TECHNISCHE UNIVERSITÄT MÜNCHEN

FAKULTÄT FÜR CHEMIE

LEHRSTUHL FÜR ANORGANISCHE UND METALLORGANISCHE CHEMIE

Positioning of Coordination-Network Materials at Surfaces

– *Case Studies Targeting Vectorial Catalysis Based on Nanometre-Sized Metal-Organic Frameworks Integrated into Microfluidic Devices, Ferroelectric Capacitors Built from Organic Perovskites, and Zr-based Metal-Organic Framework Thin Films*

ANNA LISA SEMRAU

Vollständiger Abdruck der von der Fakultät für Chemie der Technischen Universität München zur Erlangung des akademischen Grades eines

Doktors der Naturwissenschaften (Dr. rer. nat.)

genehmigten Dissertation.

Vorsitzender:	Prof. Dr. Torben Gädt
Prüfer der Dissertation:	1. Prof. Dr. Dr. h.c. Roland A. Fischer
	2. Prof. Dr. Bettina V. Lotsch
	3. Prof. Dr. Han Zuilhof

Die Dissertation wurde am 01.04.2021 bei der Technischen Universität München eingereicht und durch die Fakultät für Chemie am 04.05.2021 angenommen.

POSITIONING OF COORDINATION-NETWORK MATERIALS AT SURFACES

– Case Studies Targeting Vectorial Catalysis Based on Nanometre-Sized Metal-Organic Frameworks Integrated into Microfluidic Devices, Ferroelectric Capacitors Built from Organic Perovskites, and Zr-based Metal-Organic Framework Thin Films

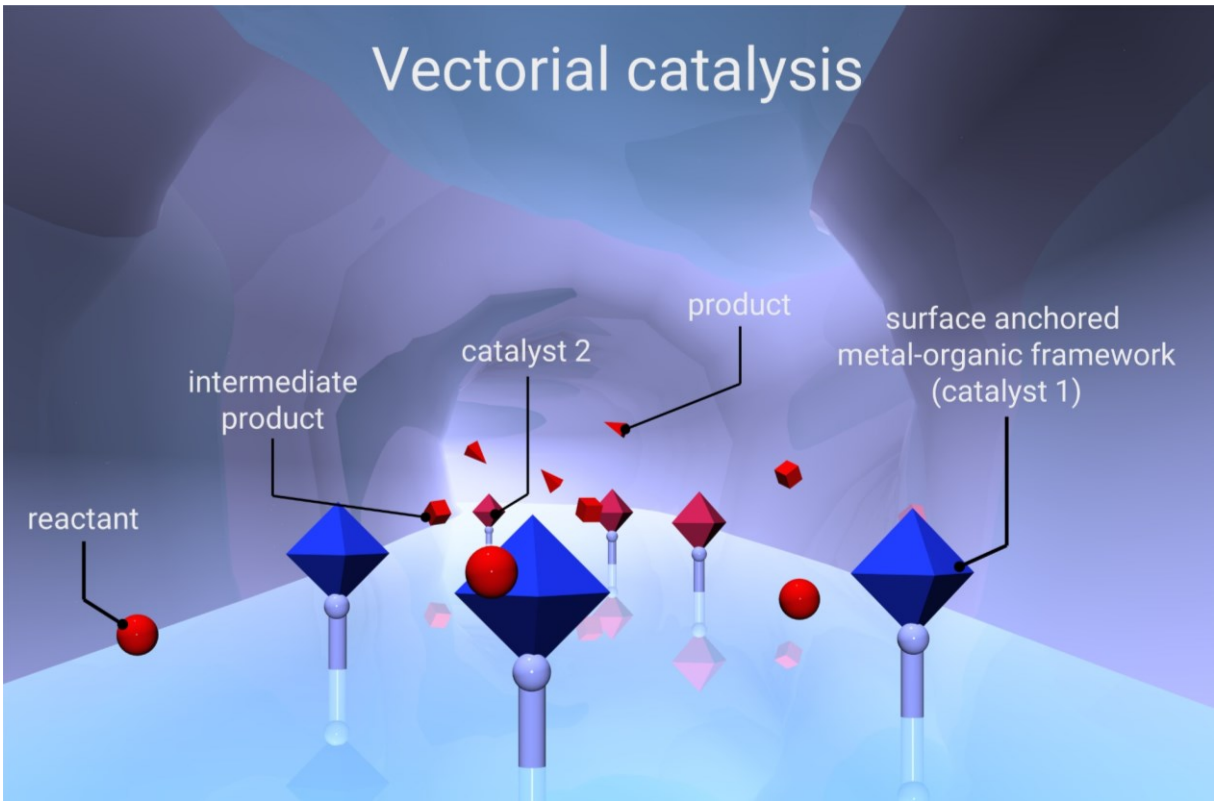

Dissertation

Anna Lisa Semrau

Die vorliegende Arbeit wurde im Zeitraum von November 2017 bis März 2021 im Fachgebiet Anorganische und Metallorganische Chemie der Technischen Universität München angefertigt.

DANKSAGUNG

Zuerst möchte ich mich bei **Prof. Dr. Dr. h.c. Roland A. Fischer** bedanken. Sie, Hr. Fischer, haben mich über lange Strecken meiner universitären Ausbildung begleitet und geprägt. Damals haben wir uns in der Allgemeinen Chemie Vorlesung in Bochum kennen gelernt. Mit ihrer ansteckenden Begeisterung für Chemie („Kemie“) und Wissenschaft haben Sie mich damals sehr beeindruckt. Meine Entwicklung über die nächsten Jahre haben Sie eng begleitet, mich gefördert und unterstützt - von Stipendienanträgen, über persönliche Ratschläge sowie im Fakultätsrat. Final habe ich mich dann nach meinem Auslandsaufenthalt in Cardiff dazu entschieden bei Ihnen (dann in München) meine Masterarbeit zu schreiben. Während meiner Master- und anschließend dann auch meiner Doktorarbeit haben mir ihr Vertrauen und die große wissenschaftliche Freiheit am Lehrstuhl sehr gut gefallen. Mit Begeisterung und vielen neuen Ideen haben Sie mich jedes Mal überrascht, wenn ich Ihnen meine neusten Ergebnisse aus dem Labor präsentiert habe. Neben ihrem Input zu meiner Forschung, möchte ich Ihnen auch insbesondere für Ihre Unterstützung bei der Bewerbung für das Kekulé Stipendium und für das Nobelpreisträgertreffen in Lindau bedanken. Auch bei der Bewerbung/Finanzierung für internationale Konferenzen haben Sie mir immer geholfen. Die bleibenden Erinnerungen aus den Niederlanden (Delft, Wageningen) Neuseeland (Auckland) und Japan (Fukuoka, Kyoto und Sapporo) bleiben mir bestimmt noch lange im Gedächtnis – insbesondere der Karaokeabend mit Pia, Miho und Ihnen. Vielen Dank für Ihr Engagement, Hr. Fischer!

Next, I would like to thank the other PIs, affectionately called the Hateful-Eight (**Gregor Kieslich, Julien Warnan, Mirza Cokoja, Alex Pöthig, Christian Gemel, Gabi Raudaschl-Sieber, Markus Drees,** and **Mr. Fischer**) (plus our newest addition **Dominik Halter**). Gregor, Julien, and Mirza in particular have helped me a lot in designing and executing projects and in writing and revising manuscripts. Without all your hard work and our secretaries **Dr. Dana Weiß** and **Martin Schellerer,** our chair would be in chaos.

Den hilfsbereiten Angestellten und Technikern an der TUM: **Katia Rodewald, Jürgen Krudermann, Maria Weindl, Ulrike Ammari, Petra Ankenbauer, Bircan Dilki, Rodica Dumitrescu** und **Tobias Kubo** möchte ich für ihre Unterstützung im Laboralltag, bei den Analysen und beim Messen der zahlreichen SEM Bilder danken.

Meinen Bachelor-/sowie Forschungs- und Master-Studenten **Sonia Mackewicz, Markus Schilling, Claire Stark, Paul Tacutu-Ertel, Patrick Schlachta, Sarah Dummert,** und insbesondere **Philip Stanley** möchte ich für ihr Engagement für meine Forschung danken. Alle haben an verschiedenen Punkten meiner Promotion mit mir zusammengearbeitet und jede/r hat mir sehr weitergeholfen.

Besonderer Dank gehört an dieser Stelle vor allem **Philip Stanley** der mit seiner unfassbaren guten Laune und seiner Energie meinen Alltag bereichert hat. Die gemeinsame Begeisterung für die Oberflächenkatalyse hat meine Forschung auf jeden Fall interessanter und facettenreicher gemacht. Mit dir waren sowohl das gemeinsame Schreiben von Publikationen wie auch das Quatschen über Bücher, Serien sowie über alles andere immer unterhaltsam. Zuletzt möchte ich mich ausdrücklich für das Korrekturlesen alle meiner Texte danken.

Suttipong Wannapaiboon, my former master thesis advisor, has been a huge help in getting started as a PhD student and was a constant source of experience and wisdom for me. Besides that, he is a great friend and colleague.

Pia Vervoorts möchte ich für die Freundschaft während der gemeinsamen Zeit am Lehrstuhl danken. Als die letzten beiden Bochumerinnen hatten wir immer viel Spaß beim gemeinsamen 'Unfug stiften'. Ob vor Ort im Labor, auf gemeinsamen Parties, den Wandertouren in den Alpen, sonntags beim gemeinsamen Kochen oder auf den vielen gemeinsamen Reisen nach Japan, die Niederlande oder Neuseeland. Auch den gemeinsamen Urlaub mit Christian, Konsen und Miguel in Neuseeland sowie die gemeinsame Kollaborationsreise nach Japan werde ich nicht vergessen.

Dem AMC Lehrstuhl – alten und jetzigen Mitgliedern – möchte ich für die positive Arbeitsatmosphäre danken. Sowohl im Labor als auch nach Feierabend habe ich die Zeit mit euch sehr genossen. Insbesondere möchte ich an dieser Stelle **Pia Vervoorts**, **Philip Stanley, Christian Schneider, Suttipong Wannapaiboon, Jana Wessing, Karina Hemmer, Jan Berger, David Mayer, Kathrin Kratzl, Kathrin Kollmannsberger, Dardan Ukaj, Miho Tsuji** und **Lena Staiger** erwähnen.

Christian Eckel und **Prof. Dr. Thomas Seitz** möchte ich für die Polarisationsmessungen des ferroelektrischen Kondensators danken. Obwohl auf dem Papier sehr einfach, stellte die Messung doch einige Herausforderungen an alle Beteiligten. Für Christians Durchhaltevermögen trotz der etlichen Rückschläge möchte ich mich bei ihm herzlich bedanken.

I would like to acknowledge **Prof. Dr. Bettina Lotsch (Max Planck Institute for Solid State Research), Dr. Bauke Albada, and Prof. Dr. Han Zuilhof (University and Research Wageningen)** for welcoming me into their groups and helping me with my research. Especially, Bettina's group, who took me in for two months during one of the CRC shutdowns. Moreover, **Bettina Lotsch** and **Han Zuilhof** agreed to be my PhD examiners for which I am very grateful.

Additionally, I would like to acknowledge my funding namely the **Chemical Industry Fund (FCI)** for a Kekulé Fellowship, **DAAD** for a 'Programm des Projektbezogenen

Personenaustauschs', which allowed me to travel to Japan, and finally the **DFG** for conference funding for the MOF 2018 in New Zealand.

Meinen Studienfreunden (**Henning, Stefan, Huong, Jan, Jonas** und **Jens**) sowie den Nicht-Chemikern **Nina** und **Marc** und den Chemie FSRs von 2013 bis 2016 möchte ich für die großartige und ereignisreiche Studienzeit in Bochum danken.

Liebe **Mama**, lieber **Papa** und **Robin**! Ich möchte mich bei euch für eure Unterstützung während meines Studiums und meiner Promotion bedanken. Ich weiß, dass es euch schwer gefallen ist mich nach Cardiff und dann nach München gehen zu lassen. Vielen Dank, dass ihr mich trotzdem bei all meinen Entscheidungen unterstützt.

Zuletzt möchte ich **Henning Jansen** für seine Liebe, seine Geduld und sein Verständnis während der Zeit dieser Arbeit danken. Du findest immer die richtige Balance dazwischen mich in unserer kostbaren gemeinsamen Zeit arbeiten zu lassen und mich von der Arbeit abzulenken. Unsere gemeinsamen Wandertouren mit der finalen fast erfolgreichen Alpenüberquerung sind das Highlight meiner Zeit in Bayern gewesen. Auf viele gemeinsame Abenteuer, wo auch immer es uns als nächstes hin verschlägt.

"Words are, in my not-so-humble opinion, our most inexhaustible source of magic. Capable of both inflicting injury and remedying it."—

Albus P. W. B. Dumbledore

in *Harry Potter and the Chamber of Secrets*

by Joanne K. Rowling

TABLE OF CONTENTS

KURZZUSAMMENFASSUNG

Die vorliegende Dissertation befasst sich mit der Herstellung von anorganisch-organischen Koordinationsnetzwerken in Form von Dünnfilmbeschichtungen auf Substraten und der Untersuchung der funktionalen Eigenschaften dieser Verbundmaterialien (Sorption, Katalyse, und Ferroelektrizität).

Die Kombination anorganischer und organischer Komponenten zu kristallinen Koordinationsnetzwerken eröffnet viele faszinierende Möglichkeiten für die Gewinnung neuer, grundlegender Erkenntnisse auf der einen und für praktische Anwendungen auf der anderen Seite. Bei Koordinationsnetzwerken unterscheidet man zwischen dichten Strukturen einerseits und nanoporösen Materialien andererseits. Letztere werden auch als metallorganische Gerüststrukturen (MOFs = Metal-Organic Frameworks) bezeichnet. Die Verankerung dieser Materialien als Beschichtungen auf Trägermaterialien, bzw. die selektive Positionierung dieser Strukturen auf Oberflächen erweitert dabei signifikant ihr Anwendungsspektrum. Beispielsweise ebnet dies den Weg für ihre Verwendung in mikroelektronischen oder mikrosystemtechnischen Bauelementen, wie z.B. neuartige Kondensatormaterialien für die Datenverarbeitungs-Elektronik oder als Bestanteile von Membranen für die Trinkwasseraufbereitung (z.B. in Entsalzungsanlagen). Motiviert von diesen Herausforderungen befasst sich diese Arbeit mit verschiedenen Strategien zur Oberflächenpositionierung von Koordinationsnetzwerken.

In einem Teil der Arbeit (Kapitel 3) untersuchen wir die selektive Positionierung von diskreten UiO-66 ($Zr_6O_4(OH)_4(bdc)_6$; bdc^{2-} = Terephthalat) und MIL-101 ($Cr_3O(OH_2)_2(OH)(bdc)_3$) Nanopartikeln mittels kovalenter Bindungen auf strukturierten Trägermaterialoberflächen (z.B. Silizium). Diese oberflächenverankerten Nano-MOFs (SA-NMOFs) wurden anschließend in zwei katalytischen Reaktionen getestet. Es zeigte sich eine Erhöhung der Umsatzfrequenzen (TOFs) um bis zu vier Größenordnungen im Vergleich zu dichten MOF-Dünnfilmen oder mikrokristallinen Pulvern (aus aggregierten Primär-Kristalliten) als Referenz. In einem zweiten Schritt wurden die SA-NMOFs in einen mikrofluidischen Aufbau integriert. Dieser basierte auf einer aus Polydimethylsiloxan (PDMS) geformten Kanalstruktur, die auf einem Trägermaterial (z.B Glass oder PDMS) aufgebracht wird. Die Vorrichtung erlaubt die sequenzielle Verankerung zweier verschiedener SA-NMOFs in zwei Abschnitten der Kanalstruktur und deren anschließender Anwendung als Katalysatoren in einer zweistufigen Katalysesequenz. Der Nachweis eines MOF-basierten zweistufigen, sogenannten vektoriellen Katalysesystems wurde damit erbracht.

Der andere Teil der Arbeit (Kapitel 2 und Kapitel 4) befasst sich mit dem Wachstum von kristallinen, phasenreinen, dichten und glatten anorganisch-organischen

Gerüststrukturdünnfilmen. Die Systeme UiO-66 und UiO-66-NH_2 ($Zr_6O_4(OH)_4$(bdc-NH_2))$_6$, bdc-NH_2^{2-} = 2-Aminobenzol-1,4-dicarboxylat) sind prototypische MOFs mit hoher Porosität und chemischer Stabilität (z.B. gegen Wasser), die neben der Katalyse auch im Bereich der Nanofiltration (Membrantechnologie) für die Wasseraufbereitung angewandt werden. Da für diese Anwendungen besonders glatte, dünne und dichte Dünnfilmbeschichtungen benötigt werden, haben wir für diese Systeme das stufenweise, Lage-für-Lage Wachstum untersucht. Die Methode ist dafür bekannt Filme hervorragender Qualität mit ausgezeichneter Kontrolle über die Schichtdicke und Kristallitorientierung zu erzeugen. Aufgrund der vielstufigen Reaktionskinetik und des komplizierten Koordinationsgleichgewichts von Metallknoten mit hoher Konnektivität (8-12) ist die Prozessoptimierung der Lage-für-Lage Abscheidung von UiO-66 und verwandten MOFs jedoch sehr anspruchsvoll. Bisher war dieses Verfahren nur für MOFs mit geringer Metallknotenkonnektivität erfolgreich, wie z.B. für Schaufelrad-basierte MOFs (Konnektivität: 4), MOF-5-Isotypen (Konnektivität: 4) oder Hofmann-MOFs (Konnektivität: 4-6). Um dennoch kristalline UiO-66 Filme (Konnektivität: 12) zu erhalten, haben wir einen sogenannten Koordinationsmodulator eingesetzt. Nach Optimierung auch der Substratvorbehandlung wurden schließlich rissfreie, glatte UiO-66-NH_2-Dünnschichten mit der erwarteten, sehr hohen spezifischen Sorptionskapazität erhalten.

Gegenüber UiO-66 handelt es sich bei [HMDABCO](NH_4)I_3 ([HMDABCO^{2+}] = 1-Methyl-1,4-diazabicyclo[2.2.2]octan-1,4-diium) um ein nicht auf Metallionen-koordination basierendes Koordinationsnetzwerk. Stattdessen besteht es aus rein organischen Ionen, welche ein dichtes Koordinationswerk bilden. Aufgrund der Knappheit der meisten Metalle stellen rein organische Koordinationsnetzwerke eine kostengünstige und zukunftssichere Lösung dar. Seine ferroelektrische und optischen Eigenschaften sowie elektrokalorische Stärke machen HMDABCO](NH_4)I_3 als neuartiges Material für verschieden Anwendungen (z.B. in der Mikroelektronik) interessant. Für die Herstellung von Bauelementen, z.B. von ferroelektrischen Kondensatoren, müssen jedoch wieder kristalline, dichte und glatte Dünnschichten erzeugt werden. Deshalb haben wir für die Abscheidung von [HMDABCO](NH_4)I_3 verschiedene Fabrikationstechniken wie die Spray-, Tropf- und Tauchbeschichtung untersucht. Durch Variation der Menge der Tropfenbeschichtungslösung konnten wir zudem die Dünnschichtdicke kontrollieren und die Kristallorientierung bei der Verwendung verschiedener funktionalisierter Träger-materialien beeinflussen. Zwar gelang es uns noch nicht einen funktionierenden ferroelekrischen Kondensator herzustellen, jedoch könnten die Ergebnisse den Weg für [HMDABCO](NH_4)I_3 und verwandte Materialien dorthin ebnen.

Abstract

This dissertation deals with fabricating inorganic-organic coordination network thin film coatings on substrates and investigating their functional properties in the areas of sorption, catalysis, and ferroelectricity.

Combining inorganic and organic building blocks to form crystalline coordination networks paves the way for many fascinating possibilities, ranging from new, fundamental science to practical applications. Coordination networks can be partitioned into dense materials on the one hand and nanoporous structures on the other, with the latter, also referred to as metal-organic frameworks (MOFs). Depositing these structures as coatings on support materials, or selectively positioning these materials on surfaces, significantly expands their application range. For example, this includes microelectronics or microsystem components, such as novel capacitor materials for data processing electronics or membrane components for drinking water treatment (e.g. in desalination plants). Inspired and motivated by these challenges, this thesis addresses different strategies for surface positioning of coordination networks.

One part of this thesis (chapter 3), investigates selective positioning of UiO-66 ($Zr_6O_4(OH)_4(bdc)_6$; bdc^{2-} = terephthalate) and MIL-101 ($Cr_3O(OH_2)_2(OH)(bdc)_3$) discrete nanoparticles by utilizing covalent bonds on structured substrate surfaces (e.g. silicon). Subsequently, these surface-anchored nano-MOFs (SA-NMOFs) were tested in two Lewis acid-catalyzed reactions, where they illustrated a remarkably high catalytic activity, increasing turnover frequencies (TOFs) by up to four orders of magnitude in comparison to dense MOF thin films and microcrystalline powders (from aggregated primary crystallites). Thereafter, the SA-NMOFs were integrated into a microfluidic device, based on a channel structure formed from polydimethylsiloxane (PDMS) deposited on glass or PDMS substrates. In this device two different SA-NMOFs were selectively anchored in two separate sections of the channel structure and subsequently applied as catalysts in a two-step catalytic sequence, yielding a proof-of-concept for a MOF-based vectorial catalytic system.

The other part of this thesis (chapter 2 /4) deals with the growth of crystalline, phase-pure, dense, and smooth inorganic-organic framework structure thin films. The systems UiO-66 and UiO-66-NH_2 ($Zr_6O_4(OH)_4(bdc\text{-}NH_2)_6$, bdc NH_2^{2-} = 2-aminobenzene-1,4-dicarboxylate) are prototypical MOFs with high porosity and chemical stability (water stability), which can be applied as catalysts or in the area of nanofiltration (membrane technology) for water treatment. As these applications require particularly smooth, thin, and dense thin film coatings, we investigated stepwise, layer-by-layer growth for these systems. This method is known to produce pristine films of high quality with excellent control over film thickness and crystallographic orientation. However, due to the multi-step reaction kinetics and the

complex coordination equilibrium of metal nodes with high connectivity (8-12), process optimization of layer-by-layer deposition of UiO-66 and related MOFs is very challenging. Previously, this process was only successful for MOFs with a low metal node connectivity, such as paddle-wheel-based MOFs (connectivity: 4), MOF-5 isotypes (connectivity: 4), or Hofmann MOFs (connectivity: 4-6). In order to obtain crystalline UiO-66 films (connectivity: 12) despite these challenges, we used a so-called coordination modulator. After optimization of substrate pre-treatment, crack-free, smooth UiO-66-NH_2 thin films with the expected high specific sorption capacity were obtained.

Compared to UiO-66, [HMDABCO]$(NH_4)I_3$ ([HMDABCO^{2+}] = 1 methyl-1,4-diazabicyclo[2.2.2]octane-1,4-diium) is a dense coordination network that is not based on metal ion coordination. In contrast, it consists of organic ions in its entirety. Due to the scarcity of most metals, purely organic coordination networks offer a cost-efficient and future-proof solution. Owing to its ferroelectricity, electrocaloric strength and non-linear optical activity, HMDABCO]$(NH_4)I_3$ is an interesting new material for many applications (e.g. in microelectronic devices). However, for the production of device components, e.g. ferroelectric capacitors, crystalline, dense, and smooth thin films are required. Different fabrication techniques such as spray, drop, and dip coating were investigated for the fabrication of [HMDABCO]$(NH_4)I_3$ thin films. By varying the amount of drop coating solution, we were additionally able to control the thin film thickness and influence the crystal orientation when using different functionalized support materials. Although we have not yet succeeded in producing a functioning ferroelectric capacitor, we are on route to achieve this goal in the future.

LIST OF ABBREVIATIONS

°	Degree
°C	Degree Celsius
2-mim	2-Methyl Imidazole
ADA	12-Azido-dodecane-1-amine
COC	Cyclic Olefin Copolymers
COF	Covalent Organic Framework
CO_2RR	Carbon Dioxide Reduction Reaction
CSA	Controlled SBU Approach
3D	Three Dimensional
AES	Auger Electron Microscopy
AFM	Atomic Force Microscopy
ALD	Atomic Layer Deposition
APTES	(3-Aminopropyl)triethoxysilane
bdc^{2-}	Benzene-1,4-dicarboxylate
$Bdc(\text{-}NH_2^{2-})$	Benzene-1,4-dicarboxylate and/or 2-Amino-benzene-1,4-dicarboxylate
$bdc\text{-}NH_2^{2-}$	2-Amino-benzene-1,4-dicarboxylate
BA	Benzaldehyde
BACN	2-Benzylidene malononitrile
BADMA	Benzaldehyde dimethylacetal
BAOH	Benzyl alcohol
BAOTMSCN	2-Phenyl-2 ((trimethylsilyl)oxy)acetonitrile
BET	Brunauer-Emmett-Teller
bipy	4,4′-Bipyridine
$BME\text{-}bdc^{2-}$	2,5-Bis(2-methoxyethoxy)-1,4-benzene dicarboxylate
$bpdc^{2-}$	Biphenyl-4,4′-dicarboxylate
btc^{3-}	Benzene-1,3,5-tricarboxylate
CALB	Candida Antarctica Lipase B
CCDC	The Cambridge Crystallographic Data Centre
CM	Coordination Modulation
COF	Covalent Organic Framework
CSD	Crystalline Domaine Sizes
CuAAC	Copper-Catalyzed Azide-Alkyne Cycloaddition
CVD	Chemical Vapour Deposition
DABCO/dabco	1,4-Diazabicyclo[2.2.2]octane
DAD	1,12-Diamino dodecane
DCM	Dichloromethane
DIC	*N,N'*-Diisopropyl carbodiimide
DLS	Dynamic Light Scattering
DMF	*N,N-D*imethylformamide
DMSO	Dimethyl sulfoxide
EDX	Energy-Dispersive X-ray Spectroscopy
E_F	Coercive Field
EHU-30	$[Zr_6O_4(OH)_4(bdc)_6]_n$
equiv.	Equivalents
ESI	Electrospray ionization

EtOH	Ethanol
EXAFS	Extended X-ray Absorption Fine Structure
F_4bdc^{2-}	Tetrafluorobenzene-1,4-dicarboxylate
fcu	Face-Centred Cubic
fu-ip	Functionalized Isophthalate
FTO	Fluorine-Doped Tin Oxide
FWHM	Full Width at Half Maximum
GC	Gas Chromatography
GIXRD	Grazing Incidence X-ray Diffraction
GOX	Glucose Oxidase
H_2bdc	Benzene-1,4-dicarboxylic acid
$H_2bdc(-NH_2)$	Benzene-1,4-dicarboxylic acid and/or 2-Amino-1,4-benzenedicarboxylic acid
$H_2bdc-NH_2$	2-Amino-1,4-benzenedicarboxylic acid
$H_2dmcapz$	3,5-dimethyl-4-carboxypyrazole
$H_2mipcapz$	3-methyl-5-isopropyl-4-carboxypyrazole
HIOP	Hybrid Inorganic Organic Perovskites
HER	Hydrogen Evolution Reaction
HKUST-1	$[Cu_3btc_2]_n$
$HMDABCO^{2+}$	N-Methyl-1,4-diazabicyclo[2.2.2] octane-1,4-diium
$HMDABCO(NH_4)I_3$	N-Methyl-1,4-diazabicyclo[2.2.2] octane-1,4-diium ammonium iodide
HOMO	Highest Occupied Molecular Orbital
HRP	Horseradish Peroxidase
ICP	Inductively Coupled Plasma
IR	Infrared
IR-ATR	Attenuated Total Reflectance Infrared Spectroscopy
IRMOFs	Isoreticular MOFs
IRRAS	Infrared Reflection Absorption Spectroscopy
ITO	Indium Tin Oxide
IUPAC	International Union of Applied Chemistry
L	Layer/Deposition Cycles
LbL	Layer-by-Layer
LED	Light-Emitting Diode
LEI	Lower Secondary Electron Detector
LPE	Liquid-Phase Epitaxy
LUMO	Lowest Unoccupied Molecular Orbital
MAN	Malononitrile
McOH	Methacrylic acid
MeCN	Acetonitrile
MeOH	Methanol
MIL	Matérial Institut Lavoisier
MIL-101 (Cr)	$Cr_3O(OH)(OH_2)_2(bdc)_3$
MIP	Molecular Imprinted Polymers
MLD	Molecular Layer Deposition
MMM	Mixed MOF Membranes
MN	Mandelonitrile
MOC	Metal Organic Clusters
MOF	Metal-Organic Framework
MOF-5	$[Zn_4O(bdc)_3(DMF)_x]_n$
MS	Mass Spectrometry

MS	Metal Source
ndc^{2-}	1,4-Naphtalene dicarboxylate
NHS	*N*-hydroxysuccinimide
NMOF	Nanometer-Sized Metal-Organic Framework
NMR	Nuclear Magnetic Resonance
OAc^{-}	Acetate
OER	Oxygen Evolution Reaction
OFET	Organic Field-Effect Transistor
OMc^{-}	Methacrylate
ORR	Oxygen Reduction Reaction
PCO	Propylene Carbonate
pdc^{2-}	Pyridine-2,6-dicarboxylate
PDMS	Polydimethylsiloxane
PET	Polyethylene Terephthalate
PIZA	Porphyrinic Illinois Zeolite Analog
ppm	Part Per Million
P_R	Remanent Polarisation
P_S	Spontaneous Polarisation
PSD	Pore Size Distribution
PSE	Post Synthetic Encapsulation
PSM	Post Synthetic Modification
PS_PIAS	$Polystyrene_{40}$-b-poly(lisocyanoalanine (2-thiophen-3-ylethyl)amide)$_{50}$
PXRD	Powder X-ray Diffraction
pz	Pyrazine
QCM	Quartz Crystal Microbalance
R	Rate
rpm	Rounds Per Minute
RT	Room Temperature
SAM	Self-Assembling Monolayer
SA-NMOF	Surface-Anchored NMOFs
SAW	Surface Acoustic Wave
SBU	Secondary Building Unit
SCXRD	Single Crystal X-ray Diffraction
SEI	Upper Secondary Electron In-lens Detector
SEM	Scanning Electron Microscopy
SURMOF	Surface-Mounted Metal-Organic Framework
t	Time
T	Temperature
tBITC	*tert*-Butyl isothiocyanate
tBuOOH	tert-Butyl hydroperoxide
TCNQ	7,7,8,8-Tetracyanoquinodimethane
TEMPO	2,2,6,6-Tetramethylpiperidinyloxyl
TFA	Trifluoracetic acid
TGA	Thermal Gravimetric Analysis
THF	Tetrahydrofuran
TMSCN	Trimethylsilyl cyanide
TOF	Turnover Frequency
TON	Turnover Number
TTP^{2-}	5,15-bis-(3,4,5-trimethoxyphenyl)-10,20-bis- (4-carboxyphenyl) porphyrinato zinc(II)

UiO	Universitet i Oslo
UiO-66 (Zr)	$[Zr_6O_4(OH)_4(bdc)_6]_n$
UiO-66(-NH_2)	UiO-66 (Zr) and/or UiO-66-NH_2(Zr)
UiO-66-NH_2(Zr)	$[Zr_6O_4(OH)_4(bdc\text{-}NH_2)_6]_n$
UV	Ultraviolet
VAC	Vapour Assisted Conversion
VOC	Volatile Organic Compounds
WD	Working Distance (distance between SEM final aperture in the objective lens and specimen)
XPS	X-ray Photoelectron Spectroscopy
ZIF	Zeolitic Imidazolate Framework
ZIF-8	$[Zn(2\text{-}mim)_2]_n$

1. INTRODUCTION

1.1. Functional Composite Materials

Today the world faces many challenges such as global warming,[1] biodiversity mass extinction[1], or the corona pandemic.[1] Many of these global challenges can be split up into smaller problems and challenges, e.g. inefficient CO_2 capture and recovery technology, or the need for an effective test system for infection monitoring. Additionally, new problems can be caused by these challenges such as dwindling drinking water resources[1] or the need for energy-efficient electronics.[2] The development of functional materials can help to address challenges by offering smarter, cheaper, and more sustainable solutions. Particularly, the combination of different functional materials forming a functional composite material can offer new perspectives.

Coordination networks offer a great platform for the design of functional materials due to the variety of possible combinations and their broad range of exciting properties such as (nano)porosity, catalytic activity, or ferroelectricity. By immobilizing and selectively positioning these coordination polymers on or coating them onto substrate surfaces, new functional composite materials can be created. These can allow for material-device-integration e.g in microfluidic devices, capacitors, or membranes. An important step is to analyze how surface material interactions can influence or determining the composite properties. Understanding structure-property relationships can pave the way for the targeted design of new, more suitable composite materials, could reduce the cost of research, and improve performance optimization as materials could be designed more effectively.

Therefore, this thesis focuses on the development of functional composite materials by employing different coating methods for the positioning of coordination networks. The fabricated functional composites were characterized and investigated. Overall, we targeted the areas of (vectorial) catalysis, nanofiltration/desalination, and capacitor fabrication.

1.2. Coordination Networks

The field of coordination frameworks has evolved into one of the fastest-growing research areas in materials chemistry. Often divided into the class of nanoporous coordination polymers, known as metal-organic frameworks (MOFs) and dense inorganic-organic frameworks, the virtually unlimited range of organic building units presents a plethora of opportunities for creating technologically relevant properties. In science, coordination networks offer a great platform for studying structure-property relationships.

1.2.1. Metal-Organic Frameworks

The term metal-organic frameworks (MOF) – describing nanoporous metal-organic coordination polymers – first emerged in the late 1990s and was coined by O. Yaghi. At that time, a couple of landmark publications initially described MOFs with a relatively high thermal (330 °C[3] - 450°C[4,5]) and chemical stability and extraordinarily high porosity.[6,7] Since then, the research in MOFs intensified considerably, a trend that culminated in more than 68,000 publications available on the topic today.[8] The research on MOFs is rooted in the chemistry of metal-organic coordination polymers, which were initially discovered and investigated by K. A. Hofmann (1870 - 1940).

Three MOF generations. Conceptually, Yaghi's MOFs and Hofmann's metal-organic coordination polymers differ i.a. in their structural integrity after removal of the adsorbed solvents. While Yaghi's MOFs are rigid after the removal of absorbed solvents, Hofmann's coordination polymers collapse upon the removal of the adsorbed guest molecules (*e.g.* solvent molecules). The confusion about the term 'metal-organic framework' was resolved by the International Union of Pure and Applied Chemistry (IUPAC) in 2013[9] and a landmark publication by S. Kitagawa.[10] The IUPAC defines a MOF as "a coordination network with organic ligands containing potential voids"[9], further specified by Kitagawa's publication which defines MOFs according to their response towards guest molecule removal from their pores (see Figure 1).

In detail, three types (generations) of MOFs are distinguished. The 1st generation collapses upon the removal of guest molecules in the pores, whereas the 2nd generation retains their structure after guest removal. The iconic MOFs HKUST-1 (Cu_3btc_2, HKUST = Hong Kong University of Science and Technology, btc^{3-} = benzene-1,3,5-tricarboxylate) and MOF-5 ($[Zn_4O(bdc)_3(DMF)_x]$, DMF= dimethylformamide, bdc^{2-} = benzene-1,4-dicarboxylate) published by Williams *et al*.[7] and Yaghi *et al*.[6] in the late 1990s can be assigned to this category.

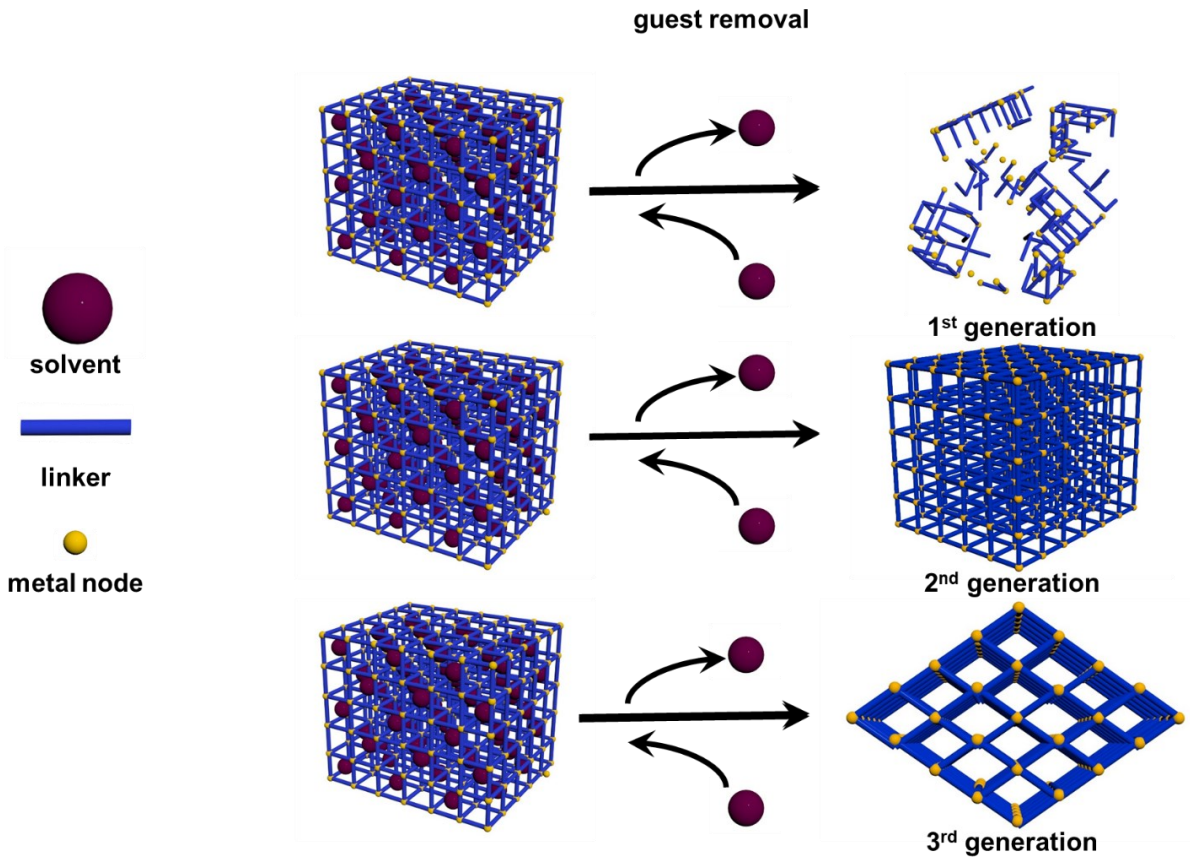

Figure 1: The metal-organic frameworks are constructed from metal nodes and organic linkers resulting in a crystalline 3D scaffold. Upon the removal of the guest (solvent) molecules from the scaffold the 1st generation of MOFs collapses, while the 2nd generation retains the structure, and the 3rd generation undergoes a phase transition. This scheme was created with 3ds Max.

As part of the intensified research after the emergence of the 2nd generation of MOFs, the 3rd generation of MOFs was discovered a few years later. Also known as soft porous crystals, this generation responds to external physical or chemical stimuli by a reversible phase transition.[10] Further research, also resulted in covalent organic frameworks (COFs), which are metal-free, crystalline, porous, organic polymers with permanent porosity and ordered structures. In contrast to MOFs, which are dominated by coordinative bonds, COFs are polymers with covalent bonds.

Building blocks. In general, the structural principles of MOF assembly can be summed up as the connection of metal ions or clusters, sometimes referred to as inorganic nodes, linked by polytopic organic ligands, often describes as organic linkers. In this context, the term secondary building unit (SBU) is often mentioned, which refers to the metal node including the coordinating functional groups. The topology of the resulting framework is a combination of the topologies and connectivities of the linker and SBUs. Metal ions or clusters employed in MOF assembly are typically first-row transition metal ions such as Zn^{2+}, Cu^{2+}, or Ni^{2+} but also second and third-row transition metals (Zr^{4+}, $Rh^{2+/3+}$, $Ru^{2+/3+}$) or lanthanide-based MOFs[11] are known. Although stable bonds should allow the formation of stable crystalline 3D polymers, a coordination

bond formation equilibrium is of great importance. This enables a reversible bond formation and breakage equilibrium, which allows for the replacement of incorrectly attached building blocks. The MOFs crystallization should be regarded as a highly complex topic as kinetic, thermodynamic, and entropic factors play a role. Different reaction conditions and additives have been introduced to the MOF synthesis to manipulate the kinetics of MOF formation. Typically, MOF syntheses are carried out in high boiling organic solvents like DMF at high temperatures and under solvothermal conditions. For the modulation of the bond formation kinetics, accelerating bases or decelerating monotopic carboxylic acids can be added. As the modulators in small quantities often remain part of the assembled MOF, this gave rise to research into defect-engineered MOFs, which are discussed in chapter 3.1.1.

1.2.1.1. Properties and Commercial Applications of MOFs

Investigating properties and applications of MOFs started due to their extraordinarily large surface area offering possible applications in gas storage, gas separation, as carriers for bioactive molecules and heterogeneous catalysis. In this field, MOFs compete with other nano- and mesoporous materials like zeolites and porous carbon. While MOFs sometimes lack sufficient thermal stability e.g. for industrial heterogeneous catalysis, they can be promising precursors for MOF-derived catalytically active metal oxides or hydroxides.[12,13] Due to the high investment costs for the application of MOFs on an industrial scale, they are still unattractive for most large-scale companies. Smaller companies like NUMat Technology manufacture MOF-filled gas cylinders for the low-pressure storage of toxic gases for the semiconductor industry.[14] Another industrial application was started in 2014 by a start-up named MOFworx. They invented a novel packaging that prevents fruits and vegetables from ripening. Here, a MOF is employed to store and slowly release 1-methyl cyclopropene, a synthetic plant growth regulator that stifles ripening. Therefore, enabling longer delivery times and reducing the loss of crop from harvest to consumer.[15] Another interesting application would be water recovery in arid climates. As reported in Science, Yaghi and other researchers developed a MOF-based water-harvesting machine that can recover water in arid climates.[16–18] As water shortage is a global socio-economic challenge, MOF-based materials could help address these issues. While the high price associated with MOFs limits their attractiveness for large-scale applications, this is not an issue for research.

In science, MOFs offer a great platform for research as the design of linkers and nodes offers a broad range of possible topologies and structures. This enables the recognition of structure-property relationships and facilitates the transfer to other structures and material classes.

1.2.2. Coordination Networks as Coatings

The fabrication of coordination networks as thin films offers a multitude of opportunities as this allows for their integration into devices and broadens their application spectrum. Additionally, the fabrication of high-quality thin films can improve material properties like electrical conductivity or filtration performance e.g. by the reduction of grain boundaries.

In literature, multiple methods were reported to create coordination networks as coatings onto different kinds of substrates. The different techniques can be divided into two major categories, the bottom-up or top-down approaches. Top-down coatings can be achieved by immobilizing pre-synthesized crystals onto substrate surfaces, while bottom-up coatings can be produced by the crystallization of the coordination networks from the (molecular) precursors directly on the surface (see Figure 2).

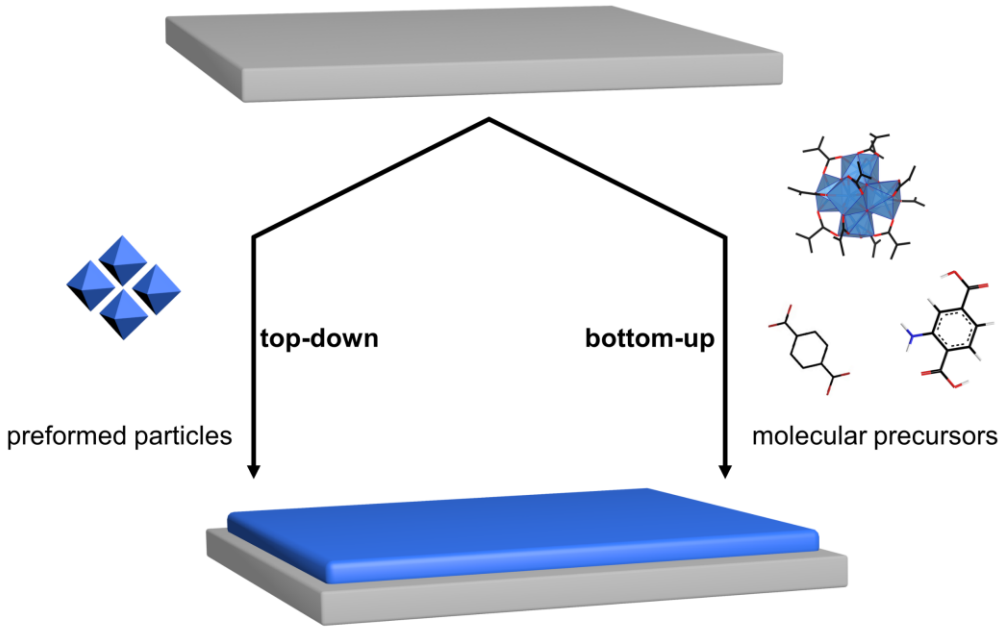

Figure 2: Schematic illustration of the bottom-up and top-down thin film fabrication approaches. Bottom-up growth is defined here as any protocol which grows MOF crystals on the surface, whereas top-down patterning is defined as the deposition of pre-existing MOF crystals.

Both strategies were employed in this thesis, and the details and reasoning are provided in the associated chapters.

2. FABRICATION OF ZR-BASED MOF THIN FILMS

Preamble. This introduction chapter is based on an invited feature article in Langmuir:

Anna Lisa Semrau,† Zhenyu Zhou,† Soumya Mukherjee, Min Tu, Weijin Li, Roland A. Fischer, Langmuir **2021**, *37*, 6847-6863. (Surface-mounted metal-organic frameworks: past, present, and future perspectives).

The structure of the invited article was designed by R. A. Fischer and W. Li. A. L. Semrau sorted the literature and wrote and draft for the introduction and the chronology of key developments as well as designing the figures for the manuscript (besides the last figure). The future perspective's part was drafted together with Z. Zhou, who additionally wrote the preparation of SURMOFs as well as the state-of-the-art SURMOFs and current benchmarks. M. Tu, S. Mukherjee, and W. Li revised the manuscript. Additionally, S. Mukherjee designed the last figure in the publication, which is not printed in this thesis.

2.1. Introduction to Layer-by-Layer Liquid Phase Epitaxy

MOF thin films: top-down vs. bottom-up techniques. As mentioned in the introduction, top-down or bottom-up methods can be used to manufacture coordination network-based thin films. In the case of metal-organic frameworks, top-down thin film coatings are mainly dominated by relatively weak physisorption interactions, which oft-encounters two limitations: high surface roughness and low surface coverage. Additionally, the processability of MOFs is reduced by the low solubility of MOF in solvents, limiting the likelihood to produce MOF thin films by top-down methods. In contrast to this, chemisorption interactions dominate the bottom-up route coating, inducing stronger adhesion forces between MOF coating and surface. Therefore, bottom-up routes have been the main approach to fabricate MOF coatings. During the last years, several techniques for the bottom-up fabrication of MOF thin films have been reported, such as the direct growth/solvothermal deposition,[19] vapour-assisted conversion,[20] gas-phase depositions (including atomic layer deposition or molecular layer deposition and chemical vapour deposition),[21,22] electrochemical deposition,[23] and liquid-phase epitaxy layer-by-layer (LPE-LbL).[24] The scope of applications is determined by each technique's advantages and disadvantages.

Bottom-up techniques: direct growth. The so-called ''direct growth'' technique is the simplest and most straightforward method to obtain bottom-up coatings. Therefore, a substrate is immersed into a mother solution (consisting of metal precursor and

organic linker) and the solvothermal reaction is performed. Ideally yielding a MOF thin film attached to the substrate surface. However, this strategy lacks control over the thin film thickness and usually inhomogeneous thin films are obtained.

Gas-phase-based techniques. Gas-phase-based techniques such as atomic layer deposition (ALD), molecular layer deposition (MLD), and chemical vapour deposition (CVD) usually yield highly homogenous thin films. All these techniques utilize precursor molecules that are deposited from the gas phase onto the substrate, forming MOF thin films. Compatible with conventional semiconductor fabrication processes these techniques can facilitate the integration into electronic devices. Due to the process conditions, the precursors require volatile yet stable precursors and a high process temperature. This limits the scope of substrates (e.g. polymers) and linkers, as thermally unstable linkers or linkers with a low vapour pressure are challenging.[25–27]

Vapour-assisted conversion. Vapour-assisted conversion (VAC, see Figure 3) developed by Bein and co-workers is another bottom-up technique. Initially targeting covalent organic thin films, this method was later translated to MOF thin films. [20,28] Experimentally, a droplet of a solution containing the metal precursor and organic linker is staged on a substrate, which is placed on a platform in a closed vessel accompanied by a volatile solvent/vapour source. By heating the sealed system, a MOF thin film is formed on top of the substrate. While VAC lacks a precise thickness control and usually requires a dense, non-macroporous solid support, it provides a reasonable control over the thin-film homogeneity.

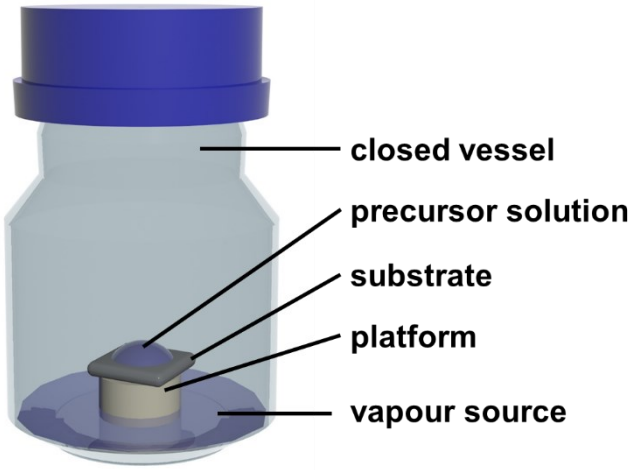

Figure 3: Experimental setup for the vapour assisted conversion (VAC). Therefore, a solid substrate is placed on a platform in a Schott bottle. The precursor solution is then placed on top of the substrate. The bottle is partly filled with a vapour source to assist the formation of a MOF thin-film.

Liquid-phase epitaxy. Liquid-phase epitaxy (LPE) describes crystal growth or material deposition from the liquid phase, in which new crystalline layers are formed with a well-defined orientation concerning the crystalline substrate. This term implies that the deposited layer has the same crystalline orientation as the substrate or that the orientation of the substrate has a direct influence on the orientation of the growing thin film.[29] In the area of MOFs, LPE is often synonymously used for a layer-by-layer deposition. In this case, the orientation e.g. of the silicon wafer does not influence the

orientation of the SURMOF thin film. However, the functionalization of a substrate with a self-assembling monolayer (SAM, see chapter 3.1.2) can trigger the growth of a thin film with a preferred orientation.[30,31] Due to the different use of this term in thin-film physics and the MOF thin-film community, respectively, it can lead to misunderstandings. The LbL-LPE operates at relatively low temperatures and is, therefore, an energy-efficient, solution-based technique for thin-film fabrication. Experimentally, native (fluorine-doped tin oxide (FTO), indium tin oxide (ITO), silica, or alumina) or functionalized (e.g., formed via self-assembly) surfaces are alternatively immersed in a metal precursor and organic linker solution (Figure 4).[32] In between, the substrate is rinsed with solvent to remove unreacted molecules from the surface. The LBL-LPE process usually yields crystalline, smooth, and oriented MOF thin films, which are classified as surface-mounted MOFs (SURMOFs).[33] In order to obtain these high-quality SURMOF thin films, a systematic optimization of the thin-film deposition parameters is required (e.g. targeted MOF precursors, temperature, metal precursor concentration, linker concentration, solvent, etc.).

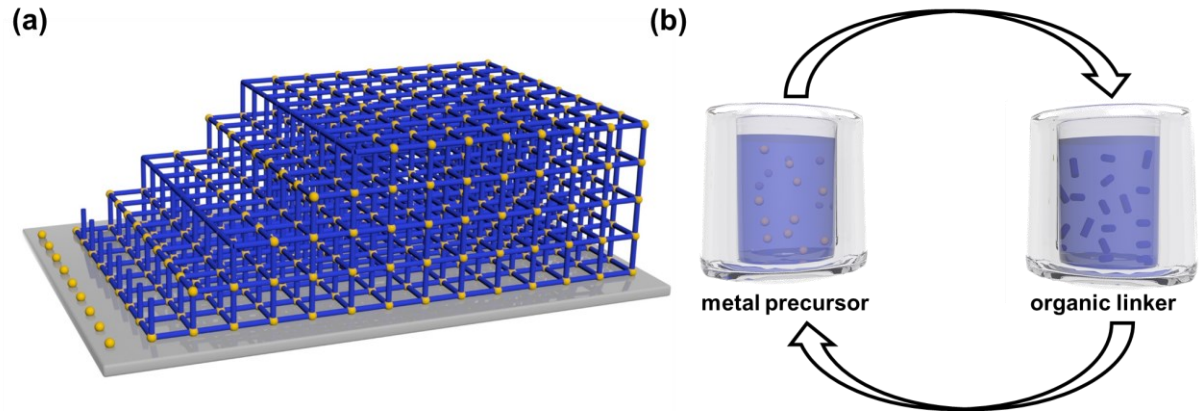

Figure 4: Schematic representation of the layer-by-layer liquid phase epitaxy (LPE) process yielding a SURMOF (a). The layered structure of the SURMOF (a) is achieved by the alternative immersion of the substrate in a metal precursor and an organic linker solution (b). This scheme was created with 3ds max.

Advantages. LbL-LPE presents key advantages over other bottom-up techniques. These include i) the precise control of the deposited thin film thickness, which can be targeted by adjusting the number of deposition cycles. By utilizing quartz crystal microbalances the deposition can be tracked in situ and conclusions about the underlying growth mechanisms can be drawn. SURMOFs are especially known for their low roughness.[32] ii) another key advantage is the direct control over the crystallographic orientation, which can be induced by substrate functionalization.[30,34] iii) Furthermore, LbL-LPE is associated with a low process temperature, which allows expanding the range to substrates like polymers which are unstable at high temperatures.[35] iv) Due to the repetitiveness of the SURMOF growth process, LbL-LPE is compatible with the instrumentation of automatic deposition, thereby allowing for

easy processability and high reproducibility.[36] v) The specific manufacturing process offers precise control over the deposited structure, which in turn can enable a) strategic control over the level of interpenetration,[37] and/or b) the formation of otherwise inaccessible structures.[38]

Deriving from the many advantages, LbL-LPE has been proven as a valuable tool to grow high-quality MOF thin films, with a plethora of applications. In this chapter, we start with a chronological survey, whereby we provide a detailed account of the major developments of SURMOFs, relevant to the optimization of the process parameters. Then we follow up on the recent trends, by summarizing the SURMOFs' performances in the context of different applications. Finally, summing up this chapter with a perspective on the future of SURMOFs, particularly in terms of their preparation, applications, and challenges.

2.2. Chronology of Key Discoveries

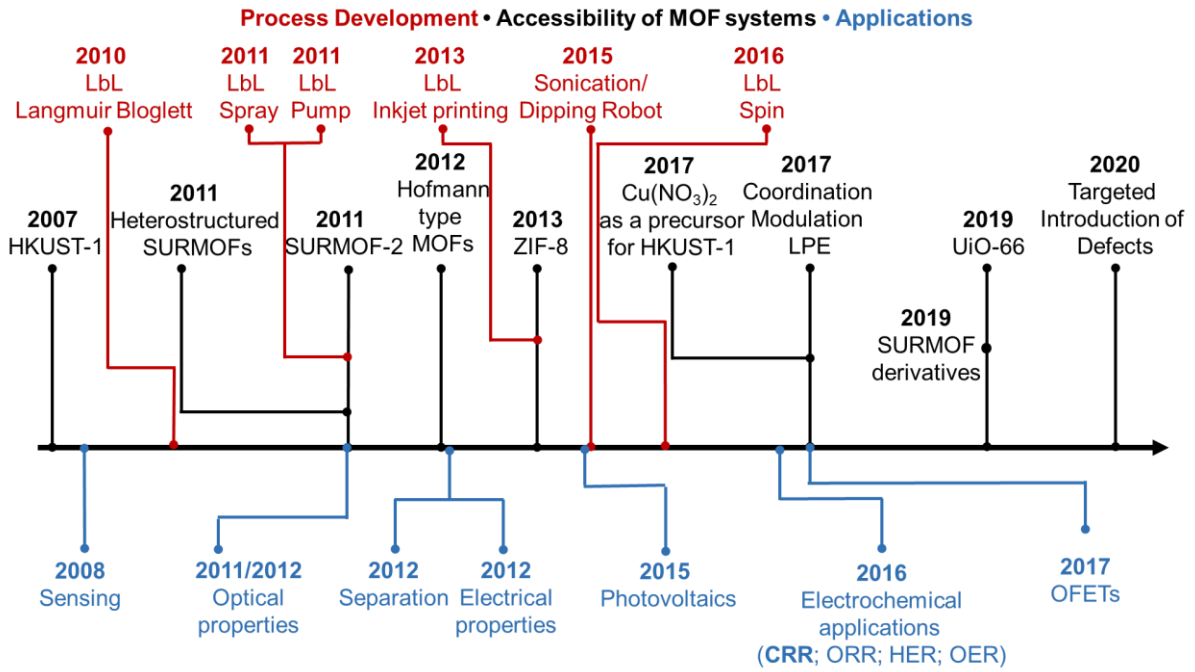

Figure 5: Chronological order of the key discoveries leading to the development of SURMOFs, consisting of technological development (red), new structure development (black), and the exploration of new applications (blue).

In this section, we discuss the key findings, that in our opinion, had the most profound impacts on the development of SURMOFs since their discovery in 2007. These include process development and advancement, as well as the ease of access to new, tailor-made MOF systems, and thereby unlock several applications.

Technological development. Initially, we focus on the chronological development of the process technologies of LbL-LPE. 2007 the investigation of the LPE process started with the invention of a manual LbL dipping process. Later this was replaced by automated processes and different process variants. The first step towards the automatization of the LbL-LPE process was achieved by the introduction of an automated pump system in 2011.[36] Therefore, the substrate is placed in a temperature-controlled double-wall cell, which is automatically filled with either the metal precursor, an organic linker solution, or the solvent in an alternative matter. The automatization of the process led in turn to easier processability and reproducibility of the resulting SURMOF thin films. Similar advantages were observed for an automated dipping robot developed in 2015.[39] The robot dips the substrate automatically in various solutions following the required SURMOF protocol. While both techniques have advantages, they are still time-consuming, require large amounts of solvents and chemicals. Minimizing these disadvantages, while embracing the advantages of automated processes, the automated LbL spray coating (2011),[40] inkjet printing (2013),[41] and spin coating (2016) were developed. Experimentally, the different solutions are computer-programmed to alternatively get spray-coated, or printed, or spin-coated onto the substrate. Moreover, manual LbL Langmuir Blodgett was developed in 2010.[42] It enabled the fabrication of so far inaccessible crystalline MOF nanofilms. However, due to the incompatibility with automation and the requirement of a specific Langmuir Blodgett setup, its potential for SURMOF fabrication is weakened. Another process advancement was introduced by Gu *et al.* alongside the development of a dip-coating robot in 2015. They observed a reduction of the defect content, enhanced homogeneity, and reduced surface roughness of $[Cu_3(btc)_2]$, HKUST-1 thin films.

Accessibility of different SURMOFs. Staring in 2007, the landmark publication of C. Wöll, R. A. Fischer, and co-workers seminally reported the LbL growth of HKUST-1 (Figure 5).[32] Compared with directly grown HKUST-1 thin films, the SURMOFs exhibited enhanced crystallinity, uniform coverage, and low surface roughness. Based on these pioneering results an intense research effort was fostered which lead to the systematic expansion of SURMOF systems, broadening their spectrum of applications. One major step in developing LPE-LbL was the utilization of molecular secondary building units (SBUs)[43,44] to improve the nucleation of the MOF particles. Due to the occasional facile formation of the metal node, using mononuclear metal salts at times afforded amorphous or non-existent coatings. For example, instead of other mononuclear metal salts e.g. $Cu(NO_3)_2$ (copper nitrate), the paddlewheel-containing $Cu_2(OAc)_4$ (copper acetate), was required to deposit HKUST-1, which is known as the controlled SBU (second building unit) approach (CSA). For the formation of HKUST-1, the acetate ligands of $Cu_2(OAc)_4$ need to be exchanged with btc^{3-} resulting in the

formation of a 3D scaffold. This approach enabled the fabrication of other metal-carboxylate SURMOFs, namely MOF-5,[45] $Zn_4O(bdc)_3$ and its isoreticular variants (*e.g.* Zn_4OL_3 (L^{2-} = 3,5-dialkyl-4-carboxypyrazolate).[46]

Pursuing further process optimization, however, Weckhuysen and co-workers reveal that $Cu(NO_3)_2$ can be used as the metal source in order to deposit HKUST-1 thin films.[47] In contrast to common observations among SURMOFs so far documented, they observed that defects in the HKUST-1 structure mainly arise from retained acetate ligands stemming from the $Cu_2(OAc)_4$ metal precursor. Due to the weaker coordinative bond between Cu and the nitrate ions as compared to Cu and acetate, this could be prevented by employing $Cu(NO_3)_2$ as a metal source instead of $Cu_2(OAc)_4$.[47]

LPE-LbL enables a high degree of control over orientation and surface functionality. Combined with the mild growth conditions that prevent dissolution/decomposition of the preformed MOF films, LPE-LbL allows creating heteroepitaxial MOF-on-MOF coatings.[48] Additionally, the interactions between the MOF and the surface can stabilize otherwise thermodynamically metastable systems and therefore allow the fabrication of otherwise inaccessible MOFs such as SURMOF-2 and its isoreticular variants.[36] Solvothermal reaction of $M_2(OAc)_4$ (M = Zn(II), Cu(II)) paddlewheels and ditopic carboxylic acids results in the typical MOF-2 structure, which exhibits a low *P2* or *C2* symmetry due to a shift of the M_2L_2 layers.[49] In contrast, the SURMOF-2 structure nucleates in the symmetric *P4* structure as the carboxylic acid groups exposed on the surface stabilize a coplanar arrangement of the Cu dimers. The symmetric arrangement of the stacked linkers in the SURMOF-2 structure type contributes to many photophysical properties, due to the enhanced interaction between the organic linkers.[50–52] Variation of the organic linker in the SURMOF formation led to a multitude of SURMOF-2 structural analogues.[38]

To expand the library of accessible SURMOFs amenable to the LbL deposition method further research was conducted. In this regard, the Hofmann type SURMOF [Fe(pz)[Pt(CN)$_4$] (pz: pyrazine) was fabricated H. Kitagawa and co-workers in 2012.[53] Likewise successful was the manufacturing of Zeolitic imidazolate framework 8 (ZIF-8) SURMOFs.[54] Due to the rather atypical structure (the metal nodes consist of a single metal ion instead of multinuclear metal(-oxo)-cluster), the deposition of these SURMOFs was particularly challenging .[55–58]

In 2017, a new strategy to improve the film homogeneity was implemented by Wannapaiboon *et al.*[46]. Thereto, they added a monotopic carboxylic acid, acetic acid, as a coordination modulator (CM) to the LbL process growing pyrazolate MOF Zn_4OL_3 (L: di-substituted carboxypyrazolates). Coordination modulation slowed down the growth rate, resulting in the fabrication of thinner films with enhanced homogeneity and crystallographic orientation. This study paved the way to crystallize MOFs with

higher node connectivity, which are typically very hard to crystallize. The addition of a CM enabled the LbL growth of UiO-66 ($Zr_6O_4(OH)_4(bdc)_{12}$, see chapter 2.8 in this thesis)[59] in the first place, which was later complemented by other related MOFs like UiO-66-NH_2 ($Zr_6O_4(OH)_4(bdc\text{-}NH_2)_{12}$, bdc-$NH_2$ = 2-amino-benzene-1,4-dicarboxylate)[60] and started investigations into the LbL deposition of porphyrin-based Zr(IV) MOFs[61] (Zhenyu Zhou's thesis).

Exploration of new applications. After SURMOFs were developed, the investigation of their properties linked to various applications began. As MOFs were initially renowned for their porosity and extraordinary high surface area, the investigations started by evaluating their gas/vapour sorption (such as, for sensing purposes) and separation abilities. This later shifted to optical, electrical, and catalytic applications. While this section deliberates over the first key publications regarding the application-relevant properties of SURMOFs, chapter 2.4 covers further in-depth discussions.

In regards to sensing, Allendorf *et al.*[62] seminally contributed by depositing HKUST-1 SURMOF onto a microcantilever with an incorporated piezoresistive sensor. Thereby, they were able to detect vapours of different volatile organic solvents and water. In 2011, shifting from adsorption to sieving, Liu *et al.*[63] initially demonstrated that a racemic mixture can be enantioselectively adsorbed by a chiral SURMOF. Later, the development of heteroepitaxial grown MOF-on-MOF films empowered for advanced sieving and gas separation investigations.[64]

The investigation of optical/photophysical properties of SURMOFs started in 2011/2012.[36,65] Due to the coplanar arrangement of linker molecules in SURMOF-2 structure analogues, these were motifs of interest for studying optical interactions. This phenomenon was also utilized by Liu *et al.*, who fabricated the first porphyrin SURMOF-2-based photovoltaic.[66] These were classified as indirect band-gap semiconductors, facilitating fast and highly efficient charge separation that suppresses charge-carrier recombination. Consequently, these properties were linked to the highly porous, ordered, and oriented porphyrin SURMOFs.

Most MOFs are classified as electrical insulators, however, loading them with some redox-active molecules like ferrocene[67] or 7,7,8,8-tetracyanoquinodimethane (TCNQ)[68,69] can render them semiconducting. Leveraging the insulating properties Gu *et al.* [70] manufactured a SURMOF-based organic field-effect transistor (OFET) in 2017, whereby he used an HKUST-1 SURMOF as a high k dielectric layer. Another application struggling with the low conductivity of (SUR)MOFs, is their ability to act as electrocatalysts. The electrochemical carbon dioxide reduction reaction (CO_2RR),[71] oxygen reduction reaction (ORR),[13] hydrogen evolution reaction (HER),[72] oxygen evolution reaction (OER),[12,73,74] became target reactions for different SURMOFs (mainly Fe/Co/Ni composites) based catalysts. Enhancing their conductivity and potential as

electrocatalysts was attempted by the utilization of ultra-thin SURMOF films.[12] However, the harsh conditions which are essential for driving the electrochemical reactions tend to destroy the SURMOF structures and results in derived materials such as, Fe/Co/Ni hydroxides with non-coordinated organic linkers.[12] These SURMOF derived materials turned out to be excellent electrochemical catalysts.[12,13]

2.3. Strategies for SURMOF Growth

In this section, we elucidate LPE-LbL processing in the context of MOF thin-film preparation. As discussed above, the LPE-LbL process consists of two steps, a) modification of substrates with functional groups, b) alternate immersion of functionalized substrates in metal salt or organic ligand solutions with a rinse step at each interval between the two reactive steps (Figure 4). Each step is identified in the nucleation induction and growth of MOFs on substrate surfaces.[61]

For the growth of SURMOFS, the termination of the substrates (metals, metal oxides, polymers, *etc.*) with functional groups is essential, these can be achieved by utilizing native oxide surfaces or by reacting substrates with SAMs bearing functional terminal groups, such as carboxyl, hydroxyl, pyridyl, methyl, and amino groups. Au substrates, for example, can be terminated with hydroxyl or carboxyl groups by immersion in 11-mercaptoundecanol or 16-mercaptohexadecanoic acid solution, respectively. Silicon wafers, alumina, ITO and FTO, already possess a native oxide surface if exposed to air. The surface can be additionally treated with UV ozone, O_2 plasma, or piranha solution in order to remove organic residues and to enhance the hydrophilicity of the surface. These terminated functional groups can coordinate with the metal nodes or organic ligands, facilitating and tailing the nucleation of MOF films.

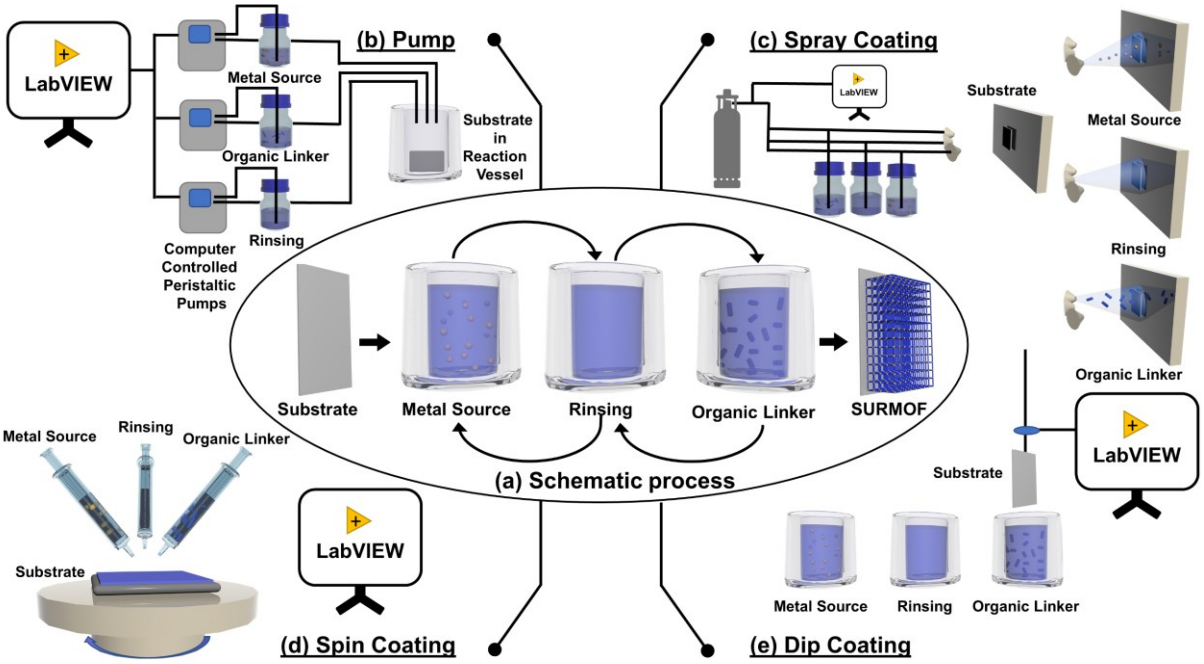

Figure 6: Schematic illustration (a) of different precursor delivery techniques involved in the LBL growth of SURMOFs. Technical realizations of the LbL processes automated pump system (b),[36] the spray coating system(c),[40] the spin-coating setup (d),[75] and the dipping robot setup (e).[39]

As mentioned in the timeline in the previous chapter, several process variants to implement the LbL-LPE strategy were developed. Chronologically, these preparative processes include manual dipping (2007),[32] as well as automated pump (2011),[36] spray coating (2011),[40] dipping robot (2015),[39] and spin coating (2016).[75] While all processes follow the stepwise deposition (Figure 6a), the major differences among these strategies lie in their disparate techniques of introducing the precursor solutions and rinse solvent to the substrate surfaces. The pumping technique relies upon the use of computer-controlled peristaltic pumps to introduce the solutions into/out of a reaction cell (Figure 6b). In the spray process, the solutions are sprayed on the surface through nozzles that generate aerosols (Figure 6c). For spin coating, the substrate is immobilized on a rotary vacuum chuck, and the centrifugal force allows the microdrops of solutions to spread homogeneously on the substrate (Figure 6d). As shown in Figures 6e, the dipping method relies on immersing the functionalized substrate in the solutions by hand (manual dipping) or by using a robot (automatic dipping).

Crystal engineering of SURMOFs. Various functionalities have been introduced to SURMOFs over the last decade, which set out paths to potential applications. Therefore, we herein discuss the progress and state-of-the-art heterostructured SURMOFs,[46,76–79] guest encapsulation,[80–83] coordination modulation assisted LPE growth,[59,84] targeted defect engineering in SURMOFs.[85]

Heterostructured SURMOFs. Due to the unique stepwise process design of the LPE process, extraordinary, otherwise inaccessible structures can be accessed. One example of these structures are heterostructured MOF-on-MOF coatings, which are hardly accessible by the solvothermal synthesis.

Multifunctionality of these MOF-on-MOF composite materials can be achieved by combining MOFs with different features, such as network topology, pore size, and reactive centres. Moreover, by LPE the distribution of functionalities along the growth direction can be achieved.

The first of the heterostructured MOF-on-MOF coatings were grown by Zacher *et al.* by employing two different pillared-layer [$M_2(L)_2(P)$] (M: metal ion/cluster; L: organic linker; P: pillar ligand) SURMOFs.[76] The film consist of two lattice-matching layers of various dicarboxylate linkers and metals, i.e. $Cu_2(F_4bdc)_2$(dabco)-on-$Cu_2(ndc)_2$(dabco) and Zn_2(BME-bdc)$_2$(dabco)-on-$Cu_2(ndc)_2$(dabco) (F_4bdc: tetrafluorobenzene-1,4-dicarboxylate; dabco: 1,4- 1,4-diazabicyclo (2.2.2)octane; ndc: 1,4-naphtalene dicarboxylate; BME-bdc: 2,5-bis(2-methoxyethoxy)-1,4-benzene dicaboxylate). The lattice matching of both structures is important for the heteroepitaxial growth, as the hetero-SURMOFs maintain the [001] crystallographic orientation of the bottom layer. The multifunctionality of the heterostructured MOFs is shown by the increased water contact angle of $Cu_2(F_4bdc)_2$(dabco)-on-$Cu_2(ndc)_2$(dabco) as compared to $Cu_2(ndc)_2$(dabco). Further exploitation of the lattice matching led to the fabrication of heterostructured MOF-5 isotype [$Zn_4O(L)_3$] MOF thin films. Based on the chosen top and bottom layer, Wannapaiboon *et al*. could show that these thin films exhibited a vapour sorption selectivity. By choosing a small pore diameter on top and a large pore diameter on the bottom a selectivity towards smaller molecules (methanol and ethanol instead of isopropanol) while maintaining larger storage capacities could be achieved.[46]

To endow hetero-SURMOFs with more versatility, layers of different lattice parameters and topologies were successfully integrated via the LPE technique. HKUST-1, with a face-centred cubic structure (space group *Fm-3m*) was deposited on $Cu_2(ndc)_2$(dabco), which has a tetragonal symmetry (space group *P4/mmm*).[77] $Cu_2(ndc)_2$(dabco) was grown along the [001] direction on a pyridyl terminated substrate. The terminal layer of the $Cu_2(ndc)_2$(dabco) layer was a dabco layer, which similarly to a pyridyl functionality, allowed for the growth along the [111] direction. However, the inverse experiment growing $Cu_2(ndc)_2$(dabco) on HKUST-1, was not successful, as HKUST-1 is terminated by btc^{3-} linkers with can not template the growth of $Cu_2(ndc)_2$(dabco). This shows the importance of the interface and the surface functionalization for the successful fabrication of (heterostructured) SURMOFs. After further investigating the $Cu_2(ndc)_2$(dabco))-on-HKUST-1 interface, the termination of

the HKUST-1 layer with different functionalized isophthalate (fu-ip) ligands enabled the successful preparation of $Cu_2(ndc)_2(dabco)$)-on-HKUST-1.[78] BuOH-ip (Bu= butoxy) ligands served as the best template for growing the [001] oriented $Cu_2(ndc)_2(dabco)$.

Heterostructured SURMOFs have multiple functionalities and are of particular relevance to chemical sensing and separation, among other emerging applications. However, some functional ligands cannot be incorporated in hetero-SURMOFs by direct LPE. Post-synthetic modification (PSM) can be utilized to modify the ligands of the prepared hetero-SURMOFs in a task-specific manner. For example, hetero-SURMOF of $Cu_2(bdc\text{-}NH_2)_2(dabco)$-on-$Cu_2(bdc)_2(dabco)$ was fabricated by Tu *et al.* and subsequently modified with *tert*-butyl isothiocyanate (tBITC).[79] This hetero-SURMOF maintains its original PXRD pattern after the chemical modification, whereas the loading of tBITC molecules on the top MOF layer reduces its pore size, the key to inducing size-selective adsorption of methanol and hexane over cyclohexane.

Guest encapsulation in SURMOFs. The ordered nanoporosity of most MOF and SURMOFs allows for the encapsulation of several nano-species (e.g., metallic nanoparticles, quantum dots, organic polymer materials) into the pores. This approach can introduce new features to the SURMOF and in turn, expand the applications of the SURMOFs composites.

For example, Liu *et al.* embedded ligand-stabilized Au_{55} clusters $[Au_{55}(PPh_3)_{12}Cl_6]$ (hexachlorododecakis(tripphenyl-phosphine)-pentapentacontagold) into highly oriented SURMOF thin films during the spray LPE process, which has been confirmed by X-ray diffraction, infrared spectroscopy, and ultraviolet−visible spectroscopy.[80] The Au_{55} clusters encapsulation leads to a substantial increase of electrical conductivity and enhanced catalytic activity for the reduction of 4-nitrophenol. Exemplifying the success of this spray LPE approach, titanium metal-organic clusters (MOCs) were encapsulated in HKUST-1 SURMOF, and a palladium nanocatalyst and $Ce(pdc)_3$ (pdc: pyridine-2,6-dicarboxylic acid) were separately encapsulated in the porphyrin-based SURMOF PIZA-1 (PIZA: porphyrinic Illinois zeolite analogue).[81,82,83]

Another approach for guest encapsulation is the post-synthetic encapsulation (PSE) of guests into the preformed SURMOFs. Dragasser *et al.* loaded ferrocene into HKUST-1 films through post-synthetic vapour-phase loading.[67] Charge transport across the insulating HKUST-1 SURMOF could be established after encapsulating ferrocene as an immobilized redox mediator.

Coordination modulation assisted LPE. The quality of SURMOF films can be extensively influenced by the crystallization process. Consequently, precise control of crystallization is highly favoured to fabricate SURMOFs with superior characteristics

(e.g., crystallinity, orientation, and porosity). One strategy of effectively influence the crystallization process is coordination modulation. Employed and explored for the solvothermal growth of bulk MOFs the addition of a coordination modulator, which typically contains the same coordinating group as the organic linker, slows down the reaction kinetics of the MOF formation. Owing to its facile integration in LPE, growing literature reports suggest CM-assisted modulation being a potentially powerful route to impact the LPE growth of SURMOFs.

The translation from solvothermal growth to LbL-LPE was first explored by Wannapaiboon *et al.* fabricating $Zn_4O(L)_3$ (L^{2-}= 3,5-dialkyl-4-carboxypyrazolate) SURMOFs using acetic acid as a modulator.[84] The CM-LPE process decelerates the growth kinetics and contributes to the enhanced crystallinity and higher degree of preferred orientation in the SURMOFs, verified by XRD measurement and SEM imaging. Moreover, the enhanced crystallinity resulted in their improved adsorption capacities for methanol.

Following up on these results, the CM-LPE technique was employed to enable the fabrication of SURMOFs with high node connectivity. So far, SURMOFs fabricated via LPE were typically limited to the tetra-connected dinuclear paddle-wheel MOFs and Hoffmann-type MOFs, while MOFs with higher connectivity (8-12 connecting metal nodes) with high porosity and crystallinity are difficult to be deposited as thin films. Utilizing CM-LPE, Semrau *et al.* achieved to prepare the 12-connected UiO-66, $Zr_6O_4(OH)_4(bdc)_6$ applying methacrylic acid as a modulator and water as an additional additive through the facilitation of the proton-dependent coordination equilibria (see chapter 2.8).[59] The SURMOF exhibited high porosity and nano-crystallinity. As a proof-of-concept, the success of this case further strengthened the CM-LPE approach, fostering new opportunities to deposit higher-connected SURMOF thin films under mild conditions.

Targeted defect engineering in SURMOFs. Defect engineering – the targeted installation of metal and/or linker vacancies in MOFs – is an effective strategy to tailor their properties. While defect engineering, similar to CM, has been thoroughly explored for bulk MOFs, its translation into the CM-LPE process has just begun. Targeted defects in MOFs may enhance the functional properties of MOFs (e.g., porosity,[86] catalytic activity,[87] and magnetic behavior[88]) or even endow new properties (e.g., charge transport[89]).

Using LPE, Wang *et al.* introduced missing linker defects in an HKUST-1 SURMOF by partially employing a set of defect-generating linkers, *i.e.* isophthalic acid, 5-hydroxyisophthalic acid, and 3,5- pyridinedicarboxylic acid alongside H_3btc. Two different strategies were used to introduce the defects: 1) mixing of both linkers

(defective and non-defective); 2) alternatively dosing the parent linker and the defective linker solution. They conclude that the mixing method is more efficient for the incorporation of defects into SURMOFs, while the alternating method shows a higher degree of control in distributing defects. Overall, these strategies offer control over the defect formation (e.g., type, quantity, and distribution) in SURMOFs.

2.4. State-of-the-Art SURMOFs and the Summary of Current Benchmarks

Due to the unique advantages, such as controllable growth orientation, well-regulated thickness, and smooth, homogeneous morphologies, SURMOFs have delivered properties relevant to a miscellany of applications. In this section, we discuss the structure-surface-function relationships in SURMOFs contextualizing their thoroughly studied properties such as sensing, adsorption/separation, optical applications, electrical applications, and catalysis. (see Table 1).

Table 1: Summary of SURMOF structures described in this review.

Applications	MOFs	Properties	Substrates	Ref.
Adsorption and separation	$[Zn_4O(L)_3]_n$ (L=H_2dmcapz, H_2mipcapz)	High VOCs adsorption selectivity	-COOH terminated Au	46
	Cu_3btc_2 on Cubdc; Cu_3btc_2 on Cubpdc; Cu_3btc_2 on CuTFbdc	Higher VOCs storage capacity versus the two SURMOF components	-COOH terminated Au	90
	$[Zn_2((+)cam)_2(dabco)]_n$	Significant enantioselectivity towards R-HDO and S-HDO	-COOH, -pyridyl terminated Au	63
	$Cu_2(bdc)_2(dabco)$ and $Cu_2(atbdc)_2(dabco)$	Highly selective uptake for Fe(III) and Pd(II)	-OH terminated Au; quartz glass	91
Sensing	HKUST-1	Ultrasensitive humidity detection	Quartz SAW	92
	HKUST-1	High optical reflectivities and colour tunability over the whole visible range.	Modified Si wafers; ITO	93
	$Ni_3(C_{18}H_6(NH)_6)_2$, $Cu_3(C_{18}H_6(NH)_6)_2$ and $Cu_3(C_{18}H_6(NH)_6)_2$	Photodetector and gas sensor	-OH terminated Si wafer	94

Optical	Cu_2(AB-BPDC)$_2$(bipy) on Cu_2(BPDC)$_2$(bipy)	Uptake and release of guest molecules by the photoswitch	-OH terminated Au	95
	Zn(TPP) and C_{60}@Zn(TPP)	Photo-conductivity with an on-off photocurrent ratio of two orders of magnitude.	Quartz	96
	Porphyrin-based Zn-SURMOF 2	Photovoltaic device	FTO, -COOH terminated Au	66
	HUKST-1	White-light emission	Quartz	97
	PIZA-1	third-order nonlinear optical property	Quartz	98
Electrical	HKUST-1	Tunable conductivity after the loading of TCNQ	Si wafers with Pt pads	69
	HUKST-1	Thermoelectrics	Quartz	99
	HUKST-1	OFETs	Modified Si wafers	70
	HUKST-1	Memristors	Au coated PET	100
Catalysis	PIZA-1	Tandem oxidation–acetalization catalysis	-OH terminated Au	82
	Re-SURMOFs	electrocatalytic CO_2 reduction	FTO glass	101
	NiCo-bdc SURMOFDs	OER electrocatalyst	-COOH terminated Au	12
	NiFe-bdc (X) SURMOFDs	Bifunctional ORR/OER electrocatalyst	-COOH terminated Au	13

Abbreviations: H_2dmcapz: 3,5-dimethyl-4-carboxypyrazole; H_2mipcapz: 3-methyl-5-isopropyl-4-carboxypyrazole; btc: 1,3,5-benzentricarboxylate; bdc：benzene-1,4-dicarboxylate；bpdc: biphenyl-4,4′-dicarboxylate; TFbdc: tetrafluoroterephthalate; (+)cam = (1R,3S)- (+)-camphoric acid; dabco: 1,4-diazabicyclo[2.2.2]octane; R-HDO: (2R,5R)-2,5-hexanediol; S-HDO: (2S,5S)-2,5-hexanediol; atbdc: 2,5-bis-(allylthio)terephthalic acid; SAW：surface acoustic wave; $C_{18}H_6(NH)_6$: 2,3,6,7,10,11-hexaaminotriphenylene；bipy: 4,4′-bipyridine; AB-BPDC: 2-azobenzene 4,4′-biphenyldicarboxylic acid; BPDC: biphenyl-4,4′-dicarboxylic acid; TPP: 5,15-bis-(3,4,5-trimethoxyphenyl)-10,20-bis- (4-carboxyphenyl) porphyrinato zinc(II); TCNQ: 7,7,8,8-tetracyanoquinodimethane; OFETs: organic field-effect transistors; PET: polyethylene terephthalate.

Adsorption and separation. Owing to their nanoporosity, adsorption and separation were the first investigated for SURMOFs. In this regard, especially heterostructured MOFs combining the properties of both individual SURMOFs have been proven

useful. In this respect, Wannapaiboon *et al*. combined $[Zn_4O(dmcapz)_3]_n$ and $[Zn_4O(mipcapz)_3]_n$ which were subsequentially grown on a substrate. The combination allowed for the size-selective adsorption of ethanol/methanol as compared to isopropanol, while maintaining the higher sorption capacity of $[Zn_4O(dmcapz)_3]_n$.[46] Further investigations confirm the advantages of heteros-SURMOFs in adsorptive separation.[79,102,103] The combination of multiple SURMOFs in a layered fashion usually leads to a combination of the sorption properties of both materials. However, a rather surprising observation was recently made by Wang *et al.*. They observed that the heterostructured SURMOF (Cu_3btc_2 on CuTFbdc) boosted the mesitylene sorption capacity of the individual MOFs capacity by the factor 4.5. They attribute this phenomenon to a funnelling effect as CuTFbdc usually does not adsorb much VOC due to a high pore entrance barrier. This entrance barrier is probably reduced by the $Cu_3(btc)_2$ top layer. This interesting phenomenon still requires further investigation as the interface between the SURMOFs layers and the diffusion processes are challenging to investigate.

Differences in biological and pharmacological properties of chiral molecules necessitate efficient enantiomeric separation in pharmaceutical research. Homochiral MOFs are promising candidates for the efficient separation of enantiomers owing to their large surface areas and structural/compositional diversity. In this regard, Liu *et al.* investigated the adsorption kinetics of enantiomers, *viz.* (2R,5R)-2,5-hexanediol and (2S,5S)-2,5-hexanediol with the chiral SURMOFs $[Zn_2((+)cam)_2(dabco)]$ and $[Zn_2((-)cam)_2(dabco)]$.[63] Selective adsorption capacities and different diffusion kinetics were observed for the chosen enantiomers. Following up on this work, several homochiral SURMOFs and derivatives were fabricated for the chiral separation.[81,104–106]

Another sorption and separation application is the adsorption of metal ions instead of gases. Optimized linkers in $[Cu_2(atbdc)_2(dabco)]$ enhance the maximum sorption capacity for Fe(III) and Pd(II) ions to six metal ions per MOF pore. This is twice the amount that can be captured by the isostructural $Cu_2(bdc)_2(dabco)$ SURMOFs.[91] Moreover, the functionalized linkers of $[Cu_2(atbdc)_2(dabco)]$ reduce the diffusion constant. The highly selective capture of metal ions in these SURMOFs highlights the so-far untapped potentials of SURMOF for applications including, metal-ion sensing and metal-ion separation and purification.

Sensing. Due to the responsiveness and nanoporosity of selected MOFs, SURMOFs are extensively used for chemical sensing applications. Experimentally, chemical responses must be transduced to physical signals for detection. Various mechanisms, such as optical, electrical, and mechanical mechanisms, have been incorporated into the MOF films to achieve chemical detection.

The most straightforward methods for SURMOF-based sensing are gravimetric sensors, such as quartz crystal microbalance substrates, surface acoustic wave sensors, and microcantilevers. In this regard, a humidity sensor was prepared by growing HKUST-1 on a surface acoustic wave (SAW) sensor, which could detect a broad humidity detection range, from 3 to 14800 parts per million by volume (ppmv).[92] In this study by Robinson *et al.* several other interesting observations were made. They noticed that HKUST-1 thin films, which were obtained by the direct growth method and displayed a rougher and irregular surface, displayed a broader detection range. Moreover, thicker LBL HKUST-1 SURMOFs (50 deposition cycles) show a higher sensitivity than the thinner SURMOF thin films (20-30 deposition cycles). However, the increasing longer response times render thicker films unattractive for their use in humidity sensors. As the humidity detection is based on the mass change occurring upon the adsorption of water vapour molecule(s) on the studied SURMOF film, similar SURMOF sensors can also be developed to detect various gas molecules, such as volatile organic compounds (VOCs),[102,107–109] and volatile plant oils.[110]

Apart from gravimetric sensing, optical sensors based on multi-layered Bragg stacks are an option for SURMOF-based sensors. A proof-of-concept for this approach was presented by Liu *et al.* which prepared a Bragg stack by fabricating several alternating layers of HKUST-1 and ITO.[93] In this case, HKUST-1 SURMOF features a low refractive index (RI), whereas the sputtered ITO represents the high RI material. They report that by modifying the individual layer thicknesses (80–135 nm/ITO-layer of 62-85 nm), the Bragg stack photonic band-gap material displays a high reflectivity of up to 80% with a tunable colour over the whole visible range. Additionally, the porosity of HKUST-1 can be used to alter the reflected wavelength by 20-40 nm by loading various guest molecules. They attributed this effect to a change in the overall refraction upon guest inclusion, instead of swelling of the SURMOF pores.

Schottky diodes fabricated with electrically conductive SURMOFs as interlayer materials as self-powered photodetectors were first reported by Cao *et al.*.[110] In the Schottky diode, SURMOF layer was used to modulate the height of the Schottky barrier, resulting in an enhanced separation efficiency in photo-generated electron/hole pairs. Surprisingly, this diode achieved the highest external quantum efficiency (84%), broadest detectable spectrum range (250 to 1500 nm), high on-off ratio (~103), as well as short rise (0.007s) and fall time (0.03s) if compared to other self-powered photodetectors. Moreover, owing to the porosity of the SURMOF, this diode can sense some typical harmful gases and vapours.

Optical properties. Due to the high control over thickness, structure, and crystallographic orientation, SURMOFs are highly interesting candidates for studying photophysical properties like photoswitching,[95,111] photoconductivity,[96]

photovoltaic,[66,112] photoluminescence[97,113] which could culminate in the fabrication of optical devices.

A key for the optical properties is often the choice of functional linkers which is the standard route to endow SURMOFs with specific optical properties. By incorporating photoswitchable linkers, for example, the permeability of the resulting SURMOFs can be rendered switchable by light. In this regard, Heinke *et al.* prepared the heterostructured Cu_2(AB-BPDC)$_2$(bipy) on the lattice-matching Cu_2(BPDC)$_2$(bipy). After loading the bottom layer with molecules, the top layer can be optically triggered to release or take up the guest molecules.[95] This is enabled by the azobenzene-based linkers, which can switch from *trans* to *cis* state or the reverse under the irradiation of ultraviolet light or red light, respectively. Remote control switching of SURMOFs is one of the interesting properties which might lead to the fabrication of smart SURMOF devices. Extending this work, a series of similar photo-switchable SURMOFs have been fabricated for storage and separation of guest molecules,[111,114,115] and proton conduction.[116]

Photoconductivity was introduced to SURMOFs by Liu *et al.* employing C_{60}@Zn(TPP) SURMOF films. These feature porphyrinic linkers as electron donors and infiltrated C_{60} as an electron acceptor, which displays a typical on-off photocurrent under light irradiation. [96] The infiltration with C_{60} as a guest enhanced the separation and transport of the photoactivated electron through the SURMOF material, after the optical excitation of the Soret band of the porphyrin, resulting in its photoconductivity. Benefiting from the high density of donor-acceptor interfaces, in combination with the spatially continuous network of interpenetrating donor and acceptor domains of C_{60}@Zn(TPP) SURMOF, culminating in enhanced photoconductivity. Photoconductivity is a characteristic property of semiconductors, and this work has unlocked potential paths of SURMOFs to applications such as photoresponsive transistors and light-sensing.

Besides electron donors porphyrins can also act as light-harvesters and photoelectrics, enabling porphyrin-based SURMOFs to function as photovoltaic devices.[66,112,117] Liu *et al.* investigated this by fabricating a prototype photovoltaic device based on porphyrin SURMOF-2.[66] As porphyrin-based SURMOFs are indirect bandgap semiconductors, they enable fast and efficient charge separation and thereby suppress charge-carrier recombination. The photovoltaic device based on Pd porphyrin Zn-SURMOF revealed a remarkable photocarrier generation efficiency of 0.45% with an open-circuit voltage of 0.7 V, a short circuit current density of 0.71 mA $cm^{-2,}$ and a fill factor of 0.65. By loading the electroactive molecules into the pores, the oriented crystalline SURMOF films achieved higher performances, particularly reflected in improved charge separation.

SURMOFs can pose as excellent platforms for photoluminescence emission by introducing photoluminescent guests, such as organic chromophores,[113,118,119], and lanthanide ions[97,120]. Due to the layered assembly, guest molecules can be efficiently encapsulated into the SURMOF. $Ln(pdc)_3$ (Ln = Eu, Tb, and Gd) infiltrated HUKST-1 SURMOF were prepared by LbL-LPE. Emission photoluminescence colour could be tuned by adjusting the ratio of these compounds, as each emits one of the RGB colours (red (Eu), green (Tb), and blue(Tb)).[97] White-light emission was enabled by the precise control of the Gd/Eu/Tb ratio in $Ln(pdc)_3$, leading to the fabrication of a white LED by depositing Ln(pdc)@HKUST-1 SURMOF on an ultraviolet LED chip. This LED showed strong white light emission under 350 mA forward bias current. Efficient encapsulation of photoluminescent guests into the uniformly ordered SURMOF in a well-defined LPE process materializes a new perspective to develop high-performance photoluminescent emission devices and sensors.

Electrical properties. While the homogeneous, continuous morphology of SURMOFs is sought-after in electronics, the low dielectric constant of most SURMOFs deems them only suitable as insulating layers. The infiltration with guest molecules can render them semiconducting, however, their application is generally limited by their poor electrical conductivity.

An advantage of SURMOFs lies in their amenability to manifest controlled electronic properties by the use of appropriate linkers,[66,109] or by loading with guest molecules, such as ferrocene,[67,121,122] 7,7,8,8-tetracyanoquinodimethane (TCNQ),[69,123] iodine[124], or 1-hexyne[125]. Talin *et al.* observed that after infiltrating an insulating HKUST-1 SURMOF with TCNQ increases its electrical conductivity by *ca.* six orders of magnitude to 7 S m^{-1}.[69] They attribute the enhanced conductivity to a new charge transfer band between HKUST-1 and TCNQ, which was established by inserting the unoccupied TCNQ molecular orbitals into the HOMO-LUMO gap of HKUST-1.

Further investigations by Erickson *et al.* investigated the TCNQ infiltrated HKUST-1 SURMOFs as candidates for thermoelectric devices.[99] The thermoelectric properties of the TCNQ@HKUST-1 film were measured using Peltier temperature control elements to create a temperature gradient. TCNQ@HKUST-1 possessed a surprisingly large positive Seebeck coefficient of 375 $\mu V\ K^{-1}$, attributed to hole transport in the MOF valence band. Temperature-dependent conductivity measurements revealed a linear dependence associated with a temperature-activated charge carrier transport with an energy barrier of 0.052 eV. Simply put, this work investigated thermal conductivity among SURMOFs for the first time and underscored its yet untapped potentials for thermoelectric applications.

Organic field-effect transistors (OFETs) have drawn significant attention for their application in phototransistors, light-emitting transistors, memory devices, and

display devices. Gu *et al.* utilized HKUST-1 SURMOF to fabricate the first SURMOF based OFETs.[70] Therefore, HKUST-1 was grown on a SiO_2 layer and subsequently coated with PTB7-Th (poly[4,8-bis(5-(2-ethylhexyl)thiophen-2-yl)benzo[1,2-*b*:4,5-*b'*]dithiophene-*co*-3-fluorothieno[3,4-*b*]thiophene-2-carboxylate]) as a semiconductive polymer layer. The final layer consisted of two Au electrodes at opposite sides of the Si wafer. It was found that the performance of the OFETs, such as charge mobility, threshold voltage, and current on/off ratio, was significantly improved after the modification with only a few (e.g 4) LPE deposition cycles of HUKST-1. Investigating the hole mobility ($(1.32\pm 0.20) \times 10^{-2}$ cm^2 V^{-1} s^{-1}), the threshold voltage (10 V), and an on/off ratio (10^3), the HKUST-1 based OFET displays superior properties as compared to bare SiO_2 substrates. The enhanced performance of this device is mainly ascribed to the high crystallinity, homogeneity, and low dielectric constant of HKUST-1. This work highlights the benefit of SURMOFs modified dielectric and indicates future scopes to design and study new SURMOFs modified dielectrics, targeting OFET applications.

Memristors[126] - defined as non-linear two-terminal electrical components connecting electric charge with magnetic flux linkage - are considered promising candidates to replace complementary metal-oxide-semiconductor technology. Since the discovery, applying homogeneous SURMOFs with controlled thickness has been the general research trend. In this regard, bipolar resistive switching behaviour is the characteristic property of memristors and has been found in SURMOF-based devices.[100,122,127] Pan *et al.* fabricated an HKUST-1 layer on Au coated polyethylene terephthalate (PET) substrates, resulting in Au/HKUST-1/Au PET memory devices.[100] The SURMOF-based devices showed uniform and reproducible resistive switching effect from –70 to +70 °C, which allows their applications to cover a wide temperature range. The observed resistive switching resulted from the formation of highly conducting filaments caused by electric field-induced migration of the Cu(II) ions and then pyrolysis of the trimesate linkers. Very recently, a stable and reproducible ambipolar resistive switching mediated by controlled humidity was found on a SURMOF-based, rolled-up and scalable device.[127] The device showed a high on/off ratio of 10^6 under high humidity (90%) and low threshold voltages (< 1 V). The excellent performance is caused by structural defects associated with the water molecules, thereby the occasional appearance of additional states in the bandgap region. The authors declared that further studies are in progress to explore charge transport mechanisms in these devices at low temperatures (< 20 K), beneficial to their versatile applications.

Catalysis. Catalytic applications emerged for SURMOFs during the last years, owing to the exposed active sites,[74,101,128], or the encapsulation of catalysts.[82] Moreover, SURMOF derived film materials (SURMOFDs), such as carbon-based materials,[83,129–131] hydroxides[12,13,132] and metal oxides[133] were investigated as catalysts.

Liquid phase organic reactions were catalyzed by SURMOF encapsulated metal-organic catalysts. The one-pot tandem oxidation-acetalization catalysis of benzyl alcohol and ethylene glycol was catalyzed by the bifunctional catalyst $Pd[P(C_6H_5)_3]_4$@porphyrin-based SURMOF PIZA-1.[82] Combining the Lewis acidic properties of PIZA-2 and the oxidative properties of $Pd[P(C_6H_5)_3]_4$ enabled the successful catalysis. Controlling the top layer ($Co(OAC)_2$, TCPP ligand, or Pd-Cs), affected the respective reaction conversions (85.0%, 71.9%, and 70.0%), and enabled a deeper understanding into the mechanism and the control that is offered by SURMOFs, thereby guiding future researchers to develop functional SURMOF films with tailored catalytic properties.

CO_2 reduction to higher-value chemicals is one of the most interesting reaction pathways facing global warming. In this regard, SURMOFs and derived materials were investigated for their potential application as electrocatalysts.[101,134] First, Liu *et al.* employed a monolithic and oriented Re-SURMOF thin film grown on an FTO substrate, which revealed a CO_2 reduction potential of −1.3 V vs. NHE (normal hydrogen electrode).[101] Higher selectivity and Faraday efficiency (93 ± 5%) of CO_2 to CO conversion at −1.6 V vs. NHE with a turnover number of 580 were observed for the SURMOF compared to Re-based organic linkers, which was attributed to the effective charge transport along [001] direction. However, it should be noted, that the stability of the catalysts remains a challenge.

Another highly desired process for sustainable and environmentally clean energy conversion is the electrocatalytic water splitting, which can be divided into two half-reactions: oxygen evolution reaction (OER)[12,74,83,132,133] and hydrogen evolution reaction (HER).[130,135,136] Recently, SURMOF derived materials emerged as catalysts in that area. Established by Li *et al.*, the mixed nickel/cobalt double-layered hydroxides derived from [M(bdc)] (M = Ni(II) and Co(II)) SURMOFs by immersion in KOH solution reveal excellent OER performance.[12] The simultaneous abundance of exposed Ni(II) and Co(II) sites in SURMOFDs induces an electronic coupling, synergistically contributing to the electrocatalytic performance. Especially, thin films (10 deposition cycles instead of 50) can drastically improve the mass activity from ~0.8 to ~2.5 $mA \cdot \mu g^{-1}$ at an overpotential of 300 mV. This can be attributed to the enhanced electron/mass transport and the higher density of accessible active sites. The observed mass activity even challenges other (precious metal) benchmark electrocatalysts.

Multifunctional electrocatalysts, effectively catalyzing both half-cell water splitting reactions are the holy grail of electrocatalysis. While the tailored design of the multifunctional electrocatalysts is still in its infancy, very recently, derived from oriented NiFe-bdc(X) SURMOFs, Li *et al.* developed an advanced bifunctional electrocatalyst for both ORR and OER.[13] Fabrication was conducted by introducing

various functional groups such as -Br, -OCH_3 and -NH_2 into the bdc^{2-} linkers. After treating the SURMOFs with KOH, the derived Fe/Ni double-layer hydroxides were obtained. The use of different functional groups can alter the lattice strain of the double layer hydroxides, therefore inducing an improved electrocatalytic activity. Excellent OER performance and an "overpotential window" $\Delta E_{ORR-OER}$ of 0.69 V were observed for bdc-NH_2 as the organic linker. This makes this double layer hydroxide the bifunctional electrocatalyst with the narrowest overpotential window documented thus far.

2.5. Conclusion and Future Perspectives

So far we discussed the chronology of developments in the field of SURMOFs and covered recent key developments concerning the fabrication and application of SURMOFs. The as-prepared SURMOF thin films feature advantages of controlled thickness, well-defined orientation, and homogeneous compact surface, all of which culminate in manifold properties, *viz.* adsorptive selectivity/separation, sensing, optical applications, electrical applications, and catalysis. Despite the aforementioned advantages of SURMOF thin films and their versatility in applications, some challenges continue to plague the development of SURMOFs and their further applications. The main challenges/perspectives are summed up in Figure 7.

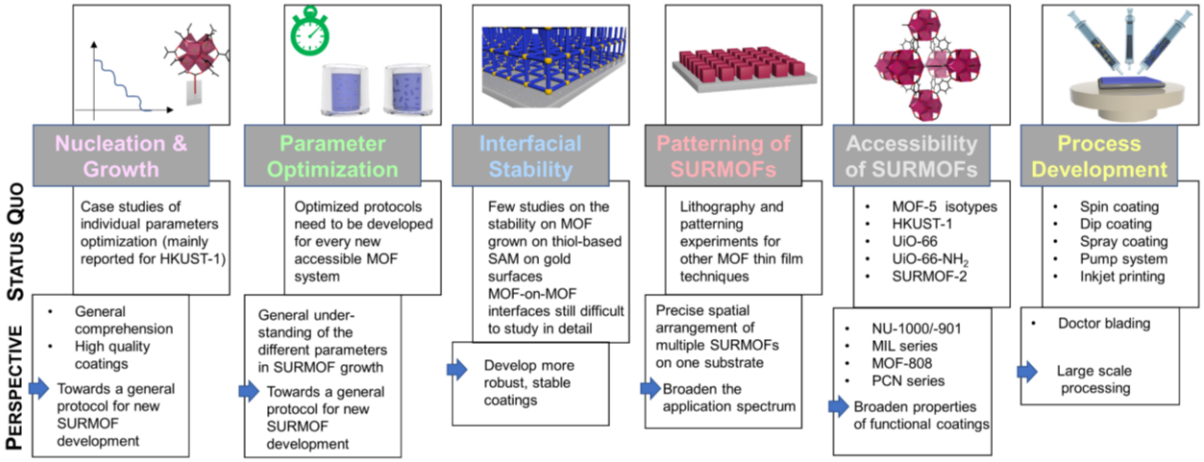

Figure 7: Potential "*low-lying*" areas where SURMOF research is most likely to flourish.

To establish a more general protocol for the deposition of SURMOFs, further in-depth studies into the growth mechanism of various SURMOFs are needed. While a couple of publications were published on this topic and discussed in this review,[47,137–139] further insights could help to fabricate high-quality SURMOFs, for example, in terms of affording less or well-regulated defects, grain boundaries, substantial wafer-scale uniformity, and in-plane orientation, or even single-crystalline SURMOFs.

Alongside the growth mechanisms, systematic investigation of the growth parameters is highly recommended to optimize specific SURMOF films. These include the

optimization of metal node precursors, concentrations, solvent, modulator, temperature, reaction time, and the sequence of dosing.[137,140–144] The listed parameters evidently influence the nucleation and growth of the SURMOFs, and the investigation will potentially offer reference points for the preparation of high-quality SURMOFs targeting various applications.

The long-term goal of these two research strategies would be to establish an optimized protocol for each SURMOF, and ideally translating the research towards the development of a general protocol for the deposition of new SURMOFs.

Another area that demands more attention is the investigation of the interfaces, including the substrate/SURMOF interface or the interfaces between MOF in heterostructured MOF-on-MOF coatings. Due to the facile task, investigations on the topic are rare and therefore highly encouraged.[145] Studying the interface can in turn be used to improve the anchoring of the SURMOF onto the substrate, which will affect the properties of SURMOF based devices, such as, charge transfer on electrochemical devices, therefore crucial to elicit their applications.

In comparison with the large number of bulk MOFs, only a limited number of MOFs, such as HKUST-1, SUMOF-2, Hofmann type MOFs, pillared $[M_2(L)_2(P)]$ SURMOFs and MOF-5 isotypes, are established by LPE-LbL. Recently, ZIF-8 and UiO-66 thin films were also prepared using advanced LbL-LPE strategies such as CM-LPE. However, many other typical MOFs, such as PCN and MIL series, are still not accessible by LbL-LPE[61] Only further expansion of this SURMOF films library will realize their full potential.

The large-scale industrial applications of SURMOFs, or any MOF thin films in this regard, are still in the far future. One factor that could limit the utilization of SURMOFs in large-scale applications is the vast amount of solvents and chemicals as well as the long process durations needed for the manufacturing process – in short, so far, the process is highly cost-intensive. However, the development of the LbL spray coating and LbL spin coating processes reduces the process duration and solvent consumption drastically. Combined with investigations of the growth mechanism, this can help to reduce the process duration further, and additionally reduce the thin film roughness and defect content, enhancing the orientations at the same time. Further investigations in this area can help to reduce the process cost and make SURMOFs more attractive.

In conclusion, despite early performances demonstrated by SURMOF thin films in various fields, the above challenges should be investigated before they might find applications in real-world devices and/or industrially relevant processes. We believe that more applications of the SURMOF films will certainly be a reality in the near future, not only in the aforementioned applications but also in dormant fields.

2.6. Selected MOF Systems in this Thesis

UiO-66(-NH_2) is a prototypical example of a MOF exhibiting extremely high surface areas as well as high chemical and thermal stability. As the structure is key for the next chapter as is discussed here.

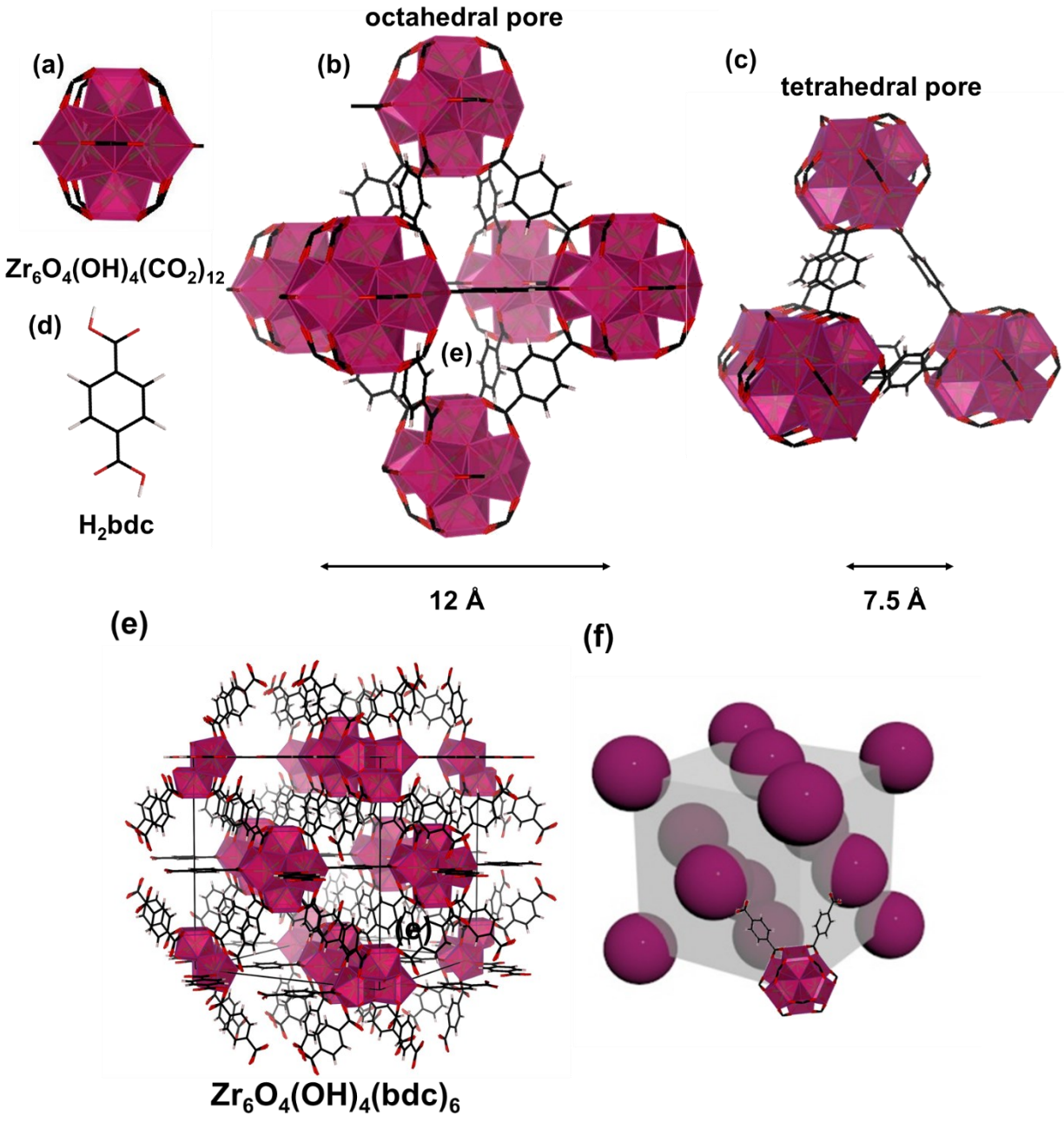

Figure 8: Structure of UiO-66 (e) consisting of the $Zr_6O_4(OH)_4(COO)_{12}$(a) and H_2bdc (d) as an organic linker forming a face-centred cubic structure (f) with the unit cell with $[Zr_6O_4(OH)_4(bdc)_6]_4$ atoms forming 4 octahedral (b) and 8 tetrahedral pores (c). Each sphere represents $Zr_6O_4(OH)_4(bdc)_6$ atoms, and the cube represents one unit cell. The images were created with Vesta or 3ds max based on the CCDC entry 1018045.

The zirconium-based MOF UiO-66 was discovered in 2009 at the University of Oslo (Universitet i Oslo), where its name stems from.[146] The framework consists of hexazirconium $Zr_6O_4(OH)_4^{12+}$ nodes, where the zirconium atoms occupy the corners of an octahedron and are alternatively bridged by μ_3-oxo and μ_3-hydroxy groups, which are centred on the faces of the octahedron. The inorganic hexazirconium-oxo node in combination with 12 carboxylic acid groups forms the secondary building unit (SBU) $[Zr_6O_4(OH)_4(COO)_{12}]$ of UiO-66. This molecular complex can be utilized in the transformation of this fragment into extended porous networks by using the ditopic bdc^{2-} linker. The resulting scaffold has a face-centred cubic (fcu) structure. Each unit cell contains $[Zr_6O_4(OH)_4(bdc)_6]_4$ atoms with four octahedral and eight tetrahedral cavities (see Figure 8).

Due to its exceptionally high connectivity and stability (strong Zr-O bonds), the framework is stable towards chemicals,[147–149] pressure,[150,151] and heat (up to 540 °C).[152] These properties make UiO-66 an interesting system for investigation resulting in 4037 publications until August 2020.[153] Besides other applications, UiO-66(Zr) is a convincing option for Lewis acid-catalyzed reactions, with good activities and reusability. It has thus been employed in esterifications,[154,155] in phosphodiester hydrolysis,[156–159] in cross-aldol condensations,[160,161] CO_2 fixation,[162,163] isomerizations[164,165] and for cyanosilylations.[166–168]

2.7. Motivation & Objective

The first part of my thesis is inspired by the goal to fabricate Zr-based metal-organic frameworks as thin-film coatings. Their broad application spectrum and exceptional stability towards temperature and chemicals make them interesting targets for thin-film coatings. As mentioned in the introduction, prior to my master thesis (in 2017) no Zr-based MOFs fabricated by LbL-LPE were reported. However, in 2017 Wannapaiboon *et al*.[46] implemented a new strategy to improve the film homogeneity, by adding one simple monotopic carboxylic acid, acetic acid, as a coordination modulator (CM) to the LbL deposition of the pyrazolate MOF Zn_4OL_3 (L: di-substituted carboxypyrazolates). The addition of acetic acid decelerated the growth rate. This study paved the way to crystallize MOFs with higher node connectivity. Therefore, the goal of my master thesis and part of my dissertation was to deposit Zr-based MOFs by CM LbL-LPE.

2.8. Highly Porous Nanocrystalline UiO-66(-NH_2) Thin Films via Coordination Modulation Controlled Step-by-Step Liquid-Phase Growth

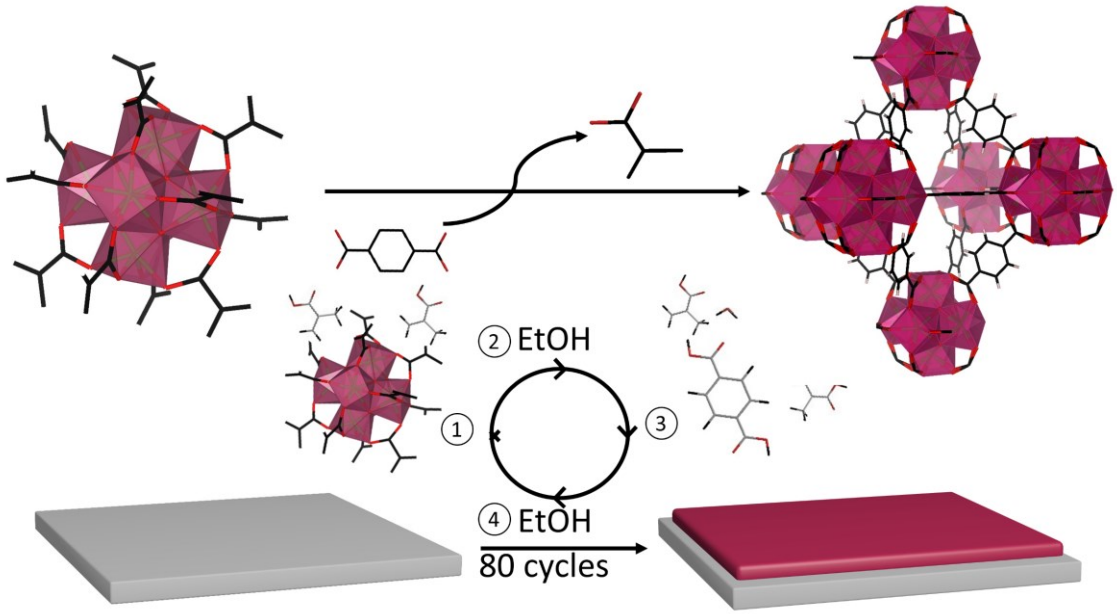

This chapter is based on two publications, which have been published by Crystal Growth Design and Chemistry-A European Journal:

A. Lisa Semrau, Suttipong Wannapaiboon, Sidharam P. Pujari, Pia Vervoorts, Bauke Albada, Han Zuilhof, Roland A. Fischer, Highly Porous Nanocrystalline UiO-66 Thin Films via Coordination Modulation Controlled Step-by-Step Liquid-Phase Growth, *Cryst. Growth Des*. **2019**, *19*, 1736-1747.

The project was designed by A. L. Semrau, S. Wannapaiboon, and R. A. Fischer. The experiments (powder synthesis, CM-LPE experiments) and most of the characterizations (IR, GIXRD, PXRD, Sorption experiments for the thin films) were performed by A. L. Semrau. Part of this work was performed in the context of A. L. Semrau's master thesis, which was supervised by S. Wannapaiboon. The progress was regularly discussed with S. Wannapaiboon and R. A. Fischer. P. Vervoorts measured and processed N_2 adsorption experiments. S. Wannapaiboon measured the EXAFS data at the Synchrotron Light Research Institute in Thailand and evaluated and fitted the data. S. P. Pujari contributed by measuring and processing XPS, AFM, SEM, and Auger Electron Microscopy (AES). The data (SEM, AFM, XPS, and N_2 adsorption) was analyzed by A. L. Semrau and discussed with all co-authors. The final manuscript was written by A. L. Semrau and edited by all co-authors.

A. Lisa Semrau, Roland A. Fischer, High-Quality Thin Films of UiO-66-NH_2 by Coordination Modulated Layer-by-Layer Liquid Phase Epitaxy, Chem.-A Eur. J., **2021**, *27*, 8509-8516.

The project was designed by A. L. Semrau. The experiments (powder synthesis, CM-LPE experiments) and the characterizations (IR, GIXRD, PXRD, XPS, sorption experiments for the thin films) were performed and analyzed by A. L. Semrau. The final manuscript was written by A. L. Semrau and edited by R. A. Fischer.

2.8.1. Zr-based SURMOFs: A Challenge

UiO-66 and in particular UiO-66-NH_2 thin films are focus areas of MOF-based membranes for desalination and nanofiltration applications. Different approaches are commonly used to produce these membranes such as the fabrication of mixed MOF membranes[169] or the deposition of a UiO-66-NH_2 thin film onto membranes. These can be done by directed/solvothermal growth.[170,171]. However, the quality of the UiO-66-NH_2 films is a key factor for efficient sieving of these membranes. Therefore, we tried to improve the thin film quality by employing LbL-LPE instead of the direct growth method.

LbL-LPE is a technique to fabricate surface-mounted metal-organic frameworks (SURMOFs), often with excellent thin-film quality. Nevertheless, LPE was so far limited to MOFs with lower connected nodes, typically tetra-connected di-nuclear paddlewheels. In our study, we employed LPE to fabricate nano-crystalline UiO-66(Zr) and UiO-66(Zr)-NH_2 ($Zr_6O_4(OH)_4(bdc(\text{-}NH_2))_6$ abbreviated as UiO-66(-NH_2)) thin films from $Zr_6O_4(OH)_4(OMc)_{12}$ (OMc^-: methacrylate) by ligand exchange with bdc(-NH_2). Several techniques were used to investigate the film morphology, nano-crystalline structure, sorption properties, and elemental composition of the fabricated thin films. Highly porous UiO-66 with 12-fold connecting nodes were previously hard to deposit by any liquid-based synthetic process. Our results provide a proof-of-concept of a systematic methodology, some insight into the deposition mechanism, and the importance of various deposition parameters to expand the scope of the LbL-LPE for the fabrication of higher connected MOF thin films.

One aspect, which will be discussed in detail is substrate activation for the deposition of UiO-66-NH_2 by CM-LPE. By ideal surface activation, crack-free, smooth thin films with a thickness of ~2.6 μm were fabricated in an ethanol-based coordination modulated liquid phase epitaxy process and have excellent thin-film quality as demonstrated by grazing incidence X-ray diffraction (GIXRD), X-ray photoelectron spectroscopy (XPS), scanning electron microscopy (SEM), atomic force microscopy (AFM), infrared spectroscopy (IR) and sorption experiments.

2.8.2. UiO-66 Powder Synthesis via the Controlled Secondary Building Unit Approach

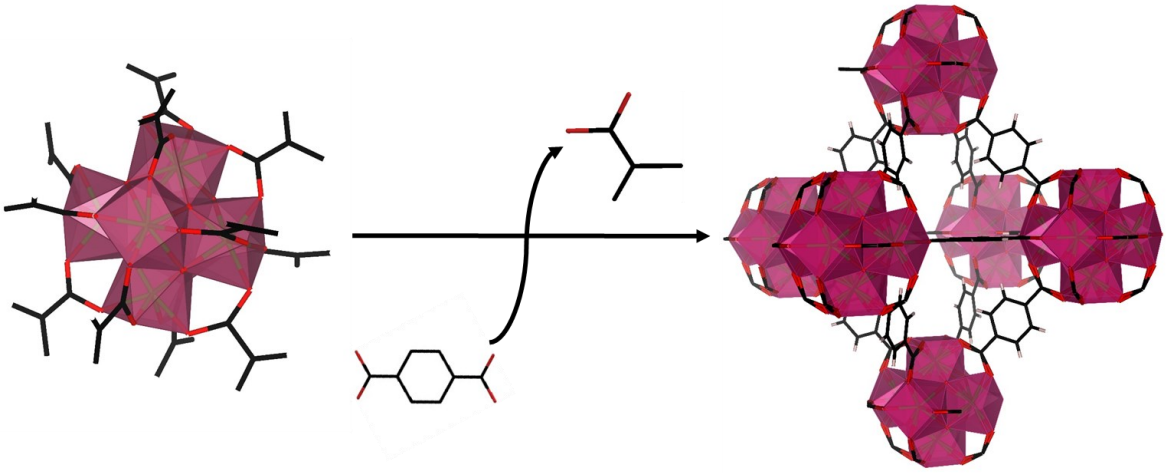

Figure 9: Schematic representation of the controlled secondary building unit approach (CSA). The preformed secondary building unit $Zr_6O_4(OH)_4(OMc)_{12}$ is reacted with the bdc linkers forming the fcu UiO-66 structure.

For the fabrication of UiO-66 thin films by LPE, we utilized the secondary building unit (SBU) $Zr_6O_4(OH)_4(OMc)_{12}$ as a metal source for the LPE. Based on this SBU, the formation of the UiO-66 thin films was attempted by ligand exchange of McO^- with bdc^{2-} which is referred to as the controlled SBU approach (see Figure 9). However, previously unpublished results from our group and other groups suggest that simple ligand exchange does not yield crystalline thin films, but rather amorphous, porous coatings. Due to this observation, we attempted the formation of crystalline UiO-66 thin films by the addition of methacrylic acid to the reaction mixture as a modulator.

Due to the various process parameters during the LPE process, the reaction conditions were first optimized for the UiO-66 solvothermal powder synthesis using the CSA. Specific emphasis was placed on the investigation of the influence of methacrylic acid (McOH) and water as reaction modulating additives. The results of these experiments are discussed in this chapter, while the next chapter deals with the transfer of these observations to the LPE process.

We started the optimization by using an ethanol-based solution with $Zr_6O_4(OH)_4(OMc)_{12}$ as the metal source and $H_2bdc(-NH_2)$ as a linker. These reaction conditions differ significantly from the solvothermal synthesis conditions reported for UiO-66 in literature, where mononuclear zirconium sources like $ZrCl_4$ or $ZrOCl_2$ are

utilized in DMF-based solutions with relatively harsh reaction temperatures of up to 220 °C. Additionally, acetic acid is added as a coordination modulator to control nucleation and crystal growth, improve the reproducibility of the synthesis, and optimize the crystallinity and crystal shape.[172] However, these reactions conditions are not suitable for the growth of a thin film by LPE.

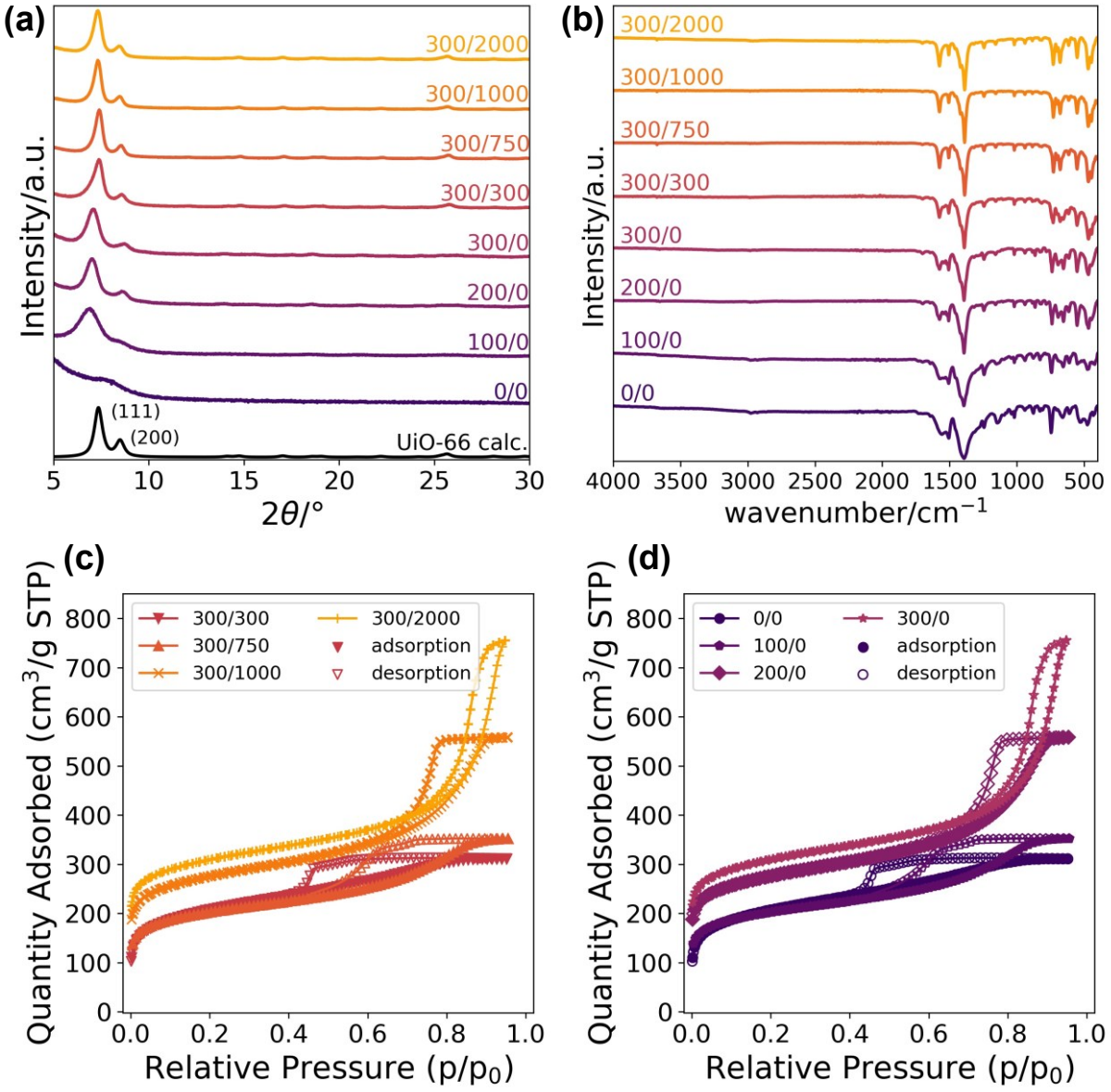

Figure 10: Characterization of the UiO-66 powders synthesized by CSA. PXRD (a), IR spectra (b), and nitrogen adsorption experiments (c,d) of UiO-66 powders synthesized via the controlled SBU approach with different amounts of methacrylic acid (0-300 equiv.) as a modulator and water (0-2000 equiv.) as an reaction additive, denoted as McOH equiv. /H_2O equiv.. The reference pattern of UiO-66 was calculated with Vesta using the single crystal structure (CCDC 733458, FWHM=0.5).

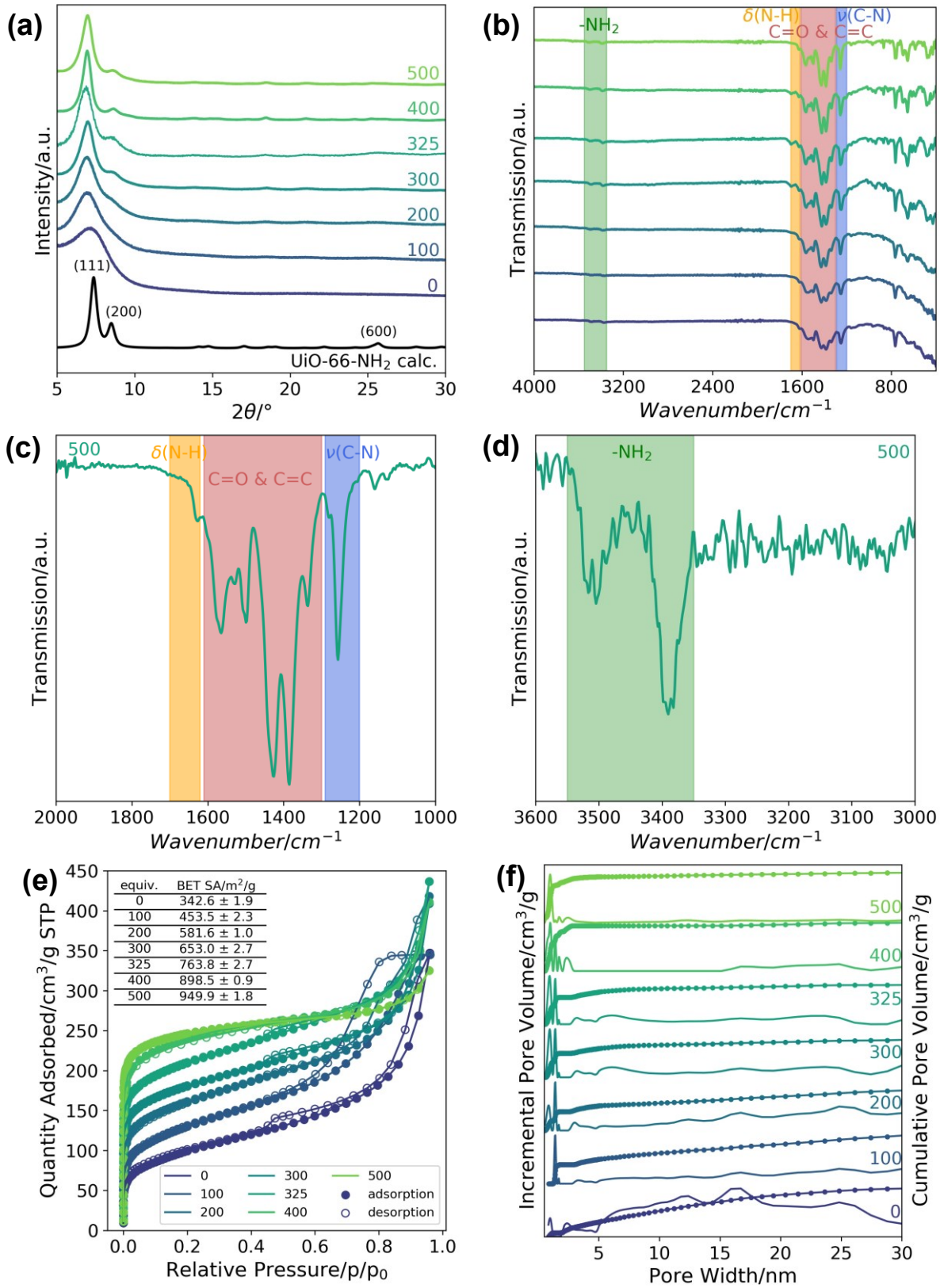

Figure 11: Characterization of UiO-66-NH_2 powders. Powder diffractograms (a), IR full spectra (b) and enlarged areas of the IR spectrum (c,d), and N_2 adsorption (e) and pore size distribution (PSD) (f) of dried UiO-66-NH_2 powders synthesized with 0-500 equiv. of methacrylic acid as a modulator. (a) The calculated powder pattern was simulated from the single-crystal structure of UiO-66-NH_2 (CCDC 1405751, FWHM(2θ)=0.5) with Vesta. (f) The scattered plot displays the cumulative pore volume, while the incremental pore volume is displayed by the continuous lines.

The high reaction temperature necessary for the formation of the $[Zr_6O_4(OH)_4]^{12+}$ are not needed for the CSA approach as the cluster is already pre-formed. The synthesis of UiO-66 with the Zirconium oxo cluster $[Zr_6O_4(OH)_4(OMc)_{12}]$ as a metal source was already reported by Feréy and co-workers in DMF at 100 °C.[173] Due to the slow crystallization in DMF and the environmental impact we used ethanol-based solutions instead.

Experimentally, $[Zr_6O_4(OH)_4(OMc)_{12}]$ and $H_2bdc(-NH_2)$ were both dissolved in ethanol separately and 0-300 molar equivalents of McOH were added to the $[Zr_6O_4(OH)_4(OMc)_{12}]$ solution, while 0-2000 equiv. H_2O were added to the $H_2bdc(-NH_2)$ solution. Finally, the solutions were combined and placed in an oven for 24 h. Afterwards, the powders were washed three times with ethanol and activated at 150°C in an oil pump vacuum. Subsequently, the powders were investigated by PXRD, IR, and BET measurements (Figure 10-11). In the following the UiO-66 samples are displayed in colours from lilac to yellow (colourmap inferno), the UiO-66-NH_2 samples are displayed in colours from violet to green (colourmap viridis).

Unfortunately, the direct reaction of $Zr_6O_4(OH)_4(OMc)_{12}$ and $H_2bdc(-NH_2)$ yielded an amorphous, yet porous powder (BET: 757 m^2/g(UiO-66)/342.6 m^2/g(UiO-66-NH_2)) as described before. This indicates that the structure, even though it does not contain a highly ordered, repetitive motif, probably still contains a similar coordination environment and short-range order as the UiO-66 structure. To enhance the reversibility of the ligand exchange and enable the slower formation of a crystalline, porous 3D UiO-66-NH_2 MOF, the addition of McOH as a modulator was necessary. The samples are denoted with the molar equivalents of modulator and water, if added, in relation to $Zr_6O_4(OH)_4(OMc)_{12}$, which were added to the reaction solution Upon the addition of McOH to the reaction mixture, the crystalline domain size, expands, which can be observed in the PXRD as the reflections sharpen. The CDSs were calculated by the Scherrer equation (see chapter 3.3.3) with FWHM of the 111 reflection and can be found in Table 2 for the UiO-66 samples. The addition of 300 equiv. of McOH yielded nanocrystalline, highly porous (1149 m^2/g) UiO-66 powders. In difference to UiO-66, the addition of water did not enhance the formation of UiO-66-NH_2, therefore no water was added. Another difference was that the formation of UiO-66-NH_2 required higher amounts of modulator, probably due to the protonation of the amino group. For 500 equiv. of McOH a CDS of 11 nm and a BET surface of 949 m^2/g was observed.

Finally, the N_2 adsorption isotherms (Figure 10 c-d-Figure 11 e) of the UiO-66(-NH_2)powder samples display that the isotherms' shape as well as the BET surface area changes with increasing modulator concentration. The UiO-66-NH_2 samples **0** and **100** (synthesized with either 0 or 100 equiv. McOH) exhibit a type II or type IV isotype, corresponding non-porous/macroporous or mesoporous samples, respectively. The same phenomenon is observed for all UiO-66 samples, indicating the formation of mesopores. However, the UiO-66-NH_2 samples **300**-**500** feature a typical

type I isotherm with minor contributions from a type II isotherm, which confirms the micro-porosity of the powders. The calculated pore size distributions (PSDs, Figure 11 f) depict the same trend as observed from the analysis of the isotherms. The amount of macro- and mesopores is decreasing with an increasing modulator amount. Thus, larger (equivalent) BET surface areas were calculated for samples with higher modulator concentrations. The highest BET surface area (949.9 ± 1.8 m^2/g) within the series was **500**. This obtained BET surface area is in line with the intermediate range of surface areas reported for UiO-66-NH_2 reference samples obtained by high temperature and high-pressure solvothermal synthesis, which range from 675 m^2/g[147] up to 1250 m^2/g[174] with most reported values around 1000 m^2/g.[175–177] and optimized synthetic protocols for UiO-66 (*e.g.* protocol A:[178] DMF, H_2O, 120 °C, 24 h: 1069 m^2/g; protocol B:[179] DMF, H_2O, 120 °C, 72 h: 1158 m^2/g), and with theoretical expectations (1290 m^2/g)[180].

Table 2: Specific surface areas (BET) and crystalline domain sizes (CDS) of UiO-66 powders synthesized with different molar equivalents of McOH and water.

McOH/H_2O	**0/0**	**100/0**	**200/0**	**300/0**	**300/1000**	**300/2000**
BET Surface area/ m^2/g	757	749	1018	1149	1234	1237
CDS/nm	-	-	12.0	11.6	21.2	22.4

The addition of water to the process in the case of UiO-66, alongside the addition of methacrylic acid, seems to expand the CDS further and additionally increase the BET surface area from 1149 to 1237 m^2/g. Mechanistically, the water probably acts as a base, thereby enhancing the CSD and the BET surface area.

The IR spectra (Figure 10 b-Figure 11 b-d) display that the peaks at 1200 and 1660 cm^{-1} sharpen upon the addition of methacrylic acid to the synthesis. These vibrations originate from the asymmetric and symmetric stretching of the C=C and carboxylic acid bonds. The distance between the C=O stretching peaks corresponds to the coordination mode of the carboxylate linker to the Zr-oxo node.[60,181] For low amounts of modulator the coordination mode of the carboxylate at the Zr node is not well defined and shifts to a predominately bridging coordination mode at higher concentrations of the modulator, as displayed by the sharpening of the peaks in the IR spectra. In the UiO-66(-NH_2) spectra an additional -NH_2 vibration is visible.

Furthermore, the UiO-66 powders were synthesized with 0-400 equiv. of McOH were investigated by EXAFS (Zr K-edge) to explore their local coordination environment. After the measurement, the obtained spectra were fitted and analyzed (see appendix Figure S11-S16, Table S5). The fitted spectra of all powder samples indicate that the material exhibits a similar local coordination environment of Zr as in the reported single-crystal XRD data of UiO-66 (CCDC 733458). However, a site splitting is

observed for the first shell data in R-Space of the EXAFS data, after the addition of more than 200 equiv. of McOH to the reaction mixture. This can be attributed to a different shift of the O species in the first shell (the distance from Zr centre of the O atoms of the O^{2-} and OH^- is shortened whereas the one the of bdc linker is elongated).[182] This indicates that after the addition of more than 200 equiv. of McOH the resulting powder shows a distinct long-range order which was not present in the samples synthesized with lower concentrations of the modulator. This is supported by the observation, that this phenomenon is only observed when the UiO-66 powders are highly crystalline. Overall, the EXAFS measurement support and highlight the results which were obtained from PXRD: the addition of small amounts (0-200equiv.) of McOH yield porous, amorphous coating, with short-range orders and the addition of higher modulator concentrations (300-400 equiv.) enables the formation of crystalline UiO-66 powders with long-range orders.

Summing up the results of these experiments with the UiO-66(-NH_2) powders, it is evident, that the addition of 300 equiv. of McOH in case of UiO-66 and 325-500 equiv. of McOH in case of UiO-66-NH_2 to the rection solution yields nanocrystalline and porous UiO-66(-NH_2). The share of macro- and mesopores is decreasing with an increasing modulator concentration, whereas the CDS increases. At a first glance, this might be counterintuitive due to the numerous reports on defect engineering in MOFs. They report the utilization of modulators as a tool to target defective structures and in turn e.g. increase their catalytic activity. However, the employed controlled SBU approach differs a lot from the solvothermal synthesis conditions employed for the defect engineering approach. Due to the fast, but incomplete exchange of McO^- ligands by bdc-NH_2^{2-} ligands, high modulator concentrations are needed to reduce the reaction speed and precipitation. Finally, we conclude that the use of 325-500 equiv. of methacrylic acid as a modulator is a suitable parameter window for CM-LPE experiments.

2.8.3. UiO-66 SURMOFs by Coordination Modulated Liquid-Phase Epitaxy

After successful optimization of the UiO-66(-NH_2) powder synthesis reaction parameters yielding crystalline, porous powders, we tried to transfer this approach to the LPE deposition protocol – starting with UiO-66. While the optimization of the process parameters for the powder synthesis was a useful tool to narrow the parameter window for the LPE, it should be noted, that due to the significant differences in the process the powders and films synthesized with similar amounts of McOH cannot be compared directly.

While a lot of parameters were investigated, we will discuss in this chapter mainly the influence of the reaction modulating additives water and methacrylic acid. However, a comprehensive table and more details can be found in my master thesis. The CM-LPE process required further optimization of the process parameters, which included the temperature, the immersion times, the number of deposition cycles, the substrate, substrate activation protocol, the concentrations of the preformed SBU, linker, McOH, and water.

Thus, we develop the following protocol: Initially, native silicon dioxide substrates were activated by UV light generated O_3 for 30 min. The Si/SiO_2 substrates were placed in a double-walled temperature-controlled vessel (40 mL) and the vessel was set at isothermal conditions of 70 °C. Peristaltic pumps operated by LabView were used to immerse the substrate to the zirconium methacrylate cluster and the linker solution in an alternating fashion for 10 min in each step. In between the steps, the substrate was rinsed with ethanol for 5 min. The McOH was added to both solutions, the Zr methacrylate cluster, and linker solution, whereas the water was only added to the linker solution due to the instability of the Zr methacrylate towards water forming ZrO_2.

The resulting thin films were investigated by GIXRD, IR spectroscopy, XPS, methanol adsorption experiment, SEM, and AFM.

Crystallinity. The out of plane GIXRD diffractograms were recorded for thin films fabricated with various amounts of McOH and water as reaction

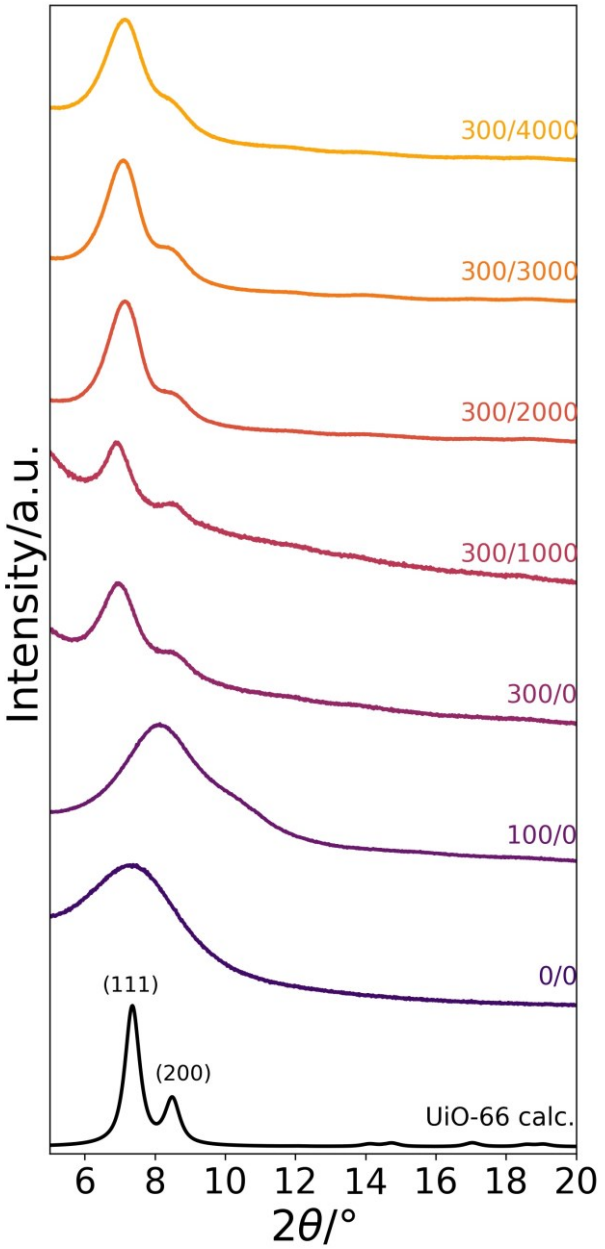

Figure 12: Out of plane GIXRD pattern recorded UiO-66 thin films fabricated by CM-LPE with methacrylic acid (0-300 equiv.) as a modulator and water (0-4000 equiv.) as an reaction additive, denoted as McOH equiv. /H_2O equiv.. The reference pattern of UiO-66 was calculated with Vesta using the single crystal structure (CCDC 733458, FWHM=0.5).

modulating additives (Figure 12). The GIXRD pattern for the thin film fabricated without any modulator displays no reflections indicating its amorphous structure. Upon the addition of more McOH, the formation of (broad) reflections can be observed. The largest CDS was observed after the addition of 300 equiv. McOH and 1000 equiv. of H_2O. It should be noted that the addition of 300 equiv. McOH to both solutions, instead of just the Zr source of linker solution resulted in significantly enhanced thin films.

The FWHM for the 111 reflection is between 1.27457° (for 300 equiv. McOH /4000 equiv. H_2O) and 0.7812° (300 equiv. McOH/1000 equiv. H_2O), and corresponds to a crystalline size of 6.2 and 10.2 nm according to the Scherrer equation, respectively. As opposed to the powder formation, we observe that for the thin film formation the addition of large amounts (2000-4000 equiv.) of water are not beneficial. Small amounts, however, can still increase the CDS. The additional investigation of the thin-films via EXAFS was not possible due to the limitation of the X-ray absorption spectroscopy (XAS) experimental set-up being operated in the transmission mode, which is not suitable for the targeted samples on non-transparent substrates like Si/SiO_2.

Elemental composition and defects. The elemental composition and defect content of the thin film was analyzed by XPS spectroscopy (Figure 13). Therefore, we recorded

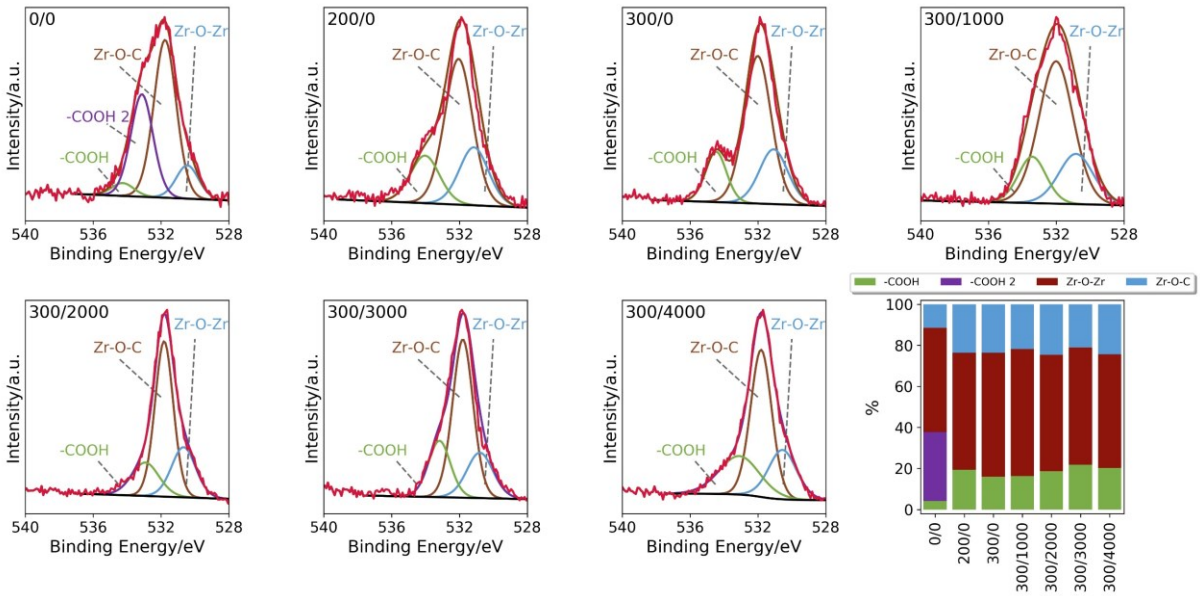

Figure 13: O 1s narrow scan XPS spectra (a-g) recorded from UiO-66 thin films grown with different amounts of methacrylic acid (0-300 equiv.) and water (0-4000 equiv.) applied the CM-LPE process, denoted as McOH equiv./H_2O equiv. in the right corner of the XPS spectra. The deconvoluted species can be assigned to dangling carboxylic acid groups (-COOH, green), Zr bound oxo groups (Zr-O-Zr, blue), carboxylic acid groups coordinated to the Zr atoms (Zr-O-C, brown), and non-coordinating carboxylic acid in a bridging mode (-COOH 2, lilac) (h) Integrated areas of the deconvoluted species in the O 1s narrow scans, coloured in the same colours as in the corresponding spectra.

the survey scan, and narrow scans of the O 1s, C 1s, and Zr 3p of all thin films (Figure S17-S23). While most of the samples contain similar amounts as calculated for the ideal UiO-66 (6.98 at% of Zr, 37.21 at% of O, and 55.81 at% of C), the 0/0 thin film sample has considerably lower zirconium and oxygen content. This can be ascribed to a higher amount of linker loading or to the remaining McOH coordinated to the cluster. Additionally, carbon contamination might lower the measured Zr and O content. According to Wang et al.[182], the O1s narrow scans can be evaluated to determine the amount of free carboxylic acid groups in the MOF. Free carboxylic acids (green) exhibit higher oxygen binding energies compared to the zirconium-bound carboxylate groups (brown); for an analogous comparison of O1s energies see Carvalho *et al.*[183] and Wang *et al.*[182]

Therefore, the number of defects can be calculated. In an ideal, infinite UiO-66 crystal the amount of free –COOH linkers would be 0 %. Assuming the total number of linkers contains the free dangling carboxylic acid groups and the bridging linkers the integrated peaks (PI) can be used to calculate the assumed sum formula:

$$PI\ (Linker) = PI\ (-COOH) + PI\ (Zr - OOC)$$

$$at\ \%\ (-COOH) = \frac{PI\ (-COOH)}{PI\ (Linker)}$$

$$at\ \%\ (Zr - OOC) = \frac{PI\ (Zr - OOC)}{PI\ (Linker)}$$

e.g. for 300 equiv. of McOH the integrated areas are –COOH: 16.0 % and Zr-OOC: 60,3 %.

The film synthesized with 300 equiv. of McOH has 20.9 % of free carboxylic acids and 79.1 % of bridging carboxylic acids. The addition of water to the fabrication of the UiO-66 thin-film leads to an increase of free carboxylic acids (26.9 % for 4000 equiv. of water). The fourth deconvoluted species (lilac) is observed in the thin-film fabricated without a modulator. This could originate from non-coordinating carboxylic acid in a bridging mode (IR, see below). The presence of Si in the thin films seemed surprising due to the surface sensitivity of the XPS method. However, as evident by SEM imaging (SEM, see below) suggested the substrates were not fully covered by UiO-66.

Morphology and thickness. The morphology and thickness of the thin films were studied by SEM (Figure 14-15 and Figure S24-S30), AFM (Figure S31-S37), and Auger spectroscopy (Figure 16). The morphology of the thin films reveals that the films are not homogenously covered, but rather an island structure with non-covered bare silica areas is observed. Depending on the modulating additives the observed islands differ significantly in size. While the addition of 300 equiv. of McOH leads to the formation of islands with a diameter of ~2 μm, the further addition of 3000 equiv. of water leads

to rather large islands (diameter: ~15 µm). Despite the rather small islands observed for the 300/0 thin film, it was still the film with the least non-covered areas. Further investigations by Auger spectroscopy were made, to elucidate the nature of the non-covered areas (Figure 16). The highly surface sensitive method revealed that the bare areas indeed mainly consist of SiO_x (Si, O, and C (carbon contamination)), whereas the islands mainly consist of C, O, and Zr.

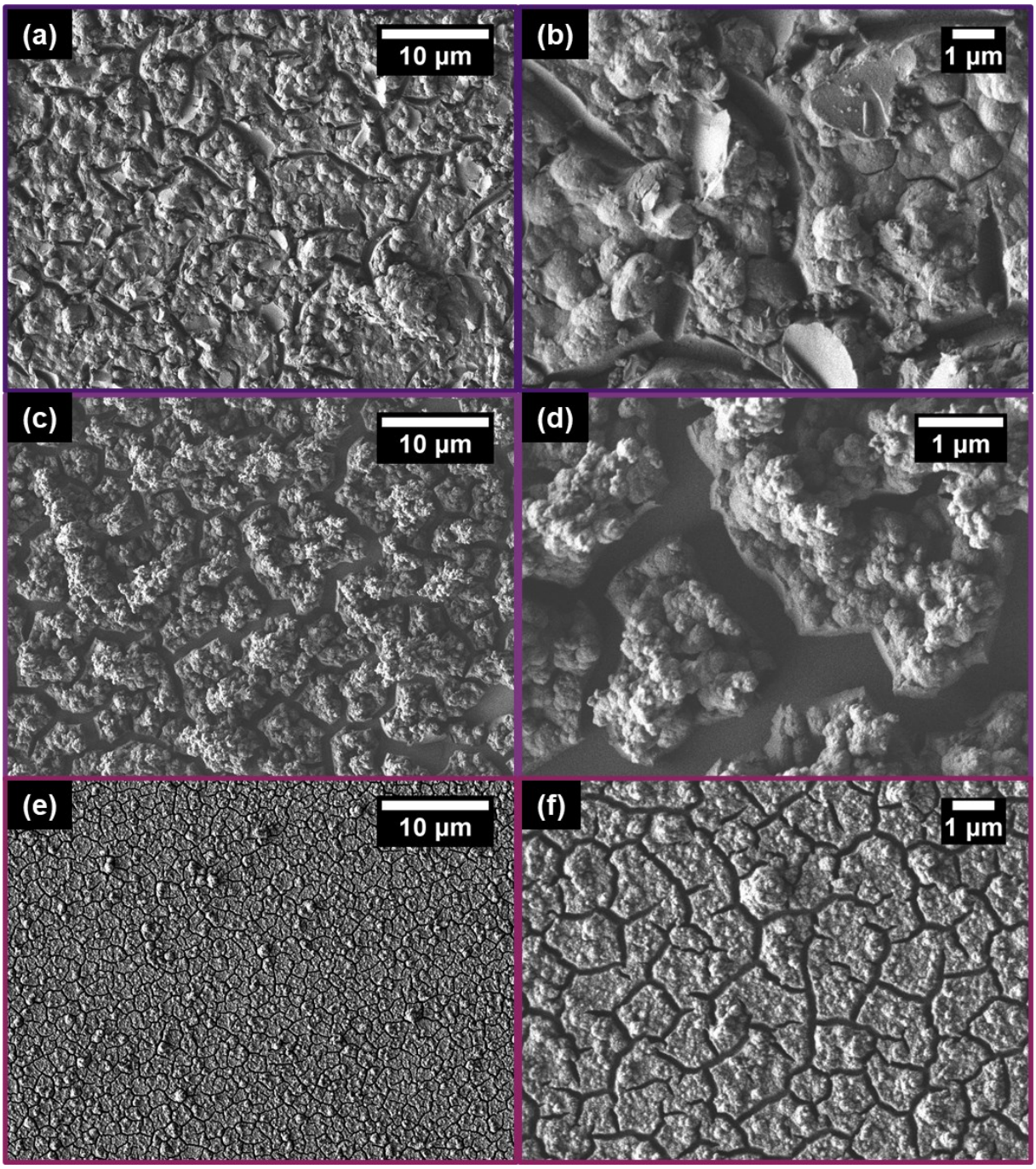

Figure 14: SEM images of UiO-66 thin films fabricated by CM-LPE with 0 equiv. (a,b), 200 equiv. (c,d), and 300 equiv. (e,f) of methacrylic acid as a modulator.

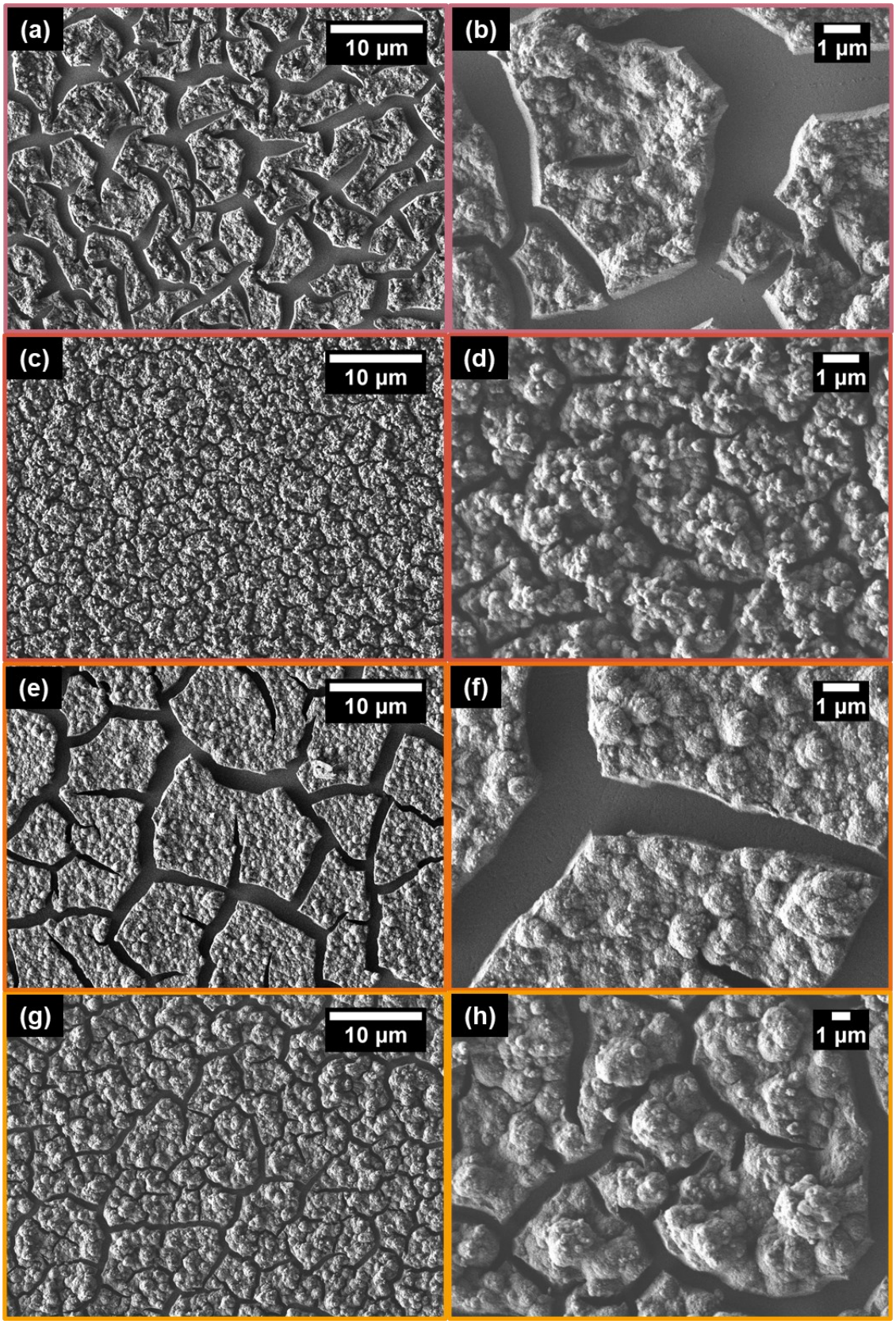

Figure 15: SEM images of UiO-66 thin films fabricated by CM-LPE with 300 equiv. of methacrylic acid as a modulator, and 1000, 2000, 3000, and 4000 equiv. of water as an additive.

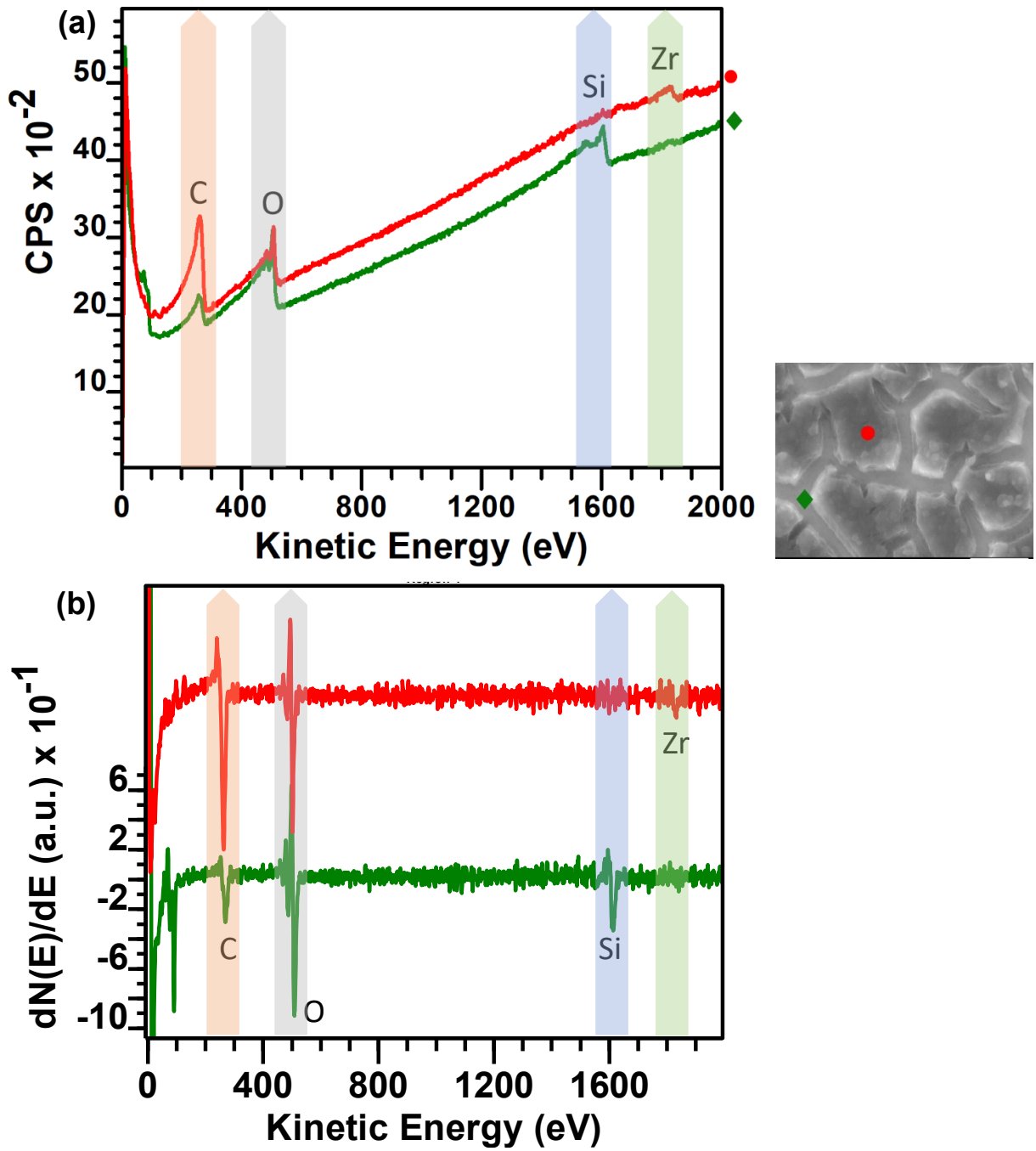

Figure 16: Auger spectroscopy of the activated UiO-66 thin-film fabricated by CM-LPE with 300 equiv. of McOH as modulator marked with C-KLL (263 eV), O-KLL (502 eV), Si-KLL (1610 eV), and Zr-LMM (1830 eV): (a) without differentiated [N(E)], and (b) with differentiated [dN(E)/dE]. SEM image shows that spot on UiO-66 thin-film are (red) and silicon area (green). This Figure was taken from Semrau, *et al.*[59] permission from ACS Crystal Growth & Design. Copyright (2019) American Chemical Society.

While the island growth mode is observed for many thin films, including SURMOFs, partial substrate coverage for UiO-66 is not reported as often. There are some possible explanations: (i) Due to the long initiation period of the thin film deposition, which is further discussed later, an inhibited nucleation at the Si/SiO_2 substrate due to the lack of active binding functional groups on the substrate surface is observed. (ii) The low solubility of H_2bdc in ethanol, which enhanced the island formation further. (iii) The formation of cracks during the activation procedure before the SEM measurements or the high vacuum in the SEM chamber. The formation of dense, fully covered thin-films should be possible if the nucleation process is optimized for a more thorough substrate activation, modification, or via the choice of different and more nucleation active substrates (see chapter 2.8.4).

Finally, due to the island structure of the thin films, the AFM amplitude plots could be used to determine the average thickness of the UiO-66 thin films which are listed in Table 3. The considerable decrease in the thickness of the coating after the addition of McOH can be explained by the etching effect of an additional modulator in the solutions. The addition of water as a base, however, leads again to a significant increase in thickness. The mechanism of the thin film formation and further analysis of the function of water and McOH is discussed below.

Table 3: Average thickness of UiO-66 thin-films determined by AFM and deposited mass measured by QCM.

McOH/H_2O	**0/0**	**200/0**	**300/0**	**300/1000**	**300/2000**	**300/3000**	**300/4000**
Average Thickness /nm	744	390	82	312	361	425	678
Deposited Mass/ng	33200	25900	9700	9800	22900	29100	30500

Porosity measurements. To determine the porosity of the UiO-66 thin films, we measured the mass-specific methanol adsorption capacity with a quartz crystal microbalance (QCM). Therefore, special electrode contacted quartz substrates with various top coatings such as Au, SiO_2, or Ti are used. Due to the piezoelectric effect, the application of a voltage to this quartz crystal will induce oscillations. By applying an alternating current between the electrodes, a standing shear wave is generated. The frequency of the shear wave is altered by the adsorption or desorption of species at the surface of the quartz crystal, which is exploited by the QCM technology for sensing. According to the Sauerbrey equation, the direct connection between the change in the oscillation frequency and the mass can be described as:

$$\Delta f = \frac{2f_0^2}{A\sqrt{p_q \mu_p}} \Delta m$$

Where Δm is the mass difference, Δf is the resonance frequency difference, f_0 is the initial resonance frequency, μ_q is the shear modulus (2.947 10^{10} kg m^{-1} s^{-2}), ρ_q is the density of quartz (2648 kg m^{-3}), and A is the piezo-electrical active area. If average parameters are applied, the frequency change of 1 Hz equals ~1 ng.

For the methanol sorption experiments, UiO-66 thin films grown on QCM substrates with a SiO_2 top coating were introduced to a sealed QCM adsorption chamber and exposed to various relative methanol pressure while the oscillation frequency was recorded. Thereby, the relative uptake of methanol is recorded for the different samples (Figure 17). By comparing their MeOH uptake, it becomes clear that their adsorption capacity depends significantly on the applied CM-LPE conditions. The thin-films with the largest crystalline domain sizes (McOH/H_2O: 300/0 equiv. and 300/1000 equiv., respectively) adsorb about 3.6 mmol/g of methanol (MeOH), while the thin-films fabricated with higher amounts of water (1000 equiv.) adsorb up to 6.6 mmol/g. As reference material to compare the obtained values to an ideal UiO-66 sample, we used solvothermal synthesized UiO-66 (**UiO-66-HCl**), which was dispersed ethanol and drop cast onto a QCM substrate. **UiO-66-HCl** exhibits a similar adsorption capacity (3.5 mmol/g) as the 300/0 and the 300/1000 sample.

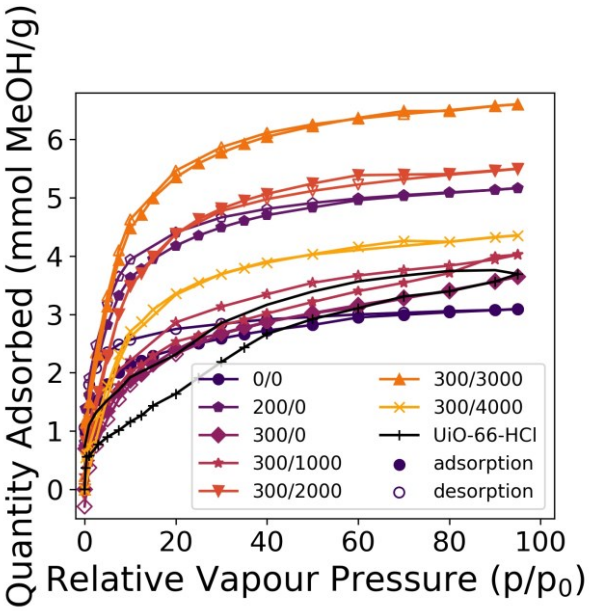

Figure 17: Methanol adsorption of UiO-66 thin films fabricated with 0-300equiv. of McOH and 0-4000 equiv. of H_2O, denoted as McOH equiv./H_2O equiv. The adsorption and desorption are shown in solid and open symbols, respectively.

For the fabrication of thin films, the addition of water to the process seems to boost the adsorption capacity. Even though a similar trend was observed for the powder samples for N_2 adsorption the relative increase is quite different. While the BET area increases about 7% upon the addition of 2000 equiv. of water, the MeOH uptake doubles. This boost in adsorption capacity can be ascribed to the combination of structural defects in UiO-66 structure, the increased roughness of the films, and the small primary crystalline domain sizes. Additionally, residual water, which was not removed during the activation procedure can cause an increased adsorption capacity of the samples, if exchanged with methanol during the adsorption process.

CM-LPE mechanism. So far, we observed that the morphology, adsorption capacity, defect content, and crystallinity correlate to the amount of methacrylic acid and water applied in the fabrication of the thin films. In particular, the addition of McOH facilitates the formation of smoother islands and more densely packed films (higher surface coverage), as well as a reduction in the thin film thickness. The addition of water, however, increases the deposited mass and thickness. These observations coincide with the following mechanistic considerations: during UiO-66 thin-film growth, the dissolved methacrylate-capped zirconium cluster binds to the substrate surface (HO-S).

$$Zr_6O_4(OH)_4(OMc)_{12}+HO\text{-}S \rightleftharpoons [Zr_6O_4(OH)_4(OMc)_{11}]O\text{-}S + McOH \quad (1)$$

$$H_2bdc + H_2O \rightleftharpoons H_3O^+ + Hbdc^- \quad (2)$$

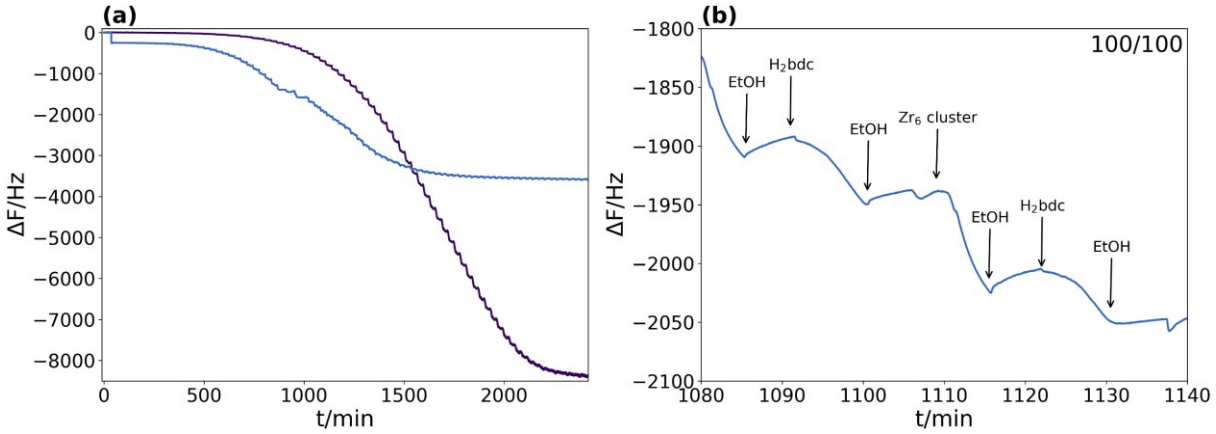

Figure 18: QCM oscillator frequency (ΔF) as a function of time during the fabrication of UiO-66 thin-films on Si/SiO_2 substrates at 40 °C using different amounts 100 equiv. McOH and 0 (lilac), 100 equiv. (blue) of water as an additive.

Upon binding of the Zr-oxo-cluster to the surface, McOH is released involving a proton-coupled coordination equilibrium. Therefore, additional McOH (as a modulator) shifts the equilibrium towards the dissolved cluster, resulting in a reduced nucleation density and crystal growth efficiency. However, the etching of loosely bound and probably disoriented or less connected clusters improves the thin-film quality. The control of these equilibria enables the formation of highly crystalline UiO-66 thin-films.

A detailed analysis of the growth mechanism was achieved by the in-situ monitoring of the thin film growth by QCM microbalance (see Figure 18). Due to the restrictions of the instrument, the measurements were conducted at 40°C instead of 70°C. Despite the different conditions, we are confident that the observed mechanistic details are valid for higher temperatures as well.

It can be observed that the oscillation frequency of the quartz crystal decreased with the number of cycles, which correlates to a mass increase (thin film growth) on the

substrate surface. In detail, the immersion of the film in Zr-oxo-Cluster solution and terephthalic acid corresponds to a mass increase, whereas the rinsing with ethanol decreases the mass on the surface, which is important for the CM-LPE process. The addition of McOH to the reaction solution prolongs the initial nucleation period (up to 900 min), during this time no significant mass gain is detected. The addition of water to the CM-LPE process reduces the initial nucleation period, facilitating a faster MOF formation. Nucleation is followed by rapid growth and a stationary plateau is observed at long deposition times and a large number of cycles (> 2000 min). The stationary plateau at the end can be ascribed to the formation of powder-like structures on the surface. The investigations of the resulting films by PXRD and MeOH adsorption show that the films are amorphous yet porous. This can be ascribed to the different temperatures (40°C instead of 70°C).

Kinetically favourable polymorph. The investigation of the thin film formation at different temperatures reveals fascinating results. After the addition of 100-200 equiv. of McOH the formation of another phase is observed (see Figure 19). At the time of the publication of this chapter in Cryst. Growth Des., this phase could not be assigned to the other literature known UiO-66 polymorphs, like the reo-UiO-66 structure.[184] However, since then two publications were published which described another, kinetically stable UiO-66 phase namely EHU-30.[185,186] For the formation of EHU-30, they applied similar conditions: H_2bdc as the linker, $Zr(OPr)_4$ as the metal source, and McOH as a modulator. They observed a $Zr_6O_4(OH)_4(COO)_{12}$ SBU connected by twelve phenyl linkers to the eight surrounding clusters, leading to an 8-connected uni nodal three-dimensional net with a hexagonal primitive topology (hex) and a (3^6•4^{18}•5^3•6) point symbol, while in UiO-66 each SBU is 12-connected into a fcu-type net (see Figure 20). This structure is especially observed with methacrylic acid as the modulator, as contains extremely strained bdc linkers, which is templated by methacrylic acid as a modulator. Due to

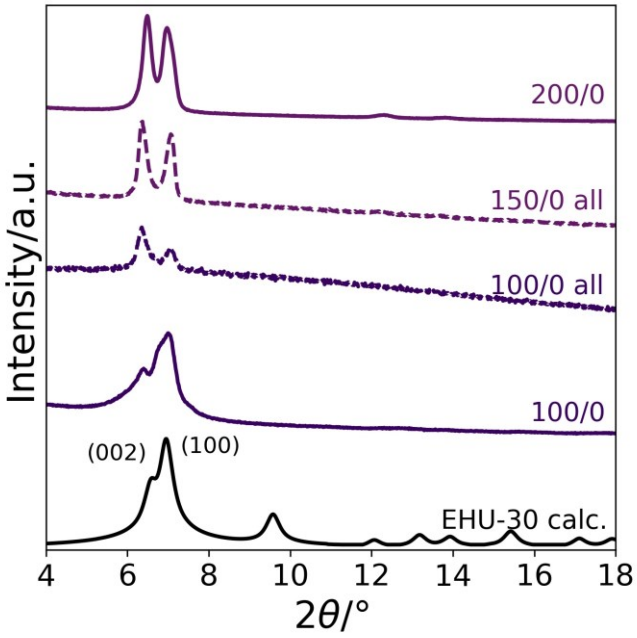

Figure 19: Out of plane GIXRD patterns of EHU-30, fabricated at 60°C with 100-200equiv. of McOH as modulator applied to the H_2bdc and Zr -oxo-cluster solutions or to all solutions. The reference diffraction pattern was calculated from the single crystal structure of EHU-30 (CCDC 1894173, FWHM=0.3).

this stain, the structure is only kinetically favorable. By the reduction of the reactant concentrations or by the addition of water to the reaction mixture the formation of UiO-66 instead of EHU-30 is observed. Additionally, EHU-30 can be transformed into UiO-66 by heating to 100°C in DMF for several hours. Due to the similar reaction conditions and matching of the grazing incidence diffraction pattern, the so-far unidentified phase is probably EHU-30.

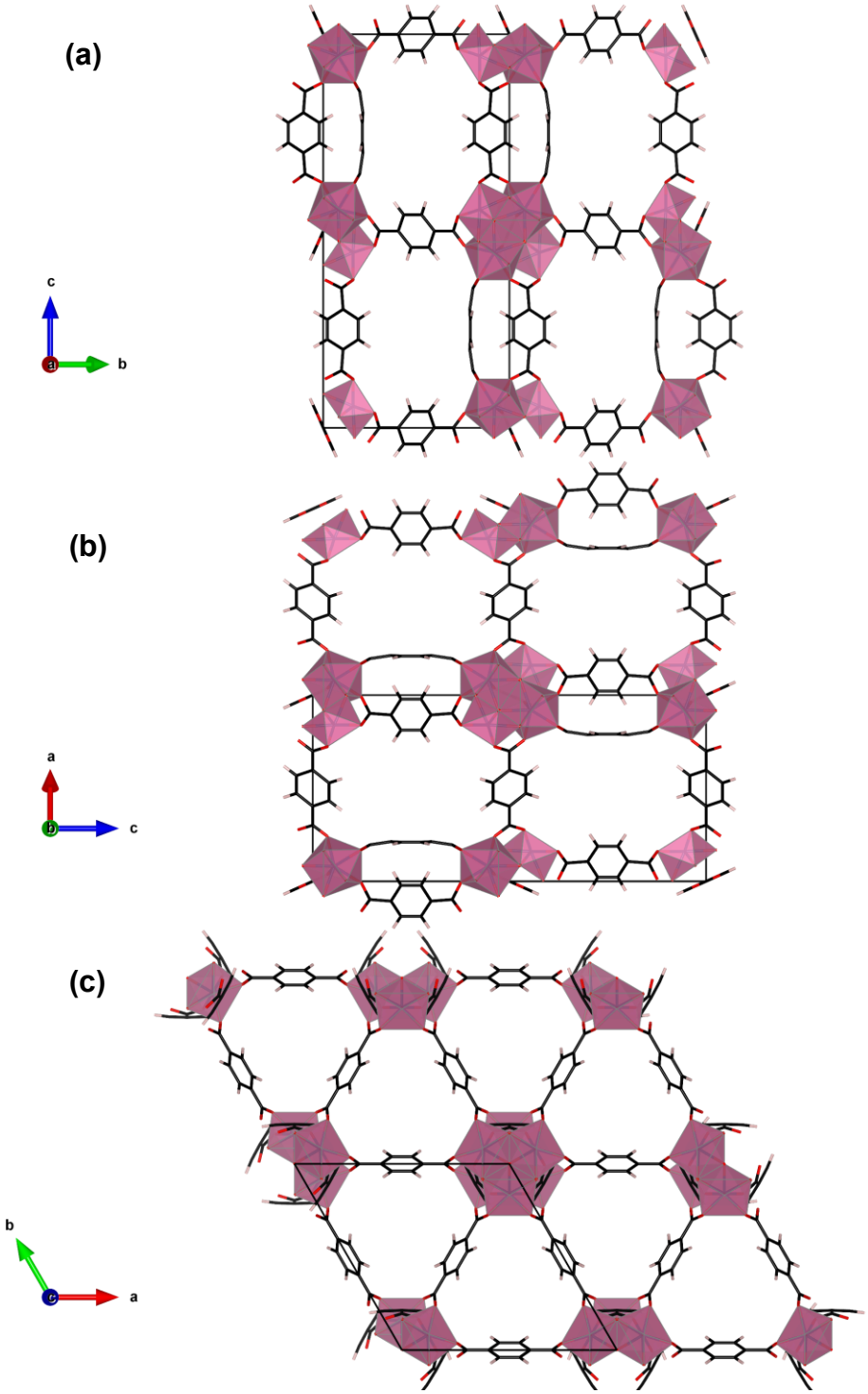

Figure 20: Structure of EHU-30 with the $Zr_6O_4(OH)_4(RCOO)_{12}$ SBUs and bdc as organic linker shown along the a (a), b (b) and c (c) axis.[185,186]

Coordination mode of H_2bdc in UiO-66 films obtained by CM-LPE. IR spectra were measured to examine the binding mode between bdc^{2-} and the SBU. In this context, Verpoort *et al*.[181] investigated the coordination mode between carboxylates and metals. They observed that the difference between the symmetric stretching vibration at 1400 cm^{-1} and the most prominent peak between 1500-1700 cm^{-1}, correlating to the asymmetric stretching vibrations, reveal the coordination mode of the carboxylate to the metal. The difference of the two bands can therefore be used to distinguish between a monodentate (>200 cm^{-1}), bidentate (50-150 cm^{-1}), or bridging (130-200 cm^{-1}) coordination mode of the bdc linker to the metal (Figure 21).

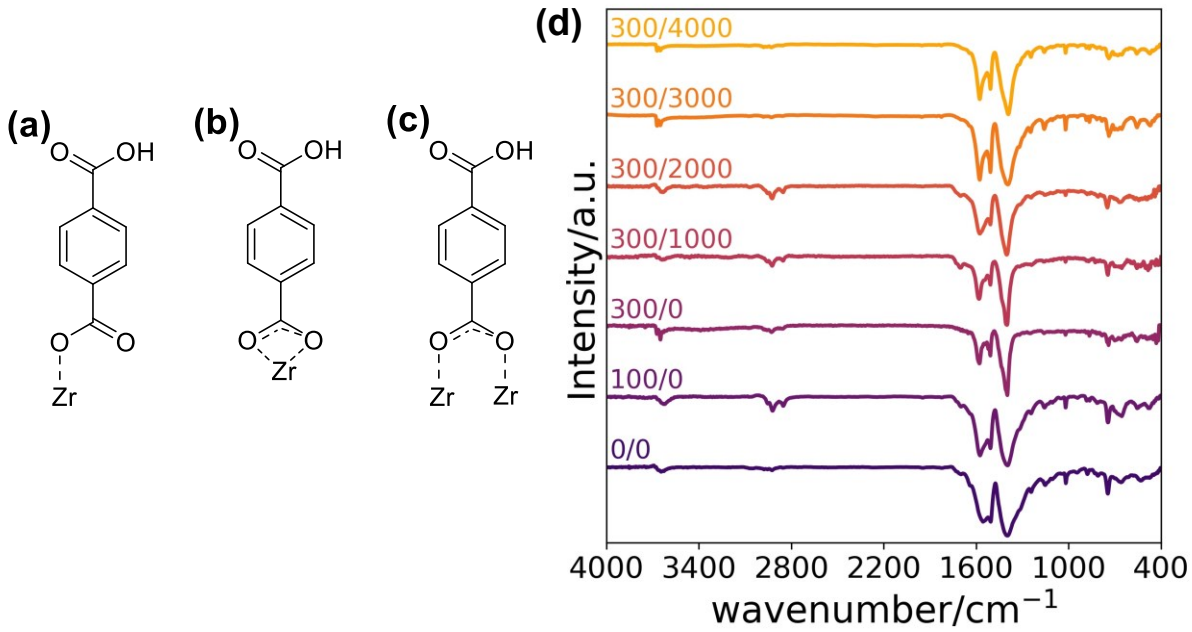

Figure 21: (a-c) monodentate (a), bidentate (b), and bridging (c) coordination mode of the bdc linker to the Zr cluster. (d) IR spectra of the UiO-66 thin-films fabricated with various molar ratios of McOH and water in respect to the amount of the metal SBU.

By comparing the IR spectra with an increasing amount of McOH and water it becomes evident that the IR band around 1400-1600 cm^{-1} sharpens. This observation can be correlated to a less diverse coordination mode between the metal and linker. The broader peaks of the samples **0/0** and **0/200** can be ascribed to different coordination modes at the same time, which agrees with the XPS results. All in all, the IR spectra confirmed that the CM-LPE fabricated films **300/0-300/4000** exhibit the expected bridging coordination mode.

Comparison with literature results. The range of methods to deposit UiO-66 thin films on various substrates have been explored in the past (Table 4). So far, the UiO-66 thin film fabrication has been reported by electrochemical deposition, solvothermal/direct deposition, ALD, and VAC. In comparison to these other UiO-66 thin-film fabrication methods (film thicknesses of 200 nm[20] – 5 μm[187]), CM-LPE allows for more precise and simple control of the film thickness even below 100 nm, by the number of deposition cycles which are applied. The calculated CSDs (18 nm) of the obtained CM-LPE films are in the range of the reported domain sizes of 10 nm[21] – 40 nm[20] of other UiO-66 thin-films. Importantly, the CM-LPE fabricated UiO-66 thin-films are highly porous and can take up to 3.3-6.6 mmol MeOH/g. We showed that the specific uptake of methanol for conventionally synthesized UiO-66 powder samples and the obtained thin-films is equal. The results show that the CM-LPE technique is a powerful tool in the growth of so far inaccessible MOF thin films.

Table 4: Comprehensive overview about UiO-66 thin films fabricated with different techniques.

	Thickness [nm]	Roughness [nm]	FWHM of 111 reflection	Uptake mmol/g	Preferred orientation
CM-LPE	82 nm	24.36 nm	0.7812	3.9-6.6 MeOH	no
Electrochem. deposition[187]	4-5 μm	-	0.42	-	no
Solvotherm[188]	2-5 μm	-	0.285	-	no
ALD[21,+]	~ 500 nm	-	1.05	0.057 5s water	no
Solv. ass.[20]	~200 nm	-	0.20	-	yes

[+]UiO-66 thin films obtained by ALD were not crystalline after the growth, only the post-synthetic treatment with acetic acid vapour yielded crystalline UiO-66 thin films.

2.8.4. Dense UiO-66-NH_2 SURMOFs: The Importance of Substrate Surface Activation

Following up on the presented results, we wanted to improve the thin film coverage and morphology of the UiO-66 thin films, as the crack-infused surface was a problem for any application. Therefore, we fabricated UiO-66-NH_2 thin films by the CM-LPE process. Experimentally, 1 equiv. $Zr_6O_4(OH)_4(OMc)_{12}$ and 6 equiv. of H_2bdc-NH_2 were separately dissolved in ethanol and an activated Si substrate was alternatively treated with both solutions for 80 deposition cycles. The modulator, X equiv. McOH was added to both solutions equally. If 400 equiv. or more were added to the solutions, no thin-film formation was observed. This can be attributed to the etching effect of McOH:

$$Zr_6O_4(OH)_4(OMc)_{12}+HO\text{-}S \rightleftharpoons [Zr_6O_4(OH)_4(OMc)_{11}]O\text{-}S + McOH \quad (1)$$

If more methacrylic acid is added, the surface attached Zr cluster $[Zr_6O_4(OH)_4(OMc)_{11}]O$-S reacts with McOH to $Zr_6O_4(OH)_4(OMc)_{12}$ and detaches from the surface. After the reduction to 325 equiv. McOH the thin film fabrication yielded a macroscopically homogenous thin film, which was subsequently investigated by GIXRD, IR spectroscopy, and MeOH adsorption measurements.

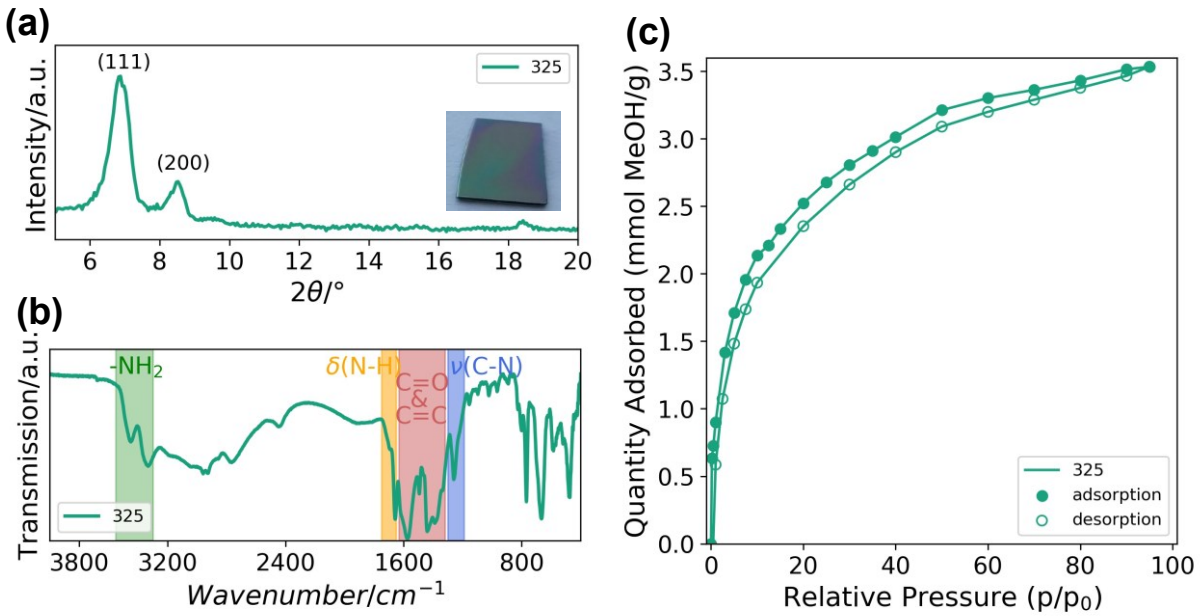

Figure 22: Characterization of an 80L UiO-66-NH_2 thin film fabricated by CM-LPE: (a) GIXRD, and image, (b) IR spectrum, and (c) methanol adsorption measurement.

The evaluation of the GIXRD (Figure 22 a) shows that the fabrication yields a crystalline film, with a mean CDS of 14.7 ± 2 nm. Additionally, the IR spectrum shows the presence of carbonyl, N-H, and C-N vibrations associated with the formation of UiO-66-NH_2. Finally, the mass-specific methanol (MeOH) adsorption isotherm of the fabricated UiO-66-NH_2 film was measured with a QCM. The overall MeOH adsorption capacity was determined as 3.53 mmol g^{-1} MeOH (at 25 °C, 95 % MeOH; Figure 22 c) and the shape of the isotherm matches a microporous type I isotherm. The small

deviation of the adsorption and desorption branches can be attributed to a slow desorption process.

The comparison of the obtained methanol uptake with the measurements reported in literature is challenging, as methanol was so far not reported for UiO-66-NH_2 thin films. However, on the one hand, the ethanol uptake of UiO-66-NH_2 thin films fabricated by the VAC methods was reported as 2.9 mmol g^{-1}(at 25 °C, 99 % EtOH). The 22% higher uptake of methanol reported in this work, in comparison to ethanol, is expected as the size of the molecule increases from methanol to ethanol, reducing the sorption capacity of the MOF in turn. On the other hand, the methanol uptake for solvothermally synthesized **UiO-66-HCl** was determined by QCM measurements. These powders adsorb 3.6 mmol g^{-1}, which is slightly higher than the 3.53 mmol g^{-1} MeOH measured for UiO-66-NH_2.

As a next step, we investigated the morphology of the obtained sample by scanning electron microscopy. Surprisingly, the morphology of the 80 deposition cycles (abbreviated as L) UiO-66-NH_2 thin film fabricated by CM-LPE does not show any cracks when compared to the UiO-66 samples. Probably, this can be attributed to a higher solubility of H_2bdc-NH_2 compared to H_2bdc and correspondingly a faster nucleation process. Additionally, we varied the surface activation procedure as a key to achieving excellent thin-film quality is the careful and efficient activation of the chosen substrate to remove any impurities and maximize the amount of nucleation active, functional groups for the MOF thin film formation. We utilized ozone and piranha acid treatment (*Caution: Piranha is a very strong oxidizer and can react explosively with organic compounds*) of the substrate surfaces prior to the thin film fabrication, in order to compare the thin film quality of the resulting thin films. The SEM images of these thin films show that the pre-treatment indeed has a significant effect on the thin film surface roughness. Piranha treated thin films are smoother after 20 and 80 deposition layers compared to their ozone-activated counterparts (Figure 23). This is attributed to enhanced chemisorption of the molecules at the substrate surface resulting in higher nucleation density.

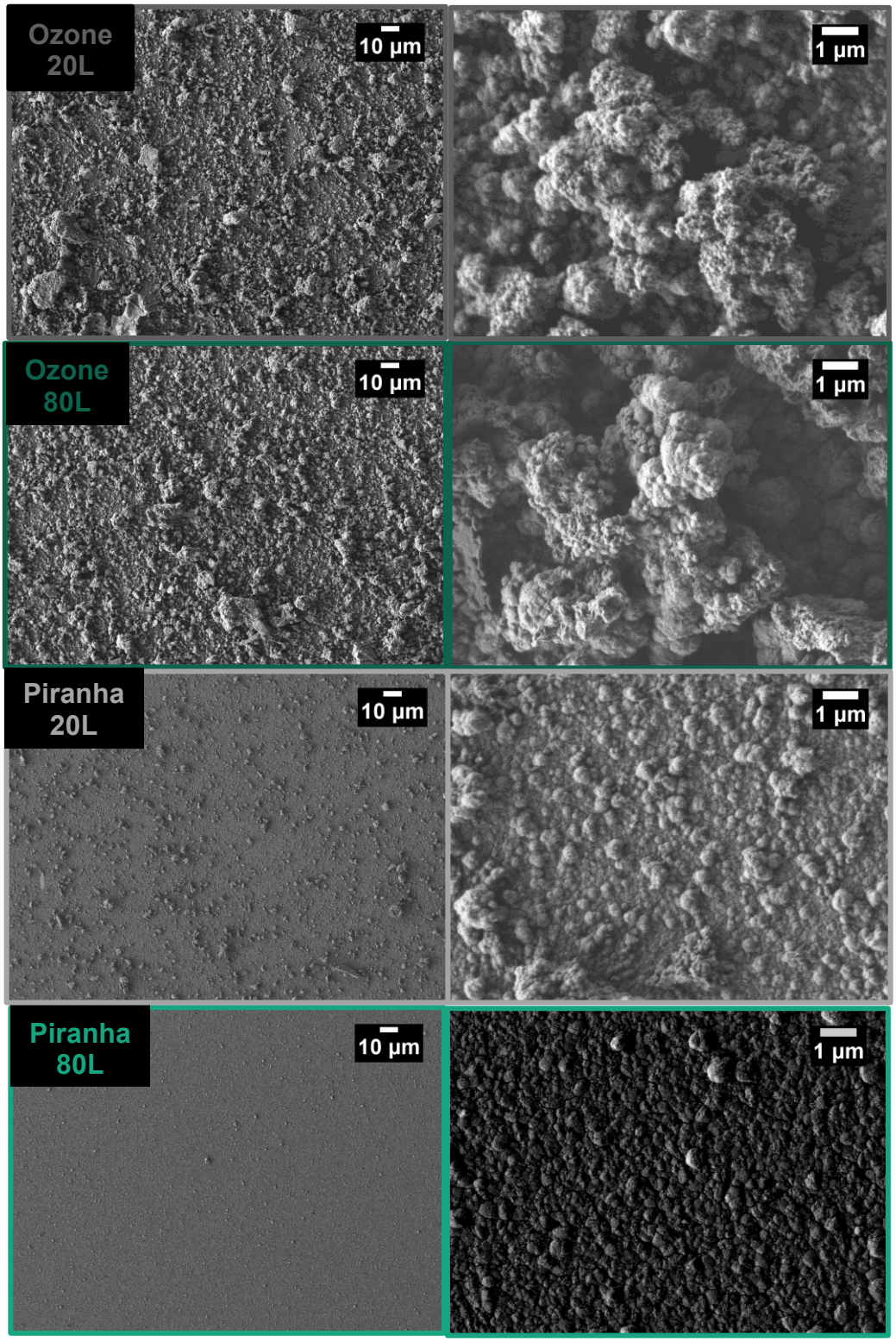

Figure 23: SEM images of UiO-66-NH_2 thin films fabricated with 325 equiv. of McOH as the modulator. The substrates were activated by either ozone treatment or piranha acid and the CM-LPE process was performed for 20 or 80 cycles.

Settings: 500 (left) and 10,000-fold (right) magnification, 1.0 kV LEI, WD 8.0 mm.

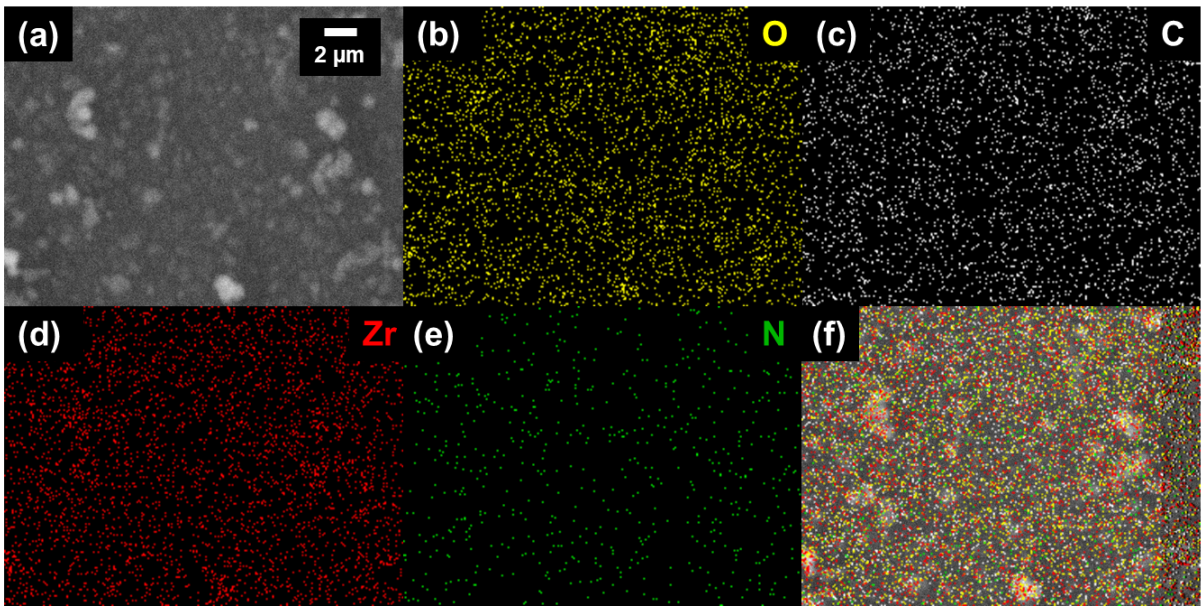

Figure 24: Full EDX elemental mapping for O (b), C (c), Zr (d), and N (e) and overlapped spectra (f) of a 60L UiO-66-NH2 film (a) deposited via CM-LPE on a silicon <100> wafer activated in piranha acid for 30 min.

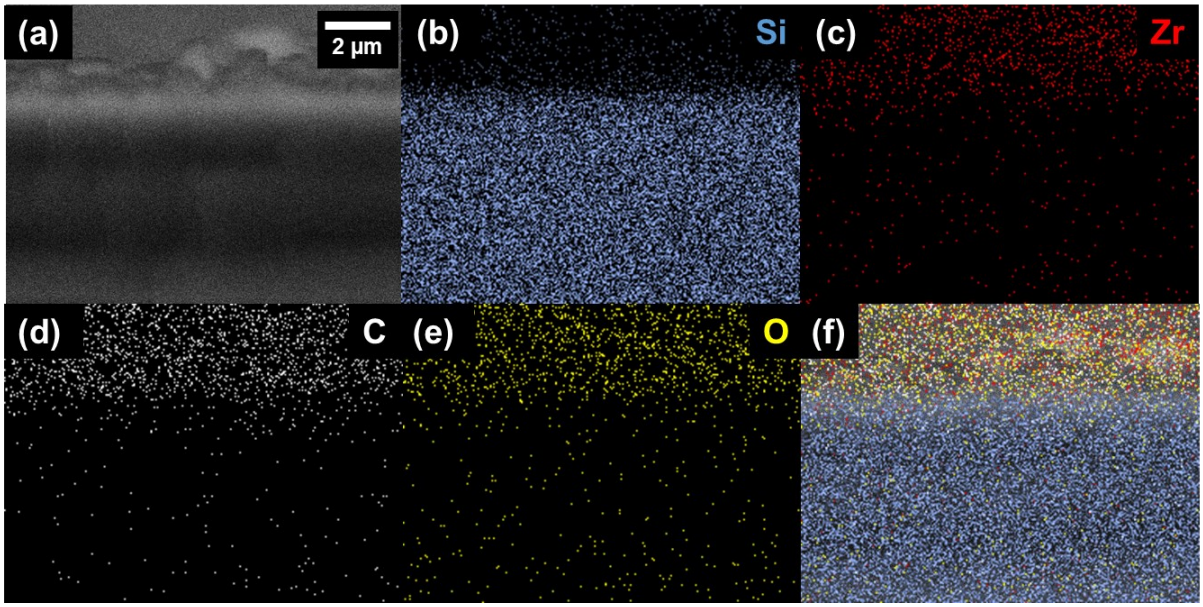

Figure 25: Full EDX elemental mapping for Si (b), Zr (c), O (d), and C (e) and overlapped spectra (f) of a 60L UiO-66-NH2 thin film 90° cross-section (a) deposited via CM-LPE on a silicon <100> wafer activated in piranha acid for 30 min.

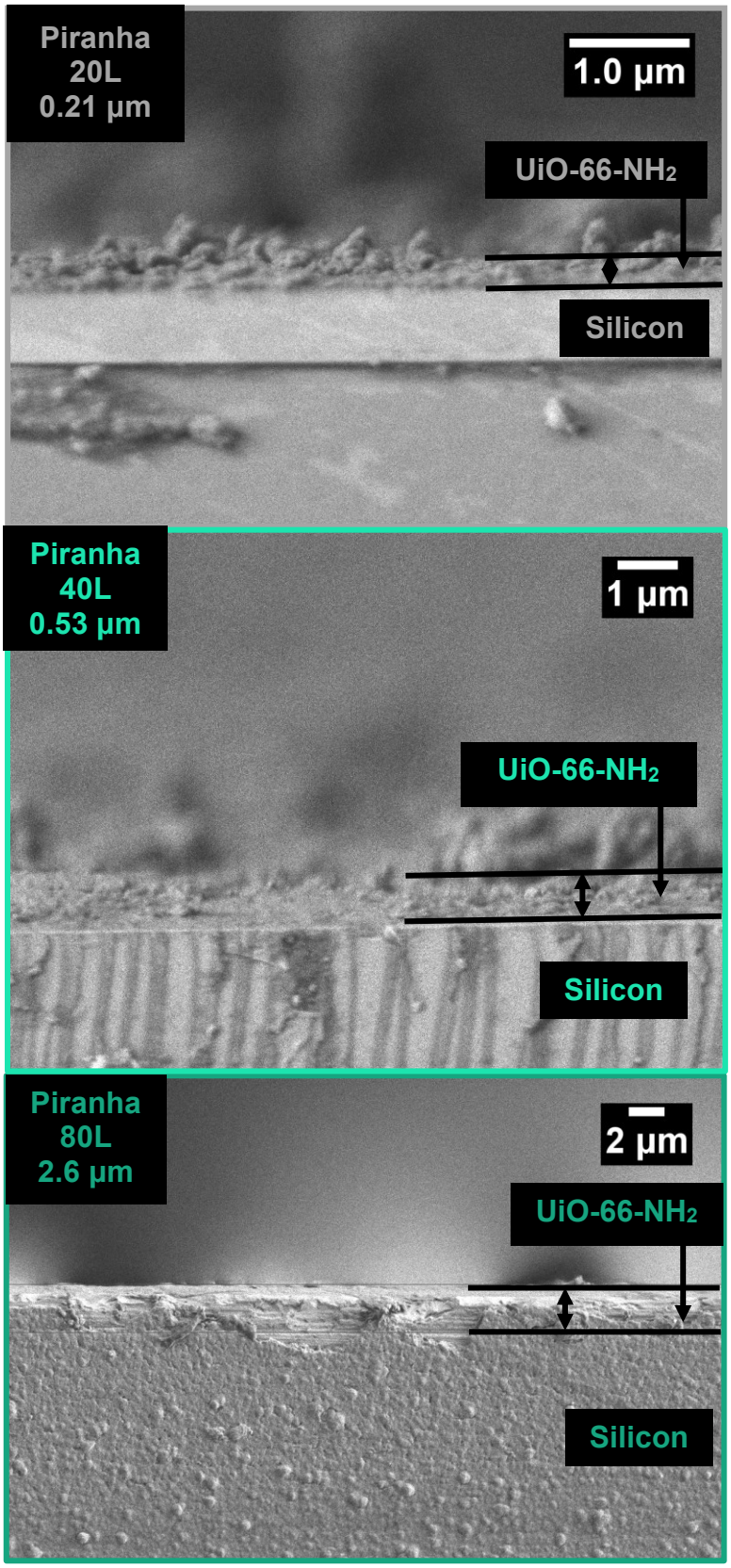

Figure 26: 90° cross-section SEM images of a 20/40/80L UiO-66-NH_2 film deposited via CM-LPE on silicon <100> wafer activated in piranha acid for 30 min.
Settings: (top) 20,000-fold magnification, 1.0 kV LEI, WD 7.9 mm., (middle) 10,000-fold magnification, 2.0 kV LEI, WD 7.9 mm, (bottom) 3,500-fold magnification, 1.0 kV LEI, WD 8.1 mm.

Contact angle measurements of freshly activated silicon substrates reveal H_2O contact angles of 20° for ozone and 10° for piranha acid treatment (appendix, Figure S39), which corresponds to the available hydroxyl groups on the surface. Additionally, piranha etching removes organic residues from the surface,[189] creating a cleaner and thus more hydrophilic surface, which in turn leads to more efficient nucleation. The surface roughness and homogeneity improve with an increasing number of deposition cycles. The SEM cross-section analysis (Figure 26) revealed a thickness of 2.60 μm for 80L, which can be easily adjusted by the number of deposition cycles, as the 20L film results in 210 nm, and 40L yielded 530 nm thick, thin films. Similarly, to the UiO-66 thin films, the thin film growth of UiO-66-NH_2 includes a nucleation period with a low growth rate which then increases, explaining the non-linear growth of the thin film thickness. The 80L piranha activated film exhibits a root mean squared roughness of 2.0 nm on a 200 x 200 nm sample (obtained by Atomic Force Microscopy, AFM, Figure S38). Additionally, SEM energy-dispersive x-ray (EDX) elemental mapping was conducted with a UiO-66-NH_2 thin film showing strong peaks at 0.277, 0.392, 0.525, 1.739, and 2.042 keV, assigned to the characteristic X-ray energy of C, N, O, Si, and Zr, respectively (see Figure 24-25). Elemental mapping provided insight into the distribution of the elements within the sample, revealing a uniform elemental distribution. The EDX cross-section analysis enabled a clearer differentiation between the substrate and the UiO-66-NH_2 coating. Overall, we observed a smooth surface without any cracks, which is a significant advancement compared to UiO-66 thin films.

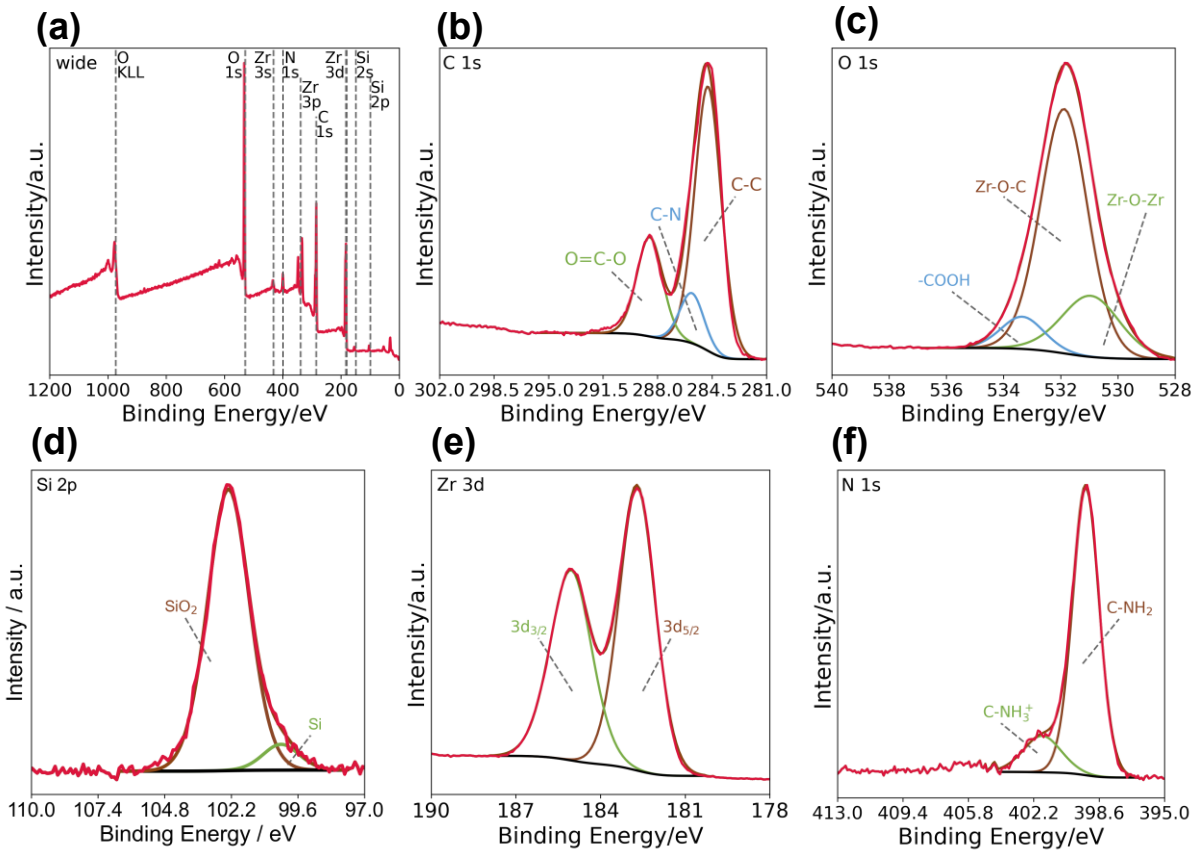

Figure 27: XPS survey scan (a) of a UiO-66-NH_2 thin film as well as narrow scans for 1s carbon (b), 1s oxygen (c), 2p silicon (d) and 3d zirconium (e), 1s nitrogen (f) including assignments of characteristic chemical species.

Subsequently, we investigated the obtained UiO-66-NH_2 thin films by X-ray photoelectron spectroscopy (XPS, Figure 27) to evaluate the defect content, to ensure the correct elemental composition, and to probe for impurities. The XPS survey scan (Figure 27 a) displays an elemental composition of C: 57.3 At%, N: 5.0 At%, O: 32.2 At%, Zr: 5.6 At%, and no further impurities. This is in reasonable agreement with the calculated composition of C: 52.1 At%, N: 6.5 At%, O: 34.7%, Zr: 6.5 At%. As carbon contamination might influence the ratios, comparing N and Zr ratios is more meaningful in this case. The calculated ratio is 1/1 and similar to the measured ratio of 1.12/1.0. In literature, deconvoluted XPS spectra were used to determine the relative defect content of UiO-66 thin-films.[190]According to Wang *et al.* the three different species in the O1s narrow scan can be assigned to the oxygen atoms in free, dangling carboxylic acid groups, which do not coordinate to Zr ions, to Zr coordinated carboxylate groups, and to bridging η3-O-Zr_3 groups. As our measurement yielded an O1s peak with no shoulders it is difficult to deconvolute the signal and fit the different components. Due to the absence of a distinct shoulder of the peak, which was observed for other highly defective samples [190], however, it can be concluded that the defect content is relatively low. Therefore, the XPS results suggest that the synthesis of a relatively low-defect and impurity-free UiO-66-NH_2 thin film was successful.

As the last step, we investigated the long-term stability in air and water in order to verify processability and longevity for manufacturing nanofiltration membranes. For this purpose, freshly fabricated thin films were exposed to air for 4 months or immersed in deionized water for 14 days. After certain time intervals, the films were investigated by GIXRD to observe if the films retain their structure (Figure 28). After the immersion in water, a slight decrease in the diffraction intensity can be observed over time, which can be attributed to a slow amorphization of the thin film. However, even after 2 weeks of water immersion, the thin film remains mainly crystalline. Long-term stability experiments in the literature were primarily reported time-dependent membrane performance tests. Typically, the UiO-66-NH_2 containing membranes display a slight decrease in flux and rejection but are overall stable for 70-160 h at elevated pressures up to 16 bar.[191–195] A comprehensive overview of membrane performances can be found in the appendix, Table S7. Besides these membrane performance tests, Wöll *et al.*[196] reported that their UiO-66-NH_2 thin films are stable in boiling water for at least 1 h. Overall, these experiments are hard to compare due to the different techniques for thin-film fabrication and the precise conditions of the stability measurements. However, all the experiments show that the UiO-66-NH_2 thin films are at least for some time stable in water, which is a prerequisite for their application in desalination membranes.

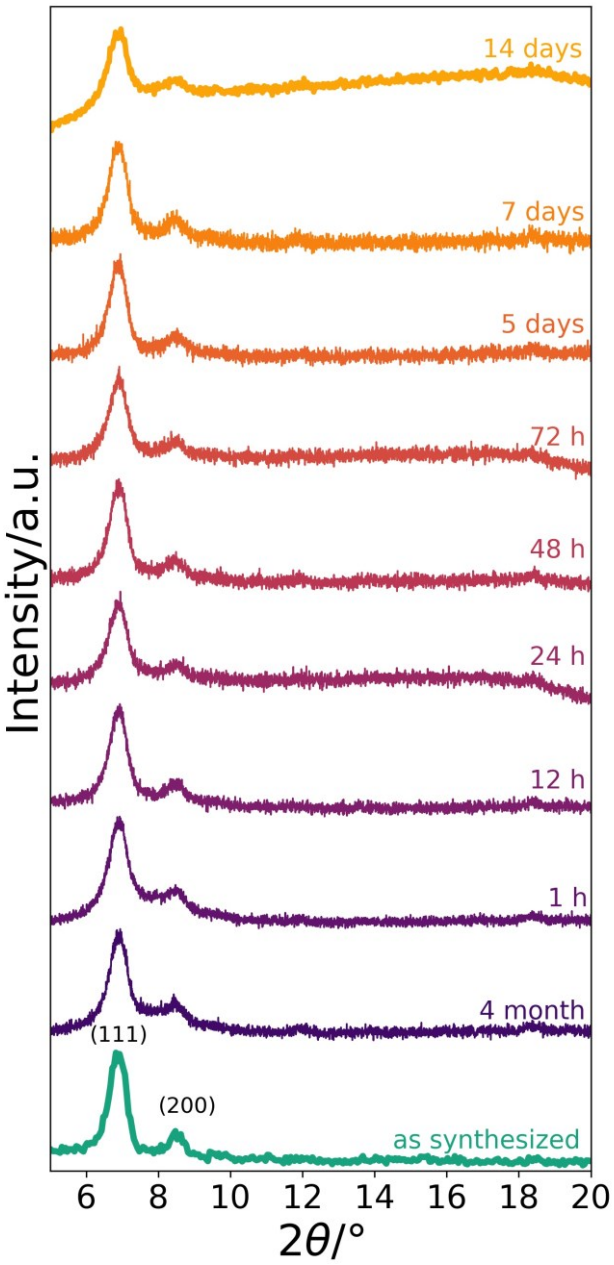

Figure 28: Long term stability of UiO-66-NH_2 films in water. GIXRDs investigating the stability of UiO-66-NH_2 samples after 4 months in air, and after 1h-14 days in water.

2.9. Conclusion & Outlook

The first part of my thesis with the fabrication of UiO-66 (Zr)(-NH_2) by coordination modulated LbL-LPE (Figure 29). UiO-66 (Zr) is notoriously hard to crystallize due to its high, 12-fold connectivity. Herein, we demonstrated a systematic approach that combines coordination modulation (CM) with the controlled SBU approach to facilitate solvothermal bulk powder synthesis (1st step) and transfer this knowledge to the CM-LPE for film deposition (2nd step). Thereby, achieving the formation of the 12-fold connecting node-based UiO-66, which was previously hard to deposit by any liquid-based synthetic process. Due to the two-step process, we were able to effectively reduce the parameter space for the CM-LPE process and obtain meaningful reference data for the related thin-film materials. In particular, we investigated the influence of water and methacrylic acid, as reaction modulating additives, on the formation of UiO-66. By varying the temperature and modulator concentrations we were also able to fabricate EHU-30 thin films, a hexagonal phase of UiO-66.

Additionally, we were able to grow macroscopically and microscopically homogenous UiO-66-NH_2 by CM-LPE. The UiO-66-NH_2 thin film fabrication yielded crack-free thin film coatings, which are essential for their applications in membranes (see Table S6-S7 for literature comparison). Efficient substrate activation was determined as a key factor for the formation of smooth and crack-free UiO-66-NH_2 thin-film coatings. By utilizing piranha acid-activated silicon substrates UiO-66-NH_2 thin films of uniform coverage, minimal roughness of 2 nm, and a high methanol adsorption capacity of 3.53 mmol g^{-1} were obtained. Additionally, the CM-LPE allows for high control over the thin film thickness, by adjusting the number of deposition cycles thin film thicknesses between 200 nm (20L) and 2.60 μm (80L) can be targeted. The investigation of the thin film stability revealed that the thin films are stable in water for at least two weeks, which coincides with other literature reports. As UiO-66-NH_2 membranes play an important role in desalination and nanofiltration, we are convinced that our method can improve the performance of these membranes in the future.

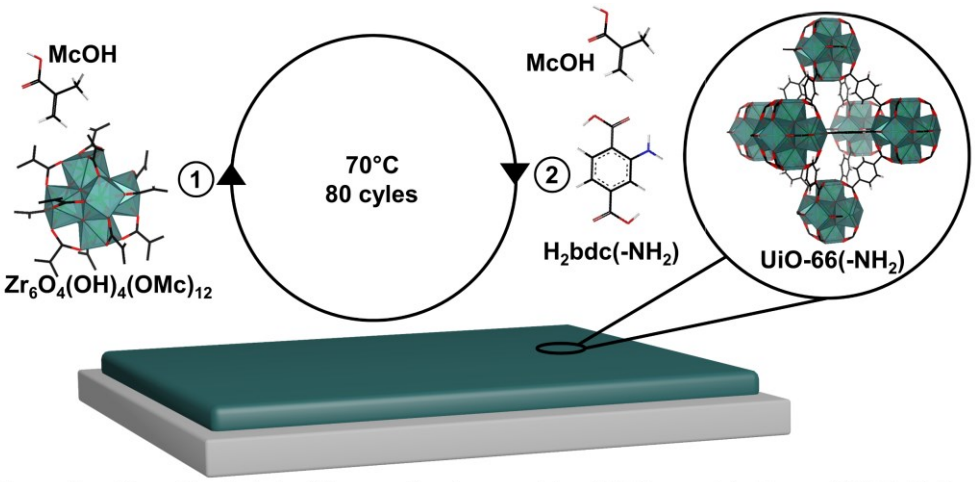

Figure 29: For the CM-LPE process, a substrate is alternatively immersed in a solution of the $Zr_6O_4(OH)_4(OMc)_{12}$/McOH and $H_2bdc(-NH_2)$/McOH for 80 cycles at 70°C yielding a porous, (nano-) crystalline UiO-66(-NH_2) coating.

Furthermore, these results could enable the formation of dense SURMOF-based membranes and broaden the accessible structures for LPE growth towards structures of higher connectivity (i.e. 8-12 fold) such as other Zr-based systems (NU-901, NU-1000, PCN-222, PCN-224, and MOF-525) and the MIL family of metal-organic frameworks.

3. SELECTIVE COVALENT IMMOBILIZATION OF PREFORMED NANO-MOFS IN MICROFLUIDIC DEVICES TARGETING VECTORIAL CATALYSIS

3.1. Vectorial Catalysis – An Introduction

Catalysis is key both to a sustainable development that is critical to transitioning from the current sources of energy and raw materials for chemistry towards a carbon-neutral, renewable future. Currently, estimates state that 90% of all chemical products and energy carriers are made using catalysts in at least one of the processing steps.[197] Thus, a comparatively small investment in catalysis research and development directly impacts the orders of magnitude larger overall chemical and refining industry.

Such effort requires, however, fundamentally new approaches in chemical transformations. One of these approaches is inspired by the design of biocatalysis: controlling multiple reactions in a programmed sequence and defined spatial localization – often referred to as **vectorial catalysis** (see Figure 30).[198]

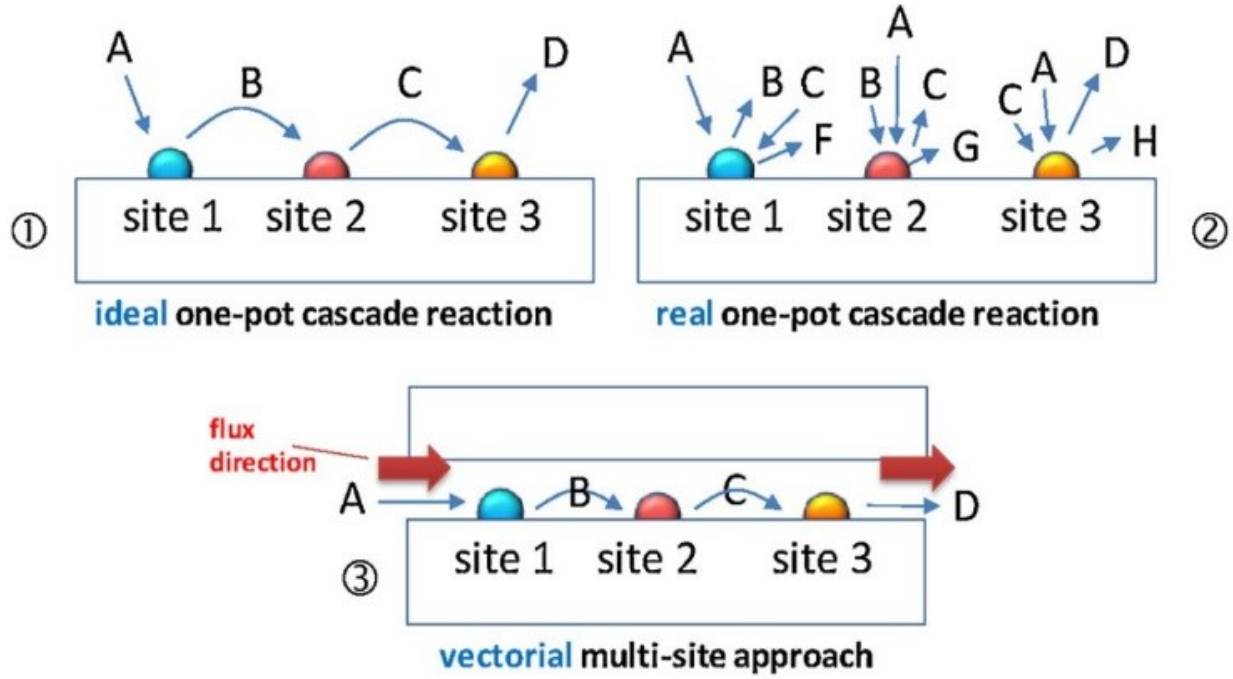

Figure 30: Concept of ideal (1) and real (2) one-pot cascade reaction as compared to the vectorial multi-side approach (3). This Figure was taken from Centi *et al.*[198] and is reprinted with permission from Elsevier.

As shown in Figure 30, a reaction cascade requires different catalytically active centers, which are present in the reaction and accessible to the reactant. In an ideal version, the reactant (A) reacts sequentially with the catalytically active sites 1 to 3 thereby transforming B and C and finally ending up as the product D (1). Unfortunately, reactants or intermediate products can often interact with more than one active site,

resulting in the formation of multiple side products (2). The additional introduction of a vector e.g. a flux can lead to an ideal version of cascade reaction, whereby the flux enables a degree of reaction control and reduces the side products (3).

Selection problem. Hence, vectorial reaction space essentially addresses the coupling of localized chemical transformations by the spatial arrangement of the catalytically active sides enabling a reaction-specific environment. Experimentally, the described requirements for multi-step vectorial catalysis are intrinsically challenging to achieve. Every reaction requires specific reaction conditions such as temperature, pressure, solvents, pH values, etc. The reaction conditions for one specific reaction might interfere with the reaction conditions of the subsequent reaction, resulting in catalyst deactivation or inhibition of reaction intermediates. Additionally, tailoring reaction vectors to match the targeted reaction sequence and employed catalysts can be equally challenging, as various scales of length and time need to be addressed. This targets the directed and active mass transport for example by anisotropic di- and multipolar force fields, orientation, and alignment of reactants within confined space, as well as responsive reaction centres.

Translation towards inorganic catalysts. Translating vectorial catalysis from biological systems towards inorganic/metal-organic catalysts, potentially entails many advantages such as increased scalability, enhanced robustness, and tailored adaptivity, as well as many challenges mimicking enzyme design principles (**catalyst design**), the compartmentation of biological systems (**reactor design**) and tailored mass transport (**suitable reaction vectors**). Among many suitable inorganic/metal-organic catalysts, MOFs represent an ideal design platform for targeting vectorial catalysis. Their building block design principles and coordination chemistry allow the tailoring of cages,[199,200] cavities,[201] and channels[43] (1D-transport and size confinement) together with implementing additional functional properties of the environment such as light-harvesting[202] or ion conduction[203]. Another tool for the additional introduction of functionalities can be the targeted inclusion and immobilization of catalysts in the pore architecture of the MOF.[204–206] Utilizing stimuli-responsive 3rd generation MOFs for the regulated accessibility of reaction centres (mimicking cell compartmentation) or using core-shell MOFs[207,208] for the controlled spatial organization of the catalytic active centres (catalysts/reactor design) are potential ideas for mimicking biological systems.

Reactor dimensions. The scales of length and time in vectorial catalysis can differ widely. The reactor dimension can include nanometer distances (between enzymes), micrometre-sized distances in or between cell compartments, or millimetre/centimetre distances in microfluidic reactors, or between different organs in organisms. Controlling the spatial arrangement of the catalytic active sides and designing suitable reaction vectors becomes increasingly difficult if the reactor dimensions are reduced or the time scales of vectorial catalysis are shortened.

State of the art – artificial vectorial catalysis. Due to the challenging nature of adapting vectorial catalysis into artificial reactors, not many examples are reported in the literature so far (a brief overview can be found in the appendix Table S8). Most examples mimic the biological systems closely, using various enzymes with a novel reactor design as shown by Van Hest and Zuilhof *et al* (2011) [209] and van Hest et al. [210] (2007) (Figure 31).

The first publication reported the immobilization of two enzymes in a fused silica microchannel and could therefore catalyze the hydrolysis of glucose acetate to glucose in the first step, then the second enzyme in the mobile phase catalyzes the oxidation to gluconolactone in the second sequential step. In the final step, the immobilized horseradish peroxidase oxidizes a dye with H_2O_2, a by-product of the second reaction step, the dye radical can then be easily detected by UV Vis spectroscopy.

The latter describes the formation of a nanoreactor mimicking cellular compartmentation by the diblock copolymer polystyrene$_{40}$-b-poly(lisocyanoalanine (2-thiophen-3-ylethyl)amide)$_{50}$ (PS-PIAT). The block copolymer is an amphiphile that resembles phospholipidic membranes only permeable for small molecules. Horseradish peroxidase (HRP) is immobilized in the artificial membrane, whereas the second enzyme glucose oxidase (GOX) is solvated inside of the nanoreactor and the third enzyme is Candida antarctica lipase B (CALB) is on the outside. Initially, the substrate 1,2,3,4-tetra-O-acetyl-β-glucopyranose (GAc4) is hydrolyzed in solution by CALB yielding glucose, which diffuses into the nanoreactor and gets oxidized by GOX. Products of this reaction are gluconolactone and hydrogen peroxide. The latter is converted in the third catalytic reaction, where HRP catalyzes the oxidation of the dye, inducing the reaction detection by UV/Vis.

Nanoreactors do not always mimic cellular behaviour so closely, which was for example presented by Li and co-workers,[211] which build a bifunctional nanoreactor based on molecularly imprinted polymers (MIPs) containing platinum nanoparticles at the end of the imprinted channels. In this case, the vector in the reaction sequence is induced by the diffusion pathway of the substrate molecules inside the nanoreactor. The first reaction is catalyzed by acidic sides in the channel, hydrolyzing 4-nitrophenyl acetate to 4-nitrophenol, which then diffuses further into the channel to the Pt NP. Subsequentially, these catalyze the reduction to 4-aminophenol.[211]

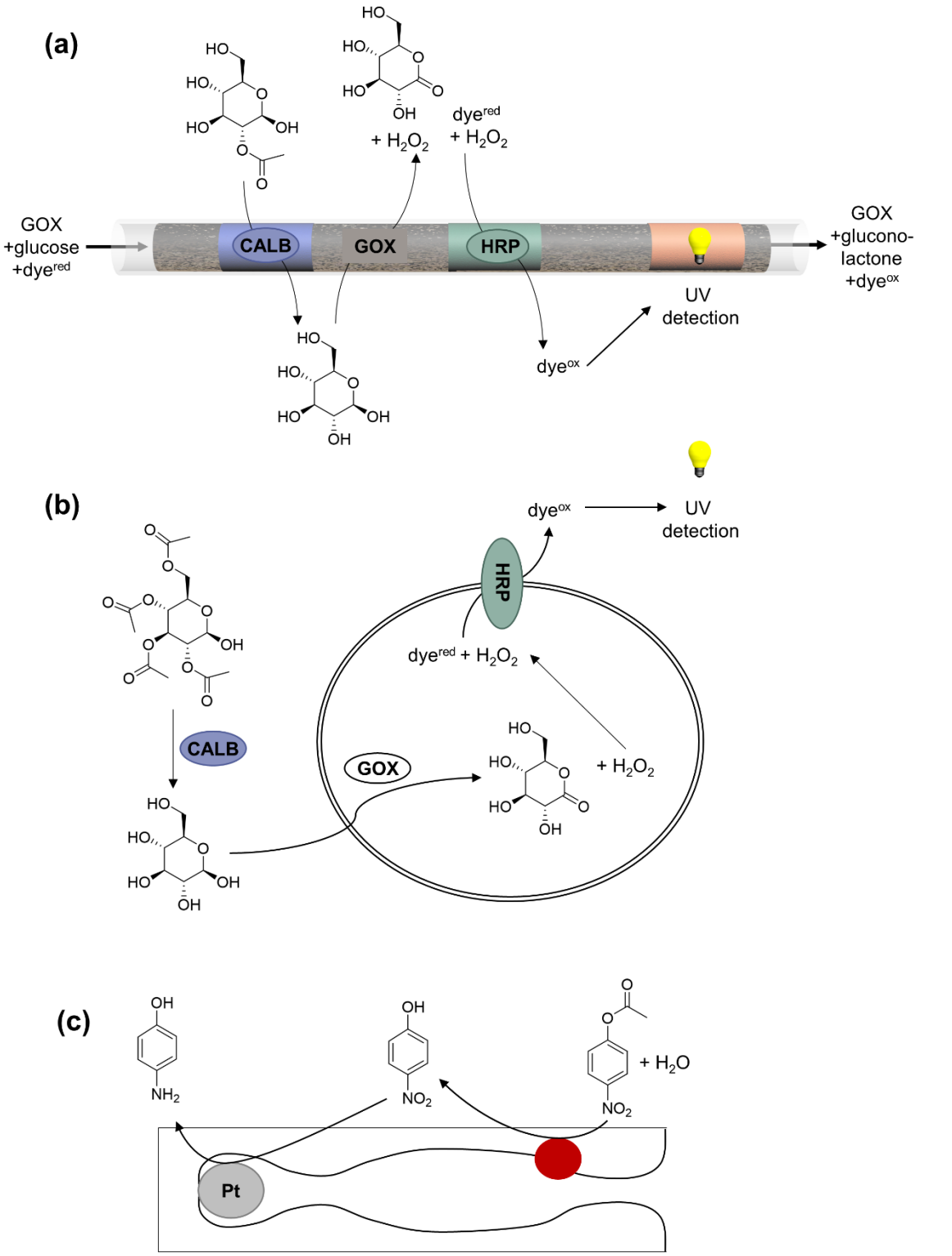

Figure 31: Examples for artificial vectorial catalysis from literature. Differentiation between closely mimicking the biological systems (a,b) or other nanoreactors (c). Van Hest and Zuilhof *et al.*[209] utilize a fused silica microchannel (a) or diblock copolymer formed micelle[210] (b) where a glucose acetate ester is hydrolysed by Candida antarctica lipase B (CALB) yielding glucose, which subsequentially oxidized to gluconolactone and H_2O_2 by glucose oxidase (GOX) and finally a dye oxidation enabled by H_2O_2 is catalyzed by Horseradish peroxidase (HRP). The last example shows molecular imprinted polymers containing Pt NP (c). The first reaction is catalyzed by lewis acidic sides in the polymer, hydrolyzing 4-nitrophenyl acetate to 4-nitrophenol, which then diffuses further into the channel to the Pt NP. Subsequentially, these catalyze the reduction to 4-aminophenol.[211]

Tandem catalysis vs. vectorial catalysis. While the reports on vectorial catalysis with MOFs as reaction platforms or with MOFs as catalytically active centres are rare in literature, the number of publications targeting tandem catalysis with different catalytically active centres available in the same MOF (bifunctional catalyst) and without a directed mass transport (vector) are abundant in literature. A brief overview can be found in the appendix Table S9-S10.

Realizing artificial vectorial catalysis with MOF as catalysts. Adapting the vectorial concept towards MOFs would require overcoming several challenges/ adaptation steps:

1. **Catalyst design**. Inspired by the highly selective and effective enzymes, MOFs are reported as rather sluggish catalysts. Due to their high inner surface area and the microporous nature of most MOFs, most reactions are diffusion-limited and possess low turnover frequencies. As a key requirement for vectorial catalysis, the diffusion limitation needs to be drastically reduced.
2. **Compartmentation**. Compartmentation in MOFs needs to be achieved either by the targeted structural design of MOFs as reaction platforms (catalytically active centres are selectively positioned inside of the MOF) or in the overall reactor design to target MOFs as catalytic active centres.
3. **Suitable reaction vector**. The reaction vector is most difficult to design, it can be an artificially induced flux in a flow reactor or by an anisotropic di- and multipolar force fields (directed diffusion).

The challenges and several ideas on how to overcome these are presented in the following chapters.

3.1.1. Catalyst Design: Defect-Engineering vs. Downsizing

For several years, MOFs have been reported as catalysts or platforms for immobilizing catalysts. However, most reactions are diffusion-limited and show low turnover frequencies, especially when compared to enzymes. Two approaches, namely downsizing MOFs, and defect engineering, were presented in literature since then to overcome this issue.

Defect engineering. The ideal conception of crystalline materials is an infinite number of repetitive units. As we live in a finite (expanding) world, real-world crystalline materials exhibit structural irregularities, also referred to as defects, especially on their surfaces. The major driving force for the formation of defects is the entropy gain associated with the formation of defects. Often these defects shape the material properties like conductivity (Si doping),[212] stability (steel research)[213] or reactivity (heterogeneous catalysis).[214,215] Therefore, the investigation and the intentional

introduction of defects (defect engineering) to alter the materials' properties is a major research field.

Defects can be defined as a feature that locally breaks the crystal structure's periodicity. Based on their dimensions, defects can be classified as point defects[216] (e.g. vacancies), line defects (e.g. dislocations), planar defects (e.g. boundaries and stacking faults), and micro- and mesoscale volume defects (e.g. inclusions and voids).[217] For MOFs, mainly point defects were investigated and can be categorized as (i) missing linker defects, (ii) missing node defects, (iii) modified linker defects, and (iv) modified node defects.[215,218,219]

In the context of defect engineering, two MOF model systems were established, namely UiO-66 (Universitet i Oslo, $Zr_6O_4(OH)_4(bdc)_6$) and HKUST-1. The latter is prone to form defects upon thermal activation.[220,221] Additionally, linkers with deviating connectivities/defective linkers (*e.g.* isoterephthalate or pyridine-3,5-dicarboxylate instead of btc^{3-}) were introduced by a solid solution approach causing defects in the crystal structure.[88,222,223]

Advantages of defect engineered compared to pristine MOFs were mainly discovered in heterogeneous catalysis and gas adsorption. In these cases, missing linker defects create vacant positions at the metal nodes. In turn, this leads to more catalytically active centres or increased interaction between the sorbent and the framework boosting the catalytic activity and sorption properties. In general, defect-engineering in MOF synthesis has proven useful to manipulate material properties.

Downsizing. Another approach besides defect engineering to control and manipulate the properties of MOFs is to influence and target the shape and size of the MOF particles. In other research areas (e.g. noble metal nanoparticles for electro- or heterogeneous catalysis),[224,225] the influence of the particle size on the materials' properties have been investigated.[226] It has been shown that the photophysical,[227] catalytic,[228] and physiochemical properties[229] can strongly depend on the particle size. Therefore, investigating the properties of MOFs as a function of their particle size is an interesting research topic.

Nanometre-sized MOFs (NMOFs) crystals typically have a dimension of 5-500 nm and can be synthesized by solvothermal reactions like their bulk counterparts. Recently, Brozek *et al*.[230] started an elaborate investigation of NMOF sizes of ZIF-8 and HKUST-1 depending on the solution's acidity, ligand excess, and reactant concentrations. They state that the ligand excess has the greatest ability to decrease the particle size of the MOF, although low acidity and high concentrations can exhibit similar effects.

In terms of application, the downsizing of MOF also leads to stable colloidal NMOF solutions. Monodisperse colloidal solutions can be an interesting opportunity for the fabrication of MOF-based thin-film coatings. Maspoch *et al.*[231,232] showed that colloidal ZIF-8 solutions can be utilized for the formation of highly ordered superstructures with photonic properties.

In terms of catalytic properties, NMOFs have shown to be of particular interest in the context of heterogeneous catalysis.[233,234] Nano-sizing the MOF catalysts can (1) present a higher density of catalytic sites on the surface and (2) allow faster and more facile substrate-catalyst interaction due to lower diffusion barriers and/or reducing diffusion limitations. Therefore, rendering them interesting catalysts. This strong correlation between size and catalytic activity was among others reported by Farha *et al.*[158] and Janiak *et al.*[235].

Downsizing as the catalysts design principle of this thesis. By comparing both strategies, defect-engineering, and downsizing of MOF, we think that the downsizing approach entails more potential than the defect-engineering approach. Despite the intense research efforts in this area (prior 2017), a report of colloidal NMOF particles with particle diameters significantly less than 100 nm in catalysis has not been reported yet. Therefore, the potential to investigate the behaviour of NMOFs with particle diameters below ~20 nm or less might be interesting and offers opportunities to further boost the catalytic activity/turnover frequencies of MOFs.

3.1.2. Reactor Design/Compartimentation: Surface Functionalization and Patterning

In order to create compartmentation allowing the first reaction to proceed subsequentially followed up by the next, an orthogonal bonding approach needs to be developed, selectively positioning the NMOF catalysts at different positions in the reactor.

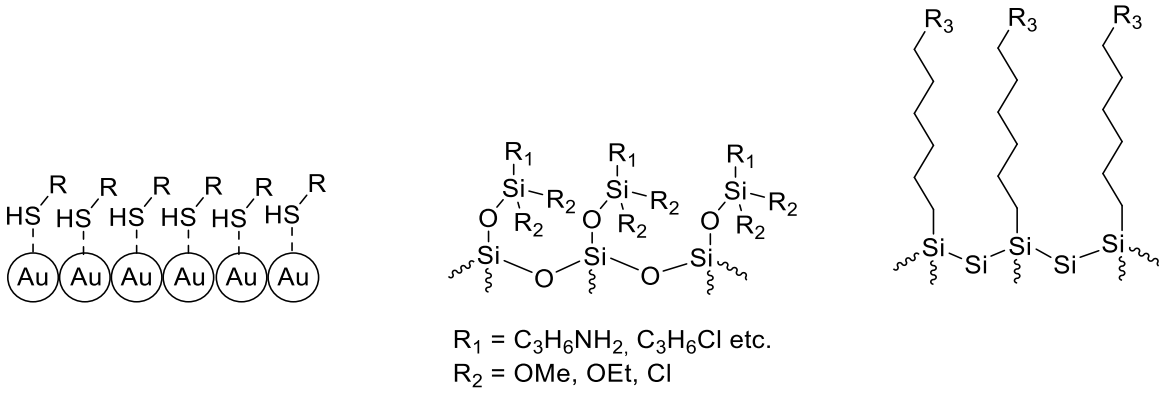

Figure 32: Schematic representation for the functionalization of gold with alkyl thiols (a), alkylsilanes on silica (b), and 1-alkenes on silicon (c).

Surface functionalization. Surface functionalization of materials or substrates is a useful technique to alter chemical and physical properties such as chemical reactivity or hydrophilicity/hydrophobicity of a surface while still retaining the structural properties of the substrate.[236] In general, two strategies are known to functionalize surfaces, namely physical adsorption, and covalent conjugation. As the latter produces more stable and persisting surfaces, this is in this case the method of choice.

For this work, in particular, the surface functionalization of gold, silicon, glass, and polydimethylsiloxane (PDMS) is important (see Figure 32).

Gold surfaces are usually functionalized by thiol terminated self-assembling monolayers (SAMs). To achieve this, gold surfaces are typically immersed in aqueous or ethanol-based solutions of the corresponding thiol. The nature of the thiol gold interaction has long been described as a chemisorption interaction, where the formation of the bond requires the loss of the hydrogen atom.[237,238] Only recently, Venkataraman *et al.*[238] published an article, where conclude from single-molecule conductance measurements that the gold surface sulfur bond can be better rationalized as a physisorption interaction.

The chemical surface properties of the substrate play a major role in the choice of the functionalization method. Substrates that have intrinsic/native hydroxyl or oxide terminated surfaces can be often functionalized similarly. Glass, silicon with its native

SiO_2 surface, and polydimethylsiloxane can be activated through ozone/UV treatment,[239,240] oxygen plasma,[241] corona discharges,[242,243] or a solution-phase oxidation reaction.[244] These activation processes render the surfaces hydrophilic by the creation of reactive silanol groups. In a follow-up step, these can be utilized for surface functionalization. UV mediated polymerization,[245,246] free radical polymerization,[247–249] and silanization[250] are methods that were reported in the literature. The latter exploits the free hydroxyl group to form covalent bonds with highly reactive alkoxysilanes.[251–253] Major advantage of this method is the simple applicability in the lab and the easy availability of alkoxylsilanes. Noteworthy disadvantages can include the self-condensation of silanes due to the high reactivity and therefore the formation of multilayers.[250,253] Due to the reactive nature of the alkoxysilanes only certain functional groups can be introduced by this method like perfluorinated alkyl chains, amino groups, thiol groups, halides, vinyl groups.[254]

Another approach includes the etching of the silicon surface in the first step e.g. by aqueous HF or NH_4F to generate hydrogen-terminated Si surfaces (H-Si). In a second step, 1-alkene or 1-alkynes are utilized to react with the etched substrates.[255–257] Several methods like thermal-,[258] catalytic-,[259] photo-,[260,261] electro-,[262] mechano-[263], and sonochemical[264] methods are known to promote the formation of these monolayers. The accepted mechanism for the formation - regardless of the method - is described via a radical-chain mechanism, which was supported by scanning tunnelling microscopy.[265] These covalent Si-C bonds are non-polar and therefore very stable and can prevent the Si surfaces from oxidation, which is useful for example for electronic applications in the semiconductor industry, where Si plays a dominant role. Another major advantage is the high monolayer quality, producing typically very smooth and stable surfaces. Compared to the variety of available monolayers facilitated by thiol-based functionalization chemistry, this method still lacks a multitude of functional groups. Due to their reactivity, the direct formation of amino, hydroxyl, or aldehyde terminated layer is not feasible. Nevertheless, carboxylic acid (-COOH),[266]-COF,[267] alkenes,[268] -alkyne terminated monolayers[269] can be produced today.

Surface patterning. Lateral control of the functionalization can be achieved by surface patterning such as soft lithography (Figure 33).[270,271] A stamp is dipped/soaked in the functionalization agent, and then reacted with the substrate surface. The subsequent reaction of the unreacted sites with another functionalization agent is called backfilling and can create regions with different properties on one substrate.

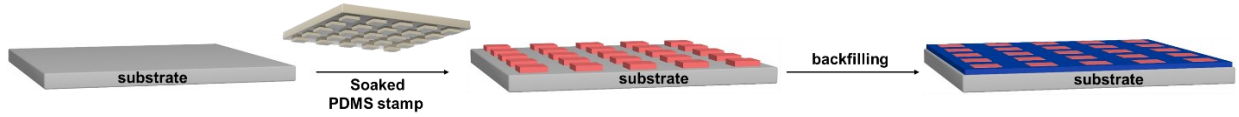

Figure 33: For the soft lithography process, a PDMS stamp soaked in a functionalization agent is positioned on a substrate and form a reaction pattern on the surface. Subsequently, the unreacted surface sites can be backfilled with another functionalization agent.

As mentioned above, the formation of functionalized surfaces can alter the chemical reactivity of the surface by introducing different functional groups like acid, amino, or alkyne groups. In a second step, these functional groups can be utilized to immobilize desired molecules/materials on these surfaces. Different (macro)-molecules or particles with different optical, magnetic, or biological properties have been reacted with functionalized/patterned surfaces, e.g. by the copper-catalyzed azide-alkyne cycloaddition (CuAAC) reaction, amide formation, or Diels alder reaction.[272] In such cases soft lithography can be used to soak a PDMS stamp into a solution of the reacting molecule and thereby create a pattern of the reacting molecule onto a homogeneously functionalized surface.[272]

Orthogonal anchoring approaches. To immobilize the preformed NMOFs at the functionalized or patterned substrate surfaces, covalent bonds between the NMOF catalysts and the substrate surface allow for a precise size and shape control, while strengthening the interaction between substrate and particles as compared to purely physisorption interactions. Therefore, reactive groups on the substrate surface are reacted with moieties on the outer surface of the NMOF.

3.1.3. Tailored Mass Transport/Suitable Reaction Vectors: Microfluidic Devices

For introducing a tailored mass transport enabling vectorial catalysis, the fabrication of microfluidic devices with a defined channel structure and the opportunity to generate a flow velocity is the final step.

Microfluidic devices. Microfluidic devices allow the handling of small amounts of fluids. Compared to their macroscale counterparts they offer some distinct advantages such as excellent control of mass and heat transport. This is important for complex systems such as novel drug delivery systems and biosensors.[273] One goal for microfluidic devices is a Lab on a chip approach, where assay operations such as detection, as well as sample pre-treatment, and sample preparation are integral on one chip.[274] As a consequence, these devices need less sample or reagent for analysis or operation, saving money and time, and are easy to handle.[273,274] Therefore, these can be multiplied into parallel structures for high trough put systems.

Due to the small quantity of volume and high surface-to-volume ratio, the mass transport in microfluidics is dominated by diffusion, resulting in a laminar fluid flow with thermal homogeneity and rapid heat transfer.[275] The make the process highly controllable and reproducible.

Microfluidic devices can be fabricated by different methods. PDMS-based microfluidic devices are one of the most commonly used systems (see Figure 34). Therefore, a two-component polymer is molded by mixing an elastomer and curing agent, often on photolithographic molds.[275] The resulting PDMS channel structure is then sealed with a glass slide or silicon wafer to yield a microfluidic device. The advantages include its low polymerization temperature, its transparency, and its straightforward handling.[276] A major drawback of PDMS-based microfluidic devices is the incompatibility with most organic solvents, as the PDMS swells upon contact with many organic solvents.[277]

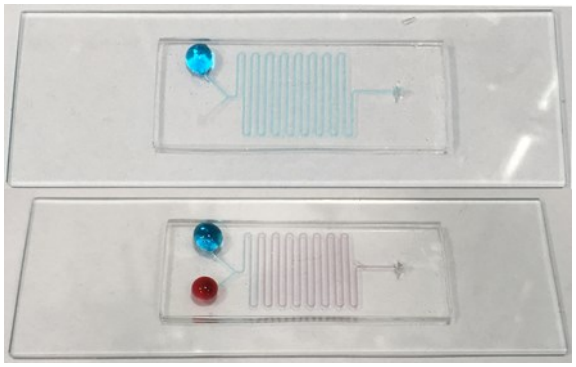

Figure 34: PDMS channel structure sealed with a glass slides to fabricate PDMS based microfluidic devices.

As another alternative, cyclic olefin copolymers (COCs) are emerging as an increasingly popular substrate material for microfluidic devices. These can be fabricated by various techniques, such as micro-milling, hot-embossing, and injection molding.[278,279] Due to their optical transparency, chemical resistance, low water absorption properties, and good biocompatibility they gained a lot of attention during the last years.[280] However, COC being quite inert toward chemical modification hinders the ability to covalently functionalize the surface, therefore hindering their application for biobased microfluidics.[280]

Design flexibility, small required sample volumes, reproducibility, and portability are the main advantages of microfluidic devices, which led to their application in medicine, fine chemical production, life sciences, and catalysis.[281–283] We hope that this technology will enable the translation of artificial vectorial catalysis with NMOFs as catalytically active sides as selectively positioned at defined areas of the microfluidic device.

3.2. Motivation & Objective

The second part of my doctoral thesis is derived from a proposal for the Horizon 2020 call from the European Union in cooperation with Bauke Albada and Han Zuilhof in Wageningen. The proposal's ultimate aim is the selective integration of different NMOFs as catalysts into the channels of microfluidic devices targeting artificial vectorial catalysis (Figure 35). Additionally, stimuli-responsive hydrogels that can switch between different states (e.g. non-permeable, permeable) if exposed to suitable stimuli (e.g. pH change, illumination) will be integrated into the channel to act as a switch between the steps of a multi-step vectorial catalysis reaction. Therefore, the resulting microfluidic device regulates itself during the catalytic process generating a self-regulating autofluidic device. These very ambitious goals mimic nature in its ability for the self-regulating production of chemicals.

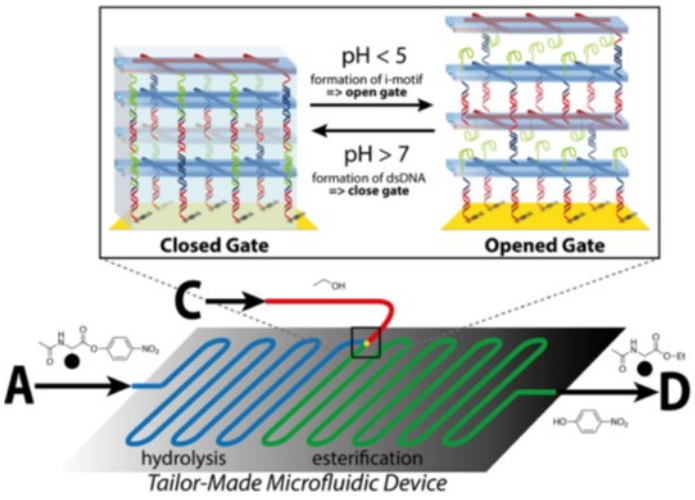

Figure 35: The overarching goal is fabrication of a tailor-made microfluidic device, which uses chemo-responsive hydrogel gates for flow control and positioning of NMOFs in the blue and green areas as catalysts for targeting vectorial catalysis. This image was taken from the Horizon 2020 proposal, with permission from the author.

Aiming for preliminary and preparatory work related to this collaborative project, I am interested in the following questions:

- Is it possible to selectively immobilize different NMOFs at certain positions of a substrate? What kind of surface functionalization of the substrate and the NMOFs are necessary to achieve that goal?
- Are the surface anchored NMOFs still catalytically active? Are we able to measure such low turn-over frequencies? How are the stability and catalytic activity of these NMOFs?
- Are we able to catalyze a reaction with NMOFs as catalysts in a controlled fashion with a microfluidic device? Are we able to extend the scope by introducing multi-step reaction cascades with different NMOFs as catalytically active species?

According to these questions, we start the investigation of the surface anchoring of NMOFs on different substrates. As model systems, UiO-66 (Zr) and MIL-101 (Cr) sparked my interest as they are known for their chemical and thermal stability. Moreover, their catalytic abilities are well investigated, and the size-selective synthesis of their nanometer-sized particles have already been reported in the literature. For the covalent immobilization of UiO-66 nanoparticles (UiO-66 NP), we will investigate different, orthogonal chemical bonding strategies such as amide bonds and click chemistry. As the NMOFs need to provide the chemical functionalization for the follow-up immobilization we will chemically modify the exterior surface of the NMOFs with functional groups. This approach ensures broad transferability to many different MOF systems. Additionally, this exterior surface functionalization might prevent agglomeration of the NMOFs by acting as a capping agent. Afterwards, these NMOFs will be covalently immobilized on different substrates (such as functionalized gold, silicon, or PDMS surfaces) yielding surface-anchored NMOF composite materials (SA-NMOF) at selected positions of the substrate (see chapter 3.3). In a follow-up step, the investigation of the catalytic activity of these SA-NMOFs on different substrates will be investigated for Lewis acid-catalyzed reactions where UiO-66 and MIL-101 can act as a catalyst. As a long-term goal, the final step of the project is the integration of different NMOFs as catalysts in microfluidic devices and the investigation of their catalytical activity inflow. Cumulating in the fabrication of microfluidic device which features two separately functionalized regions with two different catalysts respectively, allowing for a proof-of-concept MOF-based two-step vectorial catalysis system.

3.3. Study I: Selective Positioning of Nano-Sized Metal-Organic Frameworks Particles at Patterned Substrate Surfaces

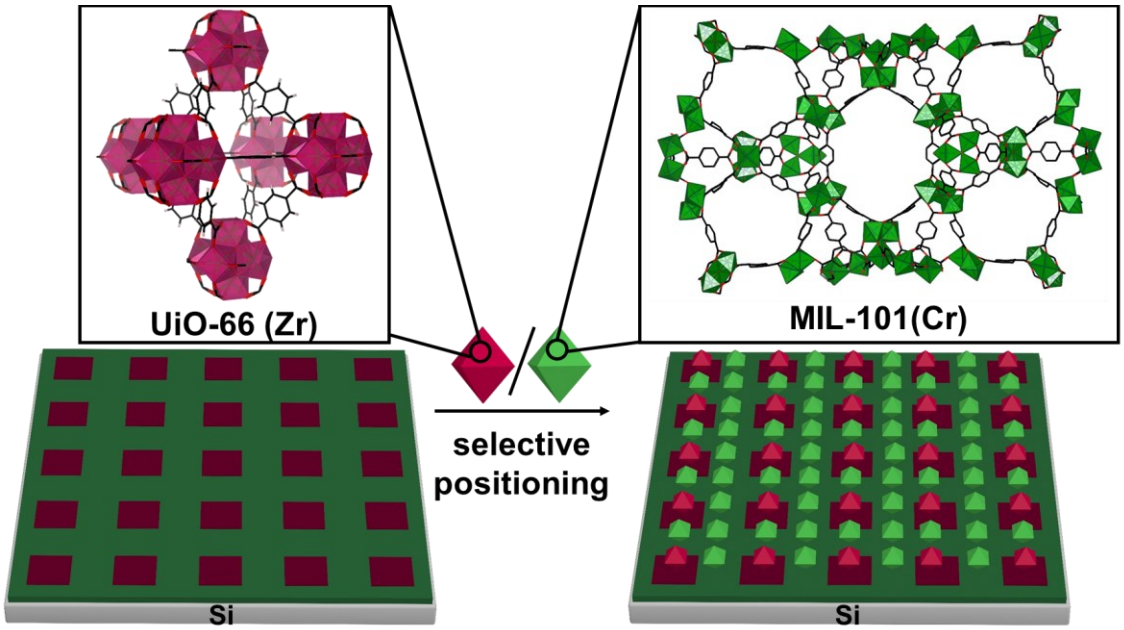

This chapter is based on the publication:

Anna Lisa. Semrau, Sidharam P, Pujari, Philip M. Stanley, Suttipong Wannapaiboon, Bauke Albada, Han Zuilhof, and R. A. Fischer, Selective positioning of nano-sized metal-organic frameworks particles at patterned substrate surfaces, *Chem. Mater*., **2020.**

The project was designed by A. L. Semrau and discussed with S. Wannapaiboon and R. A. Fischer. The experiments and characterization were performed by A. L. Semrau, S. P. Pujari and P. M. Stanley. S. P. Pujari additionally measured SEM, IRRAS, and XPS. The results were analyzed by A.L. Semrau. Subsequently, final results were discussed with all co-authors. Finally, the manuscript was written by A. L. Semrau and edited by all co-authors.

3.3.1. Surface Engineering: Selectively Positioning of NMOFs

The motivation for this project is derived from the recent literature reports investigating the catalytic activity of NMOFs as compared to bulk MOF particles. Janiak *et al.*[235] and Farah *et al.*[284] showed that NMOFs exhibit enhanced catalytic activities compared to their bulk counterparts (see chapter 3.1.1). Some applications, e.g. their integration into microfluidic devices or other catalytic set-ups might benefit from anchoring NMOFs to substrate surfaces, for example by preventing their aggregation.
In the past, MOFs were selectively grown (bottom-up approach) on patterned substrates, which has been among others[285] shown by Ocal *et al.*[286] and Falcaro *et al.*[287] In contrast to these literature reports, we chose the top-down immobilization of pre-synthesized NMOF particles on patterned surfaces, which has not been reported, yet. Due to the high control over the preformed particle shape and size, the top-down approach offers distinct advantages. Therefore, we tried to establish a reliable route with a transferable approach to selectively position NMOFs on substrate surfaces.

Synthetic approach. For this approach, we used the well-established and broadly applicable NMOFs UiO-66[152] and MIL-101[288] (Matérial Institut Lavoisier, $Cr_3O(OH)(H_2O)_2(bdc)_3$), since both compounds are known for their physical and chemical stability.[147,149,289] Additionally, their crystallization behaviour has been thoroughly investigated and therefore literature reports on the synthesis of nanometer-sized crystals were available.[290,291]

In the first step, NMOFs were functionalized on their outer surface to create reactive groups for selective positioning. Therefore, UiO-66 (**NMOF 1**) or MIL-101 (**NMOF 3**) nanoparticles were functionalized on their nano crystalline particles' exterior surface with ω-functionalized alkane-α-amines, whereas the functional group was either a ω-azido or ω-amino group. The reaction with the NMOFs yielded azide-functionalized UiO-66 (**NMOF 2**) or amine-functionalized MIL-101 (**NMOF 4**).

To position them onto surfaces, the silicon substrates have to be prepared and functionalized accordingly. For this purpose, the native silicon oxide on the silicon surface was removed by etching with NH_4F. Afterwards, the etched surfaces were reacted with neat alkyne or alkene solutions at 100°C overnight. This resulted in the formation of a self-assembled organic monolayer (SAM) terminated with either an alkyne, carboxylic acid, or both groups at the surface. Lateral control over the surface functionalization pattern was achieved by microcontact printing (μCP) (see Figure 36b), i.e., by treating the etched surfaces with a PDMS stamp in the glovebox (O_2 < 0.1 ppm, and H_2O <0.1 ppm) overnight, and additional backfilling afterwards yielding a

patterned surface consisting of specific areas with alkyne, or carboxylic acid termination.

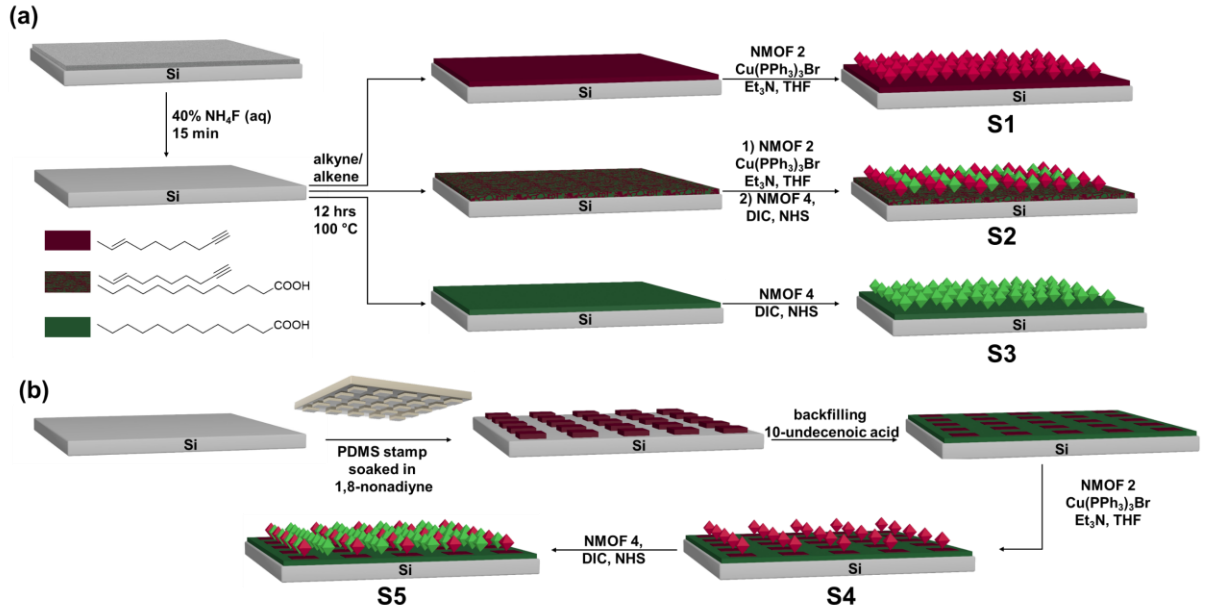

Figure 36: Schematic representation of the goal of this chapter: the selective positioning of **NMOF 2** and **4** on silicon substrates. **(a)** In the first step, silicon substrates are treated with a 40% aqueous NH_4F solution to remove the native silicon oxide layer. This step is followed by reacting the silicon substrates in neat 1,8-nonadiyne, 10-undecenoic acid, or a 1:1 molar solution of 1,8-nonadiyne and 10-undecenoic acid. Finally, the functionalized silicon surfaces are reacted with **NMOF 2** or **4** or both, respectively, to form **S1-3**. **(b)** Selective anchoring of the **NMOFs 2** and **4** was shown by surface patterning via micro-contact printing on a silicon surface. Therefore, an etched silicon substrate was contacted with an 1,8-nonadiyne soaked PDMS stamp. The backfilling procedure was performed for 12 h at room temperature with 10-undecenoic acid. The patterned silicon surface was then sequentially reacted with **NMOF 2** (**S4**) and **NMOF 4** (**S5**).

In the last step, the different reactive moieties on the surfaces were exploited for the selective immobilization of the NMOFs at the functionalized Si surfaces. The alkyne-terminated Si surfaces (alkyne, mixed and patterned surface) were reacted with **NMOF 2** in a copper-catalyzed alkyne azide cycloaddition yielding a triazole bond. Subsequently, the carboxylic acid-terminated Si surfaces (carboxylic acid, mixed and patterned surface) were reacted with **NMOF 4**. Whereas the amide bond formation is facilitated by diisopropyl carbodiimide (DIC) and N-hydroxysuccinimide (NHS). We used several techniques like Scanning Electron Microscopy (SEM), X-ray Photoelectron Spectroscopy (XPS), Infrared Reflection Absorption Spectroscopy (IRRAS), Attenuated Total Reflectance Infrared Spectroscopy (IR-ATR), Dynamic Light Scattering (DLS), Powder X-ray Diffraction (PXRD), and nitrogen adsorption experiments (BET) to demonstrate the properties of the synthesized NMOFs and to prove that they were successfully and selectively positioned.

3.3.2. Silicon Substrate Functionalization

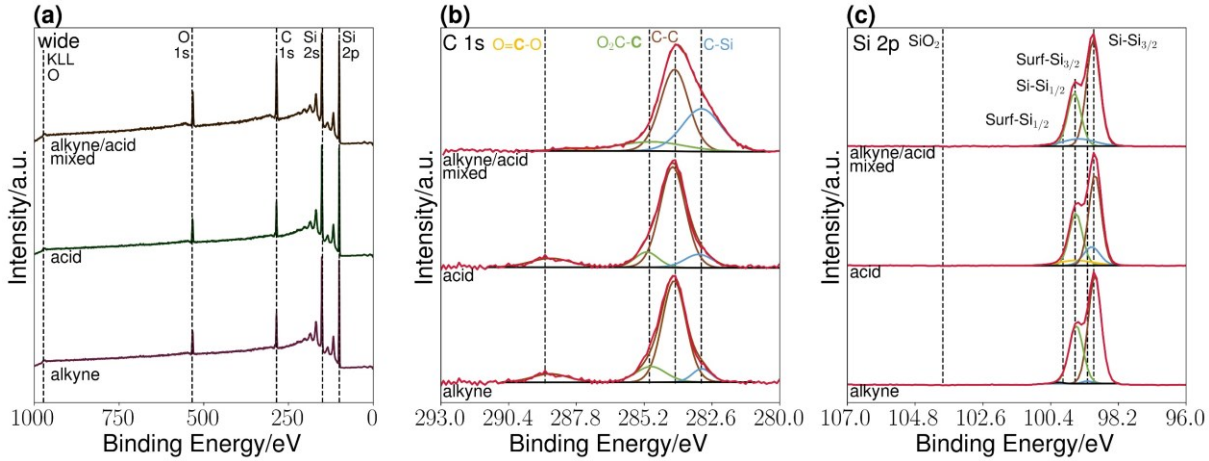

Figure 37: XPS survey scan (a), C 1s (b), and Si 2p (c) XPS narrow scans of alkyne, acid, and alkyne/acid-terminated monolayers on Si substrates.

The silicon substrates were functionalized as previously reported in the literature. Therefore, the native oxide is removed by etching with a degassed, aqueous 40w% solution of NH_4F resulting in a hydrogen-terminated silicon surface. These substrates can be utilized for the Si-C bond formation by the reaction with alkynes or alkenes as described in chapter 0. For this reason, the hydrogen-terminated substrates were immersed in degassed, neat 1,8-nonadiyne, 10-undecenoic acid, or a 1/1 molar mixture of both for 12 h at 100°C.

After rinsing, the resulting substrates were investigated by XPS, IRAAS, and contact angle measurements. The XPS spectra of the three modified surfaces show the presence of Si, C, and O as reported in the literature (see Figure 37).[269,292] In the case of the 1,8-nonadiyne, the oxygen content can be explained by covalently bound oxygen, which presumably originates from the 1,8-nonadiyne.[269] The XPS C 1s narrow scans can be deconvoluted into different components which can be assigned to a C-C bond peak (285.0 eV), Si-**C**=C bonds (284.0 eV), **C**-O/**C**-CO_2H (286.0 eV), and C-**C**O_2H (290.0 eV).[269,292,293] Evaluating the Si 2p narrow scan reveals that the Si-O peak at 101-104 eV is non-existent. This observation indicates the formation of densely packed SAMs that prevented the oxidation of the etched Si-H substrate surfaces. The related O 1s narrow scans of the three surfaces can be found in the appendix (see Figure S40).

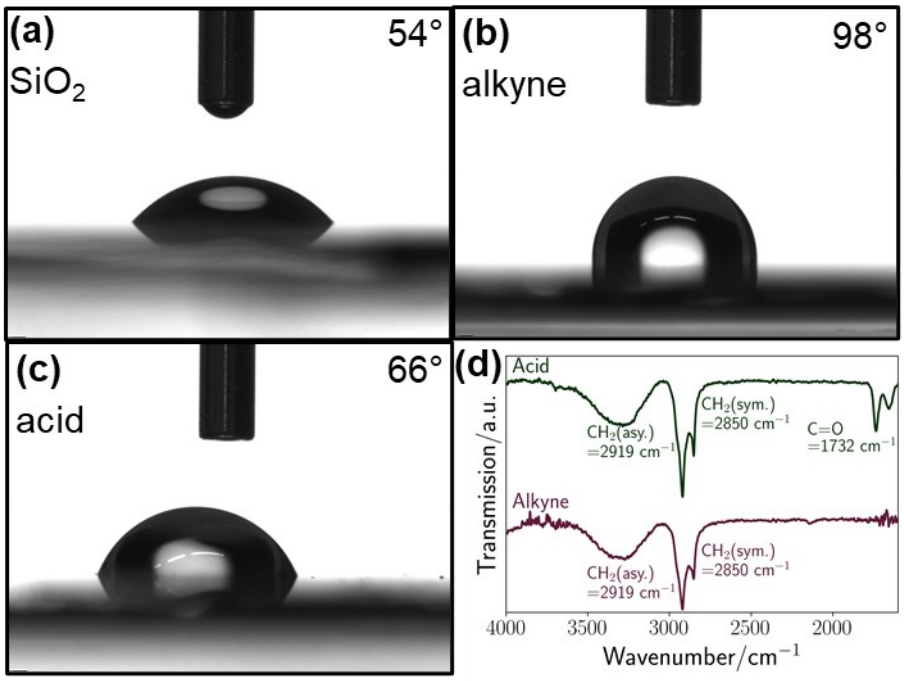

Figure 38: Contact angle measurements of untreated silicon surfaces with an native oxide surface (a), alkyne terminated surface (b) and carboxylic acid (c) terminated silicon surfaces. IR spectra (d) of alkyne terminated surface and carboxylic acid functionalized silicon surfaces.

Further investigations of the surfaces, by IRRAS spectra, show the symmetric and antisymmetric C-H stretch vibrations as well as the C=O stretching vibration for the carboxylic acid-terminated self-assembled monolayer, which is in accordance with the literature and confirms the formation of SAMs (see Figure 38 d).[294,295] The static water contact angle (see Figure 38 a-c) of the surfaces can indicate a change in surface polarity and therefore prove successful surface functionalization. The contact angles were determined as 93 ± 3° for the alkyne terminated monolayer,[269,293] 65° for the -COOH terminated monolayers,[296] and 54° for the pristine, native oxide surface on silicon. Similar to the results reported by XPS and IRRAS, the measured contact angles are in good agreement with the values measured in the literature. Moreover, this corroborates the successful preparation of alkyne, acid, and alkyne/acid mixed terminated surfaces.

3.3.3. NMOF Preparation, Functionalization, and Characterization

Preparation. Nanometer-sized UiO-66 (N-UiO-66, **NMOF 1**) and MIL-101 (N-MIL-101, **NMOF 3**) particles were synthesized via two different approaches. **NMOF 1** was prepared by the solvothermal synthesis of H_2bdc, acetic acid, and $ZrOCl_2$ in DMF at 90°C for 18 h, which resulted in a white colloidal solution.[290] **NMOF 3** was prepared by harsh reaction conditions (H_2O, 200 °C, 1 min) in a microwave reactor,[291] resulting after filtration in a green colloidal solution of MIL-101. The correlation between these parameters and the particle size was recently published, together with an investigation

of the influence of acidity, the concentration of the ligand, and modulator on the particle size.[297] (see chapter 3.1.1).

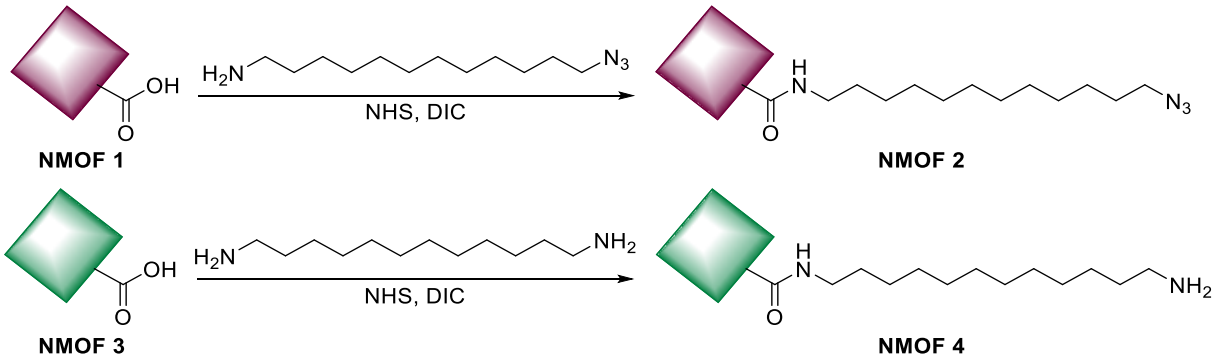

Figure 39: UiO-66 (**NMOF 1**) and MIL-101 (**NMOF 3**) are reacted with 12-azido dodecane-1-amine (ADA) and 1,12-diamino dodecane (DAD), respectively, to form functionalized MOF NPs **NMOF 2** and **NMOF 4**.

Functionalization. NMOF 1 and **NMOF 3** were functionalized on their outer surface as shown in Figure 39. For this reason, the carboxylic acid groups of the dangling bdc linkers on the outer surface of the NMOFs are reacted with 12-azido-dodecane-1-amine (ADA) or 1,12-diamino dodecane (DAD), respectively, to form the functionalized **NMOFs 2** and **4**. It should be noted, that the surface functionalization of the NMOFs can act as a capping agent, stabilizing the NMOF in solution and preventing agglomeration, and additionally introducing functional groups to the outer NMOF surface. Subsequent experiments, which we will not discuss in detail, showed that the utilization of shorter alkyl chains (C_3 (isopropylamine)-C_8 (octyl amine) can have similar stabilizing effects.

Characterization. NMOFs 1-4 were further characterized by SEM, PXRD, DLS, XPS, IR, TGA, BET, and NMR following nanoparticle digestion.

Particle size determination. The particle diameter of **NMOFs 1-4** was determined by electron microscopy imaging (see Figure 40). Different images of the **NMOFs** were recorded at different magnifications. Analyzing the recorded images with Image J, the size of at least 200 particles was measured and histograms were created from these measurements (see Figure S49-S56). An average size of ~23 nm for all NMOFs was calculated (see Table 5).

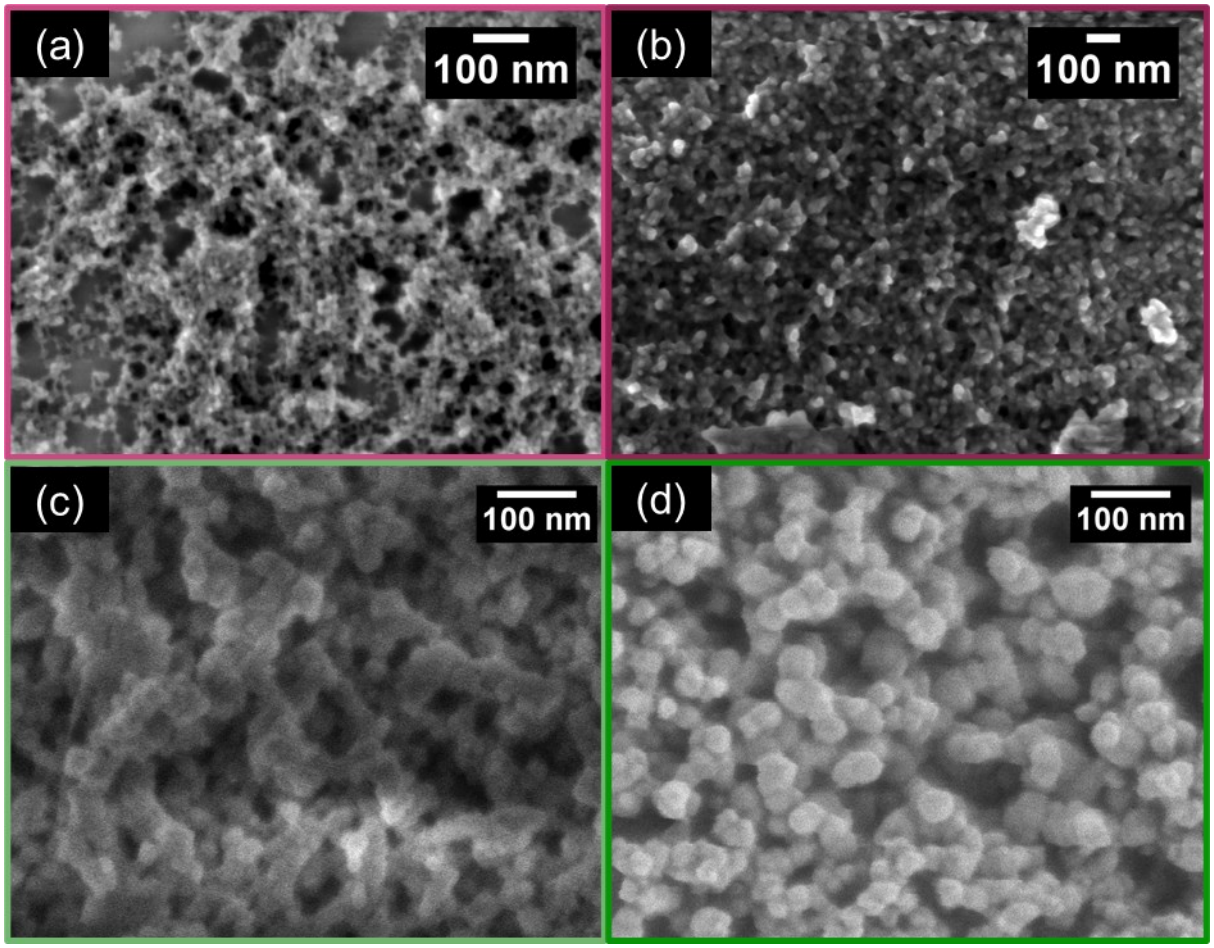

Figure 40: SEM images of **NMOF 1-4** (a-d). The SEM samples were prepared by drop coating of a colloidal ethanol solution onto pristine silicon substrates. If the samples were activated (at 100°C, oil pump vacuum) before the measurement, we observed severe particle aggregation.

Table 5: Particle diameter, hydrodynamic diameters, and crystalline domain sizes of NMOF 1-4 determined by SEM, DLS, and PXRD, respectively.

determined by	SEM	PXRD	DLS	
sample	Particle diameter [nm]	Crystalline domain size [nm]	Hydrodynamic diameter [nm]	Hydrodynamic diameter [nm] after 4 weeks
NMOF 1	21.0 ± 3.3	17.7 ± 2.1	164 ± 24	531 ± 76
NMOF 2	23.4 ± 2.5	16.9 ± 1.5	91 ± 38	78 ± 24
NMOF 3	26.7 ± 3.9	12.4 ± 2.8	79 ± 33	106 ± 47
NMOF 4	24.6 ± 3.8	13.0 ± 2.3	91 ± 34	91 ± 46

Upon surface functionalization, the measured size distribution changes slightly. However, unfunctionalized as well as functionalized particles are similar to the values reported for **NMOF 1** and **3** in literature: 22 nm ± 8 nm for **NMOF 1**[290] and 22 nm ± 5 nm for **NMOF 3**[291].

The DLS number distributions (see appendix, Figure S41-S44, see Table 5) show the average hydrodynamic diameter of the particles in solution. Due to the subsequent

application of these colloidal solutions in catalysis, the size of the particles in solution and their stability over time is important: DLS measurements, which measure the hydrodynamic radius, usually result in larger diameters compared to SEM imaging due to the solvent shell adsorbed at the surface of the NMOF. The measured diameter of the NMOF shows that **NMOF 1** aggregates over time resulting in an increased hydrodynamic radius and precipitation of the particles from the solution. In contrast to this, **NMOF 3** forms a more stable colloidal solution. A slight increase in the hydrodynamic radius is observed over time, but the solution is still colloidal, and any increase after 4 weeks is still within the margin of error. Hence, **NMOF 2** and **4** are stable colloidal solutions, which do not aggregate over time.

Crystallinity. Further investigations, by PXRD, show that the synthesized NMOFs 1-4 (see Figure 41 a,b) feature the targeted structure of bulk UiO-66 and MIL-101, respectively. The major reflections at 7.3°, 8.5°, and 25.7° corresponding to the (111), (200), and (600) lattice planes for **NMOF 1** and 5.2°, 8.4°, and 16.3° corresponding to the (531), (822), (911), and (15 7 1) lattice planes for **NMOF 2.** Moreover, they illustrate that the structure is retained during the particle functionalization process. The line broadening in reference to the calculated patterns relates to a reduced crystalline domain size (CDS), indicating their nano crystallinity. The average crystalline domain size can be determined by the calculation with the Scherrer equation from all major reflections of UiO-66 and MIL-101 and averaging those for each NMOF separately.

The Scherrer equation is a powerful tool in the analysis of powder patterns to calculate the size of the crystalline domains. The CDS relates to the line broadening of the reflections depending on the size of the crystalline domains. However, it should be noted that the equation is only valid for CDS below 100-200 nm as for larger CDS the size-dependent broadening is hard to separate from other (i. a. instrument-specific) line broadening effects.[298]

Scherrer equation, as depicted in Equation 1 with τ being the mean ordered crystalline domain size [nm], K the shape factor (if spherical K=0.9), λ the X-ray wavelength [nm], β the line broadening at half the maximum intensity (FWHM) and θ the Bragg angle. Equation 1:

$$\tau = \frac{K\lambda}{\beta \cos(\theta)}$$

Example for **NMOF 1**: K=0.9 (for spherical objects); λ=0.154 nm; 2θ = 7.31° (for the 111 reflection; θ = 3.65°; in radian: 0.0637) and FWHM: 0.482 (in radian: 0.00841)

$$\tau = \frac{0.9 \cdot 0.154\ nm}{0.00841 \cdot \cos(0.0637)} = 16.5\ nm$$

The CSDs for the **NMOFs 1-4** are shown in Table 5. Note that, the CDS should not be confused with the particle size. A large particle of 200 μm can either contain one crystalline domain, in which case it would be a single crystal, or it could contain, 10 crystalline domains of 20 nm each. In turn, this shows that **NMOF 1** and **2** contain ~ 1

crystalline domain per NP, whereas **NMOF 3** and **4** contain ~ 2 crystalline domains per NP. The analysis of the PXRD patterns showed, that **NMOF 1-4** possesses the expected nano-crystalline structures, and the structures are retained after functionalization.

Vibrational Spectroscopy. Additionally, the NMOFs were examined with IR spectroscopy (see Figure 41c,d). These reveal that **NMOFs 2** and **4** are blended materials consisting of ADA and **NMOF 1** and DAD and **NMOF 3,** respectively. The CH_2 stretching vibrations from the ω-functionalized alkane-α-amines (~2900 cm^{-1}), which are absent in the spectra of **NMOF 1** and **3**, become visible in the spectra of **NMOF 2** and **4**. Additionally, the azide stretching vibration around 2100 cm^{-1} can be observed for **NMOF 2** indicating the presence of an azide group in **NMOF 2.** Moreover, it is clearly visible that the band at 1664 cm^{-1}, which originates from the OH bending vibration of the free carboxylic acid, is absent in **NMOF 2**. This suggests that the ω-functionalized alkane-α-amines reacted with the dangling bdc linkers on the exterior surface of the NMOFs forming amide bonds. These observations corroborate the successful surface functionalization of **NMOF 1** and **NMOF 3** to form **NMOF 2** and **4**, respectively.

Mass fraction of ADA/DAD. Another critical aspect was to calculate the amount of ADA or DAD that was incorporated into the NMOF structure. Therefore, **NMOFs 2** and **4** were digested in a solution of DMSO-d_6/DCl (37w%) (0.4/0.1 mL), and the NMR spectra were measured subsequently (see appendix, Figure S45-S48).[299] In the first step, the H_2bdc peak (δ = 7.01 ppm) was integrated and set to 24 H (12 H) (6x4H (3x4H) in formula unit). Afterwards, the integrals, which were ascribed to the 12-azido-dodecan-1-amine or 12-diamino-dodecane, were then used to calculate the mol% and w%. Note, that we also tried to determine the amount of ADA or DAD by solid-state NMR, which yielded similar results. Due to the very broad signals, we decided to use digestion NMR instead.

If a formula unit has 6 (3) H_2bdc molecules with 6 (3) free acid groups, 100 mol% would mean that one formula unit would react with 6 (3) molecules 12-azido-dodecan-1-amine corresponding to 24 x 6 H atoms.

$$mol\%\ (NMOF\ 2) = \frac{22.77}{24\ \cdot 6} \cdot 100 = 15.81\ mol\%$$

$$mol\%\ (NMOF\ 4) = \frac{15.1}{24\ \cdot 3} \cdot 100 = 20.97\ mol\%$$

To calculate the mass fraction (w%) of ADA and DAD we have to consider the molar masses:

$$wt\%\ (\mathbf{NMOF\ 2}) = \frac{m_{N3}}{m_{ges}} = \frac{15.81\ mol\% \cdot 224.37\frac{g}{mol}\ \cdot 6}{\left(15.81\ mol\% \cdot 224.37\frac{g}{mol} \cdot 6 + 1664\frac{g}{mol}\right)} = 11.34\ wt\%$$

$$wt\%\ (\mathbf{NMOF\ 4}) = \frac{m_{-COOH}}{m_{ges}} = \frac{20.97 mol\% \cdot 200.23\frac{g}{mol} \cdot 3}{\left(20.97 mol\% \cdot 200.23\frac{g}{mol} \cdot 3 + 717.0\frac{g}{mol}\right)} = 14.94\ wt\%$$

The obtained functionalization of **NMOF 2** is 15.8 mol% (11.3 w%) and for **NMOF 4** about 21.0 mol% (14.9 w%). This again demonstrates the successful functionalization of the NMOF particles.

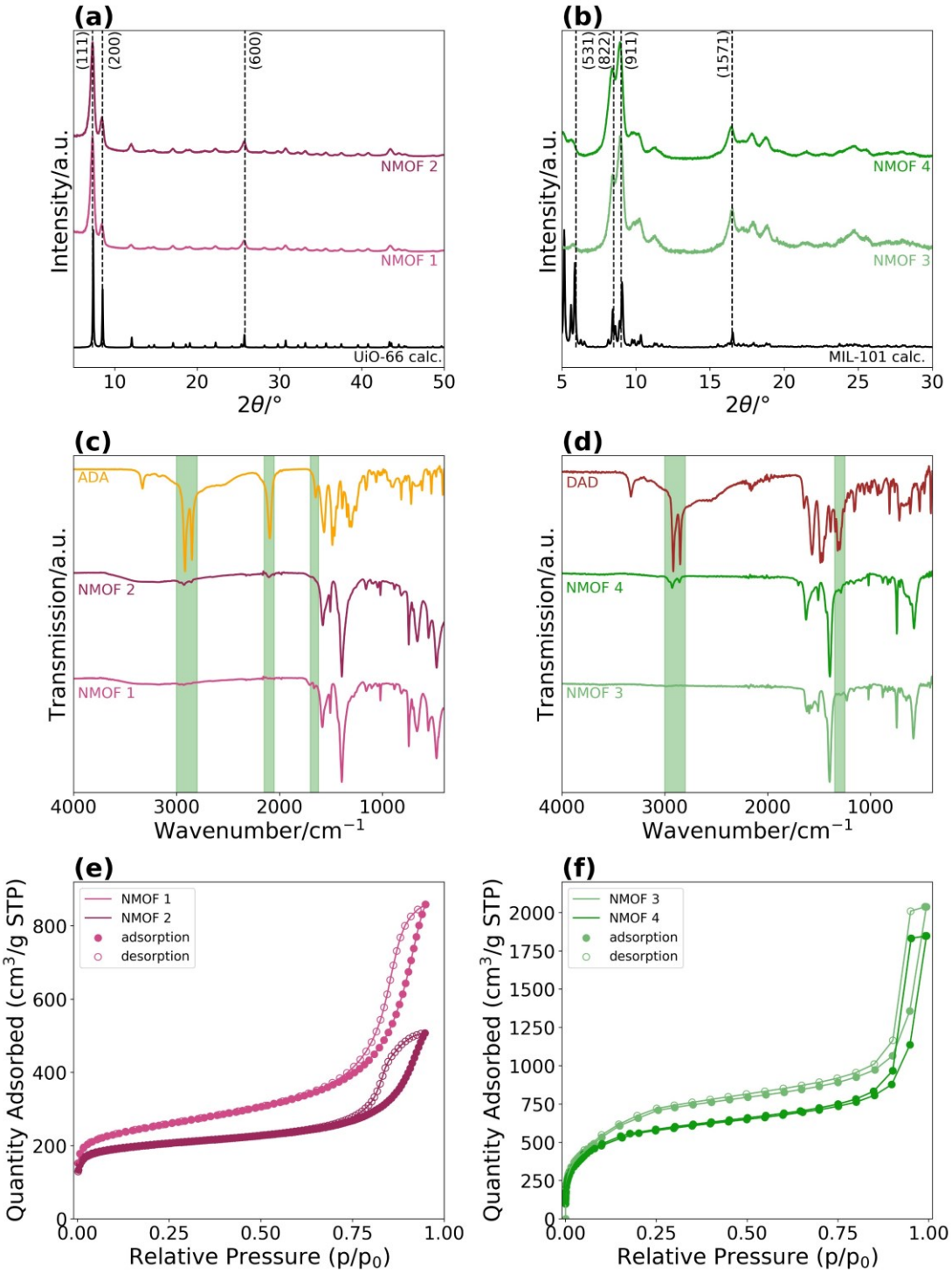

Figure 41: PXRD diffractograms of the activated (100 °C, 12 h) **NMOFs 1-2** (light/dark pink) (a) and **NMOF 3-4** (light/dark green) (b). The PXRD reference patterns (black) were calculated with Vesta from the single crystal structure of UiO-66 (CCDC 733458) and MIL-101 (Cr) (CCDC 605510), respectively. The IR spectra of **NMOFs 1-2** and **ADA** (orange) as well as **NMOF 3-4** and **DAD** (brown) are shown in (c) and (d). Specific areas of interest are highlighted in green. Nitrogen adsorption measurements (e,f) were recorded from the activated NMOFs (100 °C, 12 h, oil-pump vacuum). Adsorption and desorption isotherms are shown with full and empty symbols, respectively. BET surface areas are 918 ± 1 m^2/g (**NMOF 1**), 777 ± 1 m^2/g (**NMOF 2**),1856 m^2/g (**NMOF 3**), and 1632 m^2/g (**NMOF 4**), respectively.

N_2 sorption experiments. Further investigations of the NMOFs required the analysis of its accessible *inner* surface area before and after the exterior NMOF particle surface functionalization with nitrogen adsorption experiments (see Figure 41 e,f). Due to their possible application, a rather large accessible surface area is of utmost importance. In the past, the functionalization of the outer surface sometimes led to drastic changes in the accessible inner surface. A reduction of up to 65% (1260 m^2 g^{-1} to 450 m^2 g^{-1}) was reported.[290] The obtained weight-specific BET surface areas for **NMOF1-4**, however, show only a slight reduction by 15.3% (**NMOF 2** (918; 777 m^2/g)) and 12.0 % (**NMOF 4** (1856; 1632 m^2/g)), respectively. The observed reduction in the BET area matches with the range of the weight-specific NMOF particle surface functionalization. Overall, the BET measurements show that the obtained NMOFs exhibit only a slightly reduced *inner* surface area, which is still accessible. All results obtained for the characterization are summed up in Table 6.

Table 6: Summed up characterization results of **NMOF 1-4** obtained by SEM (particle diameter), PXRD (CDS), DLS (Hydrodynamic radius), N_2 adsorption experiments (BET surface area), and NMR digestion experiments (mass fraction of ADA and DAD), respectively.

	Particle diameter [nm]	CDS [nm]	Hydrodynamic diameter [nm]	BET surface [m^2/g]	ADA/DAD mass fraction w%
NMOF 1	21.0 ± 3.3	17.7 ± 2.1	164 ± 24	918	-
NMOF 2	23.4 ± 2.5	16.9 ± 1.5	91 ± 38	777	15.3 %
NMOF 3	26.7 ± 3.9	12.4 ± 2.8	79 ± 33	1856	-
NMOF 4	24.6 ± 3.8	13.0 ± 2.3	91 ± 34	1632	12.0 %

3.3.4. Targeted NMOF Anchoring

In the final step, the **NMOFs 2** and **4** were anchored to the matching surfaces. For this reason, **NMOF 2** was reacted with the alkyne terminated and alkyne/acid mixed surface in a CuAAC reaction forming covalent triazole linkages between the NMOFs and the functionalized surfaces. **NMOF 4** was covalently immobilized on the carboxylic acid and alkyne/acid mixed surfaces by utilizing DIC and NHS to form amide bonds. The resulting surfaces **NMOF 2**@alkyne-Si (**S1**), **NMOF 2** and **4**@alkyne/acid mixed-Si (**S2**), and **NMOF 4**@acid-Si (**S3**) were investigated by XPS and SEM. A schematic illustration of the different approaches can be found in Figure 36.

XPS. XPS spectra reveal the presence of N, O, and C as expected in all samples (see Figure 42). Zr and Cr, however, are only present in **NMOF 2**, **S1**, and **S2** and **NMOF 4**, **S3,** and **S2**, respectively. Si is only detected for the samples **S1-3**, as the NMOF samples are not measured on silicon substrates.

The absence of a peak at ~933 eV (Cu $2p_{3/2}$) in samples **S1** and **S2** indicates that the Cu catalyst for the CuAAC has been fully removed by washing and sonication.

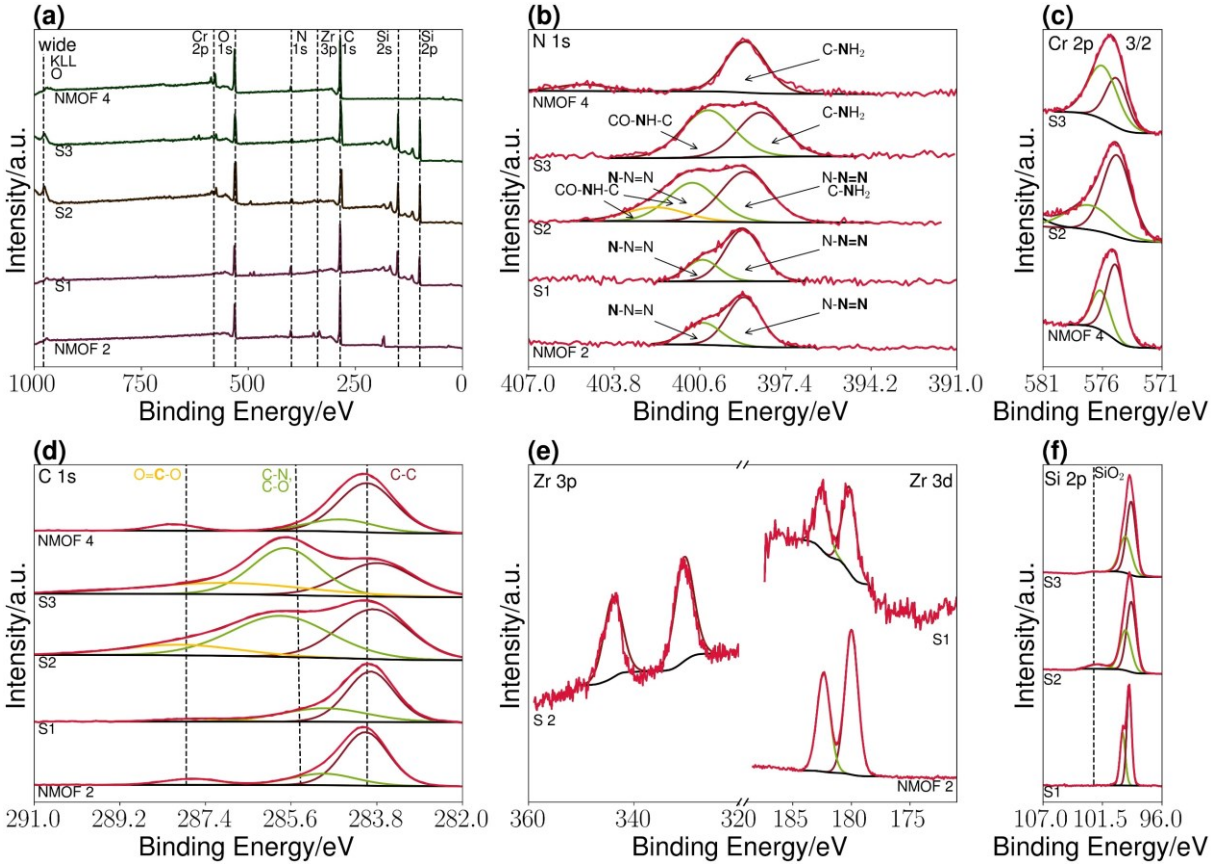

Figure 42: XPS survey spectra (a) of **NMOFs 2** and **4** and **S1-3** as well as the corresponding narrow scan spectra for N1s (b), Cr 2p 3/2 (c), C 1s (d), Zr 3p/3d (e), and Si 2p (f).

The C 1s and N 1s XPS narrow scans are particularly interesting. The N 1s narrow scan of **NMOF 2** and **S1** can be deconvoluted into two components at 400 and 401.6 eV, which can be assigned to N-**N**=N and **N**-N=N as part of the azide group or the triazole linkages.[300,301] The calculated ratio of both areas of 1:2 resembles the measured ratio of 1:2.1. The N 1s narrow scan of **NMOF 4** on the other hand can be deconvoluted in two components, which can be assigned to the dangling amine groups on the NMOF exterior surface (399.0 eV) and partly protonated amine groups (~405 eV). **S3** shows a similar spectrum as **NMOF 4** but with an additional peak at 400.8 eV, which can be assigned to the formed amide bonds between **NMOF4** and the carboxylic acid terminated surface. The **S2** N1s narrow scan combines the C-NH_2 groups, visible in the spectrum of **NMOF 4,** and the N_3 groups (see N1s spectrum of **NMOF 2**), which are partly free dangling groups and partly involved in an amide or triazole bond to the surface resulting in a highly complicated spectrum.

The major peak in the C1s spectra for all samples at 285.0 eV originates from C-C bonds, either from the surface modification, from the bdc linker of the NMOF, or the alkyl chains of the ω-functionalized alkane-α-amines covalently attached to the bdc linkers. The peak around 286.4 eV stems from C bound to electronegative atoms like O or N. Due to the additional triazole and amide bonds which are formed during the

anchoring, this peak is more pronounced in the spectra of **S1-3**. Furthermore, the peak at 289.0 eV can be assigned to C=O species, which are either present in the carboxylic acid of the surface functionalization or at the bdc linker of the NMOFs. In summary, the XPS spectra prove the successful immobilization of **NMOF 2** at the alkyne surface, **NMOF 4** at the carboxylic acid surface, and both NMOFs at the mixed alkyne/acid surface by the formation of a covalent bond.

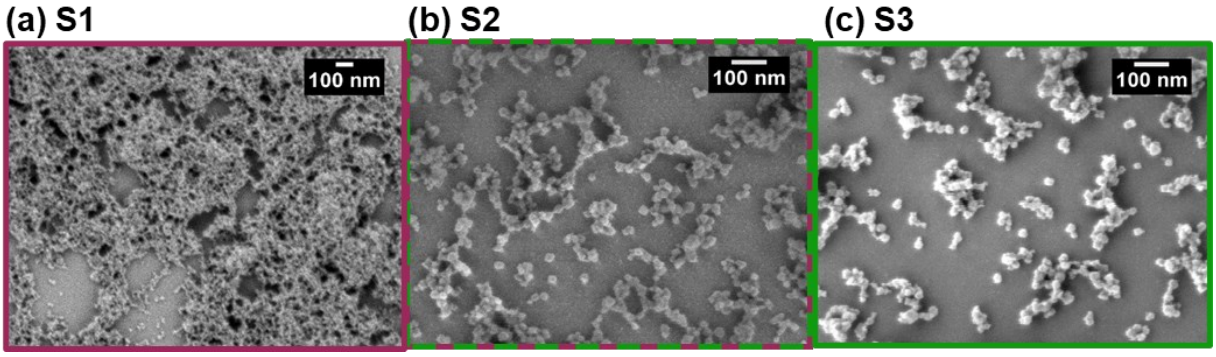

Figure 43: SEM images of **S1-3** (a-c). The additional SEM images and histograms of the size distributions can be found in the SI, chapter S11. Compare with Figure 36 for the different synthetic routes to obtain **S1-3.**

SEM. Finally, the substrate surfaces **S1-3** were investigated by electron microscopy (Figure 43, appendix Figure S57-S64). These images reveal the distribution and arrangement of the NMOFs on the surfaces. The first observation from these images is, that the particles deposited on the surface exhibit a similar size as reported and measured for the NMOFs. The anchored NMOFs are slightly agglomerated, but only to a small extent and the individual particles are still visible. A more detailed analysis of 200 particles each reveals that the average particle diameter of the NMOFs is 18.0 ± 2.8 nm (**S1**), 22.4 ± 3.3 nm (**S2**), and 24.2 ± 3.3 nm (**S3**), which similar to the measured sizes of **NMOF 2** and **4** (see Table 5). **NMOF 2** seems to agglomerate more during the reaction, which might be caused by the Cu catalyst. Therefore, we observed a denser particle structure than for **NMOF 4**.

3.3.5. Orthogonal Anchoring by Surface Patterning

For the final evidence, that NMOFs can be selectively positioned on substrate surfaces, patterned surfaces were prepared. Therefore, a 1,8-nonadiyne PDMS stamp with a pattern of 20 x 20 μm elevations was placed on top of an etched silicon substrate under inert conditions for 12h. Afterwards, the stamp was removed and the unreacted sides of the substrate were backfilled with 10-undecanoic acid, creating a pattern of alkyne and acid terminated sides on the silicon substrate (see Figure 36).

Subsequently, this patterned substrate was then reacted with **NMOF 2** forming **S4** at first, followed by the reaction with **NMOF 4** yielding **S5**. The surfaces **S4** and **S5** were then investigated by SEM (see Figure 44).

SEM. Figure 44 b-d shows the patterning of the surface after the reaction with **NMOF 2** resulting in distinct patterns on the silicon surface. The lighter colour in the 20 μm x 20 μm indicates the positioning of insulating **NMOF 2** onto the surface. Further magnification shows that the NMOFs still have a similar shape and size as observed in previous images. These surfaces subsequently reacted with **NMOF 4** resulting in **S5** (Figure 44 f-i). The overall light colour of the images indicates that the NMOFs are then bound to the whole surface. Different magnifications of the areas show that NMOFs are attached to different areas of the substrate. We additionally tried to prove the selective positioning by labelling the NMOFs with dyes or by elemental mapping by SEM-Energy-dispersive X-ray spectroscopy (EDX). Unfortunately, this proved difficult due to the small amount of NMOFs/dyes deposited on the surface and the large penetration depth of the SEM-EDX surface. Only revealing the silicon surface below.

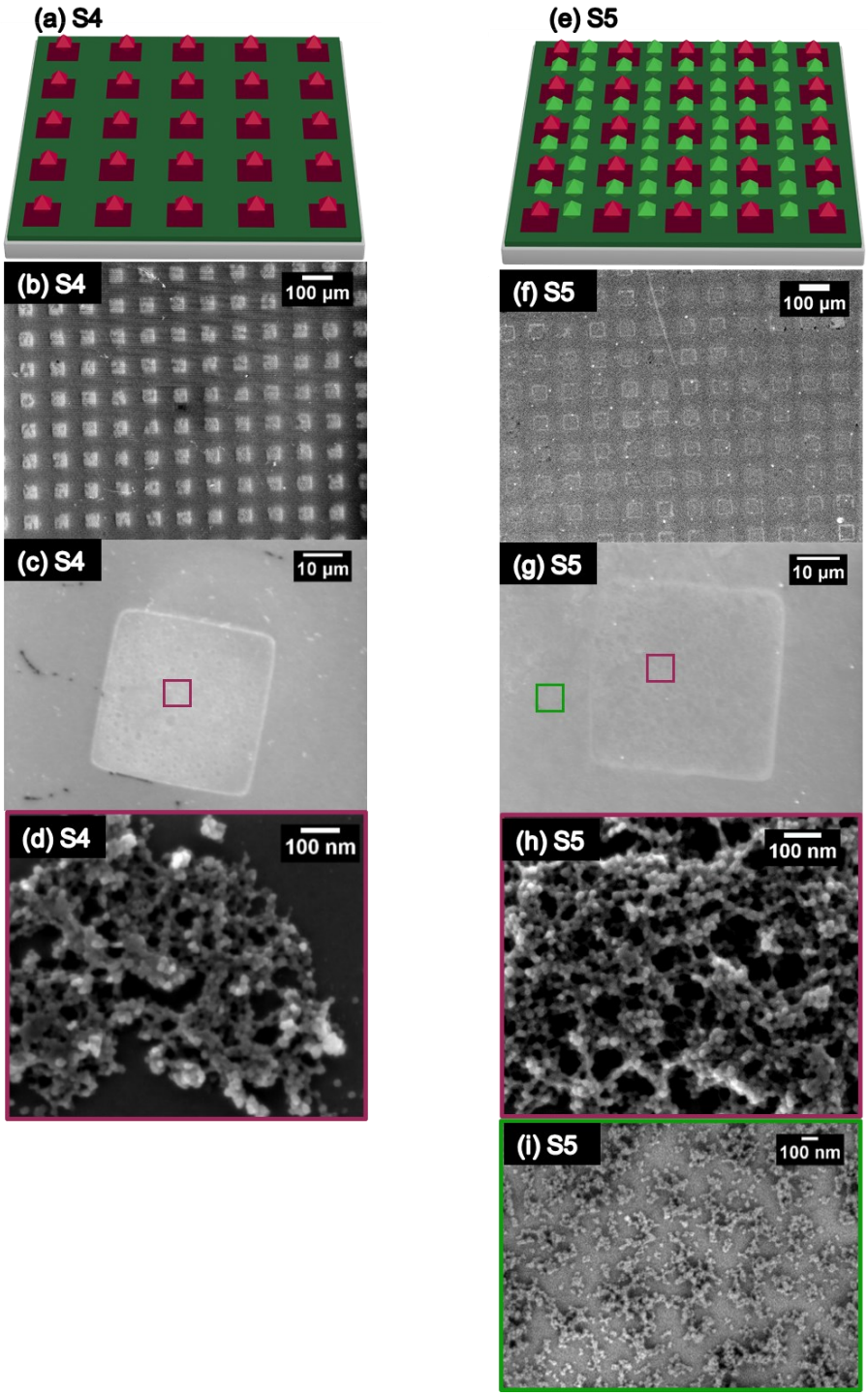

Figure 44: Schematic representation of **NMOF 2** (pink spheres) at the patterned alkyne (light pink), carboxylic acid (dark green) terminated surface **S4** (a) and **NMOF 2 and NMOF 4** (green spheres) at a similarly patterned surface **S5** (b) as well as the corresponding SEM images of patterned Si surface **S4** (b-d) and **S5** (f-i) after the reaction with **NMOF 2** and **NMOF 2** and **4** respectively. The images show the surfaces in different magnifications. The pink and green framed images are magnifications of the coloured areas in the images (c) and (g), respectively. An image of the patterned surface without any NMOF and further SEM images can be found in the appendix, Figure S65-Figure S70).

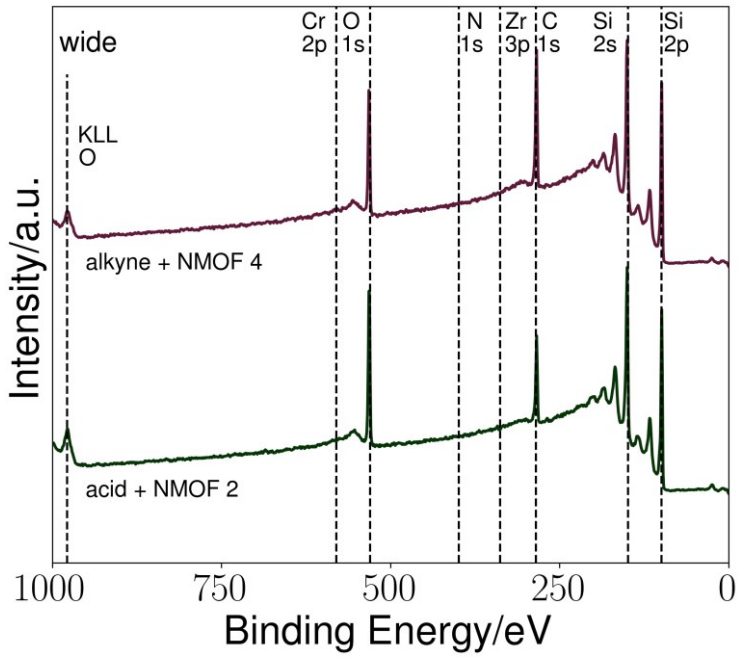

Figure 45: XPS spectra of the alkyne functionalized surface after immersion in a solution of NMOF 4 and DIC/NHS and acid terminated surfaces after immersion in a solution of NMOF 2, $Cu(PPh_3)_3Br$, THF for 24 h. Before the measurement, the substrates were washed with copious amounts of water and ethanol and sonicated in water, ethanol, and DCM for 5 min each.

Control experiments. To further elucidate the nature of the patterning experiments, two sets of control experiments were conducted. In detail, an alkyne terminated surface was reacted with **NMOF 4** and the acid terminated surface was reacted with **NMOF 2**, resulting in no selective binding or physisorption to the substrate surface. This proves that the NMOFs which are present at the surface after rinsing and sonication are covalently bonded to the surface (see Figure 45).

XPS. Further experimental investigation on the selective positioning (spatial distribution) was conducted by XPS analysis (Figure 46). To enable the XPS analysis an analogous macro-patterned surface was created. As a typical XPS measurement required 700 x 700 µm of surface and the micro-pattern is hard to spot a macro-pattern surface with two differently functionalized areas with dimensions of 0.35 x 0.4 cm were created. Therefore, two PDMS substrates with dimensions of 0.34 x 0.4 cm were immersed in either 1,8-nonadiyne or 10-undecanoic acid. These prepared PDMS stamps were then placed on top of an etched silicon substrate under inert conditions for 12 h, which then created a functionalized macro-pattern on the silicon surface.

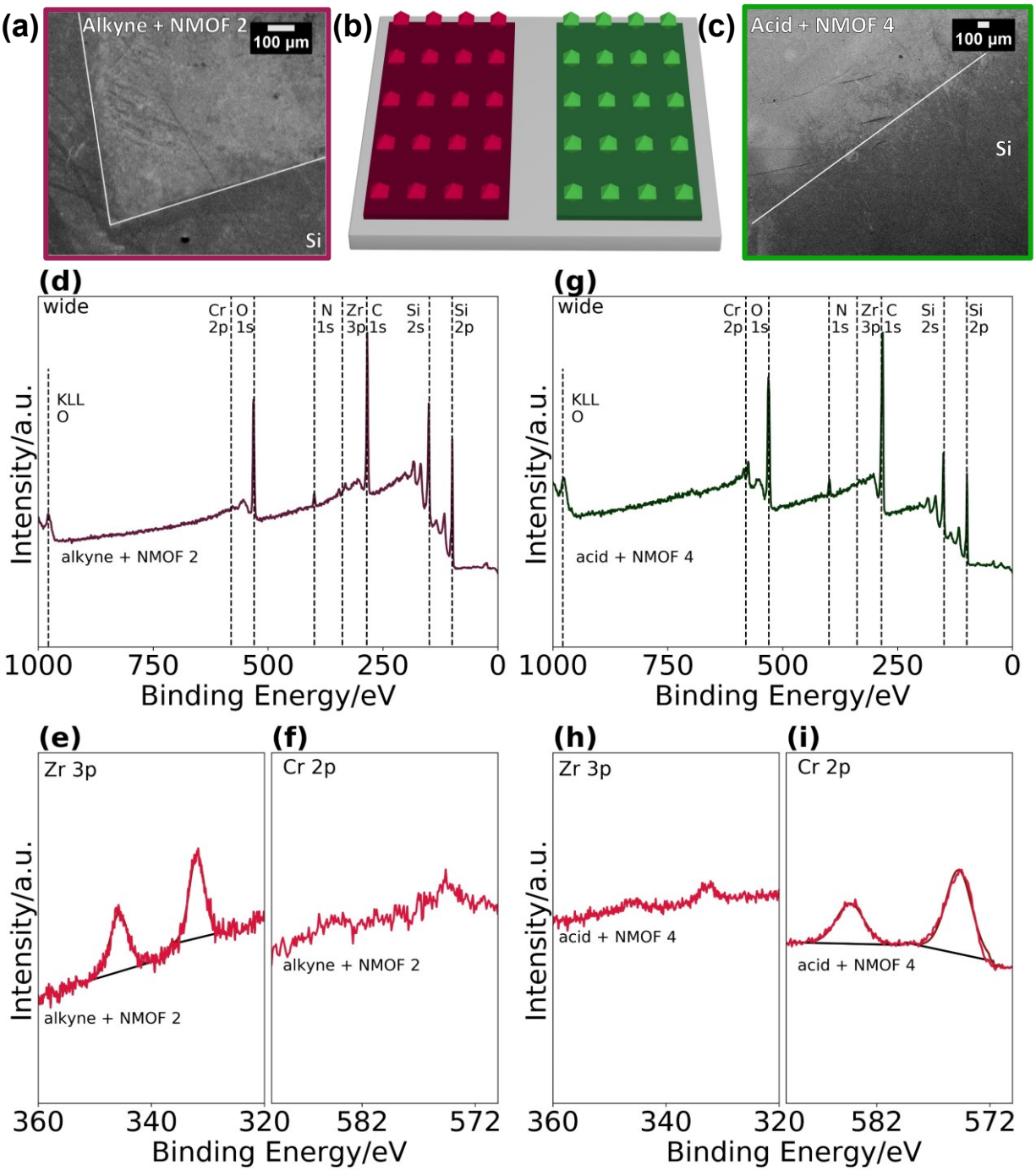

Figure 46: Selective NMOF positioning on macro-patterned substrate surfaces. Schematic representation of a silicon surface with a functionalization pattern created with PDMS substrates of 0.35x0.4 cm dimension. The left side of the substrate was functionalized with 1,8-nonadiyne (dark red), while the right side was functionalized with 10-undecenoic acid (dark green). After consecutive reactions with **NMOF 2** (light red) and **NMOF 4** (light green), the substrate (a) was obtained and investigated by SEM (a,b) and XPS (b-g). The survey spectra (d,g), and the Zr 3p (e,h), and the Cr 2p(f,i) narrow scan were recorded for the alkyne terminated side (red, d-f) and the acid-functionalized side (green, g-i), respectively.

The latter was washed and subsequentially reacted with **NMOF 2** and then subsequentially with **NMOF 4**. The resulting surface (see Figure 46 b) was investigated by SEM and XPS using the characteristic Zr and Cr signals to identify the respective MOFs. The XPS analysis of the left (alkyne, red) side shows the presence of Zr and the absence of Cr, indicating that **NMOF 2** (Zr) (Figure 46 e,f) selectively binds to the surface. On the right side, however, Cr is present and Zr absent showing the presents of **NMOF 4** (Cr) (Figure 46 h, i). This provides unequivocal evidence of selective positioning of the NMOFs on the macro-patterned surface. It is reasonable to conclude, that the same situation holds for the micro-patterned substrates (see Figure 44).

3.3.6. Summary

In this chapter, we successfully synthesized, characterized, and selectively immobilized two different NMOFs on a substrate surface. As a first step, nanometer-sized UiO-66 and MIL-101 particles were synthesized according to the literature. Subsequently, these NMOFs were functionalized on their exterior surface likewise to several silicon substrates exhibiting matching surface functionalizations. This was followed by the reaction of the azide-terminated UiO-66 NP with alkyne-functionalized Si surfaces, resulting in the triazole formation by click chemistry and their immobilization on the surface. Amino functionalized MIL-101 NP were combined with carboxylic acid-terminated Si surfaces yielding their covalent immobilization via amide bonds. Multiple characterization methods, e.g. XPS and SEM, revealed the successful immobilization. Finally, a surface patterning experiment demonstrated that the positioning of the NMOFs is selective and can be actively controlled by the choice of pattern. Specifically, azide-functionalized NMOFs only interact with alkyne-terminated surfaces, and amine-functionalized NMOFs only with carboxylic acid terminated surfaces. This paves the way for the application of selective positioning of desired materials at targeted parts in microfluidic devices and further provides the possibility for selective, tandem, or cascade catalysis.

3.4. Study II: Substantial Turnover Frequency Enhancement of MOF Catalysts by Crystallite Downsizing Combined with Surface Anchoring

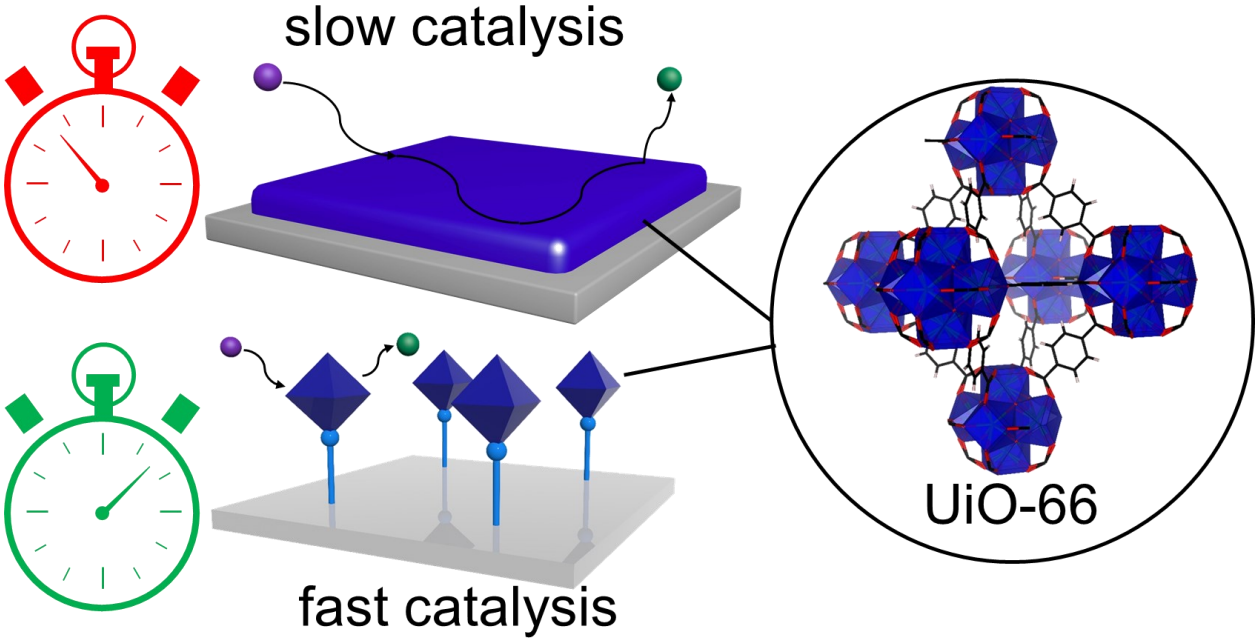

The results of this chapter were published in ACS catalysis as described below:

A. Lisa Semrau,† Philip M. Stanley,† Alexander Urstoeger, Michael Schuster, Mirza Cokoja, and Roland A. Fischer, Substantial turnover frequency enhancement of MOF catalysts by crystallite downsizing combined with surface anchoring, *ACS Catal.* **2020**, *10*, 3203-3011.

The project was designed by A. L. Semrau and R. A. Fischer. The experiments (synthesis, catalysis) and characterization were performed by A. L. Semrau and P. M. Stanley. This project was part of P. M. Stanley's master thesis, which was supervised by A. L. Semrau. The progress was regularly discussed with M. Cokoja and R. A. Fischer. The ICP-MS experiments were conducted and evaluated by A. Urstöger and M. Schuster. The final manuscript was written by A. L. Semrau and edited by all co-authors. Most of the editing and shaping of the manuscript was done by P. M. Stanley and M. Cokoja.

3.4.1. Prevent Agglomeration by Surface Anchoring

MOFs attract a lot of attention as heterogeneous catalysts at moderate temperatures, especially for liquid-phase reactions. Tuning their catalytic activity in these reactions has been the focus of numerous articles. Defect engineering has been described as one of the most effective methods to enhance the catalytic activity of MOFs.[302] Another approach, focusing on the size dependence of MOF particles was investigated by Janiak *et al.*[235] and Farha *et al.*[158] They concluded that MOF powders consisting of small primary particles (~100 nm) are more active in catalysis than larger primary particles. Despite the intense research efforts in this area, a report of colloidal NMOF particles with particle diameters significantly less than 100 nm in catalysis has not been reported yet (prior to 2017). The investigation of stability and applicability of NMOF (<<100 nm) colloidal solutions in catalysis is very important from a fundamental point of view and for future applications.

In this chapter, we present the comparison of bulk, defect-engineered MOF particles and colloidal dispersed NMOFs in different test reactions as Lewis acidic catalysts. Our results show that colloidal NMOF particles (~20 nm) tend to aggregate during the catalysis, making them less active in catalytic applications. Preventing aggregation by surface anchoring of NMOFs to substrate surfaces (SA-NMOF) enhances their catalytic properties substantially. Thus, they are 50,000-100,000 times more active than defect-engineered MOF powders. Additionally, we compared the catalytic activity of the SA-NMOF with bottom-up grown thin-films. We observed that SA-NMOFs are significantly more active in catalysis as compared to thin films, which we ascribe to the higher diffusion barrier.

3.4.2. Size Matters: Downsizing Enhances Catalytic Properties

For the catalytic investigations in this chapter, we utilized **NMOF 1** and **2** whose synthesis and characterization were already described in the previous chapter. However, it should be noted, that for better differentiation other colours (blue (**NMOF 1**), green (**NMOF 2**)) were used.

After their successful characterization, the NMOFs were utilized as catalysts for the cyanosilylation of benzaldehyde. The catalysis was conducted with 3 mol% of Zr loading in toluene as a solvent. Every experiment was carried out at least three times, resulting in the time-yield plots displayed in Figure 47. It should be noted that the yield equals the conversion since no side products were detected. More details about the calculation of the time yield plot can be found in chapter 6.3.2.6.

.

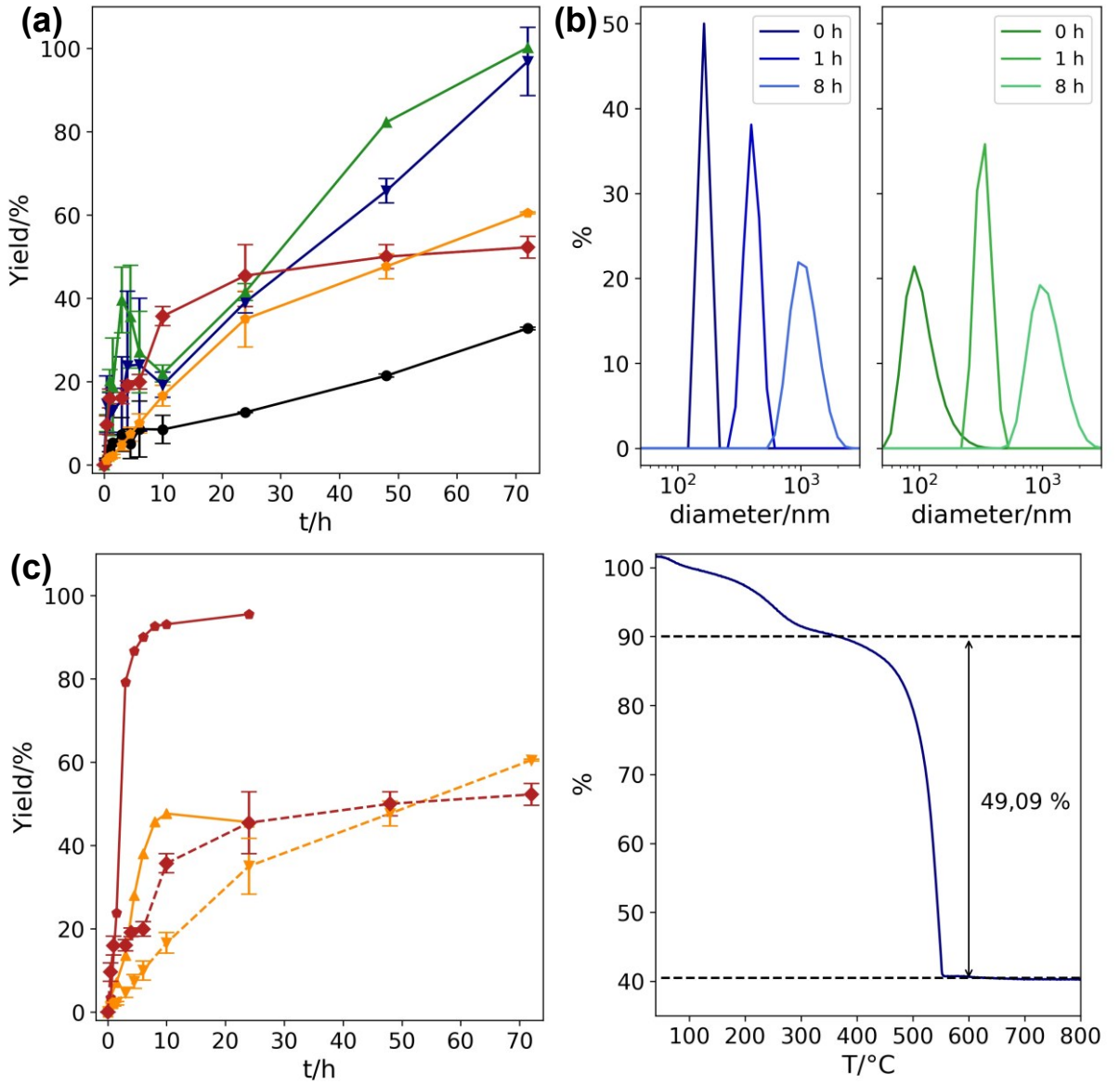

Figure 47: (a) Time-yield plot of cyanohydrin (2-phenyl-2-((trimethylsilyl)oxy) acetonitrile) produced by cyanosilylation of benzaldehyde and 2.0 equiv. TMSCN in toluene catalyzed by 3 mol% of Zr of **NMOF 1** (blue), **NMOF 2** (green), **UiO-66-HCl** (orange), **UiO-66-10TFA** (red), and without any catalyst (blank, black). (b) DLS spectra (number distribution) of **NMOF 1** and **2** were recorded before catalysis (0 h), after 1 h, and after 8 h of catalysis. TGA curves of activated (12 h, 100 °C) **NMOF 1** recorded under air from 30°C to 800 °C with a heat ramp of 10 K/min.

The kinetic curves of **NMOFs 1** (blue) and **NMOF 2** (green) shown in Figure 47a initially display a strong catalytic activity with low reproducibility. After this initial period, rapid deactivation of the catalyst can be observed, due to aggregation of the NMOF during the reaction. Further time-dependent investigation by DLS showed that that the initial hydrodynamic diameter of **NMOF 1** drastically increases from 164 nm to 396 nm after 1 h and 1110 nm after 8 h (see Figure 47). Unfortunately, ADA cannot

prevent the agglomeration of **NMOF 2** during the catalytic reaction as a similar trend was observed.

Reference samples/ control experiments. As a comparison, we wanted to employ bulk, defect-engineered UiO-66, and defect-free UiO-66 as reference catalysts. The comparison of the catalytic activities reported in the literature was complicated, due to different reaction conditions that were employed.[166] Therefore, we synthesized **UiO-66-HCl**, a sample with low defect content, and **UiO-66-10TFA**, a defect-engineered UiO-66 sample synthesized with 10 equiv. of trifluoroacetic acid (TFA), (see chapter 6.3.2.1 and appendix Figure S71) and repeated the catalytic experiments in dichloromethane (DCM) and toluene. We observed that the bulk catalysts are very sensitive towards the change of the solvent, as the reaction is significantly faster in DCM as compared to toluene (see Figure 47). When comparing the catalytic activity of bulk UiO-66 samples and the colloidal NMOFs, we observe that the catalytic activity of the colloidal NMOFs is higher than the bulk particles despite the agglomeration of the particles during the reaction. As this could be caused by a high defect content of the NMOFs, we calculated the missing linker defect content of **NMOF 1.** It was calculated from TGA data (see Figure 47) according to established procedures[179] and was determined at 13.7 % (see calculation below). This corresponds to the chemical formula of $Zr_6O_{6.82}(bdc)_{5.18}$ of the activated **NMOF 1** and is comparably low compared with defect-engineered MOFs. Their overall enhanced activity contrasts with the comparably low defect content and thus must be related to the reduced characteristic primary particle size.

Ideal mass loss of the dehydroxylated species:

$$w\% = \frac{M(Zr_6O_6BDC_6)}{6 \cdot M(ZrO_2)} = \frac{1628.1\ g/mol}{739.3\ g/mol} = 220.2\ \%$$

Weight contribution per bdc Linker (Wt. PL_{theo}):

$$Wt.PL_{theo} = \frac{220.2 - 100}{6} = 20.03\%$$

$$W_{Exp.Plat.} = \frac{100}{0{,}4909} = 203.7\%$$

$$NLexp. = (6 - x) = \frac{(W_{Exp.Plat.} - W_{End})}{Wt.PL_{theo}} = \frac{203.7 - 100}{20.03} = 5.18$$

⇨ $Zr_6O_{6.82}(bdc)_{5.18}$ (=> NMOF 1: 13.7 % missing linker defect)

3.4.3. Covalent Anchoring of the NMOFs at Substrate Surfaces

In the following step, we immobilized the NMOF catalysts chemically on substrate surfaces to prevent their deactivation by agglomeration. While the general idea is similar to the last chapter, the experimental part differs significantly. Due to the chosen model substrates polydimethylsiloxane (PDMS) and silicon (Si), a surface functionalization approach based on functionalized silanes instead of alkynes/alkenes was used. The surface anchoring (SA) of the NMOFs was achieved via two different routes, utilizing amide bond chemistry (**SA-NMOF 3**) and click chemistry (**SA-NMOF 4**) (see Figure 48) as already discussed in chapter 3.3.

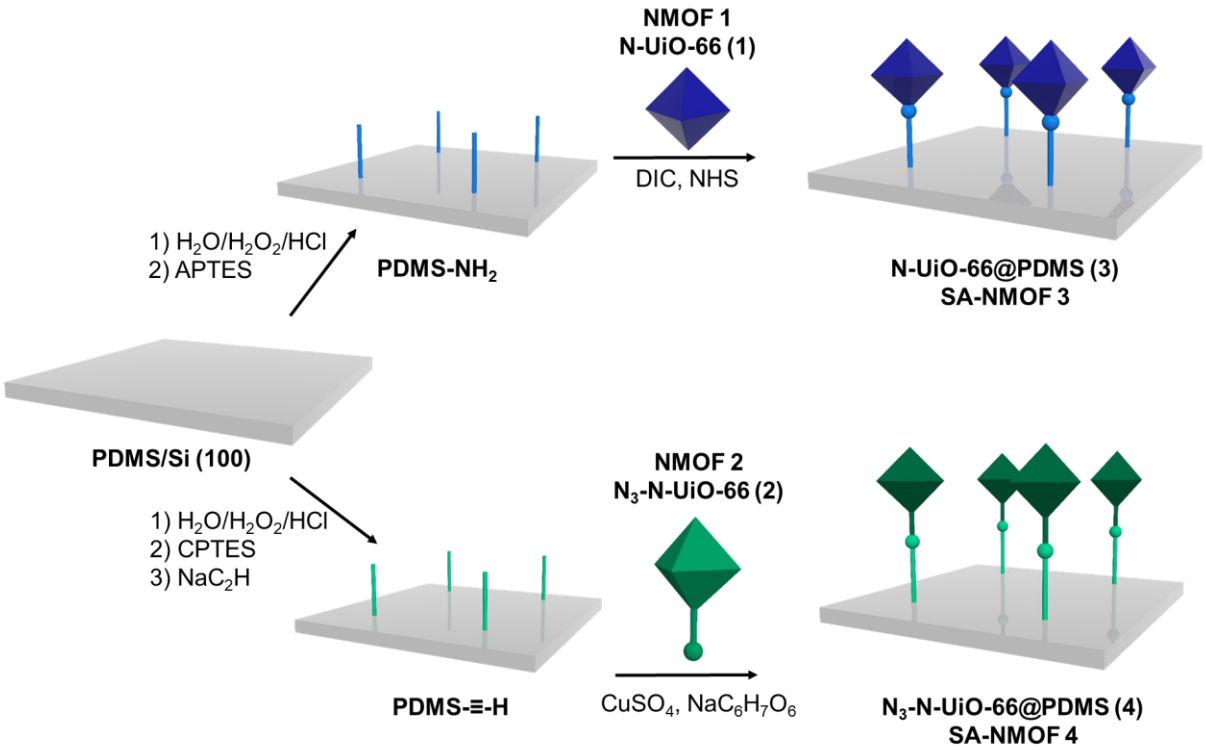

Figure 48: Surface anchoring of **NMOF 1** and **2** on functionalized PDMS or Si surfaces. For the amide bond approach, the HCl/H_2O_2 activated PDMS substrates are treated with 3-aminopropyl)triethoxysilane (APTES) to yield amino terminated PDMS surfaces. These surfaces are then reacted with **NMOF 1**, *N,N*-diisopropyl carbodimide (DIC), and *N*-hydroxysuccinimide (NHS) to form **SA-NMOF 3**. For the second route, similarly activated substrates are reacted with 3-chloroproyl)trimethoxy-silane (CPTES) and sodium acetylide to form alkyne terminated PDMS surfaces, which are treated with **NMOF 2**, $CuSO_4$, and sodium ascorbate for the CuAAC forming **SA-NMOF 4**.

First, the PDMS and silicon substrates were activated with HCl/H_2O_2 or piranha acid (*Caution: Piranha is a very strong oxidizer and can react explosively with organic compounds*) to generate more reactive hydroxyl groups on their surface. Then, the activated surfaces were reacted with (3-aminopropyl)triethoxysilane (APTES) or (3-chloroproyl)trimethoxysilane (CPTES), to yield amino- or chlorine-terminated surfaces, respectively. The chlorine terminated surfaces were treated with a sodium

acetylide/xylene slurry at 130 °C for 5 h to form alkyne terminated PDMS surfaces. The successful functionalization of the PDMS/Si substrates was investigated and confirmed by contact angle measurements, IR spectroscopy, and staining experiments (as discussed below).

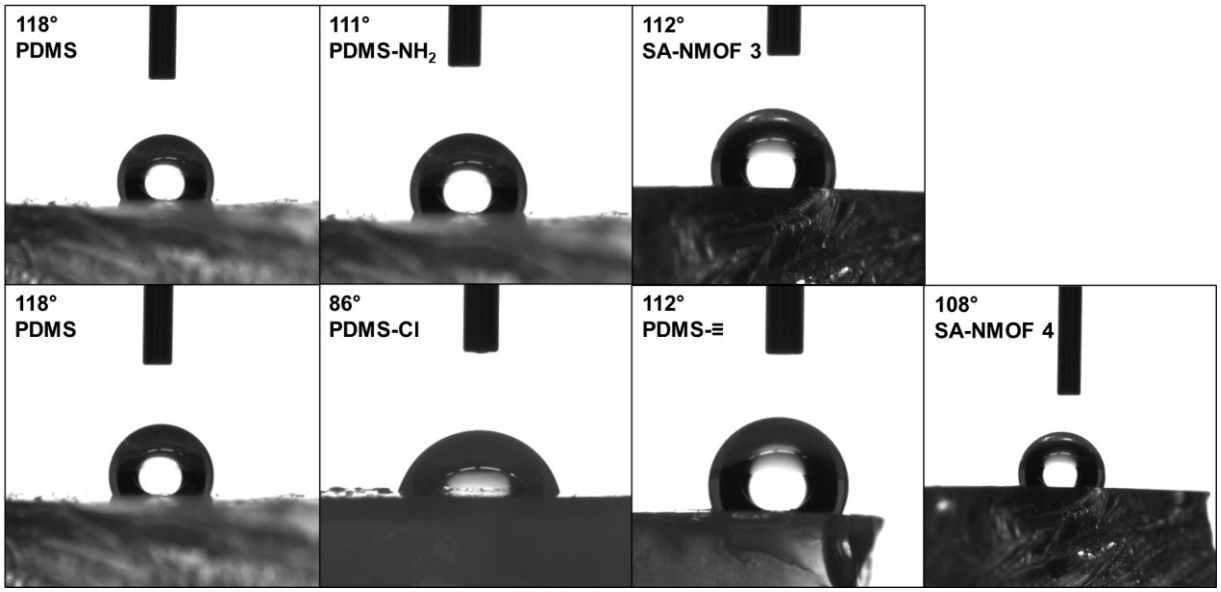

Figure 49: Contact angle measurements of various PDMS samples. From left to right and top to bottom: Native PDMS, PDMS after functionalization with APTES, forming amine-terminated surfaces, subsequent reaction with **NMOF 1** forming **SA-NMOF-3**. In the lower row, the contact angle measurements of native PDMS, Cl-terminated, and alkyne-terminated PDMS and finally reacted with **NMOF 2** yielding **SA-NMOF 4**. Each value is measured three times with a 2.5 µL water droplet, respectively.

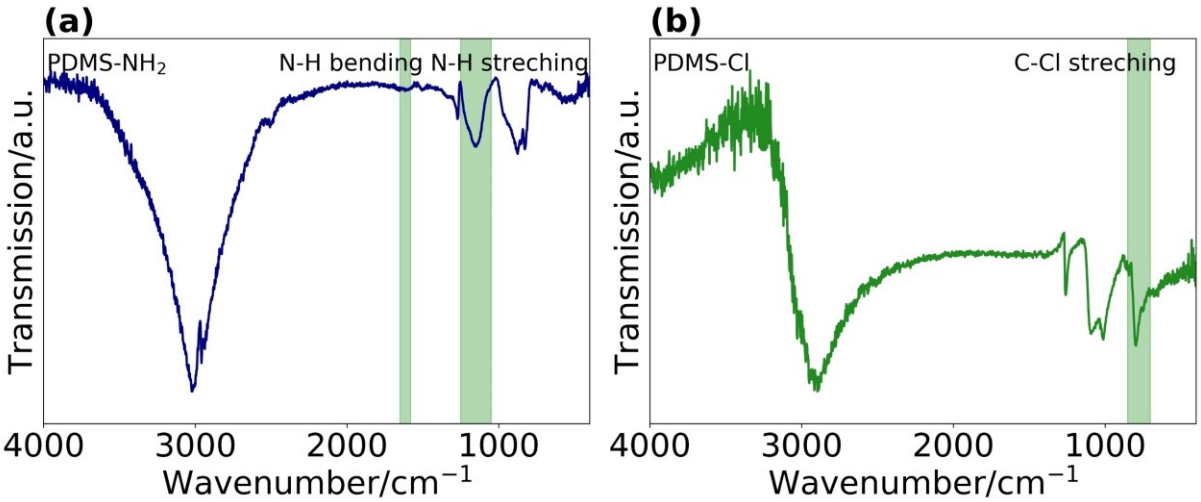

Figure 50: IR spectra of functionalized PDMS. Baseline-corrected IR spectra of PDMS functionalized with APTES (a) and CPTES (b), measured in reflection mode and with native PDMS as a background. Regions highlighted in green represent the expected bands for a free primary amine group.

Secondly, the functionalized surfaces were reacted with **NMOF 1** or **NMOF 2** to form the two SA-NMOFs 1 (N-UiO-66@PDMS, **SA-NMOF 3**) and 2 (N_3-N-UiO-66@PDMS, **SA-NMOF 4**), respectively. For the first approach (**SA-NMOF 3**), which utilizes amide bonds for the chemical immobilization, the PDMS substrate was immersed in an ethanol dispersion of **NMOF 1**, *N*,*N*-diisopropyl carbodimide, and *N*-hydroxysuccinimide. For the second approach (**SA-NMOF 4**), **NMOF 2**, $CuSO_4$, and ascorbic acid (to generate the Cu(I) catalyst for click chemistry) were dispersed in ethanol and the PDMS substrates were added.

Contact angle measurements. The contact angle measurements (Figure 49) can allow for the qualitative validation of whether a surface modification has occurred in terms of polarity. The determined value for native PDMS is 118.2 ± 2.5°, which matches with other values reported in literature.[303,304] The contact angle measured after the subsequent reaction with APTES, yielding amino-terminated PDMS decreases slightly. This matches expectations and literature values as the amine group is more polar than the native PDMS surface.[305] The surface termination of the latter is predominantly composed of methyl groups. Upon anchoring of **NMOF 1** forming **SA-NMOF 3** no change in surface polarity was observed, which can neither confirm the presence nor the absence of the NMOF.

For the second strategy, we observe a substantial reduction in the contact angle (86.0 ± 2.1°) after the initial reaction of native PDMS (118.2 ± 2.5°) with CPTES. Subsequent replacement of the chloride group with a less polar alkyne group increases the value once more. This is especially interesting, as the reaction that we used, was not applied to surfaces before. Immobilizing NMOFs on the surface provides a similar value to the amide bonding approach (112.0 ± 1.0°).

Vibrational spectroscopy. Further investigation by IR spectroscopy showed characteristic infrared bands for primary amines and chlorides, respectively. These can be used to identify successful surface modification. For primary amines, N-H bending should occur between 1590 and 1650 cm^{-1}, while C-N stretching should feature from 1020 to 1250 cm^{-1}.[306] Aliphatic organochlorides show C-Cl stretching, which should be visible between 700 and 800 cm^{-1}.[306] The received spectra (Figure 50) were taken in reflection mode and with native PDMS as a background. The desired bands are present and highlighted in green. Additionally, a broad peak from 2500 to 3500 cm^{-1} is visible in both spectra, corresponding to free hydroxyl groups. These stem from the initial activation with HCl/H_2O_2 prior to the reaction.

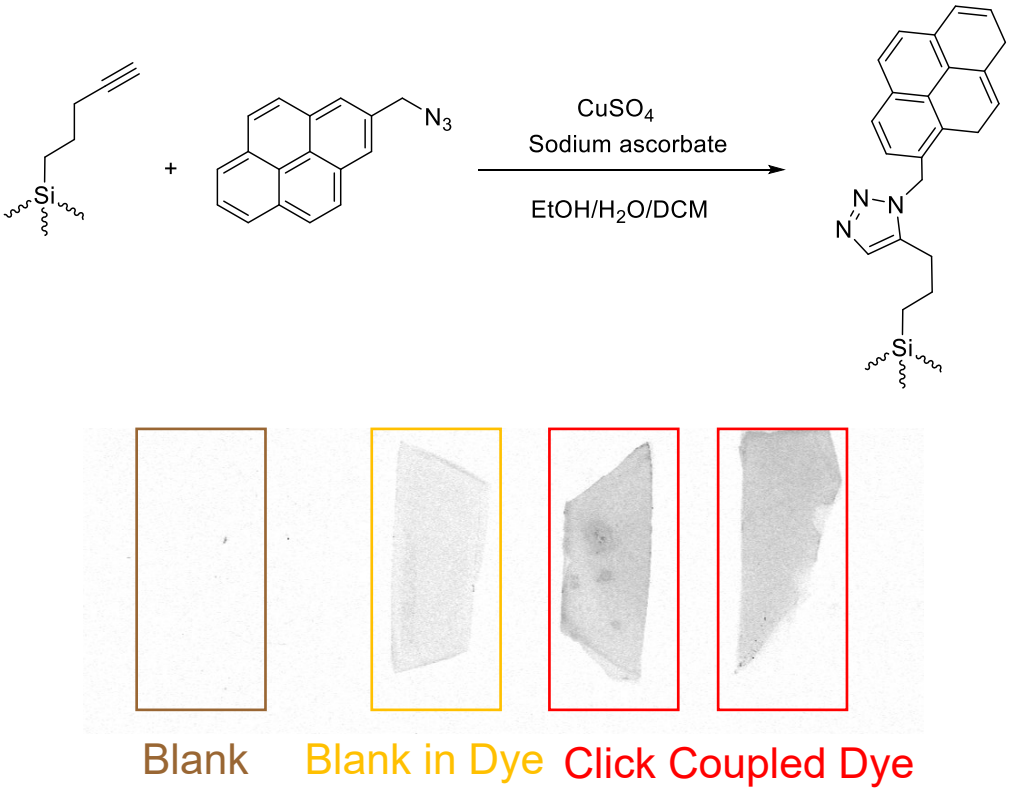

Figure 51: Fluorescence detection of PDMS samples probed by a fluorescence image scanner. From left to right: Native PDMS as a blank, native PDMS immersed in azide functionalized dye solution prior to the measurement, alkyne functionalized PDMS reacted in a CuAAC with a pyrene dye.

Staining experiments. As mentioned before, the introduction of the alkyne groups to PDMS by this reaction was not reported in literature so far. Therefore, a thorough investigation of the successful introduction of the alkyne group was important. Additionally, as the alkyne groups should be utilized for click chemistry, we wanted to test the feasibility of click coupling by staining experiments. Therefore, a pyrene-based dye was synthesized (see chapter 6.3.2.2) and reacted with the PDMS surface in a CuAAC (see Figure 51). Fluorescence is then probed via an imaging scanner with a green excitation laser (532 nm). To further elucidate the validity of our approach, two sets of control experiments were conducted. Therefore, the fluorescence of native PDMS, with and without prior immersion in the dye solution, is examined with a fluorescence image scanner. The penultimate also displays fluorescence (yellow box). However, the observed emission intensity is significantly higher for the click coupled samples (red margin), implying a successful anchoring of the dye to the polymer surface.

The fluorescence of the immersed sample can be explained by the permeable nature of PDMS as a network polymer structure. Its porosity allows small molecules, e.g. dyes,

to diffuse into the bulk polymer. In fact, this has allowed PDMS to be used in microextraction applications for removing trace organic compounds. This swelling behaviour becomes very important in the following chapter.

The resulting SA-NMOFs were further investigated by SEM with the corresponding images shown in Figure 52. The recorded images confirm a dense surface coating of the substrate surface with **NMOF 1** and **NMOF 2**, respectively. Evaluation of the particle size distribution by Image J resulted in the histograms display in Figure 52 (e,f). The size is determined as 14.4 nm (**NMOF 1**) and 14.8 nm (**NMOF 2**). The non-ideal dispersion of nanocrystallites on the surface is not fully elucidated, but presumably originates from the self-condensation of the silanes during functionalization.[307] As surface microscopic imaging techniques, such as atomic force microscopy and SEM, are challenging and non-specific for the PDMS substrates, the images shown here are recorded for the silicon substrates.

SA-NMOF Zr loading determination. The amount of Zr deposited on the 1 cm^2 PDMS substrates was determined by inductively coupled plasma-mass spectrometry (ICP-MS) measurements after the subsequent digestion of the SA-NMOFs in HNO_3/H_2O_2 for 5 min at 150°C. The exact PDMS substrate sizes were determined with a calliper and these values were used to calculate the amount of Zr/cm^2 (see calculation below). The calculation yielded 4.05 ± 0.53 nmol for **SA-NMOF 3** and 4.09 ± 0.51 nmol for **SA-NMOF 4** (see Table 7).

The calculation for the substance quantity (n) and the associated error (Δn) for **SA-NMOF 3**, whereas the m is the mass in ng determined by ICP-MS, A is the area in cm^2, m* is the mass per area (ng/cm^2), and Δm, ΔA, and Δm* are the associated errors.

$$m^* = \frac{m}{A} = \frac{369.00}{1.00} = 369\ ng/cm^2$$

$$\Delta m^* = \left(\frac{\Delta m}{m} + \frac{\Delta A}{A}\right) \cdot m^* = \left(\frac{11.28\ ng}{369.00\ ng} + \frac{0.10\ cm^2}{1.00\ cm^3}\right) \cdot 369\,\frac{ng}{cm^2} = 48\ \frac{ng}{cm^2}$$

$$n = \frac{m}{M} = \frac{369\,\frac{ng}{cm^2}}{91.224\,\frac{g}{mol}} = 4.05\,\frac{nmol}{cm^2}$$

$$\Delta n = \left(\frac{\Delta m}{m}\right) \cdot n = \frac{48\,\frac{ng}{cm^2}}{369\,\frac{ng}{cm^2}} \cdot 4.05\,\frac{nmol}{cm^2} = 0.53\ nmol/cm^2$$

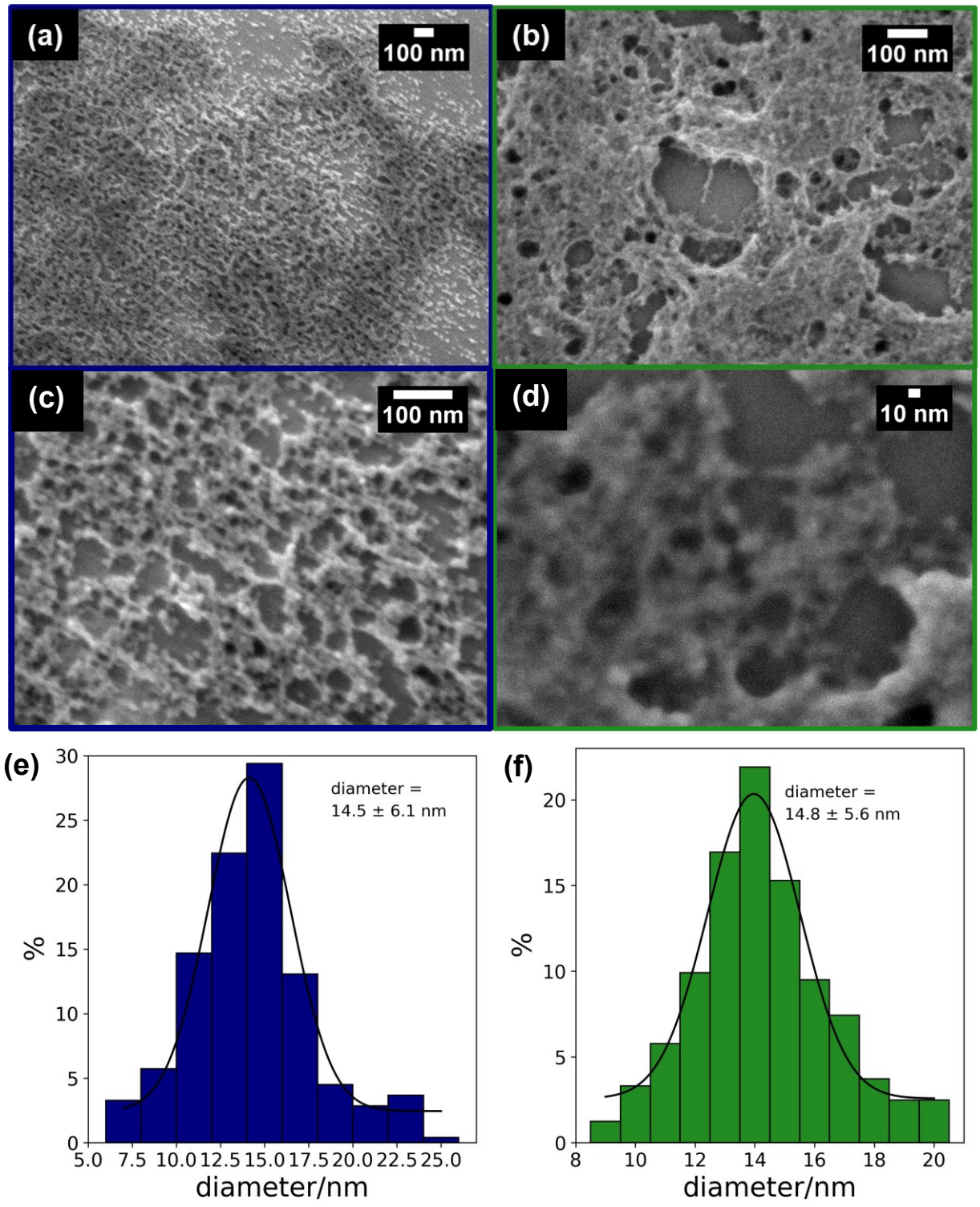

Figure 52: SEM images and histograms for **SA-NMOF 5** and **6**. SEM images and histograms recorded for **NMOF 1**@Si (**SA-NMOF 5**) (a,c,e) and **NMOF 2**@Si (**SA-NMOF 6**) (b,d,f). Settings: (a) 50,000-fold magnification, 0.80 kV SEI, working distance (WD) 2.9 mm.(b) 100,000-fold magnification, 0.80 kV SEI, WD 3.2 mm. (c) 150,000-fold magnification, 0.80 kV SEI, WD 2.9 mm. (d) 300,000-fold magnification, 0.80 kV SEI, WD 3.2 mm.

Table 7: Amount of Zirconium in the surface anchored NMOFs determined by ICP-MS.

Name	Substrate	Zirconium Mass (m) [ng]	Sample area (A) [cm^2]	Zirconium Mass (m*) [ng/cm^2]	Catalyst amount[1] [nmol per cm^2]
SA-NMOF 3	PDMS	369.00 ± 11.28	1.00 ± 0.10	369 ± 48	4.05 ± 0.53
SA-NMOF 5	Si	58.41 ± 2.14	1.00 ± 0.10	58.4 ± 8.0	$6.40 \cdot 10^{-1}$ ± $0.10 \cdot 10^{-1}$
SA-NMOF 4	PDMS	373.48 ± 9.59	1.00 ± 0.10	373 ± 47	4.09 ± 0.51
SA-NMOF 6	Si	128.63 ± 5.10	1.00 ± 0.10	129 ± 18	1.41 ± 0.20
UiO-66-film	PDMS	10485.97 ± 113.98	1.00 ± 0.10	$10.5 \cdot 10^3$ ± $12 \cdot 10^2$	115 ± 13
UiO-66-film	Si	23097.48 ± 178.51	1.00 ± 0.10	$23.1 \cdot 10^3$ ± $25 \cdot 10^2$	253 ± 27
UiO-66-HCl	PDMS	2218.62 ± 27.50	1.05 ± 0.10	$21.1 \cdot 10^2$ ± $23 \cdot 10^1$	23.2 ± 2.5
UiO-66-HCl	Si	104.58 ± 2.10	1.00 ± 0.10	105 ± 13	1.15 ± 0.14
blank	PDMS	4.28 ± 1.11	1.05 ± 0.10	4.08 ± 1.50	$4.46 \cdot 10^{-2}$ ± $1.58 \cdot 10^{-2}$
blank	Si	5.04 ± 2.49	1.00 ± 0.10	5.04 ± 2.99	$5.52 \cdot 10^{-2}$ ± $3.28 \cdot 10^{-2}$

[1]Calculated with the molar mass of Zr = 91.224 $g \cdot mol^{-1}$

In conclusion, this confirms the successful surface anchoring or chemical immobilization of **NMOF 1** and **2** on the corresponding surfaces forming a dense coating of the NMOFs on top of the surfaces.

3.4.4. Surface Anchoring Boosts Catalytic Activity

SA-NMOFs as catalysts in the cyanosilylation of benzaldehyde. After a short activation at 80°C for 30 min, the catalytic activity of the SA-NMOFs was tested in the cyanosilylation of benzaldehyde. Therefore, the 1 cm² of **SANMOF-3** and **4** were immersed in the toluene solution of benzaldehyde, and TMSCN, and stirred at 40°C for 4 h. At various points in time, reaction-equivalents were taken to determine the time yield plots shown in Figure 53. These show a remarkably high catalytic activity and good reproducibility, especially when compared to the **NMOF 1** and **2,** or bulk UiO-66 samples displayed in Figure 47.

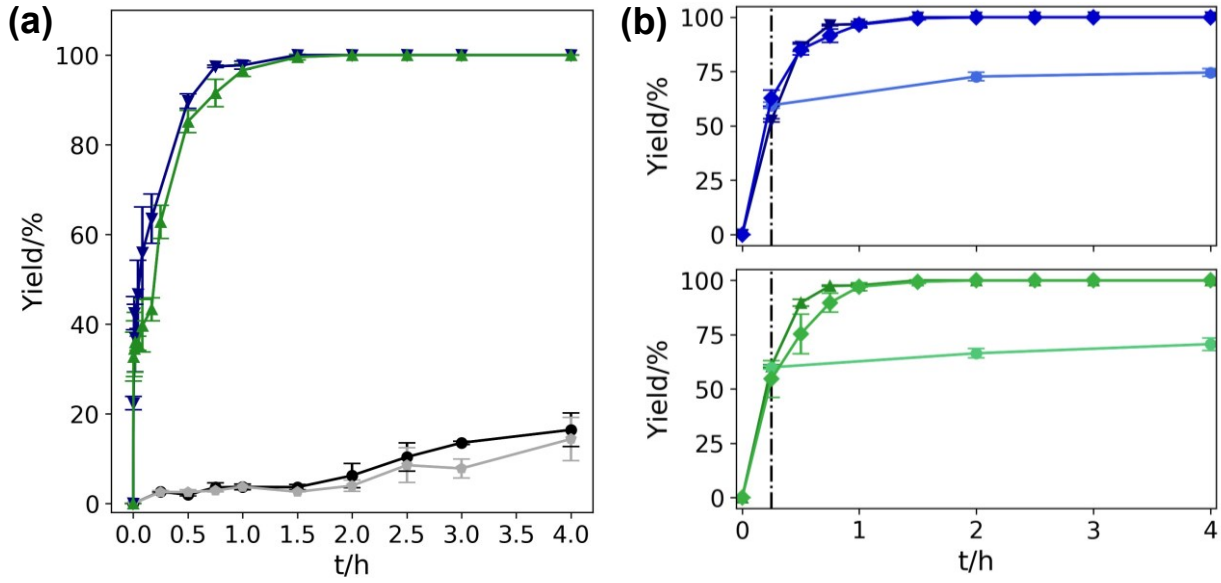

Figure 53: Time-yield plot of the cyanohydrin (2-phenyl-2-((trimethylsilyl)oxy)acetonitrile) resulted from cyanosilylation of benzaldehyde and 2.0 equiv. of TMSCN in toluene catalyzed by 1 cm² of the composites (a) **SA-NMOF 3** (blue, ▼), **SA-NMOF 4** (green, ▲), blank PDMS (grey, ⬟) and without any catalyst (blank, black, ●). (b) Time-yield plot for the same reaction conditions for the first (▲) and the second catalytic cycle (◆) of **SA-NMOF 3** and **4** as well as for the hot filtration of the reaction solution after 15 min (▼).

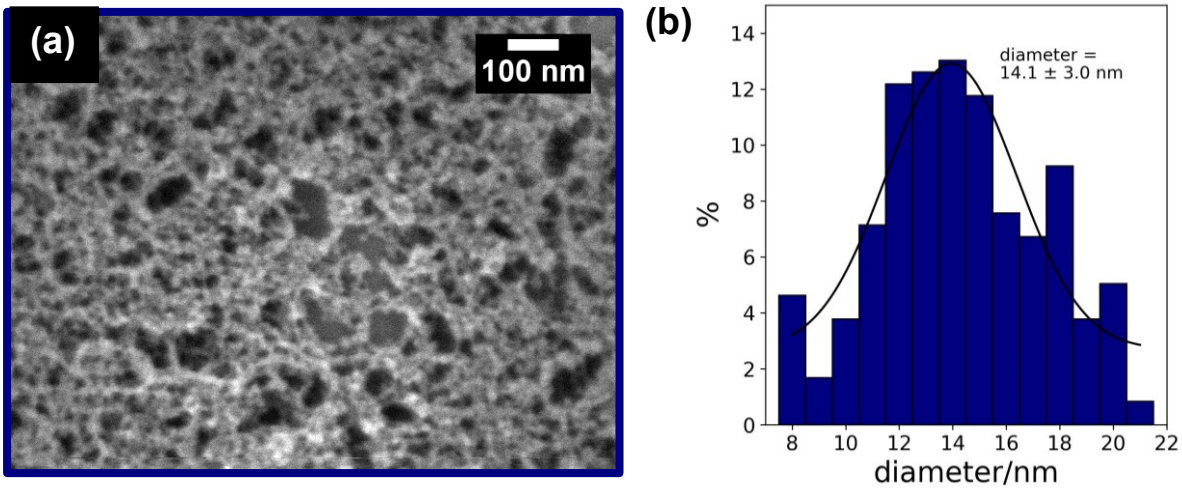

Figure 54: SEM image (a) and histogram (b) of **SA-NMOF 3** recorded after cyanosilylation. Instrument settings after recording: (a) 100,000-fold magnification, 0.80 kV SEI, WD: 3.3 mm.

Reusability and hot filtration. Further investigation included recyclability and hot filtration tests. For the recyclability experiments, the samples were washed with copious amounts of toluene and reactivated at 80°C for 12 h to remove the toluene from the material. The second catalytic cycle revealed a small deviation as compared to the first catalytic cycle. Due to the small amount of NMOFs on the surface, leaching of catalytic active NMOFs in the solution would significantly reduce the catalytic activity of the sample. Similar results were observed for the hot filtration test, which additionally proved negligible leaching of the catalyst species into the solution. Additional SEM images were recorded after the catalysis (Figure 54) and show that the microstructure of the composite is retained, which supports the previous findings of reusability.

Turnover frequencies and calculations. The initial reaction rates and turnover frequencies (TOF) for the investigated systems were calculated (see below) to allow for a comparison with other reported TOF values for coordination polymers as catalysts. Whereas r' is the reaction rate, $n_{catalyst}$ is the substance quantity calculated in the previous chapter, c(BA) is the concentration of benzaldehyde at the start of the reaction (t_0) and after a certain time (t_1).

Table 8: Calculated initial reaction rate (r') and TOFs for the cyanosilylation of benzaldehyde with 2.0 equiv. TMSCN catalyzed by colloidal solutions of **NMOF 1** and **2**, **SA-NMOF 3** and **4,** and **UiO-66-10TFA** and **UiO-66-HCl** in toluene.

	Bulk UiO-66 samples		colloidal solution		**SA-NMOF**	
	UiO-66-10TFA	**UiO-66-HCl**	**NMOF 1**	**NMOF 2**	**3**	**4**
r' [mmol h^{-1}]	$2.13 \cdot 10^{-2} \pm 3.3 \cdot 10^{-3}$	$1.89 \cdot 10^{-1} \pm 4.3 \cdot 10^{-2}$	$2.87 \cdot 10^{-1} \pm 1.3 \cdot 10^{-1}$	$1.97 \cdot 10^{-1} \pm 3.9 \cdot 10^{-2}$	79.0 ± 5.3	116 ± 19
TOF [h^{-1}]	$7.29 \cdot 10^{-1} \pm 1.6 \cdot 10^{-1}$	6.45 ± 1.87	9.79 ± 5.14	6.74 ± 1.76	$1.96 \cdot 10^{7} \pm 3.9 \cdot 10^{6}$	$2.82 \cdot 10^{7} \pm 8.3\ 10^{6}$

As an example, the reaction rate (r'), the TOF value, and the corresponding errors are calculated for **SA-NMOF 3**.

$$TOF = \frac{r'[\frac{nmol}{h}]}{n_{catalyst}\ [nmol]}$$

$$r'\ \left[\frac{nmol}{h}\right] = \frac{c(BA)_{t_1} - c(BA)_{t_0}}{t_1 - t_0}$$

$n_{catalyst/area}$ = 4.05 ± 0.53 nmol/cm² (ICP-MS);

$A_{catalyst}$ = 1.00 ± 0.10 cm²;

c_{0h} = 9.81 · 10⁵ nmol;

$Yield_{10s}$ = 22.38 ± 1.50 %

$$c_{10s} = \frac{100 - \mathrm{Y}}{100} \cdot c_0 = \frac{100 - 22.38}{100} \cdot 9.81 \cdot 10^5\ nmol = 7.61\ \cdot 10^5\ nmol$$

$$\Delta c_{10s} = \frac{\Delta Y}{Y} \cdot c_{10s} = \frac{1.50}{22.38} \cdot 7.61\ \cdot 10^5\ nmol = 0.51 \cdot 10^5\ nmol$$

$$r'\left[\frac{nmol}{h}\right] = \frac{9.81\ \cdot\ 10^5\ \mathrm{nmol} - 7.61\ \cdot\ 10^5\ \mathrm{nmol}}{0.00278\ h} = 7.92 \cdot\ 10^7\ \mathrm{nmol/h}$$

$$TOF = \frac{7.92 \cdot\ 10^7\ \mathrm{nmol/h}}{4.05\ nmol/cm^2 \cdot 1\ cm^2} = 1.96\ \cdot\ 10^7\ \frac{1}{h}$$

$$\Delta r = \frac{0.51\ \cdot\ 10^5\ \mathrm{nmol}}{7.61\ \cdot\ 10^5\ \mathrm{nmol}} \cdot\ 7.92 \cdot\ 10^7\ \mathrm{nmol/h}\ = 5.31 \cdot\ 10^6\ \frac{nmol}{h}$$

$$\Delta n = 0.53\ \mathrm{nmol}$$

$$\Delta TOF = \left(\frac{\Delta r}{r} + \frac{\Delta n}{n}\right) \cdot TOF = \left(\frac{5.31 \cdot\ 10^6\ \frac{nmol}{h}}{7.92 \cdot\ 10^7\ \frac{\mathrm{nmol}}{\mathrm{h}}} + \frac{0.53\ \mathrm{nmol}}{4.05\ \mathrm{nmol}}\right) \cdot 1.96\ \cdot\ 10^7\ \frac{1}{h} = 3.9 \cdot\ 10^6\ \frac{1}{h}$$

Table 9: Comparison of previously reported TOF values for the cyanosilylation of benzaldehyde. A comprehensive list of cyanosilylation reactions catalyzed by coordination networks can be found in the appendix, Table S10.

Catalyst	equiv. TMSCN	T/°C	TOF	Ref.
SA-NMOF 3	2	40	$1.96 \cdot 10^7$	this work
SA-NMOF 4	2	40	$2.82 \cdot 10^7$	this work
UiO-66-HCl	2	40	9.6	this work
UiO-66-10TFA	2	40	1.02	this work
InPF-15	1.5	80	2158	[308]
Mg(ABTC) (DMI)	2	25	990	[309]
InPF-16	1	25	582	[310]

3,3',5,5'-azobenzene-tetracarboxylate ($ABTC^{4-}$), 1,3-dimethy-2-imidazolidinone (DMI)

SA-NMOF 3 and **4** show impressively high TOF values for the cyanosilylation of BA in the range of 20,000,000 h^{-1} (see Table 9). If compared to industrial benchmarks for catalyst, these usually at least require TOF values in the medium to high ten thousand or low hundred thousand for selected processes.[311,312] Therefore, a TOF value in the range of 20,000,000 h^{-1} is remarkably high. This is particularly true for

MOF catalysts, which typically show significantly lower TOF, with most compounds ranging between negligible values up to the low thousands.[313–315] Hence, we compared the calculated TOF values for **SA-NMOF 3** and **4** with those reported for various coordination polymers in literature (see

Table 9). The TOF values that we measured are four orders of magnitudes higher than those that were previously reported in literature. The substantial enhancement can be attributed to two factors: on the one hand the downsizing effect, which reduces diffusion barriers and/or diffusion limitations by exhibiting a higher density of catalytic sites on the MOF surface, and on the other hand the prevention of particle aggregation during the catalysis.

Solvent scope. To investigate the nature of the SA-NMOFs further, the cyanosilylation of benzaldehyde with **SA-NMOF 3** as a catalyst was studied in different solvents such as DCM, toluene, and DMF (see Figure 55 a). It is apparent, that the reaction is extremely efficient in all solvents, reaching full conversion and visibly showing no deactivation effects. Best results were observed for toluene reaching full conversion after one hour. The efficiency of the reaction in different solvents might be related to the swelling ratios of PDMS in the different solvents (toluene: 1.31; DCM: 1.22, and DMF: 1.01, whereas 1.01 means that the initial PDMS substrate increases its size by 1 %)[277] or to the overall faster reaction of cyanosilylation in apolar solvents. However, in comparison to the defect engineered UiO-66-TFA and pristine UiO-66-HCl the SA-NMOFs show a high catalytic activity relatively independent of the solvent.

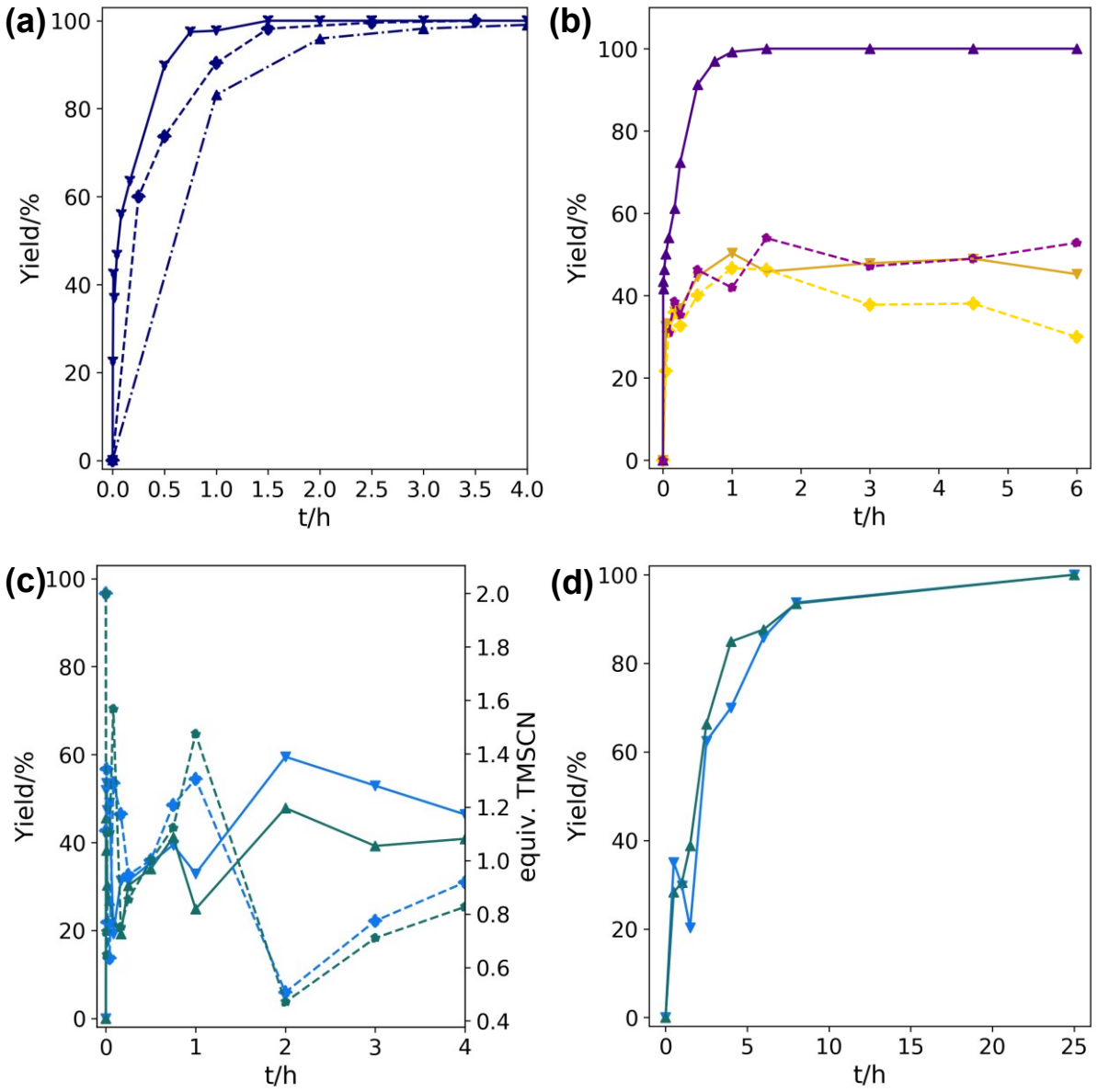

Figure 55: Time-yield plot of the cyanohydrin formation (2-phenyl-2-((trimethylsilyl)oxy)-acetonitrile) resulted from cyanosilylation of benzaldehyde and 2.0 equiv. of TMSCN in toluene catalyzed by 1 cm^2 of the composites (a) **SA-NMOF** 3 in different solvents toluene, DCM, and DMF. (b) UiO-66 thin films on PDMS and Si, and UiO-66-HCl particles immobilized by amide bonds on PDMS and Si. (c,d) **SA-NMOF 5** (blue) and **SA-NMOF 6** (green) catalyzed with 2 equiv. of TMSCN (c) and 10 equiv. of TMSCN(d), respectively. The dashed lines in (c) show the amount of TMSCN left in the reaction.

Support substrate scope. In the next experiment, we varied the substrate, employing Si instead of PDMS and testing the resulting catalysts **NMOF 1**@Si (**SA-NMOF 5**), and **NMOF 2**@Si (**SA-NMOF 6**) in the cyanosilylation of benzaldehyde (see Figure 55 c,d). The investigated systems show an equally strong initial activity compared to **SA-NMOF 3** and **4**, but do not reach full conversion. Presumably, this can be attributed to the degradation of TMSCN during the reaction. After the addition of 10 equiv. of TMSCN (see Figure 55 d), instead of 2 equiv., full conversion is reached, ruling out

catalyst deactivation phenomena. Furthermore, we investigated the catalytic activity of bottom-up grown UiO-66 thin films[59] and surface anchored **UiO-66-HCl** particles immobilized on two different substrate surfaces namely Si and PDMS (see Figure 55 b). **UiO-66-HCl** particles anchored to PDMS or Si via the amide approach showed similar time yield plots compared to **SA-NMOF 3** or **5**, respectively. This shows that the concept also works for larger particles. However, due to the higher amount of zirconium, due to the larger particle size, we observe lower TOF values as compared to **SA-NMOF 3**. UiO-66 thin-films grown by the LbL approach exhibit a reduced catalytic activity compared to the SA-NMOFs, due to the higher diffusion barrier in films as opposed to single particles.

Table 10: Reaction rates and TOF values for the cyanosilylation of benzaldehyde catalyzed by either **SA-NMOF 5** or **6**, UiO-66 thin films, or UiO-66-HCl particles immobilized on the substrate surface.

Samples	Substrate	r' [mmol· h^{-1}][e]	TOF [h^{-1}]
SA-NMOF 5	Si	183	$2.86 \cdot 10^{8} \pm 3.9 \cdot 10^{7}$
SA-NMOF 6	Si	161	$1.14 \cdot 10^{8} \pm 1.6 \cdot 10^{7}$
UiO-66-HCl	PDMS	153	$6.30 \cdot 10^{6} \pm 7.1 \cdot 10^{5}$
UiO-66-HCl	Si	3.64	$3.17 \cdot 10^{6} \pm 3.8 \cdot 10^{5}$
UiO-66-Film	PDMS	7.67	$66.7 \cdot 10^{4} \pm 7.4 \cdot 10^{3}$
UiO-66-Film	Si	5.10	$2.01 \cdot 10^{4} \pm 2.2 \cdot 10^{3}$

CO_2 cycloaddition. As a second model reaction, the cycloaddition of carbon dioxide with propylene oxide was investigated. This is one of the reactions involving CO_2 that has already been intensively studied in the past and which should prove the versatility and applicability of our approach.[316–318]

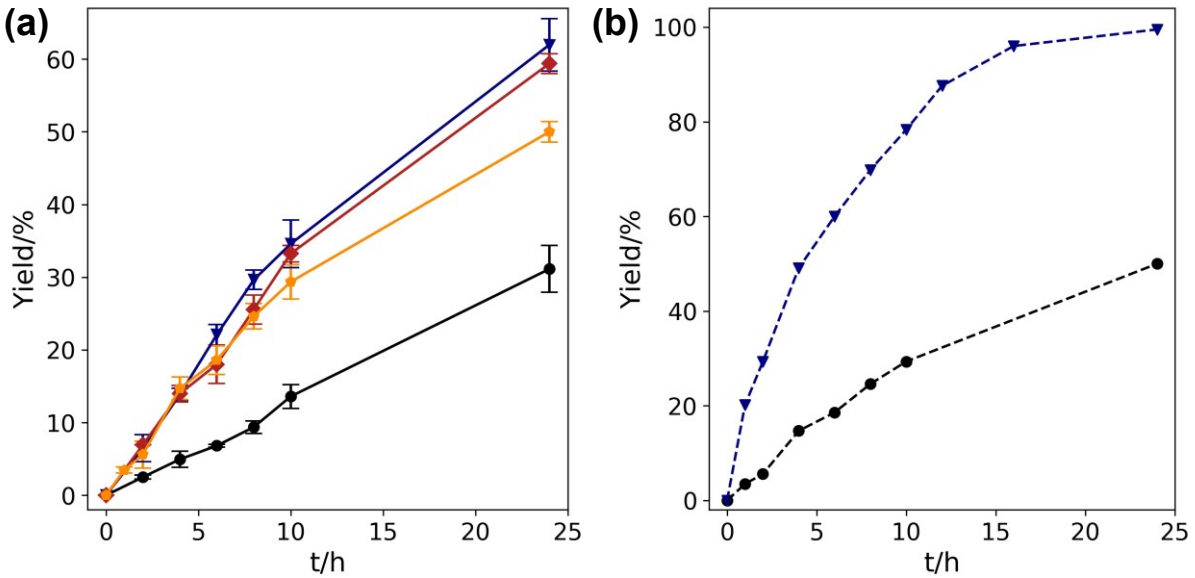

Figure 56: Time-yield plot of propylene carbonate formed by the insertion of CO_2 into propylene oxide. For all through lines, the general conditions of p(CO_2)=1 bar, 31.05 mmol propylene oxide, and 2.49 mmol Bu_4NBr (as co-catalyst) were applied. The reaction was catalyzed by either 2 cm^2 of **SA-NMOF 3** (blue), 0.5 mol% of Zr of **UiO-66-HCl** (orange), 0.5 mol% of Zr of **UiO-66-10TFA** (red) applied as microcrystalline powders or without any catalyst (black). The dotted line was recorded with p(CO_2) = 3 bar, T = 100 °C, and 2 cm^2 of **SA-NMOF 3** (blue, dotted) as a catalyst. The respective blank text without any catalyst is shown as the dotted black curve.

Table 11: Reaction rates and TOF values reported for the cycloaddition of carbon dioxide with propylene oxide-forming propylene carbonate catalyzed by SA-NMOF 3, or UiO-66-HCl and UiO-66-TFA powders and without any catalyst (blind), respectively.

Catalysts	r' [mmol·h^{-1}][e]	TOF [h^{-1}]
SA-NMOF 3[a]	6.26 [e]	$7.74 \cdot 10^6 \pm 1.01 \cdot 10^6$ [e]
SA-NMOF 3[b]	1.00 ± 0.29 [f]	$1.24 \cdot 10^6 \pm 5.16 \cdot 10^5$ [f]
UiO-66-HCl[c]	0.87 ± 0.29 [f]	5.15 ± 1.76 [f]
UiO-66-10TFA[c]	1.07 ± 0.02 [f]	6.38 ± 0.17 [f]
Blind[d]	0.38 ± 0.04 [f]	

[a] p(CO_2)=3 bar, T=100 °C, 31.05 mmol propylene oxide, 2.5 mmol Bu_4NBr, 2 cm^2 of SA-NMOF 3; [b] p(CO_2)=1 bar, T=50 °C, 31.05 mmol propylene oxide, 2.5 mmol Bu_4NBr, 2 cm^2 of SA-NMOF 3; [c] p(CO_2)=1bar, T=50 °C, 31.05 mmol propylene oxide, 2.5 mmol Bu_4NBr, 0.5mol% of Zr; [d] p(CO_2)=1bar, T=50 °C, 30.7 mmol propylene oxide, 2.5 mmol Bu_4NBr; [e] calc. after 1 h; [f] calc. after 2 h

Time-yield plots illustrate that 2 cm^2 of **SA-NMOF 3,** corresponding to a catalyst mass loading of 2.25 μg of UiO-66 (8.08 ng Zr) are more active than 43 mg of **UiO-66-HCl** or **UiO-66-10TFA** (see Figure 56 a). Full conversion after 24 h was reached by increasing both the CO_2 pressure (3 bar) and the temperature (100 °C) with **SA-NMOF 3** as the catalyst (see Figure 56 b). Following the results observed for the cyanosilylation of benzaldehyde remarkably high TOF values were observed for **SA-NMOF 3**: $1.24 \cdot 10^6 \pm 5.16 \cdot 10^5$ h^{-1} ($p(CO_2)$ = 1 bar, 50 °C) and $7.74 \cdot 10^6 \pm 1.01 \cdot 10^6$ h^{-1}, ($p(CO_2)$ = 3 bar, 100 °C) (see Table 11, Table 12). A comprehensive list with TOF values reported in literature for MOF as catalysts can be found in the appendix (see Table S2). The calculated TOF values for **SA-NMOF 3** are two orders of magnitude higher than the ones reported in literature.

Table 12: Comparison of previously reported TOF values for the cycloaddition of CO_2 to PO catalyzed by different coordination polymers (among others **SA-NMOF 3**). A full overview of the literature can be found in the appendix, Table S11).

Catalyst	$p(CO_2)$/bar	T/°C	TOF	Ref.
SA-NMOF 3	3	100	$7.74 \cdot 10^6$	this work
SA-NMOF 3	1	50	$1.24 \cdot 10^6$	this work
UiO-66-HCl	1	50	5.2	this work
UiO-66-10TFA	1	50	6.4	this work
Int-MOF-5	1	50	5400	[319]
IL-[$In_2(dpa)_3$ (1,10phen)$_2$]*	100 W^2	12	3100	[320]
DMAP-Zr-bdc-MOF	10	50	1095	[321]

*microwave assisted; 1,10-phenanthroline (phen), diphenic acid (H_2dpa), 4-dimethylamino-pyridine (DMAP)

3.4.5. Summary

Surface anchoring of NMOF crystallites drastically enhances their catalytic performance indicated by their substantially increased turnover frequencies from $2.82 \cdot 10^7$ h^{-1} (cyanosilylation of benzaldehyde) to $7.74 \cdot 10^6$ h^{-1} (CO_2 cycloaddition with propylene oxide). In comparison to microcrystalline powders, colloidal dispersions of NMOFs, and thin-films, SA-NMOFs clearly outperform all other catalysts in terms of turn-over frequencies. As visualized in Figure 57, SA-NMOFs also clearly outperform other coordination network-based catalysts which were reported in literature. Combing our results with related research of Tang et al.[322] and Fischer et al.[12] implies that the concept of MOF immobilization on substrates may offer a new strategy to overcome drawbacks in the utilization of MOFs as catalysts.[323]

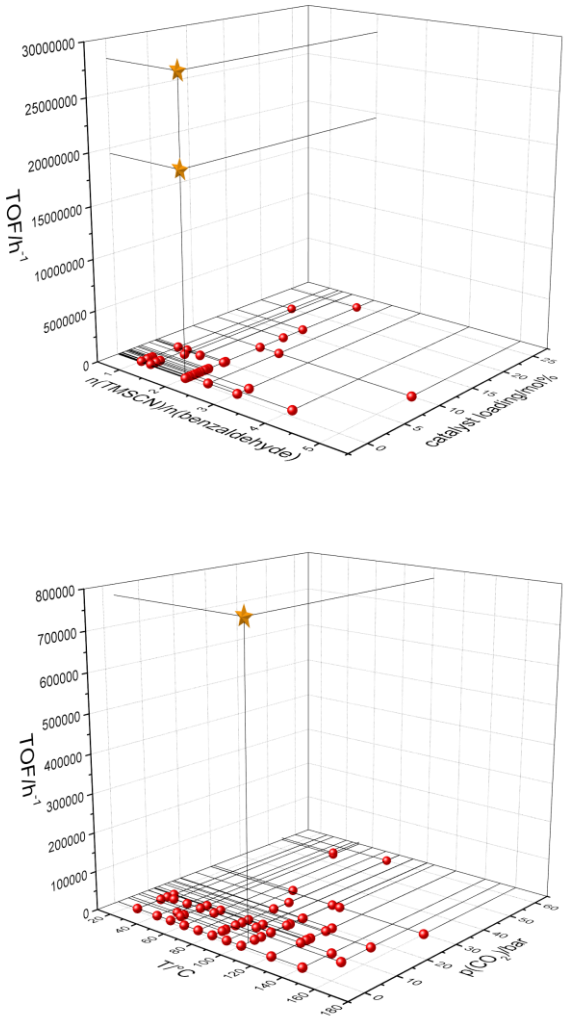

Figure 57: Turn over frequency as a function of TMSCN equivalents and catalyst loading for the cyanosilylation reaction (a) and as function of the CO_2 partial pressure of and the reaction temperature for the CO_2 insertion into propylene oxide (b), respectively. The SANMOF catalysts are marked with stars.

3.5. Study III: Targeting Vectorial Catalysis in Surface Anchored Metal-Organic Framework Based Microfluidic Devices

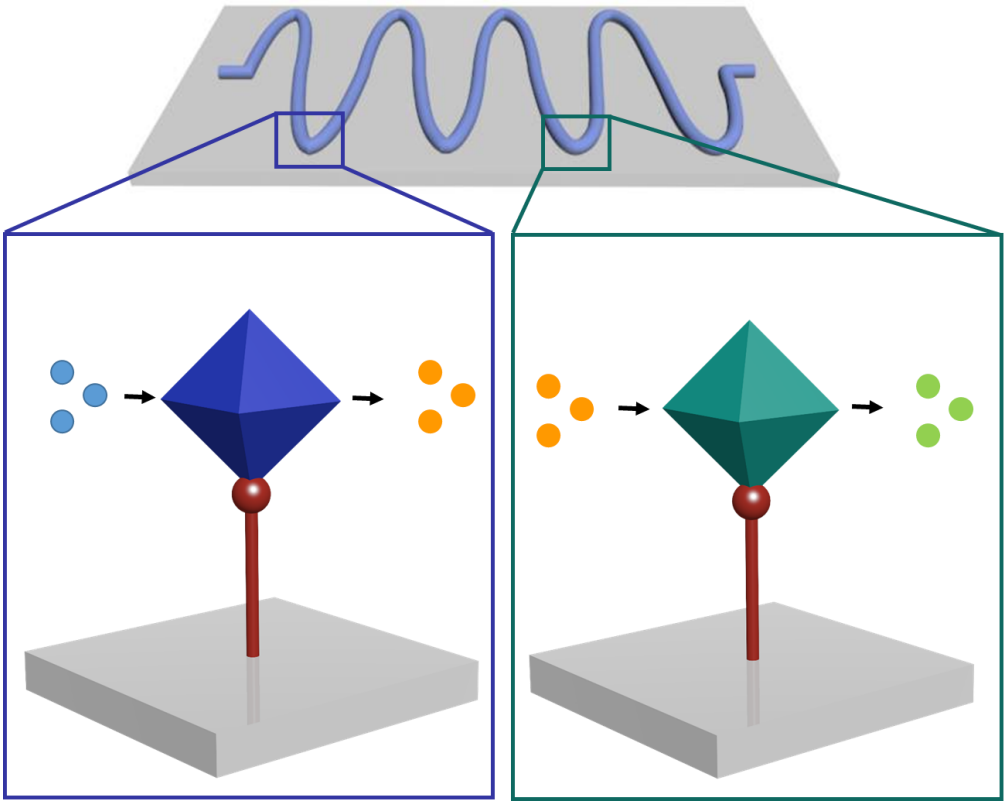

This chapter is based on a manuscript in preparation.

A. Lisa Semrau, Philip M. Stanley, Dominik Huber, Michael Schuster, Bauke Albada, Mirza Cokoja, and Roland A. Fischer, Vectorial Catalysis in Surface-Anchored Nanometer-sized Metal-Organic Frameworks-based Microfluidic Devices, submitted.

The project was designed by B. Albada, Roland A. Fischer, and A. L. Semrau as part of a Horizon 2020 proposal. The progress was regularly discussed with P. M. Stanley, M. Cokoja, and R. A. Fischer. The experiments and characterization were performed and analyzed by A. L. Semrau, except the ICP-MS measurements which were conducted and evaluated by D. Huber and M. Schuster.

3.5.1. Targeting Vectorial Catalysis

Vectorial catalysis – controlling multiple reactions in a programmed sequence and at defined spatial locations is a major challenge in catalysis science. Inspired by vectorial principles in biocatalysis, translation into artificial systems is still in its infancy.[198]

Metal-organic Frameworks (MOFs) provide a platform for the design of multifunctional material properties and are employed to explore concepts and routes towards vectorial catalysis. Thus, we report on our results of integrating different catalytically active MOFs at predefined regions within a microfluidic reactor.

In this chapter, we investigate the catalytic properties of selected suitable MOFs, namely UiO-66 ($Zr_6O_4(OH)_4(bdc)_6$), MIL-101-SO_3H ($Cr_3OX(OH_2)(bdc\text{-}SO_3H)_3$), MIL-101 ($Cr_3OX(OH_2)(bdc)_3$), MIL-101-$NH_2$ ($Cr_3OX(OH_2)(bdc\text{-}NH_2)_3$) or CoBTC ($Co_3(H_2O)_4(btc)(btc)$) to catalyze single steps in a reaction sequence whereof three were investigated: hydrolysis/Knoevenagel condensation; cyanosilylation/hydrolysis and oxidation/cyanosilylation. These reaction sequences are particularly interesting as at least individual reactions or similar reactions were previously investigated and can be catalyzed by different MOFs in various solvents. More information is provided in each chapter. After careful optimization of the reaction conditions, the reaction sequences were translated into polydimethylsiloxane (PDMS) based microfluidic reactors. In these reactors, NMOFs anchored to surfaces by covalent amide bonds serve as catalysts. Finally, a reactor featuring two different SA-NMOFs immobilized as catalysts at two separate regions of the reactor was fabricated, allowing for a proof-of-concept of a MOF-based two-step vectorial catalysis system.

3.5.2. Manufacturing SA-NMOF-based Microfluidic Devices

The final aim of this project was the proof-of-concept of vectorial catalysis with different surface anchored (N)MOFs (SA-NMOFs) as catalytically active species. In comparison to catalysis in a batch reactor (see chapter 3.2), the inclusion of the SA-NMOFs into a microfluidic flow reactor introduces the flow direction as a 'vector' for the reaction sequence. Therefore, we investigated different reactor designs and finally decided to use PDMS-based microfluidic reactors, as they combine a low polymerization temperature, transparency, and straightforward handling.[276] However, they also have major drawbacks like the incompatibility with most organic solvents, as the PDMS swells upon contact with many organic solvents and therefore disassembles the microfluidic reactor.[277]

Experimentally, the PDMS-based microfluidic reactors were manufactured starting with a silicon master mold (see Figure 59) as similarly reported in the past.[324–327] Purchased by microLIQUID this master mold is a Si wafer with a photolithographic imprinted channel structure. Freshly mixed PDMS elastomer and curing agent are molded onto the Si master mold, degassed, and cured at 70°C for 1 h. Afterwards, the cured PDMS stamp with the imprinted hollowed-out pathway is sealed onto a glass or PDMS substrate in an oven at 100°C overnight. Prior to the sealing, the NMOFs are immobilized onto the amino-functionalized glass or PDMS surface by DIC/NHS amide bond formation (see Figure 58). Therefore, the final reactors contain SA-NMOFs in the channel structures as active catalysts. Subsequentially, these reactors were used to investigate the catalytic conversion of several reactions.

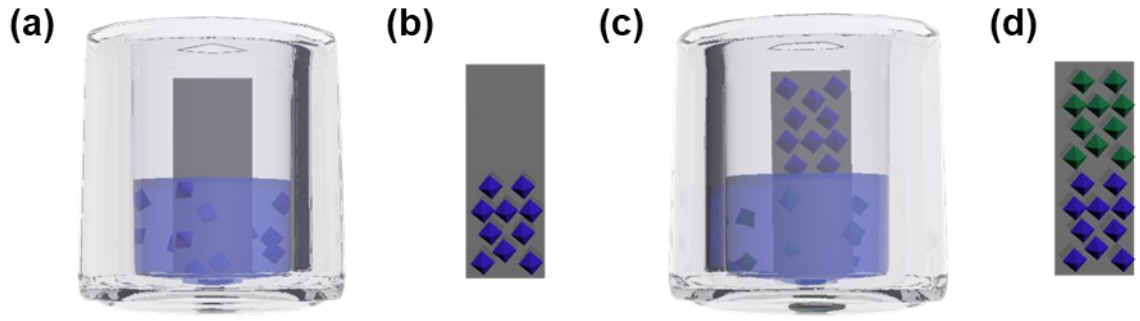

Figure 58: Schematic representation of the stepwise process of anchoring two different NMOFs onto the bottom substrate of a microfluidic device by DIC/NHS catalysed amide bond formation (a,c) resulting in the formation of a substrate with two separately NMOF anchored areas (d).

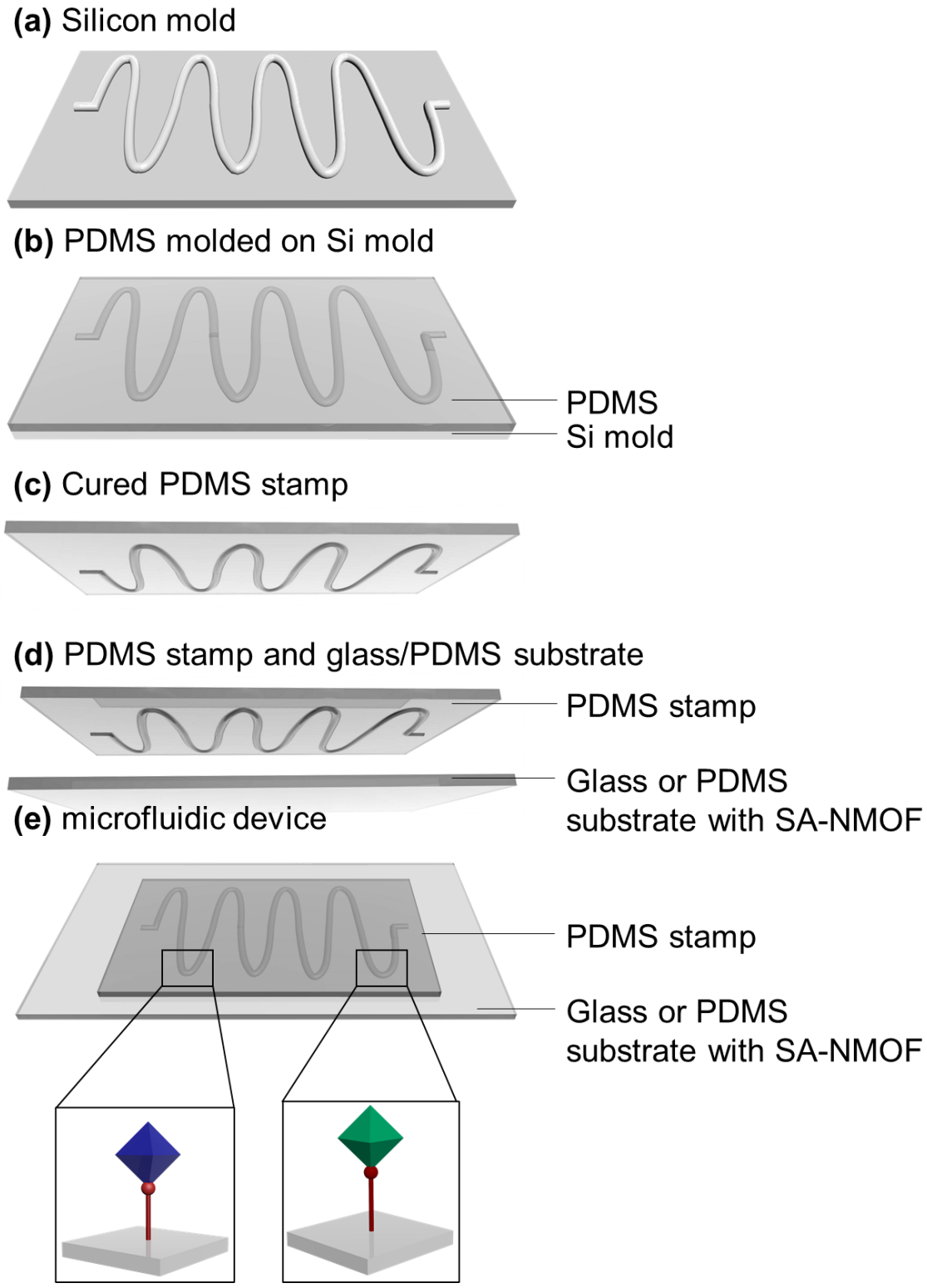

Figure 59: Schematic representation of the manufacturing process of a microfluidic device. (a) Silicon master mold manufactured by mircoLIQUID by photolithography. (b) PDMS is molded on top of the Si master mold. (c) Cured PDMS stamp after the molding process removed from the master mold, yielding a hollowed-out pathway. (d) Subsequently, the PDMS stamp is sealed to a substrate such as glass or PDMS, which is functionalized with SA-NMOFs prior. (e) Complete microfluidic device after assembly and functionalization.

3.5.3. NMOF Synthesis, Characterization, and Surface Anchoring

Prior to the investigation of the reaction sequences, we synthesized several (N)MOF powders which were identified as prospective catalysts for one of the respective reactions in this chapter.

NMOF synthesis. Therefore, various (N)MOFs, namely UiO-66 ($Zr_6O_4(OH)_4(bdc)_6$), MIL-101-SO_3H ($Cr_3OX(OH_2)(bdc\text{-}SO_3H)_3$), MIL-101 ($Cr_3OX(OH_2)(bdc)_3$), MIL-101-$NH_2$ ($Cr_3OX(OH_2)(bdc\text{-}NH_2)_3$), and CoBTC ($Co_3(H_2O)_4(btc)(btc)$) were synthesized according to (slightly) adapted established synthetic routes (see chapter 6.3.2.1). The corresponding obtained (N)MOF particles were investigated by PXRD, DLS, and SEM to determine their crystallinity and crystalline domain sizes, their hydrodynamic radii, and their primary particle size distributions in turn.

Characterization-crystallinity and crystalline domain size. The recorded PXRD patterns (Figure 60) show, that the respective NMOFs exhibit the expected reflex positions, compared to the theoretical pattern based on the structural model from single-crystal XRD (obtained from cif files from the CCDC). However, slight deviations in the intensity patterns were observed. We attribute this to insufficient grinding and/or solvent residues in the MOF pores (texture effects), which are probably caused by the flat sample holders.

Furthermore, we were interested in determining the crystalline domain size (CDS) by the Scherrer equation. As discussed before, the PXRD line broadening can be used to determine the crystalline domain size. Besides the CoBTC sample, which features larger CDS, all samples clearly show the characteristic line broadening indicating their nano crystallinity. Therefore, we determined the CDS for all samples, summed up in Table 13. All samples show a certain nano crystallinity, however, MIL-101, UiO-66, and MIL-101-NH_2 reveal pronounced nano crystallinity with CDSs between 10-20 nm.

Table 13: Crystalline domain sizes (CDS), primary particle sizes, and hydrodynamic radii determined by PXRD, SEM, and DLS, respectively, of MIL-101-SO_3H, MIL-101, MIL-101-NH_2, UiO-66, and CoBTC.

MOF	CDS/nm	Primary Particle Size/nm	Hydrodynamic radius/nm
MIL-101-SO_3H	25.8 ± 4.4	157 ± 39	1019 ± 188
MIL-101	12.4 ± 2.8	26.7 ± 3.9	79 ± 33
MIL-101-NH_2	14.9 ± 1.5	25.9 ± 5.8	128 ± 59
UiO-66	17.7 ± 2.1	21.0 ± 3.3	164 ± 24
CoBTC	45.3 ± 3.3	5840 ± 3570	529 ± 68

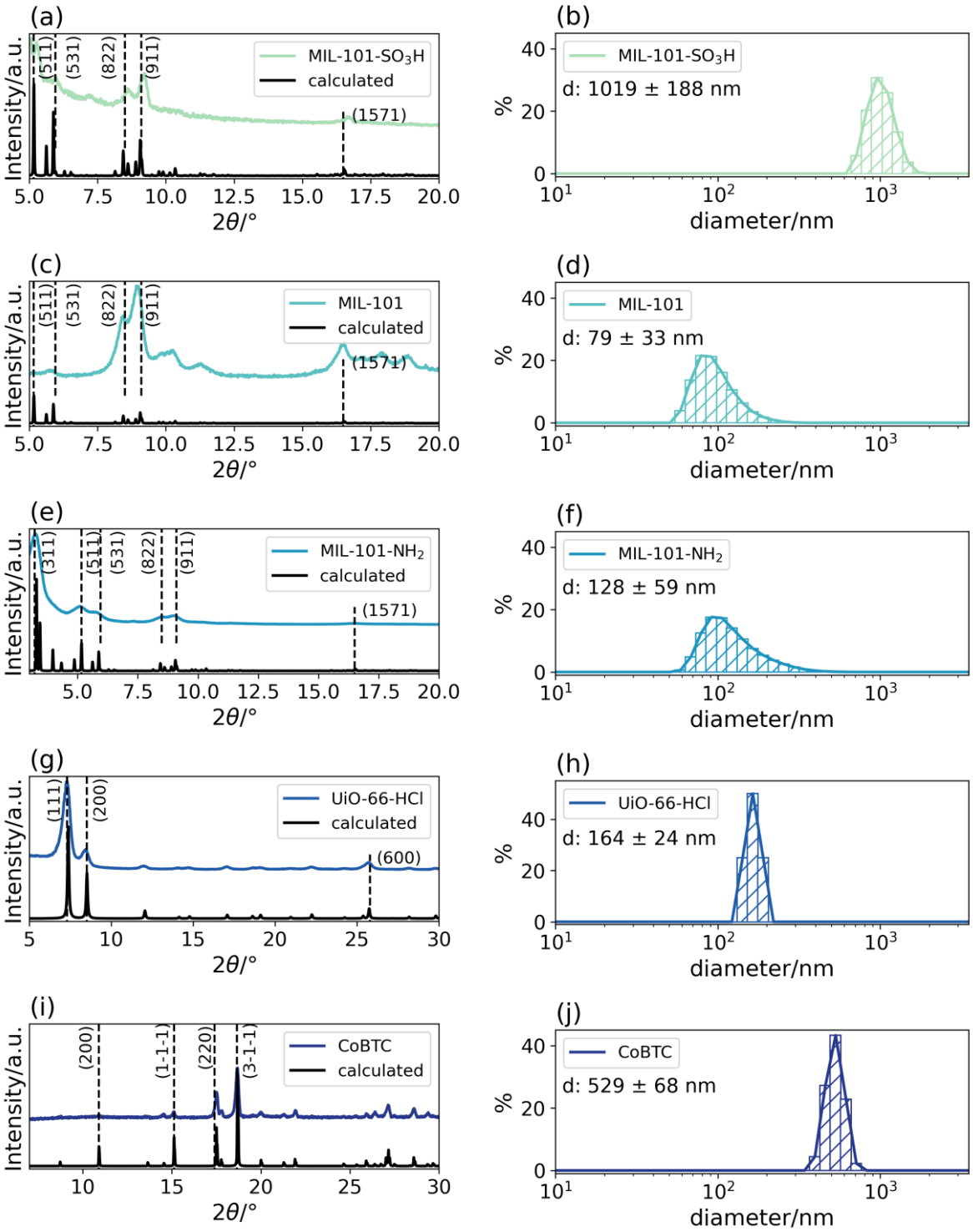

Figure 60: PXRD (a,c,e,g,i) and DLS (b,d,f,h,jj) of MIL-101-SO_3H (a,b), MIL-101 (c,d), MIL-101-NH_2 (e,f), UiO-66-HCl (g,h), and CoBTC (i,j). The reference patterns were calculated using the cif fies for MIL-101(CCDC 605510), UiO-66 (CCDC 733458), and CoBTC (CCDC 1274034).

Hydrodynamic radii. In the next step, the hydrodynamic radii of the samples were determined by DLS (Figure 60, Table 13), wherefore (N)MOF solutions were dispersed in ethanol, sonicated for 5 min, and their light-scattering properties measured in turn, determining their hydrodynamic radii in ethanol. The radii of MIL-101, UiO-66, and MIL-101-NH_2, which exhibited already very small CDS, were in between 80 and 170 nm in the range of solvated NMOFs. CoBTC (529 ± 68 nm) and MIL-101-SO_3H (1019 ± 188 nm), however, exhibited much larger hydrodynamic radii, which corresponds to their larger CDS and primary particle size (determined by SEM). Additionally, we observed that the larger CoBTC particles did not disperse well and instead precipitated from the dispersion, which reduces the corresponding hydrodynamic radius.

Primary particle size. Finally, by scanning electron microscopy we analyzed the primary particle size and morphology of the samples (see **Figure 61**). All samples, besides CoBTC, display spherically shaped primary particles. CoBTC shows rectangular particles with much larger primary particle sizes (1-10 μm), additionally the particles do not show a narrow size distribution instead the particles differ significantly in their primary particle size. Moreover, we observed that the particles have a rectangular shape, wherein the particles preferably grow in one spatial direction. Therefore, the corresponding size distribution is not particularly meaningful.

As mentioned before, the other samples exhibit a spherical primary particle morphology, with a much narrower size distribution as compared to the CoBTC samples. The histograms were determined by surveying 200 primary particles in the corresponding SEM with Image J, then evaluating the mean size, deviation, and histogram, respectively. The primary particle sizes of UiO-66, MIL-101, and MIL-101-NH_2 were determined between 21 and 26 nm, which coincides with the corresponding CDS, and the hydrodynamic radii. As both values (hydrodynamic radius and CDS) were larger for MIL-101-SO_3H, it is not surprising that the primary particle size (157 ± 39 nm) was also larger than for the other samples. Smaller particles of MIL-101-SO_3H with a narrower size distribution would have been favourable for catalysis. However, due to the complex synthetic route, starting with $Cr(VI)O_3$ in HCl/H_2O for 6 days at 180°C a thorough study to optimize the primary particle size of MIL-101-SO_3H would have been challenging and was omitted due to the time constraints of this thesis. However, according to recent publications,[297] an enhanced ligand concentration respective to the metal precursor, a higher concentration of both metal precursor and ligand in solution, and increased HCl concentration should reduce the primary particle size of MIL-101-SO_3H.

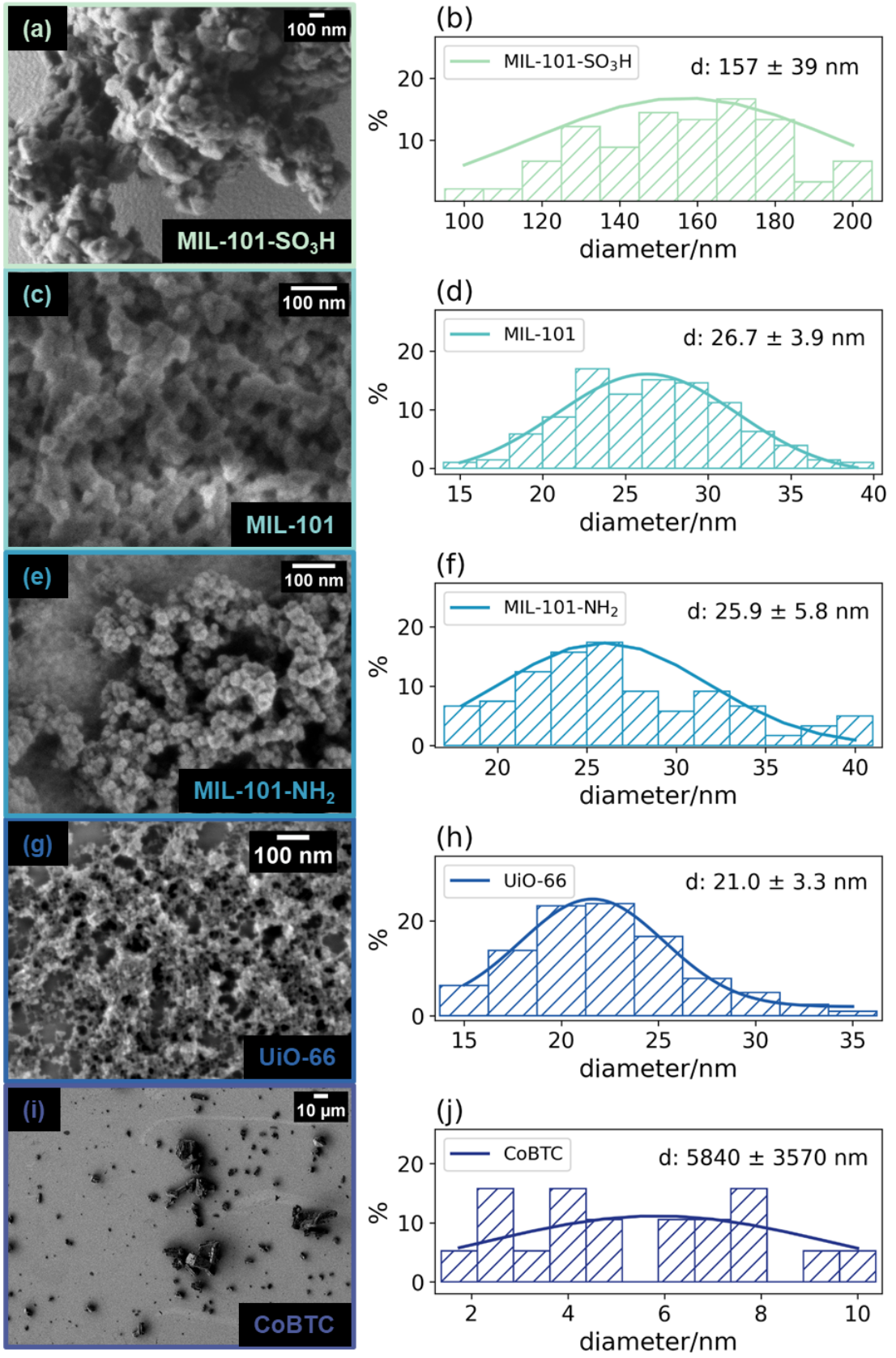

Figure 61: SEM images and histograms of the primary particle size of MIL-101-SO_3H (a,b), MIL-101 (c,d), MIL-101-NH_2 (e,f), UiO-66 (g,h), and CoBTC (i,j).

Surface anchoring. In the next step, the corresponding (N)MOF particles were immobilized onto amino-functionalized PDMS, glass, and Si substrates. The substrates were prepared as described in the previous chapter by reaction with APTES creating amino-functionalized surfaces (see chapter 6.3.2.3 and 6.3.2.4). Subsequentially, the surfaces were reacted with the (N)MOF particles creating covalently amide anchored NMOFs enabled by DIC/NHS chemistry.

The resulting SA-NMOFs were investigated by SEM and ICP-MS to evaluate the morphology, particle size distribution, and total metal content on the surfaces.

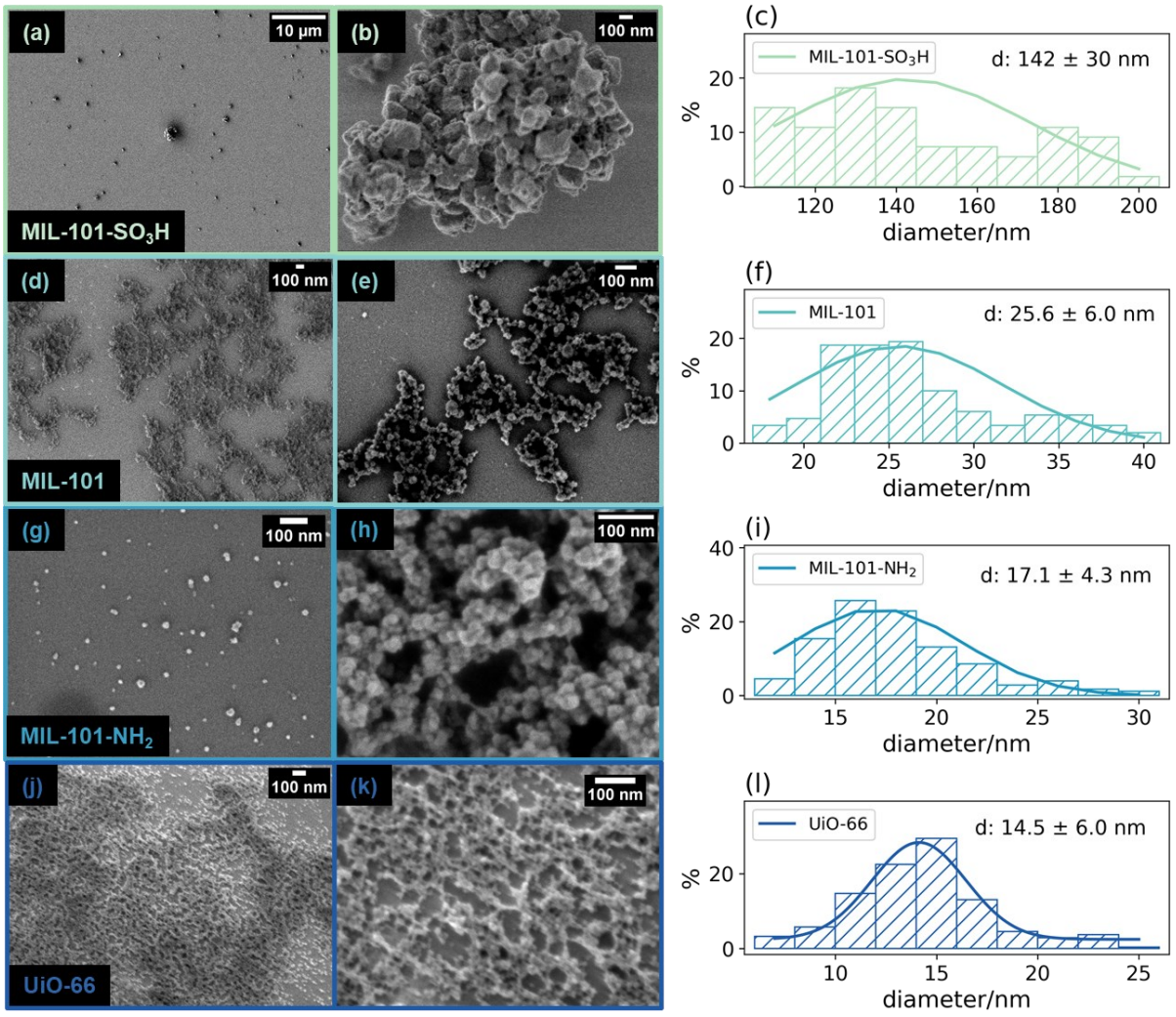

Figure 62: SEM images and histograms of surface anchored MIL-101-SO_3H (a-c), MIL-101 (d-f), MIL-101-NH_2 (g-i), and UiO-66 (j-l) immobilized on (3-aminopropyl)triethoxysilane functionalized silicon substrates.

Surface coverage and morphology. The SEM images (see Figure 62) display the surface coverage and morphology of the SA-NMOFs. The best coverage was observed after reaction with MIL-101 and UiO-66, where a dense coating with spherical nanoparticles was found. MIL-101-NH_2 and MIL-101-SO_3H, on the other hand, display

a lower particle density of anchored particles. However, the particles are distributed evenly and as singular particles on the surface which probably enhanced their accessibility and reactivity during the catalytic reactions. The lower particle density probably correlates to the functionalization of the bdc linker and therefore slightly reduced reactivity.

The histograms obtained from the SA-NMOF SEM images reveal a similar morphology and similar size distributions as the MOFs powders (see Figure 62 and Table 13). All the images reveal a spherical particle shape. In terms of particle size, the mean particle sizes are slightly smaller for the SA-NMOFs, which could be either attributed to the electron beam applied during SEM imaging, which is probably more damaging than for the MOF particles themselves, due to the overall smaller amount of MOFs on the surface, or the anchoring process might favour smaller particles over larger ones.

SA-NMOFs metal content. Finally, we investigated the overall metal content of the samples by ICP-MS (see Table 14) after digesting the SA-NMOFs in HNO_3/H_2O_2 at 150°C for 5 min. The obtained metal amounts show that the SA-NMOFs were successfully anchored on the surface, supporting the observations from SEM. Upon comparing the amount of Cr of all three chromium-containing samples, it is evident, that the MIL-101-SO_3H sample contains the highest amount of Cr. This can be attributed to the large crystals, which determine the absolute chromium content of the sample. An even higher metal content can be observed for the CoBTC samples, which show even larger primary particle sizes. For MIL-101 and MIL-101-NH_2, which show similar primary particle sizes, MIL-101-NH_2 reveals a lower Cr content, which correlates to the lower coverage density. The generally lower coverage of the silicon substrates could be explained by the unpolished, passivated backsides of the Si substrates which do not react with the NMOF particles. In this respect, the PDMS substrates have approximately twice the reaction surface and greater surface roughness, which could provide a larger reaction surface. Overall, the metal content deposited on the substrate surfaces shows similarly high metal content as the previously characterized SA-NMOF 3 (UiO-66@PDMS) and SA-NMOF 5 (UiO-66@Si).

Table 14: Amount of Chromium, Zirconium, and Cobalt in the surface anchored NMOFs determined by ICP-MS.

Name	M*	Substrate	Metal Mass (m) [ng]	Sample area (A) [cm^2]	Metal Mass (m*) [ng/cm^2]	Catalyst amount[1] [nmol per cm^2]
MIL-101-SO_3H	Cr	PDMS	296.29 ± 8.20	1.07 ± 0.10	276.15 ± 26.85	5.31 ± 0.52
MIL-101-SO_3H	Cr	Si	236.35 ± 7.01	1.00 ± 0.10	236.35 ± 24.64	4.55 ± 0.47
MIL-101-NH_2	Cr	PDMS	40.10 ± 6.21	1.15 ± 0.10	34.83 ± 6.19	0.67 ± 0.12
MIL-101-NH_2	Cr	Si	34.42 ± 3.98	1.00 ± 0.10	34.42 ± 5.26	0.66 ± 0.10
MIL-101	Cr	PDMS	89.72 ± 4.90	1.08 ± 0.10	83.44 ± 9.00	1.60 ± 0.17
MIL-101	Cr	Si	33.00 ±6.48	1.00 ± 0.10	33.00 ± 7.27	0.63 ± 0.14
blank	Cr	PDMS	29.22 ± 8.74	1.10 ± 0.10	29.22 ± 8.74	0.51 ± 0.1
blank	Cr	Si	17.42 ± 10.90	1.00 ± 0.10	17.42 ± 11.04	0.34 ± 0.21
CoBTC	Co	PDMS	3192.04 ± 17.65	1.12 ± 0.10	2827.62 ± 250.97	54.38 ± 4.83
blank	Co	PDMS	1.82 ± 0.46	1.10 ± 0.10	1.65 ±0.44	0.03 ± 0.01
UiO-66 (SA-NMOF 3)	Zr	PDMS	369.00 ± 11.28	1.00 ± 0.10	369 ± 48	4.05 ± 0.53
UiO-66 (SA-NMOF 5)	Zr	Si	58.41 ± 2.14	1.00 ± 0.10	58.4 ± 8.0	$6.40 \cdot 10^{-1}$ ± $8.8 \cdot 10^{-2}$
blank	Zr	PDMS	4.28 ± 1.11	1.05 ± 0.10	4.08 ± 1.50	$4.46 \cdot 10^{-2}$ ± $1.58 \cdot 10^{-2}$
blank	Zr	Si	5.04 ± 2.49	1.00 ± 0.10	5.04 ± 2.99	$5.52 \cdot 10^{-2}$ ± $3.28 \cdot 10^{-2}$

[1]Calculated with the molar mass of Cr=51.996 $g \cdot mol^{-1}$, Co=58.933 $g \cdot mol^{-1}$, Zr=91.224 $g \cdot mol^{-1}$

*Metal

3.5.4. Reaction Sequence I: Acetal Hydrolysis/Knoevenagel Condensation

The first reaction sequence investigated was the hydrolysis of benzaldehyde dimethyl acetal (BADMA, blue) to benzaldehyde (BA, green) and the subsequent Knoevenagel condensation of BA and malononitrile (MAN) to 2-benzylidene malononitrile (BACN, red) (see Figure 63). This reaction is particularly interesting as both reactions or similar reactions were previously investigated and can be catalyzed by different MOFs (MIL-101-SO_3H-NH_2, PCN-124, and MIL-101-NH_2 (Al)) in various solvents (dioxane, nitromethane, DMSO).[328–331]

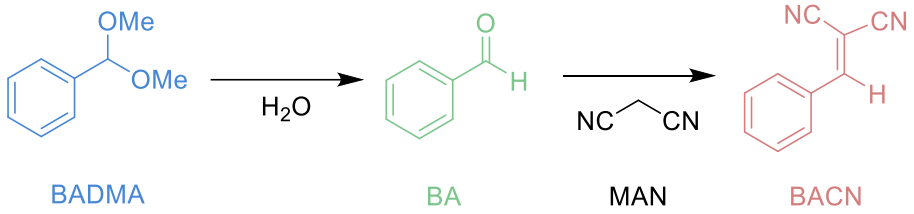

Figure 63: Subsequential reaction of benzaldehyde dimethyl acetal (BADMA) hydrolyzed first to benzaldehyde (BA), and then reacted with malononitrile (MAN) to 2-benzylidene malononitrile (BACN).

Reaction parameter optimization. Every reaction in a reaction sequence requires specific reaction conditions such as temperature, pressure, solvents, pH values, etc. The reaction conditions for one specific reaction might interfere with the reaction conditions of the subsequent reaction, resulting in catalyst deactivation or inhibition of reaction intermediates. Therefore, a thorough parameter optimization to determine the optimal conditions for both individual reactions in a reaction sequence is key.

Therefore, we optimized the solvent, water content, employed catalyst and reaction temperature for both subsequent reactions separately, and later decided which conditions we would apply for the subsequent reactions. Due to easier handling, we performed the reaction optimization in batch reactors and transferred the knowledge to the microfluidic reactors in the second step.

Hydrolysis of BADMA. Initially, we optimized the reaction parameters for the hydrolysis of BADMA to BA. Besides typical reaction parameters like temperature, catalyst, and solvent another focus was the water content in the reaction mixture as water is important for acetal hydrolysis. Experimentally, 75 µL BADMA (1 equiv.) was dissolved in 4 mL of solvent (acetonitrile (MeCN), tetrahydrofuran, dioxane, propylene carbonate, or dimethyl formamide) and 5 mg of activated catalyst powder (MIL-101 (Cr), MIL-101-NH_2 (Cr), MIL-101-SO_3H (Cr), UiO-66, and CoBTC) were reacted in a vial for usually 13 h. Afterwards, a sample was taken and analyzed by GC-

MS. Previously, a GC calibration for all reactants was performed to normalize the measured integrals (see Figure S1).

Analyzing the yields of BA by hydrolysis of BADMA with different catalysts (see Figure 65 (a)) indicated that MIL-101 (Cr), MIL-101-NH_2 (Cr), and MIL-101-SO_3H (Cr) show a high catalytical activity towards the hydrolysis of BADMA to BA as they reached full conversion after 6h. To investigate which of these catalysts is the most promising, we repeated the experiments and analyzed the reactant composition after 1 min, 15 min, 30 min, and 1 h. Our results show that in contrast to previous observations by Lee *et al.*[330] MIL-101-NH_2 has the highest catalytical activity, closely followed by MIL-101-SO_3H. In their publications, they report, that the hydrolysis of BADMA is attributed to the acidic SO_3H groups and that the Knoevenagel condensation is catalyzed by the basic amino groups MIL-101-SO_3H-NH_2(Cr) (see Figure 64).[330] (It should be noted that the reaction cascade they investigated was slightly different including the hydrolysis of BADMA followed up by the nitroaldol condensation to 2-nitrovinyl benzene.

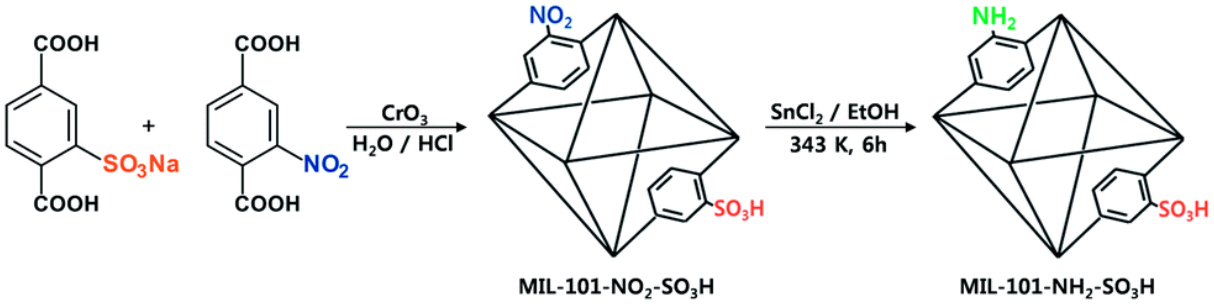

Figure 64: Synthesis route to obtain MIL-101-SO_3H-NH_2 (Cr).[330] The bifunctional catalyst was then used as a tandem catalyst in the hydrolysis of BADMA followed up by the nitroaldol condensation to 2-nitrovinyl benzene. The figure was taken from Lee *et al.* with permission from RCS.[330]

However, we observed, that MIL-101-NH_2 catalyzes the hydrolysis of BADMA preferentially and as described later, even inhibits the Knoevenagel condensation: This could be caused by protonated amino groups, due to the acidic reaction conditions during the synthesis.

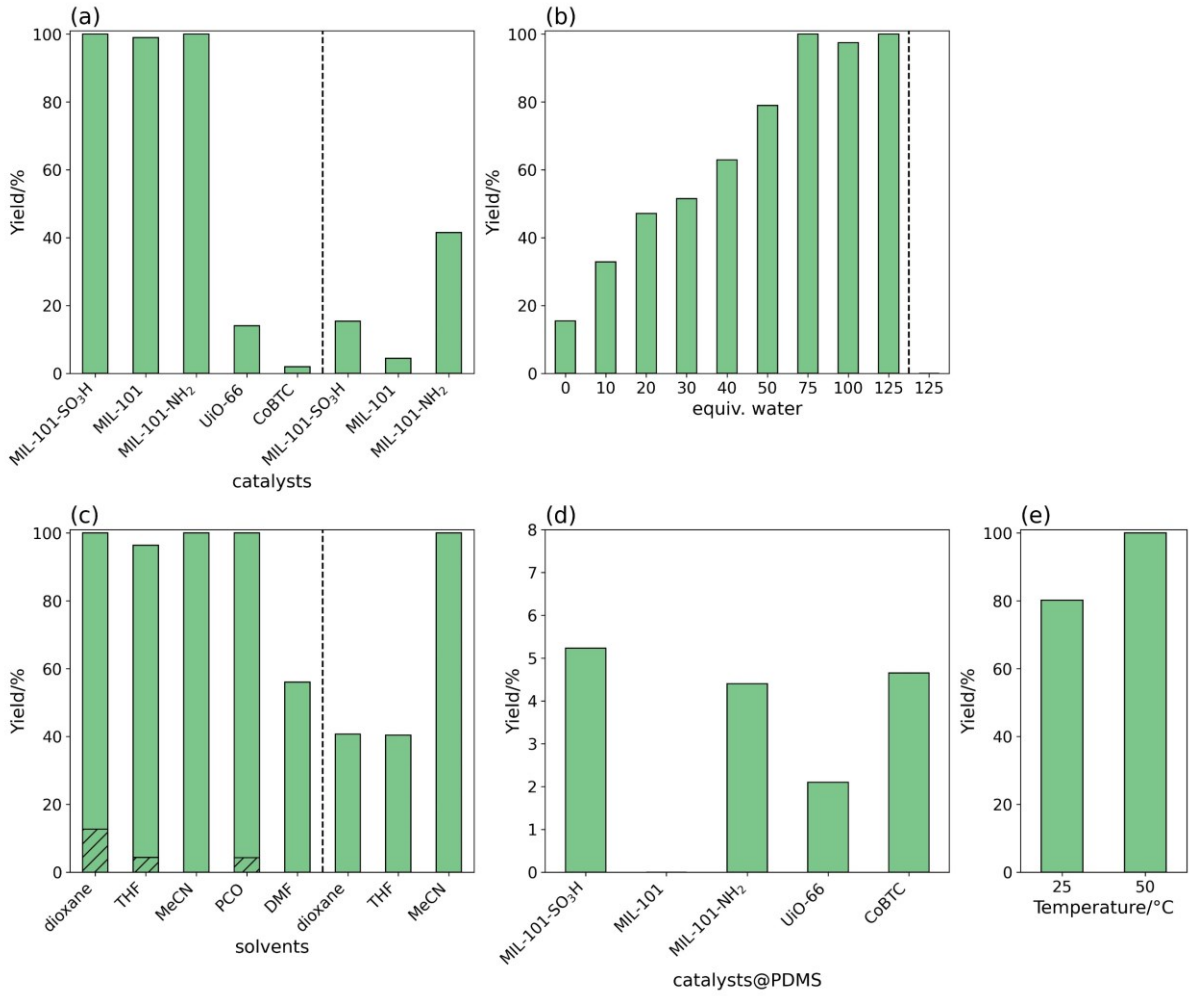

Figure 65: Optimization of the reaction conditions: catalysts (a), water content (b), the solvent (c), the catalysts immobilized on PDMS (d), and temperature (e) on the hydrolysis of BADMA to BA. The blind yields are displayed in hatch.

Experimental details: (a) solvent: MeCN, water: 125 equiv. (1.10 mL), m (catalysts= 5 mg), t: 6 h; 1min (behind the dotted line), T: 50°C; (b) solvent: MeCN, catalyst: MIL-101-SO_3H, blank (behind the dotted line), m(catalyst): 5 mg, t: 13 h, T: 50°C; (c) water: 125 equiv. (1.10 mL), catalyst: MIL-101-SO_3H, m (catalysts): 5 mg, t: 6 h,1 h (behind the dotted line), T: 50°C; (d) solvent: MeCN, water: 125 equiv. (1.10 mL), A (catalysts): 1 cm^2, t: 13 h, T: 50°C. (d) solvent: MeCN, water: 125 equiv. (1.10 mL), catalyst: MIL-101-SO_3H, m (catalysts): 5 mg, t: 6 h.

The effect of the water content on the product formation was determined in the following experiment (see Figure 65 (b)). Due to the reaction type (hydrolysis), it is clear, why the water content in the reaction mixture could enhance the product formation. The reaction yield shows that 75-125 equiv. of water enhance the product formation significantly, yielding full conversion after 13 h. Especially, for short reaction times – essential for microfluidic channels – a particularly high water content leads to a fast product formation.

Furthermore, several solvents that are compatible with microfluidic devices and miscible with water were investigated for the reaction (see Figure 65 (c)). After 6 h of reaction, dioxane, THF, MeCN, and PCO yielded full conversion. However, PCO was not miscible with 1.1 mL water yielding a two-phase system. As this is difficult for the reaction in the microfluidic channel and overall reduces the reproducibility, PCO was excluded from further investigations. For the other solvents (dioxane, THF, and MeCN) the experiments were repeated, and the yields were determined after 1 min, 15 min, 30 min, and 60 min. Figure 65 (c, left of the dashed line) shows the yields of BA in dioxane, THF, and MeCN after 60 min of reaction. While THF and dioxane yield ~40% BA, MeCN already reached full conversion. Therefore, MeCN is the best solvent for the hydrolysis of BADMA to BA.

The next parameter, that we investigated was the conversion with typical SA-NMOF catalysts. Therefore, PDMS was functionalized in a two-step process, described in the last chapter, to yield amino-functionalized PDMS. This was subsequently reacted with (N)MOF particles to form SA-NMOFs. They were cut into 1 cm^2 pieces and added to the reaction solution. After 13 h, the catalyst reached low conversion rates of <10%, with MIL-101-SO_3H@PDMS and MIL-101-NH_2@PDMS. Even though the TOF frequencies of the reaction are still high, due to the low amount of catalyst immobilized on the PDMS, the low overall conversion of the SA-NMOFs in this reaction is a problem due to the short dwell times in the microfluidic reactors.

The final parameter, that was investigated is the temperature. The catalytic activity is higher at 50°C (100%) compared to 25°C (80 %) after 6 h of reaction, which can be explained by the lower activation energy barrier at higher reaction temperatures.

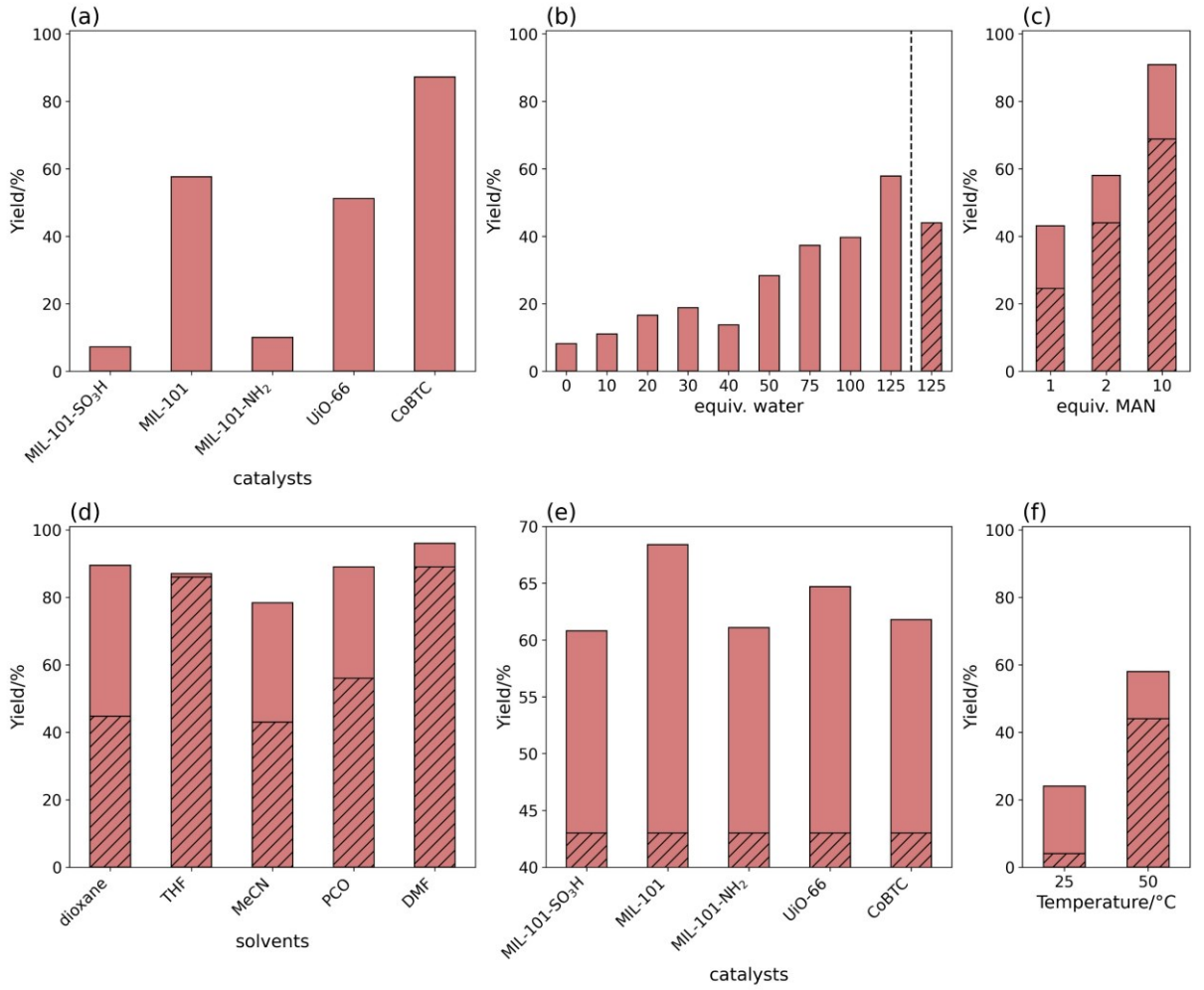

Figure 66: Optimization of the reaction conditions: catalysts (a), water content (b), MAN content (c), the solvent (d), the catalysts immobilized on PDMS (e), and temperature (f) on the Knoevenagel reaction of BA and MAN to BACN. The blind yields are displayed in hatched

Experimental details: (a) solvent: MeCN, water: 125 equiv. (1.10 mL), MAN: 2 equiv., m (catalysts= 5 mg), t: 1 h, T: 50°C; (b) solvent: MeCN, MAN: 2 equiv., catalyst: MIL-101, m(catalyst): 5 mg, t: 1 h, T: 50°C; (c) solvent: MeCN, water: 125 equiv. (1.10 mL), catalyst: MIL-101, m(catalyst): 5 mg, t: 1 h, T: 50°C; (d) water: 125 equiv. (1.10 mL), MAN: 2 equiv., catalyst: MIL-101, m (catalysts): 5 mg, t: 6 h; 1 h (behind the dotted line), T: 50°C; (e) solvent: MeCN, water: 125 equiv. (1.10 mL), MAN: 2 equiv., A (catalysts): 1 cm^2, t: 1 h, T: 50°C. (f) solvent: MeCN, water: 125 equiv. (1.10 mL), MAN: 2 equiv., m (catalysts): 5 mg, t: 1 h, T: 25°C.

Knoevenagel condensation. Subsequently, the same parameters investigated for the hydrolysis of BADMA were similarly investigated for the Knoevenagel reaction of BA and MAN to BACN.

Various catalysts were investigated for the Knoevenagel reaction (see Figure 66 a). For vectorial catalysis, two independent catalysts, which selectively catalyze one of the subsequential reactions (hydrolysis of BA and the Knoevenagel reaction) are ideal.

Due to the fact, that both reactions are catalyzed by Lewis acids, this is impossible to accomplish. However, we were able to select catalysts that preferentially catalyze one of the reactions. In terms of MOF powders, MIL-101 (Cr) and CoBTC, were the best catalysts for the Knoevenagel condensation, that we tested. Furthermore, both catalysts are not very effective as catalysts in the hydrolysis of BADMA. Additionally, the catalysts with were most effective for the hydrolysis of BADMA, MIL-101-NH_2 and MIL-101-SO_3H, seem not only to not catalyze the reactions, but they also seem to actively inhibit the reaction, as the conversions are lower than the ones observed for the blind conversion (44.0 %). This could be explained, by fact that the Knoevenagel condensation is catalyzed by basic sites. Due to the presence of acid groups (e.g. -SO_3H), the total basicity of the MOF/reaction mixture is reduced, therefore the reaction is inhibited. As mentioned before, a similar effect was observed for MIL-101-NH_2, which hints at its acidity, probably caused by the protonation of the amino group. The high overall blind conversion is dependent on many factors: high reaction temperature and water content enhance it significantly. Which makes the catalyst sequence of MIL-101-SO_3H/MIL-101 or MIL-101-NH_2/MIL-101 reasonable.

The next point that was studied was the effect of the water content on the catalytic performance (see Figure 66 b). The yield of BACN increased from 8.2 % (0 equiv. H_2O) to 57.6 % (125 equiv. H_2O) after 1 h, which shows that water enhanced the product formation. However, alongside the gain in catalytic performance, the blind conversion is also increased to 44 % (125 equiv.). Overall, these results are surprising, as the Knoevenagel reaction is a condensation reaction that produces water. Therefore, excessive amounts of water should hinder this reaction. Probably, water acts as a base, deprotonates MAN, and therefore enhances the product formation. As water accelerate both reactions at once, the addition of water is a useful tool to enhance the product formation.

Another factor that certainly influences the product formation is the equivalents of malononitrile added to the reaction mixture (see Figure 66 c), while 1 equiv. results in 43.1% BACN formation after 1 h, 90.9 % was obtained by the addition of 10 equiv. MAN.

Subsequently, dioxane, THF, MeCN, PCO, and DMF were evaluated as solvents for the Knoevenagel condensation (see Figure 66 d). Due to the particularly high blind conversions for DMF and THF, these solvents are not suitable for the reaction. Additionally, PCO is not miscible with 125 equiv. of water and is therefore not a suitable solvent for the reaction. However, MeCN and dioxanes are both suitable solvents for the Knoevenagel reaction.

Following up, different catalysts were immobilized on PDMS as SA-(N)MOFs and applied as catalysts in the formation of BACN (see Figure 66 e). Similarly, to the dispersed bulk catalysts, MIL-101 (Cr) (see Figure 66 a) shows the highest catalytic performance. Due to the particularly low performance of MIL-101@PDMS in the hydrolysis of BADMA, this is a very promising catalyst for the Knoevenagel reaction in the microfluidic setup.

The final parameter, that was investigated is the temperature. The catalytic activity is higher at 50°C (57.9 %) as compared to 25°C (24.0 %) after 1 h of reaction, which can be explained by the lower activation energy barrier at higher reaction temperatures. However, the ratio of catalyst performance to the blind conversion is higher for lower temperatures – so the effect of the catalysts is more pronounced at lower temperatures.

Summary: parameter optimization. Overall, these experiments show that vectorial catalysis where one catalyst catalyzes the initial reaction and the second catalyst catalyzed the second reaction could be achieved, with the best parameters for this being:

- MIL-101-SO_3H@PDMS or MIL-101-NH_2@PDMS for the hydrolysis of BADMA and MIL-101@PDMS for the Knoevenagel reaction
- MeCN or dioxane as solvents
- High water (125 equiv. or higher) content
- Higher temperature enhances the product formation; difficult to probe in microfluidic reactors as both solvents have a low boiling point, evaporate easily, and form bubbles in the microfluidic reactor channels.
- Higher amount of MAN can enhance the product formation as well.

There are also some challenges that the initial experiments revealed, that should be addressed:

- The hydrolysis catalyzed by SA-NMOF is rather slow the results indicate that this is reaction is the rate-determining step of the reaction sequence. Even higher water contents could help to tackle this problem.
- The Knoevenagel condensation has a high blind conversion for the optimized reaction conditions, therefore it might be hard to detect the influence of the catalyst in this step. However, we tried to investigate that problem further by running by investigating the kinetics of the catalyzed reaction after one another.

Vectorial catalysis – A experimentalist's guide. The process of identifying interesting reaction sequences and optimizing the process further for its implementation into microfluidic devices can be summed up in a flow chart (Figure 67). A thorough screening for relevant and feasible reactions is the starting point for the optimization process. The chosen reaction sequence should be able to be catalyzed by MOFs, meet the requirements of the vectorial catalysis (similar temperatures, pH value, solvent, etc.), and at the same time meet the requirements of the microfluidic device. In terms of the applied PDMS-based microfluidic devices, the limitations include a limited choice of polar solvents and a process temperature to room temperature. Additionally, the reaction sequence needs to include two reactions that can be selectively catalyzed by one catalyst. Further process optimization includes the catalysis parameter optimization and the catalyst design.

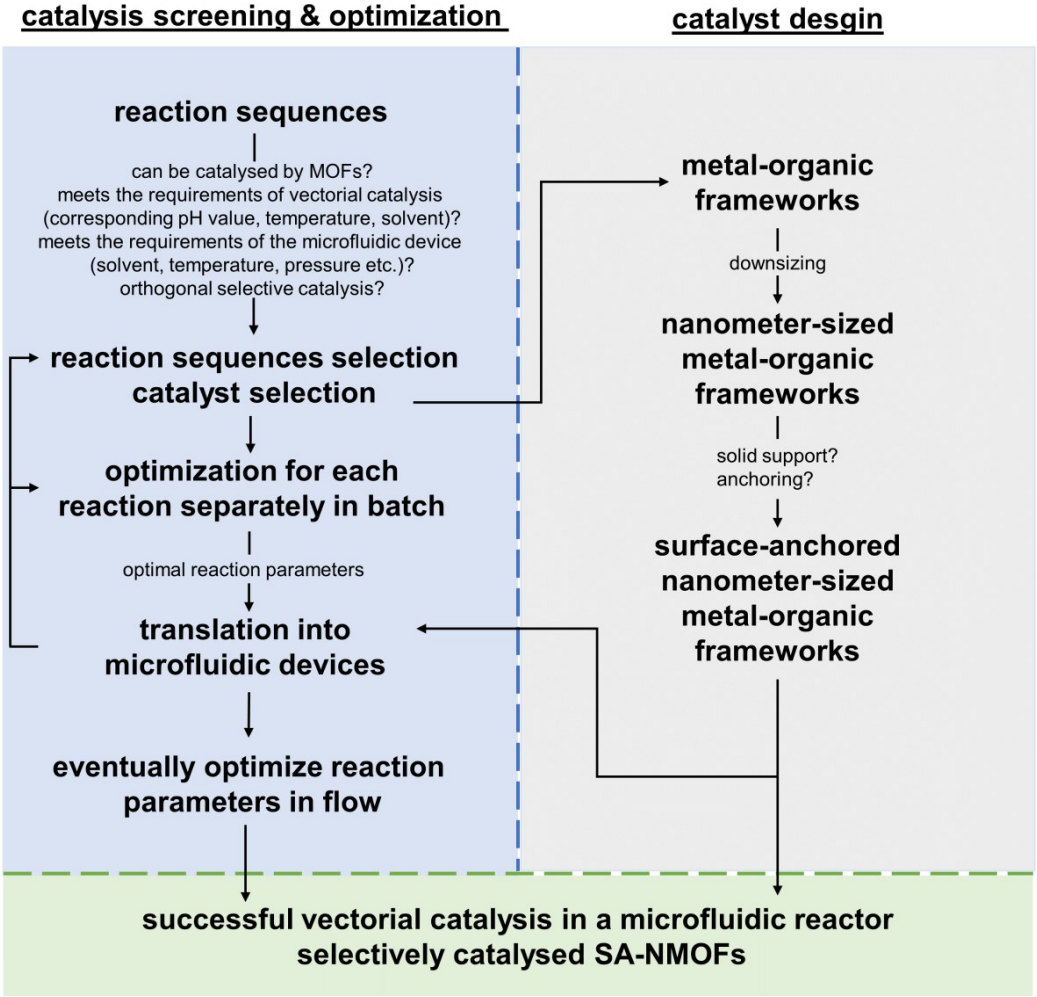

Figure 67: Flow chart of the process optimization towards the realization of vectorial catalysis in microfluidic reactors selectively catalyzed by SA-NMOFs. The optimization is slitted into catalysis screening/optimization and catalyst design.

The catalysis optimization includes the parameter optimization for all reactions in the reaction sequence separately, finding the optimal parameters for the combined reaction sequence. Then, the reaction sequence can be transferred to microfluidic devices. In parallel, the catalyst design needs to be developed: downsizing MOFs, then anchoring them to a substrate surface. After their application as catalysts in microfluidic devices, the reaction can be further optimized in flow. If the translation into the microfluidic device failed it might be necessary to repeat the other steps or to focus on other reaction sequences.

Reaction kinetics. Before translating the reaction sequence to microfluidic devices, we decided to investigate the catalysts' performances in detail in a sequential manner (see Figure 68 a). Therefore, 5 mg of MIL-101-SO_3H were dispersed in dioxane/H_2O (4/1.1 v%, 125 equiv.) and 75 µL BADMA were added and stirred for 6 h at 50°C. After 6 h MIL-101-SO_3H was filtered off and replaced by 5 mg of MIL-101 and 66 mg MAN (2 equiv.). This dispersion was stirred for 6 h at 50°C. By GC, we tracked the time-dependent yields of BADMA, BA, and BACN. The yield of BA increased over time after the catalyst was added, after 6 h full conversion was achieved. Subsequently, MAN and MIL-101 were added and the Knoevenagel reaction starts. The two equivalents of methanol formed during the hydrolysis of BADMA, seem not to interfere with the consecutive reaction, as BACN is formed as expected.

During the hydrolysis of BADMA without any catalyst (see Figure 68 b),~14% of BA is formed, with is not converted into BACN by Knoevenagel reaction. This result is slightly surprising due to the previous results, which showed a high blind conversion for the Knoevenagel reaction. Although, this is promising for the follow-up translation into microfluidic devices.

Additionally, we investigated the reaction with the catalysts in reverse order, first applying MIL-101 followed by either MIL-101-SO_3H (c) or MIL-101-NH_2 (d). The results highlight that MIL-101 cannot catalyze the hydrolysis of BADMA sufficiently. However, MIL-101-SO_3H and MIL-101-NH_2 catalyze the hydrolysis of BADMA very efficiently, but only small amounts of BACN (<20%) are formed. Hence, this indicates the importance of both catalysts being in the correct reaction sequence to catalyze this stepwise reaction as desired.

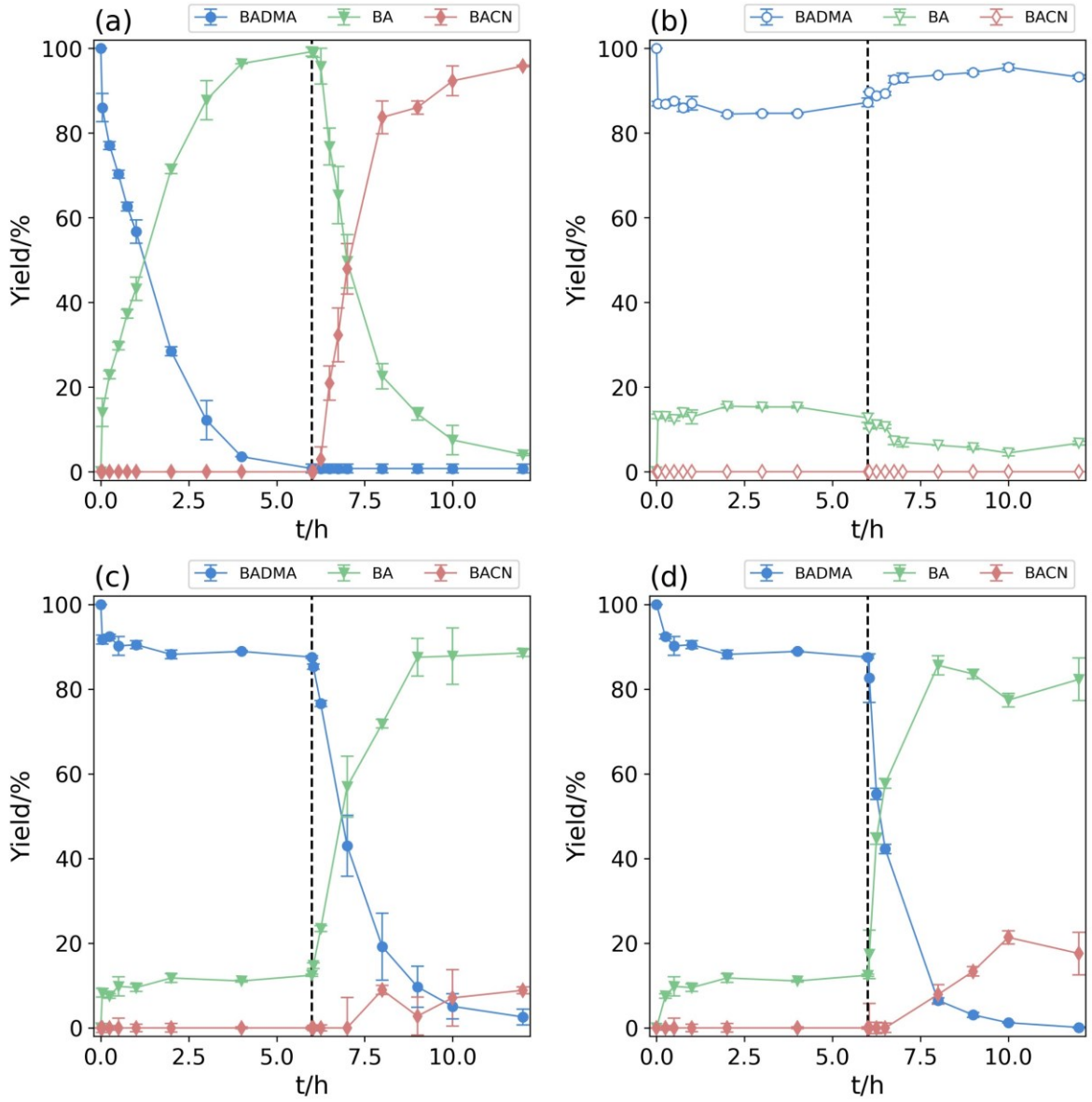

Figure 68: Time-yield plots of BA, BADMA, and BACN formed by the subsequential hydrolysis of BADMA to BA followed up by the Henry reaction to BACN catalyzed without catalyst (b), by MIL-101-SO_3H (Cr) (0-6 h), and MIL-101 (Cr) (6-12 h) (a), by MIL-101 (Cr) (0-6 h) and MIL-101-SO_3H (Cr) (6-12 h) (c) or by MIL-101 (Cr) (0-6 h) and MIL-101-NH_2 (Cr) (6-12 h) (d) performed in a batch reactor. (The reactant concentrations were 100 µM BADMA and 200 µM (2 equiv.) MAN in 4:1.1 (v %) dioxane/water.)

Finally, we translated the reaction sequence from batch to a microfluidic device. Therefore, we investigated the manufacturing of microfluidic devices. The microfluidic devices consist of a PDMS mold with an imprinted channel pattern which is molded on top of a glass, silicon, or PDMS slide (see Figure 63). The (N)MOFs can be anchored to the bottom half of the microfluidic devices and sealed to the channel.

Table 15: Conversion of BADMA, and yields of BA, and BACN after vectorial catalysis (acetal hydrolysis followed up by a Knoevenagel reaction) performed in microfluidic reactors. The reactant concentrations were 125 µM BADMA and 1.25 mM (10 equiv.) MAN in 1:1 (v %) acetonitrile/water at room temperature.

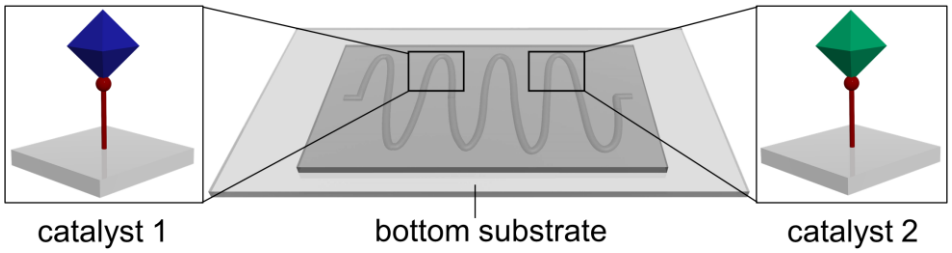

No	catalyst 1	catalyst 2		Equiv. MAN	bottom substrate	Conversion % BADMA	yield % BA	% BACN
1	-	-		10	-	9.9	9.9	0.0
2	-	-		2	-	6.4	6.4	0.0
3	-	-		10	PDMS	0	0.0	0.0
4	MIL-101-NH_2	MIL-101-NH_2		10	PDMS	59.0	59.0	0.0
5	MIL-101-SO_3H	MIL-101-SO_3H		10	PDMS	41.3	41.3	0.0
6	MIL-101	MIL-101		10	PDMS	15.5	15.5	0.0
7	MIL-101-NH_2	MIL-101		10	PDMS	85.1	12.8	72.3
8	**MIL-101-NH_2**	**MIL-101**	**c4**	**10**	**PDMS**	**100**	**18.9**	**81.1**
9	MIL-101-NH_2	MIL-101	2nd	10	PDMS	48.8	32.8	16.0
10	MIL-101-NH_2	MIL-101	*	10	PDMS	26.5	26.5	0.0
11	MIL-101-NH_2	MIL-101		2	PDMS	8.7	8.7	0.0
12	MIL-101-NH_2	MIL-101		10	glass	51.4	51.4	0.0
13	**MIL-101-SO_3H**	**MIL-101**		**10**	**PDMS**	**90.3**	**7.9**	**82.4**
14	MIL-101-SO_3H	MIL-101	2nd	10	PDMS	47.5	12.2	35.3
15	MIL-101-SO_3H	MIL-101		2	PDMS	0	0	0
16	MIL-101	MIL-101-SO_3H		10	PDMS	25.5	25.5	0

c4: cycle solution four times through the reactor; 2nd: recycle the reactor for the next reaction; *solvent- dioxane/H_2O (2/1 v/ %).

Several experiments with the microfluidic devices were performed, and the results are summed up in Table 15. Column entries 1-3 show the blind conversion after mixing 75 µL BADMA, 2 mL MeCN, 2 mL H2O, and 2 or 10 equiv. MAN (66; 330 mg) for 1 min at room temperature, Afterward the solutions were applied to the microfluidic reactors. The mean retention time was 30 s for the solutions in a 9 µL microfluidic reactor with 14 coils (13 mm x 0,3 mm x 0.15 mm).

A PDMS reactor without any functionalization yields no conversion of BADMA. However, if MIL-101-NH_2 (entry 4), MIL-101-SO_3H (entry 5), or MIL-101 (entry 6) are anchored to PDMS the conversion of BADMA to yield BA is partly successful, but the Knoevenagel condensation does not take place.

If the catalysts are arranged in a reasonable sequence, either MIL-101-SO_3H or MIL-101-NH_2 first, followed up by MIL-101; the microfluidic reactors can catalyze both reactions one after another, yielding either 9.7 % BADMA, 7.9 % BA, and 82.4 % BACN for MIL-101-SO_3H/MIL-101 or 14.9 % BADMA, 12.8 % BA, and 72.3 % BACN for MIL-101-NH_2/MIL-101 (entries 7 and 13, respectively). If the reaction solution is passed through the same reactor four times, the yield can be increased even further to 18.9 % BA and 81.1% BACN in a MIL-101-NH_2/MIL-101 reactor (entry 8). The recycling of the reactors is possible; however, we observe slightly reduced yields (entry 9, 14). We attribute this observation to the difficult cleaning procedure, which makes the re-use slightly more difficult (as the reactors cannot be immersed in solvents for hours). The possibilities to re-use the SA-NMOF have already been demonstrated in the previous chapter, by intensive washing and drying at 100°C.

Further insight was enabled by varying the solvent, the equiv. of MAN, and the substrate. By choosing dioxane instead of MeCN (entry 10), 2 instead of 10 equiv. of MAN (entry 11, 15), or glass instead of PDMS (entry 12) we see the significantly lower conversion of BADMA, yielding BA, but no BACN.

Finally, we calculated the turnover frequencies for the different catalysts. The TOF numbers are calculated as shown in the previous chapter, however, due to the reaction conditions (microfluidic reactor, vectorial catalysis) we had to make a couple of adjustments and assumptions. The calculation is demonstrated for Table 15, entry 4):

$$TOF = \frac{r'[\frac{nmol}{h}]}{n_{catalyst}\ [nmol]}$$

$$r'\ \left[\frac{nmol}{h}\right] = \frac{c(BA)_{t_1} - c(BA)_{t_0}}{t_1 - t_0}$$

$n_{catalyst/area}$ (MIL-101-NH_2) = 0.67 ± 0.12 nmol/cm^2 (ICP-MS);

$n_{catalyst/area}$ (MIL-101) = 1.60 ± 0.17 nmol/cm^2 (ICP-MS)

We assume that the catalytically active centre for the acetal hydrolysis is the protonated NH_2 group, as we cannot determine the linker itself by ICPMS, we assume that the linker and metal are in a 1:1 ratio ($Cr_3O(OH)_2(H_2O)(bdc\text{-}NH_2)_3$). Similarly, we assume that the Knoevenagel condensation is catalyzed by the basic ligands (OH^-, H_2O) coordinating to the metal centre, in turn, a 1:1 ratio of Cr:L is assumed.

$A_{catalyst}$ (MIL-101-NH_2) = 30 mm^2; $A_{catalyst}$ (MIL-101) = 30 mm^2;

The assessable area of the SA-NMOFs is determined by the dimensions of the channels (A = 9 µL/0.15 mm (V/height)=60 mm^2), where half of the area is covered with MIL-101-NH_2 and the other half with MIL-101.

n_{0h} = 1120 nmol (in 9 µL)

The material quantity of BADMA at the beginning of the experiment was determined for 9 µL as this is the volume of the microfluidic reactor with dimensions of 14 coils (13 mm x 0,3 mm x 0.15 mm; 9 µL) (further details about the reactor design can be found in the appendix chapter 6.3.2.7). Subsequentially, the relative quantity of BADMA, BA, and BACN at the end of the reactor was determined by GC/MS. For BA, we added the amount of BACN as BACN was formed from BA.

$Yield_{30s}$ (BA) = 12.8 %

$Yield_{30s}$ (BACN) = 72.3 %

$$n_{30s}(BADMA) = \frac{100 - \mathrm{Y1} - \mathrm{Y2}}{100} \cdot c_0 = \frac{100 - 12.8 - 72.3}{100} \cdot 1120\ nmol = 167\ nmol$$

$$n_{30s}(BA) = \frac{\mathrm{Y(BA)} + \mathrm{Y(BACN)}}{100} \cdot c_0 = \frac{12.8 + 72.3}{100} \cdot 1120\ nmol = 953\ nmol$$

$$n_{30s}(BACN) = \frac{\mathrm{Y}}{100} \cdot c_0 = \frac{72.3}{100} \cdot 1120\ nmol = 810\ nmol$$

Then we determined the initial reaction rates, with the measured mean retention times of the solution in the microfluidic reactor.

$$r'\,(BA)\left[\frac{nmol}{h}\right] = \frac{953\ \mathrm{nmol}}{0.00833\ h} = 1.14 \cdot 10^5\ \mathrm{nmol/h}$$

$$r'\,(BACN)\left[\frac{nmol}{h}\right] = \frac{810\ \mathrm{nmol}}{0.00833\ h} = 9.72 \cdot 10^4\ \mathrm{nmol/h}$$

For the calculation of the TOF values, we assumed that the acetal hydrolysis is exclusively catalyzed by MIL-101-NH_2, and the Knoevenagel condensation is exclusively catalyzed by MIL-101, which is not entirely correct, but a reasonable approximation. Additionally, we assumed that the ~1cm^2 SA-NMOF PDMS substrates possess an actual area of 2 cm^2, as the PDMS substrates show functionalized top and bottom sites. Therefore, the amount of accessible catalyst has to be divided by a factor of 2.

$$TOF\ (cat\ 1) = \frac{1.14 \cdot 10^6 \frac{\mathrm{nmol}}{\mathrm{h}}}{\frac{0.67 \frac{nmol}{cm^2}}{2} \cdot 0.3\ cm^2} = 1.13 \cdot 10^6 \frac{1}{h}$$

$$TOF\ (cat\ 2) = \frac{9.72 \cdot\ 10^5 \frac{\text{nmol}}{\text{h}}}{\frac{1.60 \frac{nmol}{cm^2}}{2} \cdot 0.3\ cm^2} = 4.05\ \cdot\ 10^5 \frac{1}{h}$$

$$\Delta TOF\ (cat\ 1) = \left(\frac{\Delta n}{n}\right) \cdot TOF = \left(\frac{0.12\ \text{nmol}}{0.67\ \text{nmol}}\right) \cdot 1.13 \cdot\ 10^6 \frac{1}{h} = 0.20 \cdot\ 10^6 \frac{1}{h}$$

$$\Delta TOF\ (cat\ 2) = \left(\frac{\Delta n}{n}\right) \cdot TOF = \left(\frac{0.17\ \text{nmol}}{1.60\ \text{nmol}}\right) \cdot 4.05\ \cdot\ 10^5 \frac{1}{h} = 0.43 \cdot\ 10^5 \frac{1}{h}$$

The values were calculated for the various samples and are summed up in Table 16.

Table 16: Turnover frequencies calculated for the different catalysts applied in vectorial catalysis of acetal hydrolysis followed up by a Knoevenagel reaction performed in microfluidic reactors.

No	catalyst I	catalyst 2		Equiv. MAN	bottom substrate	TOF/h^{-1} Catalyst I	TOF /h^{-1} Catalyst II
1	MIL-101-NH_2	MIL-101-NH_2		10	PDMS	(3.96 ± 1.40) $\cdot 10^5$	-
2	MIL-101-SO_3H	MIL-101-SO_3H		10	PDMS	(3.50 ± 0.68) $\cdot 10^4$	-
3	MIL-101	MIL-101		10	PDMS	(4.34 ± 0.46) $\cdot 10^4$	-
4	MIL-101-NH_2	MIL-101		10	PDMS	(1.13 ± 0.20) 10^6	(4.05 ± 0.43) $\cdot 10^5$
5	MIL-101-NH_2	MIL-101	c4	10	PDMS	(3.36 ± 0.60) 10^5	(1.13 ± 0.20) $\cdot 10^5$
6	MIL-101-NH_2	MIL-101	2^{nd}	10	PDMS	(6.55 ± 0.12) $\cdot 10^5$	(8.97 ± 0.87) $\cdot 10^5$
7	MIL-101-SO_3H	MIL-101		10	PDMS	(1.53 ± 0.15) $\cdot 10^5$	(4.62 ± 0.50) $\cdot 10^5$
8	MIL-101-SO_3H	MIL-101	2^{nd}	10	PDMS	(8.04 ± 0.78) $\cdot 10^4$	(1.97 ± 0.19) $\cdot 10^5$

c4: cycle solution four times through the reactor; 2^{nd}: recycle the reactor for the next reaction;

The SA-NMOFs show impressively high TOF values for the vectorial catalysis comprised of acetal hydrolysis and Knoevenagel condensation in the range of ~100,000-1,000,000 h^{-1} (see Table 16). The values could probably be improved further by reducing the primary particle size of MIL-101-SO_3H to 20-30 nm. The absolute TOF values reflect the enhanced reaction process and show the enhanced activity of the SA-NMOF catalysts combined with the subsequential reaction sequence. The TOF values are in the same range as reported in the previous chapter.

Table 17: Comparison of TOFs obtained from vectorial catalysis in microfluidic reactors for the reaction sequence consisting of hydrolysis of BADMA to BA, and Knoevenagel condensation to BACN with the tandem catalysis of the same reaction sequence catalyzed by bifunctional catalysts. The TOF frequencies were not given by the authors but calculated with the information given in the publications with are listed in the table.

+ this chapter

catalyst	Solvent	T/°C	t/h	n_{cat}/ mol%	Y/% BA	Y/% BACN	TOF/h^{-1} (R1)	TOF/h^{-1} (R2)	Ref.
MIL-101-NH_2 (Cr)	MeCN, H_2O	RT	30s	0.008	12.8	72.3	$1.13 \cdot 10^6$	-	+
MIL-101 (Cr)	MeCN, H_2O	RT	30s	0.02	12.8	72.3	-	$4.05 \cdot 10^5$	+
PCN-124 (Cu)	DMSO	50	12	1.0	0	100	16.8	16.8	[329]
MIL-101-NH_2 (Al)	dioxane	90	3	43	6	94	0.76	0.74	[328]
UiO-67(-NH_2)$_2$	ethanol	60	10	3.6	1	98	2.8	2.7	[332]
MIL-101(Cr) @citosan	MeCN	80	12	3.6	0	99	2.3	2.3	[333]
Cr-MIL-101-AB-x	DMF	90	0.08	4.0	44	17	180	51	[334]
Yb-bdc-NH_2	DMSO	50	24	2.0	0	97	2.0	2.0	[335]
Zn-MOF 1	DMF	80	0.5	1.0	16	10	52	20	[336]
Zn-MOF 2	DMF	80	0.5	1.0	27	5	64	10	[336]
Cd-MOF 1	DMF	90	5	0.56	0	84	30	30	[337]
Cd-MOF 2	DMF	90	5	0.56	0	95	34	34	[337]
PCN-905(Eu)-SO_2-SO_3H	toluene, H_2O	90	1	10	4.5	95.5	10	9.6	[338]

For comparison, we calculated various TOFs from publications (see Table 17) which investigated the reaction sequence in tandem catalysis catalyzed by one bifunctional catalyst. Due to the fact, that that the conversion and yields at short reaction times are often not reported in the publications, a direct comparison between the TOFs obtained from our microfluidic devices and the calculated ones from the literature are difficult to compare. However, even if the estimated values are qualitatively less accurate, we still observe that the TOF observed for the microfluidic devices are still several orders of magnitude higher than the ones derived from published data. This demonstrates how powerful the SA-NMOF-based microfluidic devices can be. A comprehensive comparison with more details from the publications shown in Table 17 and a complete overview of the publications for this reaction are comprised in Table S12.

3.5.5. Substrate Preparation Reaction Sequence II: Cyanosilylation/Hydrolysis

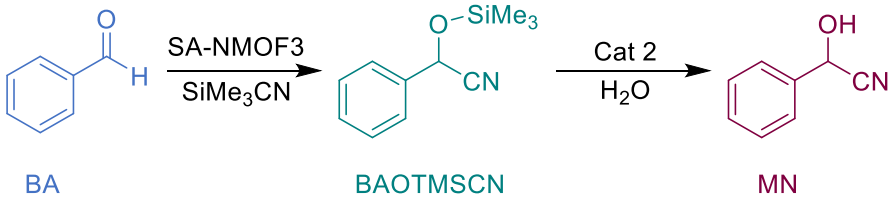

Figure 69: Subsequential reaction of benzaldehyde (BA) and trimethylsilyl cyanide (TMSCN) to 2-phenyl-2 ((trimethylsilyl)oxy)acetonitrile (BAOTMSCN), and then finally hydrolyzed to mandelonitrile (MN).

Another very appealing reaction sequence is the cyanosilylation of BA to 2-phenyl-2 ((trimethylsilyl)oxy)acetonitrile (BAOTMSCN) followed by the hydrolysis of BATMSCN to mandelonitrile (MN) (Figure 69). Due to the investigation of the first reaction in the previous chapter, the reaction sequence was a natural target for further investigations.

Based on the previous experiments, it was evident that SA-NMOF 3 (UiO-66-NPs@PDMS) is a suitable catalyst for the cyanosilylation of BA, however, the catalyst for the follow-up hydrolysis needed to be determined. Therefore, we investigated different catalysts (CoBTC, MIL-101-NH_2, MIL-101, and MIL-101-NH_2) immobilized on PDMS for this reaction. Experimentally, 213 µL BAOTMSCN were dissolved in 4 mL of DMF, and 1cm^2 of MOF@PDMS was added and stirred at 500 rpm at 40 °C. Aliquots were taken at several intervals. MIL-101-SO_3H@PDMS was the best of the investigated catalysts and resulted in a conversion of BAOTMSCN yielding 58.8% BA (blank PDMS: 8.5%; blind: 3.2%) after 2.5 min.

Therefore, PDMS-PDMS-based reactors were fabricated with UiO-66-NPs@PDMS (SA-NMOF 3) or MIL-101-SO_3H@PDMS or a combination of both to catalyze either the cyanosilyation, the hydrolysis, or both consecutive reactions, respectively. Experimentally, a solution of 25 µL BA, 62 µL (2 equiv.) or 300 µL (10 equiv.) TMSCN and 1 mL DMF was applied to PDMS-PDMS-based microfluidic reactors. The solution was collected at the end of the reactor and analyzed via GC.

Analysis methods. The analysis turned out to be particularly difficult, as MN decomposes at 170°C to BA and HCN and is therefore indistinguishable via GC. Consequently, we tried to analyze the reaction mixture by HPLC. There we observed that MN decomposed on the HPLC column, therefore we refrained from using this method as well.

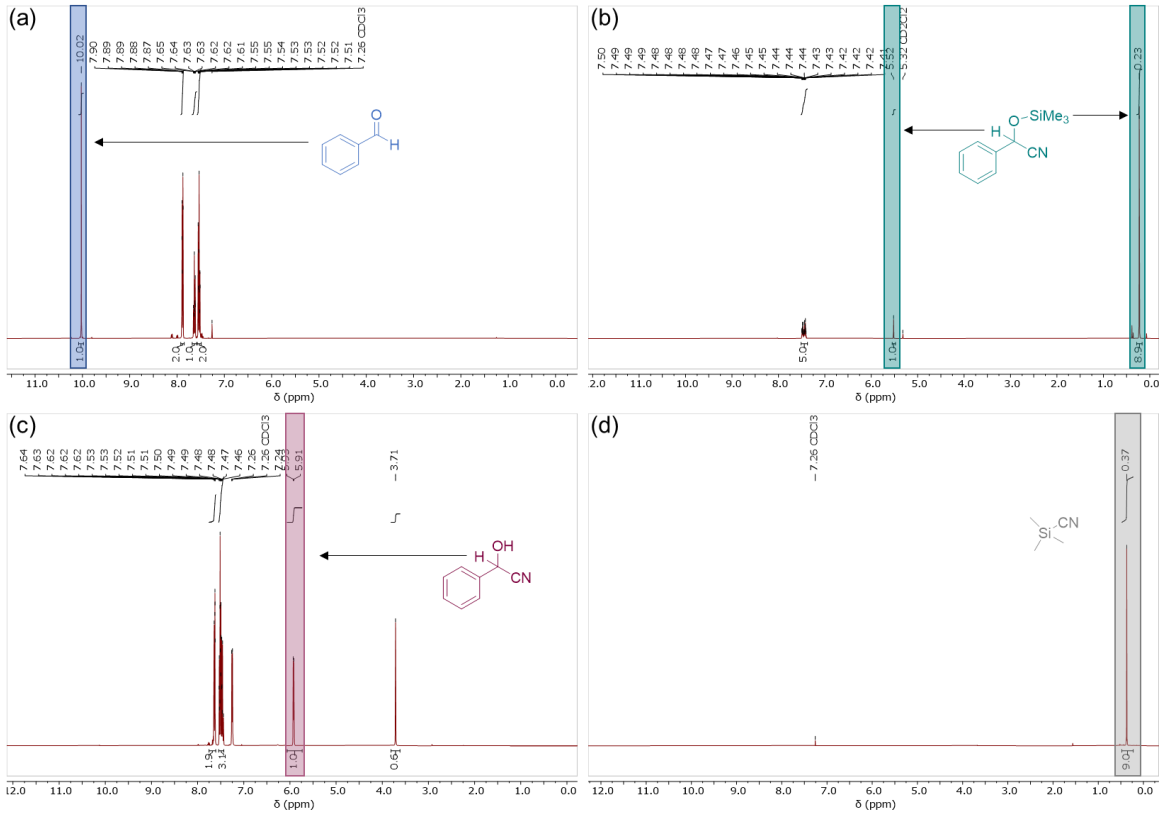

Figure 70: ^{1}H NMR spectra of BA (a), BAOTMSCN (b), MN (c), and TMSCN (d).

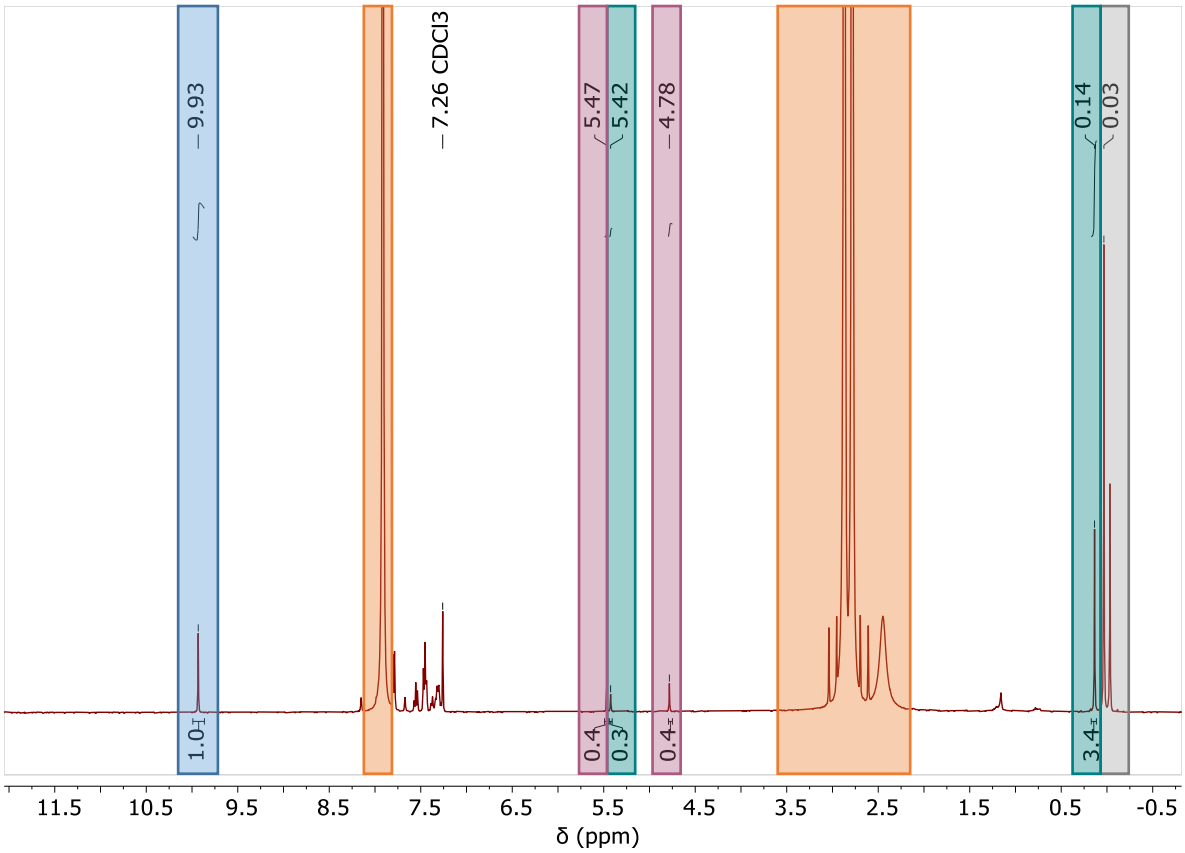

Figure 71: ^{1}H NMR spectra of the reaction mixture collected after the microfluidic device BA (blue), BAOTMSCN (turquoise), MN (red), DMF (orange) and TMSCN (grey).

Finally, we choose a combined method: determine the BAOTMSCN: (MN+BA) ratio by GC and then analyzing the BA/(MN+BAOTMSCN) ratio by ^{1}H NMR. The ^{1}H NMR spectra of BA (a), BAOTMSCN (b), MN (c), and TMSCN(d) are shown in Figure 70. The particularly interesting areas to distinguish the different components are highlighted. The analysis of the solution from the microfluidic device by ^{1}H NMR is shown below in Figure 71. We refrained from the full analysis by ^{1}H-NMR as $DCCl_3$ enhanced the decomposition of BAOTMCN at low concentrations due to the residual HCl/DCl content. Additionally, we tried to reduce the HCl content by filtration over basic Al_2O_3. In the end, we decided to use a two-analysis method strategy by ^{1}H NMR (with $DCCl_3$ as a solvent) and GC (with DMF as a solvent).

Table 18: Conversion of BA and yield of BAOTMSCN as well as MN after vectorial catalysis (cyanosilylation followed up by hydrolysis) performed in microfluidic reactors. The reactant concentrations were 125 µM BA and 1.25 mM (10 equiv.) TMSCN in DMF at room temperature.

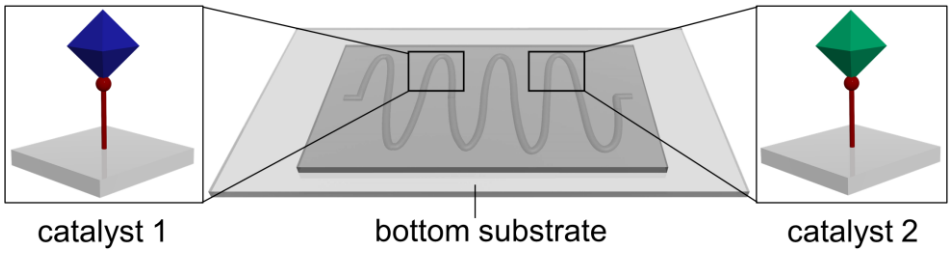

No	catalyst 1	catalyst 2	Equiv. TMSCN	bottom substrate	c%	y%	
					BA	BAOTMSCN	MN
1	-	-	2	-	94.3	5.7	0
2			10		82.6	17.4	0
3	UiO-66	UiO-66	2	PDMS	7.6	86.2	6.2
4	UiO-66	UiO-66	10	PDMS	0	96.0	4.0
5	MIL-101-SO_3H	MIL-101-SO_3H	2	PDMS	59.2	22.4	18.4
6	MIL-101-SO_3H	MIL-101-SO_3H	10	PDMS	7.2	74.6	18.2
7	UiO-66	MIL-101-SO_3H	2	PDMS	26.6	67.5	5.9
8	UiO-66	MIL-101-SO_3H	10	PDMS	3.8	92.2	4.4
9	MIL-101-SO_3H	MIL-101-SO_3H	*	PDMS	0	84.5	15.5
10	MIL-101-SO_3H	MIL-101-SO_3H	**10	PDMS	0	81.8	18.2
11	UiO-66	HCl(aq) in DMF	2$^{\#}$	PDMS	8	0	92
12	UiO-66	HCl(aq) in DMF	10$^{\#}$	PDMS	0	0	100

* 213 µL BAOTMSCN in 4 mL of DMF **53 µL BAOTMSCN; 300 µL TMSCN in 1 mL of DMF (c: conversion, y: yield)

Vectorial catalysis in microfluidic reactors. After evaluating different strategies to quantify the amount of BA, BAOTMSCN, and MN, we ran several experiments to assess the catalytic activity of the different surface anchored MOF on the reaction sequence (see Table 18).

After determining the blind conversions at room temperature and 1 min of stirring (entries 1-2), we investigated the conversions after the reaction in the microfluidic reactors. The mean retention time was 60 s for the solutions in a 9 μL microfluidic reactor with 14 coils (13 mm x 0,3 mm x 0.15 mm). The SA-NMOF 3 (UiO-66) (see Table 18, entries 3,4) based microfluidic reactor performed the cyanosilylation reaction sequence excellently, resulting in 86.2% BAOTMSCN for 2 equiv. TMSCN. However, the catalytic performance of SA-NMOF 3 in the follow-up hydrolysis (6.2% MN) is significantly lower. Full conversion of BA is observed for 10 equiv. TMSCN, resulting in 96% BAOTMSCN and 4.0% MN. This shows that surface anchored UiO-66 is an excellent catalyst for the cyanosilylation, as observed in the previous chapter. However, the catalytic performance for the hydrolysis is low.

In the next step, the performance of MIL-101-SO_3H in both reactions is investigated (see Table 18, entries 5,6,9,10). First, the same experiment as described above is performed. In these experiments, MIL-101-SO_3H shows a moderate catalytic performance for the cyanosilylation, which results in 59.2% of BA after the reaction. However, compared to UiO-66 it is still significantly lower, especially for lower TMSCN concentrations. The yields determined for MN are in the range of 15-19 %, independent of the amount of TMSCN and concentration of BAOTMSCN in the reaction mixture.

The ability of MIL-101-SO_3H@PDMS based microfluidic device to hydrolyze BATOMSCN was additionally tested by applying a BAOTMSCN solution and a BAOTMSCN solution with 10 additional equiv. of TMSCN to the reactor. The reaction solution was collected and analyzed by GC. The conversion rates were similarly high with a yield of 15.5 % and 18.8% of MN, respectively.

In summary, MIL-101-SO_3H is a moderate catalyst for both reactions, the cyanosilylation, and the hydrolysis. It outperforms UiO-66 in the hydrolysis of BAOTMSCN and is moderately active in the cyanosilylation.

Finally, mixed reactors with UiO-66 immobilized on one side and MIL-101-SO_3H immobilized on the other were tested (entries 7-8). After applying both solutions, we observe that the conversion of BA is higher for 10 equiv. TMSCN as compared to 2 equiv. The yields of BAOTMSCN are 67.5 % and 92.2% for 2 and 10 equiv. of TMSCN, respectively. The sequential arrangement of the catalysts, however, does not have the desired function, as the cyanosilylation is less pronounced as in the UiO-66 based

reactors and the hydrolysis less pronounced as in the MIL-101-SO_3H channels. However, the concept itself is still valid and could be further investigated by more experiments concerning the length of the reactor, etc.

Overall, UiO-66 is a great catalyst for the cyanosilylation of BA and shows a low activity in the hydrolysis of BAOTMSCN. MIL-101-SO_3H shows moderate catalytic activity for both reactions the cyanosilylation and the hydrolysis. The sequential positioning did not enhance both reactions, rather averaged the yields.

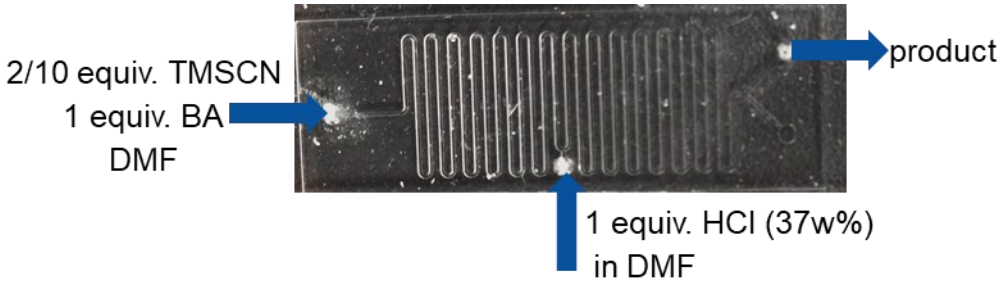

Figure 72: Microfluidic device design for the addition of HCl.

Full conversion of BA, yielding 100%- MN can be achieved if 1 equiv. of HCl (37w%) are dissolved in DMF and the solution is added after 14 coils of the microfluidic reactor (see Figure 72 and Table 18, entry 11/12).

Turnover frequencies. Finally, we calculated the TOF for the reaction sequence of cyanosilylation and hydrolysis. Similar assumptions as for the first reaction example were made, with one notable exception. For the mixed catalyst reactors, we assumed that both NMOFs act as catalysts in the cyanosilylation, but the hydrolysis is exclusively catalyzed by MIL-101-SO3H. The TOF values for all reactions are summed up in Table 19.

Table 19: Turnover frequencies calculated for the cyanosilylation of BA in DMF, followed up by the hydrolysis of BAOTMSCN in SA-NMOF-based microfluidic reactors.

No	catalyst 1	catalyst 2	Equiv. TMSCN	bottom substrate	TOF/h^{-1} Reaction 1	TOF/h^{-1} Reaction 2
1	UiO-66	UiO-66	2	PDMS	(1.00± 0.26) $\cdot 10^5$	(6.76 ± 1.77) $\cdot 10^3$
2	UiO-66	UiO-66	10	PDMS	(1.09 ± 0.29) $\cdot 10^5$	(4.36 ± 1.14) $\cdot 10^3$
3	MIL-101-SO_3H	MIL-101-SO_3H	2	PDMS	(3.39 ± 0.66) $\cdot 10^4$	(1.53 ± 2.97) $\cdot 10^4$
4	MIL-101-SO_3H	MIL-101-SO_3H	10	PDMS	(7.71 ± 1.50) $\cdot 10^4$	(1.51 ± 0.29) $\cdot 10^4$
5	UiO-66	MIL-101-SO_3H	2	PDMS	(6.92 ± 1.58) $\cdot 10^4$	(9.81 ± 0.95) $\cdot 10^3$
6	UiO-66	MIL-101-SO_3H	10	PDMS	(9.11 ± 1.77) $\cdot 10^4$	(7.31 ± 0.71) $\cdot 10^3$
7	MIL-101-SO_3H	MIL-101-SO_3H	*	PDMS	-	(1.29 ± 0.25) $\cdot 10^4$
8	MIL-101-SO_3H	MIL-101-SO_3H	**10	PDMS	-	(1.51 ± 0.29) $\cdot 10^4$

2.09* 213 µL BAOTMSCN in 4 mL of DMF **53 µL BAOTMSCN; 300 µL TMSCN in 1 mL of DMF

Similarly, to the reaction of previous reactions, the SA-NMOFs again show exceptionally high turnover frequencies in the range of 100,000 h^{-1} for the cyanosilylation and 10,000 h^{-1} for the hydrolysis. Besides the absolute yields, these TOF frequencies are exceptionally high for MOF-based catalysts. As the reaction sequence has not been reported for other MOF-based systems, we cannot provide a comparison with other MOF-based systems. However, for the cyanosilylation, further comparison with literature can be found in chapter 3.4.4 or Table S10.

3.5.6. Reaction Sequence III: Oxidation/Cyanosilylation

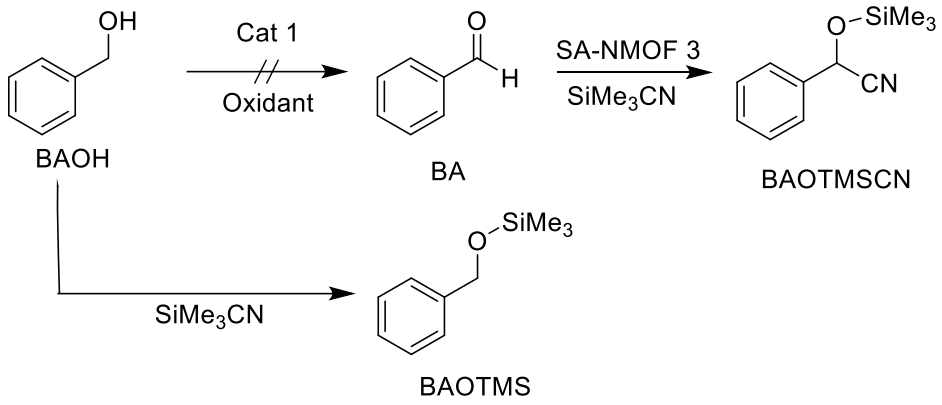

Figure 73: Third investigated reaction sequence: subsequential oxidation of benzyl alcohol (BAOH) to benzaldehyde, and then cyanosilylation to 2-phenyl-2 ((trimethylsilyl)oxy) acetonitrile (BAOTMSCN).

After we investigated the cyanosilylation-hydrolysis reaction sequence (see above), we tried to advance this knowledge towards another reaction sequence which consists of oxidation of benzyl alcohol (BAOH) to BA followed up by a cyanosilylation to BAOTMSCN (Figure 73). Conceptually, this reaction sequence is interesting due to the different reaction types (redox reaction followed up by a Lewis acid-catalyzed reaction), which would make the vectorial catalysis even more appealing. We studied several oxidants such as tert-butyl hydroperoxide (tBuOOH), hydrogen peroxide, 2,2,6,6-tetramethylpiperidinyloxyl (TEMPO); catalysts like CoBTC, MIL-101, and Au-NP@MIL-101;[223,314,339,340] and additives *e.g.* K_2CO_3, Na_2CO_3, and 1-Methylimidazol at different reaction temperatures (40°C/95°C). The best conditions for this reaction in a batch reactor were achieved with 2 equiv. tBuOOH as an oxidant, Au-NP@MIL-101 as a catalyst, Na_2CO_3 as an additive in DMF as a solvent at 95°C. After 24 h a yield of 55.4% BA was achieved as compared to 10.9% BA for the blind reaction, however, the desired oxidation illustrates comparatively slow reaction kinetics, which makes the translation into microfluidic devices very challenging. When the catalyst (AU-NP@MIL-101) was removed after full conversion of BAOH and 2-10 equiv. TMSCN and SA-NMOF 3 or UiO-66-HCl were added the cyanosilylation did not take place. Instead, TMSCN reacts with tBuOH (a by-product formed during the oxidation), residual tBuOOH, or water.

If the reaction is translated to the microfluidic devices, we do not observe any BA formation. Instead, we observe the silylated by-product benzyloxy(trimetylsilane) (BAOTMS). Due to these challenges, we did not pursue this reaction sequence further.

3.5.7. Summary

In resumé, this chapter provides insights into the catalysis of SA-NMOFs under flow conditions, by manufacturing SA-NMOF-based microfluidic devices. We investigated three different reaction sequences, namely the hydrolysis of benzaldehyde dimethyl acetal to benzaldehyde, followed by the Knoevenagel condensation to 2-benzylidene malononitrile; the cyanosilylation of benzaldehyde, followed by the hydrolysis to mandelonitrile, and finally the oxidization of benzyl alcohol towards benzaldehyde, followed by the cyanosilylation.

The observations differ significantly between these three reaction sequences, while the first reaction sequence (hydrolysis/Knoevenagel condensation) is vectorial catalysis with two different catalysts, where each catalyst mainly catalyzes one of the reactions. For the second reaction sequence (cyanosilylation/hydrolysis) UiO-66 selectively catalyzes the cyanosilylation, and the second catalyst MIL-101-SO3H shows a moderate catalytic activity for both reactions. Finally, the third reaction sequence (oxidation/cyanosilylation), was not successful due to side reactions, the high reaction temperature needed for the reaction sequence, and the remaining oxidation agents.

This chapter shows, that with careful process optimization, vectorial catalysis in a microfluidic device with MOFs immobilized onto PDMS substrates can be achieved. The substantial TOF enhancement described in the previous chapter supported the fabrication of SA-NMOF-based microfluidic devices significantly and enabled the fabrication of extremely efficient microfluidic reactors. Finally, we would like to emphasize that this successful proof-of-principle, vectorial catalysis is an SA-NMOF-based microfluidic reactor, is a major step towards a more efficient multi-step reaction sequence catalyzed by MOFs.

3.6. Conclusion & Outlook

Conclusion. The second part of my thesis deals with the translation of vectorial catalysis from biological systems towards metal-organic catalysts targeting increased scalability, enhanced robustness, and tailored adaptivity. As a first step, the selective positioning (compartmentation) of the NMOFs was explored (chapter 3.3). Subsequentially, the design and influence of the catalyst on the catalytic properties are explored (chapter 3.4). Finally, we investigate the integration of different NMOFs into microfluidic devices realizing artificial vectorial catalysis (chapter 3.5, Figure 74).

As a first step, the possibilities to synthesize, stabilize, and characterize nanometer-sized MOFs were explored. Therefore, we employed the well-established UiO-66(Zr) and MIL-101(Cr) as model systems. We synthesized these NMOFs in a reproducible fashion and modified their exterior surface through amide bond formation with dangling carboxylic acid groups from the terephthalic acid linkers. This allowed for functional group introduction, e.g. an azide group, or an amine group which tied into the follow-up aim to anchor these NMOFs to material surfaces e.g. by amide bond formation or the Copper-catalyzed alkyne azide cycloaddition (CuAAC). In the first study, we showed by SEM and EDX that we can anchor these functionalized NMOFs selectively to carboxylic acid and alkyne terminated patterned silicon substrates.

In a second step, we employed these SA-NMOFs (on silicon and PDMS) as Lewis acid catalysts for the cyanosilylation of benzaldehyde (CS-BA) and the insertion of CO_2 into propylene oxide. We could show that the covalent immobilization of nanometer-sized UiO-66 (Zr) particles substantially increases the turn over frequency of the reaction ($1.96 \cdot 10^7\ h^{-1}$, *CS-BA*) as compared to colloidal NMOF solutions ($9.79\ h^{-1}$, *CS-BA*), pristine UiO-66 ($6.45\ h^{-1}$, *CS-BA*) or defect engineered samples ($7.29\ h^{-1}$, *CS-BA*). We attribute this boost in catalytic activity to the prevention of particle aggregation, which we observed for the colloidal nanoparticle solutions during catalysis. Another benefit of the SA-NMOFs is the retained high catalytic activity in different solvents like DCM, DMF, and toluene, especially when compared to the well-established defect engineered UiO-66.

In a final step, we integrated the SA-NMOFs into microfluidic devices to utilize their catalytic properties for vectorial catalysis. Therefore, we selectively immobilized different NMOFs onto a glass or PDMS substrate and sealed the microfluidic device with a PDMS mold. Within the microfluidic device, we could show the vectorial catalysis of independent reaction cascades in a programmed fashion, namely the deacetalization and consecutive Knoevenagel condensation of benzaldehyde dimethyl acetal and the cyanosilylation of benzaldehyde followed up by the hydrolysis to the cyanohydrin. Hence, realizing the goal of proof-of-principle for artificial vectorial catalysis with NMOFs as catalysts.

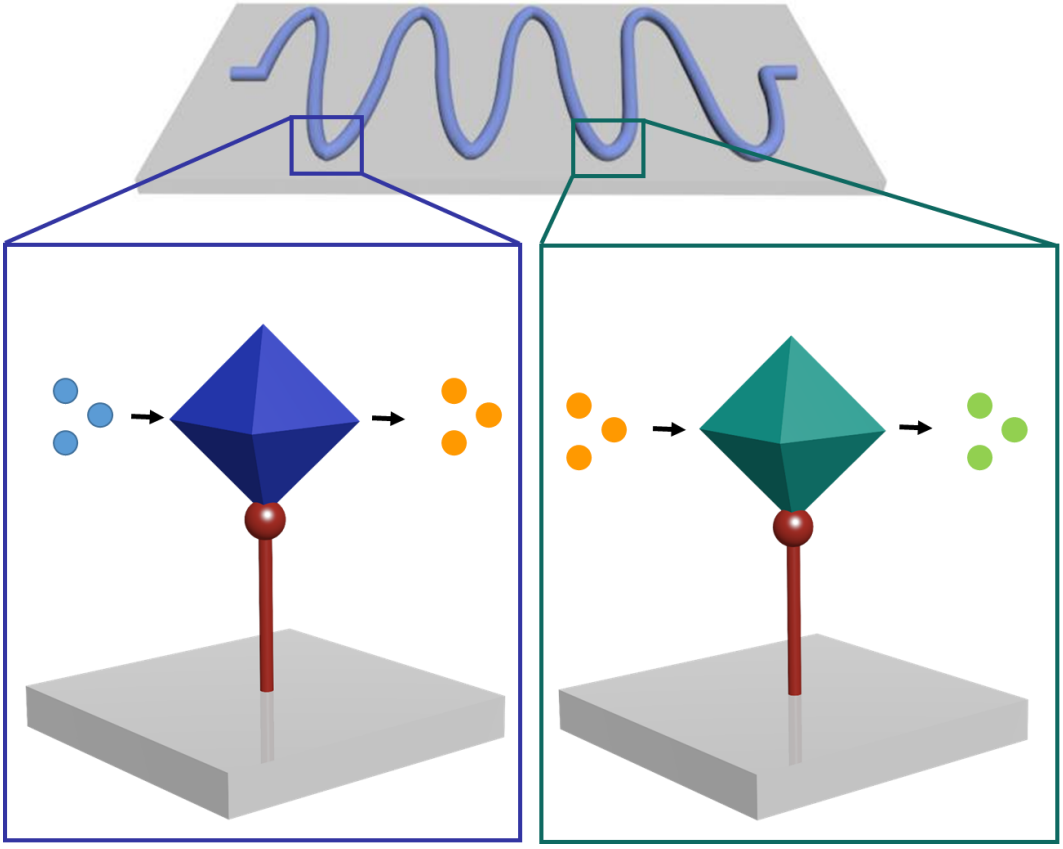

Figure 74: Schematic representation of vectorial catalysis in a microfluidic device. The different surface anchored NMOFs (blue and red cubes) catalyze the two-step reaction from A (blue spheres) to C (green spheres) via the intermediate B (orange spheres).

Lessons learned. Realizing artificial vectorial catalysis with NMOFs as catalysts in microfluidic channels was the most challenging topic of my thesis. Several parameters could be further optimized to improve the obtained results, however, due to the time restrictions could not be investigated any further. The flow chart (see Figure 75) schematically illustrates the experimentalist's approach realizing artificial vectorial catalysis. In order to improve the obtained results, the most crucial changes would be the chosen microfluidic device and the catalyst's design.

Altering the **microfluidic device design** from PDMS-based microfluidic devices towards cyclic olefin copolymers(COC)-based reactors or polymethylmethacrylate (PMMA)-based microfluidic devices offers increased control over the flow regulation allowing for more reproducible results. Additionally, the stability towards organic solvents and increased temperature can be used to access more reaction sequences. Further optimization could be targeted by improving the applied NMOF catalysts. The work shown in this thesis was meant as a proof-of-principle. However, if instead of model catalysts like UiO-66 or MIL-101 (Cr)/-NH_2/-SO_3H **targeted catalyst design** would be used the reaction sequence scope and overall artificial vectorial catalysis could be improved. This could be addressed by in-depth literature research for the

already explored MOF catalysts, after deciding on a targeted reaction sequence. The reaction conditions for a selection of already highly active MOF catalysts would be optimized to reduce the particle size. Finally, anchoring these NMOFs to selected positions in the microfluidic devices via the anchoring methods which were already explored.

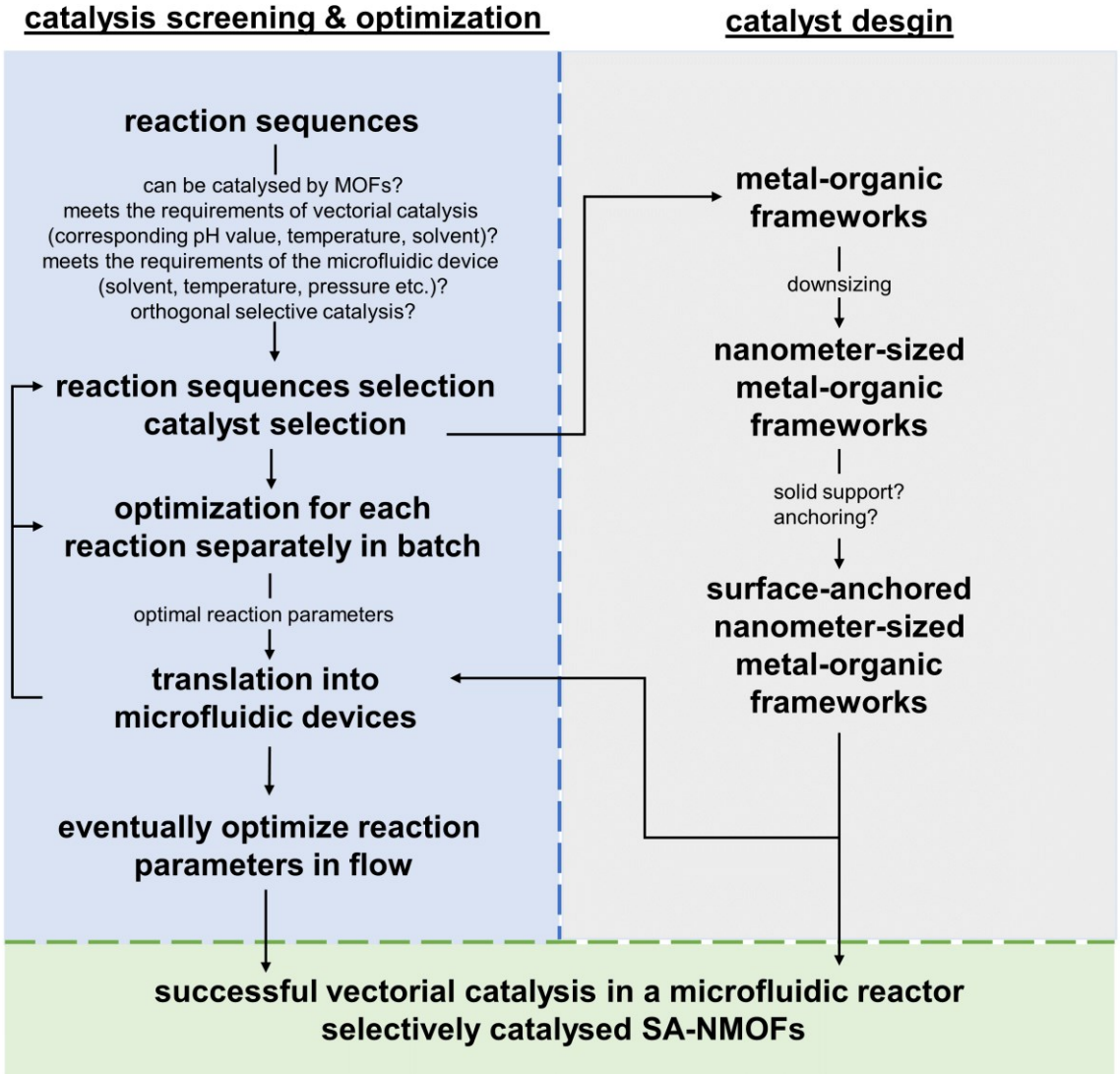

Figure 75: Flow chart of the process optimization towards the realization of vectorial catalysis in microfluidic reactors selectively catalysed by SA-NMOFs. The optimization is slitted into catalysis screening/optimization and catalyst design.

Outlook. Interesting ideas, that would not improve the obtained results but rather provide more insight on the reaction mechanism include the in-situ reaction monitoring by in-situ Raman spectroscopy as recently reported by Weckhuysen *et al.*[341] instead of GC reaction monitoring.

Highly challenging and rewarding would be the manufacturing of self-regulating autofluidic devices which was initially proposed. Therefore, in a combined effort

relevant multi-step reaction and NMOF catalysts would be matched with suitable stimuli responsible hydrogels targeted by customized stimuli. All these points would finally enable the fabrication of an autofluidic device for the self-regulating vectorial catalysis of high-value chemicals.

4. FERROELECTRIC METAL-FREE PEROVSKITE [HMDABCO](NH$_4$)I$_3$ THIN FILMS

4.1. Ferroelectricity

Ferroelectricity is the characteristic property of certain nonconducting materials, or dielectrics, that exhibit spontaneous electric polarization which can be reversed in direction by the application of an external electric field. The major criterion for these materials is, that the crystalline symmetry allows a polar axis.[342] By shifting differently charged ions in the crystal lattice, spontaneous polarization can occur. Such ferroelectric crystals consist of many domains which are regions with the same direction of polarization. From domain to domain, the direction of polarization changes within a few atomic layers.

In contrast to regular dielectrics, the induced polarization P is not a linear function of the applied electric field E (see Figure 76).[343] Additionally, ferromagnetic materials always demonstrate a spontaneous polarization, even without any electric field. However, if a suitably strong electric field is applied, the spontaneous polarization can be reversed. If the polarization is now plotted against the applied electric field, a hysteresis loop is observed. Ferroelectric materials can be characterized by three parameters: the coercive field (E_F), the spontaneous polarization (P_s), and the remanent polarization (P_r). The remanent polarization is the polarization that can be measured when no external electrical field is applied. The coercive field is the electrical field that is needed to reverse the remanent polarization and the spontaneous polarization is the maximum polarization of the material.

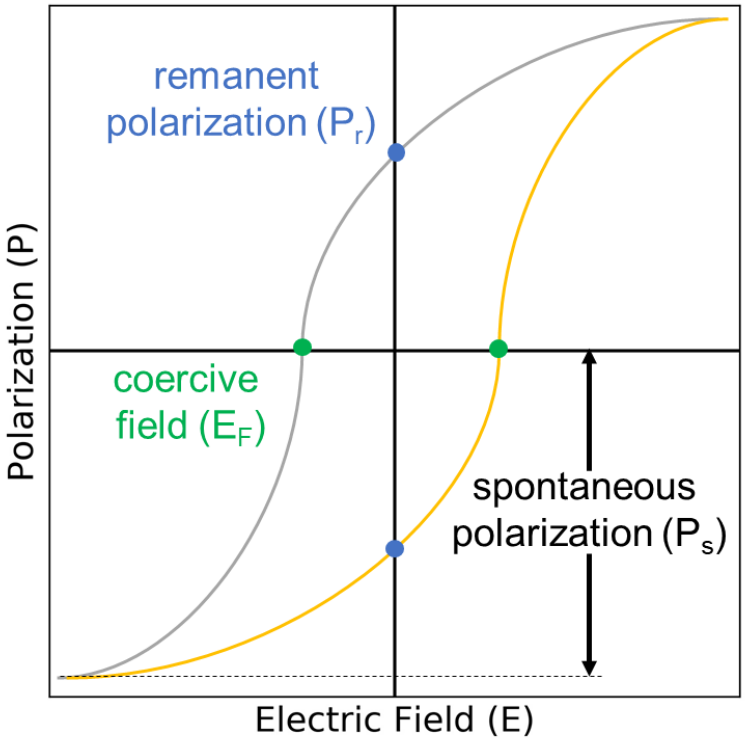

Figure 76: Polarization measurement of an ideal ferroelectric capacitor whereas P_r is the remanent polarization, P_s is the spontaneous polarization, and E_F is the coercive field.

Above a certain temperature, the Curie temperature, these materials lose their ferroelectric properties.[342] They display no spontaneous polarization and no permanent electric dipole. Macroscopically, this temperature-dependent behaviour can be regarded as a phase transition.[342]

For applications in capacitors, the nonlinearity of the polarization of ferroelectrics is utilized.[344] Due to the remanent/spontaneous polarization ferroelectric devices can be used as a memory element. Nowadays, a variety of companies are making FRAM (ferroelectric random-access-memory) devices that are used in computers. The main advantages of ferroelectric non-volatile information storage are the high electric permittivity and the switching of the polarization at a moderate voltage which allow for the increase of areal storage density.

4.2. Inorganic-Organic Perovskites

Inorganic-organic perovskites often referred to as hybrid inorganic-organic perovskites (HIOPs) are a class of compounds, which are named after the structure type of their all-inorganic perovskite counterparts. HIOPs crystallize in the 3D perovskite-motif where the B-site cation and X-site anion form a ReO_3-type network and the A-site cation is located in the void of this network forming a dense, cubic structure (see Figure 77). Like MOFs, HIOPs are hybrid materials, where either A, B or X ion is an organic, molecular building unit. Additionally, both are dominated by coordinative interactions. However, due to their dense structure, HIOPs are non-porous, which sets them apart from MOFs.

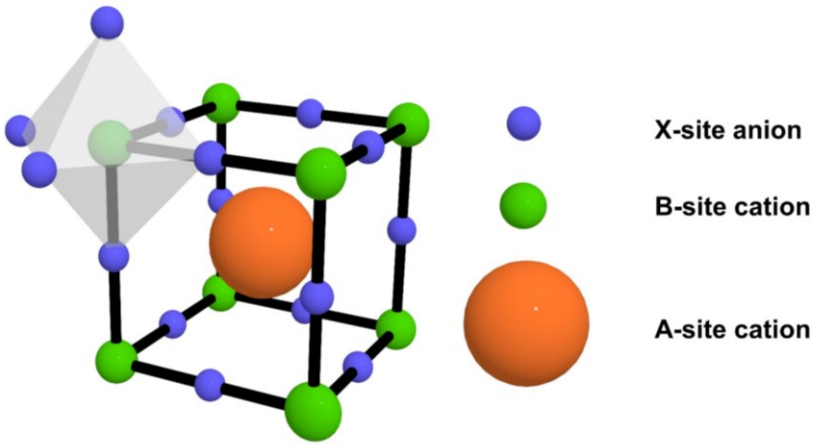

Figure 77: Schematic representation of the cubic perovskite structure motif with the general formula ABX_3.

The rational design of perovskites was introduced by Victor Goldschmidt, who synthesized and analyzed many inorganic perovskites. From his experiments he concluded, that the A-site cation can vary in size depending on the radii of the B-site

cation and X-site anion, while still maintaining the perovskite structure.[345] This concept of the 'tolerance factor' was later adjusted for HIOPs by Kieslich *et al.*.[346]

The schematic representation of the perovskite structure in Figure 77 suggests that perovskites all exhibit a simple cubic O_h symmetry. This is often not the case, as the ions must be of rather defined relative sizes to one another to crystallize in the cubic phase. Due to small deviations in size, most perovskites crystallize in symmetry reduced orthorhombic or tetragonal phases. Owing to the narrow energy landscape, many HIOPs exhibit phase transitions, which can be triggered by changes in temperature or pressure. For all-inorganic perovskites, their transitions are primarily driven by the displacement of the A- and/or B-site cation and the tilting of the BX_6 octahedral units. The existence of molecular ions on the A-, B- and/or X-sites makes the situation more complicated. In this context, the nature of the interactions in perovskites is of particular interest. While all-inorganic perovskites are dominated by ionic interactions, the interactions in HIOPs can be characterized as a combination of ionic interactions, coordinative bonds, hydrogen bonding, and van-der-Waals interactions. Especially, the latter two can have a major effect on phase transitions in HIOPs as compared to all-inorganic perovskites.[347]

Such further structural degrees of freedom caused by additional and diverse interactions were a major motivation to investigate HIOPs in the first place. Additionally, the processing of all-inorganic perovskites often requires harsh conditions and are often environmentally problematic. Due to their interesting properties and widespread use, a greener, easier-to-process alternative would be beneficial. The research investigating HIOPs to date lead to the discovery of many interesting HIOPs such as $[CH_3NH_3]PbI_3$ and $[(CH_3)_2NH_2]Mn(HCOO)_3$. While $[CH_3NH_3]PbI_3$ has fascinating photophysical properties,[348] facilitating use in photovoltaics, $[(CH_3)_2NH_2]Mn(HCOO)_3$ shows multiferroic properties.[349]

4.3. Metal-free Organic Perovskites

The perovskite of particular relevance to this work is [HMADBCO](NH4)I3 ([HMDABCO], 1-methyl-1,4-diazabicyclo[2.2.2]octane-1,4-diium), which was discovered by Ye *et al.* in 2018.[350,351]

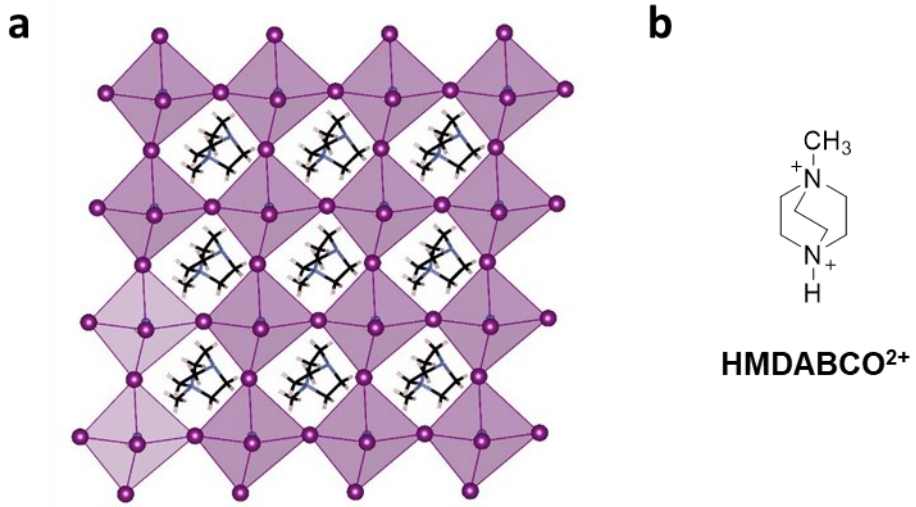

Figure 78: (**a**) Crystal structure of [HMDABCO](NH4)I3 in its ferroelectric phase at 293 K shown along the c axis. This structure is based on the CCDC entry 1836325 and was created with VESTA.[352] The (NH4)I6 octahedra are visualized in purple polyhedrons. HMDABCO2+ cations (see **b** for Lewis structure) are located in the voids between the octahedra.

This metal-free perovskite exhibits a 3D network of corner-shared (NH4)I6 octahedra, locating the A-site cation HMDABCO2+ in the enclosed cavity. As the coordination bonds of perovskites are not present in this compound, the stability of the structure is provided by ionic, van-der-Waals, and hydrogen bonding interactions. Especially the latter, play a significant role in the chemistry and phase transitions of [HMADBCO](NH4)I3. The choice of the A-site cation, HMDABCO2+, which has C3v symmetry, causes the perovskite to exhibit the non-centrosymmetric space group R3 along with a unique crystallographic axis. This induces the ferroelectric properties due to the rotational freedom and the dipolar moment of the HMDABCO ions. As mentioned before, many HIOPs feature phase transitions caused by temperature or pressure changes. Above its Curie temperature of 448 K [HMADBCO](NH4)I3 crystallizes in a cubic structure, whereas the ferroelectric phase exhibits a trigonal crystal system (see Figure 78).[350]

Upon comparing ferroelectric potentials, [HMDABCO](NH4)I3 can compete with established and applied ferroelectric perovskites $BaTiO_3$[353] or $Pb(Zr_{1-x}Ti_x)O_3$.[354] It shows a similarly large spontaneous polarization of 22 μC cm^{-2} and can be easily synthesized at room temperature in water.[350] Challenging for applications remains the long-term stability towards moisture and mechanical stress.[347] Besides its ferroelectric properties, [HMDABCO](NH4)I3 also has interesting non-linear optical properties[355] and high

electrocaloric strength.[356] To take advantage of the ferroelectric properties, this work deals with the implementation of [HMADBCO](NH4)I3 as thin films into capacitors.

4.4. Perovskites as Thin Films

Due to different interatomic and intermolecular interactions, many HIOP and metal-free perovskites can be crystallized directly from highly concentrated precursor solutions instead of requiring solvothermal synthesis conditions.[357] Therefore, in contrast to MOFs, solution deposition techniques like spin, dip, or spray coating do not require pre-synthesized particles but rather concentrated precursor solutions, which are deposited onto the substrate yielding a crystalline film after evaporation of the solvent.

Especially known for its application in the perovskite thin-film fabrication is spin coating. Significant progress to improve the thin film quality of perovskites e.g. methylammonium lead iodide ($MAPbI_3$) was made in the last years[358] including the anti-solvent approach[359] and different post-synthetic treatments.[360,361]

In the course of this work, only solution-based methods were used, namely spray coating, drop-casting, and dip coating.

4.5. Motivation & Objective

The third and final part of my thesis is inspired by the goal to fabricate thin-film coatings of different coordination networks to allow for their integration into ferroelectric capacitors, while their properties are retained. As mentioned in the introduction [HMDABCO](NH4)I3 is an interesting material combining ferroelectric properties, with non-linear optical activity,[355] and is a material with high prospective electrocaloric strength.[356] Especially, the ferroelectric properties with a substantial spontaneous polarization of 22 $\mu C\ cm^{-2}$, the high Curie temperature (446 K), and the multiple polarization directions make it an interesting material for thin-film ferroelectric devices.[350,351] Due to its easy room-temperature synthesis, an easy drop-cast or spin coating preparation of these films was expected/predicted[351,362] but to the best of our knowledge that has not been reported to this date.

Due to the urgent need for [HMDABCO](NH4)I3 thin films for their application in ferroelectric devices, we investigated the thin film formation of this compound by different chemicals solution deposition methods such as spin coating, spray coating, dip coating, and vapor assisted conversion. Finally, we succeeded in the fabrication of dense thin films of phase pure [HMDABCO](NH4)I3. This is a significant step towards the application of these films in ferroelectric devices.

4.6. Organic Ferroelectrics: [HMDABCO](NH4)I3 –A Thin Film Case Study

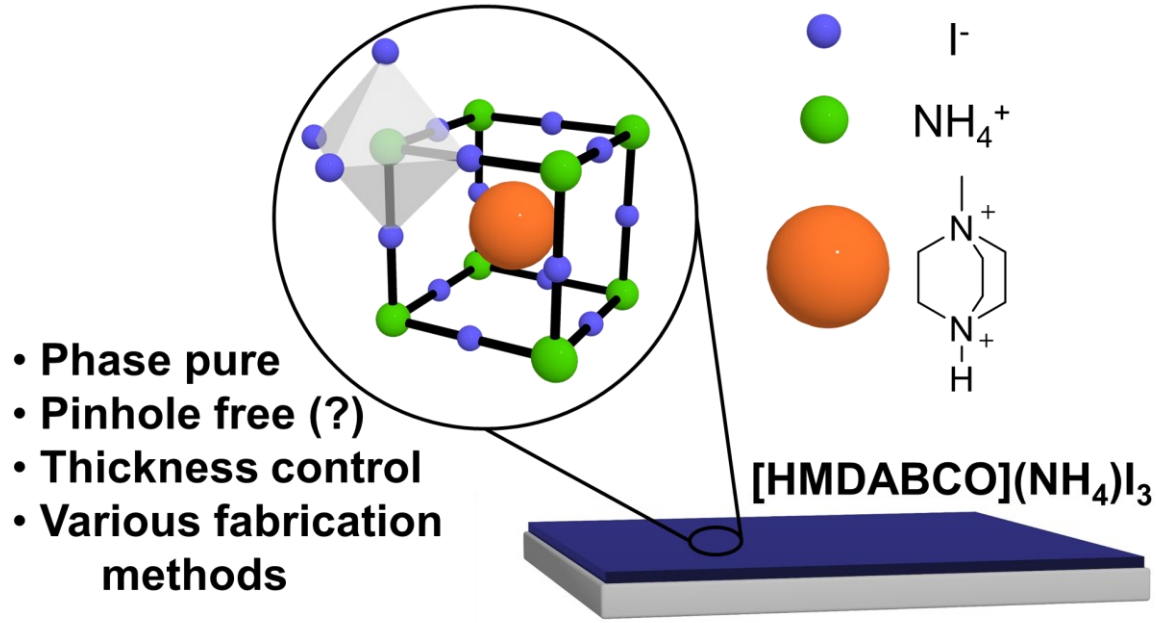

The project was conceived by G. Kieslich and designed by A. L. Semrau and the progress was regularly discussed with G. Kieslich. The experiments in this project were performed by A. L. Semrau, S. Mackewicz, and S. V. Dummert, who investigated the organic perovskite thin films as part of their bachelor thesis and research internship as well as a master thesis, respectively. However, the results achieved by S. Mackewicz (dealing with the VAC method) and S. V. Dummert (dealing with the spin coating) are not discussed in this thesis. The thin-film fabrication and characterization experiments displayed in this chapter were performed and analyzed by A.L. Semrau, and the investigation of the ferroelectric properties was carried out by Christian Eckel, M.Sc. student of Prof. Dr. Thomas Weitz, Ludwig Maximilian University Munich.

4.6.1. Challenges in the Thin Film Fabrication of [HMDABCO](NH4)I3

Phase purity. The first challenge in this project was the fabrication of phase pure [HMDABCO](NH4)I3 thin films and powders. The synthesis and purification of MDABCOI prior to the synthesis of [HMDABCO](NH4)I3 was not described in the original publication of Ye *et al.*[363]. After some experiments, we found out that the MDABCOI purification and synthesis conditions are crucial for the synthesis of phase pure [HMDABCO](NH4)I3, especially for thin-film fabrication. Different protocols for the synthesis of MDABCOI can be found in the literature. Usually, 1,4-diazabicyclo[2.2.2]octane (DABCO) is methylated with methyl iodide (MeI) in different solvents ranging from ethanol[364] to ethyl acetate[365]. The reported purifications range from no purification at all to the addition of a base (K2CO3) followed by filtration and solvent removal under reduced pressure. First, we synthesized MDABCOI in ethyl acetate without further purification, which yielded a white powder. After the characterization by ^{1}H NMR, ^{13}C NMR, and EA a minor impurity at 4.07 ppm in the ^{1}H NMR was detected (see Figure 79 b). This impurity can be removed by the corresponding base treatment, which could ascribe the impurity to the partial protonation of MDABCOI. Both MDABCOI sources were used for the synthesis of [HMDABCO](NH4)I3 powders. This was achieved by a procedure described by Ye *et al.*[363]: MDABCOI and NH4I were dissolved in water and reduced HI was added to the solution, resulting in sudden precipitation of a white powder. Despite the minor impurity, the synthesis of the [HMDACO](NH4)I3 powder with the untreated MDABCOI (Figure 79 b, green) lead to the formation of phase pure [HMDACO](NH4)I3 (see Figure 79 c), whereas the utilization of base treated MDABCOI yielded a white powder with various phases.

In the next step, we investigated the impact of different MDABCOI sources on the [HMDABCO](NH4)I3 thin film formation. Inspired by the fabrication techniques for other HIOP thin films, we investigated different techniques and solvents. As a starting point, we employed spray coating as a simple and straightforward method to fabricate thin films. Due to the low boiling point, low viscosity, and protic nature, which are detrimental to the fabrication, we changed the solvent from water to dimethyl formamide (DMF). For the thin film fabrication, a DMF-based solution of 3 M MDABCOI (untreated or base purified) and 3 M NH4I solution was spray coated onto activated silicon substrates and dried on preheated microscope glass slides at 120°C in an oven. Afterwards, the phase purity of these films was investigated by grazing incidence X-ray diffraction (GIXRD) (see Figure 79 a). In contrast to the powder, both films show distinct side phase impurities. Single Crystal XRD measurements revealed that some side phases could be attributed to [HMDACBO]I2. This could be caused by the missing second molar HI equivalent, which was added in the water-based powder

synthesis to induce crystallization. Therefore, an additional HI source is needed to protonate the $MDABCO^+$ to form $HMDABCO^{2+}$. However, if HI is added directly to the DMF solution it induces crystallization and the solution cannot be spray coated. Therefore, we synthesized $HMDABCOI_2$ (MDABCOI•HI) to add additional HI to the solution. Similar to the other precursor, it was dissolved in DMF, and NH_4I was added. After sonication, the precipitate was filtered off and the supernatant was used for the spray coating experiments. However, this resulted in two obstacles: (i) the solubility of MDABCOI•HI in DMF is significantly lower than MDABCOI and (ii) the resulting thin films are not phase pure. Therefore, the investigation into other, indirect sources of HI was necessary.

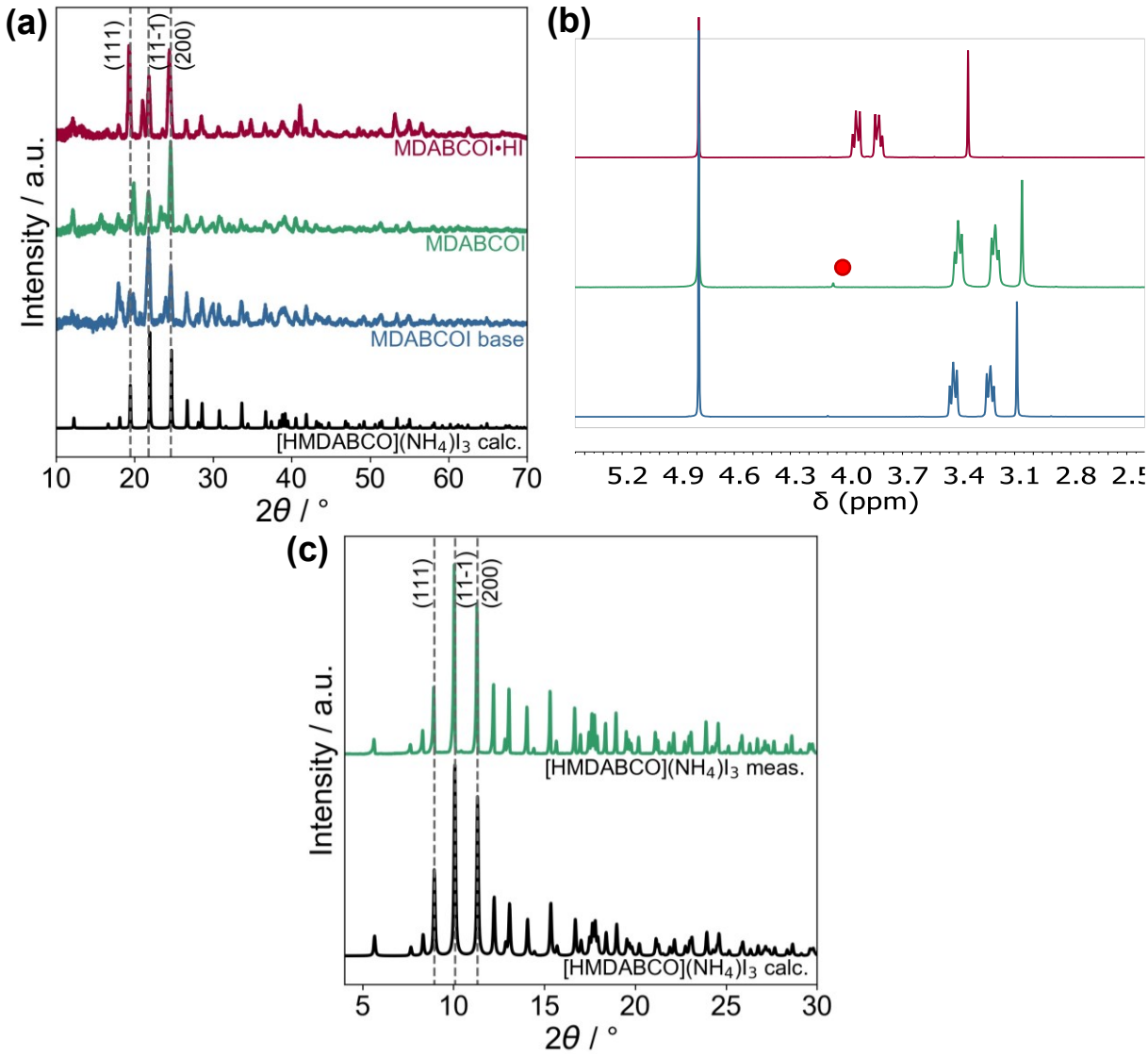

Figure 79: (a) GIXRD patterns of $[HMDABCO](NH_4)I_3$ thin films fabricated on Si/SiO_2 substrates with different MDABCOI precursors: base-treated MDABCOI (blue), MDABCOI (green), and MDABCOI•HI (red). (b) Corresponding ^1H NMR spectra of based treated MDABCOI (blue), MDABCOI (green), and MDABCOI•HI (red) dissolved in D_2O. (c) PXRD patterns of $[HMDABCO](NH_4)I_3$ powder synthesized with MDABCOI (green), HI, and NH_4I in water. The PXRD measurements were conducted with a Mo source.

NH_4I as an indirect HI source. NH_4I is an integral part of the perovskite structure and can be easily removed after the proton transfer from NH_4^+ to $MDABCO^+$ due to the volatility of NH_3. Therefore, we added 1,1.5, and 2 equiv. of NH_4I to the stock solutions, as the excessive molar equivalents could be utilized as an artificial HI source.

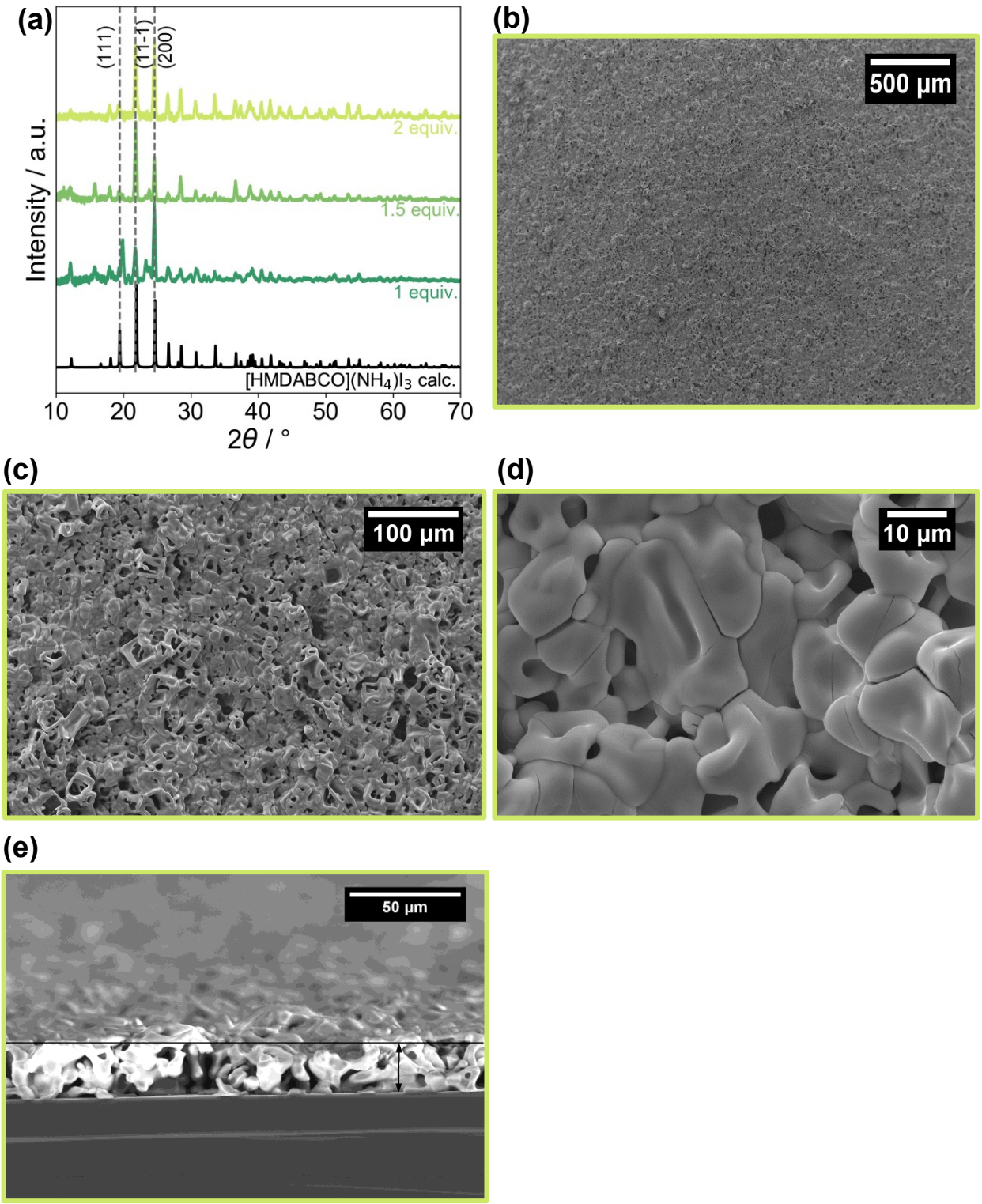

Figure 80: (a) GIXRD diffractograms of $[HMDABCO](NH_4)I_3$ produced with 1-2 equiv. of NH_4I as an indirect HI source. (b-d) SEM image of the phase pure $[HMDABCO](NH_4)I_3$ fabricated with 2 equiv. of NH_4I with different magnifications (40-1500-fold), 15kV.(e) 90° cross-section image of the $[HMDABCO](NH_4)I_3$ fabricated with 2 equiv. of NH_4I. The measured thickness was determined at 23 µm.

The films were investigated by GIXRD and we observed that the phase impurities vanished with an increasing amount of NH_4I. After the addition of 2 equiv. of NH_4I

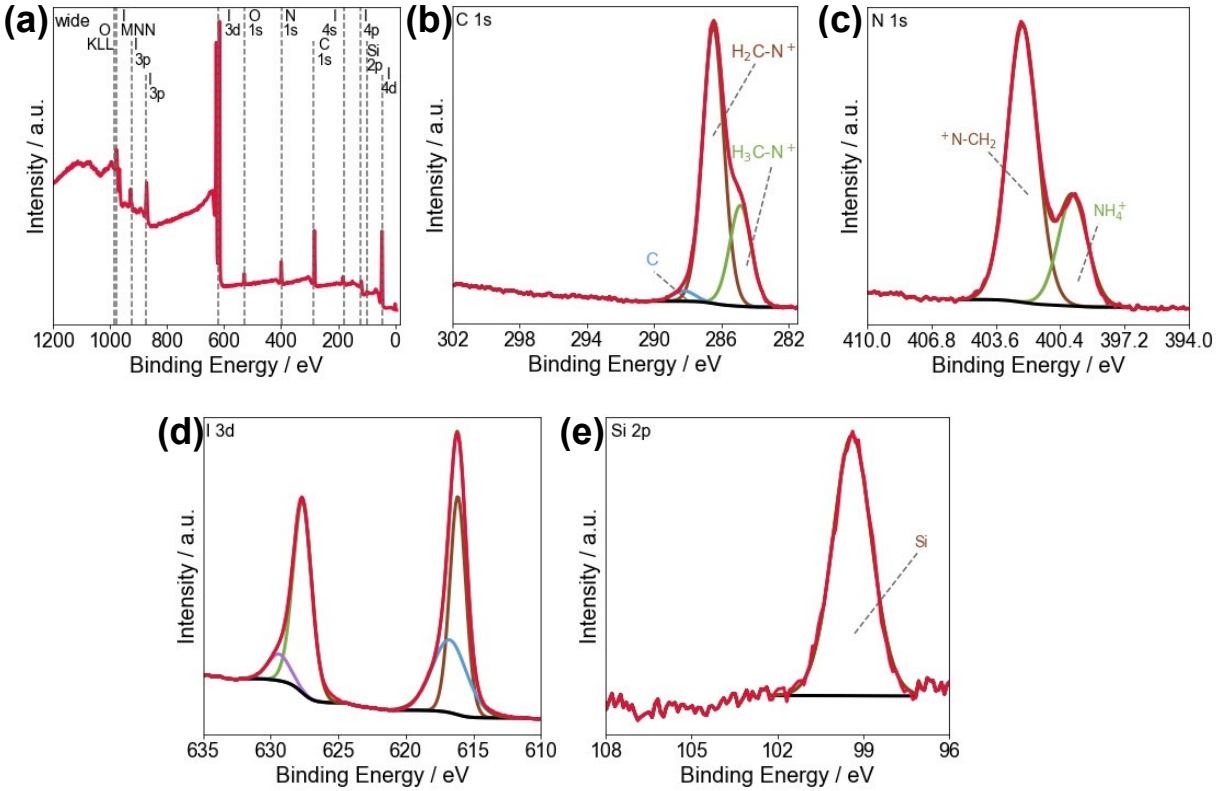

Figure 81: XPS survey scan (a) of [HMDABCO](NH4)I3@Si deposited by spray coating dried at 120 °C as well as C1s (b), N1s (c), I 3d (d), and Si 2p (e) XPS narrow scans.

phase pure [HMDABCO](NH4)I3 thin films were formed. This film was then investigated by scanning electron microscopy (SEM) in order to investigate the homogeneity, roughness, and thickness of the films. The images reveal a dense coating of the surface, with particles ~25x15 µm. 90° cross-section SEM images show, that the thin film thickness is ~23 µm. However, if the substrates are contemplated in detail, coatings are dense, but a major drawback is the large thickness and relative high roughness of the thin films.

X-ray photoelectron spectroscopy (XPS) was performed to ensure that the film has the correct chemical composition and to investigate the oxidation state of the elements. The XPS wide scan shows the expected elements such as C, I, N, and Si. The determined composition of C 67.3 At%, N 15.6 At%, and I 16.9 At% is a reasonable agreement with the theoretical values of C 53.8 At%, N 23.1 At%, and I 23.1 At% if we account for carbon surface contaminations. Consequently, we compare the theoretical I/N ratio of 1/1 to the experimentally determined one of 1.08/1, which is in good agreement. Additionally, small amounts of oxygen were measured, which we assign to residues of water. The small amount of additional carbon that we measured can be assigned to surface contamination with carbon (see Figure 81b, blue). The de-convoluted signals of the C 1s narrow scan can be assigned to the ethyl (brown) and methyl groups (green), respectively. The N 1s narrow scan can be de-convoluted in

alkylammonium (brown) and ammonium N atoms (green). The narrow scan for 3d I displays the typical 5/2 3/2 3d splitting, which can be expected for Iodine compounds. However, the deconvolution of the XPS spectra shows two species. Probably, this could be assigned to I^- at ~619 eV and I(0) at ~620 eV. Due to the volatility of elemental iodine in the XPS chamber, XPS is not the right technique to quantify the ratio of I^-/I(0). An observation that could support the presence of I(0) in the [HMDABCO](NH4)I3 thin films, is that the colour of the fabricated thin films changes from white to brown over a couple of months. This colour change could be associated with the formation of I_2 and I_3^- over time. The investigation of this phenomenon by spectroscopic methods will be part of Sarah Dummert's master thesis and additional discussion of this phenomenon can be found in the following subsection.

Thin-film roughness/ density. The thin-film fabrication process via spin coating involves different steps, namely (i) the preparation of the spin coating solution, (ii) the activation of the substrate (iii) spray coating, and (vi) the drying of the resulting film. Therefore, a huge number of parameters can be optimized to achieve an optimal thin film quality. Herein, we investigate the variation of the drying process after the spin coating step. Different methods could be used to dry the thin films, such as a heating plate, vacuum drying with an oil pump vacuum, and oven drying. In this case, the best results were achieved for oven drying. Various drying temperatures were tried and the corresponding light microscopy images and SEM images are displayed in Figure 82 and Figure 85, respectively. The light microscopy images illustrate that the thin film coverage increases and roughness decreases with increasing temperature for Au substrates and Si substrates with a native SiO_2 layer (Si/SiO_2) alike. SEM images show that the size of the crystallites/primary particles decreases with increasing temperature, which is also reflected by broader PXRD reflexes (see appendix, Figure S72). According to many articles, the essence for homogenous thin films with minimal surface roughness is fast nucleation and slow crystallization which nicely aligns with these observations.[366] However, the SEM images recorded at 150°C display pinhole-like structures on the surface of the thin film, which could be detrimental to the density of the thin film. Therefore, a good compromise between decreasing primary particle size/crystallinity and increasing surface coverage and homogeneity was identified to be 120°C. Another parameter that should be considered is the duration of the drying procedure. Once the solvent is completely evaporated (10-15 min), the substrates should be removed from the oven. Afterwards, the colour changes from white to yellowish-white to brown indicating the formation of I_2/I_3^-. Additionally, we noticed that the Au substrates were damaged/etched exposing the underlying SiO_2 partially. Similar etching processes were already described in the literature for Au nanorods:[367]

$$I_2 + I^- \rightarrow I_3^-$$

$$2\,Au + I_3^- + I^- \rightarrow 2\,AuI_2^-$$

While the Au etching (complex formation) is known in literature, the exact mechanism of the Iodine formation in the films is not studied yet. However, molecular oxygen can already oxidize I^- to I_2, a process with is accelerated by humidity and high temperature, therefore, this reaction might take place. This can be partially prevented by limiting the exposure to high temperatures and air e.g. by storing the thin films in the glovebox.

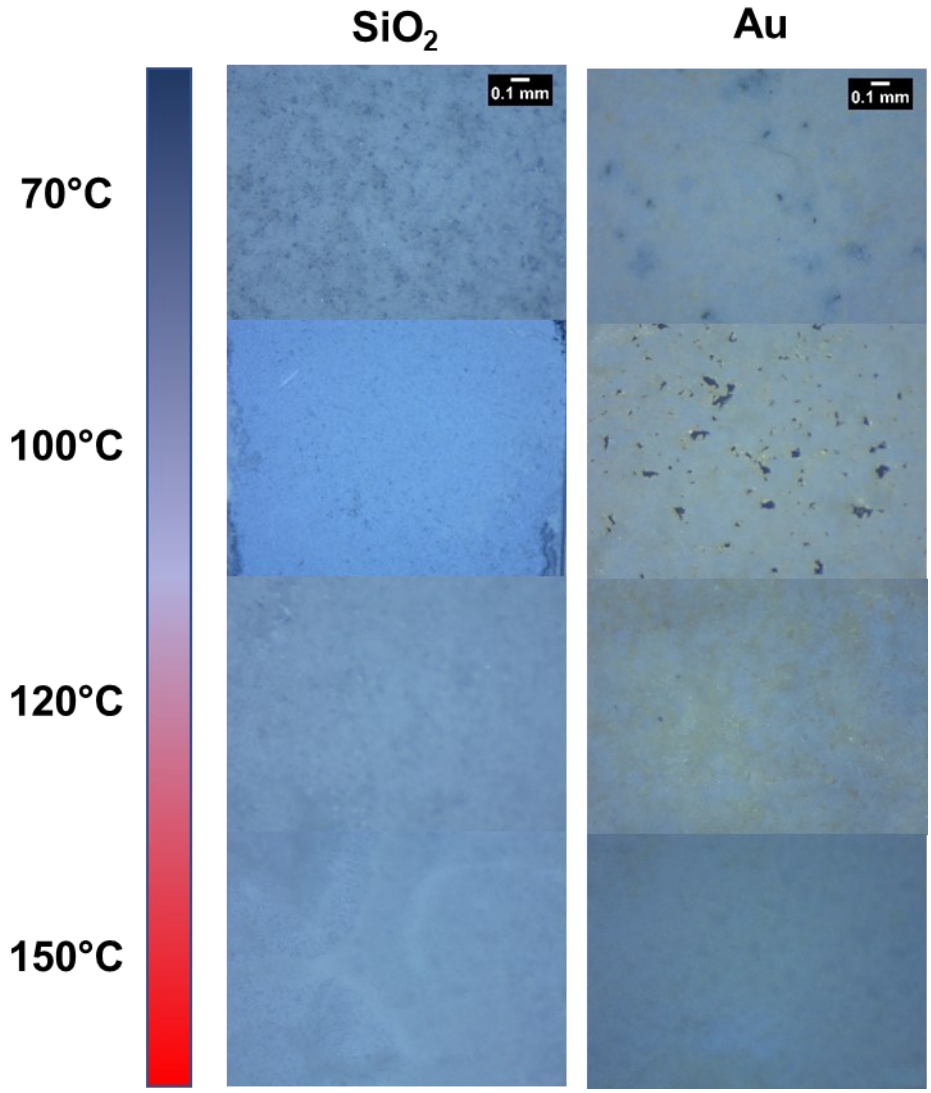

Figure 82: Light microscopy images of [HMDABCO](NH4)I3 spray coating thin films on Au or Si/SiO2 substrates dried at various temperatures between 70-150°C.

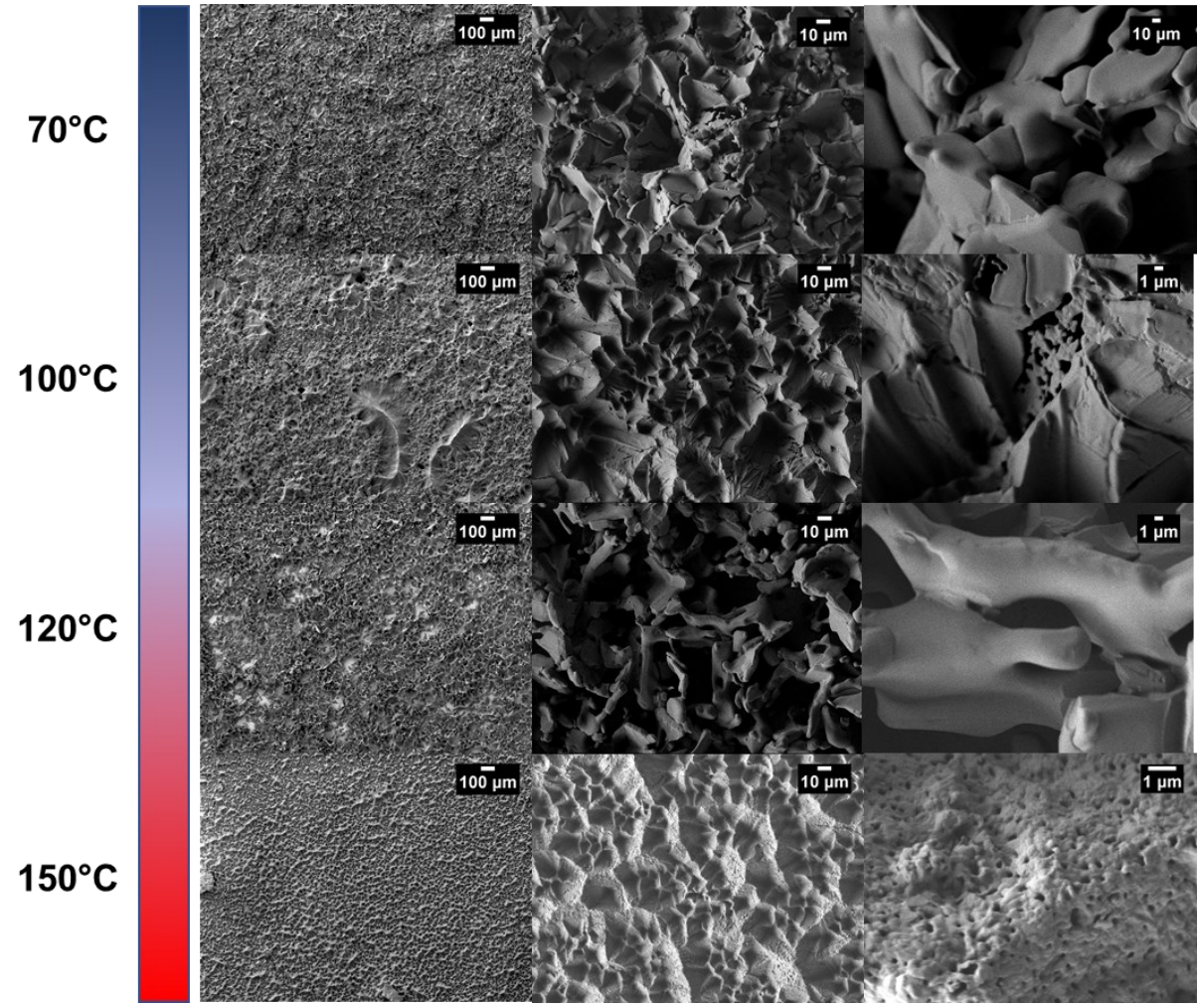

Figure 83: SEM images of [HMDABCO](NH4)I3 spray coating thin films on Si/SiO2 substrates between 70-150°C.

Settings: 50-10,000-fold magnification, 1.0 kV LEI, WD 8.0 mm.

Variation of the substrate. Another important process parameter, that was investigated was the choice and surface activation/preparation of the substrate surface. The variation of the substrate is interesting for several reasons. On the one hand, conductive substrates (like Au) are interesting to facilitate the construction of capacitors with [HMDABCO](NH4)I3 as a dielectric. On the other hand, self-assembled monolayers (SAMs) on different surfaces might help to control the oriented growth of [HMDABCO](NH4)I3 on different materials.

Therefore, we immersed Au substrates in different thiol-based SAM solutions, resulting in the formation of monolayers with various functional terminal groups which drastically altered the surface properties of the corresponding Au surfaces. The successful formation was confirmed by contact angle measurements (appendix, Figure S73). Afterwards, the surfaces were spray-coated with the previously used solution of

1 equiv. MDABCOI and 2 equiv. NH_4I dissolved in dry DMF. Then the substrates were dried for 10 min in an oven at 70 and 150°C.

The investigation by GIXRD shows that the substrate choice and its surface functionalization indeed influence the growth of the perovskite. The hydroxyl and carboxylic acid terminated gold substrate promotes a preferred orientation along the (100) axis especially at low temperatures and slow crystallization rates. The fabrication at 150°C, however, triggered the formation of some side phases, which were not observed for lower temperatures. This might be related to the oxidation of iodide ions and gold etching, which is especially observed for higher temperatures. Therefore, 150°C is not recommended as a drying temperature as discussed before (Figure 84 b). Therefore, the lower temperatures seem favourable. The GIXRD dried at 70°C shows a phase pure [HMDABCO](NH_4)I_3 thin film, with a preferred orientation in the (100) direction. But in contrast to the films dried at 150°C, the thin films dried at 70°C lack full surface coverage and smoothness, which were observed at 120/150°C (see Figure 85). Therefore, the optimal drying temperature was observed at 120°C. The corresponding GIXRD patterns (see Figure 84c) reveal (i) that the thin films do not contain any side phases, and (ii) that the hydroxyl-terminated thin films lead to a preferred orientation in (100) direction. This preferred orientation is more distinctive at 70°C, but still visible at 120°C. This shows that most of the results of the silicon substrates can be transferred to gold substrates. The introduction of SAM functionalized gold substrates offers a certain degree of control over the orientation of the particles on the substrate.

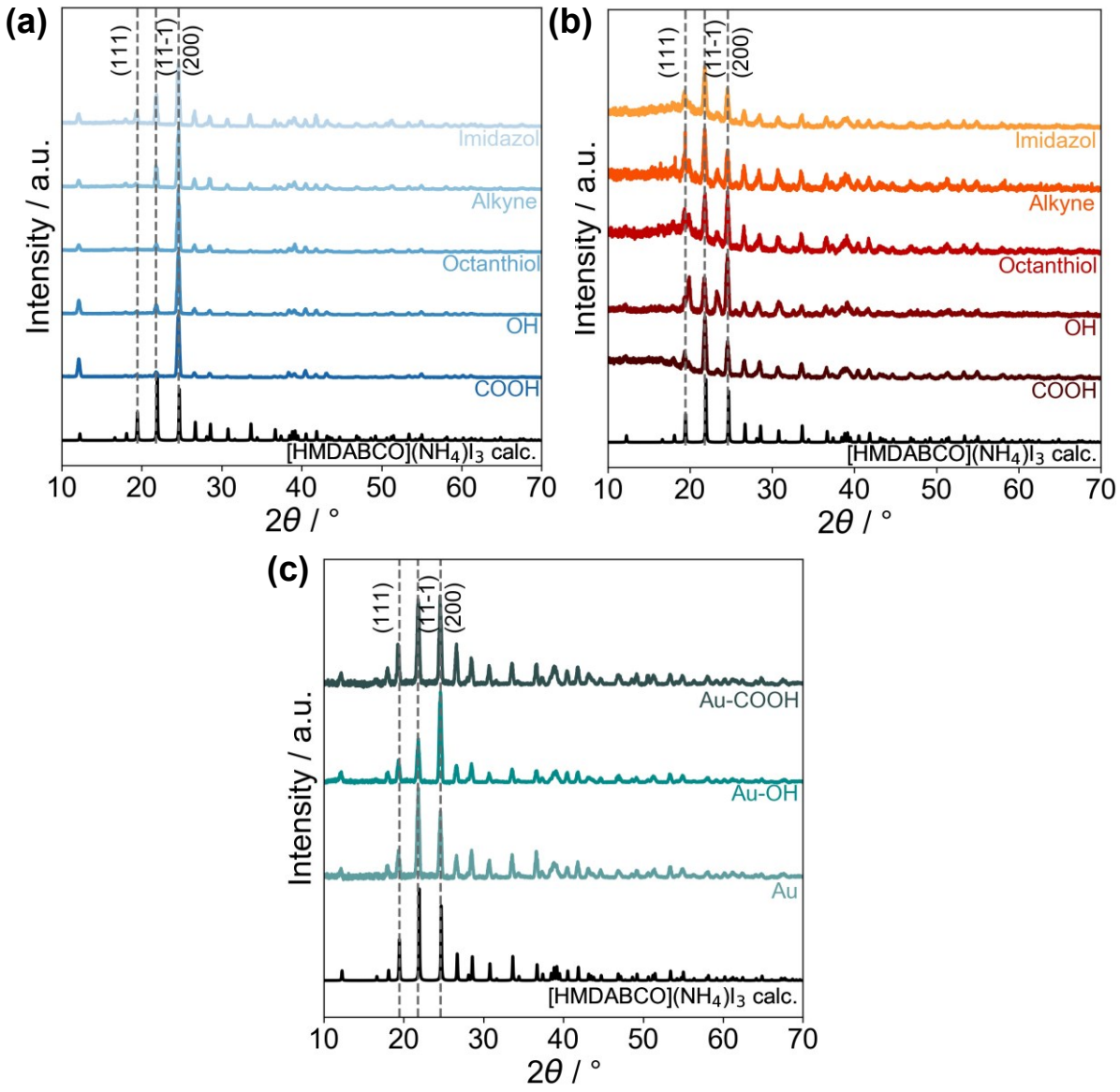

Figure 84: Investigation of the [HMDABCO](NH_4)I_3 perovskite thin films on SAM terminated gold substrates. The thin films were fabricated by spray coating of an MDABCOI (1 equiv.) and NH_4I (2 equiv.) solution in DMF at 70°C (a), 150°C (b), and 120°C (c), respectively.

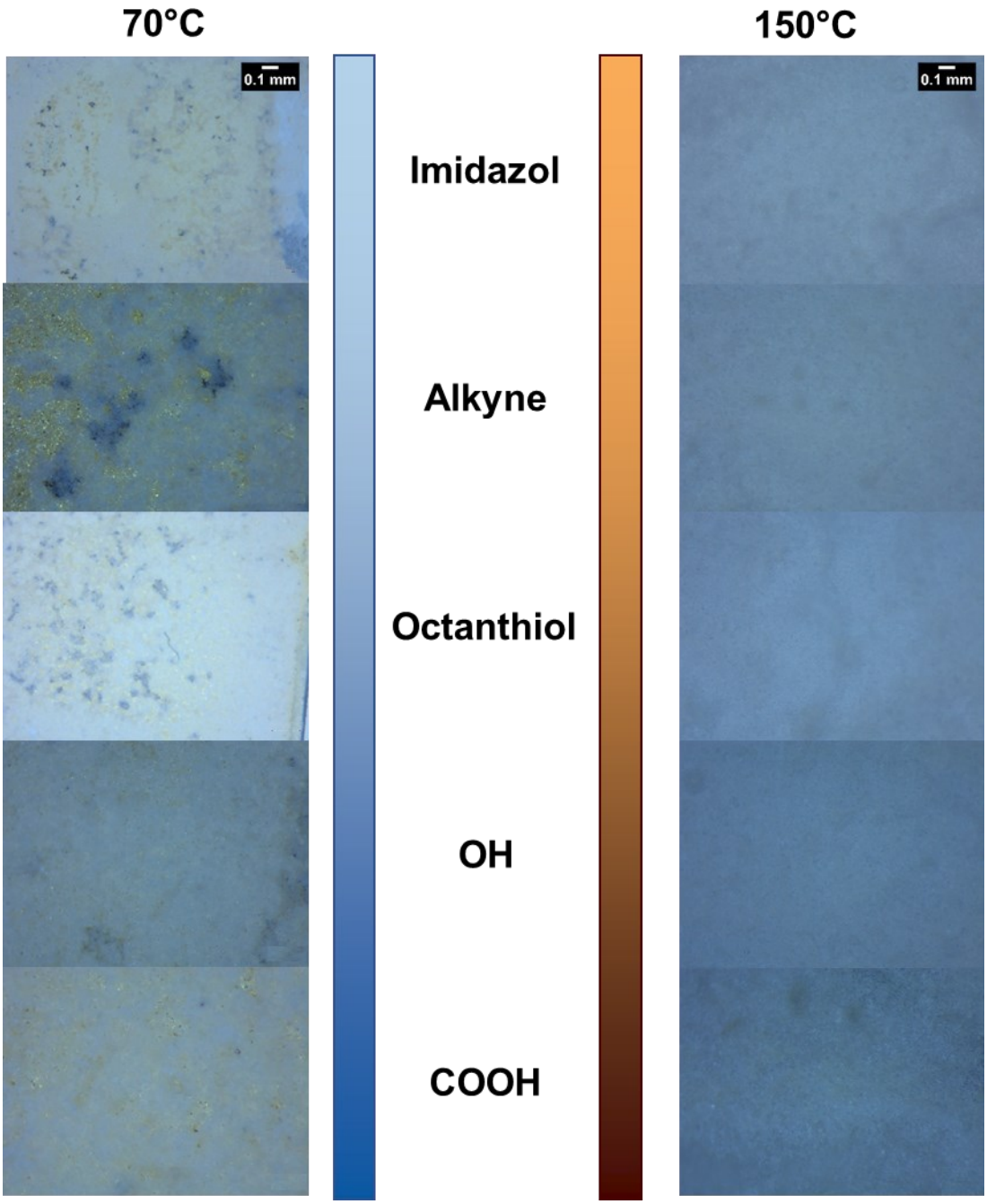

Figure 85: Light microscopy images of [HMDABCO](NH4)I3 spray coating thin films on SAM terminated Au thin films dried at 70 °C (left) or 150°C (right).

Surface activation. Besides the choice of substrate, a proper surface activation procedure is beneficial for a smooth coating and high surface coverage. For this reason, different activation procedures were used, and the thin films were investigated by light microscopy. For the silicon substrates, maximum hydrophilicity determines the thin film quality. Therefore, we compared no activation, ozone treatment, and piranha acid etching (*Caution: Piranha is a very strong oxidizer and can react explosively with organic compounds*). Surface coverage and homogeneity improved from no activation to ozone treatment, with the best results achieved for piranha etching. For unfunctionalized Au substrates, no pre-treatment, ozone treatment, and preheating of the substrates were compared. In this case, the best results were achieved for the preheating procedure.

Variation of deposition method and thickness. Besides spray coating, other chemical solution deposition techniques like dip and drop coating can be employed as well to produce [HMDABCO](NH$_4$)I$_3$ thin films. In particular, drop coating offers a high degree of control over the thin film thickness. By easily adjusting the drop coating volume of the stock solution in DMF a thickness control can be achieved. Cross-section measurements of the thin films (see Figure 86) display that the thickness can be adjusted from 50-100 µm by placing different amounts (7.5-15 µL) of the stock solution on Au coated silicon substrates and drying them at 120°C in the oven. However, the investigated surfaces are still very rough.

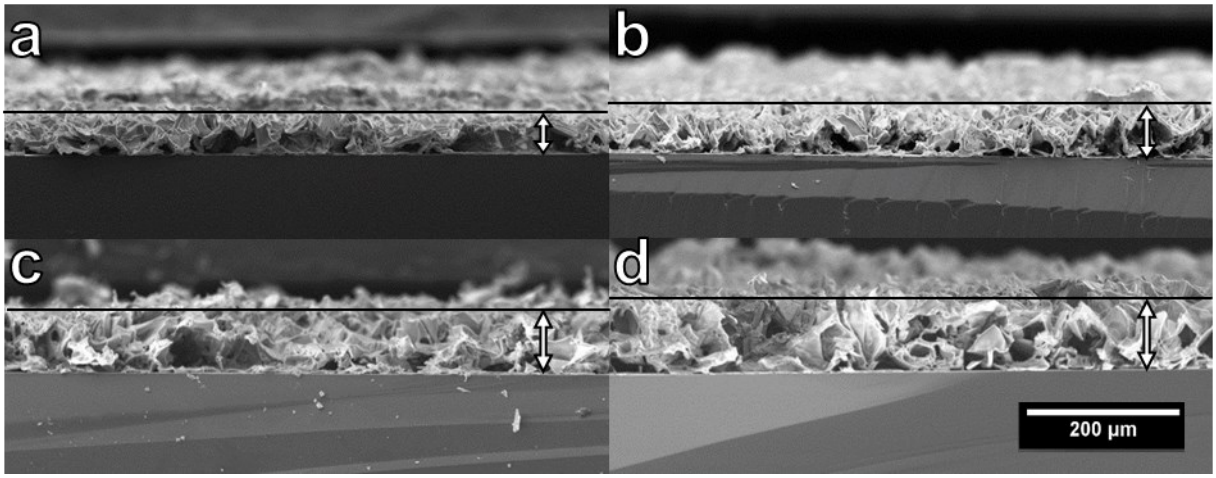

Figure 86: 90° cross-section measurements of [HMDABCO](NH$_4$)I$_3$ thin films supported on Si/SiO$_2$, prepared by drop coating of different volumes (7.5 µL (a, 53 µm), 10 µL (b, 64 µm), 12.5 µL (c, 88 µm), 15 µL (d, 102 µm)) onto the surface and followed up by drying in an oven at 120°C for 10 min.

Capacitor fabrication. The final goal of this project was the design of an [HMDABCO](NH4)I3 based capacitor to characterize its ferroelectric properties which was attempted in close cooperation with Christian Eckel, M.Sc. from Thomas Weitz' research group at the Ludwig Maximilian University, Munich. A detailed description of ferroelectricity and its origin can be found in chapter 4.1.

A capacitor consists of two conductive electrodes and a dielectric layer in between. Hence, a Si substrate with a silicon dioxide layer (Si/SiO2) on the surface was used as the substrate. By adding a Ti adhesion and top Au layer the bottom electrode was created, where the [HMDABCO](NH4)I3 thin film was deposited onto. Finally, the Au top electrode was sputtered or evaporated on top of the [HMDABCO](NH4)I3 layer. The final challenge was the contacting of the [HMDABCO](NH4)I3 thin film, which was achieved with silver varnish and thin Au wires. The targeted design as shown below (Figure 87), should prevent short circuits by diffusion of the silver varnish through the [HMDABCO](NH4)I3 thin film, as the contacting areas are not an integral part of the capacitor.

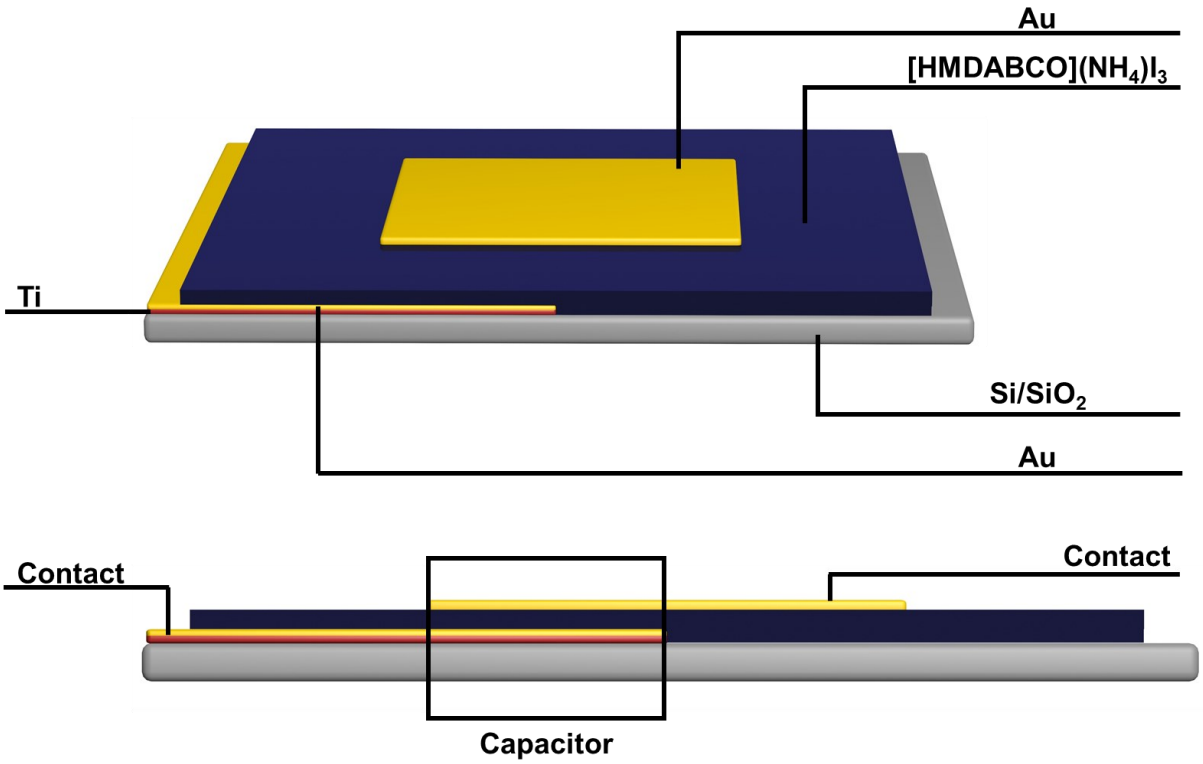

Figure 87: Schematic representation of a capacitor consisting of two gold electrodes separated by an [HMDABCO](NH4)I3 dielectric.

After contacting the [HMDABCO](NH4)I3 thin films, they were exposed to a triangular voltage generated by a Keysight 3350B wave generator and amplified by a voltage amplifier. The resulting current was then recorded by an oscilloscope via the voltage drop over a series resistor. After the measurement, the time-dependent currents can

be integrated over time to calculate the charge (C). By dividing the charge by the area of the capacitator, the polarization (P) can be obtained. By plotting P against the electric field (E, E=U/d), where d is the thickness of the capacitor and U is the applied voltage, the classical P-E hysteresis loop can be visualized. Finally, the ferroelectric polarizability (α) can be calculated by dividing the polarization by the electrical field.

Unfortunately, we were not able to record a meaningful ferroelectric response of the material so far. Two key issues remain a challenge until today: (i) the ideal activation of the mixed (Au/SiO_2) substrate surface and (ii) the roughness of the thin film (Figure 88). The first issue arises from the design of the capacitor, as the surface for the thin film fabrication consists of a mixed substrate consisting of Au and SiO_2 areas. The ideal activation procedure for the silicon substrates involves the treatment of the substrates with piranha acid, which in turn destroys the gold layer. The gold substrates were pre-treated at 110°C in an oven, which did not work for the silicon substrates yielding insufficient surface coverage. A balance between both activation procedures could be achieved by ozone/UV treatment followed up by 10 min of heating, rendering both areas hydrophilic. Even though the achieved results were better, the thin film quality observed for the single SiO_2 or Au surfaces could not be achieved so far. Another method that potentially could help to solve this issue might be an oxygen plasma generator, which will be investigated in the future.

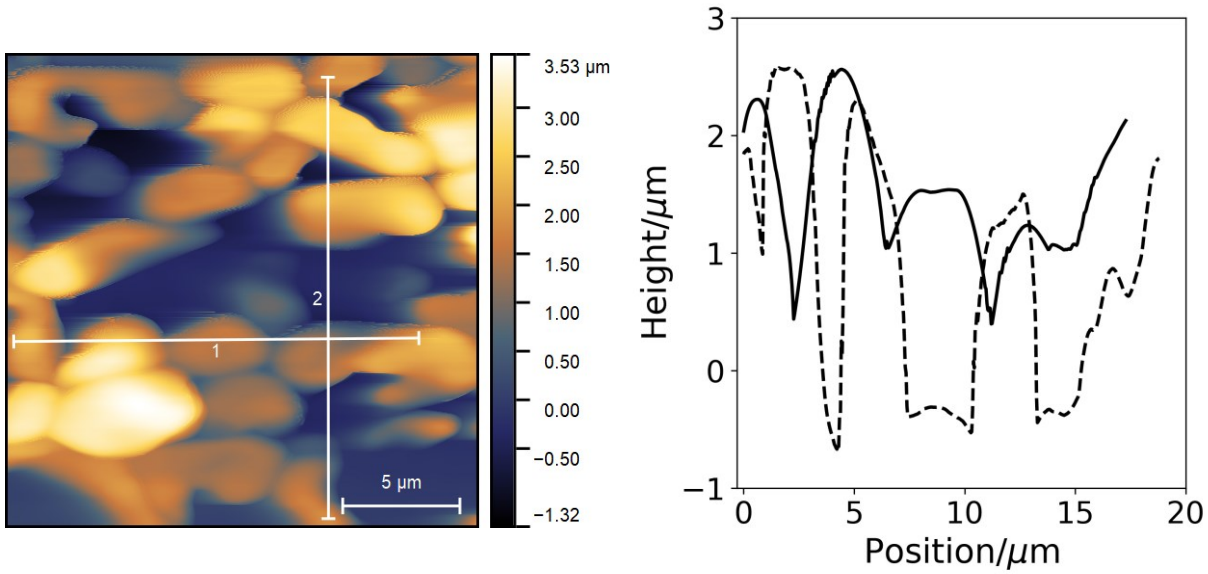

Figure 88: AFM image (a) and height profile of the lines marked in a (b) of [HMDABCO](NH4)I3 spray-coated thin film on top of an Au/SiO_2 mixed substrate.

The second challenge, that we faced for the capacitor fabrication is the surface roughness of the obtained thin films. The surface roughness was determined by AFM and revealed an RMS value of 1.043 µm. This is problematic on two accounts: (i) the top Au contact of the capacitor is only 60 nm thick, if the height differences span a

couple of microns the gold top layer might not be completely continuous, which prevents a meaningful measurement. (ii) the determined thin film thickness is needed to calculate the polarizability of the ferroelectric material. Even if the contacting and measurement issues are solved, it would be not possible to extract the ferroelectric properties out of the data. Due to the high differences in thicknesses in the capacitor area, no electric field value can be calculated. Therefore, the investigation into the fabrication of thinner, fully covered, and smoother [HMDABCO](NH4)I3 thin films are needed. This will be part of Sarah Dummert's master thesis, but due to time constraints not further discussed in this thesis.

4.7. Conclusion & Outlook

In this chapter, the thin film deposition of [HMDABCO](NH4)I3 thin films was discussed. Phase pure thin films were achieved by the introduction of an artificial HI source, namely NH4I. Further investigations included the variation of the substrate, the deposition method, as well as the drying technique, and the temperature. By varying the substrate type and activation thereof, a preferred orientation of the [HMDABCO](NH4)I3 thin films could be introduced. Emphasizing the possibilities derived from our approach we showed that a multitude of chemical deposition methods like dip, spray, and drop coating can be used to fabricate [HMDABCO](NH4)I3 thin films. We additionally showed that it is possible to control the thickness of the films by adjusting the drop coating volume, opening up possibilities to tailor-made thin films, which can be produced with minimum effort. Moreover, based on our results, we tried to build a capacitor. Due to the absolute surface roughness, however, we were not able to measure the ferroelectric properties so far. Further investigations optimizing the surface roughness, thin-film thickness, and coverage could enable the final fabrication of a [HMDABCO](NH4)I3 thin film ferroelectric capacitor.

5. REFERENCES

(1) World Economic Forum. *Global Risks Report 2019*; 2019.

(2) Project, E. *Electronics Enabling Efficient Energy Usage*; 2009.

(3) Stassen, I.; Burtch, N.; Talin, A.; Falcaro, P.; Allendorf, M.; Ameloot, R. An Updated Roadmap for the Integration of Metal–Organic Frameworks with Electronic Devices and Chemical Sensors. *Chem. Soc. Rev.* **2017**, *46*, 3185–3241.

(4) Mohamed, S. A.; Chong, S.; Kim, J. Thermal Stability of Methyl-Functionalized MOF-5. *J. Phys. Chem. C* **2019**, *123*, 29686–29692.

(5) Yang, J.; Grzech, A.; Mulder, M.; Dingemans, T. J. Methyl Modified MOF-5: A Water Stable Hydrogen Storage Material. *Chem. Commun.* **2011**, No. 47, 5244–5246.

(6) Li, H.; Eddaoudi, M.; O'Keeffe, M.; Yaghi, O. M. Design and Synthesis of an Exceptionally Stable and Highly Porous Metal-Organic Framework. *Nature* **1999**, *402*, 276–279.

(7) Chui, S. S.; Lo, S. M.; Charmant, J. P. H.; Orpen, A. G.; Williams, I. D. A Chemically Functionalizable Nanoporous Material $[Cu_3(TMA)_2(H2O)_3]_N$. *Science* **1999**, *283*, 1148–1151.

(8) Searching for the term "metal-organic frameworks" at scifinder.cas.org on 2021-03-10.

(9) Chadwick, A. V.; Sherwood, J. N. Point Defects in Molecular Solids. In *Point Defects in Solids*; Springer US: Boston, MA, 1975; Vol. 85, pp 441–475.

(10) Horike, S.; Shimomura, S.; Kitagawa, S. Soft Porous Crystals. *Nat. Chem* **2009**, *1*, 695–704.

(11) Wang, X.; Zhang, L.; Yang, J.; Liu, F.; Dai, F.; Wang, R.; Sun, D. Lanthanide Metal-Organic Frameworks Containing a Novel Flexible Ligand for Luminescence Sensing of Small Organic Molecules and Selective Adsorption. *J. Mater. Chem. A* **2015**, *3*, 12777–12785.

(12) Li, W.; Watzele, S.; El-Sayed, H. A.; Liang, Y.; Kieslich, G.; Bandarenka, A. S.; Rodewald, K.; Rieger, B.; Fischer, R. A. Unprecedented High Oxygen Evolution Activity of Electrocatalysts Derived from Surface-Mounted Metal-Organic Frameworks. *J. Am. Chem. Soc.* **2019**, *141*, 5926–5933.

(13) Li, W.; Xue, S.; Watzele, S.; Hou, S.; Fichtner, J.; Semrau, A. L.; Zhou, L.; Welle, A.; Bandarenka, A. S.; Fischer, R. A. Advanced Bifunctional Oxygen Reduction and Evolution Electrocatalyst Derived from Surface-Mounted Metal–Organic Frameworks. *Angew. Chem. Int. Ed.* **2020**, *59*, 5837–5843.

(14) Trager, R. MOFs Offer Safer Toxic Gas Storage. *Chemistry World*. 2016.

(15) Urquhart, J. Worls's First Commerial MOF Keeps Fruit Fresh. *Chemistry World*. 2016.

(16) Kim, H.; Yang, S.; Rao, S. R.; Narayanan, S.; Kapustin, E. A.; Furukawa, H.; Umans, A. S.; Yaghi, O. M.; Wang, E. N. Water Harvesting from Air with Metal-Organic Frameworks Powered by Natural Sunlight. *Science* **2017**, *356*, 430–434.

(17) Kim, H.; Rao, S. R.; Kapustin, E. A.; Zhao, L.; Yang, S.; Yaghi, O. M.; Wang, E. N.

Adsorption-Based Atmospheric Water Harvesting Device for Arid Climates. *Nat. Commun.* **2018**, *9*, 1191.

(18) Hanikel, N.; Prévot, M. S.; Fathieh, F.; Kapustin, E. A.; Lyu, H.; Wang, H.; Diercks, N. J.; Glover, T. G.; Yaghi, O. M. Rapid Cycling and Exceptional Yield in a Metal-Organic Framework Water Harvester. *ACS Cent. Sci.* **2019**, *5*, 1699–1706.

(19) Zacher, D.; Shekhah, O.; Wöll, C.; Fischer, R. A. Thin Films of Metal–Organic Frameworks. *Chem. Soc. Rev.* **2009**, *38*, 1418.

(20) Virmani, E.; Rotter, J. M.; Mähringer, A.; von Zons, T.; Godt, A.; Bein, T.; Wuttke, S.; Medina, D. D. On-Surface Synthesis of Highly Oriented Thin Metal–Organic Framework Films through Vapor-Assisted Conversion. *J. Am. Chem. Soc.* **2018**, *140*, 4812–4819.

(21) Lausund, K. B.; Nilsen, O. All-Gas-Phase Synthesis of UiO-66 through Modulated Atomic Layer Deposition. *Nat. Commun.* **2016**, *7*, 13578.

(22) Stassen, I.; Styles, M.; Grenci, G.; Gorp, H. Van; Vanderlinden, W.; Feyter, S. De; Falcaro, P.; Vos, D. De; Vereecken, P.; Ameloot, R. Chemical Vapour Deposition of Zeolitic Imidazolate Framework Thin Films. *Nat. Mater.* **2016**, *15*, 304–310.

(23) Zhang, X.; Wan, K.; Subramanian, P.; Xu, M.; Luo, J.; Fransaer, J. Electrochemical Deposition of Metal–Organic Framework Films and Their Applications. *J. Mater. Chem. A* **2020**, *8*, 7569–7587.

(24) Wang, Z.; Wöll, C. Fabrication of Metal–Organic Framework Thin Films Using Programmed Layer-by-Layer Assembly Techniques. *Adv. Mater. Technol.* **2019**, *4*, 1–22.

(25) Bilger, D.; Homayounfar, S. Z.; Andrew, T. L. A Critical Review of Reactive Vapor Deposition for Conjugated Polymer Synthesis. *J. Mater. Chem. C* **2019**, *7*, 7159–7174.

(26) Weber, M.; Julbe, A.; Kim, S. S.; Bechelany, M. Atomic Layer Deposition (ALD) on Inorganic or Polymeric Membranes. *J. Appl. Phys.* **2019**, *126*.

(27) Kim, H. G.; Lee, J. G.; Kim, S. S. Surface Modification of Polymeric Substrates to Enhance the Barrier Properties of an Al_2O_3 Layer Formed by PEALD Process. *Org. Electron.* **2017**, *50*, 239–246.

(28) Medina, D. D.; Rotter, J. M.; Hu, Y.; Dogru, M.; Werner, V.; Auras, F.; Markiewicz, J. T.; Knochel, P.; Bein, T. Room Temperature Synthesis of Covalent–Organic Framework Films through Vapor-Assisted Conversion. *J. Am. Chem. Soc.* **2015**, *137*, 1016–1019.

(29) Scheel, H. J. Introduction to Liquid Phase Epitaxy. In *Liquid Phase Epitaxy of Electronic, Optical and Optoelectronic Materials*; Wiley Online Books; John Wiley & Sons, Ltd: Chichester, UK, 2007; pp 1–19.

(30) Biemmi, E.; Scherb, C.; Bein, T. Oriented Growth of the Metal Organic Framework $Cu_3(BTC)_2(H_2O)_3 \cdot xH_2O$ Tunable with Functionalized Self-Assembled Monolayers. *J. Am. Chem. Soc.* **2007**, *129*, 8054–8055.

(31) Liu, J.; Shekhah, O.; Stammer, X.; Arslan, H. K.; Liu, B.; Schüpbach, B.; Terfort, A.; Wöll, C. Deposition of Metal-Organic Frameworks by Liquid-Phase Epitaxy: The Influence of Substrate Functional Group Density on Film Orientation. *Materials* **2012**, *5*, 1581–1592.

(32) Shekhah, O.; Wang, H.; Kowarik, S.; Schreiber, F.; Paulus, M.; Tolan, M.; Sternemann, C.; Evers, F.; Zacher, D.; Fischer, R. A.; Wöll, C. Step-by-Step Route for the Synthesis of Metal−Organic Frameworks. *J. Am. Chem. Soc.* **2007**, *129*, 15118–15119.

(33) Zacher, D.; Schmid, R.; Wöll, C.; Fischer, R. A. Surface Chemistry of Metal-Organic Frameworks at the Liquid-Solid Interface. *Angew. Chem. Int. Ed.* **2011**, *50*, 176–199.

(34) Gliemann, H.; Wöll, C. Epitaxially Grown Metal-Organic Frameworks. *Mater. Today* **2012**, *15*, 110–116.

(35) Meilikhov, M.; Yusenko, K.; Schollmeyer, E.; Mayer, C.; Buschmann, H. J.; Fischer, R. A. Stepwise Deposition of Metal Organic Frameworks on Flexible Synthetic Polymer Surfaces. *Dalt. Trans.* **2011**, *40*, 4838–4841.

(36) Arslan, H. K.; Shekhah, O.; Wieland, D. C. F.; Paulus, M.; Sternemann, C.; Schroer, M. A.; Tiemeyer, S.; Tolan, M.; Fischer, R. A.; Wöll, C. Intercalation in Layered Metal-Organic Frameworks: Reversible Inclusion of an Extended π-System. *J. Am. Chem. Soc.* **2011**, *133*, 8158–8161.

(37) Shekhah, O.; Wang, H.; Paradinas, M.; Ocal, C.; Schüpbach, B.; Terfort, A.; Zacher, D.; Fischer, R. A.; Wöll, C. Controlling Interpenetration in Metal–Organic Frameworks by Liquid-Phase Epitaxy. *Nat. Mater.* **2009**, *8*, 481–484.

(38) Liu, J.; Lukose, B.; Shekhah, O.; Arslan, H. K.; Weidler, P.; Gliemann, H.; Bräse, S.; Grosjean, S.; Godt, A.; Feng, X.; Müllen, K.; Magdau, I. B.; Heine, T.; Wöll, C. A Novel Series of Isoreticular Metal Organic Frameworks: Realizing Metastable Structures by Liquid Phase Epitaxy. *Sci. Rep.* **2012**, *2*, 1–5.

(39) Gu, Z. G.; Pfriem, A.; Hamsch, S.; Breitwieser, H.; Wohlgemuth, J.; Heinke, L.; Gliemann, H.; Wöll, C. Transparent Films of Metal-Organic Frameworks for Optical Applications. *Microporous Mesoporous Mater.* **2015**, *211*, 82–87.

(40) Arslan, H. K.; Shekhah, O.; Wohlgemuth, J.; Franzreb, M.; Fischer, R. A.; Wöll, C. High-Throughput Fabrication of Uniform and Homogenous MOF Coatings. *Adv. Funct. Mater.* **2011**, *21*, 4228–4231.

(41) Zhuang, J. L.; Ar, D.; Yu, X. J.; Liu, J. X.; Terfort, A. Patterned Deposition of Metal-Organic Frameworks onto Plastic, Paper, and Textile Substrates by Inkjet Printing of a Precursor Solution. *Adv. Mater.* **2013**, *25*, 4631–4635.

(42) Makiura, R.; Motoyama, S.; Umemura, Y.; Yamanaka, H.; Sakata, O.; Kitagawa, H. Surface Nano-Architecture of a Metal-Organic Framework. *Nat. Mater.* **2010**, *9*, 565–571.

(43) Rosi, N. L.; Kim, J.; Eddaoudi, M.; Chen, B.; O'Keeffe, M.; Yaghi, O. M. Rod Packings and Metal−Organic Frameworks Constructed from Rod-Shaped Secondary Building Units. *J. Am. Chem. Soc.* **2005**, *127*, 1504–1518.

(44) Schoedel, A.; Li, M.; Li, D.; O'Keeffe, M.; Yaghi, O. M. Structures of Metal–Organic Frameworks with Rod Secondary Building Units. *Chem. Rev.* **2016**, *116*, 12466–12535.

(45) Münch, A. S.; Lohse, M. S.; Hausdorf, S.; Schreiber, G.; Zacher, D.; Fischer, R. A.; Mertens, F. O. R. L. Room Temperature Preparation Method for Thin MOF-5 Films on Metal and Fused Silica Surfaces Using the Controlled SBU Approach. *Microporous Mesoporous Mater.* **2012**, *159*, 132–138.

(46) Wannapaiboon, S.; Tu, M.; Fischer, R. A. Liquid Phase Heteroepitaxial Growth of Moisture-Tolerant MOF-5 Isotype Thin Films and Assessment of the Sorption Properties by Quartz Crystal Microbalance. *Adv. Funct. Mater.* **2014**, *24*, 2696–2705.

(47) Delen, G.; Ristanović, Z.; Mandemaker, L. D. B.; Weckhuysen, B. M. Mechanistic Insights into Growth of Surface-Mounted Metal-Organic Framework Films Resolved by Infrared (Nano-) Spectroscopy. *Chem. - A Eur. J.* **2018**, *24*, 187–195.

(48) Shekhah, O.; Hirai, K.; Wang, H.; Uehara, H.; Kondo, M.; Diring, S.; Zacher, D.; Fischer, R. A.; Sakata, O.; Kitagawa, S.; Furukawa, S.; Wöll, C. MOF-on-MOF Heteroepitaxy: Perfectly Oriented $[Zn_2(Ndc)_2(Dabco)]_n$ Grown on $[Cu_2(Ndc)_2(Dabco)]_n$ Thin Films. *Dalt. Trans.* **2011**, *40*, 4954.

(49) Li, H.; Eddaoudi, M.; Groy, T. L.; Yaghi, O. M. Establishing Microporosity in Open Metal-Organic Frameworks: Gas Sorption Isotherms for Zn(BDC) (BDC = 1,4-Benzenedicarboxylate). *J. Am. Chem. Soc.* **1998**, *120*, 8571–8572.

(50) Oldenburg, M.; Turshatov, A.; Busko, D.; Wollgarten, S.; Adams, M.; Baroni, N.; Welle, A.; Redel, E.; Wöll, C.; Richards, B. S.; Howard, I. A. Photon Upconversion at Crystalline Organic–Organic Heterojunctions. *Adv. Mater.* **2016**, *28*, 8477–8482.

(51) Adams, M.; Kozlowska, M.; Baroni, N.; Oldenburg, M.; Ma, R.; Busko, D.; Turshatov, A.; Emandi, G.; Senge, M. O.; Haldar, R.; Wöll, C.; Nienhaus, G. U.; Richards, B. S.; Howard, I. A. Highly Efficient One-Dimensional Triplet Exciton Transport in a Palladium-Porphyrin-Based Surface-Anchored Metal-Organic Framework. *ACS Appl. Mater. Interfaces* **2019**, *11*, 15688–15697.

(52) Ahmad, S.; Liu, J.; Gong, C.; Zhao, J.; Sun, L. Photon Up-Conversion via Epitaxial Surface-Supported Metal–Organic Framework Thin Films with Enhanced Photocurrent. *ACS Appl. Energy Mater.* **2018**, *1*, 249–253.

(53) Otsubo, K.; Haraguchi, T.; Sakata, O.; Fujiwara, A.; Kitagawa, H. Step-by-Step Fabrication of a Highly Oriented Crystalline Three-Dimensional Pillared-Layer-Type Metal–Organic Framework Thin Film Confirmed by Synchrotron X-Ray Diffraction. *J. Am. Chem. Soc.* **2012**, *134*, 9605–9608.

(54) Shekhah, O.; Eddaoudi, M. The Liquid Phase Epitaxy Method for the Construction of Oriented ZIF-8 Thin Films with Controlled Growth on Functionalized Surfaces. *Chem. Commun.* **2013**, *49*, 10079–10081.

(55) Valadez Sánchez, E. P.; Gliemann, H.; Haas-Santo, K.; Wöll, C.; Dittmeyer, R. ZIF-8 SURMOF Membranes Synthesized by Au-Assisted Liquid Phase Epitaxy for Application in Gas Separation. *Chemie Ing. Tech.* **2016**, *88*, 1798–1805.

(56) Knebel, A.; Geppert, B.; Volgmann, K.; Kolokolov, D. I.; Stepanov, A. G.; Twiefel, J.; Heitjans, P.; Volkmer, D.; Caro, J. Defibrillation of Soft Porous Metal-Organic Frameworks with Electric Fields. *Science* **2017**, *358*, 347–351.

(57) Li, K.; Olson, D. H.; Seidel, J.; Emge, T. J.; Gong, H.; Zeng, H.; Li, J. Zeolitic Imidazolate Frameworks for Kinetic Separation of Propane and Propene. *J. Am. Chem. Soc.* **2009**, *131*, 10368–10369.

(58) Piñeiro-López, L.; Valverde-Muñoz, F. J.; Seredyuk, M.; Muñoz, M. C.; Haukka, M.; Real, J. A. Guest Induced Strong Cooperative One- and Two-Step Spin Transitions in Highly Porous Iron(II) Hofmann-Type Metal–Organic Frameworks. *Inorg. Chem.* **2017**, *56*,

7038–7047.

(59) Semrau, A. L.; Wannapaiboon, S.; Pujari, S. P.; Vervoorts, P.; Albada, B.; Zuilhof, H.; Fischer, R. A. Highly Porous Nanocrystalline UiO-66 Thin Films via Coordination Modulation Controlled Step-by-Step Liquid-Phase Growth. *Cryst. Growth Des.* **2019**, *19*, 1738–1747.

(60) Hashem, T.; Valadez Sánchez, E. P.; Weidler, P. G.; Gliemann, H.; Alkordi, M. H.; Wöll, C. Liquid-Phase Quasi-Epitaxial Growth of Highly Stable, Monolithic UiO-66-NH_2 MOF Thin Films on Solid Substrates. *ChemistryOpen* **2020**, *9*, 524–527.

(61) Zhou, Z.; Mukherjee, S.; Warnan, J.; Li, W.-J.; Wannapaiboon, S.; Hou, S.; Rodewald, K.; Rieger, B.; Weidler, P. G.; Wöll, C.; Fischer, R. A. Porphyrin Based Metal–Organic Framework Films: Nucleation and Growth. *J. Mater. Chem. A* **2020**, *8*, 25941–25950.

(62) Allendorf, M. D.; Houk, R. J. T.; Andruszkiewicz, L.; Talin, A. A.; Pikarsky, J.; Choudhury, A.; Gall, K. A.; Hesketh, P. J. Stress-Induced Chemical Detection Using Flexible Metal−Organic Frameworks. *J. Am. Chem. Soc.* **2008**, *130*, 14404–14405.

(63) Liu, B.; Shekhah, O.; Arslan, H. K.; Liu, J.; Wöll, C.; Fischer, R. A. Enantiopure Metal-Organic Framework Thin Films: Oriented SURMOF Growth and Enantioselective Adsorption. *Angew. Chem. Int. Ed.* **2012**, *51*, 807–810.

(64) Tu, M.; Wannapaiboon, S.; Fischer, R. A. Liquid Phase Stepwise Growth of Surface Mounted Metal–Organic Frameworks for Exploratory Research and Development of Applications. *Inorg. Chem. Front.* **2014**, *1*, 442–463.

(65) Streit, H. C.; Adlung, M.; Shekhah, O.; Stammer, X.; Arslan, H. K.; Zybaylo, O.; Ladnorg, T.; Gliemann, H.; Franzreb, M.; Wöll, C.; Wickleder, C. Surface-Anchored MOF-Based Photonic Antennae. *ChemPhysChem* **2012**, *13*, 2699–2702.

(66) Liu, J.; Zhou, W.; Liu, J.; Howard, I.; Kilibarda, G.; Schlabach, S.; Coupry, D.; Addicoat, M.; Yoneda, S.; Tsutsui, Y.; Sakurai, T.; Seki, S.; Wang, Z.; Lindemann, P.; Redel, E.; Heine, T.; et al. Photoinduced Charge-Carrier Generation in Epitaxial MOF Thin Films: High Efficiency as a Result of an Indirect Electronic Band Gap? *Angew. Chem. Int. Ed.* **2015**, *54*, 7441–7445.

(67) Dragässer, A.; Shekhah, O.; Zybaylo, O.; Shen, C.; Buck, M.; Wöll, C.; Schlettwein, D. Redox Mediation Enabled by Immobilised Centres in the Pores of a Metal–Organic Framework Grown by Liquid Phase Epitaxy. *Chem. Commun.* **2012**, *48*, 663–665.

(68) Chen, X.; Wang, Z.; Hassan, Z. M.; Lin, P.; Zhang, K.; Baumgart, H.; Redel, E. Seebeck Coefficient Measurements of Polycrystalline and Highly Ordered Metal-Organic Framework Thin Films. *ECS J. Solid State Sci. Technol.* **2017**, *6*, P150–P153.

(69) Talin, A. A.; Centrone, A.; Ford, A. C.; Foster, M. E.; Stavila, V.; Haney, P.; Kinney, R. A.; Szalai, V.; El Gabaly, F.; Yoon, H. P.; Léonard, F.; Allendorf, M. D. Tunable Electrical Conductivity in Metal-Organic Framework Thin-Film Devices. *Science* **2014**, *343*, 66–69.

(70) Gu, Z. G.; Chen, S. C.; Fu, W. Q.; Zheng, Q.; Zhang, J. Epitaxial Growth of MOF Thin Film for Modifying the Dielectric Layer in Organic Field-Effect Transistors. *ACS Appl. Mater. Interfaces* **2017**, *9*, 7259–7264.

(71) Kornienko, N.; Zhao, Y.; Kley, C. S.; Zhu, C.; Kim, D.; Lin, S.; Chang, C. J.; Yaghi, O. M.; Yang, P. Metal–Organic Frameworks for Electrocatalytic Reduction of Carbon

Dioxide. *J. Am. Chem. Soc.* **2015**, *137*, 14129–14135.

(72) Zhu, B.; Zou, R.; Xu, Q. Metal–Organic Framework Based Catalysts for Hydrogen Evolution. *Adv. Energy Mater.* **2018**, *8*, 1801193.

(73) Xiao, Y.-H.; Gu, Z.-G.; Zhang, J. Surface-Coordinated Metal–Organic Framework Thin Films (SURMOFs) for Electrocatalytic Applications. *Nanoscale* **2020**, *12*, 12712–12730.

(74) Li, D.-J.; Li, Q.-H.; Gu, Z.-G.; Zhang, J. A Surface-Mounted MOF Thin Film with Oriented Nanosheet Arrays for Enhancing the Oxygen Evolution Reaction. *J. Mater. Chem. A* **2019**, *7*, 18519–18528.

(75) Chernikova, V.; Shekhah, O.; Eddaoudi, M. Advanced Fabrication Method for the Preparation of MOF Thin Films: Liquid-Phase Epitaxy Approach Meets Spin Coating Method. *ACS Appl. Mater. Interfaces* **2016**, *8*, 20459–20464.

(76) Zacher, D.; Yusenko, K.; Bétard, A.; Henke, S.; Molon, M.; Ladnorg, T.; Shekhah, O.; Schüpbach, B.; de los Arcos, T.; Krasnopolski, M.; Meilikhov, M.; Winter, J.; Terfort, A.; Wöll, C.; Fischer, R. A. Liquid-Phase Epitaxy of Multicomponent Layer-Based Porous Coordination Polymer Thin Films of $[M(L)(P)_{0.5}]$ Type: Importance of Deposition Sequence on the Oriented Growth. *Chem. - A Eur. J.* **2011**, *17*, 1448–1455.

(77) Tu, M.; Fischer, R. A. Heteroepitaxial Growth of Surface Mounted Metal–Organic Framework Thin Films with Hybrid Adsorption Functionality. *J. Mater. Chem. A* **2014**, *2*, 2018–2022.

(78) Wang, Z.; Wannapaiboon, S.; Rodewald, K.; Tu, M.; Rieger, B.; Fischer, R. A. Directing the Hetero-Growth of Lattice-Mismatched Surface-Mounted Metal–Organic Frameworks by Functionalizing the Interface. *J. Mater. Chem. A* **2018**, *6*, 21295–21303.

(79) Tu, M.; Wannapaiboon, S.; Fischer, R. A. Programmed Functionalization of SURMOFs via Liquid Phase Heteroepitaxial Growth and Post-Synthetic Modification. *Dalt. Trans* **2013**, *42*, 16029–16035.

(80) Liu, J.; Heidrich, S.; Liu, J.; Guo, B.; Zharnikov, M.; Simon, U.; Wenzel, W.; Wöll, C. Encapsulation of Au_{55} Clusters within Surface-Supported Metal–Organic Frameworks for Catalytic Reduction of 4-Nitrophenol. *ACS Appl. Nano Mater.* **2020**, acsanm.0c02842.

(81) Gu, Z. G.; Fu, H.; Neumann, T.; Xu, Z. X.; Fu, W. Q.; Wenzel, W.; Zhang, L.; Zhang, J.; Woll, C. Chiral Porous Metacrystals: Employing Liquid-Phase Epitaxy to Assemble Enantiopure Metal-Organic Nanoclusters into Molecular Framework Pores. *ACS Nano* **2016**, *10*, 977–983.

(82) Vohra, M. I.; Li, D. J.; Gu, Z. G.; Zhang, J. Insight into the Epitaxial Encapsulation of Pd Catalysts in an Oriented Metalloporphyrin Network Thin Film for Tandem Catalysis. *Nanoscale* **2017**, *9*, 7734–7738.

(83) Li, D.-J.; Gu, Z.-G.; Zhang, W.; Kang, Y.; Zhang, J. Epitaxial Encapsulation of Homodispersed CeO2 in a Cobalt–Porphyrin Network Derived Thin Film for the Highly Efficient Oxygen Evolution Reaction. *J. Mater. Chem. A* **2017**, *5*, 20126–20130.

(84) Wannapaiboon, S.; Sumida, K.; Dilchert, K.; Tu, M.; Kitagawa, S.; Furukawa, S.; Fischer, R. A. Enhanced Properties of Metal-Organic Framework Thin Films Fabricated via a Coordination Modulation-Controlled Layer-by-Layer Process. *J. Mater. Chem. A* **2017**, *5*, 13665–13673.

(85) Wang, Z.; Henke, S.; Paulus, M.; Welle, A.; Fan, Z.; Rodewald, K.; Rieger, B.; Fischer, R. A. Defect Creation in Surface-Mounted Metal-Organic Framework Thin Films. *ACS Appl Mater Interfaces* **2020**, *12*, 2655–2661.

(86) Behrens, K.; Mondal, S. S.; Nöske, R.; Baburin, I. A.; Leoni, S.; Günter, C.; Weber, J.; Holdt, H.-J. Microwave-Assisted Synthesis of Defects Metal-Imidazolate-Amide-Imidate Frameworks and Improved CO_2 Capture. *Inorg. Chem.* **2015**, *54*, 10073–10080.

(87) Fan, Z.; Wang, J.; Wang, W.; Burger, S.; Wang, Z.; Wang, Y.; Wöll, C.; Cokoja, M.; Fischer, R. A. Defect Engineering of Copper Paddlewheel-Based Metal–Organic Frameworks of Type NOTT-100: Implementing Truncated Linkers and Its Effect on Catalytic Properties. *ACS Appl. Mater. Interfaces* **2020**, *12*, 37993–38002.

(88) Fang, Z.; Dürholt, J. P.; Kauer, M.; Zhang, W.; Lochenie, C.; Jee, B.; Albada, B.; Metzler-Nolte, N.; Pöppl, A.; Weber, B.; Muhler, M.; Wang, Y.; Schmid, R.; Fischer, R. A. Structural Complexity in Metal–Organic Frameworks: Simultaneous Modification of Open Metal Sites and Hierarchical Porosity by Systematic Doping with Defective Linkers. *J. Am. Chem. Soc.* **2014**, *136*, 9627–9636.

(89) Stassen, I.; Burtch, N.; Talin, A.; Falcaro, P.; Allendorf, M.; Ameloot, R. An Updated Roadmap for the Integration of Metal-Organic Frameworks with Electronic Devices and Chemical Sensors. *Chem. Soc. Rev.* **2017**, *46*, 3185–3241.

(90) Wang, Z.; Wannapaiboon, S.; Henke, S.; Paulus, M.; Rodewald, K.; Rieger, B.; Fischer, R. A. The Synergistic Effect of Heterostructured Dissimilar Metal–Organic Framework Thin Films on Adsorption Properties. *J. Mater. Chem. A* **2020**, *8*, 12990–12995.

(91) Guo, W.; Zha, M.; Wang, Z.; Redel, E.; Xu, Z.; Wöll, C. Improving the Loading Capacity of Metal-Organic Framework Thin Films Using Optimized Linkers. *ACS Appl. Mater. Interfaces* **2016**, *8*, 24699–24702.

(92) Robinson, A. L.; Stavila, V.; Zeitler, T. R.; White, M. I.; Thornberg, S. M.; Greathouse, J. A.; Allendorf, M. D. Ultrasensitive Humidity Detection Using Metal–Organic Framework-Coated Microsensors. *Anal. Chem.* **2012**, *84*, 7043–7051.

(93) Liu, J.; Redel, E.; Walheim, S.; Wang, Z.; Oberst, V.; Liu, J.; Heissler, S.; Welle, A.; Moosmann, M.; Scherer, T.; Bruns, M.; Gliemann, H.; Wöll, C. Monolithic High Performance Surface Anchored Metal-Organic Framework Bragg Reflector for Optical Sensing. *Chem. Mater.* **2015**, *27*, 1991–1996.

(94) Cao, L.-A.; Yao, M.-S.; Jiang, H.-J.; Kitagawa, S.; Ye, X.-L.; Li, W.-H.; Xu, G. A Highly Oriented Conductive MOF Thin Film-Based Schottky Diode for Self-Powered Light and Gas Detection. *J. Mater. Chem. A* **2020**, *8*, 9085–9090.

(95) Heinke, L.; Cakici, M.; Dommaschk, M.; Grosjean, S.; Herges, R.; Bräse, S.; Wöll, C. Photoswitching in Two-Component Surface-Mounted Metal-Organic Frameworks: Optically Triggered Release from a Molecular Container. *ACS Nano* **2014**, *8*, 1463–1467.

(96) Liu, X.; Kozlowska, M.; Okkali, T.; Wagner, D.; Higashino, T.; Brenner-Weiß, G.; Marschner, S. M.; Fu, Z.; Zhang, Q.; Imahori, H.; Bräse, S.; Wenzel, W.; Wöll, C.; Heinke, L. Photoconductivity in Metal–Organic Framework (MOF) Thin Films. *Angew. Chem. Int. Ed.* **2019**, *58*, 9590–9595.

(97) Gu, Z. G.; Chen, Z.; Fu, W. Q.; Wang, F.; Zhang, J. Liquid-Phase Epitaxy Effective Encapsulation of Lanthanide Coordination Compounds into MOF Film with Homogeneous and Tunable White-Light Emission. *ACS Appl Mater Interfaces* **2015**, *7*, 28585–28590.

(98) Li, D. J.; Gu, Z. G.; Zhang, J. Auto-Controlled Fabrication of a Metal-Porphyrin Framework Thin Film with Tunable Optical Limiting Effects. *Chem. Sci.* **2020**, *11*, 1935–1942.

(99) Erickson, K. J.; Léonard, F.; Stavila, V.; Foster, M. E.; Spataru, C. D.; Jones, R. E.; Foley, B. M.; Hopkins, P. E.; Allendorf, M. D.; Talin, A. A. Thin Film Thermoelectric Metal–Organic Framework with High Seebeck Coefficient and Low Thermal Conductivity. *Adv. Mater.* **2015**, *27*, 3453–3459.

(100) Pan, L.; Ji, Z.; Yi, X.; Zhu, X.; Chen, X.; Shang, J.; Liu, G.; Li, R.-W. Metal-Organic Framework Nanofilm for Mechanically Flexible Information Storage Applications. *Adv. Funct. Mater.* **2015**, *25*, 2677–2685.

(101) Ye, L.; Liu, J.; Gao, Y.; Gong, C.; Addicoat, M.; Heine, T.; Wöll, C.; Sun, L. Highly Oriented MOF Thin Film-Based Electrocatalytic Device for the Reduction of CO_2 to CO Exhibiting High Faradaic Efficiency. *J. Mater. Chem. A* **2016**, *4*, 15320–15326.

(102) Meilikhov, M.; Furukawa, S.; Hirai, K.; Fischer, R. A.; Kitagawa, S. Binary Janus Porous Coordination Polymer Coatings for Sensor Devices with Tunable Analyte Affinity. *Angew. Chem. Int. Ed.* **2013**, *52*, 341–345.

(103) Wannapaiboon, S.; Tu, M.; Sumida, K.; Khaletskaya, K.; Furukawa, S.; Kitagawa, S.; Fischer, R. A. Hierarchical Structuring of Metal–Organic Framework Thin-Films on Quartz Crystal Microbalance (QCM) Substrates for Selective Adsorption Applications. *J. Mater. Chem. A* **2015**, *3*, 23385–23394.

(104) Gu, Z. G.; Fu, W. Q.; Wu, X.; Zhang, J. Liquid-Phase Epitaxial Growth of a Homochiral MOF Thin Film on Poly(L-DOPA) Functionalized Substrate for Improved Enantiomer Separation. *Chem Commun* **2016**, *52*, 772–775.

(105) Gu, Z.-G.; Bürck, J.; Bihlmeier, A.; Liu, J.; Shekhah, O.; Weidler, P. G.; Azucena, C.; Wang, Z.; Heissler, S.; Gliemann, H.; Klopper, W.; Ulrich, A. S.; Wöll, C. Oriented Circular Dichroism Analysis of Chiral Surface-Anchored Metal-Organic Frameworks Grown by Liquid-Phase Epitaxy and upon Loading with Chiral Guest Compounds. *Chem. - A Eur. J.* **2014**, *20*, 9879–9882.

(106) Gu, Z.-G.; Fu, W.-Q.; Liu, M.; Zhang, J. Surface-Mounted MOF Templated Fabrication of Homochiral Polymer Thin Film for Enantioselective Adsorption of Drugs. *Chem. Commun.* **2017**, *53*, 1470–1473.

(107) Li, D. J.; Gu, Z. G.; Vohra, I.; Kang, Y.; Zhu, Y. S.; Zhang, J. Epitaxial Growth of Oriented Metalloporphyrin Network Thin Film for Improved Selectivity of Volatile Organic Compounds. *Small* **2017**, *13*.

(108) Stavila, V.; Schneider, C.; Mowry, C.; Zeitler, T. R.; Greathouse, J. A.; Robinson, A. L.; Denning, J. M.; Volponi, J.; Leong, K.; Quan, W.; Tu, M.; Fischer, R. A.; Allendorf, M. D. Thin Film Growth of Nbo MOFs and Their Integration with Electroacoustic Devices. *Adv. Funct. Mater.* **2016**, *26*, 1699–1707.

(109) Wu, A.-Q.; Wang, W.-Q.; Zhan, H.-B.; Cao, L.-A.; Ye, X.-L.; Zheng, J.-J.; Kumar, P. N.;

Chiranjeevulu, K.; Deng, W.-H.; Wang, G.-E.; Yao, M.-S.; Xu, G. Layer-by-Layer Assembled Dual-Ligand Conductive MOF Nano-Films with Modulated Chemiresistive Sensitivity and Selectivity. *Nano Res.* **2020**.

(110) Okur, S.; Zhang, Z.; Sarheed, M.; Nick, P.; Lemmer, U.; Heinke, L. Towards a MOF E-Nose: A SURMOF Sensor Array for Detection and Discrimination of Plant Oil Scents and Their Mixtures. *Sensors Actuators, B Chem.* **2020**, *306*, 127502.

(111) Wang, Z.; Knebel, A.; Grosjean, S.; Wagner, D.; Brase, S.; Woll, C.; Caro, J.; Heinke, L. Tunable Molecular Separation by Nanoporous Membranes. *Nat Commun* **2016**, *7*, 13872.

(112) So, M. C.; Jin, S.; Son, H.-J.; Wiederrecht, G. P.; Farha, O. K.; Hupp, J. T. Layer-by-Layer Fabrication of Oriented Porous Thin Films Based on Porphyrin-Containing Metal–Organic Frameworks. *J. Am. Chem. Soc.* **2013**, *135*, 15698–15701.

(113) Oldenburg, M.; Turshatov, A.; Busko, D.; Jakoby, M.; Haldar, R.; Chen, K.; Emandi, G.; Senge, M. O.; Wöll, C.; Hodgkiss, J. M.; Richards, B. S.; Howard, I. A. Enhancing the Photoluminescence of Surface Anchored Metal-Organic Frameworks: Mixed Linkers and Efficient Acceptors. *Phys. Chem. Chem. Phys.* **2018**, *20*, 11564–11576.

(114) Yu, X.; Wang, Z.; Buchholz, M.; Fullgrabe, N.; Grosjean, S.; Bebensee, F.; Brase, S.; Woll, C.; Heinke, L. Cis-to-Trans Isomerization of Azobenzene Investigated by Using Thin Films of Metal-Organic Frameworks. *Phys Chem Chem Phys* **2015**, *17*, 22721–22725.

(115) Wang, Z.; Müller, K.; Valášek, M.; Grosjean, S.; Bräse, S.; Wöll, C.; Mayor, M.; Heinke, L. Series of Photoswitchable Azobenzene-Containing Metal–Organic Frameworks with Variable Adsorption Switching Effect. *J. Phys. Chem. C* **2018**, *122*, 19044–19050.

(116) Muller, K.; Helfferich, J.; Zhao, F.; Verma, R.; Kanj, A. B.; Meded, V.; Bleger, D.; Wenzel, W.; Heinke, L. Switching the Proton Conduction in Nanoporous, Crystalline Materials by Light. *Adv Mater* **2018**, *30*.

(117) Liu, J.; Zhou, W.; Liu, J.; Fujimori, Y.; Higashino, T.; Imahori, H.; Jiang, X.; Zhao, J.; Sakurai, T.; Hattori, Y.; Matsuda, W.; Seki, S.; Garlapati, S. K.; Dasgupta, S.; Redel, E.; Sun, L.; et al. A New Class of Epitaxial Porphyrin Metal–Organic Framework Thin Films with Extremely High Photocarrier Generation Efficiency: Promising Materials for All-Solid-State Solar Cells. *J. Mater. Chem. A* **2016**, *4*, 12739–12747.

(118) Liu, B.; Ma, M.; Zacher, D.; Bétard, A.; Yusenko, K.; Metzler-Nolte, N.; Wöll, C.; Fischer, R. A. Chemistry of SURMOFs: Layer-Selective Installation of Functional Groups and Post-Synthetic Covalent Modification Probed by Fluorescence Microscopy. *J. Am. Chem. Soc.* **2011**, *133*, 1734–1737.

(119) Baroni, N.; Turshatov, A.; Adams, M.; Dolgopolova, E. A.; Schlisske, S.; Hernandez-Sosa, G.; Wöll, C.; Shustova, N. B.; Richards, B. S.; Howard, I. A. Inkjet-Printed Photoluminescent Patterns of Aggregation-Induced-Emission Chromophores on Surface-Anchored Metal–Organic Frameworks. *ACS Appl. Mater. Interfaces* **2018**, *10*, 25754–25762.

(120) Chen, D.; Haldar, R.; Neumeier, B. L.; Fu, Z.; Feldmann, C.; Wöll, C.; Redel, E. Tunable Emission in Heteroepitaxial Ln-SURMOFs. *Adv. Funct. Mater.* **2019**, *29*, 1903086.

(121) Liu, J.; Wächter, T.; Irmler, A.; Weidler, P. G.; Gliemann, H.; Pauly, F.; Mugnaini, V.; Zharnikov, M.; Wöll, C. Electric Transport Properties of Surface-Anchored Metal-Organic Frameworks and the Effect of Ferrocene Loading. *ACS Appl. Mater. Interfaces* **2015**, *7*, 9824–9830.

(122) Wang, Z.; Nminibapiel, D.; Shrestha, P.; Liu, J.; Guo, W.; Weidler, P. G.; Baumgart, H.; Wöll, C.; Redel, E. Resistive Switching Nanodevices Based on Metal-Organic Frameworks. *ChemNanoMat* **2016**, *2*, 67–73.

(123) Thürmer, K.; Schneider, C.; Stavila, V.; Friddle, R. W.; Léonard, F.; Fischer, R. A.; Allendorf, M. D.; Talin, A. A. Surface Morphology and Electrical Properties of Cu_3BTC_2 Thin Films Before and After Reaction with TCNQ. *ACS Appl. Mater. Interfaces* **2018**, *10*, 39400–39410.

(124) Lee, D. Y.; Kim, E. K.; Shrestha, N. K.; Boukhvalov, D. W.; Lee, J. K.; Han, S. H. Charge Transfer-Induced Molecular Hole Doping into Thin Film of Metal-Organic Frameworks. *ACS Appl Mater Interfaces* **2015**, *7*, 18501–18507.

(125) Klyatskaya, S.; Kanj, A. B.; Molina-Jirón, C.; Heidrich, S.; Velasco, L.; Natzeck, C.; Gliemann, H.; Heissler, S.; Weidler, P.; Wenzel, W.; Bufon, C. C. B.; Heinke, L.; Wöll, C.; Ruben, M. Conductive Metal–Organic Framework Thin Film Hybrids by Electropolymerization of Monosubstituted Acetylenes. *ACS Appl. Mater. Interfaces* **2020**, *12*, 30972–30979.

(126) Chua, L. Memristor-The Missing Circuit Element. *IEEE Trans. Circuit Theory* **1971**, *18*, 507–519.

(127) Albano, L. G. S.; Vello, T. P.; De Camargo, D. H. S.; Da Silva, R. M. L.; Padilha, A. C. M.; Fazzio, A.; Bufon, C. C. B. Ambipolar Resistive Switching in an Ultrathin Surface-Supported Metal-Organic Framework Vertical Heterojunction. *Nano Lett.* **2020**, *20*, 1080–1088.

(128) Zhao, Q.; Fan, Y.; Zhang, Y.; Liu, J.; Li, W.; Weng, Y. Copper-Based SURMOFs for Nitric Oxide Generation: Hemocompatibility, Vascular Cell Growth, and Tissue Response. *ACS Appl Mater Interfaces* **2019**, *11*, 7872–7883.

(129) Gu, Z.-G.; Zhang, D.-X.; Fu, W.-Q.; Fu, Z.-H.; Vohra, M. I.; Zhang, L.; Wöll, C.; Zhang, J. Facile Synthesis of Metal-Loaded Porous Carbon Thin Films via Carbonization of Surface-Mounted Metal–Organic Frameworks. *Inorg. Chem.* **2017**, *56*, 3526–3531.

(130) Jia, G.; Zhang, W.; Fan, G.; Li, Z.; Fu, D.; Hao, W.; Yuan, C.; Zou, Z. Three-Dimensional Hierarchical Architectures Derived from Surface-Mounted Metal-Organic Framework Membranes for Enhanced Electrocatalysis. *Angew. Chem. Int. Ed.* **2017**, *56*, 13781–13785.

(131) Chen, H.; Gu, Z. G.; Mirza, S.; Zhang, S. H.; Zhang, J. Hollow Cu-TiO_2/C Nanospheres Derived from a Ti Precursor Encapsulated MOF Coating for Efficient Photocatalytic Hydrogen Evolution. *J. Mater. Chem. A* **2018**, *6*, 7175–7181.

(132) Begum, S.; Hashem, T.; Tsotsalas, M.; Wöll, C.; Alkordi, M. H. Electrolytic Conversion of Sacrificial Metal–Organic Framework Thin Films into an Electrocatalytically Active Monolithic Oxide Coating for the Oxygen-Evolution Reaction. *Energy Technol.* **2019**, *7*, 1900967.

(133) Lei, S.; Li, Q.-H.; Kang, Y.; Gu, Z.-G.; Zhang, J. Epitaxial Growth of Oriented Prussian

Blue Analogue Derived Well-Aligned $CoFe_2O_4$ Thin Film for Efficient Oxygen Evolution Reaction. *Appl. Catal. B Environ.* **2019**, *245*, 1–9.

(134) De Luna, P.; Liang, W.; Mallick, A.; Shekhah, O.; García de Arquer, F. P.; Proppe, A. H.; Todorović, P.; Kelley, S. O.; Sargent, E. H.; Eddaoudi, M. Metal–Organic Framework Thin Films on High-Curvature Nanostructures Toward Tandem Electrocatalysis. *ACS Appl. Mater. Interfaces* **2018**, *10*, 31225–31232.

(135) Yoo, H.; Welle, A.; Guo, W.; Choi, J.; Redel, E. Electrodeposition of WO_3 Nanoparticles into Surface Mounted Metal-Organic Framework HKUST-1 Thin Films. *Nanotechnology* **2017**, *28*, 115605.

(136) Wang, D.-W.; Zhu, Y.-D.; Lei, S.; Chen, S.-M.; Gu, Z.-G.; Zhang, J. Epitaxial Growth of Prussian Blue Analogue Derived NiFeP Thin Film for Efficient Electrocatalytic Hydrogen Evolution Reaction. *J. Solid State Chem.* **2021**, *293*, 121779.

(137) Zhuang, J. L.; Kind, M.; Grytz, C. M.; Farr, F.; Diefenbach, M.; Tussupbayev, S.; Holthausen, M. C.; Terfort, A. Insight into the Oriented Growth of Surface-Attached Metal-Organic Frameworks: Surface Functionality, Deposition Temperature, and First Layer Order. *J. Am. Chem. Soc.* **2015**, *137*, 8237–8243.

(138) Summerfield, A.; Cebula, I.; Schröder, M.; Beton, P. H. Nucleation and Early Stages of Layer-by-Layer Growth of Metal Organic Frameworks on Surfaces. *J. Phys. Chem. C* **2015**, *119*, 23544–23551.

(139) Ohnsorg, M. L.; Beaudoin, C. K.; Anderson, M. E. Fundamentals of MOF Thin Film Growth via Liquid-Phase Epitaxy: Investigating the Initiation of Deposition and the Influence of Temperature. *Langmuir* **2015**, *31*, 6114–6121.

(140) Shekhah, O.; Wang, H.; Zacher, D.; Fischer, R. A.; Wöll, C. Growth Mechanism of Metal-Organic Frameworks: Insights into the Nucleation by Employing a Step-by-Step Route. *Angew. Chem. Int. Ed.* **2009**, *48*, 5038–5041.

(141) Li, Q.; Gies, J.; Yu, X. J.; Gu, Y.; Terfort, A.; Kind, M. Concentration-Dependent Seeding as a Strategy for Fabrication of Densely Packed Surface-Mounted Metal–Organic Frameworks (SURMOF) Layers. *Chem. - A Eur. J.* **2020**, *26*, 5185–5189.

(142) Wang, Z.; Rodewald, K.; Medishetty, R.; Rieger, B.; Fischer, R. A. Control of Water Content for Enhancing the Quality of Copper Paddle-Wheel-Based Metal-Organic Framework Thin Films Grown by Layer-by-Layer Liquid-Phase Epitaxy. *Cryst. Growth Des.* **2018**, *18*, 7451–7459.

(143) Wannapaiboon, S.; Sumida, K.; Dilchert, K.; Tu, M.; Kitagawa, S.; Furukawa, S.; Fischer, R. A. Enhanced Properties of Metal–Organic Framework Thin Films Fabricated via a Coordination Modulation-Controlled Layer-by-Layer Process. *J. Mater. Chem. A* **2017**, *5*, 13665–13673.

(144) Yu, X.-J.; Zhuang, J.-L.; Scherr, J.; Abu-Husein, T.; Terfort, A. Minimization of Surface Energies and Ripening Outcompete Template Effects in the Surface Growth of Metal-Organic Frameworks. *Angew. Chem. Int. Ed.* **2016**, *55*, 8348–8352.

(145) Wang, Z.; Weidler, P. G.; Azucena, C.; Heinke, L.; Wöll, C. Negative, Anisotropic Thermal Expansion in Monolithic Thin Films of Crystalline Metal-Organic Frameworks. *Microporous Mesoporous Mater.* **2016**, *222*, 241–246.

(146) Cavka, J. H.; Jakobsen, S.; Olsbye, U.; Guillou, N.; Lamberti, C.; Bordiga, S.; Lillerud, K.

P. A New Zirconium Inorganic Building Brick Forming Metal Organic Frameworks with Exceptional Stability. *J. Am. Chem. Soc.* **2008**, *130*, 13850–13851.

(147) DeCoste, J. B.; Peterson, G. W.; Jasuja, H.; Glover, T. G.; Huang, Y.; Walton, K. S. Stability and Degradation Mechanisms of Metal–Organic Frameworks Containing the $Zr_6O_4(OH)_4$ Secondary Building Unit. *J. Mater. Chem. A* **2013**, *1*, 5642.

(148) Dhakshinamoorthy, A.; Alvaro, M.; Corma, A.; Garcia, H. Delineating Similarities and Dissimilarities in the Use of Metal Organic Frameworks and Zeolites as Heterogeneous Catalysts for Organic Reactions. *Dalt. Trans.* **2011**, *40*, 6344–6360.

(149) Mondloch, J. E.; Katz, M. J.; Planas, N.; Semrouni, D.; Gagliardi, L.; Hupp, J. T.; Farha, O. K. Are Zr_6-Based MOFs Water Stable? Linker Hydrolysis vs. Capillary-Force-Driven Channel Collapse. *Chem. Commun.* **2014**, *50*, 8944–8946.

(150) Dissegna, S.; Vervoorts, P.; Hobday, C. L.; Düren, T.; Daisenberger, D.; Smith, A. J.; Fischer, R. A.; Kieslich, G. Tuning the Mechanical Response of Metal–Organic Frameworks by Defect Engineering. *J. Am. Chem. Soc.* **2018**, *140*, 11581–11584.

(151) Hobday, C. L.; Marshall, R. J.; Murphie, C. F.; Sotelo, J.; Richards, T.; Allan, D. R.; Düren, T.; Coudert, F.-X.; Forgan, R. S.; Morrison, C. A.; Moggach, S. A.; Bennett, T. D. A Computational and Experimental Approach Linking Disorder, High-Pressure Behavior, and Mechanical Properties in UiO Frameworks. *Angew. Chem. Int. Ed.* **2016**, *55*, 2401–2405.

(152) Cavka, J. H.; Jakobsen, S.; Olsbye, U.; Guillou, N.; Lamberti, C.; Bordiga, S.; Lillerud, K. P. A New Zirconium Inorganic Building Brick Forming Metal Organic Frameworks with Exceptional Stability. *J. Am. Chem. Soc.* **2008**, *130*, 13850–13851.

(153) Research of "UiO-66" at www.scifinder.cas.org.

(154) Desidery, L.; Chaemcheun, S.; Yusubov, M.; Verpoort, F. Di-Methyl Carbonate Transesterification with EtOH over MOFs: Basicity and Synergic Effect of Basic and Acid Active Sites. *Catal. Commun.* **2018**, *104*, 82–85.

(155) Fang, Z.; Bueken, B.; De Vos, D. E.; Fischer, R. A. Defect-Engineered Metal-Organic Frameworks. *Angew. Chem. Int. Ed.* **2015**, *54*, 7234–7254.

(156) Mondal, S. S.; Holdt, H.-J. Breaking Down Chemical Weapons by Metal-Organic Frameworks. *Angew. Chem. Int. Ed.* **2016**, *55*, 42–44.

(157) Zhao, J.; Lee, D. T.; Yaga, R. W.; Hall, M. G.; Barton, H. F.; Woodward, I. R.; Oldham, C. J.; Walls, H. J.; Peterson, G. W.; Parsons, G. N. Ultra-Fast Degradation of Chemical Warfare Agents Using MOF-Nanofiber Kebabs. *Angew. Chem. Int. Ed.* **2016**, *55*, 13224–13228.

(158) Li, P.; Klet, R. C.; Moon, S.-Y.; Wang, T. C.; Deria, P.; Peters, A. W.; Klahr, B. M.; Park, H.-J.; Al-Juaid, S. S.; Hupp, J. T.; Farha, O. K. Synthesis of Nanocrystals of Zr-Based Metal–Organic Frameworks with Csq-Net: Significant Enhancement in the Degradation of a Nerve Agent Simulant. *Chem. Commun.* **2015**, *51*, 10925–10928.

(159) Islamoglu, T.; Ortuño, M. A.; Proussaloglou, E.; Howarth, A. J.; Vermeulen, N. A.; Atilgan, A.; Asiri, A. M.; Cramer, C. J.; Farha, O. K. Presence versus Proximity: The Role of Pendant Amines in the Catalytic Hydrolysis of a Nerve Agent Simulant. *Angew. Chem. Int. Ed.* **2018**, *57*, 1949–1953.

(160) Wang, Y.; Zhang, W.; Guo, J.; Duan, W.; Liu, B. Synthesis of Well-Defined Internal-Space-Controllable UiO-66 Spherical Nanostructures Used as Advanced Nanoreactor. *ACS Appl. Mater. Interfaces* **2019**, *11*, 38016–38022.

(161) Nguyen, K. D.; Kutzscher, C.; Ehrling, S.; Senkovska, I.; Bon, V.; de Oliveira, M.; Gutmann, T.; Buntkowsky, G.; Kaskel, S. Insights into the Role of Zirconium in Proline Functionalized Metal-Organic Frameworks Attaining High Enantio- and Diastereoselectivity. *J. Catal.* **2019**, *377*, 41–50.

(162) Kurisingal, J. F.; Rachuri, Y.; Gu, Y.; Kim, G.; Park, D. Binary Metal-Organic Frameworks: Catalysts for the Efficient Solvent-Free CO_2 Fixation Reaction via Cyclic Carbonates Synthesis. *Appl. Catal. A Gen.* **2019**, *571*, 1–11.

(163) Noh, J.; Kim, Y.; Park, H.; Lee, J.; Yoon, M.; Park, M. H.; Kim, Y.; Kim, M. Functional Group Effects on a Metal-Organic Framework Catalyst for CO_2 Cycloaddition. *J. Ind. Eng. Chem.* **2018**, *64*, 478–483.

(164) de Mello, M. D.; Tsapatsis, M. Selective Glucose-to-Fructose Isomerization over Modified Zirconium UiO-66 in Alcohol Media. *ChemCatChem* **2018**, *10*, 2417–2423.

(165) Vermoortele, F.; Bueken, B.; Le Bars, G.; Van de Voorde, B.; Vandichel, M.; Houthoofd, K.; Vimont, A.; Daturi, M.; Waroquier, M.; Van Speybroeck, V.; Kirschhock, C.; De Vos, D. E. Synthesis Modulation as a Tool To Increase the Catalytic Activity of Metal–Organic Frameworks: The Unique Case of UiO-66(Zr). *J. Am. Chem. Soc.* **2013**, *135*, 11465–11468.

(166) Dissegna, S.; Hardian, R.; Epp, K.; Kieslich, G.; Coulet, M.-V.; Llewellyn, P.; Fischer, R. A. Using Water Adsorption Measurements to Access the Chemistry of Defects in the Metal–Organic Framework UiO-66. *CrystEngComm* **2017**, *19*, 4137–4141.

(167) Jin, F.-Z.; Zhao, C.-C.; Ma, H.-C.; Chen, G.-J.; Dong, Y.-B. Homochiral BINAPDA-Zr-MOF for Heterogeneous Asymmetric Cyanosilylation of Aldehydes. *Inorg. Chem.* **2019**, *58*, 9253–9259.

(168) Xi, F.-G.; Yang, Y.; Liu, H.; Yao, H.-F.; Gao, E.-Q. Different Acidity and Additive Effects of Zirconium Metal–Organic Frameworks as Catalysts for Cyanosilylation. *RSC Adv.* **2015**, *5*, 79216–79223.

(169) Liu, T.-Y.; Yuan, H.; Liu, Y.; Ren, D.; Su, Y.; Wang, X. Metal–Organic Framework Nanocomposite Thin Films with Interfacial Bindings and Self-Standing Robustness for High Water Flux and Enhanced Ion Selectivity. *ACS Nano* **2018**, *12*, 9253–9265.

(170) Zhang, C.; Zhao, Y.; Li, Y.; Zhang, X.; Chi, L.; Lu, G. Defect-Controlled Preparation of UiO-66 Metal-Organic Framework Thin Films with Molecular Sieving Capability. *Chem. - An Asian J.* **2016**, *11*, 207–210.

(171) Aghili, F.; Ghoreyshi, A. A.; Rahimpour, A.; Van der Bruggen, B. New Chemistry for Mixed Matrix Membranes: Growth of Continuous Multilayer UiO-66-NH_2 on UiO-66-NH_2-Based Polyacrylonitrile for Highly Efficient Separations. *Ind. Eng. Chem. Res.* **2020**, *59*, 7825–7838.

(172) Schaate, A.; Roy, P.; Godt, A.; Lippke, J.; Waltz, F.; Wiebcke, M.; Behrens, P. Modulated Synthesis of Zr-Based Metal-Organic Frameworks: From Nano to Single Crystals. *Chem. - A Eur. J.* **2011**, *17*, 6643–6651.

(173) Guillerm, V.; Gross, S.; Serre, C.; Devic, T.; Bauer, M.; Férey, G. A Zirconium

Methacrylate Oxocluster as Precursor for the Low-Temperature Synthesis of Porous Zirconium(IV) Dicarboxylates. *Chem. Commun.* **2010**, *46*, 767–769.

(174) Kim, S.-I.; Yoon, T.-U.; Kim, M.-B.; Lee, S.-J.; Hwang, Y. K.; Chang, J.-S.; Kim, H.-J.; Lee, H.-N.; Lee, U.-H.; Bae, Y.-S. Metal–Organic Frameworks with High Working Capacities and Cyclic Hydrothermal Stabilities for Fresh Water Production. *Chem. Eng. J.* **2016**, *286*, 467–475.

(175) Azarifar, D.; Ghorbani-Vaghei, R.; Daliran, S.; Oveisi, A. R. A Multifunctional Zirconium-Based Metal-Organic Framework for the One-Pot Tandem Photooxidative Passerini Three-Component Reaction of Alcohols. *ChemCatChem* **2017**, *9*, 1992–2000.

(176) Lee, D. T.; Zhao, J.; Peterson, G. W.; Parsons, G. N. Catalytic "MOF-Cloth" Formed via Directed Supramolecular Assembly of UiO-66-NH_2 Crystals on Atomic Layer Deposition-Coated Textiles for Rapid Degradation of Chemical Warfare Agent Simulants. *Chem. Mater.* **2017**, *29*, 4894–4903.

(177) Amer Hamzah, H.; Crickmore, T. S.; Rixson, D.; Burrows, A. D. Post-Synthetic Modification of Zirconium Metal–Organic Frameworks by Catalyst-Free Aza-Michael Additions. *Dalt. Trans.* **2018**, *47*, 14491–14496.

(178) Valenzano, L.; Civalleri, B.; Chavan, S.; Bordiga, S.; Nilsen, M. H.; Jakobsen, S.; Lillerud, K. P.; Lamberti, C. Disclosing the Complex Structure of UiO-66 Metal Organic Framework: A Synergic Combination of Experiment and Theory. *Chem. Mater.* **2011**, *23*, 1700–1718.

(179) Shearer, G. C.; Chavan, S.; Bordiga, S.; Svelle, S.; Olsbye, U.; Lillerud, K. P. Defect Engineering: Tuning the Porosity and Composition of the Metal-Organic Framework UiO-66 via Modulated Synthesis. *Chem. Mater.* **2016**, *28*, 3749–3761.

(180) Gómez-Gualdrón, D. A.; Moghadam, P. Z.; Hupp, J. T.; Farha, O. K.; Snurr, R. Q. Application of Consistency Criteria to Calculate BET Areas of Micro- and Mesoporous Metal-Organic Frameworks. *J. Am. Chem. Soc.* **2016**, *138*, 215–224.

(181) Verpoort, F.; Haemers, T.; Roose, P.; Maes, J. P. Characterization of a Surface Coating Formed from Carboxylic Acid-Based Coolants. *Appl. Spectrosc.* **1999**, *53*, 1528–1534.

(182) Zybaylo, O.; Shekhah, O.; Wang, H.; Tafipolsky, M.; Schmid, R.; Johannsmann, D.; Wöll, C. A Novel Method to Measure Diffusion Coefficients in Porous Metal–Organic Frameworks. *Phys. Chem. Chem. Phys.* **2010**, *12*, 8092.

(183) Carvalho, R. R.; Pujari, S. P.; Vrouwe, E. X.; Zuilhof, H. Mild and Selective C–H Activation of COC Microfluidic Channels Allowing Covalent Multifunctional Coatings. *ACS Appl. Mater. Interfaces* **2017**, *9*, 16644–16650.

(184) Cliffe, M. J.; Wan, W.; Zou, X.; Chater, P. A.; Kleppe, A. K.; Tucker, M. G.; Wilhelm, H.; Funnell, N. P.; Coudert, F.-X.; Goodwin, A. L. Correlated Defect Nanoregions in a Metal–Organic Framework. *Nat. Commun.* **2014**, *5*, 4176.

(185) Lee, S.-J.; Mancuso, J. L.; Le, K. N.; Malliakas, C. D.; Bae, Y.-S.; Hendon, C. H.; Islamoglu, T.; Farha, O. K. Time-Resolved in Situ Polymorphic Transformation from One 12-Connected Zr-MOF to Another. *ACS Mater. Lett.* **2020**, *2*, 499–504.

(186) Perfecto-Irigaray, M.; Beobide, G.; Castillo, O.; da Silva, I.; García-Lojo, D.; Luque, A.; Mendia, A.; Pérez-Yáñez, S. $[Zr_6O_4(OH)_4(\text{Benzene-1,4-Dicarboxylato})_6]_n$: A Hexagonal Polymorph of UiO-66. *Chem. Commun.* **2019**, *55*, 5954–5957.

(187) Hod, I.; Bury, W.; Karlin, D. M.; Deria, P.; Kung, C.-W.; Katz, M. J.; So, M.; Klahr, B.; Jin, D.; Chung, Y.-W.; Odom, T. W.; Farha, O. K.; Hupp, J. T. Directed Growth of Electroactive Metal-Organic Framework Thin Films Using Electrophoretic Deposition. *Adv. Mater.* **2014**, *26*, 6295–6300.

(188) Fei, H.; Pullen, S.; Wagner, A.; Ott, S.; Cohen, S. M. Functionalization of Robust Zr(IV)-Based Metal-Organic Framework Films via a Postsynthetic Ligand Exchange. *Chem. Commun.* **2015**, *51*, 66–69.

(189) Paredes, V.; Salvagni, E.; Rodríguez-Castellón, E.; Manero, J. M. Comparative Study of Surface Chemical Composition and Oxide Layer Modification upon Oxygen Plasma Cleaning and Piranha Etching on a Novel Low Elastic Modulus $Ti_{25}Nb_{21}Hf$ Alloy. *Metall. Mater. Trans. A* **2017**, *48*, 3770–3776.

(190) Wang, Y.; Li, L.; Dai, P.; Yan, L.; Cao, L.; Gu, X.; Zhao, X. Missing-Node Directed Synthesis of Hierarchical Pores on a Zirconium Metal–Organic Framework with Tunable Porosity and Enhanced Surface Acidity via a Microdroplet Flow Reaction. *J. Mater. Chem. A* **2017**, *5*, 22372–22379.

(191) Gong, Y.; Gao, S.; Tian, Y.; Zhu, Y.; Fang, W.; Wang, Z.; Jin, J. Thin-Film Nanocomposite Nanofiltration Membrane with an Ultrathin Polyamide/UiO-66-NH_2 Active Layer for High-Performance Desalination. *J. Memb. Sci.* **2020**, *600*, 117874.

(192) He, Y.; Tang, Y. P.; Ma, D.; Chung, T. UiO-66 Incorporated Thin-Film Nanocomposite Membranes for Efficient Selenium and Arsenic Removal. *J. Memb. Sci.* **2017**, *541*, 262–270.

(193) Xu, T.; Shehzad, M. A.; Yu, D.; Li, Q.; Wu, B.; Ren, X.; Ge, L.; Xu, T. Highly Cation Permselective Metal–Organic Framework Membranes with Leaf-Like Morphology. *ChemSusChem* **2019**, *12*, 2593–2597.

(194) Golpour, M.; Pakizeh, M. Preparation and Characterization of New PA-MOF/PPSU-GO Membrane for the Separation of KHI from Water. *Chem. Eng. J.* **2018**, *345*, 221–232.

(195) Fang, S.; Zhang, P.; Gong, J.; Tang, L.; Zeng, G.; Song, B.; Cao, W.; Li, J.; Ye, J. Construction of Highly Water-Stable Metal-Organic Framework UiO-66 Thin-Film Composite Membrane for Dyes and Antibiotics Separation. *Chem. Eng. J.* **2020**, *385*, 123400.

(196) Hashem, T.; Valadez Sánchez, E. P.; Weidler, P. G.; Gliemann, H.; Alkordi, M. H.; Wöll, C. Liquid-Phase Quasi-Epitaxial Growth of Highly Stable, Monolithic UiO-66-NH_2 MOF Thin Films on Solid Substrates. *ChemistryOpen* **2020**, *9*, 524–527.

(197) *Catalytic Process Technology*; National Academies Press: Washington, D.C., 2000.

(198) Centi, G.; Perathoner, S. Creating and Mastering Nano-Objects to Design Advanced Catalytic Materials. *Coord. Chem. Rev.* **2011**, *255*, 1480–1498.

(199) Liu, Q.; Song, Y.; Ma, Y.; Zhou, Y.; Cong, H.; Wang, C.; Wu, J.; Hu, G.; O'Keeffe, M.; Deng, H. Mesoporous Cages in Chemically Robust MOFs Created by a Large Number of Vertices with Reduced Connectivity. *J. Am. Chem. Soc.* **2019**, *141*, 488–496.

(200) Gándara, F.; Gómez-Lor, B.; Iglesias, M.; Snejko, N.; Gutiérrez-Puebla, E.; Monge, A. A New Scandium Metal Organic Framework Built up from Octadecasil Zeolitic Cages as Heterogeneous Catalyst. *Chem. Commun.* **2009**, No. 17, 2393.

(201) Wang, T.; Gao, L.; Hou, J.; Herou, S. J. A.; Griffiths, J. T.; Li, W.; Dong, J.; Gao, S.; Titirici, M. M.; Kumar, R. V.; Cheetham, A. K.; Bao, X.; Fu, Q.; Smoukov, S. K. Rational Approach to Guest Confinement inside MOF Cavities for Low-Temperature Catalysis. *Nat. Commun.* **2019**, *10*, 1–9.

(202) Goswami, S.; Yu, J.; Patwardhan, S.; Deria, P.; Hupp, J. T. Light-Harvesting "Antenna" Behavior in NU-1000. *ACS Energy Lett.* **2021**, *6*, 848–853.

(203) Horike, S.; Umeyama, D.; Kitagawa, S. Ion Conductivity and Transport by Porous Coordination Polymers and Metal–Organic Frameworks. *Acc. Chem. Res.* **2013**, *46*, 2376–2384.

(204) Rösler, C.; Esken, D.; Wiktor, C.; Kobayashi, H.; Yamamoto, T.; Matsumura, S.; Kitagawa, H.; Fischer, R. A. Encapsulation of Bimetallic Nanoparticles into a Metal-Organic Framework: Preparation and Microstructure Characterization of Pd/Au@ZIF-8. *Eur. J. Inorg. Chem.* **2014**, *2014*, 5514–5521.

(205) Rösler, C.; Fischer, R. a. Metal–Organic Frameworks as Hosts for Nanoparticles. *CrystEngComm* **2015**, *17*, 199–217.

(206) Semrau, A. L.; Pujari, S. P.; Stanley, P. M.; Wannapaiboon, S.; Albada, B.; Zuilhof, H.; Fischer, R. A. Selective Positioning of Nanosized Metal–Organic Framework Particles at Patterned Substrate Surfaces. *Chem. Mater.* **2020**, *32*, 9954–9963.

(207) Orr, K. W. P.; Collins, S. M.; Reynolds, E. M.; Nightingale, F.; Boström, H. L. B.; Cassidy, S. J.; Dawson, D. M.; Ashbrook, S. E.; Magdysyuk, O. V; Midgley, P. A.; Goodwin, A. L.; Yeung, H. H.-M. Single-Step Synthesis and Interface Tuning of Core–Shell Metal–Organic Framework Nanoparticles. *Chem. Sci.* **2021**.

(208) Wu, M.-X.; Wang, Y.; Zhou, G.; Liu, X. Core–Shell MOFs@MOFs: Diverse Designability and Enhanced Selectivity. *ACS Appl. Mater. Interfaces* **2020**, *12*, 54285–54305.

(209) Vong, T.; Schoffelen, S.; van Dongen, S. F. M.; van Beek, T. A.; Zuilhof, H.; van Hest, J. C. M. A DNA-Based Strategy for Dynamic Positional Enzyme Immobilization inside Fused Silica Microchannels. *Chem. Sci.* **2011**, *2*, 1278.

(210) Vriezema, D. M.; Garcia, P. M. L.; Sancho Oltra, N.; Hatzakis, N. S.; Kuiper, S. M.; Nolte, R. J. M.; Rowan, A. E.; van Hest, J. C. M. Positional Assembly of Enzymes in Polymersome Nanoreactors for Cascade Reactions. *Angew. Chem. Int. Ed.* **2007**, *46*, 7378–7382.

(211) Wang, J.; Zhu, M.; Shen, X.; Li, S. A Cascade-Reaction Nanoreactor Composed of a Bifunctional Molecularly Imprinted Polymer That Contains Pt Nanoparticles. *Chem. - A Eur. J.* **2015**, *21*, 7532–7539.

(212) Kitagawa, H.; Tanaka, S. Iron-Related Defect Model in n-Type Silicon Based on the Electrical and Diffusion Properties. *Phys. B Condens. Matter* **1999**, *273–274*, 416–419.

(213) Gupta, R. K.; Birbilis, N. The Influence of Nanocrystalline Structure and Processing Route on Corrosion of Stainless Steel: A Review. *Corros. Sci.* **2015**, *92*, 1–15.

(214) Campos, M. A. C.; Paulusse, J. M. J.; Zuilhof, H. Functional Monolayers on Oxide-Free Silicon Surfaces via Thiol–Ene Click Chemistry. *Chem. Commun.* **2010**, *46*, 5512–5514.

(215) Zhu, W.; Guo, J.; Agola, J. O.; Croissant, J. G.; Wang, Z.; Shang, J.; Coker, E.;

Motevalli, B.; Zimpel, A.; Wuttke, S.; Brinker, C. J. Metal–Organic Framework Nanoparticle-Assisted Cryopreservation of Red Blood Cells. *J. Am. Chem. Soc.* **2019**, *141*, 7789–7796.

(216) Chadwick, A. V; Sherwood, J. N. Point Defects in Molecular Solids. In *Point Defects in Solids: Volume 2 Semiconductors and Molecular Crystals*; Crawford, J. H., Slifkin, L. M., Eds.; Springer US: Boston, MA, 1975; pp 441–475.

(217) Crocker, A. G. Defects in Crystalline Materials and Their Relation to Mechanical Properties. *Exp. Mech.* **1966**, *6*, 266–272.

(218) St. Petkov, P.; Vayssilov, G. N.; Liu, J.; Shekhah, O.; Wang, Y.; Wöll, C.; Heine, T. Defects in MOFs: A Thorough Characterization. *ChemPhysChem* **2012**, *13*, 2025–2029.

(219) Ameloot, R.; Vermoortele, F.; Hofkens, J.; De Schryver, F. C.; De Vos, D. E.; Roeffaers, M. B. J. Three-Dimensional Visualization of Defects Formed during the Synthesis of Metal-Organic Frameworks: A Fluorescence Microscopy Study. *Angew. Chem. Int. Ed.* **2013**, *52*, 401–405.

(220) Szanyi, J.; Daturi, M.; Clet, G.; Baer, D. R.; Peden, C. H. F. Well-Studied Cu–BTC Still Serves Surprises: Evidence for Facile Cu^{2+}/Cu^{+} Interchange. *Phys. Chem. Chem. Phys.* **2012**, *14*, 4383.

(221) Nijem, N.; Bluhm, H.; Ng, M. L.; Kunz, M.; Leone, S. R.; Gilles, M. K. Cu^{1+} in HKUST-1: Selective Gas Adsorption in the Presence of Water. *Chem. Commun.* **2014**, *50*, 10144–10147.

(222) Barin, G.; Krungleviciute, V.; Gutov, O.; Hupp, J. T.; Yildirim, T.; Farha, O. K. Defect Creation by Linker Fragmentation in Metal–Organic Frameworks and Its Effects on Gas Uptake Properties. *Inorg. Chem.* **2014**, *53*, 6914–6919.

(223) Marx, S.; Kleist, W.; Baiker, A. Synthesis, Structural Properties, and Catalytic Behavior of Cu-BTC and Mixed-Linker Cu-BTC-PyDC in the Oxidation of Benzene Derivatives. *J. Catal.* **2011**, *281*, 76–87.

(224) Liu, Y.; He, L.; Liu, Y.; Liu, J.; Xiong, Y.; Zheng, J.; Tang, Z. Core-Shell Noble-Metal@metal-Organic-Framework Nanoparticles with Highly Selective Sensing Property. *Angew. Chem. Int. Ed.* **2013**, *52*, 3741–3745.

(225) Pumera, M.; Aldavert, M.; Mills, C.; Merkoçi, A.; Alegret, S. Direct Voltammetric Determination of Gold Nanoparticles Using Graphite-Epoxy Composite Electrode. *Electrochim. Acta* **2005**, *50*, 3702–3707.

(226) Khan, I.; Saeed, K.; Khan, I. Nanoparticles: Properties, Applications and Toxicities. *Arab. J. Chem.* **2019**, *12*, 908–931.

(227) Ray, P. C. Size and Shape Dependent Second Order Nonlinear Optical Properties of Nanomaterials and Their Application in Biological and Chemical Sensing. *Chem. Rev.* **2010**, *110*, 5332–5365.

(228) Astruc, D. Introduction: Nanoparticles in Catalysis. *Chem. Rev.* **2020**, *120*, 461–463.

(229) Yang, C. C.; Mai, Y.-W. Thermodynamics at the Nanoscale: A New Approach to the Investigation of Unique Physicochemical Properties of Nanomaterials. *Mater. Sci. Eng. R Reports* **2014**, *79*, 1–40.

(230) Majewski, M. B.; Noh, H.; Islamoglu, T.; Farha, O. K. NanoMOFs: Little Crystallites for Substantial Applications. *J. Mater. Chem. A* **2018**, *6*, 7338–7350.

(231) Troyano, J.; Carne-Sanchez, A.; Avci, C.; Imaza, I.; Maspoch, D. Colloidal Metal–Organic Framework Particles: The Pioneering Case of ZIF-8. *Chem. Soc. Rev.* **2019**, *48*, 5534–5546.

(232) Avci, C.; Imaz, I.; Carné-Sánchez, A.; Pariente, J. A.; Tasios, N.; Pérez-Carvajal, J.; Alonso, M. I.; Blanco, A.; Dijkstra, M.; López, C.; Maspoch, D. Self-Assembly of Polyhedral Metal–Organic Framework Particles into Three-Dimensional Ordered Superstructures. *Nat. Chem.* **2018**, *10*, 78–84.

(233) Zhu, W.; Guo, J.; Agola, J. O.; Croissant, J. G.; Wang, Z.; Shang, J.; Coker, E.; Motevalli, B.; Zimpel, A.; Wuttke, S.; Brinker, C. J. Metal–Organic Framework Nanoparticle-Assisted Cryopreservation of Red Blood Cells. *J. Am. Chem. Soc.* **2019**, *141*, 7789–7796.

(234) Cai, X.; Xie, Z.; Li, D.; Kassymova, M.; Zang, S.; Jiang, H. Nano-Sized Metal-Organic Frameworks: Synthesis and Applications. *Coord. Chem. Rev.* **2020**, *417*, 213366.

(235) Herbst, A.; Khutia, A.; Janiak, C. Brønsted Instead of Lewis Acidity in Functionalized MIL-101Cr MOFs for Efficient Heterogeneous (Nano-MOF) Catalysis in the Condensation Reaction of Aldehydes with Alcohols. *Inorg. Chem.* **2014**, *53*, 7319–7333.

(236) Veerbeek, J.; Huskens, J. Applications of Monolayer-Functionalized H-Terminated Silicon Surfaces: A Review. *Small Methods* **2017**, *1*, 1700072.

(237) Pacchioni, G. A Not-so-Strong Bond. *Nat. Rev. Mater.* **2019**, *4*, 226.

(238) Inkpen, M. S.; Liu, Z.; Li, H.; Campos, L. M.; Neaton, J. B.; Venkataraman, L. Non-Chemisorbed Gold–Sulfur Binding Prevails in Self-Assembled Monolayers. *Nat. Chem.* **2019**, *11*, 351–358.

(239) Efimenko, K.; Wallace, W. E.; Genzer, J. Surface Modification of Sylgard-184 Poly(Dimethyl Siloxane) Networks by Ultraviolet and Ultraviolet/Ozone Treatment. *J. Colloid Interface Sci.* **2002**, *254*, 306–315.

(240) Hillborg, H.; Tomczak, N.; Olàh, A.; Schönherr, H.; Vancso, G. J. Nanoscale Hydrophobic Recovery: A Chemical Force Microscopy Study of UV/Ozone-Treated Cross-Linked Poly(Dimethylsiloxane). *Langmuir* **2004**, *20*, 785–794.

(241) Duffy, D. C.; McDonald, J. C.; Schueller, O. J. A.; Whitesides, G. M. Rapid Prototyping of Microfluidic Systems in Poly(Dimethylsiloxane). *Anal. Chem.* **1998**, *70*, 4974–4984.

(242) Hillborg, H.; Gedde, U. W. Hydrophobicity Recovery of Polydimethylsiloxane after Exposure to Corona Discharges. *Polymer* **1998**, *39*, 1991–1998.

(243) Kim, J.; Chaudhury, M. K.; Owen, M. J. Hydrophobic Recovery of Polydimethylsiloxane Elastomer Exposed to Partial Electrical Discharge. *J. Colloid Interface Sci.* **2000**, *226*, 231–236.

(244) Seu, K. J.; Pandey, A. P.; Haque, F.; Proctor, E. A.; Ribbe, A. E.; Hovis, J. S. Effect of Surface Treatment on Diffusion and Domain Formation in Supported Lipid Bilayers. *Biophys. J.* **2007**, *92*, 2445–2450.

(245) Hu, S.; Ren, X.; Bachman, M.; Sims, C. E.; Li, G. P.; Allbritton, N. Surface Modification of Poly(Dimethylsiloxane) Microfluidic Devices by Ultraviolet Polymer Grafting. *Anal. Chem.* **2002**, *74*, 4117–4123.

(246) Hu, S.; Ren, X.; Bachman, M.; Sims, C. E.; Li, G. P.; Allbritton, N. L. Surface-Directed, Graft Polymerization within Microfluidic Channels. *Anal. Chem.* **2004**, *76*, 1865–1870.

(247) Husseman, M.; Malmström, E. E.; McNamara, M.; Mate, M.; Mecerreyes, D.; Benoit, D. G.; Hedrick, J. L.; Mansky, P.; Huang, E.; Russell, T. P.; Hawker, C. J. Controlled Synthesis of Polymer Brushes by "Living" Free Radical Polymerization Techniques. *Macromolecules* **1999**, *32*, 1424–1431.

(248) Edmondson, S.; Osborne, V. L.; Huck, W. T. S. Polymer Brushes via Surface-Initiated Polymerizations. *Chem. Soc. Rev.* **2004**, *33*, 14–22.

(249) Tsujii, Y.; Ohno, K.; Yamamoto, S.; Goto, A.; Fukuda, T. Structure and Properties of High-Density Polymer Brushes Prepared by Surface-Initiated Living Radical Polymerization; Jordan, R., Ed.; Springer Berlin Heidelberg: Berlin, Heidelberg, 2006; pp 1–45.

(250) Ulman, A. Formation and Structure of Self-Assembled Monolayers. *Chem. Rev.* **1996**, *96*, 1533–1554.

(251) Sagiv, J. Organized Monolayers by Adsorption. 1. Formation and Structure of Oleophobic Mixed Monolayers on Solid Surfaces. *J. Am. Chem. Soc.* **1980**, *102*, 92–98.

(252) Onclin, S.; Ravoo, B. J.; Reinhoudt, D. N. Engineering Silicon Oxide Surfaces Using Self-Assembled Monolayers. *Angew. Chem. Int. Ed.* **2005**, *44*, 6282–6304.

(253) Pujari, S. P.; Scheres, L.; Marcelis, A. T. M.; Zuilhof, H. Covalent Surface Modification of Oxide Surfaces. *Angew. Chem. Int. Ed.* **2014**, *53*, 6322–6356.

(254) Silane: Chemistry, Applications and Performance. **2013**.

(255) Linford, M. R.; Fenter, P.; Eisenberger, P. M.; Chidsey, C. E. D. Alkyl Monolayers on Silicon Prepared from 1-Alkenes and Hydrogen-Terminated Silicon. *J. Am. Chem. Soc.* **1995**, *117*, 3145–3155.

(256) Li, Y.; Calder, S.; Yaffe, O.; Cahen, D.; Haick, H.; Kronik, L.; Zuilhof, H. Hybrids of Organic Molecules and Flat, Oxide-Free Silicon: High-Density Monolayers, Electronic Properties, and Functionalization. *Langmuir* **2012**, *28*, 9920–9929.

(257) Buriak, J. M. Illuminating Silicon Surface Hydrosilylation: An Unexpected Plurality of Mechanisms. *Chem. Mater.* **2014**, *26*, 763–772.

(258) Sung, M. M.; Kluth, G. J.; Yauw, O. W.; Maboudian, R. Thermal Behavior of Alkyl Monolayers on Silicon Surfaces. *Langmuir* **1997**, *13*, 6164–6168.

(259) Zazzera, L. A.; Evans, J. F.; Deruelle, M.; Tirrelib, M. Bonding Organic Molecules to Hydrogen-Terminated Silicon Wafers. *J. Electrochem. Soc.* **1997**, *144*, 2184–2189.

(260) Cicero, R. L.; Linford, M. R.; Chidsey, C. E. D. Photoreactivity of Unsaturated Compounds with Hydrogen-Terminated Silicon(111). *Langmuir* **2000**, *16*, 5688–5695.

(261) Sun, Q.-Y.; de Smet, L. C. P. M.; van Lagen, B.; Wright, A.; Zuilhof, H.; Sudhölter, E. J. R. Covalently Attached Monolayers on Hydrogen-Terminated Si(100): Extremely Mild Attachment by Visible Light. *Angew. Chem. Int. Ed.* **2004**, *43*, 1352–1355.

(262) Robins, E. G.; Stewart, M. P.; Buriak, J. M. Anodic and Cathodic Electrografting of Alkynes on Porous Silicon. *Chem. Commun.* **1999**, *24*, 2479–2480.

(263) Niederhauser, T. L.; Jiang, G.; Lua, Y.; Dorff, M. J.; Woolley, A. T.; Asplund, M. C.; Berges, D. A.; Linford, M. R. A New Method of Preparing Monolayers on Silicon and Patterning Silicon Surfaces by Scribing in the Presence of Reactive Species. *Langmuir* **2001**, *17*, 5889–5900.

(264) Zhong, Y. L.; Bernasek, S. L. Mild and Efficient Functionalization of Hydrogen-Terminated Si(111) via Sonochemical Activated Hydrosilylation. *J. Am. Chem. Soc.* **2011**, *133*, 8118–8121.

(265) Cicero, R. L.; Chidsey, C. E. D.; Lopinski, G. P.; Wayner, D. D. M.; Wolkow, R. A. Olefin Additions on H−Si(111): Evidence for a Surface Chain Reaction Initiated at Isolated Dangling Bonds. *Langmuir* **2002**, *18*, 305–307.

(266) Faucheux, A.; Gouget-Laemmel, A. C.; Henry de Villeneuve, C.; Boukherroub, R.; Ozanam, F.; Allongue, P.; Chazalviel, J.-N. Well-Defined Carboxyl-Terminated Alkyl Monolayers Grafted onto H−Si(111): Packing Density from a Combined AFM and Quantitative IR Study. *Langmuir* **2006**, *22*, 153–162.

(267) Scheres, L.; ter Maat, J.; Giesbers, M.; Zuilhof, H. Microcontact Printing onto Oxide-Free Silicon via Highly Reactive Acid Fluoride-Functionalized Monolayers. *Small* **2010**, *6*, 642–650.

(268) Campos, M. A. C.; Paulusse, J. M. J.; Zuilhof, H. Functional Monolayers on Oxide-Free Silicon Surfaces via Thiol–Ene Click Chemistry. *Chem. Commun.* **2010**, *46*, 5512–5514.

(269) Wang, J.; Wu, F.; Watkinson, M.; Zhu, J.; Krause, S. "Click" Patterning of Self-Assembled Monolayers on Hydrogen-Terminated Silicon Surfaces and Their Characterization Using Light-Addressable Potentiometric Sensors. *Langmuir* **2015**, *31*, 9646–9654.

(270) Mizuno, H.; Buriak, J. M. Catalytic Stamp Lithography for Sub-100 Nm Patterning of Organic Monolayers. *J. Am. Chem. Soc.* **2008**, *130*, 17656–17657.

(271) Rogers, J. A.; Nuzzo, R. G. Recent Progress in Soft Lithography. *Mater. Today* **2005**, *8*, 50–56.

(272) Nicosia, C.; Huskens, J. Reactive Self-Assembled Monolayers: From Surface Functionalization to Gradient Formation. *Mater. Horiz.* **2014**, *1*, 32–45.

(273) Betancourt, T.; Brannon-Peppas, L. Micro- and Nanofabrication Methods in Nanotechnological Medical and Pharmaceutical Devices. *Int. J. Nanomedicine* **2006**, *1*, 483–495.

(274) Lei, K. F. Introduction: The Origin, Current Status, and Future of Microfluidics. *Microfluidics: Fundamental, Devices and Applications*. February 12, 2018, pp 1–18.

(275) Beebe, D. J.; Mensing, G. A.; Walker, G. M. Physics and Applications of Microfluidics in Biology. *Annu. Rev. Biomed. Eng.* **2002**, *4*, 261–286.

(276) Ren, X.; Bachman, M.; Sims, C.; Li, G. P.; Allbritton, N. Electroosmotic Properties of Microfluidic Channels Composed of Poly(Dimethylsiloxane). *J. Chromatogr. B Biomed. Sci. Appl.* **2001**, *762*, 117–125.

(277) Lee, J. N.; Park, C.; Whitesides, G. M. Solvent Compatibility of Poly(Dimethylsiloxane)-Based Microfluidic Devices. *Anal. Chem.* **2003**, *75*, 6544–6554.

(278) Kuo, J. S.; Chiu, D. T. Disposable Microfluidic Substrates: Transitioning from the Research Laboratory into the Clinic. *Lab Chip* **2011**, *11*, 2656–2665.

(279) Nunes, P. S.; Ohlsson, P. D.; Ordeig, O.; Kutter, J. P. Cyclic Olefin Polymers: Emerging Materials for Lab-on-a-Chip Applications. *Microfluid. Nanofluidics* **2010**, *9*, 145–161.

(280) Bruijns, B.; Veciana, A.; Tiggelaar, R.; Gardeniers, H. Cyclic Olefin Copolymer Microfluidic Devices for Forensic Applications. *Biosensors* **2019**, *9*, 85.

(281) Chiu, D. T.; deMello, A. J.; Di Carlo, D.; Doyle, P. S.; Hansen, C.; Maceiczyk, R. M.; Wootton, R. C. R. Small but Perfectly Formed? Successes, Challenges, and Opportunities for Microfluidics in the Chemical and Biological Sciences. *Chem* **2017**, *2*, 201–223.

(282) Jayamohan, H.; Romanov, V.; Li, H.; Son, J.; Samuel, R.; Nelson, J.; Gale, B. K. Advances in Microfluidics and Lab-on-a-Chip Technologies. In *Molecular Diagnostics*; Elsevier, 2017; pp 197–217.

(283) Streets, A. M.; Huang, Y. Chip in a Lab: Microfluidics for next Generation Life Science Research. *Biomicrofluidics* **2013**, *7*, 011302.

(284) Li, P.; Klet, R. C.; Moon, S.-Y.; Wang, T. C.; Deria, P.; Peters, A. W.; Klahr, B. M.; Park, H.-J.; Al-Juaid, S. S.; Hupp, J. T.; Farha, O. K. Synthesis of Nanocrystals of Zr-Based Metal–Organic Frameworks with Csq-Net: Significant Enhancement in the Degradation of a Nerve Agent Simulant. *Chem. Commun.* **2015**, *51*, 10925–10928.

(285) Falcaro, P.; Ricco, R.; Doherty, C. M.; Liang, K.; Hill, A. J.; Styles, M. J. MOF Positioning Technology and Device Fabrication. *Chem. Soc. Rev.* **2014**, *43*, 5513–5560.

(286) St. Petkov, P.; Vayssilov, G. N.; Liu, J.; Shekhah, O.; Wang, Y.; Wöll, C.; Heine, T. Defects in MOFs: A Thorough Characterization. *ChemPhysChem* **2012**, *13*, 2025–2029.

(287) Falcaro, P.; Hill, A. J.; Nairn, K. M.; Jasieniak, J.; Mardel, J. I.; Bastow, T. J.; Mayo, S. C.; Gimona, M.; Gomez, D.; Whitfield, H. J.; Riccò, R.; Patelli, A.; Marmiroli, B.; Amenitsch, H.; Colson, T.; Villanova, L.; et al. A New Method to Position and Functionalize Metal-Organic Framework Crystals. *Nat. Commun.* **2011**, *2*, 237.

(288) Férey, G.; Serre, C.; Mellot-Draznieks, C.; Millange, F.; Surblé, S.; Dutour, J.; Margiolaki, I. A Hybrid Solid with Giant Pores Prepared by a Combination of Targeted Chemistry, Simulation, and Powder Diffraction. *Angew. Chem. Int. Ed.* **2004**, *43*, 6296–6301.

(289) Bhattacharjee, S.; Chen, C.; Ahn, W. S. Chromium Terephthalate Metal-Organic Framework MIL-101: Synthesis, Functionalization, and Applications for Adsorption and Catalysis. *RSC Adv.* **2014**, *4*, 52500–52525.

(290) Wang, S.; Morris, W.; Liu, Y.; McGuirk, C. M.; Zhou, Y.; Hupp, J. T.; Farha, O. K.; Mirkin, C. A. Surface-Specific Functionalization of Nanoscale Metal-Organic Frameworks. *Angew. Chem. Int. Ed.* **2015**, *54*, 14738–14742.

(291) Demessence, A.; Horcajada, P.; Serre, C.; Boissière, C.; Grosso, D.; Sanchez, C.; Férey, G. Elaboration and Properties of Hierarchically Structured Optical Thin Films

of MIL-101(Cr). *Chem. Commun.* **2009**, *101*, 7149–7151.

(292) Coffinier, Y.; Piret, G.; Das, M. R.; Boukherroub, R. Effect of Surface Roughness and Chemical Composition on the Wetting Properties of Silicon-Based Substrates. *Comptes Rendus Chim.* **2013**, *16*, 65–72.

(293) Ciampi, S.; Böcking, T.; Kilian, K. A.; James, M.; Harper, J. B.; Gooding, J. J. Functionalization of Acetylene-Terminated Monolayers on Si(100) Surfaces: A Click Chemistry Approach. *Langmuir* **2007**, *23*, 9320–9329.

(294) Liu, H.; Duclairoir, F.; Fleury, B.; Dubois, L.; Chenavier, Y.; Marchon, J. C. Porphyrin Anchoring on Si(100) Using a β-Pyrrolic Position. *Dalt. Trans.* **2009**, *19*, 3793–3799.

(295) Voicu, R.; Boukherroub, R.; Bartzoka, V.; Ward, T.; Wojtyk, J. T. C.; Wayner, D. D. M. Formation, Characterization, and Chemistry of Undecanoic Acid-Terminated Silicon Surfaces: Patterning and Immobilization of DNA. *Langmuir* **2004**, *20*, 11713–11720.

(296) Alvarez, S. D.; Derfus, A. M.; Schwartz, M. P.; Bhatia, S. N.; Sailor, M. J. The Compatibility of Hepatocytes with Chemically Modified Porous Silicon with Reference to in Vitro Biosensors. *Biomaterials* **2009**, *30*, 26–34.

(297) Marshall, C. R.; Timmel, E. E.; Staudhammer, S. A.; Brozek, C. K. Experimental Evidence for a General Model of Modulated MOF Nanoparticle Growth. *Chem. Sci.* **2020**, *11*, 11539–11547.

(298) Holzwarth, U.; Gibson, N. The Scherrer Equation versus the "Debye-Scherrer Equation." *Nat. Nanotechnol.* **2011**, *6*, 534–534.

(299) Howarth, A. J.; Peters, A. W.; Vermeulen, N. A.; Wang, T. C.; Hupp, J. T.; Farha, O. K. Best Practices for the Synthesis, Activation, and Characterization of Metal–Organic Frameworks. *Chem. Mater.* **2017**, *29*, 26–39.

(300) Lange, S. C.; van Andel, E.; Smulders, M. M. J.; Zuilhof, H. Efficient and Tunable Three-Dimensional Functionalization of Fully Zwitterionic Antifouling Surface Coatings. *Langmuir* **2016**, *32*, 10199–10205.

(301) Zhao, J.; Gao, F.; Pujari, S. P.; Zuilhof, H.; Teplyakov, A. V. Universal Calibration of Computationally Predicted N 1s Binding Energies for Interpretation of XPS Experimental Measurements. *Langmuir* **2017**, *33*, 10792–10799.

(302) Vermoortele, F.; Bueken, B.; Le Bars, G.; Van de Voorde, B.; Vandichel, M.; Houthoofd, K.; Vimont, A.; Daturi, M.; Waroquier, M.; Van Speybroeck, V.; Kirschhock, C.; De Vos, D. E. Synthesis Modulation as a Tool To Increase the Catalytic Activity of Metal–Organic Frameworks: The Unique Case of UiO-66(Zr). *J. Am. Chem. Soc.* **2013**, *135*, 11465–11468.

(303) Kuddannaya, S.; Chuah, Y. J.; Lee, M. H. A.; Menon, N. V; Kang, Y.; Zhang, Y. Surface Chemical Modification of Poly(Dimethylsiloxane) for the Enhanced Adhesion and Proliferation of Mesenchymal Stem Cells. *ACS Appl. Mater. Interfaces* **2013**, *5*, 9777–9784.

(304) Tropmann, A.; Tanguy, L.; Koltay, P.; Zengerle, R.; Riegger, L. Completely Superhydrophobic PDMS Surfaces for Microfluidics. *Langmuir* **2012**, *28*, 8292–8295.

(305) Beal, J. H. L.; Bubendorfer, A.; Kemmitt, T.; Hoek, I.; Mike Arnold, W. A Rapid, Inexpensive Surface Treatment for Enhanced Functionality of Polydimethylsiloxane

Microfluidic Channels. *Biomicrofluidics* **2012**, *6*, 036503.

(306) *Encyclopedia of Analytical Chemistry*; Meyers, R. A., Ed.; Wiley, 2006.

(307) Qiao, B.; Wang, T. J.; Gao, H.; Jin, Y. High Density Silanization of Nano-Silica Particles Using γ-Aminopropyltriethoxysilane (APTES). *Appl. Surf. Sci.* **2015**, *351*, 646–654.

(308) Aguirre-Díaz, L. M.; Iglesias, M.; Snejko, N.; Gutiérrez-Puebla, E.; Monge, M. Á. Toward Understanding the Structure-Catalyst Activity Relationship of New Indium MOFs as Catalysts for Solvent-Free Ketone Cyanosilylation. *RSC Adv.* **2015**, *5*, 7058–7065.

(309) Li, Y. P.; Zhang, L. J.; Ji, W. J. Synthesis, Characterization, Crystal Structure of Magnesium Compound Based 3, 3′, 5, 5′-Azobenzentetracarboxylic Acid and Application as High-Performance Heterogeneous Catalyst for Cyanosilylation. *J. Mol. Struct.* **2017**, *1133*, 607–614.

(310) Aguirre-Díaz, L. M.; Iglesias, M.; Snejko, N.; Gutiérrez-Puebla, E.; Monge, M. Á. Synchronizing Substrate Activation Rates in Multicomponent Reactions with Metal-Organic Framework Catalysts. *Chem. - A Eur. J.* **2016**, *22*, 6654–6665.

(311) Vannice, M. A. *Kinetics of Catalytic Reactions*; New York, London, 2005.

(312) Bartholomew, Calvin H. Farrauto, R. J. *Fundamentals of Industrial Catalytic Processes*; WILEY-VCH Verlag: New York, 2011.

(313) Feng, Y.; Chen, C.; Liu, Z.; Fei, B.; Lin, P.; Li, Q.; Sun, S.; Du, S. Application of a Ni Mercaptopyrimidine MOF as Highly Efficient Catalyst for Sunlight-Driven Hydrogen Generation. *J. Mater. Chem. A* **2015**, *3*, 7163–7169.

(314) Brown, K.; Zolezzi, S.; Aguirre, P.; Venegas-Yazigi, D.; Paredes-García, V.; Baggio, R.; Novak, M. A.; Spodine, E. $[Cu(H_2Btec)(Bipy)]_\infty$: A Novel Metal Organic Framework (MOF) as Heterogeneous Catalyst for the Oxidation of Olefins. *Dalt. Trans.* **2009**, No. 8, 1422–1427.

(315) Aguado, S.; Canivet, J.; Farrusseng, D. Engineering Structured MOF at Nano and Macroscales for Catalysis and Separation. *J. Mater. Chem.* **2011**, *21*, 7582–7588.

(316) Wei, R.; Zhang, X.; Du, B.; Fan, Z.; Qi, G. Synthesis of Bis(Cyclic Carbonate) and Propylene Carbonate via a One-Pot Coupling Reaction of CO_2, Bisepoxide and Propylene Oxide. *RSC Adv.* **2013**, *3*, 17307–17313.

(317) Mousavinejad, A.; Rahimpour, A.; Shirzad Kebria, M. R.; Khoshhal Salestan, S.; Sadrzadeh, M.; Tavajohi Hassan Kiadeh, N. Nickel-Based Metal–Organic Frameworks to Improve the CO_2/CH_4 Separation Capability of Thin-Film Pebax Membranes. *Ind. Eng. Chem. Res.* **2020**, *59*, 12834–12844.

(318) Epp, K.; Semrau, A. L.; Cokoja, M.; Fischer, R. A. Dual Site Lewis-Acid Metal-Organic Framework Catalysts for CO_2 Fixation: Counteracting Effects of Node Connectivity, Defects and Linker Metalation. *ChemCatChem* **2018**, *10*, 3506–3512.

(319) Kim, H.; Moon, H. S.; Sohail, M.; Yoon, Y. N.; Shah, S. F. A.; Yim, K.; Moon, J. H.; Park, Y. C. Synthesis of Cyclic Carbonate by CO_2 Fixation to Epoxides Using Interpenetrated MOF-5/n-Bu_4NBr. *J. Mater. Sci.* **2019**, *54*, 11796–11803.

(320) Babu, R.; Kurisingal, J. F.; Chang, J. S.; Park, D. W. Bifunctional Pyridinium-Based Ionic-

Liquid-Immobilized Diindium Tris(Diphenic Acid) Bis(1,10-Phenanthroline) for CO_2 Fixation. *ChemSusChem* **2018**, *11*, 924–932.

(321) Rani, P.; Srivastava, R. Tailoring the Catalytic Activity of Metal Organic Frameworks by Tuning the Metal Center and Basic Functional Sites. *New J. Chem.* **2017**, *41*, 8166–8177.

(322) Iqbal, K.; Iqbal, A.; Kirillov, A. M.; Liu, W.; Tang, Y. Hybrid Metal-Organic-Framework/Inorganic Nanocatalyst toward Highly Efficient Discoloration of Organic Dyes in Aqueous Medium. *Inorg. Chem.* **2018**, *57*, 13270–13278.

(323) Yang, D.; Gates, B. C. Catalysis by Metal Organic Frameworks: Perspective and Suggestions for Future Research. *ACS Catal.* **2019**, *9*, 1779–1798.

(324) Morbioli, G. G.; Speller, N. C.; Cato, M. E.; Cantrell, T. P.; Stockton, A. M. Rapid and Low-Cost Development of Microfluidic Devices Using Wax Printing and Microwave Treatment. *Sensors Actuators B Chem.* **2019**, *284*, 650–656.

(325) Morbioli, G. G.; Speller, N. C.; Stockton, A. M. A Practical Guide to Rapid-Prototyping of PDMS-Based Microfluidic Devices: A Tutorial. *Anal. Chim. Acta* **2020**, *1135*, 150–174.

(326) You, J. B.; Kang, K.; Tran, T. T.; Park, H.; Hwang, W. R.; Kim, J. M.; Im, S. G. PDMS-Based Turbulent Microfluidic Mixer. *Lab Chip* **2015**, *15*, 1727–1735.

(327) You, J. B.; Lee, B.; Choi, Y.; Lee, C.-S.; Peter, M.; Im, S. G.; Lee, S. S. Nanoadhesive Layer to Prevent Protein Absorption in a Poly(Dimethylsiloxane) Microfluidic Device. *Biotechniques* **2020**, *69*, 46–51.

(328) Toyao, T.; Fujiwaki, M.; Horiuchi, Y.; Matsuoka, M. Application of an Amino-Functionalised Metal–Organic Framework: An Approach to a One-Pot Acid–Base Reaction. *RSC Adv.* **2013**, *3*, 21582.

(329) Park, J.; Li, J. R.; Chen, Y. P.; Yu, J.; Yakovenko, A. A.; Wang, Z. U.; Sun, L. B.; Balbuena, P. B.; Zhou, H. C. A Versatile Metal–Organic Framework for Carbon Dioxide Capture and Cooperative Catalysis. *Chem. Commun.* **2012**, *48*, 9995–9997.

(330) Lee, Y.-R.; Chung, Y.-M.; Ahn, W.-S. A New Site-Isolated Acid–Base Bifunctional Metal–Organic Framework for One-Pot Tandem Reaction. *RSC Adv.* **2014**, *4*, 23064.

(331) Li, B.; Zhang, Y.; Ma, D.; Li, L.; Li, G.; Li, G.; Shi, Z.; Feng, S. A Strategy toward Constructing a Bifunctionalized MOF Catalyst: Post-Synthetic Modification of MOFs on Organic Ligands and Coordinatively Unsaturated Metal Sites. *Chem. Commun.* **2012**, *48*, 6151.

(332) Das, A.; Anbu, N.; SK, M.; Dhakshinamoorthy, A.; Biswas, S. Highly Active Bisamino Functionalized Zr(IV)-UiO-67 Metal-Organic Framework for Cascade Catalysis. *Eur. J. Inorg. Chem.* **2020**, *2020*, 2830–2834.

(333) Zhao, Z. S.; Zhang, Y.; Fang, T.; Han, Z. B.; Liang, F. S. Chitosan-Coated Metal-Organic-Framework Nanoparticles as Catalysts for Tandem Deacetalization-Knoevenagel Condensation Reactions. *ACS Appl. Nano Mater.* **2020**, *3*, 6316–6320.

(334) Liu, H.; Xi, F.-G.; Sun, W.; Yang, N.-N.; Gao, E.-Q. Amino- and Sulfo-Bifunctionalized Metal–Organic Frameworks: One-Pot Tandem Catalysis and the Catalytic Sites. *Inorg. Chem.* **2016**, *55*, 5753–5755.

(335) Zhang, Y.; Wang, Y.; Liu, L.; Wei, N.; Gao, M.-L.; Zhao, D.; Han, Z.-B. Robust Bifunctional Lanthanide Cluster Based Metal–Organic Frameworks (MOFs) for Tandem Deacetalization–Knoevenagel Reaction. *Inorg. Chem.* **2018**, *57*, 2193–2198.

(336) Karmakar, A.; Soliman, M. M. A.; Rúbio, G. M. D. M.; Guedes Da Silva, M. F. C.; Pombeiro, A. J. L. Synthesis and Catalytic Activities of a Zn(II) Based Metallomacrocycle and a Metal-Organic Framework towards One-Pot Deacetalization-Knoevenagel Tandem Reactions under Different Strategies: A Comparative Study. *Dalt. Trans.* **2020**, *49*, 8075–8085.

(337) Mistry, S.; Sarkar, A.; Natarajan, S. New Bifunctional Metal-Organic Frameworks and Their Utilization in One-Pot Tandem Catalytic Reactions. *Cryst. Growth Des.* **2019**, *19*, 747–755.

(338) Feng, L.; Wang, Y.; Zhang, K.; Wang, K.; Fan, W.; Wang, X.; Powell, J. A.; Guo, B.; Dai, F.; Zhang, L.; Wang, R.; Sun, D.; Zhou, H. Molecular Pivot-Hinge Installation to Evolve Topology in Rare-Earth Metal–Organic Frameworks. *Angew. Chem. Int. Ed.* **2019**, *58*, 16682–16690.

(339) Paul, A.; Martins, L. M. D. R. S.; Karmakar, A.; Kuznetsov, M. L.; Novikov, A. S.; Guedes da Silva, M. F. C.; Pombeiro, A. J. L. Environmentally Benign Benzyl Alcohol Oxidation and C-C Coupling Catalysed by Amide Functionalized 3D Co(II) and Zn(II) Metal Organic Frameworks. *J. Catal.* **2020**, *385*, 324–337.

(340) Liu, H.; Liu, Y.; Li, Y.; Tang, Z.; Jiang, H. Metal−Organic Framework Supported Gold Nanoparticles as a Highly Active Heterogeneous Catalyst for Aerobic Oxidation of Alcohols. *J. Phys. Chem. C* **2010**, *114*, 13362–13369.

(341) Vis, C. M.; Nieuwelink, A.; Weckhuysen, B. M.; Bruijnincx, P. C. A. Continuous Flow Pickering Emulsion Catalysis in Droplet Microfluidics Studied with In Situ Raman Microscopy. *Chem. – A Eur. J.* **2020**, *26*, 15099–15102.

(342) Safari, A.; Akdoğan, E. K. *Piezoelectric and Acoustic Materials for Transducer Applications*; 2008.

(343) Ivanov, M.; Macutkevic, J.; Grigalaitis, R.; Banys, J. *Magnetic, Ferroelectric, and Multiferroic Metal Oxides*; Elsevier, 2018.

(344) Scott, J. F. *Ferroelectric Memories*; Springer Series in Advanced Microelectronics; Springer Berlin Heidelberg: Berlin, Heidelberg, 2000; Vol. 3.

(345) Goldschmidt, V. M. Die Gesetze Der Krystallochemie. *Naturwissenschaften* **1926**, *14*, 477–485.

(346) Hurley, P. T.; Ribbe, A. E.; Buriak, J. M. Nanopatterning of Alkynes on Hydrogen-Terminated Silicon Surfaces by Scanning Probe-Induced Cathodic Electrografting. *J. Am. Chem. Soc.* **2003**, *125*, 11334–11339.

(347) Ehrenreich, M. G.; Zeng, Z.; Burger, S.; Warren, M. R.; Gaultois, M. W.; Tan, J.-C.; Kieslich, G. Mechanical Properties of the Ferroelectric Metal-Free Perovskite [MDABCO](NH$_4$)I$_3$. *Chem. Commun.* **2019**, *55*, 3911–3914.

(348) Etgar, L.; Gao, P.; Xue, Z.; Peng, Q.; Chandiran, A. K.; Liu, B.; Nazeeruddin, M. K.; Grätzel, M. Mesoscopic $CH_3NH_3PbI_3/TiO_2$ Heterojunction Solar Cells. *J. Am. Chem. Soc.* **2012**, *134*, 17396–17399.

(349) Walker, H. C.; Duncan, H. D.; Le, M. D.; Keen, D. A.; Voneshen, D. J.; Phillips, A. E. Magnetic Structure and Spin-Wave Excitations in the Multiferroic Magnetic Metal-Organic Framework $(CD_3)_2ND_2[Mn\ (DCO_2)_3]$. *Phys. Rev. B* **2017**, *96*, 094423–094429.

(350) Ye, H.-Y.; Tang, Y.-Y.; Li, P.-F.; Liao, W.-Q.; Gao, J.-X.; Hua, X.-N.; Cai, H.; Shi, P.-P.; You, Y.-M.; Xiong, R.-G. Metal-Free Three-Dimensional Perovskite Ferroelectrics. *Science* **2018**, *361*, 151–155.

(351) Li, W.; Ji, L.-J. Perovskite Ferroelectrics Go Metal Free. *Science* **2018**, *361*, 132–132.

(352) Momma, K.; Izumi, F. VESTA 3 for Three-Dimensional Visualization of Crystal, Volumetric and Morphology Data. *J. Appl. Crystallogr.* **2011**, *44*, 1272–1276.

(353) Shieh, J.; Yeh, J. H.; Shu, Y. C.; Yen, J. H. Hysteresis Behaviors of Barium Titanate Single Crystals Based on the Operation of Multiple 90° Switching Systems. *Mater. Sci. Eng. B* **2009**, *161*, 50–54.

(354) Kamenshchikov, M.; Solnyshkin, A.; Pronin, I.; Belov, A. The Influence of Polarization on Properties of the Potential Barrier at Metal-Ferroelectric Interface. *Process. Appl. Ceram.* **2019**, *13*, 277–280.

(355) Kasel, T. W.; Deng, Z.; Mroz, A. M.; Hendon, C. H.; Butler, K. T.; Canepa, P. Metal-Free Perovskites for Non Linear Optical Materials. *Chem. Sci.* **2019**, *10*, 8187–8194.

(356) Kim, H.; Yang, S.; Rao, S. R.; Narayanan, S.; Kapustin, E. A.; Furukawa, H.; Umans, A. S.; Yaghi, O. M.; Wang, E. N. Water Harvesting from Air with Metal-Organic Frameworks Powered by Natural Sunlight. *Science* **2017**, *356*, 430–434.

(357) Yang, Z.; Zhang, S.; Li, L.; Chen, W. Research Progress on Large-Area Perovskite Thin Films and Solar Modules. *J. Mater.* **2017**, *3*, 231–244.

(358) *Metal Halide Perovskite Crystals: Growth Techniques, Properties and Emerging Applications*; Zhang, W., Ed.; MDPI, 2019.

(359) Bruening, K.; Tassone, C. J. Antisolvent Processing of Lead Halide Perovskite Thin Films Studied by in Situ X-Ray Diffraction. *J. Mater. Chem. A* **2018**, *6*, 18865–18870.

(360) Eperon, G. E.; Habisreutinger, S. N.; Leijtens, T.; Bruijnaers, B. J.; van Franeker, J. J.; DeQuilettes, D. W.; Pathak, S.; Sutton, R. J.; Grancini, G.; Ginger, D. S.; Janssen, R. A. J.; Petrozza, A.; Snaith, H. J. The Importance of Moisture in Hybrid Lead Halide Perovskite Thin Film Fabrication. *ACS Nano* **2015**, *9*, 9380–9393.

(361) Zhang, W.; Pathak, S.; Sakai, N.; Stergiopoulos, T.; Nayak, P. K.; Noel, N. K.; Haghighirad, A. A.; Burlakov, V. M.; DeQuilettes, D. W.; Sadhanala, A.; Li, W.; Wang, L.; Ginger, D. S.; Friend, R. H.; Snaith, H. J. Enhanced Optoelectronic Quality of Perovskite Thin Films with Hypophosphorous Acid for Planar Heterojunction Solar Cells. *Nat. Commun.* **2015**, *6*, 10030.

(362) Ehrenreich, M. G.; Zeng, Z.; Burger, S.; Warren, M. R.; Gaultois, M. W.; Tan, J.-C.; Kieslich, G. Mechanical Properties of the Ferroelectric Metal-Free Perovskite $[MDABCO](NH_4)I_3$. *Chem. Commun.* **2019**, *55*, 3911–3914.

(363) Ye, H. Y.; Tang, Y. Y.; Li, P. F.; Liao, W. Q.; Gao, J. X.; Hua, X. N.; Cai, H.; Shi, P. P.; You, Y. M.; Xiong, R. G. Metal-Free Three-Dimensional Perovskite Ferroelectrics. *Science* **2018**, *361*, 151–155.

(364) Marino, M. G.; Kreuer, K. D. Alkaline Stability of Quaternary Ammonium Cations for Alkaline Fuel Cell Membranes and Ionic Liquids. *ChemSusChem* **2015**, *8*, 513–523.

(365) Kazock, J. Y.; Taggougui, M.; Carré, B.; Willmann, P.; Lemordant, D. Simple and Efficient Synthesis of N-Quaternary Salts of Quinuclidinium Derivatives. *Synthesis* **2007**, No. 24, 3776–3778.

(366) Liu, C.; Cheng, Y.-B.; Ge, Z. Understanding of Perovskite Crystal Growth and Film Formation in Scalable Deposition Processes. *Chem. Soc. Rev.* **2020**, *49*, 1653–1687.

(367) Weng, G.; Dong, X.; Li, J.; Zhao, J. Halide Ions Can Trigger the Oxidative Etching of Gold Nanorods with the Iodide Ions Being the Most Efficient. *J. Mater. Sci.* **2016**, *51*, 7678–7690.

(368) Ciampi, S.; Harper, J. B.; Gooding, J. J. Wet Chemical Routes to the Assembly of Organic Monolayers on Silicon Surfaces via the Formation of Si–C Bonds: Surface Preparation, Passivation and Functionalization. *Chem. Soc. Rev.* **2010**, *39*, 2158.

(369) Standard procedure for PDMS molding http://bdml.stanford.edu/twiki/bin/view/Rise/PDMSProceSS.html#PDMS_Molding_Procedure.

(370) Sui, G.; Wang, J.; Lee, C.-C.; Lu, W.; Lee, S. P.; Leyton, J. V.; Wu, A. M.; Tseng, H.-R. Solution-Phase Surface Modification in Intact Poly(Dimethylsiloxane) Microfluidic Channels. *Anal. Chem.* **2006**, *78*, 5543–5551.

(371) Kickelbick, G.; Schubert, U. Oxozirconium Methacrylate Clusters: $Zr_6(OH)_4O_4(OMc)_{12}$ and $Zr_4O_2(OMc)_{12}$ (OMc- = Methacrylate). *Chem. Ber. Recl.* **1997**, *6*, 473–477.

(372) Zhou, Y.-X.; Chen, Y.-Z.; Hu, Y.; Huang, G.; Yu, S.-H.; Jiang, H.-L. MIL-101-SO_3H: A Highly Efficient Brønsted Acid Catalyst for Heterogeneous Alcoholysis of Epoxides under Ambient Conditions. *Chem. - A Eur. J.* **2014**, *20*, 14976–14980.

(373) Jiang, D.; Keenan, L. L.; Burrows, A. D.; Edler, K. J. Synthesis and Post-Synthetic Modification of MIL-101(Cr)-NH_2 via a Tandem Diazotisation Process. *Chem. Commun.* **2012**, *48*, 12053.

(374) Yaghi, O. M.; Li, H.; Groy, T. L. Construction of Porous Solids from Hydrogen-Bonded Metal Complexes of 1,3,5-Benzenetricarboxylic Acid. *J. Am. Chem. Soc.* **1996**, *118*, 9096–9101.

(375) Dissegna, S.; Epp, K.; Heinz, W. R.; Kieslich, G.; Fischer, R. A. Defective Metal-Organic Frameworks. *Adv. Mater.* **2018**, *30*, 1704501.

(376) Shearer, G. C.; Chavan, S.; Ethiraj, J.; Vitillo, J. G.; Svelle, S.; Olsbye, U.; Lamberti, C.; Bordiga, S.; Lillerud, K. P. Tuned to Perfection: Ironing Out the Defects in Metal–Organic Framework UiO-66. *Chem. Mater.* **2014**, *26*, 4068–4071.

(377) Ferey, G. A Chromium Terephthalate-Based Solid with Unusually Large Pore Volumes and Surface Area. *Science* **2005**, *309*, 2040–2042.

(378) Leenders, C. M. A.; Jansen, G.; Frissen, M. M. M.; Lafleur, R. P. M.; Voets, I. K.; Palmans, A. R. A.; Meijer, E. W. Monosaccharides as Versatile Units for Water-Soluble Supramolecular Polymers. *Chem. - A Eur. J.* **2016**, *22*, 4608–4615.

(379) Diesendruck, C. E.; Zhu, L.; Moore, J. S. Alkyne Mechanochemistry: Putative Activation by Transoidal Bending. *Chem. Commun.* **2014**, *50*, 13235–13238.

(380) Texier-Boullet, F.; Foucaud, A. Knoevenagel Condensation Catalysed by Aluminium Oxide. *Tetrahedron Lett.* **1982**, *23*, 4927–4928.

(381) Higuchi, K.; Onaka, M.; Izumi, Y. Solid Acid and Base-Catalyzed Cyanosilylation of Carbonyl Compounds with Cyanotrimethylsilane. *Bull. Chem. Soc. Jpn.* **1993**, *66*, 2016–2032.

(382) Toulemon, D.; Pichon, B. P.; Leuvrey, C.; Zafeiratos, S.; Papaefthimiou, V.; Cattoën, X.; Bégin-Colin, S. Fast Assembling of Magnetic Iron Oxide Nanoparticles by Microwave-Assisted Copper(I) Catalyzed Alkyne-Azide Cycloaddition (CuAAC). *Chem. Mater.* **2013**, *25*, 2849–2854.

(383) Ng, A.; Ciampi, S.; James, M.; Harper, J. B.; Gooding, J. J. Comparing the Reactivity of Alkynes and Alkenes on Silicon 100 Surfaces. *Langmuir* **2009**, *25*, 13934–13941.

(384) Miranda, A.; Martínez, L.; De Beule, P. A. A. Facile Synthesis of an Aminopropylsilane Layer on Si/SiO2 Substrates Using Ethanol as APTES Solvent. *MethodsX* **2020**, *7*, 100931.

(385) Montalbetti, C. A. G. N.; Falque, V. Amide Bond Formation and Peptide Coupling. *Tetrahedron* **2005**, *61*, 10827–10852.

(386) Zimpel, A.; Preiß, T.; Röder, R.; Engelke, H.; Ingrisch, M.; Peller, M.; Rädler, J. O.; Wagner, E.; Bein, T.; Lächelt, U.; Wuttke, S. Imparting Functionality to MOF Nanoparticles by External Surface Selective Covalent Attachment of Polymers. *Chem. Mater.* **2016**, *28*, 3318–3326.

(387) Friedman, M. Applications of the Ninhydrin Reaction for Analysis of Amino Acids, Peptides, and Proteins to Agricultural and Biomedical Sciences. *J. Agric. Food Chem.* **2004**, *52*, 385–406.

(388) Fulmer, G. R.; Miller, A. J. M.; Sherden, N. H.; Gottlieb, H. E.; Nudelman, A.; Stoltz, B. M.; Bercaw, J. E.; Goldberg, K. I. NMR Chemical Shifts of Trace Impurities: Common Laboratory Solvents, Organics, and Gases in Deuterated Solvents Relevant to the Organometallic Chemist. *Organometallics* **2010**, *29*, 2176–2179.

(389) Lee, D. G.; Chang, V. S. Oxidation of Hydrocarbons. 9. The Oxidation of Alkynes by Potassium Permanganate. *J. Org. Chem.* **1979**, *44*, 2726–2730.

(390) Sternberg, J.; Gallaway, W.; Jones, D. *The Mechanism of Response of Flame Ionization Detectors*; Brenner, N., Callen, J. E., Weiss, M. D., Eds.; Academic Press: New York, 1962.

(391) Ma, D.; Han, G.; Gao, Z. F.; Chen, S. B. Continuous UiO-66-Type Metal–Organic Framework Thin Film on Polymeric Support for Organic Solvent Nanofiltration. *ACS Appl. Mater. Interfaces* **2019**, *11*, 45290–45300.

(392) Huang, Y.; Tao, C.; Chen, R.; Sheng, L.; Wang, J. Comparison of Fabrication Methods of Metal-Organic Framework Optical Thin Films. *Nanomaterials* **2018**, *8*, 676.

(393) Chen, R.; Tao, C.; Zhang, Z.; Chen, X.; Liu, Z.; Wang, J. Layer-by-Layer Fabrication of Core–Shell Fe_3O_4@UiO-66-NH_2 with High Catalytic Reactivity toward the Hydrolysis of Chemical Warfare Agent Simulants. *ACS Appl. Mater. Interfaces* **2019**, *11*, 43156–

43165.

(394) Gao, J.; Wei, W.; Yin, Y.; Liu, M.; Zheng, C.; Zhang, Y.; Deng, P. Continuous Ultrathin UiO-66-NH_2 Coatings on a Polymeric Substrate Synthesized by a Layer-by-Layer Method: A Kind of Promising Membrane for Oil–Water Separation. *Nanoscale* **2020**, *12*, 6658–6663.

(395) Silva, R. M.; Carlos, L. D.; Rocha, J.; Silva, R. F. Luminescent Thin Films of Eu-Bearing UiO-66 Metal Organic Framework Prepared by ALD/MLD. *Appl. Surf. Sci.* **2020**, *527*, 146603.

(396) Lausund, K. B.; Nilsen, O. All-Gas-Phase Synthesis of UiO-66 through Modulated Atomic Layer Deposition. *Nat. Commun.* **2016**, *7*, 13578.

(397) Lausund, K. B.; Petrovic, V.; Nilsen, O. All-Gas-Phase Synthesis of Amino-Functionalized UiO-66 Thin Films. *Dalt. Trans.* **2017**, *46*, 16983–16992.

(398) Feng, J.; Gao, S.; Shi, J.; Liu, T.; Cao, R. C-QDs@UiO-66-$(COOH)_2$ Composite Film via Electrophoretic Deposition for Temperature Sensing. *Inorg. Chem.* **2018**, *57*, 2447–2454.

(399) Feng, J.; Gao, S.; Liu, T.; Shi, J.; Cao, R. Preparation of Dual-Emitting Ln@UiO-66-Hybrid Films via Electrophoretic Deposition for Ratiometric Temperature Sensing. *ACS Appl. Mater. Interfaces* **2018**, *10*, 6014–6023.

(400) Wagner, A.; Pullen, S.; Ott, S.; Primetzhofer, D. The Potential of Ion Beams for Characterization of Metal–Organic Frameworks. *Nucl. Instruments Methods Phys. Res. Sect. B* **2016**, *371*, 327–331.

(401) Zhang, C.; Zhao, Y.; Li, Y.; Zhang, X.; Chi, L.; Lu, G. Defect-Controlled Preparation of UiO-66 Metal-Organic Framework Thin Films with Molecular Sieving Capability. *Chem. - An Asian J.* **2016**, *11*, 207–210.

(402) Nazari, M.; Forouzandeh, M. A.; Divarathne, C. M.; Sidiroglou, F.; Martinez, M. R.; Konstas, K.; Muir, B. W.; Hill, A. J.; Duke, M. C.; Hill, M. R.; Collins, S. F. UiO-66 MOF End-Face-Coated Optical Fiber in Aqueous Contaminant Detection. *Opt. Lett.* **2016**, *41*, 1696.

(403) Nazari, M.; Rubio-Martinez, M.; Babarao, R.; Younis, A. A.; Collins, S. F.; Hill, M. R.; Duke, M. C. Aqueous Contaminant Detection via UiO-66 Thin Film Optical Fiber Sensor Platform with Fast Fourier Transform Based Spectrum Analysis. *J. Phys. D. Appl. Phys.* **2018**, *51*, 025601.

(404) Chen, S. S.; Hu, C.; Liu, C.; Chen, Y.; Ahamad, T.; Alshehri, S. M.; Huang, P.; Wu, K. C.-W. De Novo Synthesis of Platinum-Nanoparticle-Encapsulated UiO-66-NH_2 for Photocatalytic Thin Film Fabrication with Enhanced Performance of Phenol Degradation. *J. Hazard. Mater.* **2020**, *397*, 122431.

(405) Ghorbanpour, A.; Huelsenbeck, L. D.; Smilgies, D.-M.; Giri, G. Oriented UiO-66 Thin Films through Solution Shearing. *CrystEngComm* **2018**, *20*, 294–300.

(406) Nguyen Thi Thuy, V.; Luu Cam, L.; Nguyen, T.; Nguyen Phung, A.; Ha Cam, A.; Nguyen Thanh, T.; Nguyen Lam Thuy, D.; Hoang Tien, C. Kinetics of Photocatalytic Degradation of Gaseous p -xylene on UiO-66-NH_2 and $LaFeO_3$ Thin Films under Combined Illumination of Ultraviolet and Visible Lights. *Int. J. Chem. Kinet.* **2020**, *52*, 35–51.

(407) Feng, J.; Liu, T.; Shi, J.; Gao, S.; Cao, R. Dual-Emitting UiO-66(Zr&Eu) Metal–Organic Framework Films for Ratiometric Temperature Sensing. *ACS Appl. Mater. Interfaces* **2018**, *10*, 20854–20861.

(408) Bagherzadeh, M.; Bayrami, A.; Amini, M. Thin-film Nanocomposite Forward Osmosis Membranes Modified with Zr-based Metal–Organic Framework to Improve Desalination Performance. *Appl. Organomet. Chem.* **2020**, *34*, 1–12.

(409) Zhao, D. L.; Yeung, W. S.; Zhao, Q.; Chung, T.-S. Thin-Film Nanocomposite Membranes Incorporated with UiO-66-NH_2 Nanoparticles for Brackish Water and Seawater Desalination. *J. Memb. Sci.* **2020**, *604*, 118039.

(410) Guo, J.; Huang, M.; Gao, P.; Zhang, Y.; Chen, H.; Zheng, S.; Mu, T.; Luo, X. Simultaneous Robust Removal of Tetracycline and Tetracycline Resistance Genes by a Novel UiO/TPU/PSF Forward Osmosis Membrane. *Chem. Eng. J.* **2020**, *398*, 125604.

(411) Mozafari, M.; Rahimpour, A.; Abedini, R. Exploiting the Effects of Zirconium-Based Metal Organic Framework Decorated Carbon Nanofibers to Improve CO_2/CH_4 Separation Performance of Thin Film Nanocomposite Membranes. *J. Ind. Eng. Chem.* **2020**, *85*, 102–110.

(412) Mozafari, M.; Abedini, R.; Rahimpour, A. Zr-MOFs-Incorporated Thin Film Nanocomposite Pebax 1657 Membranes Dip-Coated on Polymethylpentyne Layer for Efficient Separation of CO_2/CH_4. *J. Mater. Chem. A* **2018**, *6*, 12380–12392.

(413) Xiao, F.; Hu, X.; Chen, Y.; Zhang, Y. Porous Zr-Based Metal-Organic Frameworks (Zr-MOFs)-Incorporated Thin-Film Nanocomposite Membrane toward Enhanced Desalination Performance. *ACS Appl. Mater. Interfaces* **2019**, *11*, 47390–47403.

(414) Ma, D.; Peh, S. B.; Han, G.; Chen, S. B. Thin-Film Nanocomposite (TFN) Membranes Incorporated with Super-Hydrophilic Metal–Organic Framework (MOF) UiO-66: Toward Enhancement of Water Flux and Salt Rejection. *ACS Appl. Mater. Interfaces* **2017**, *9*, 7523–7534.

(415) Zhao, Y.; Liu, Y.; Wang, X.; Huang, X.; Xie, Y. F. Impacts of Metal–Organic Frameworks on Structure and Performance of Polyamide Thin-Film Nanocomposite Membranes. *ACS Appl. Mater. Interfaces* **2019**, *11*, 13724–13734.

(416) Liu, L.; Xie, X.; Qi, S.; Li, R.; Zhang, X.; Song, X.; Gao, C. Thin Film Nanocomposite Reverse Osmosis Membrane Incorporated with UiO-66 Nanoparticles for Enhanced Boron Removal. *J. Memb. Sci.* **2019**, *580*, 101–109.

(417) Arjmandi, M.; Peyravi, M.; Pourafshari Chenar, M.; Jahanshahi, M. Channelization of Water Pathway and Encapsulation of DS in the SL of the TFC FO Membrane as a Novel Approach for Controlling Dilutive Internal Concentration Polarization. *Environ. Sci. Water Res. Technol.* **2019**, *5*, 1436–1452.

(418) Gohain, M. B.; Pawar, R. R.; Karki, S.; Hazarika, A.; Hazarika, S.; Ingole, P. G. Development of Thin Film Nanocomposite Membrane Incorporated with Mesoporous Synthetic Hectorite and MSH@UiO-66-NH_2 Nanoparticles for Efficient Targeted Feeds Separation, and Antibacterial Performance. *J. Memb. Sci.* **2020**, *609*, 118212.

(419) Guo, X.; Liu, D.; Han, T.; Huang, H.; Yang, Q.; Zhong, C. Preparation of Thin Film Nanocomposite Membranes with Surface Modified MOF for High Flux Organic Solvent Nanofiltration. *AIChE J.* **2017**, *63*, 1303–1312.

(420) Kadhom, M.; Hu, W.; Deng, B. Thin Film Nanocomposite Membrane Filled with Metal-Organic Frameworks UiO-66 and MIL-125 Nanoparticles for Water Desalination. *Membranes* **2017**, *7*, 31.

(421) Paseta, L.; Navarro, M.; Coronas, J.; Téllez, C. Greener Processes in the Preparation of Thin Film Nanocomposite Membranes with Diverse Metal-Organic Frameworks for Organic Solvent Nanofiltration. *J. Ind. Eng. Chem.* **2019**, *77*, 344–354.

(422) Wang, Y.; Li, X.; Zhao, S.; Fang, Z.; Ng, D.; Xie, C.; Wang, H.; Xie, Z. Thin-Film Composite Membrane with Interlayer Decorated Metal–Organic Framework UiO-66 toward Enhanced Forward Osmosis Performance. *Ind. Eng. Chem. Res.* **2019**, *58*, 195–206.

(423) Zhang, X.; Zhang, Y.; Wang, T.; Fan, Z.; Zhang, G. A Thin Film Nanocomposite Membrane with Pre-Immobilized UiO-66-NH_2 toward Enhanced Nanofiltration Performance. *RSC Adv.* **2019**, *9*, 24802–24810.

(424) Semrau, A. L.; Stanley, P. M.; Urstoeger, A.; Schuster, M.; Cokoja, M.; Fischer, R. A. Substantial Turnover Frequency Enhancement of MOF Catalysts by Crystallite Downsizing Combined with Surface Anchoring. *ACS Catal.* **2020**, *10*, 3203–3211.

(425) Toyao, T.; Styles, M. J.; Yago, T.; Sadiq, M. M.; Riccò, R.; Suzuki, K.; Horiuchi, Y.; Takahashi, M.; Matsuoka, M.; Falcaro, P. Fe_3O_4@HKUST-1 and Pd/Fe_3O_4@HKUST-1 as Magnetically Recyclable Catalysts Prepared via Conversion from a Cu-Based Ceramic. *CrystEngComm* **2017**, *19*, 4201–4210.

(426) Zheng, B.; Luo, X.; Wang, Z.; Zhang, S.; Yun, R.; Huang, L.; Zeng, W.; Liu, W. An Unprecedented Water Stable Acylamide-Functionalized Metal–Organic Framework for Highly Efficient CH_4/CO_2 Gas Storage/Separation and Acid–Base Cooperative Catalytic Activity. *Inorg. Chem. Front.* **2018**, *5*, 2355–2363.

(427) Wang, Z.; Luo, X.; Zheng, B.; Huang, L.; Hang, C.; Jiao, Y.; Cao, X.; Zeng, W.; Yun, R. Highly Selective Carbon Dioxide Capture and Cooperative Catalysis of a Water-Stable Acylamide-Functionalized Metal–Organic Framework. *Eur. J. Inorg. Chem.* **2018**, *2018*, 1309–1314.

(428) Zhao, J.-H.; Yang, Y.; Che, J.-X.; Zuo, J.; Li, X.-H.; Hu, Y.-Z.; Dong, X.-W.; Gao, L.; Liu, X.-Y. Compartmentalization of Incompatible Polymers within Metal-Organic Frameworks towards Homogenization of Heterogeneous Hybrid Catalysts for Tandem Reactions. *Chem. - A Eur. J.* **2018**, *24*, 9903–9909.

(429) Hu, X.-J.; Li, Z.-X.; Xue, H.; Huang, X.; Cao, R.; Liu, T.-F. Designing a Bifunctional Brønsted Acid–Base Heterogeneous Catalyst Through Precise Installation of Ligands on Metal–Organic Frameworks. *CCS Chem.* **2020**, *2*, 616–622.

(430) Gao, M. L.; Qi, M. H.; Liu, L.; Han, Z. B. An Exceptionally Stable Core-Shell MOF/COF Bifunctional Catalyst for a Highly Efficient Cascade Deacetalization-Knoevenagel Condensation Reaction. *Chem. Commun.* **2019**, *55*, 6377–6380.

(431) He, H.; Zhang, D. Y.; Guo, F.; Sun, F. A Versatile Microporous Zinc(II) Metal-Organic Framework for Selective Gas Adsorption, Cooperative Catalysis, and Luminescent Sensing. *Inorg. Chem.* **2018**, *57*, 7314–7320.

(432) Hu, Y.; Zhang, J.; Huo, H.; Wang, Z.; Xu, X.; Yang, Y.; Lin, K.; Fan, R. One-Pot Synthesis of Bimetallic Metal-Organic Frameworks (MOFs) as Acid-Base Bifunctional

Catalysts for Tandem Reaction. *Catal. Sci. Technol.* **2020**, *10*, 315–322.

(433) Peh, S. B.; Cheng, Y.; Zhang, J.; Wang, Y.; Chan, G. H.; Wang, J.; Zhao, D. Cluster Nuclearity Control and Modulated Hydrothermal Synthesis of Functionalized Zr_{12} Metal–Organic Frameworks. *Dalt. Trans.* **2019**, *48*, 7069–7073.

(434) He, H.; Sun, F.; Aguila, B.; Perman, J. A.; Ma, S.; Zhu, G. A Bifunctional Metal-Organic Framework Featuring the Combination of Open Metal Sites and Lewis Basic Sites for Selective Gas Adsorption and Heterogeneous Cascade Catalysis. *J. Mater. Chem. A* **2016**, *4*, 15240–15246.

(435) Zhu, G.; Graver, R.; Emdadi, L.; Liu, B.; Choi, K. Y.; Liu, D. Synthesis of Zeolite@metal-Organic Framework Core-Shell Particles as Bifunctional Catalysts. *RSC Adv.* **2014**, *4*, 30673–30676.

6. EXPERIMENTAL

6.1. General Information

The commercially purchased chemicals are used without further purification or drying. Air and moisture sensitive reactions are performed under an argon 4.6 (≥99.996%) atmosphere using standard Schlenk techniques. The respective reagents and products are kept at room temperature in an argon-purged glove box produced by M. Braun. Centrifugation is carried out in VWR centrifugation vials with an Eppendorf Centrifuge 5430, model F-35-6-30, at 7830 rpm.

Microwave-assisted syntheses are conducted in Teflon® autoclaves with magnetic stir bars in a CEM MARS-6 microwave digestion system at 1800 W.

6.1.1. Substrate Preparation

(a) Silicon substrates.

The silicon wafers purchased by Sigert Wafers (100) were cut into 1.0 cm x 1.0 cm pieces. Prior to reaction, the silicon surfaces were cleaned by sonication in acetone, ethanol, and DCM for 5 min each. Afterwards, they were dried under argon.

Activation of Si.[255,368] In order to enhance the hydrophilicity of the substrates and clean the surface from organic impurities, the surfaces are either activated by oxygen plasma, piranha acid, or ozone treatment.

For their activation by **oxygen plasma**, the substrates are placed in an oxygen plasma cleaner and activated for 15 min.

For the activation in **piranha acid,** the substrates are treated with H_2SO_4 (96 w% in H_2O)/ H_2O_2 (30 w% $H_2O_{2(aq)}$ (7:3 v%) (*Caution: Piranha is a very strong oxidizer and can react explosively with organic compounds*) at room temperature for 30 min. Afterwards, the substrates are thoroughly washed with deionized water and ethanol and blow-dried for further use.

For **UV light** activation, the Si substrates were placed in a UV/Vis ProCleaner manufactured by Bioforce Nanoscience for 30 min.

(b) PDMS.

Curing of PDMS.[369] 15 g Slygard 184 silicone elastomer base and 1.5 g (10:1 w%) Sylgard 184 silicone elastomer curing agent are thoroughly mixed for three minutes. Afterwards, the mixture is poured into a petri dish and degassed in a desiccator under a moderate vacuum. For the curing procedure, the dish is placed in an oven for one

hour at 70 °C. If needed the PDMS was cut into 1 cm x 1 cm pieces after cooling down to room temperature.

Activation of PDMS.[370] For the surface activation prior to the functionalization and cleaning, the PDMS samples were treated with H_2O/H_2O_2 (30 w% $H_2O_{2(aq)}$)/HCl (37 w% $HCl_{(aq)}$) (5:1:1 v%) for 30 min at room temperature. The surfaces are rinsed with deionized water, ethanol and dried with pressurized air.

(a) Gold-coated silicon substrates.

Gold-coated silicon substrates were fabricated by sputtering 50 nm gold on silicon wafers (purchase by Sigert Wafers). In between the silicon surface and the gold layer a 5 nm titanium adhesion layer was deposited. After this process, the 1.0 x 1.0 cm substrates were first cleaned with acetone and sonicated for 10 min in acetone, ethanol, and dichloromethane each. Then the substrates were dried in a stream of compressed air stream. For functionalization, they were then placed in a thiol solution in ethanol (c = 200 μM/L) for at least 24 h. For the 16-mercaptohexadecanoic acid, an additional 5 v% acetic acid was added to prevent the formation of SAM dimers. Finally, the films were once again rinsed with EtOH and dried in a compressed air stream.

6.2. Analytical Techniques

Auger spectroscopy (AES).

AES measurements were performed at room temperature with a scanning Auger electron spectroscope (JEOL Ltd. JAMP-9500F field emission scanning Auger microprobe) system. AES spectra were acquired with a primary beam of 20 keV. The take-off angle of the instrument was 0°. We used the differential energy spectrum to subtract the background from the direct Auger spectrum for calculating the band-to-band intensity. The first differential d(N(E))/d(E) Auger spectra were obtained by numerical derivation of the direct N(E) integrated Auger data displaying an absolute scale with counts/second units by a universal Savitzky–Golay (SG) Quadratic differential filter using seven points and used to calculate the band-to-band intensity of Auger electrons and derive the elemental compositions. The differential spectrum is simply the differential of the direct spectrum with respect to energy. The spectra were calibrated with the carbon band at 263.0 eV. For Auger elemental analysis an 8 nm probe diameter was used. The AES measurements were performed and analyzed by Dr. Sidharam Pujari at Wageningen University & Research.

Atomic force microscopy (AFM).

Images are recorded using a Nanosurf easyScan 2 AFM system including a Nanosurf easyScan 2 controller and a Nanosurf isoStage table. A time of 0.6 s per line and 512 points per line is used. Additionally, a setpoint of 70%, a P-Gain of 5000, an I-Gain of

1000, and a D-Gain of 0 is applied. Finally, the free vibration amplitude equals 59.97 mV. For each sample, the Z-axis orientation is adjusted by cantilever rotation to provide the best resolution. Subsequent image analysis and visualization are performed with the WSxM 5.0 Develop 9.1 software.

The AFM images were recorded and analyzed by ALS, except for chapter 4, where the AFM images were recorded by Christian Eckel, M.Sc. (Prof. Thomas Seitz, University Göttingen).

Contact angle.

Static contact angle values of water on substrates and the respective images are obtained with a Krüss GmbH FM40Mk2 EasyDrop. Onto the sample 2.5 µL Milli-Q® water is dropped and the contact angles are measured via the Drop Shape Analysis program. The experiment was repeated at least 3 times and the average static contact angle is shown.

Dynamic light scattering (DLS).

For Dynamic Light Scattering, 100 µL stock solutions from **NMOF 1-4** were diluted with 2 mL ethanol. The measurement was performed on a Zetasizer Nano by Malvern Instruments and the data was analyzed and evaluated with the Zetasizer Software 7.11 by Malvern Instruments. The shown DLS spectra are the number distributions calculated by the program and plotted with python.

Fluorescence imaging.

In order to detect fluorescent markers, a Typhoon 9200 Variable Mode Imager with a green (532 nm) laser is used. Using a 390 BP 100 filter the excitation takes place at 390 nm. To record the image 650 V PMT, high sensitivity, and a resolution of 50 microns are set.

Gas chromatography (GC).

GC is performed with an Agilent Technologies 7890B GC with a flame ionization detector (FID). The substance separation occurs via a capillary column HP-5 (length 30 m, inside diameter 0.32 mm, film 0.25 µm, stationary phase (5% phenyl) methylpolysiloxane)). Samples are prepared by taking a 50 µL aliquot from the reaction mixture, adding 1.5 mL of the respective solvent, and centrifuging for 30 minutes at 7830 rpm to remove any possible traces of NMOF.

Gas chromatography calibration.

To evaluate the amount of BADMA, BA, BACN, BAOTMSCN, and MN calibration curves were measured. Therefore, several solutions with 0, 0.5, 1, 2.5, 5, 10, 20 µmol/L of these compounds were prepared and measured by GC. Afterwards, the regression lines are calculated for each compound.

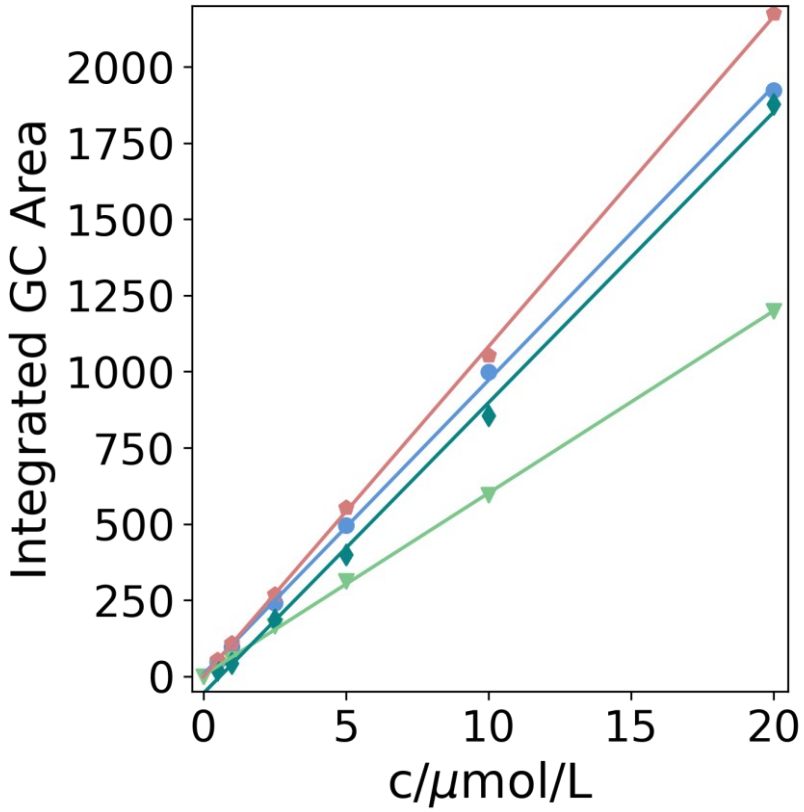

Figure S1: GC calibration of BADMA, BA, BACN, BAOTMSCN, MN measured for concentrations between 0.5 and 20 µmol/L. The retention times were determined as t (BA)~7.3 min, t (BADMA)~9.3 min, t (BACN)~11.7 min, t (BAOTMSCN)~11.3 min, and t (MN)~7.3 min. The measured values are represented by symbols, whereas the resulting regression lines are represented by lines.

$$y(BADMA) = 96.5 \cdot x + 6.9 \; (R^2 = 0.9996)$$

$$y(BA) = 59.8 \cdot x + 3.4 \; (R^2 = 0.9997)$$

$$y(BAOTMSCN) = 108.3 \cdot x - 1.4 \; (R^2 = 0.9997)$$

$$y(BACN) = 95.4 \cdot x + 6.1 \; (R^2 = 0.9985)$$

For the GC calibration, BADMA, BA, and MN were purchased from commercial vendors, and BACN and BAOTMSCN were synthesized according to literature procedures (see chapter 6.3.2.2.).

Inductively coupled plasma mass spectrometry (ICP-MS).

To obtain an accurate quantification of Zr, Cr, and Co amount anchored to PDMS and silicon wafers, ICP-MS for zirconium is conducted on an *Agilent Technologies* 7900 ICP-MS. The respective samples are immersed in concentrated 7.5 mL nitric acid and 2.5 mL H_2O_2 (30 w% in H_2O) (v%) and treated in the microwave at 150 °C for 5 min. Subsequently, 0.5 mL of this solution are diluted 1/20 and 1/200 respectively with ultra-pure water containing 1.65 % (v%) HCl. Each solvent used is extra pure and contains no traces of zirconium. ^{90}Zr, ^{52}Cr, and ^{59}Co were used as target mass for the analyte and ^{115}In for the internal standard. Zr/Cr/Co quantification was carried out in He CCT-mode to avoid isobaric and polyatomic interferences. The detection limit for Zr was 2.997 ng L^{-1} (0.15 ng). Calibration was performed in the range of 0 ng L^{-1} to 20 µg L^{-1} Zr (0 ng to 1 µg Zr). Measurements were carried out by Alexander Urstoeger, M.Sc., and Dominik Huber, M.Sc. from the research group Analytical Chemistry (Technical University of Munich).

Infrared reflection absorption spectroscopy (IRRAS) for surface analytics.

IRRAS spectra were recorded on a Bruker Tensor 27 FT-IR spectrometer using a variable-angle reflection unit (Auto Seagull, Harrick Scientific). A Harrick grid polarizer was installed in front of the detector and was used to record spectra with p-polarized (parallel) radiation with respect to the plane of incidence at the sample surface. All spectra were obtained at an incident angle of 68° (2048 scans). The resolution was set at 4 cm^{-1} per modulation centre. The final spectra were obtained using a reference surface as background. Data were collected as differential reflectance versus wavenumber. All spectra were recorded at room temperature. A linear baseline correction was applied. The IRRAS measurements were performed by Dr. Sidharam Pujari at Wageningen University & Research.

Infrared spectroscopy (IR).

IR measurements are carried out on a Bruker ALPHA-P FT-IR in the attenuated total reflectance (ATR) mode inside an argon-purged glove box. Therefore, the sample is pressed against a diamond single crystal. Unless stated otherwise, each spectrum consists of 24 accumulated scans with a 2 cm^{-1} resolution.

N_2 adsorption measurements.

Adsorption measurements with N_2 (99.999 vol%) at 77 K were carried out on a 3Flex Physisorption from Micromeritics Instrument Corp., which uses a manometric method to determine the amount adsorbed under equilibrated gas pressure. Adsorption data were processed using the 3Flex Software Version 5.01 by Micromeritics Instrument Corp. and plotted with Python. Activated samples (3h, 150°C) were transferred under dry Ar atmosphere into preweighed sample tubes and capped with Micromeritics

CheckSeals. Samples were subsequently activated again at 150°C for 3 h under a dynamic vacuum of ~ 10-3 mbar using a SmartVac Prep by Micromeritics Instrument Corp. to ensure the absence of unwanted adsorbates and identical pre-measurement states of all samples. The mass of the adsorbent was then recorded, generally in the range of 25 mg. Free space of the sample tube is determined before measuring each adsorption isotherm using helium (99.999 vol%). A liquid nitrogen bath is used for measurements at 77 K. The apparent surface area of UiO-66-NH2 samples was derived using the Brunauer-Emmett-Teller (BET) model, is hence given as the 'BET area' and based on N_2 isotherms measured at 77 K. To determine this value for microporous materials, care was taken to adhere to the Rouquerol criteria.

The pore size distribution (PSD) was derived by fitting N_2 isotherms measured at 77 K with sets of theoretical isotherms (kernel) derived from (two-dimensional non-local-) density functional theory (2D-NLDFT) based methods for specific pore sizes and geometry. As an approximation, cylindrical pores on an oxide surface are assumed for all materials to allow comparability within this series. Fitting was done using the respective kernel available via the 3Flex Software Version 5.01 by Micromeritics Instrument Corp.. The BET measurements were either performed by Dr. Pia Vervoorts or Jan Berger, M.Sc..

Nuclear magnetic resonance (NMR).

NMR spectra are recorded by a Bruker Ultrashield DRX400 (^{1}H: 400.13 MHz, ^{13}C: 100.62 MHz) at ambient temperature (298 K). The ^{1}H and ^{13}C{1H} NMR spectroscopic chemical shifts δ are reported in ppm relative to tetramethylsilane. ^{1}H and ^{13}C{^{1}H} NMR spectra are calibrated against the residual proton and natural abundance carbon resonances of the respective deuterated solvent as an internal standard ($CDCl_3$: δ (^{1}H) = 7.26 ppm and δ (^{13}C) = 77.16 ppm, DMSO-d_6: δ (1H) = 2.50 ppm).

The following abbreviations are used to describe signal multiplicities: s = singlet, d = doublet, t = triplet, quin = quintet, m = multiplet.

NMR spectra of NMOF samples are obtained by mixing the respective powder with 0.1 mL DCl and 0.4 mL DMSO-d_6 in an NMR tube. Subsequently, the latter is heated until the substance is digested.

Powder X-ray diffraction (PXRD).

PXRD measurements are performed on a silicon single-crystal wafer cut in (510) direction using Bragg-Brentano geometry in a PANalytical Empyrean diffractometer equipped with a PANalytical PIXcel 1D detector. Powder patterns of activated samples were recorded on the same instrument in capillary mode.

X-ray Cu Kα radiation is used and Kβ radiation is removed by a Ni-filter. Voltage and intensity are 45 kV and 40 mA, respectively. The measurement range is from 5.0° to 50.0° (2θ) with a scan speed of 0.015 degrees per second.

Scanning electron microscopy (SEM).

SEM images are obtained with a Jeol JSM-7500F field emission scanning electron microscope with the Gentle Beam mode with varying accelerating voltages. The images were either recorded with an upper secondary electron in-lens (SEI) or lower secondary electron (LEI) detector. The working distance, magnification, detector, and acceleration voltage used for a specific image are denoted in each figure, respectively The SEM instrument was operated by Katia Rodewald, M.Sc. at the Technical University Munich. Most SEM images in the chapter 4 were recorded by myself at a SEM benchtop instrument (Hitachi TM-1000 Tabletop scanning electron microscope with an accelerating voltage of 15 kV.).

Thermogravimetric analysis coupled with mass-spectrometry (TGA-MS).

A TGA/STA 409 PC apparatus from Mettler-Toledo Intl. Inc. is used for thermogravimetric analysis under synthetic air from 30 to 800 °C with a continuous heating ramp of 10 °C/min. The corresponding evaluation software is STARe 14.00. Roughly 3 mg of the sample are applied.

X-ray photoelectron spectroscopy (XPS).

XPS measurements were performed using a JPS-9200 photoelectron spectrometer (JEOL, Japan). A monochromatic Al Kα X-ray source (hν = 1486.7 eV; 12 kV and 20 mA) using an analyzer pass energy of 10 eV was used. The base pressure in the chamber during measurements was 3×10^{-7} Torr, and spectra were collected at room temperature. The intensity of the XPS core level electron was measured as the peak area after standard background subtraction according to the linear procedure. The take-off angle φ (angle between sample and detector) of 80° is defined with a precision of 1°. The typical sample size was $1 \times 1 cm^2$. All XPS spectra were evaluated using the Casa XPS software (version 2.3.15). All binding energies are referenced relative to the main hydrocarbon (CH_2) peak with a binding energy of 285.0 eV. The spectra were recorded by Dr. Sidharam Pujari at Wageningen University & Research or by Dr. Christian Jandl at the Technical University of Munich.

6.3. Syntheses and Analytical Characterization

6.3.1. Zr-based MOF Thin Films • (Chapter 2)

6.3.1.1. Controlled Secondary Building Unit Approach for UiO 66-(NH_2) Powders

To implement the CM-LPE technique for UiO-66(-NH_2) thin-films, the controlled SBU approach (CSA) was employed. Herein, the known methacrylate (McO^- = $H_2C{=}C(CH_3)CO_2^-$) protected zirconium-oxo cluster, ($Zr_6O_4(OH)_4(OMc)_{12}$) was selected as the source for the zirconium node. The cluster was synthesized according to modified literature procedures (see below). The CSA approach was applied due to the facilitated MOF formation and crystallization at mild conditions during the thin-film fabrication.

Synthesis of $Zr_6O_4(OH)_4(OMc)_{12}$. (Hexazirconium-tetraoxy-tetrahydroxy-dodeca-methacrylate).[371] The compound was synthesized according to the adapted procedure from Kickelbick and Schubert.[371] In a large Schlenk flask, 1 mL of 70% w/v $Zr(OPr)_4$ (3.1 mmol) in n-propanol was mixed (by shaking) at room temperature with 1 mL of methacrylic acid (McOH; 11.8 mmol, 5.3 equiv.) under inert gas atmosphere (Ar). After two weeks (no stirring), the colourless crystals were collected by filtration and washing with small quantities of n-propanol. The product was dried *in vacuo* for 12 h and yield a sample of 860 mg (0.51 mmol, 98 %).

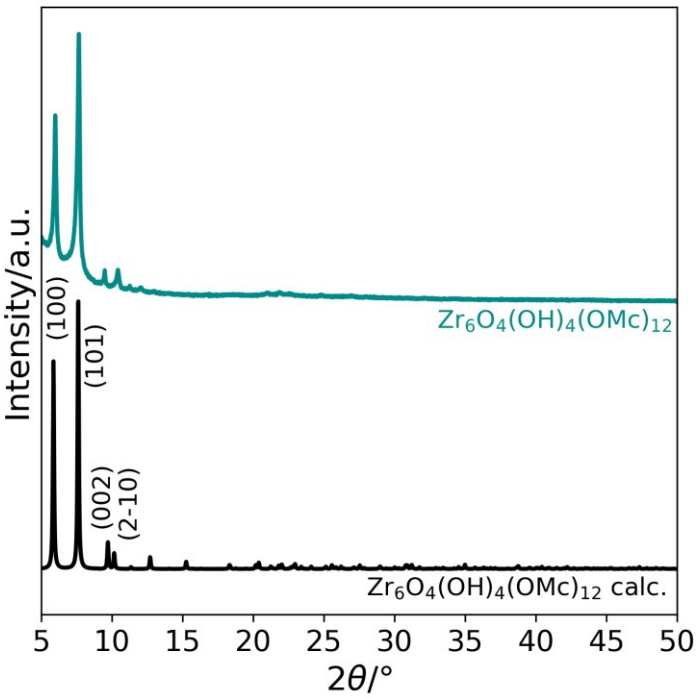

Figure S2: Experimental PXRD pattern (cyan) of the molecular methacrylate cluster ($Zr_6O_4(OH)_4(OMc)_{12}$) compared to the simulated diffraction pattern calculated from the single crystal structure (black). The simulated pattern was calculated based on the CCDC entry 106826.

Synthesis of bulk UiO-66(-NH_2) via CSA mild solution approach. A sample of 25.5 mg of $Zr_6O_4(OH)_4(OMc)_{12}$ (0.015 mmol, 1 equiv.), and x molar equivalents (x= 0-400(for UiO-66);0-500 (for UiO-66-NH_2) of the modulator (methacrylic acid, McOH) were dissolved in 4 mL ethanol and then the solution was sonicated (Sonorex

Bandelin, 350 Watt) for 60 min. Additionally, 29.9 mg of 1,4-benzene-dicarboxylic acid (H_2bdc; 0.09 mmol, 12 equiv. (UiO-66)) or 16.3 mg 4-aminotherephthalic acid (0.09 mmol, 6 equiv.)) was dissolved in 8 mL ethanol by sonicating for 60 min in a separated bottle. Then, the two solutions were combined in a 20 mL reaction vessel and then stored in the oven at 70 °C for 24 h to complete the crystallization process. The formed, white precipitate was washed three times with 5 mL ethanol each. After each washing step, a centrifuge was used to separate the precipitate (7860 rpm, 5 min). The collected colourless (white) powders were dried in the oven at 40 °C. For the activation, the powder was dried in a dynamic oil-pump vacuum overnight at room temperature and was stored under argon. For BET measurement the samples were activated at 150 °C for 3 h under vacuum.

6.3.1.2. UiO-66-(NH_2) SURMOF Fabrication by CM-LPE

Figure S3: Experimental setup for the LPE process. For the thin film deposition, a double-walled reaction vessel, which was heated with a silicon-oil thermostat was used. The solutions were pumped in and out by peristaltic pumps computer controlled by LABview. The substrate was placed in the double walled reaction vessel.

The deposition of UiO-66 thin-films was carried out in a double-walled reaction vessel, which was heated with a silicon-oil thermostat. The solutions were pumped in and out by peristaltic pumps computer-controlled by LabView (National Instruments).

For the deposition of UiO-66, QCM substrates with a silicon dioxide surface were used (Q Sense, AT-cut type, Au electrode, diameter 14 mm, thickness 0.3 mm, and fundamental frequency ca. 4.95 MHz).

The substrates were either activated by UV/ozone or piranha acid treatment as described in chapter 6.1.1.

The activated Si substrate was placed in the reaction vessel and alternatively treated with a 0.5 mM $Zr_6O_4(OH)_4(OMc)_{12}$ solution in ethanol (containing different amounts of McOH as modulator and 3 mM ethanol solution of H_2bdc or H_2bdc-NH_2 (containing different amounts of McOH as modulator and different amounts of water as an additive). The substrate was immersed in each solution for 10 min. For the UiO-66 thin films, the substrates were rinsed with pure ethanol in between these steps with pure ethanol (1000 ppm H_2O, purchased from VWR, measured via Karl-Fischer-Titration) for 5 min. These deposition cycles were repeated for X times (X=20, 40, 80 for UiO-66-NH_2 and 80 for UiO-66) at 70 °C to yield the reported UiO-66 thin-film samples.

6.3.2. Selective Covalent Immobilization of Preformed NMOFs in Microfluidic Devices Targeting Vectorial Catalysis • (Chapter 3)

6.3.2.1. Synthetic Procedures for Metal-Organic Frameworks

NMOF formation and exterior surface functionalization. In a first step, UiO-66[290] (**NMOF 1**) and MIL-101[291] (**NMOF 3**) nanometer-sized crystals were synthesized and in a second step, their exterior surface was functionalized by the formation of amide bonds to ω-functionalized alkane-α-amines to form azide-functionalized UiO-66 NP (**NMOF 2**) and amino-functionalized MIL-101 (**NMOF 4**).

UiO-66(Zr)/NMOF 1 [290] and 2. 21 mg zirconium oxychloride octahydrate (0.066 mmol, 1,0 equiv.) and 50 mg benzene dicarboxylic acid (0.30 mmol, 4.5 equiv.) were dissolved by sonication in 3 mL and 1 mL dimethylformamide (DMF). Then, both solutions were mixed, and 0.35 mL acetic acid (6.11 mmol, 20.4 equiv.) was added. Afterwards, the reaction mixture was kept at 90 °C for 12 h. The synthesis yields a white, colloidal solution. The solvent of the solution is exchanged by centrifugation three times with 4 ml of fresh DMF and three times with 4 ml ethanol each. Then, 18 mg azidododecane-1-amine (0.08 mmol) (see below), 22.3 µL N,N-diisopropylcarbodiimide (18 mg, 0.14 mmol), and catalytic amounts of N-hydroxysuccinimide, were added to 4 mL of the colloidal **NMOF 1** ethanol solution. After 4 h of stirring at room temperature, the reaction solution was exchanged for 3 times replacing it with 4 mL of fresh ethanol each time. In between the centrifugation steps, the **NMOF 2** solution was sonicated for several hours.

MIL-101 (Cr)/NMOF 3[291] and 4. 740.4 mg $Cr(NO_3)_3 \cdot 9\ H_2O$ (1.85 mmol, 1.0 equiv.) and 307.4 mg benzene dicarboxylic acid (1.85 mmol, 1.0 equiv.) were dispersed in 10 mL

deionized water in a 50 mL microwave tube. After 10 min of stirring at room temperature, the reaction solution was heated with maximum power to a set temperature of 200 °C. After about 7 min the temperature reached 190 °C and was kept at that temperature for 1 min. After the reaction mixture was cooled down to room temperature, it was filtered over a Schott filter No. 2 to filter off unreacted benzene dicarboxylic acid. The colloidal green solution of **NMOF 3** was centrifuged and the solution was replaced three times with fresh water (20 mL each) and three times with fresh ethanol (20 mL each). 20 mL of green, colloidal **NMOF 3** ethanol solution was mixed with 111.7 µL *N,N*-diisoproyl carbodiimide (90 mg, 0.71 mmol), 180 mg 1,12-diamino dodecane (DAD) (0.90 mmol) and catalytic amounts of N-hydroxysuccinimide and stirred for 4 h at room temperature. The solvent was exchanged three times after the reaction with 20 mL ethanol each. In between the centrifugation, the **NMOF 4** solution was sonicated for several hours.

MIL-101-SO_3H (Cr).[372] 0.376 g CrO_3 (3.75 mmol, 1 equiv.) and 1g Monosodium-2,5-dicarboxybenzenesulfonate (H_2bdc-SO_3Na) (3.75 mmol, 1 equiv.) were dissolved in 15 mL H_2O and mixed with 230 µL 37 w% $HCl_{(aq.)}$ (0.273 g, 2.7 mmol, 0.75 equiv.). The reaction mixture was heated in a 20 mL autoclave to 180°C for 6 days. After cooling to room temperature, the turquoise product was separated from the reaction mixture by centrifugation and washed with water and ethanol over a couple of days three times each. Afterwards, for the activation, the powder is placed at 150 °C for 12 h under an oil pump vacuum. Then, the powders were handled under inert conditions.

MIL-101-NH_2 (Cr).[373] 1.25 g $Cr(NO_3)_3 \bullet 9\ H_2O$ (3.13 mmol, 1 equiv.) and 0.58 g 2-Amino-terephthalic acid (H_2bdc-NH_2) (3.15 mmol, 1 equiv.) were dissolved in 17.5 mL H_2O. The reaction mixture was initially stirred for 3 h at room temperature and then heated in a 50 mL autoclave to 130°C for 24 h. After cooling to room temperature, the yellow-green product was separated from the reaction mixture by centrifugation and washed with water and ethanol over a couple of days three times each. For the activation, the powder is placed at 150 °C for 12 h under an oil pump vacuum. Then, the powders were handled under inert conditions.

CoBTC.[374] 0.820 g Cobalt (II) acetate tetrahydrate (3.30 mmol, 1 equiv.) and 0.400 g trimesic acid (H_3btc) (1.90 mmol, 0.58 equiv.) were dissolved in 15 mL H_2O. The reaction mixture was heated in a 20 mL autoclave to 140°C for 24 h, then to 120°C for 5 h, and finally to 100°C for 5 h. After cooling to room temperature, the pink product was separated from the reaction mixture by centrifugation and washed three times each with H_2O and ethanol. For the activation, the powder is placed at 150 °C for 12 h under an oil pump vacuum during with the colour changes from pink to purple. Afterwards, the powders were handled under inert conditions.

UiO-66-HCl. [166,375,376] 0.954 g $ZrCl_4$ (4.1 mmol, 1.00 equiv.) and 1.348 g H_2bdc (8.1 mmol, 1.99 equiv.) were dissolved in 24.3 mL DMF and mixed with 0.72 mL HCl (0.86 g of 37 w% $HCl_{(aq)}$, 0.32 g, 9.03 mmol, 2.20 equiv.). The reaction mixture was heated in a 50 mL autoclave to 220°C for 20 h. After cooling to room temperature, the white product was separated from the reaction mixture by centrifugation and dried at 60°C in an oven. Afterwards, the samples were redispersed in 50 mL DMF at 100°C for 150 min. After repeating the procedure, a second time, the powder was placed in a Soxhlet extractor. For 18 h the powder was extracted with methanol as a solvent. For the activation, the powder is placed at 250 °C for 12 h and 320°C for 3 h under an oil pump vacuum. Then, the powders were handled under inert conditions.

UiO-66-10TFA.[166,375] 5 g $ZrCl_4$ (21.5 mmol, 1.42 equiv.) and 2.5 g H_2bdc (15.1 mmol, 1.00 equiv.) were dissolved in 155 mL DMF and 1.5 mL HCl (1.8 g of 37 w% $HCl_{(aq)}$, 0.67 g HCl, 18.8 mmol, 1.25 equiv.) and 11.5 mL trifluoroacetic acid (17.2 g, 151 mmol, 10.0 equiv.) were added to the reaction mixture. In a 500 mL Schott flask the reaction mixture was placed in an oven at 120 °C for 24 h. The resulting white powder was centrifuged, and the solvent was replaced three times with DMF. Afterwards, DMF was replaced with 50 mL MeOH and it was exchanged three times. The powder was activated under an oil pump vacuum at 250 °C for 12 h and 320 °C for 3 h.

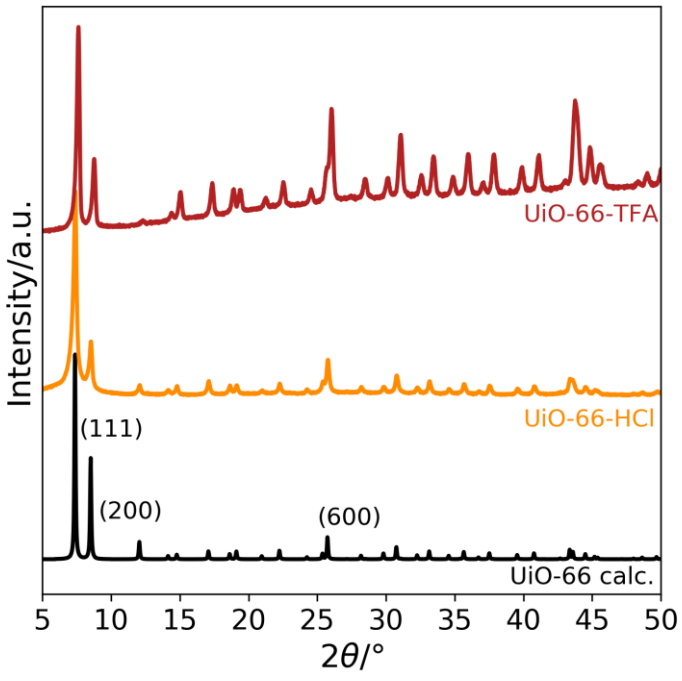

Figure S4: PXRD patterns of UiO-HCl (yellow), UiO-66-TFA(red) and the calculated UiO-66 pattern. Calculated with Vesta from the single crystal structure of UiO-66 (CCDC 733458).

Au-NP@MIL-101.[340]

MIL-101 (Cr).[377] 2.00 g $Cr(NO_3)_3 \bullet 9\ H_2O$ (5.00 mmol, 1 equiv.) and 0.82 g terephthalic acid (H_2bdc) (5.0 mmol, 1 equiv.) were dissolved in 24 mL H_2O mixed with 181 µL 48%ige HF (0.208 g, 5 mmol, 1 equiv.) *(Caution: HF is highly corrosive)*. The reaction mixture was heated in a 50 mL autoclave to 220°C for 12 h, cooled down to 150°C for 1 h, and finally cooled to room temperature for 12 h. Afterwards, the reaction mixture is centrifuged, and the supernatant quenched with $CaCl_2$ and NaOH. The precipitate is dispersed in 50 mL DMF and heated to 80°C to remove residual terephthalic acid. This procedure is repeated 3 times and the green powder is washed with water and ethanol three times each. For activation, the powder was heated to 150°C overnight under an oil pump vacuum.

23.2 mg $HAuCl_4$ and 0.607 g Polyvinylpyrrolidone (30kDa, PVP) were dissolved in 120 mL H_2O and 3.56 mL of an 0.1 M $NaBH_4$ solution in water were added over 10 min at 0°C. After stirring the reaction mixture at 0°C for 1 h, 0.623 g MIL-101 (Cr), dispersed in 4 mL in H_2O, were added to this reaction mixture and stirred for 4 hrs at room temperature. Afterwards, the powder was separated by centrifugation and washed with H_2O and ethanol three times each. Then the powder was dried under oil pump vacuum for 2 h at 100°C and heated to 200°C under 1 bar hydrogen atmosphere. Finally, the dark green-brown powder was transferred to the glovebox and kept under inert conditions.

6.3.2.2. Organic Synthesis

1-azido-dodecan-1-amine.[378] • bifunctional molecule for NMOF functionalization (chapter 3.3).

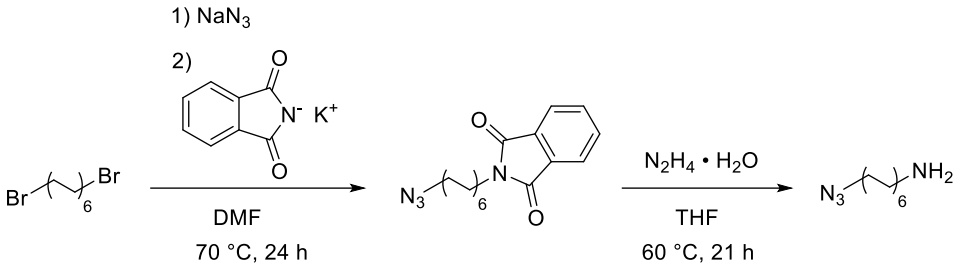

Under an atmosphere of dry argon 2.00 g 1,12-dibromododecane (6.10 mmol, 1.0 equiv.) and 322 mg sodium azide (4.95 mmol, 0.81 equiv.) are dissolved in *N,N*-dimethylformamide (9.25 mL) and stirred at 70 °C for 6 h. 5.68 g Potassium phthalimide (30.7 mmol, 5.03 equiv.) and *N,N*-dimethylformamide (2 mL) are added and the reaction mixture is stirred at 70 °C for a further 18 h. Subsequently, the solids are filtered off and the solvent is removed *in vacuo*. The resulting light-yellow substance is dissolved in dichloromethane (20 mL) and extracted with deionized water (3x 20 mL). The organic fraction is dried with $MgSO_4$, filtered, and dried *in vacuo*. This yields the light brown intermediate 1.55 g *N*-(12-azidododecyl)phthalimide (4.35 mmol, 71.4% yield).

^{1}H NMR (400 MHz, 298 K, CD_2Cl_2): δ (ppm) = 1.23-1.36 (m, 16H, aliphatic), 1.53-1.66 (m, 4H, C***H***$_2$CH$_2$N, C***H***$_2$CH$_2$N$_3$), 3.24 (t, 2H, CH$_2$C***H***$_2$N$_3$), 3.63 (t, 2H, CH$_2$C***H***$_2$N), 7.76 (ddd, 4H, phthalimide).

^{13}C NMR (101 MHz, 298 K, $CDCl_3$): δ (ppm) = 168.88, 134.36, 132.81, 123.45, 52.09, 38.51, 30.06, 30.04, 30.03, 30.01, 29.74, 29.69, 29.37, 29.10, 27.43, 27.25.

For the second reaction step, 1.55 g *N*-(12-azidododecyl)phthalimide (4.35 mmol, 1.00 equiv.) is dissolved in THF (12 mL) and 871 µL hydrazine monohydrate (80% in H_2O, 899 mg, 18.0 mmol, 4.00 equiv.) is added. The resulting solution is stirred for 21 h at 60 °C, during which a white precipitate is formed. Then the solvent is removed *in vacuo* and chloroform (40 mL) is added. Subsequently, the solution is extracted with NaOH solution (1 M, 3x 40 mL). The organic phase is dried with $MgSO_4$, filtered, and dried *in vacuo* to yield a yellow oil. This is purified by silica filtration (ethyl acetate followed by ethyl acetate/isopropyl amine 90/10 v%) to give the product 12-Azidododecan-1-amine (540 mg, 2.39 mmol, 53.2% yield) as a yellow solid.

^{1}H NMR (400 MHz, 298 K, $CDCl_3$): δ (ppm) = 1.16 (broad s, 2H, CH$_2$CH$_2$N***H***$_2$)1.26-1.36 (m, 16H, aliphatic), 1.44 (quin, 2H, C***H***$_2$CH$_2$NH$_2$), 1.59 (quin, 2H, C***H***$_2$CH$_2$N$_3$), 2.68 (t, 2H, CH$_2$C***H***$_2$N$_2$), 3.25 (t, 2H, CH$_2$C***H***$_2$N$_3$)

^{13}C NMR (100 MHz, 298 K, $CDCl_3$): δ (ppm) = 26.87, 27.03, 28.99, 29.30, 29.52, 29.62, 29.67, 29.70, 29.75, 33.75, 42.25, 51.65.

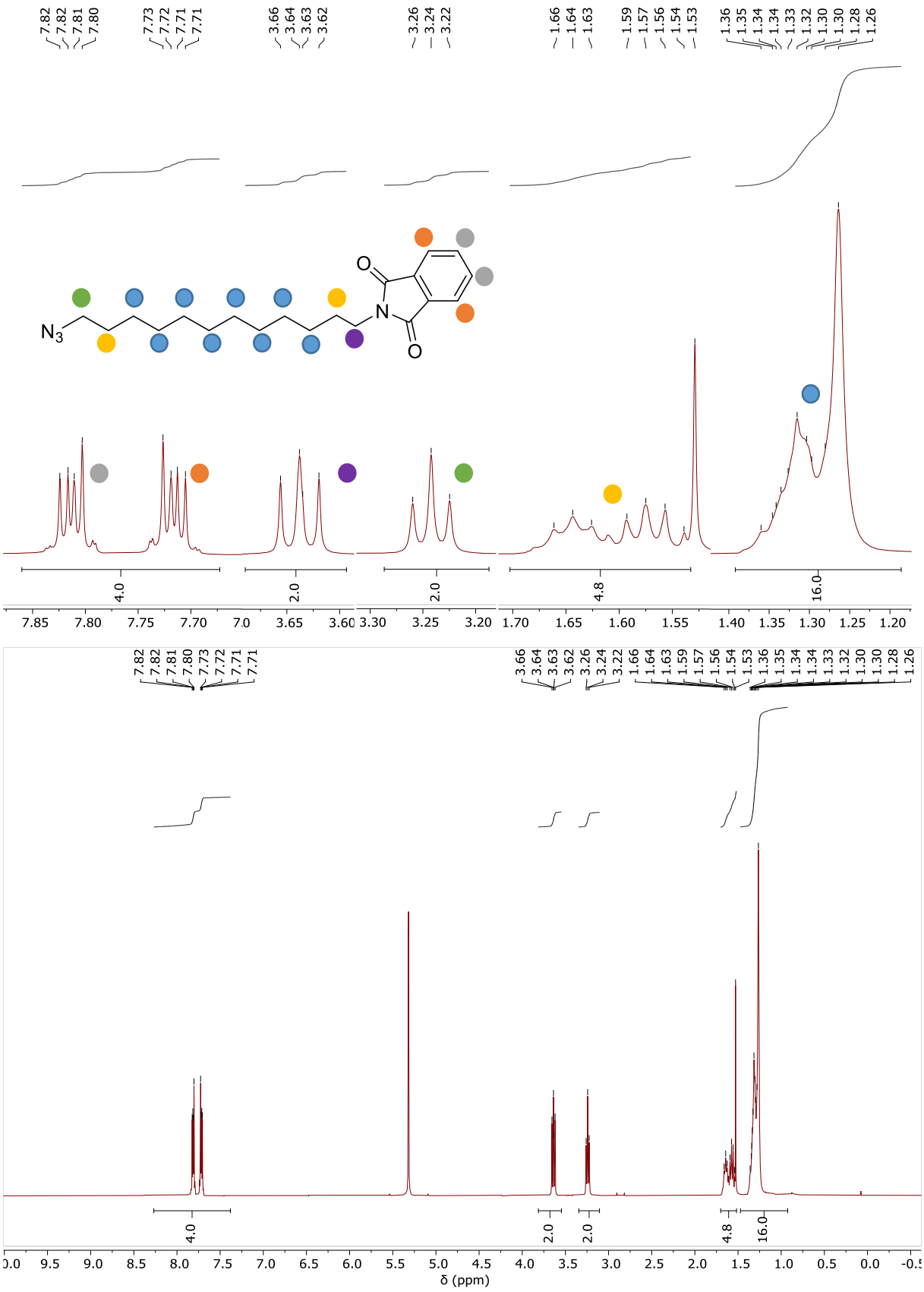

Figure S5: ^{1}H-NMR spectrum of *N*-(12-azidododecyl)phthalimide recorded in CD_2Cl_2.

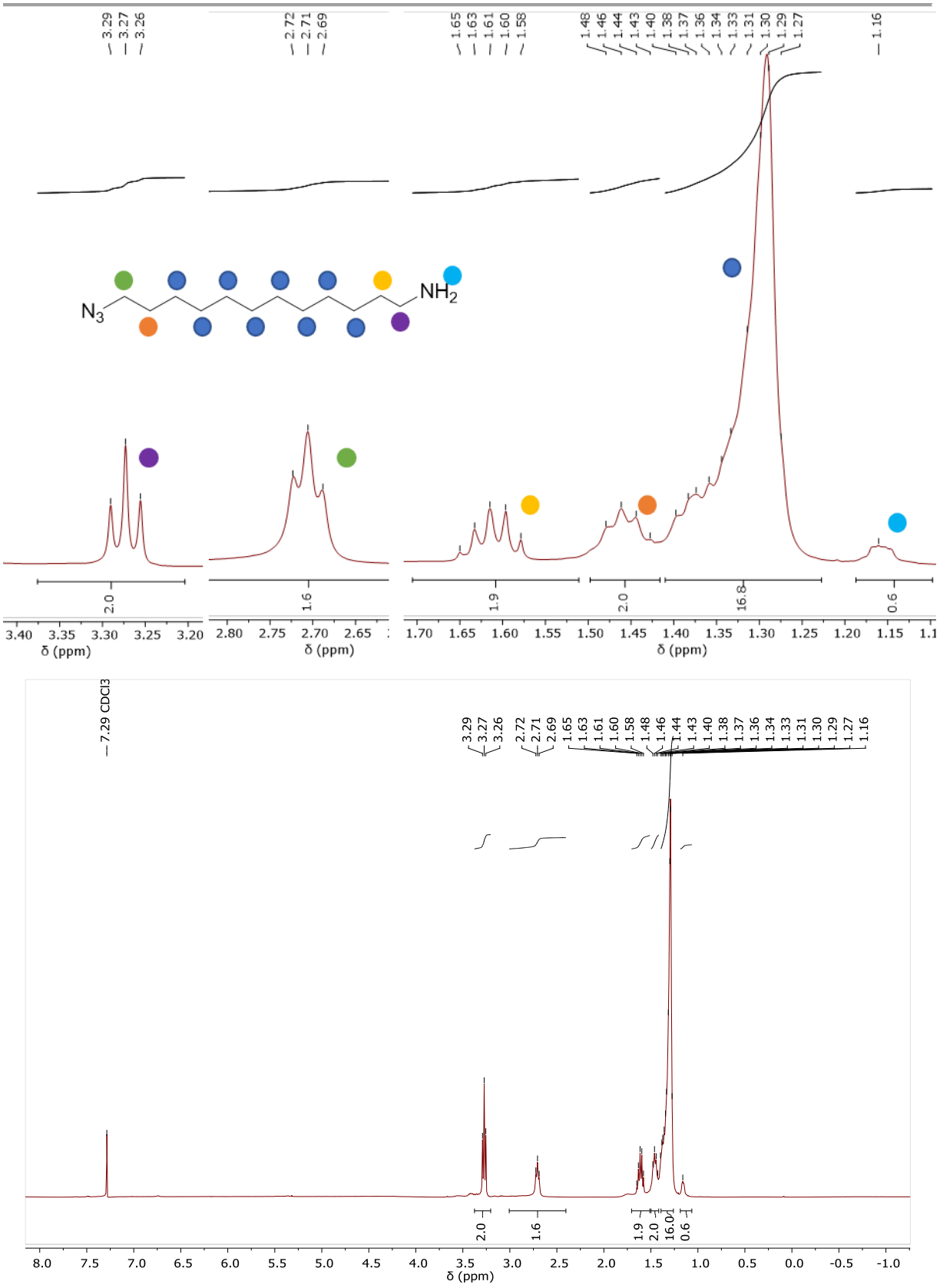

Figure S6: ^{1}H-NMR spectrum of 1-azido-dedecan-1-amine recorded in $CDCl_3$.

Synthesis of 1-(azidomethyl)pyrene[379] • Fluorescent dye for staining experiments (chapter 3.4).

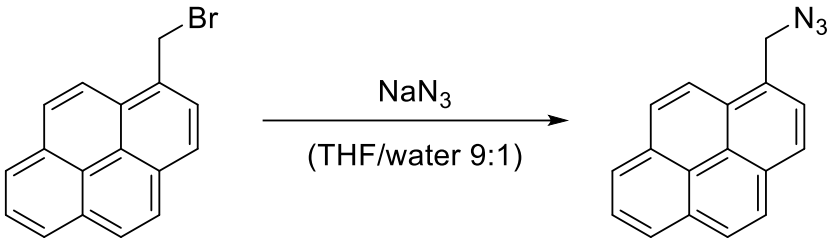

442.77 mg 1-(bromomethyl)pyrene (1.5 mmol, 1.0 equiv.) and 363.74 mg sodium azide (5.59 mmol, 3.7 equiv.) are dissolved in a solvent mixture of 10 mL THF/water (9:1 v%), and the reaction mixture is stirred at room temperature for 6 h. Afterwards, it is extracted with ethyl acetate (3x 50 mL) and the combined organic phases are washed with brine (100 mL). The organic phase is dried over $MgSO_4$ and evaporated in *vaccuo* overnight to yield 384 mg 1-(azidomethyl)pyrene (1.50 mmol, 99% yield).

^{1}H NMR (400 MHz, 298 K, $CDCl_3$): δ (ppm) = 5.08 (s, 2H, Ar-C***H***$_2$-N_3), 8.00-8.34 (m, 9H, aromatic).

^{13}C NMR (101 MHz, 298 K, $CDCl_3$): δ (ppm) = 133.35, 131.97, 131.40, 130.90, 129.44, 128.58, 128.44, 128.07, 127.66, 127.50, 126.36, 125.80, 125.73, 124.82, 122.86, 77.16, 53.28.

2-benzylidene malononitrile.[380]• reactant for GC calibration (chapter 3.5).

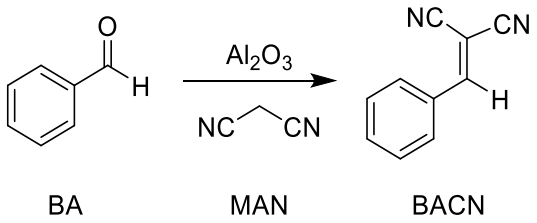

1.01 mL BA (10 mmol, 1 equiv.), 660 mg MAN (10 mmol, 1 equiv.) were mixed with 3 g Al_2O_3 and stirred at 100°C for 15 min. Afterwards, the product was extracted with DCM, and Al_2O_3 was filtered off. After DCM was removed, the product was characterized by ^{1}H NMR.

^{1}H NMR (400 MHz, CD_3CN) δ 8.11 (s, 1H, H-C=CCN), 7.98 – 7.90 (m, 2H, C-H arom.), 7.72 – 7.63 (m, 1H, C-H arom.), 7.62 – 7.55 (m, 2H, C-H arom.).

2-phenyl-2-((trimethylsilyl)oxy)-acetonitrile.[381] • reactant for GC calibration (chapter 3.5).

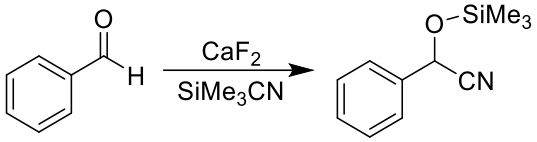

BA BAOTMSCN

10.0 g CaF_2 (128 mmol), 2 mL BA (20 mmol, 1 equiv.), 3 mL TMSCN (22 mmol, 1.1 equiv.) were dissolved in 80 mL DCM and stirred at 0°C for 4 h. Afterwards, CaF_2 is filtered off and DCM is removed to yield the product. (*Caution: remove the solvent as fast as possible at low temperatures otherwise the product decomposes.)* 3.83 g BAOTMSCN (18.7 mmol, 94.3%) was obtained as a yellowish oil.

^{1}H NMR (400 MHz, CD_2Cl_2) δ 7.54 – 7.34 (m, 5H, C-H arom.), 5.52 (s, 1H C-H), 0.23 (s, 9H Si-CH_3).

^{13}C NMR (101 MHz, CD_2Cl_2) δ 136.53 (C-H arom.), 129.32 (C-H arom.), 128.92, (C-H arom.), 126.36 (C-H arom.), 119.26 (C-N), 63.64 (q, C-H), 0.65 (TMS).

6.3.2.3. Surface Preparation and Monolayer Preparation

(a) Surface functionalization by Si-C bond formation (chapter 3.3)

Etching of the native SiO_2 surface.[255,368] After the activation by oxygen plasma, the cleaned and activated Si surfaces were then treated for 30 min in degassed 40wt % NH_4F solution, in order to remove the native oxide surface and to yield hydrogen-terminated Si (Si-H) surfaces. Finally, the substrates were washed with deionized water, blow-dried, and kept under argon for further use.

Assembly of a 1,8-nonadiyne monolayer (chapter 3.3).[269,382] Si-H substrates were placed in degassed 1,8-nonadiyne and left for 12 h at 100 °C under an argon atmosphere. After cooling to room temperature, the functionalized surface was rinsed copiously with water and sonicated in hexane and DCM for 5 min each.

Assembly of 10-undecenoic acid monolayer (chapter 3.3).[266,383] Si-H substrates were placed in the degassed 10-undecenoic acid and left for 12 h at 100 °C under an argon atmosphere. After cooling to room temperature, the functionalized surface was rinsed with water and sonicated in hexane and DCM for 5 min each.

Assembly of a 10-undecenoic acid/1,8-nonadiyne mixed monolayer (chapter 3.3).[293] The assembly of the mixed monolayer a 1/1 (n%) solution of 10-undecenoic acid and 1,8-nonadiyne is prepared and degassed. The Si-H surfaces are immersed in the solution under argon for 12 h at 100 °C. Consecutively, after cooling to room temperature the functionalized surface was rinsed with water and sonicated in hexane and DCM for 5 min each.

Patterned silicon surfaces by microcontact printing (chapter 3.3).[269] To prepare the PDMS stamps, the PDMS is poured onto a customized mold and cured according to the procedure described in chapter 6.1.1. The resulting PDMS stamps consist of rectangular islands of 20 x 20 μm diameter. For the patterning, Si-H surfaces were transferred to a glove box. The degassed 1,8-nonadiyne was dripped on a glass slide and the PDMS stamp was carefully placed on it. The 1,8-nonadiyne-soaked PDMS stamp was then placed on a silicon substrate overnight. Afterwards, the PDMS stamp was removed and the surface was cleaned by a rinse with hexane and DCM. For the backfilling, a drop of 10-undecenoic acid was placed on the silicon substrate for 12 h. After this time, the surface was rinsed with ethanol and sonicated in hexane and DCM. We also inverted the experiment, with 10-undecenonic acid in the microcontact printing step and 1,8-nonadiyne in the backfilling step.

(b) Surface functionalization by silanization (chapter 3.4/3.5)

Functionalization of PDMS substrates (chapter 3.4/3.5).[370] Amino terminated surfaces were fabricated by immersion of activated PDMS substrates in neat (3-aminopropyl)-triethoxysilane for 30 min at room temperature. Afterwards, the samples are washed with copious amounts of ethanol and deionized water and place in deionized water overnight. Alkyne terminated substrates were synthesized in a 2-step procedure, creating a chlorine terminated surface in the first step and replacing the chlorine in a second step by an alkyne group. In the first step, after activation (described in chapter 6.1.1.), the PDMS substrates are immersed in neat (3-chloropropyl)triethoxysilane for 30 min at room temperature, followed by a thorough rinse of the substrate with ethanol and deionized water. In the second step, the chlorine functionalized substrates are immersed in an 18w% slurry of sodium acetylide in xylene/mineral oil for 5 h at 150 °C. The cooled substrates are washed with a mixture of Tetrahydrofuran (THF) and Methanol (MeOH) and sonicated in MeOH for 10 min.

Functionalization of silicon substrates (chapter 3.4/3.5).[303,384] **(1)** Amino-terminated surfaces were fabricated by immersion of piranha acid-activated silicon substrates into a 10 wt.% (3-aminopropyl)-triethoxysilane solution in ethanol for 4 h at room temperature. Afterwards, the samples are washed with copious amounts of deionized water and place in deionized water overnight. Alkyne terminated substrates **(2)** were synthesized in a 2-step procedure, creating a chlorine terminated surface in the first step and replacing the chlorine in a second step by an alkyne group. In the first step, the piranha acid-activated Si substrates were immersed in a 10 w% (3-chloropropyl)triethoxysilane solution in ethanol for 4 h at room temperature, followed by a thorough rinse of the substrate with deionized water. In the second step, the chlorine functionalized substrates are immersed in an 18 w% slurry of sodium acetylene in xylene/mineral oil for 5 h at 150 °C. The cooled substrates are washed with a mixture of tetrahydrofuran (THF) and methanol (MeOH) and sonicated in MeOH for 10 min.

6.3.2.4. Surface Anchoring

Copper-catalyzed azide-alkyne cycloaddition (CuAAC) of NMOF 2 with alkyne terminated surfaces. The blow-dried, alkyne-functionalized Si (either fabricated by silanization or Si-C bond formation) or PDMS surfaces reacted with **NMOF 2** by the copper-catalyzed azide-alkyne cycloaddition (CuAAC). Thereto, three different synthetic routes were explored, which each worked best for one of the substrate types.

1) **alkyne-functionalized Si prepared by the reaction of 1,9-nonadiyne and hydrogen-terminated Si (Si-H) surfaces (chapter 3.3).**[382]

Therefore, 6.5 mg copper (I) bromide tris(triphenylphosphine) (7.0 μmol) and 0.5 mL triethylamine were dissolved in 1 mL THF. To this mixture, 1 mL **NMOF 2** ethanol solution and the alkyne-functionalized Si substrate were added and left at room temperature overnight forming **2@Si (S1).** After the reaction, the substrate was rinsed with copious amounts of water and sonicated in water, ethanol, and DCM for 5 min each. Alternatively, the CuAAC reaction can be performed by dissolving 6.5 mg $CuSO_4 \bullet 5H_2O$ (26 μmol), and 5 mg ascorbic acid (28 μmol) were in 5 mL deionized water, and 1 mL of colloidal **NMOF 2** in EtOH was added. After sonicating for 5 min the alkyne functionalized substrate was added, and the reaction was heated to 50°C at 50W for 30 min in a microwave. After the reaction, the substrate was rinsed with copious amounts of water and sonicated in water, ethanol, and DCM for 5 min each.

2) alkyne-functionalized Si manufactured by silanization(chapter 3.4). [269,293]

NMOF 2 suspended in absolute ethanol (1 mL, ca. 4.5 mg NMOF), bromotris(triphenylphosphine)copper(I) (6.50 mg, 6.99 μmol), and triethylamine (500 μL, 363 μg, 3.59 mmol) are given to THF (1 mL). Subsequently, the sample, alkyne functionalized Si (100), is immersed in the reaction solution and left at room temperature for 17 h. Then it is washed with THF and H_2O respectively and dried with compressed air to yield **SA-NMOF 6.**

3) alkyne-functionalized PDMS fabricated by silanization (chapter 3.4).[269,293]

For the triazole formation via click chemistry, (**SA-NMOF 4**), 5 mg $CuSO_4$, 20 mg ascorbic acid, and 2 mL of the azide-functionalized **NMOF 2** colloidal solution in EtOH were mixed with additional 1 mL ethanol. The alkyne terminated substrates were place in this solution for 24 h at room temperature. Afterwards, the substrates were washed with EtOH and sonicated in EtOH for 10 min.

Amide formation of NMOF 4 with carboxylic acid terminated surfaces (chapter 3.3). [295,385,386] The blow-dried, acid-functionalized Si surfaces were reacted with **NMOF 4** by NHS-catalyzed amide formation. Therefore, 23.3 μL diisopropylcarbodiimide (18 mg, 0.14 mmol) and catalytic amounts N-hydroxsuccinimide were dissolved in 1 mL ethanol. To this mixture 3 mL **NMOF 4** ethanol solution and the acid-functionalized Si substrate were added and reacted for 12 h at room temperature. After the reaction, the substrate (**4@Si (S3)**) was rinsed with copious amounts of water, ethanol, and DCM.

Reaction of the mixed monolayer (alkyne/acid) Si substrate (chapter 3.3).[382] In the final step, the surface was sequentially reacted with **NMOF 2** in the CuAAC and with **NMOF 4** via amide coupling as described above, forming **S2**.

Patterned monolayer (alkyne/acid) Si surfaces (chapter 3.3).[382] The patterned substrate was sequentially reacted with **NMOF 2** and **4** as described before, creating **S4** and **S5**.

Amide formation of NMOF 1 with amino terminated surfaces (chapter 3.4).[295,385,386] For the amide bond formation, amine-terminated substrates (PDMS or silicon) were placed in a reaction mixture consisting of 3 mL of colloidal **NMOF 1** solution in EtOH, 1 mL additional EtOH, 22.3 μL N,N-diisopropyl carbodiimide (18 mg, 0.14 mmol) and catalytic amounts of N-hydroxysuccinimide for 4 h at room temperature. Afterwards, the substrates were washed thoroughly with EtOH and were sonicated for 10 min in EtOH. The manufactured substrates are denoted as NMOF 1@PDMS (**SA-NMOF 3**) or NMOF 1@Si (**SA-NMOF 5**).

Surface anchoring of the NMOFs@substrate (Si, PDMS) (chapter 3.4/3.5). [295,385,386] For the amide bond formation amine-terminated substrates (PDMS or silicon) were placed in a reaction mixture consisting of 12 mg of the respective MOF in 4 mL EtOH, 22.3 μL N,N-diisopropyl carbodiimide (18 mg, 0.14 mmol), and catalytic amounts of N-hydroxysuccinimide for 24 h at room temperature. Prior to the addition of the substrate, the mixture is sonicated for 5 min. Afterwards, the substrates were washed thoroughly with EtOH and were sonicated for 5 min in EtOH.

6.3.2.5. Staining Experiments • (Chapter 3.4)

***Kaiser* ninhydrin test**[387,388]

In order to probe free amine functionalities on modified PDMS, the *Kaiser* test is suitable. A stock solution contains 0.3 g ninhydrin, 3 mL acetic acid, and 100 mL *n*-butanol. The respective sample is submerged in a few mL of this mixture and heated for five minutes at 100 °C. Upon a positive test result, the initially colourless solution turns dark purple due to the formation of *Ruhemann's* purple. [387,388] The latter is a strong dye, easily visible to the human eye. The test results for various PDMS samples are shown in Figure S7.

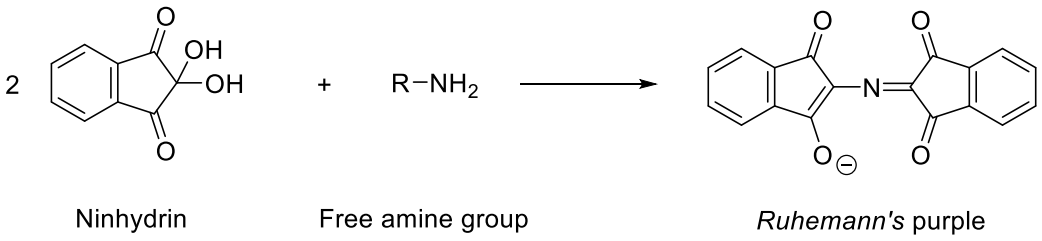

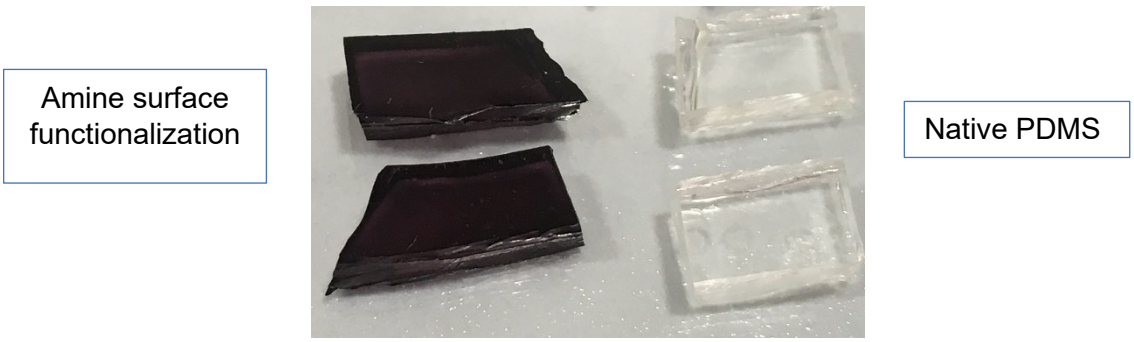

Figure S7: PDMS samples after performing the Kaiser ninhydrin test for free amine groups. Left: Surface functionalized with (3-aminopropyl)triethoxysilane and dark purple colouring visible. Right: Native PDMS illustrating no colour change after identical treatment.

For native PDMS, acting as a blank, no colour change can be observed, while amine-functionalized PDMS displays the characteristic dark purple colour. From the intense and even colour distribution it seems plausible that the modification process is successful and provides a relatively homogeneous macro-scale functionalization.

Baeyer test[389]

To test for free alkyne functionalities on chemically modified PDMS the *Baeyer* test is performed. Thus, one drop of saturated $KMnO_4$ solution is diluted with deionized water and a sample is submerged and stirred for two hours at 70 °C. A resulting yellow or light-brown substrate colouring indicates successful oxidation.[389]The resulting brown manganese(IV) oxide is apparent on the PDMS sample, as can be seen from Figure S8, implying a successful functionalization procedure.

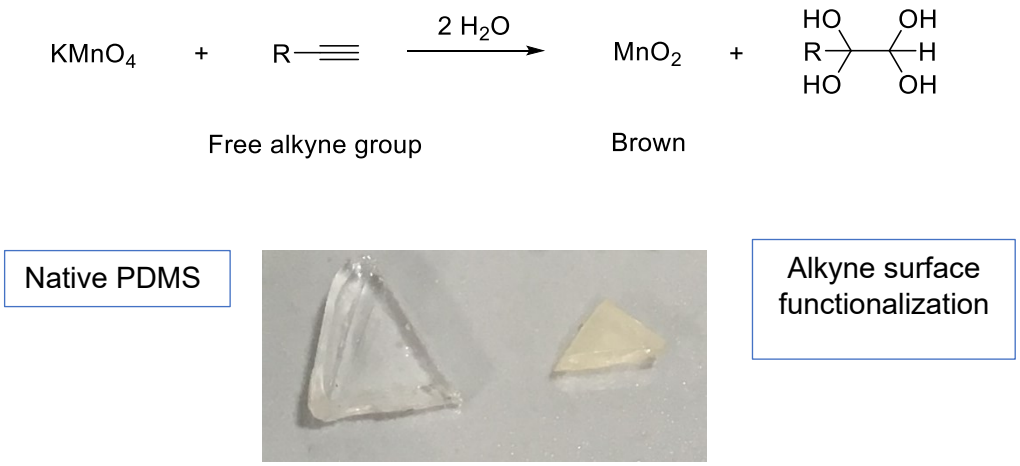

Figure S8: PDMS samples after performing the *Baeyer* test for free alkyne groups. Left: Native PDMS illustrating no colour change. Right: Surface functionalized with (3-chloropropyl)trimethoxysilane, subsequently converted to an alkyne group with sodium acetylide and a slightly brown colouring visible.

6.3.2.6. Catalytic Procedures

6.3.2.6.1. Individual Reactions in Batch • (Chapter 3.4)

Cyanosilylation of benzaldehyde to 2-phenyl-2-((trimethylsilyl)oxy)-acetonitrile.[166] **• (chapter 3.4).** The catalyst (either 8.2 mg of **NMOF 1** or **2, UiO-66-HCl** or **UiO-66-10TFA** or 1 cm^2 of **SA-NMOF 3** or **SA-NMOF 4**) were immersed in a solution of 100 µL benzaldehyde (104 mg, 980 µmol, 1.00 equiv.), 223 µL dodecane (167 mg, 980 µmol, 1.00 equiv.) 248 µL trimethylsilyl cyanide (197 mg, 1.98 mmol, 2.02 equiv.) and 4 mL toluene. Prior to the reaction SA-NMOF 4 and 5 are activated for 30 min at 80°. The resulting mixture is stirred at 40 °C and 500 rpm. After the certain time intervals, an aliquot of 50 µL is taken, diluted with the solvent (1.5 mL), centrifuged for 30 min, and analyzed via GC.

From the resulting data, the corresponding time-yield plots are obtained as follows. The integrals were normalized by dividing by the effective carbon number ((ECN) Benzaldehyde: 6, cyanohydrin (2-phenyl-2-((trimethylsilyl)oxy)acetonitrile): 8.3). The normalized product area integrals are divided through the sum of the normalized product and reagent area integrals and converted to per cent values via multiplication with 100. The validity of this approach for the studied reactions is confirmed by using dodecane as an internal standard.

The determination of the ECN values was calculated by Sternberg et al.[390]

ECN (Benzaldehyde) = 6·1.0 (carbon aromatic) + 1·0.0 (Carbon Carbonyl) = 6.0

ECN (Cyanosilylationproduct) = 6·1.0 (carbon aromatic) + 4·1.0 (Carbon alphatic) – 0.7 (Nitrile) - 1 (Ether) = 8.3

ECN (Dodecane) = 12·1.0 (carbon aromatic) = 12

Hot filtration test • (chapter 3.4).
After the specified time, the catalyst sample (NMOF on PDMS) is removed from the standard catalysis reaction solution. The latter is continuously stirred at 40 °C and 500 rpm. At time intervals an aliquot of 50 µL is taken, diluted with the solvent (1.5 mL), and analyzed via GC.

Cycloaddition of CO_2 with propylene oxide to yield 4-methyl-1,3-dioxolan-2-one (propylene carbonate).[318] • (chapter 3.4). The catalyst (either 43 mg of **UiO-66-HCl** or **UiO-66-10TFA** or 2 cm^2 of **SA-NMOF 3**) is immersed in 2.1 mL propylene oxide (1.804 g, 31.06 mmol, 1.00 equiv.) and 805 mg Bu_4NBr as co-catalyst (2.49 mmol, 0.08 equiv.) and pressurized with 1 bar CO_2 in a 50 mL Fischer-Porter bottle. The catalyst **SA-NMOF 3** was placed in an oven at 100 °C under air for 12 h prior to the reaction. The resulting mixture is stirred at 50 °C and 500 rpm. After defined time intervals aliquots of 0.05 mL are taken, diluted with the $DCCl_3$, and analyzed via ^{1}H-NMR.

For calculating the time yield plots, the reaction mixture was rapidly cooled down with liquid nitrogen and 0.05 mL of the reaction mixture was diluted with 0.5 mL of $DCCl_3$. After measuring a proton NMR, the yield was determined by integration of the signals. The normalized product area integrals are divided through the sum of the normalized product and reagent area integrals and converted to per cent values via multiplication with 100. The validity of this approach for the studied reactions is confirmed by using the cocatalyst Bu_4NBr as an internal standard.

Table S1: Total ^{1}H NMR integrals from the NMR Figure S9.

Integral (Propylene oxide)	Integral (4-methyl-1,3-dioxolan-2-one)	Integral (Bu_4NBr)
6	16.55	18.19

$$yield = \frac{6}{6 + 16.55} = 26.6\%$$

$$yield = \frac{\frac{6}{6}}{\frac{18.19}{36}} \frac{31.05\ mmol}{2.49\ mmol} = 24.7\%$$

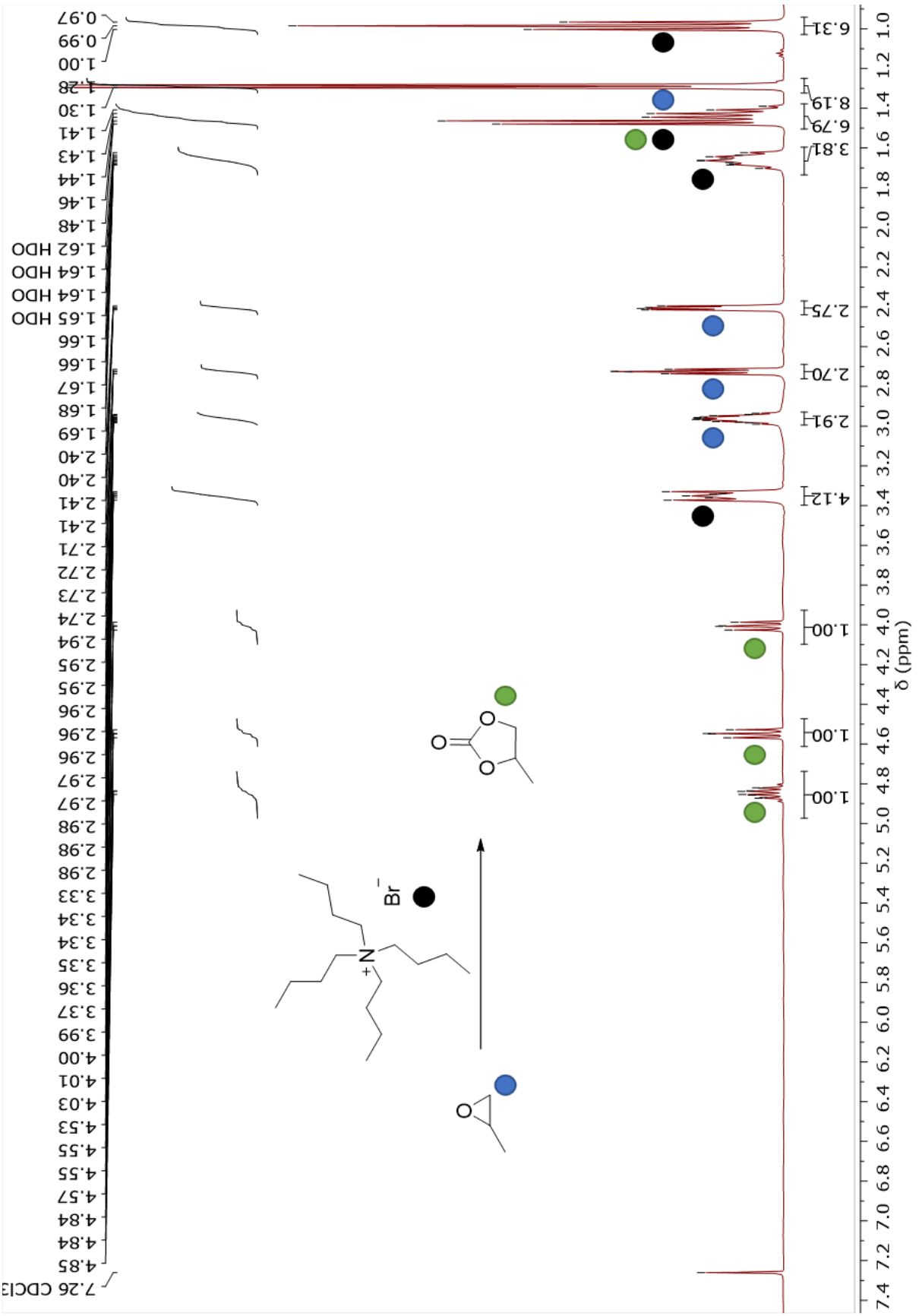

Figure S9: ^{1}H-NMR spectrum of the catalyzed reaction of propylene oxide to 4-methyl-1,3-dioxolan-2-one recorded in $CDCl_3$.

6.3.2.6.2. Reaction Sequences in Batch • (Chapter 3.5)

Reaction sequence: benzaldehyde dimethyl acetal (BADMA) to benzaldehyde (BA) and finally to 2-benzylidene malononitrile (BACN). [328–331] **• (chapter 3.5.4)**

To transfer the reaction sequence to vectorial catalysis in a microfluidic device, we needed to optimize the parameters for each reaction in batch to find the optimal reaction conditions for the reaction sequence.

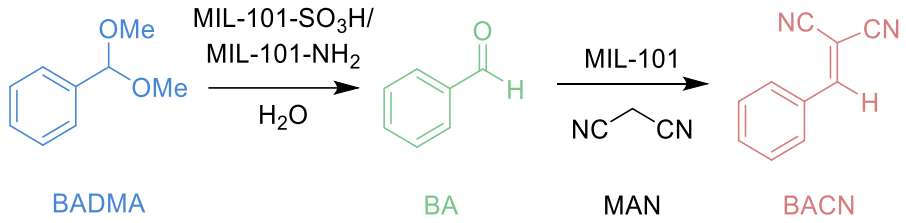

Therefore, we started optimizing the reaction conditions for the hydrolysis of BADMA to BA. The liquid phase catalysis was conducted under atmospheric pressure. Prior to their use as catalysts, the MOF powders were activated according to the procedures described in chapter 6.3.2.1, the SA-NMOFs were activated at 80°C for 30 min in an oven under atmospheric pressure. In a typical experiment, 75 µL BADMA (0.50 mmol, 1 equiv.) was dissolved in 4 mL of solvent (acetonitrile (MeCN), tetrahydrofuran, dioxane, propylene carbonate, or dimethylformamide) and 0-125 equiv. H_2O, and finally 5 mg of activated catalyst powder (MIL-101 (Cr), MIL-101-NH_2 (Cr), MIL-101-SO_3H (Cr), UiO-66, and CoBTC) were added and stirred in a 20 mL screw cap vial at various temperatures (25°C, 50°C). After certain time intervals, an aliquot of 100 µL is taken, diluted with the solvent (1.4 mL), filtered with a syringe filter, and finally analyzed by GC. For the **blind reactions (-),** the same reaction conditions were applied, but the catalyst was omitted. A table with the applied reaction conditions and yields can be found below.

Table S2: Reaction parameter optimization for the BADMA hydrolysis to BA, catalyzed by several MOF powders in batch.

Catalyst	m(cat)/ mg	Solvent	V(s)/ mL	Equiv H_2O	T/ °C	t/ h	V (BADMA)/ µL	Y% BA
MIL-101-SO_3H	5.0	MeCN	4.0	125	50	0.017	75	15.4
MIL-101-SO_3H	5.0	MeCN	4.0	125	50	0.25	75	85.4
MIL-101-SO_3H	5.0	MeCN	4.0	125	50	0.5	75	99.9
MIL-101-SO_3H	5.0	MeCN	4.0	125	50	1	75	100
MIL-101-SO_3H	5.0	MeCN	4.0	125	50	6	75	100
MIL-101	5.0	MeCN	4.0	125	50	0.017	75	4.4
MIL-101	5.0	MeCN	4.0	125	50	0.25	75	42.5
MIL-101	5.0	MeCN	4.0	125	50	0.5	75	59.9
MIL-101	5.0	MeCN	4.0	125	50	1	75	80.1
MIL-101	5.0	MeCN	4.0	125	50	6	75	99
MIL-101-NH_2	5.0	MeCN	4.0	125	50	0.017	75	41.5
MIL-101-NH_2	5.0	MeCN	4.0	125	50	0.25	75	93.4
MIL-101-NH_2	5.0	MeCN	4.0	125	50	0.5	75	100
MIL-101-NH_2	5.0	MeCN	4.0	125	50	1	75	100
MIL-101-NH_2	5.0	MeCN	4.0	125	50	6	75	100
UiO-66	5.0	MeCN	4.0	125	50	6	75	14.0
CoBTC	5.0	MeCN	4.0	125	50	6	75	2.0
MIL-101-SO_3H	5.0	dioxane	4.0	125	50	1	75	40.7
MIL-101-SO_3H	5.0	dioxane	4.0	125	50	6	75	100
MIL-101-SO_3H	5.0	MeCN	4.0	125	50	1	75	100
MIL-101-SO_3H	5.0	MeCN	4.0	125	50	6	75	100
MIL-101-SO_3H	5.0	THF	4.0	125	50	1	75	40.4
MIL-101-SO_3H	5.0	THF	4.0	125	50	6	75	96.4
MIL-101-SO_3H	5.0	PCO	4.0	125	50	6	75	100
MIL-101-SO_3H	5.0	DMF	4.0	125	50	6	75	56.0
-	5.0	dioxane	4.0	125	50	1	75	0.0
-	5.0	dioxane	4.0	125	50	6	75	12.7
-	5.0	THF	4.0	125	50	1	75	0.0
-	5.0	THF	4.0	125	50	6	75	4.3
-	5.0	MeCN	4.0	125	50	1	75	0.0
-	5.0	MeCN	4.0	125	50	6	75	0.0
-	5.0	PCO	4.0	125	50	6	75	4.3
-	5.0	DMF	4.0	125	50	6	75	0.0
MIL-101-SO_3H	5.0	MeCN	4.0	0	50	6	75	15.4
MIL-101-SO_3H	5.0	MeCN	4.0	10	50	6	75	32.9
MIL-101-SO_3H	5.0	MeCN	4.0	20	50	6	75	47.2
MIL-101-SO_3H	5.0	MeCN	4.0	30	50	6	75	51.5
MIL-101-SO_3H	5.0	MeCN	4.0	40	50	6	75	63.0
MIL-101-SO_3H	5.0	MeCN	4.0	50	50	6	75	79.0
MIL-101-SO_3H	5.0	MeCN	4.0	75	50	6	75	100
MIL-101-SO_3H	5.0	MeCN	4.0	100	50	6	75	97.5
MIL-101-SO_3H	5.0	MeCN	4.0	125	50	6	75	100
MIL-101-SO_3H	5.0	MeCN	4.0	125	25	6	75	80.2
-	5.0	MeCN	4.0	125	25	6	75	0.0
MIL-101-SO_3H@PDMS	5.0	MeCN	4.0	125	50	13	75	5.3
MIL-101@PDMS	5.0	MeCN	4.0	125	50	13	75	0
MIL-101-NH_2@PDMS	5.0	MeCN	4.0	125	50	13	75	4.4
UiO-66@PDMS	5.0	MeCN	4.0	125	50	13	75	2.1
CoBTC@PDMS	5.0	MeCN	4.0	125	50	13	75	4.7
-	5.0	MeCN	4.0	125	50	13	75	0

For the second reaction of the reaction sequence, the Knoevenagel reaction of BA and MAN yielding BACN; the MOF catalyzed reaction conditions were optimized. The liquid phase catalysis was conducted under atmospheric pressure. Prior to their use as catalysts, the MOF powders were activated according to the procedures described in chapter 6.3.2.1, the SA-NMOFs were activated at 80°C for 30 min in an oven under atmospheric pressure. In a typical experiment, 50 µL BA (0.49 mmol, 1 equiv.) and 1-10 equiv. malononitrile were dissolved in 4 mL of solvent (MeCN, tetrahydrofuran, dioxane, propylene carbonate, or dimethylformamide) and 0-125 equiv. H_2O and finally 5 mg of activated catalyst powder (MIL-101 (Cr), MIL-101-NH_2 (Cr), MIL-101-SO_3H (Cr), UiO-66, and CoBTC) were stirred in a 20 mL screw cap vial at various temperatures (25°C, 50°C). After the certain time intervals, an aliquot of 100 µL is taken diluted with the solvent (1.4 mL) and analyzed by GC. For the **blind reactions (-),** the same reaction conditions were applied, but the catalyst was omitted. A table with the applied reaction conditions can be found below.

Table S3: Reaction parameter optimization for the BADMA hydrolysis to BA, catalyzed by several MOF powders in batch.

Catalyst	m(cat)/ mg	Solvent	V(s)/ mL	Equiv H_2O	T/ °C	t/ h	Equiv. MAN	V (BA)/ µL	Y% BA
MIL-101-SO_3H	5.0	MeCN	4.0	125	50	1	2	50	6.8
MIL-101	5.0	MeCN	4.0	125	50	1	2	50	57.9
MIL-101-NH_2	5.0	MeCN	4.0	125	50	1	2	50	10.0
UiO-66	5.0	MeCN	4.0	125	50	1	2	50	51.2
CoBTC	5.0	MeCN	4.0	125	50	1	2	50	87.3
MIL-101-SO_3H @PDMS	5.0	MeCN	4.0	125	50	1	2	50	60.8
MIL-101 @PDMS	5.0	MeCN	4.0	125	50	1	2	50	68.4
MIL-101-NH_2 @PDMS	5.0	MeCN	4.0	125	50	1	2	50	61.1
UiO-66 @PDMS	5.0	MeCN	4.0	125	50	1	2	50	64.7
CoBTC @PDMS	5.0	MeCN	4.0	125	50	1	2	50	61.8
MIL-101	5.0	dioxane	4.0	125	50	1	2	50	89.5
MIL-101	5.0	MeCN	4.0	125	50	1	2	50	87.0
MIL-101	5.0	THF	4.0	125	50	1	2	50	78.4
MIL-101	5.0	PCO	4.0	125	50	1	2	50	89.1
MIL-101	5.0	DMF	4.0	125	50	1	2	50	96.0
-	5.0	dioxane	4.0	125	50	1	2	50	44.7
-	5.0	THF	4.0	125	50	1	2	50	86.3
-	5.0	MeCN	4.0	125	50	1	2	50	44.0
-	5.0	PCO	4.0	125	50	1	2	50	56.0
-	5.0	DMF	4.0	125	50	1	2	50	89.1
MIL-101	5.0	MeCN	4.0	125	25	6		75	24.2
-	5.0	MeCN	4.0	125	25	6		75	4.0

Catalyst	m(cat)/ mg	Solvent	V(s)/ mL	Equiv H_2O	T/ °C	t/ h	Equiv. MAN	V (BA)/ µL	Y% BA
MIL-101	5.0	MeCN	4.0	0	50	6	2	75	8.3
MIL-101	5.0	MeCN	4.0	10	50	6	2	75	11.1
MIL-101	5.0	MeCN	4.0	20	50	6	2	75	16.6
MIL-101	5.0	MeCN	4.0	30	50	6	2	75	18.8
MIL-101	5.0	MeCN	4.0	40	50	6	2	75	13.9
MIL-101	5.0	MeCN	4.0	50	50	6	2	75	28.4
MIL-101	5.0	MeCN	4.0	75	50	6	2	75	37.4
MIL-101	5.0	MeCN	4.0	100	50	6	2	75	39.7
MIL-101	5.0	MeCN	4.0	125	50	6	2	75	57.9
-	5.0	MeCN	4.0	125	50	6	1	75	24.5
MIL-101	5.0	MeCN	4.0	125	50	6	1	75	43.1
-	5.0	MeCN	4.0	125	50	6	2	75	44.0
MIL-101	5.0	MeCN	4.0	125	50	6	2	75	57.9
-	5.0	MeCN	4.0	125	50	6	10	75	68.8
MIL-101	5.0	MeCN	4.0	125	50	6	10	75	90.9

Reaction sequence: benzaldehyde (BA) to 2-phenyl-2-((trimethylsilyl)oxy)-acetonitrile (BAOTMSCN) and finally to malononitrile (MN). [166] **(chapter 3.5.5)**

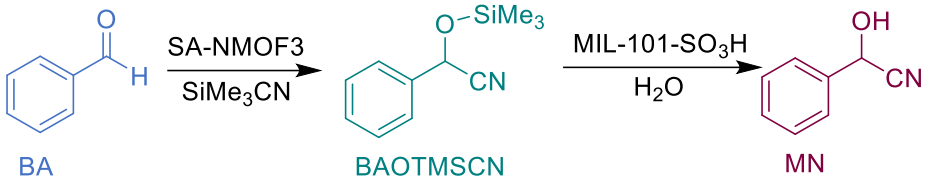

The catalysis was conducted in liquid phase under atmospheric pressure and at 95°C. Prior to their use as catalysts, the MOFs were activated according to the procedures described in chapter 6.3.2.1 the SA-NMOFs were activated at 80°C for 30 min in an oven under atmospheric pressure. In a typical procedure, 100 µL BA (104 mg, 980 µmol, 1.00 equiv.) and 248 µL trimethylsilyl cyanide (TMSCN) (197 mg, 1.98 mmol, 2.02 equiv.) were dissolved 4 mL DMF and 1 cm^2 of SA-NMOF 3 is added to the solution. The resulting solution is stirred at 40 °C and 500 rpm. After the certain time intervals, an aliquot of 25 µL is taken, diluted with $DCCl_3$, filtered through a syringe filter, and analyzed by ^{1}H-NMR (0.4 mL).

The catalyzed hydrolysis of BAOTMSCN to MN was conducted in liquid in a 20 mL screw cap vial under atmospheric pressure at 95°C. Prior to their use as catalysts, the MOFs were activated according to the procedures described in chapter 6.3.2.1 the SA-NMOFs were activated at 80°C for 30 min in an oven under atmospheric pressure. In a typical experiment, 213 µL BAOTMSCN (201 mg, 980 µmol, 1.00 equiv.) was dissolved 4 mL DMF and stirred at 500 rpm. As a catalyst, 1 cm^2 of MIL-101-SO_3H@PDMS or 5 mg activated MIL-101-SO_3H were added. After the certain time intervals, an aliquot of 25 µL is taken, diluted with $DCCl_3$, filtered through a syringe filter, and analyzed by ^{1}H-NMR (0.4 mL).

For the **blind reactions,** the same reaction conditions were applied, but the catalyst was omitted.

Prior to the analysis, $DCCl_3$ is filtered through basic Al_2O_3 to remove residual HCl/DCl to prevent the hydrolysis of BAOTMSCN.

Reaction sequence: benzyl alcohol (BAOH) to benzaldehyde (BA) and finally to 2-phenyl-2-((trimethylsilyl)oxy)-acetonitrile (BAOTMSCN). [223,314,339,340]• **(chapter 3.5.6)**

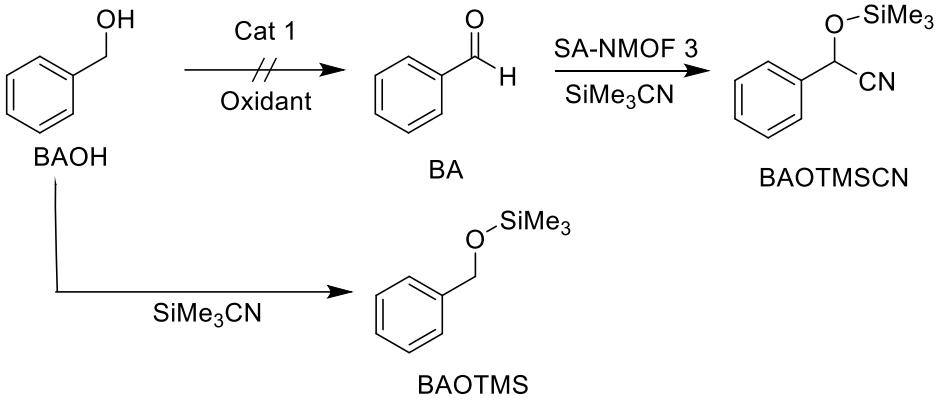

The catalysis was conducted in the liquid phase under atmospheric pressure and at 95°C. Prior to their use as catalysts, the MOFs were activated according to the procedures described in chapter 6.3.2.1 the SA-NMOFs were activated at 80°C for 1 h. In a typical catalysis procedure, 50 µL BAOH (52 mg, 490 µmol, 1.00 equiv.) and 2-10 equiv. oxidants (H_2O_2, tert-butylhydroperoxide (tBuOOH, 70 w% stabilized in water), 2,2,6,6-tetramethylpiperidinyloxyl (TEMPO)), 0-10 equiv. additives (Na_2CO_3, K_2CO_3, and 1-methyl imidazole) were dissolved 4 mL DMF and stirred at 500 rpm in a 20 mL screw cap vial For the follow-up reaction, 2-10 equiv. TMSCN were added to the solution alongside 1 cm^2 of SA-NMOF 3 or 5 mg of UiO-66-HCl. After the certain time intervals, an aliquot of 100 µL is taken, diluted with the solvent (1.4 mL), and analyzed by GC.

6.3.2.7. Microfluidic Device Manufacturing • (Chapter 3.5)

Microfluidic device manufacturing.[324–327]

Cured PDMS with the microfluidic channel structure was obtained by pouring PDMS onto a suitable mold (see Figure S10). The PDMS curing procedure is described in chapter 6.1.1.

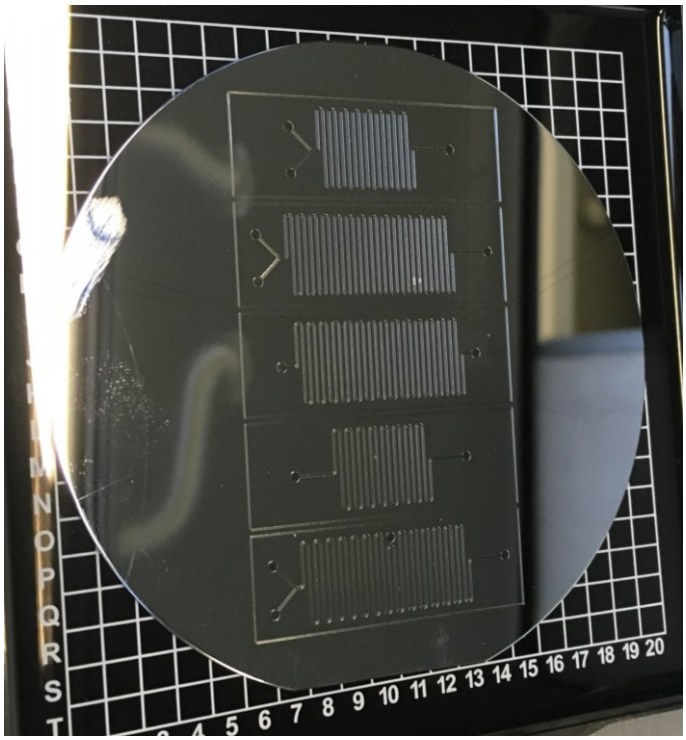

Figure S10: Silicon wafer master mold with the respective channel structure used for the fabrication of PDMS based microfluidic devices. Purchased from *microLIQUID S.L.* under communication of design needs. The diamensions are 14 coils (13 mm x 0,3 mm x 0.15 mm; 9 µL) for the small reactors and 28 coils (13 mm x 0,3 mm x 0.15 mm; 18 µL) for the larger microfluidic reactors.

Bottom substrate functionalization. [295,385,386]

The successful approach to obtain NMOFs anchored inside a microfluidic device is modifying the glass slide or PDMS substrate serving as a reactor base via the experimental procedure described in chapter 6.3.2 (b) to yield amino-functionalized glass or PDMS. Then, the glass or PDMS substrate is immersed in UiO-66(Zr), MIL-101-NH_2 (Cr), MIL-101-SO_3H (Cr), MIL-101 (Cr) NMOF suspended in absolute ethanol (9 mL, ca. 27 mg NMOF) and additional absolute ethanol is added for full submersion (roughly 15 mL). Additionally, 89.6 µL *N,N'*-diisopropylcarbodiimide (DIC) (72.0 mg, 574 µmol) and catalytic amounts of *N*-hydroxysulfosuccinimide (NHS) are weighed in. Then the reaction mixture reacted for 12 h, followed by thorough washing with absolute ethanol and drying with compressed air.

For the selectively functionalized microfluidic devices, identical reaction conditions are chosen, however, half of the amino-functionalized PDMS/glass slide is immersed in the UiO-66(Zr)/ MIL-101-NH_2 (Cr)/ MIL-101-SO_3H (Cr) solution. Subsequently, the other side is immersed in freshly synthesized MIL-101-SO_3H (Cr)/MIL-101(Cr) suspended in absolute ethanol (5 mL, ca. 25 mg NMOF). The remaining reagents and quantities for the amide bond formation described above are kept identical.

Microfluidic device sealing.[324–327]

To seal the molded PDMS sample to the modified glass slide/ PDMS substrate is kept in an oven at 100 °C for 24 hours, weighed down by an autoclave to ensure tight sealing.

6.3.2.7.1. Reaction Sequences in Microfluidic Reactors • (Chapter 3.5)

Benzaldehyde dimetylacetal hydrolysis and subsequential Knoevenagel condensation using MIL-101-SO_3H(Cr) or MIL-101-NH_2(Cr) and MIL-101(Cr) in a microfluidic reactor.[341]**• (chapter 3.5.4)**

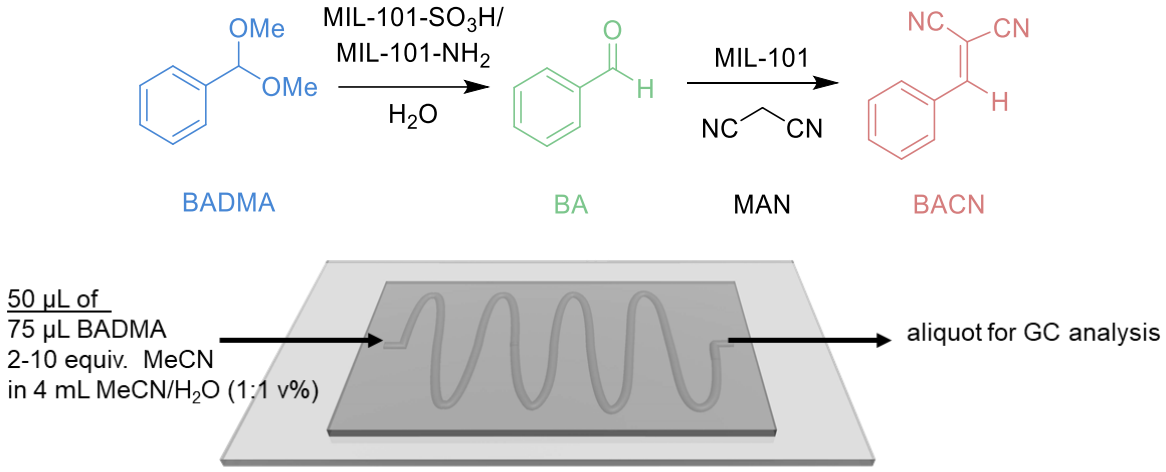

The liquid phase vectorial catalysis was conducted in microfluidic devices, which were assembled as described above. The flow catalysis was conducted in liquid phase and under ambient conditions. Prior to their use as reactors, the microfluidic devices containing the SA-NMOFs were activated at atmospheric pressure in an oven at 100°C for 30 min.

Simultaneously, a solution of 75 µL benzaldehyde dimethylacetal (79 mg, 490 µmol, 1.0 equiv.), 66 or 330 mg malononitrile (980 µmol, 2.0 equiv.; 4900 µmol, 10.0 equiv.) in 4 mL acetonitrile/water (1:1 v%) is prepared and stirred in a 20 mL screw cap vial for 1 min at room temperature for homogeneity. 50 µL of this solution is applied to the microfluidic device, at the outlet of the reactor a syringe is used to apply a vacuum, inducing the flow of the solution through the reactor. The typical retention time for the acetonitrile/water (1:1 v%) based solution in a 9 µL microfluidic device (14 coils á 13 mm x 0,3 mm x 0.15 mm) was 30s. The mean retention time was determined by dividing the total time by the total applied volume and multiplying it with the reactor volume (9 µL). The syringe is additionally used to collect the aliquot, which is diluted with MeCN (1.4 mL) and analyzed via GC.

Cyanosilylation of benzaldehyde with TMSCN and subsequential hydrolysis of BAOTMSCN using UiO-66(Zr) and MIL-101-SO_3H(Cr) in a microfluidic reactor. • (chapter 3.5.5)

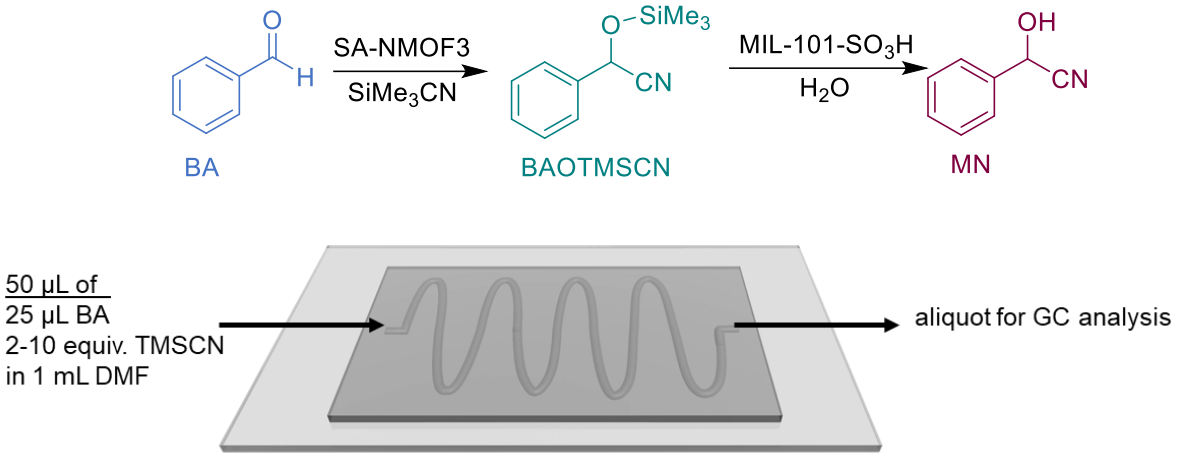

The liquid phase vectorial catalysis was conducted in microfluidic devices, which were assembled as described above. The flow catalysis was conducted in liquid phase and under ambient conditions. Prior to their use as reactors, the microfluidic devices containing the SA-NMOFs were activated under atmospheric pressure in an oven at 100°C for 30 min.

Simultaneously, a solution of 25 µL benzaldehyde (26 mg, 245 µmol, 1.0 equiv.), 60 or 300 µL trimethylsilyl cyanide (48 mg, 490 µmol, 10.0 equiv.; 238 mg, 2450 µmol, 10.0 equiv.) in 1 mL DMF is prepared and stirred in a 5 mL screw cap vial for 1 min at room temperature for homogeneity. 50 µL of this solution is applied to the microfluidic device, at the outlet of the reactor a syringe is used to apply a vacuum, inducing the flow of the solution through the reactor. The typical retention time for the DMF-based solution in a 9 µL microfluidic device (14 coils á 13 mm x 0,3 mm x 0.15 mm) was 60 s. The mean retention time was determined by dividing the total time by the total applied volume and multiplying it with the reactor volume (9 µL). The syringe is additionally used to collect the aliquot, which is partly diluted with DMF (1.4 mL) and analyzed via GC, the other half of the solution is diluted with $DCCl_3$ (0.4 mL) and analyzed via ^{1}H-NMR.

Application of HCl. Another reactor design (see below) enables the addition of 1 equiv. of HCl halfway through the reactor. The reactor design includes in total 28 coils and 3 inlets (front, after 14 coils, end). Each coil is 13 mm long, 0,3 mm wide, and 0.15 mm high. The experiment was conducted under ambient conditions. Prior to their use, the reactors were activated under atmospheric pressure in an oven at 100°C for 30 min.

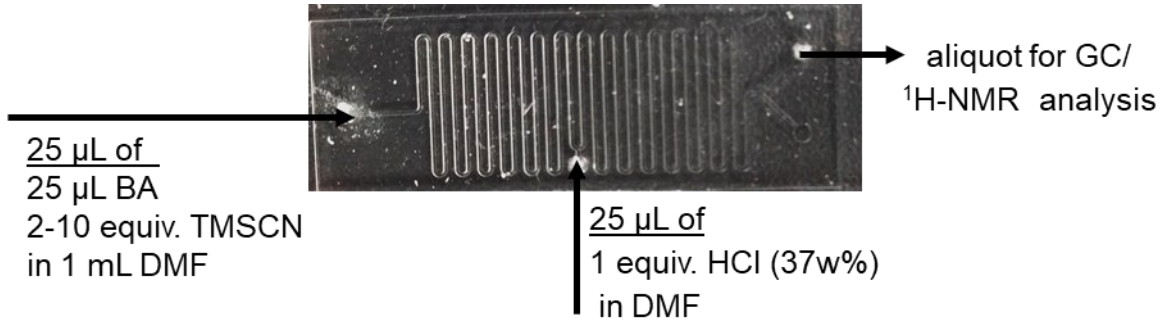

In a typical procedure, 25 µL benzaldehyde (26 mg, 245 µmol, 1.0 equiv.) and 60 or 300 µL trimethylsilyl cyanide (48 mg, 490 µmol, 10.0 equiv.; 238 mg, 2450 µmol, 10.0 equiv.) were dissolved in 1 mL DMF and stirred in a 5 mL screw cap vial for 1 min at room temperature for homogeneity. Another second solution is prepared by dissolving 19.7 µL $HCl_{(aq)}$ (37 w%, 23.4 mg, 245 µmol, 1.0 equiv.) in 1 mL DMF. 25 µL of the first solution is applied to the front inlet and 25 µL of the second solution is applied to the middle inlet (after 14 coils) of the microfluidic device. At the outlet of the reactor, a syringe is used to apply a vacuum, inducing the flow of the solution through the reactor. The typical retention time for the DMF/H_2O-based solution in an 18 µL microfluidic device (28 coils á 13 mm x 0,3 mm x 0.15 mm) was 120s. The mean retention time was determined by dividing the total time by the total applied volume and multiplying it with the reactor volume (18 µL). The syringe is additionally used to collect the aliquot, which is partly diluted with DMF (1.4 mL) and analyzed via GC, the other half of the solution is diluted with $DCCl_3$ (0.4 mL) and analyzed via ^{1}H-NMR.

Attempted vectorial catalysis: oxidation of benzyl alcohol followed up by a cyanosilylation catalyzed by Au@MIL-101(Cr) & UiO-66(Zr) in a microfluidic device• (chapter 3.5.6)

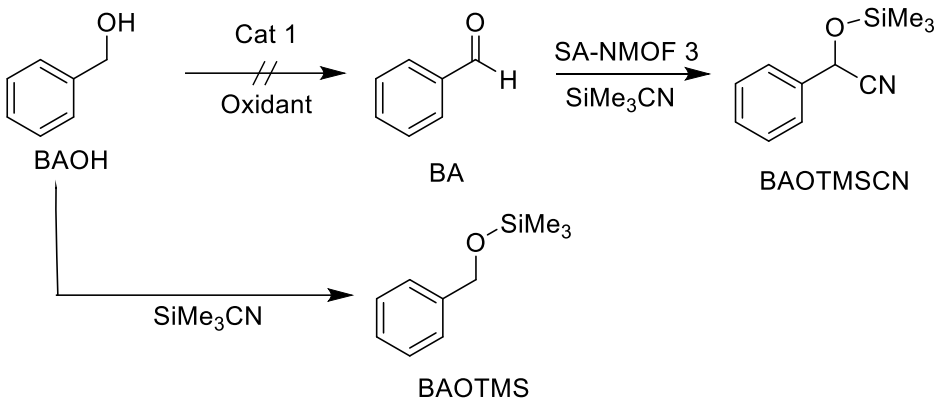

The liquid phase vectorial catalysis was conducted in microfluidic devices, which were assembled as described above. The flow catalysis was conducted in liquid phase and under ambient conditions. Prior to their use as reactors, the microfluidic devices containing the SA-NMOFs were activated under atmospheric pressure in an oven at 100°C for 30 min.

Simultaneously, a solution of 16.0 µL benzyl alcohol (16.7 mg, 154 µmol, 1.0 equiv.), 211 µL *tert*-butylhydroperoxide (70w% stabilized in water) (198 mg, 1.54 mmol, 10.0 equiv.) and 168 mg Na_2CO_3 (1.54 mmol, 10 equiv.) in 2 mL DMF is prepared and stirred briefly at 95 °C in a 5 mL screw-cap vial. 50 µL of this solution is applied to the microfluidic device, at the outlet of the reactor a syringe is used to apply a vacuum, inducing the flow of the solution through the reactor. The typical retention time for the DMF-based solution in a 9 µL microfluidic device (14 coils á 13 mm x 0,3 mm x 0.15 mm) was 60 s. The mean retention time was determined by dividing the total time by the total applied volume and multiplying it with the reactor volume (9 µL). The syringe is additionally used to collect the aliquot, which is diluted with DMF (1.4 mL) and analyzed via GC.

6.3.3. Ferroelectric Metal-Free Perovskite $[HMDABCO](NH_4)I_3$ Thin Films • (Chapter 3.5)

MDABCOI was prepared according to Kazock et al.[365] To a solution of 12.00 g DABCO (106.97 mmol, 1.50 equiv.) in 150 mL ethyl acetate, 4.50 mL methyl iodide (10.26 g, 72.28 mmol, 1.00 equiv.) were added over 15 minutes. The reaction solution was stirred for two hours at room temperature. The precipitate was then filtered off and washed with ethyl acetate and hexane (200 mL).^{1}H-NMR (D_2O, 400 MHz, 298 K): δ [ppm] = 3.40 (t, J = 7.6 Hz, 6H), 3.20 (t, J = 7.6 Hz, 6H), 3.06 (s, 3H). Anal. Calcd. For MDABCOI (M = 254.12 g/mol): C 33.09 H 5.95 N 11.02 I 49.94 found C 32.10 H 6.06 N 10.83 I 48.96 %.

There were different post-synthetic treatments performed, like base and acid treatment, but the best results were achieved without further purification:

For purification, the powder was dissolved in ethanol (350 mL) and 5.10 g K_2CO_3 was added. After stirring for two hours, the mixture was filtered again and solvent residues were removed under reduced pressure. The pure product was obtained as a white powder (16.93 g, 66.62 mmol, 93% yield). ^{1}H-NMR (D_2O, 400 MHz, 298 K): δ [ppm] = 3.43 (t, J = 9.0, 6.2 Hz, 6H, CH_2), 3.23 (t, J = 9.0, 6.2 Hz, 6H, CH_2), 3.09 (s, 3H, CH_3). Anal. Calcd. For MDABCOI (M = 254.12 g/mol): C 33.09 H 5.95 N 11.02 I 49.94 found C 31.61 H 6.09 N 10.65 I 46.82 %.

For the synthesis of MDABCOI•HI, 5.478 g MDABCOI (21.6 mmol, 1 equiv.) was dissolved in 50 mL Ethanol and 5.243 g freshly reduced HI (6 mL HI, unstabilized and 10 mL H_3PO_2 (50% in H_2O) (23.7 mmol, 1.1 equiv.) were mixed and stirred for 30 min. Afterwards, the white precipitate was filtered off and washed with an HI/Ethanol mixture. Finally, after drying under reduced pressure, the product was obtained as a white powder (7.302 g, 19.1 mmol, 88%). ^{1}H NMR (D_2O, 400 MHz, 298 K): δ [ppm] = 3.95 (dd, J = 9.4, 5.9 Hz, 6H), 3.83 (dd, J = 9.3, 6.0 Hz, 6H), 3.35 (s, 3H). Anal. Calcd. For MDABCOI•HI (M = 382.03 g/mol): C 22.01 H 4.22 N 7.33 I 66.44 found C 21.99 H 4.22 N 7.33 I 64.43 %.

For thin film deposition different stock solutions in DMF were prepared:

Therefore, generally, MDABCOI and NH_4I were dissolved in dry DMF and sonicated for 1 h. After thorough sonication, the remaining precipitate was filtered off with syringe filters. And the resulting solution was applied for the thin film deposition with piranha acid-activated Si substrates or functionalized Au substrates.

Table S4: Experimental details of the performed thin film fabrications.

$MDABCO^{2+}$ source (MS)	Substrates	m (MS) [mg]	Equiv. (MS)	m (NH_4I) [mg]	Equiv. (NH_4I)	V (DMF)	DT*/**	T/ °C
MDABCOI	Si	762	1	435	1	1	SC	120
MDABCOI base	Si	762	1	435	1	1	SC	120
MDABCOI•HI	Si	1146	1	435	1	2	SC***	120
MDABCOI	Si	762	1	652	1.5	1	SC	120
MDABCOI	Si	762	1	869	2	2	SC	120
MDABCOI	Si	762	1	869	2	2	SC	70
MDABCOI	Si	762	1	869	2	2	SC	100
MDABCOI	Si	762	1	869	2	2	SC	150
MDABCOI	Au	762	1	869	2	2	SC	70
MDABCOI	Au	762	1	869	2	2	SC	100
MDABCOI	Au	762	1	869	2	2	SC	120
MDABCOI	Au	762	1	869	2	2	SC	150
MDABCOI	Au-OH	762	1	869	2	2	SC	70
MDABCOI	Au-COOH	762	1	869	2	2	SC	70
MDABCOI	Au-imidazol	762	1	869	2	2	SC	70
MDABCOI	Au-≡	762	1	869	2	2	SC	70
MDABCOI	Au--	762	1	869	2	2	SC	70

$MDABCO^{2+}$ source (MS)	Substrates	m (MS) [mg]	Equiv. (MS)	(NH_4I) [mg]	Equiv. (NH_4I)	V (DMF)	DT*/**	T/ °C
MDABCOI	Au-OH	762	1	869	2	2	SC	150
MDABCOI	Au-COOH	762	1	869	2	2	SC	150
MDABCOI	Au-imidazol	762	1	869	2	2	SC	150
MDABCOI	Au-≡	762	1	869	2	2	SC	150
MDABCOI	Au--	762	1	869	2	2	SC	150
MDABCOI	Si	762	1	869	2	2	DiC	120
MDABCOI	Si	762	1	869	2	2	DC 7.5 µL	120
MDABCOI	Si	762	1	869	2	2	DC 10 µL	120
MDABCOI	Si	762	1	869	2	2	DC 12.5 µL	120
MDABCOI	Si	762	1	869	2	2	DC 15 µL	120

*Deposition Technique: Spray Coating (SC), Dip Coating (DiC), Drop Coating (DC)
** Amount of Volume that was used for drop coating

***Bad solubility

7. APPENDIX

7.1. Complete List of Publications

7.1.1. First Author Publications

Peer-Reviewed Journal Publications

[1] **A. L. Semrau**, S. Pujari, P. M. Stanley, S. Wannapaiboon, B. Albada, H. Zuilhof, and R. A. Fischer, *Chem. Mater.* **2020**, *10(5)*, 3203-3211 (Selective Positioning of NMOF Particles at Patterned Substrate Surfaces).

[2] **A. L. Semrau,**§ P. M. Stanley,§ A. Urstoeger, M. Schuster, M. Cokoja, R. A. Fischer *ACS Catalysis* **2020,** *10(5)*, 3203-3211 (Substantial Turnover Frequency Enhancement of MOF Catalysts by Crystallite Downsizing Combined with Surface Anchoring).

[3] **A. L. Semrau,** P. M. Stanley, D. Huber, M. Schuster,B. Albada, H. Zuilhof, M. Cokoja, R. A. Fischer (Vectorial Catalysis in Surface-Anchored Nanometer-sized Metal-Organic Frameworks-based Microfluidic Devices), submitted.

[4] **A. L. Semrau**, S. Wannapaiboon, S. P. Pujari, P. Vervoorts, B. Albada, H. Zuilhof, R. A. Fischer, *Cryst. Growth Des.* **2019**, *19(3)*, 1738–1747 (Highly Porous Nanocrystalline UiO-66 Thin-Films via Coordination Modulation Controlled Step-by-Step Liquid-Phase Growth).

[5] **A. L. Semrau**, R. A. Fischer, *Chem. - A Eur. J.* **2021** (High-Quality Thin Films of UiO-66-NH_2 by Coordination Modulated Layer-by-Layer Liquid Phase Epitaxy).

[6] **A. L. Semrau**,§ S. V. Dummert,§ S. Mackewicz and G. Kieslich (Substrate Supported, Ferroelectric Metal-Free Perovskite [HMDABCO]$(NH_4)I_3$ Thin Films), in preparation.

Review Articles:

[7] **A.L Semrau,**§ Z. Zhou, § S. Mukerjee, M. Tu, W.-J. Li, R. A. Fischer, *Langmuir* **2021** (Surface-Mounted Metal-Organic Frameworks: Past, Present, and Future Perspectives).

7.1.2. Contributions to Other Publications

Peer-Reviewed Journal Publications

[1] C. Schotten, L. G. T. Leist, **A. L. Semrau**, D. L. Browne, *React. Chem. Eng.* **2018**, *3(2)*, 210-215. (A Machine-Assisted Aapproach for the Preparation of Follow-On Pharmaceutical Compound Libraries).

Explored large parts of the substrate scope, characterized it by NMR experiments, analyzed the data and contributed to parts of the manuscript.

[2] K. Epp, **A. L. Semrau**, M. Cokoja, R. A. Fischer, *ChemCatChem* **2018**, *10(16)*, 3506-3512. (Dual Site Lewis-Acid Metal-Organic Framework Catalysts for CO_2 Fixation: Counteracting Effects of Node Connectivity, Defects and Linker Metalation)

Synthesized $Zr_6O_4(OH)_4(OMc)_{12}$, characterized it by PXRD, ^{1}H NMR, SC-XRD, analyzed the data and contributed to parts of the manuscript.

[3] S. Bhattacharya, W. W. Ayass, D. H. Taffa, A. Schneemann, **A. L. Semrau,** S. Wannapaiboon, P. J. Altmann, A. Pöthig, T. Nisar, T. Balster, N. C. Burtch, V. Wagner, R. A. Fischer, M. Wark, U. Kortz, *J. Am. Chem. Soc.* **2019**, *141(8)*, 3385–3389 (Discovery of Polyoxo-Noble-Metalate-Based Metal-Organic Frameworks).

Performed the adsorption measurements, analyzed the data, and contributed to parts of the manuscript.

[4] S. Wannapaiboon, A. Schneemann, I. Hante, M. Tu, K. Epp, **A. L. Semrau,** C. Sternemann, M. Paulus, S. J. Baxter, G. Kieslich, R. A. Fischer, *Nat. Comm.* **2019**, *10(1),* 1-10. (Control of Structural Flexibility of Layered-Pillared Metal-Organic Frameworks Anchored at Surfaces)

Collected the adsorption data and SEM images; analyzed the images and sorption experiments.

[5] W. Li, S. Xue, S. Watzele, S. Hou, J. Fichtner, **A. L. Semrau**, L. Zhou, A. Welle, A. S. Bandarenka, R. A. Fischer *Angew. Chem. Int. Ed.* **2020**, *59,* 5837–5843. (Advanced Bifunctional Oxygen Reduction and Evolution Electrocatalyst Derived from Surface-Mounted Metal-Organic Frameworks)

Helped in the analysis of the TOF-SIMS experiments and contributed to the manuscript.

[6] B. Thakur, D. T. Sun, V. V. Karve, A. L. Semrau, L. Weiß, L. Groba, R. A. Fischer, W. L. Queen, B. Wolfrum, *Adv. Mater. Technol.* **2021** (An Investigation into the Intrinsic Peroxidase-Like Activity of Fe-MOFs and Fe-MOFs/Polymer Composites), accepted

Performed the synthesis, characterization, and analysis of the MIL-101-NH_2 powders, contributions to the manuscript.

7.2. Complete List of Conference Contributions

7.2.1. First Author Presentations

[5] Regional Meeting of the scholarship holders from the Fonds of the Chemical Industry, Munich, December 2019, oral presentation: Selective Positioning of MOFs at Substrate Surfaces.

[4] 1st Symposium from the DAAD project "Fabrication of SURMOFs towards separation membrane and sensor applications", Sapporo, Japan, October 2019, oral presentation: **A. L. Semrau**, D. Mayer, R. A. Fischer, Towards the Fabrication of Highly Oriented and Transmissive Zr-based MOF Thin-Films for their Non-Linear Optical Characterization.

[3] 6th International Conference on Metal-Organic Frameworks and Open Framework Compounds, Auckland, New Zealand, December 2018, oral presentation: Selective Positioning of MOFs at Substrate Surfaces.

[2] 1st European Doctoral Symposium on Metal-Organic Frameworks, Raitenhaslach, Mai 2018, oral presentation: **A. L. Semrau,** S. Wannapaiboon, R. A. Fischer, Access to Crystalline UiO-66 Thin-Films via Coordination Modulation Liquid-Phase Epitaxy.

[1] 2nd European Conference on Metal-Organic Frameworks and Porous Polymers, Delft, Netherlands, November 2017, poster presentation: **A. L. Semrau,** S. Wannapaiboon, R. A. Fischer, Coordination Modulated Growth of Surface Attached Metal-Organic Frameworks.

7.2.2. Contributions to Other Presentations

[2] Eurotech Postdoctoral fellow meeting, Lausanne (Switzerland), September 2019, poster presentation: B.Thakur, D.T. Sun, W. L. Queen, **A. L. Semrau**, R. A. Fischer, B. Wolfrum, Metal-Organic Frameworks@Polymer Composites for Intrinsic Peroxidase-Like Activity.

[1] GSS Autumn Workshop, Dortmund, October 2016, poster presentation: B. Geissler, P. Gerschel, **A. L. Semrau,** P. Nürnberger, Ultrafast Time Resolved Spectroscopy on Thioflavin T and its Building Blocks.

7.3. Curriculum Vitae

PERSONAL DETAILS

ANNA LISA SEMRAU

Date of Birth	30. November 1992, Essen
Contact details	Bahnhofstraße 5, 85386 Eching anna.semrau@rub.de

EDUCATION

Since 10/2017	**PhD Student,** Technical University of Munich *"Selective positioning of MOFs at substrate surfaces"* Chair of Inorganic and Metal-Organic Chemistry under supervision of Prof. Dr. Dr. h.c. Roland A. Fischer
10/2015 – 09/2017	**Master of Science in Chemistry**, Ruhr University Bochum, Grade Point Average: 1.0, Ranking: 1/51 Master Thesis: *"Fabrication and characterization of zirconium-based metal-organic framework thin-films via coordination modulation-controlled layer-by-layer deposition"* Chair of Inorganic and Metal-Organic Chemistry under supervision of Prof. Dr. Dr. h.c. Roland A. Fischer
10/2012 – 08/2015	**Bachelor of Science in Chemistry**, Ruhr University Bochum, Grade Point Average: 1.1, Ranking: 1/57 Bachelor Thesis: "*Synthesis and biological evaluation of arylether substituted acylides*" Organic Chemistry under supervision of Prof. Dr. F. Schulz
06/2012	**A level** (Abitur) at Carl Friedrich von Weizsäcker-Gymnasium, Ratingen (Grade Point Average: 1.0)

SCHOLARSHIPS AND PRIZES

11/2018	**Preis an Studierenden der Ruhr Universität Bochum** Prize for outstanding scientific theses at the Ruhr University Bochum.
08/2018	**Kekulé Fellowship of the Chemical Industry Fund (FCI)** 2-year PhD fellowship for young outstanding scientists in chemistry and chemistry-related life science subjects.
09/2016 – 01/2017	**Erasmus Placement Program** for studying abroad at the University of Cardiff, United Kingdom.

2015	**Wilke-Preis** Prize for the best bachelor's degree in chemistry at the Ruhr University Bochum in 2015.
2013 – 2017	**Deutschlandstipendium** Scholarship from Ruhr University Bochum and Evonik Industries AG.
2012	**Karl von Frisch-Abiturientenpreis** Prize for excellent results in biology A-level exams.
2010	**Planspiel Börse (3rd Place)** Economy competition, where virtual capital has to be maximized by transactions over three months. 3rd Place in the district Mettmann.
2009	**Planspiel Börse (1st Place)** 1st Place in the district Mettmann.

VOLUNTARY WORK

2013 – 2016	**Student representative** at the faculty of chemistry and biochemistry, Ruhr-University Bochum, **member of the faculty council**, president of the student representative (2016)
2008 – 2014	**Trainer of the DLRG** (German Lifeguard Association)

ADDITIONAL SKILLS & HOBBIES

Languages	German (native speaker), English (C1/C2), Latin (Latinum)
Hobbies	hiking, traveling, reading, swimming

7.4. Reprint Permissions

7.4.1. Zr-based Thin Films (Chapter 2)

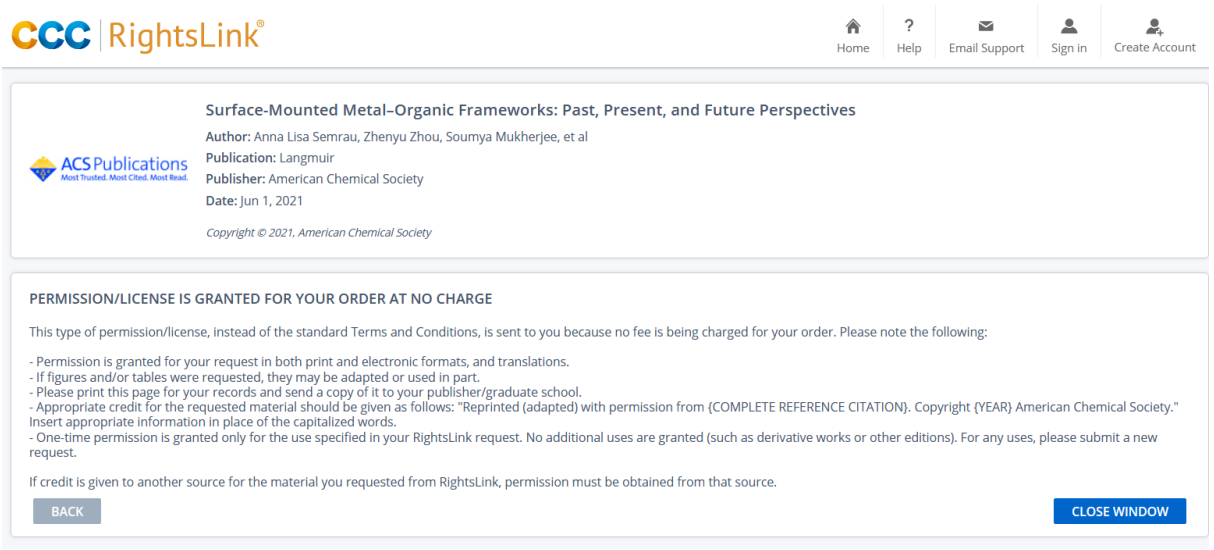

CCC | RightsLink®

Home | Help | Email Support | Sign in | Create Account

ACS Publications
Most Trusted. Most Cited. Most Read.

Surface-Mounted Metal–Organic Frameworks: Past, Present, and Future Perspectives

Author: Anna Lisa Semrau, Zhenyu Zhou, Soumya Mukherjee, et al
Publication: Langmuir
Publisher: American Chemical Society
Date: Jun 1, 2021

Copyright © 2021, American Chemical Society

PERMISSION/LICENSE IS GRANTED FOR YOUR ORDER AT NO CHARGE

This type of permission/license, instead of the standard Terms and Conditions, is sent to you because no fee is being charged for your order. Please note the following:

- Permission is granted for your request in both print and electronic formats, and translations.
- If figures and/or tables were requested, they may be adapted or used in part.
- Please print this page for your records and send a copy of it to your publisher/graduate school.
- Appropriate credit for the requested material should be given as follows: "Reprinted (adapted) with permission from {COMPLETE REFERENCE CITATION}. Copyright {YEAR} American Chemical Society." Insert appropriate information in place of the capitalized words.
- One-time permission is granted only for the use specified in your RightsLink request. No additional uses are granted (such as derivative works or other editions). For any uses, please submit a new request.

If credit is given to another source for the material you requested from RightsLink, permission must be obtained from that source.

BACK | CLOSE WINDOW

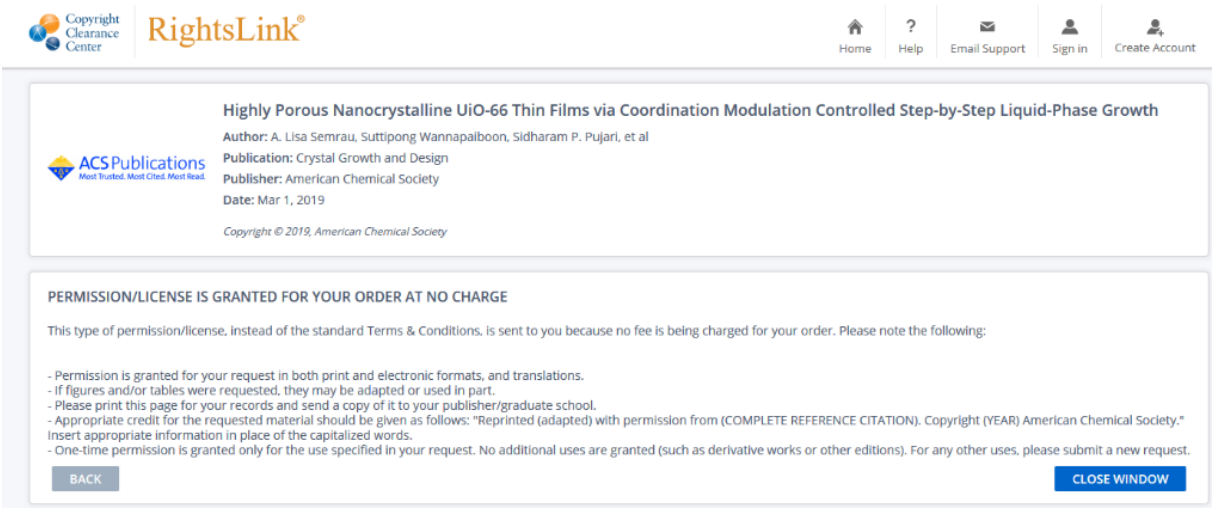

Copyright Clearance Center | RightsLink®

Home | Help | Email Support | Sign in | Create Account

ACS Publications
Most Trusted. Most Cited. Most Read.

Highly Porous Nanocrystalline UiO-66 Thin Films via Coordination Modulation Controlled Step-by-Step Liquid-Phase Growth

Author: A. Lisa Semrau, Suttipong Wannapaiboon, Sidharam P. Pujari, et al
Publication: Crystal Growth and Design
Publisher: American Chemical Society
Date: Mar 1, 2019

Copyright © 2019, American Chemical Society

PERMISSION/LICENSE IS GRANTED FOR YOUR ORDER AT NO CHARGE

This type of permission/license, instead of the standard Terms & Conditions, is sent to you because no fee is being charged for your order. Please note the following:

- Permission is granted for your request in both print and electronic formats, and translations.
- If figures and/or tables were requested, they may be adapted or used in part.
- Please print this page for your records and send a copy of it to your publisher/graduate school.
- Appropriate credit for the requested material should be given as follows: "Reprinted (adapted) with permission from (COMPLETE REFERENCE CITATION). Copyright (YEAR) American Chemical Society." Insert appropriate information in place of the capitalized words.
- One-time permission is granted only for the use specified in your request. No additional uses are granted (such as derivative works or other editions). For any other uses, please submit a new request.

BACK | CLOSE WINDOW

JOHN WILEY AND SONS LICENSE
TERMS AND CONDITIONS

Jun 30, 2021

This Agreement between Anna Lisa Semrau ("You") and John Wiley and Sons ("John Wiley and Sons") consists of your license details and the terms and conditions provided by John Wiley and Sons and Copyright Clearance Center.

License Number	5098710314655
License date	Jun 30, 2021
Licensed Content Publisher	John Wiley and Sons
Licensed Content Publication	Chemistry - A European Journal
Licensed Content Title	High-Quality Thin Films of UiO-66-NH2 by Coordination Modulated Layer-by-Layer Liquid Phase Epitaxy
Licensed Content Author	A. Lisa Semrau, Roland A. Fischer
Licensed Content Date	May 13, 2021
Licensed Content Volume	27
Licensed Content Issue	33
Licensed Content Pages	8
Type of use	Dissertation/Thesis
Requestor type	Author of this Wiley article
Format	Print and electronic
Portion	Text extract
Number of Pages	2
Will you be translating?	No
Title	Positioning of Coordination-Network Materials at Surfaces
Institution name	Technical University of Munich
Expected presentation date	Sep 2021
Portions	The images were all modified, but were inspired by the ones in the paper, as was the text but there might be single sentences that were taken from the manuscript
Requestor Location	Anna Lisa Semrau Grevenhauser Weg 53 Ratingen, 40882 Germany Attn: Anna Lisa Semrau
Publisher Tax ID	EU826007151
Total	0.00 USD

7.4.2. Selective Covalent Immobilization of Preformed NMOFs in Microfluidic Devices Targeting Vectorial Catalysis • (Chapter 3)

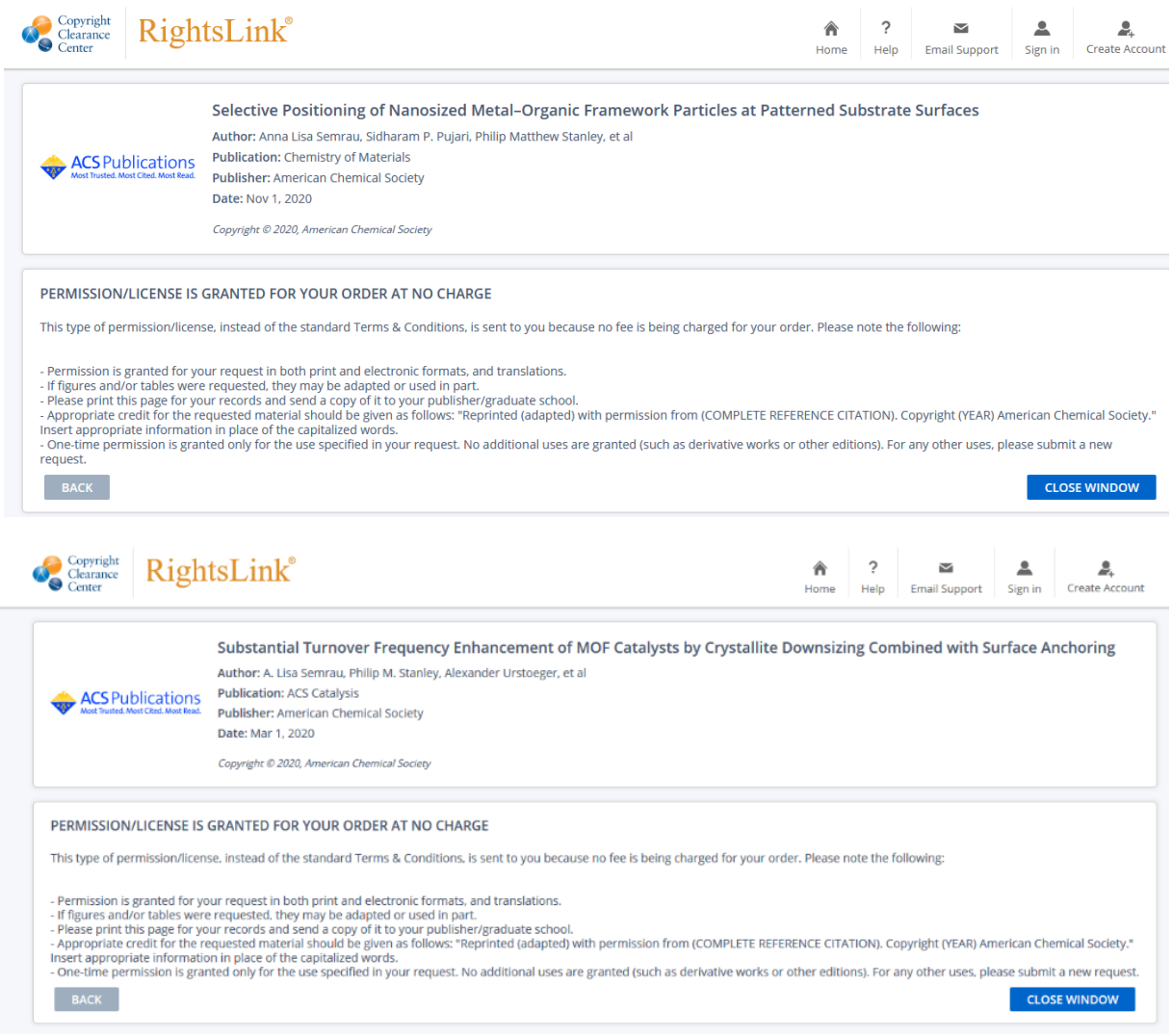

Copyright Clearance Center RightsLink®

Home | Help | Email Support | Sign in | Create Account

ACS Publications
Most Trusted. Most Cited. Most Read.

Selective Positioning of Nanosized Metal–Organic Framework Particles at Patterned Substrate Surfaces

Author: Anna Lisa Semrau, Sidharam P. Pujari, Philip Matthew Stanley, et al
Publication: Chemistry of Materials
Publisher: American Chemical Society
Date: Nov 1, 2020

Copyright © 2020, American Chemical Society

PERMISSION/LICENSE IS GRANTED FOR YOUR ORDER AT NO CHARGE

This type of permission/license, instead of the standard Terms & Conditions, is sent to you because no fee is being charged for your order. Please note the following:

- Permission is granted for your request in both print and electronic formats, and translations.
- If figures and/or tables were requested, they may be adapted or used in part.
- Please print this page for your records and send a copy of it to your publisher/graduate school.
- Appropriate credit for the requested material should be given as follows: "Reprinted (adapted) with permission from (COMPLETE REFERENCE CITATION). Copyright (YEAR) American Chemical Society." Insert appropriate information in place of the capitalized words.
- One-time permission is granted only for the use specified in your request. No additional uses are granted (such as derivative works or other editions). For any other uses, please submit a new request.

BACK CLOSE WINDOW

Copyright Clearance Center RightsLink®

Home | Help | Email Support | Sign in | Create Account

ACS Publications
Most Trusted. Most Cited. Most Read.

Substantial Turnover Frequency Enhancement of MOF Catalysts by Crystallite Downsizing Combined with Surface Anchoring

Author: A. Lisa Semrau, Philip M. Stanley, Alexander Urstoeger, et al
Publication: ACS Catalysis
Publisher: American Chemical Society
Date: Mar 1, 2020

Copyright © 2020, American Chemical Society

PERMISSION/LICENSE IS GRANTED FOR YOUR ORDER AT NO CHARGE

This type of permission/license, instead of the standard Terms & Conditions, is sent to you because no fee is being charged for your order. Please note the following:

- Permission is granted for your request in both print and electronic formats, and translations.
- If figures and/or tables were requested, they may be adapted or used in part.
- Please print this page for your records and send a copy of it to your publisher/graduate school.
- Appropriate credit for the requested material should be given as follows: "Reprinted (adapted) with permission from (COMPLETE REFERENCE CITATION). Copyright (YEAR) American Chemical Society." Insert appropriate information in place of the capitalized words.
- One-time permission is granted only for the use specified in your request. No additional uses are granted (such as derivative works or other editions). For any other uses, please submit a new request.

BACK CLOSE WINDOW

Figure 30: ELSEVIER LICENSE; Mar 22, 2021

This Agreement between Technical University Munich -- Anna Lisa Semrau ("You") and Elsevier ("Elsevier") consists of your license details and the terms and conditions provided by Elsevier and Copyright Clearance Center.

License Number	5034330744300
License date	Mar 22, 2021
Licensed Content Publisher	Elsevier
Licensed Content Publication	Coordination Chemistry Reviews
Licensed Content Title	Creating and mastering nano-objects to design advanced catalytic materials
Licensed Content Author	Gabriele Centi,Siglinda Perathoner
Licensed Content Date	Jul 1, 2011
Licensed Content Volume	255
Licensed Content Issue	13-14
Licensed Content Pages	19
Start Page	1480
End Page	1498
Type of Use	reuse in a thesis/dissertation
Portion	figures/tables/illustrations
Number of figures/tables/illustrations	1
Format	both print and electronic
Are you the author of this Elsevier article?	No
Will you be translating?	No
Title	Positioning of Coordination-Network Materials at Surfaces – Case studies targeting vectorial catalysis based on nanometre-sized metal-organic frameworks integrated into microfluidic devices, ferroelectric capacitors built from organic perovskites, and Zr-based metal-organic frameworks thin-films.
Institution name	Technical University of Munich
Expected presentation date	Apr 2021
Portions	Part of Figure 10; appears as Figure 30 in the dissertation
Requestor Location	Technical University of Munich Lichtenbergstraße 4 85748, Germany Attn: Technical University of Munich
Publisher Tax ID	GB 494 6272 12

7.5. Figures

7.5.1. Zr-based MOF Thin Films• (Chapter 2)

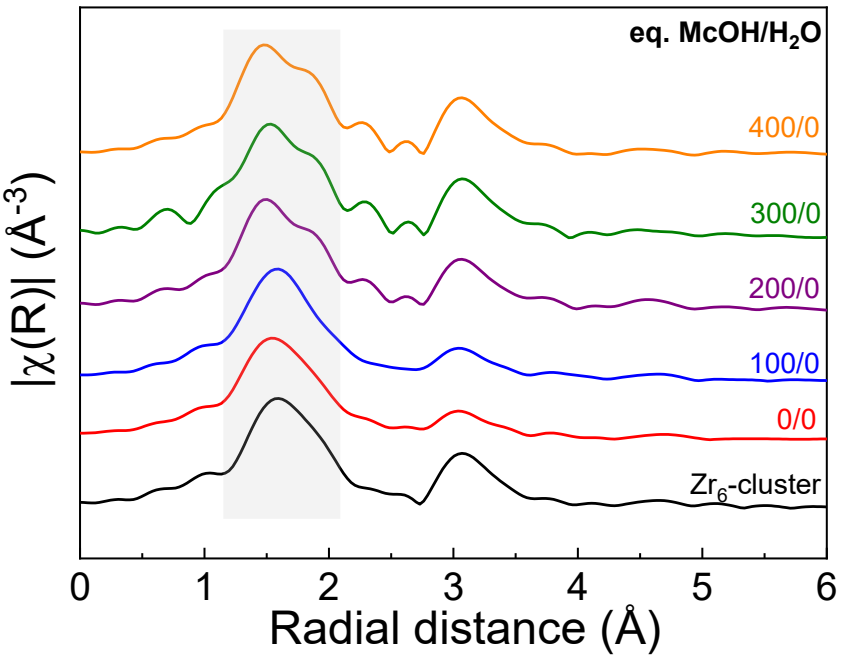

Figure S11: Comparison of the experimental k^2-weighted EXAFS data in R-Space (magnitude, $|\ \chi(R)\ |$, $Å^{-3}$) of the Zr_6-cluster secondary building units (SBUs) and the UiO-66 powders synthesized using various ratios of modulators McOH/H_2O with respect to the concentration of the Zr_6-SBUs. The light grey highlighted area indicates the difference between the first shell when varying the modulator ratio. Using of McOH for up to 100 equiv. to the SBUs shows the similar first shell to the starting SBU clusters. Using of higher McOH ratio (200, 300, and 400 equiv.) for the UiO-66 powder syntheses indicates the site splitting of the first shell and shows two different first shell distances separated more than 0.1 Å. This Figure was taken from Semrau, *et al.*[59] permission from ACS Crystal Growth & Design. Copyright (2019) American Chemical Society.

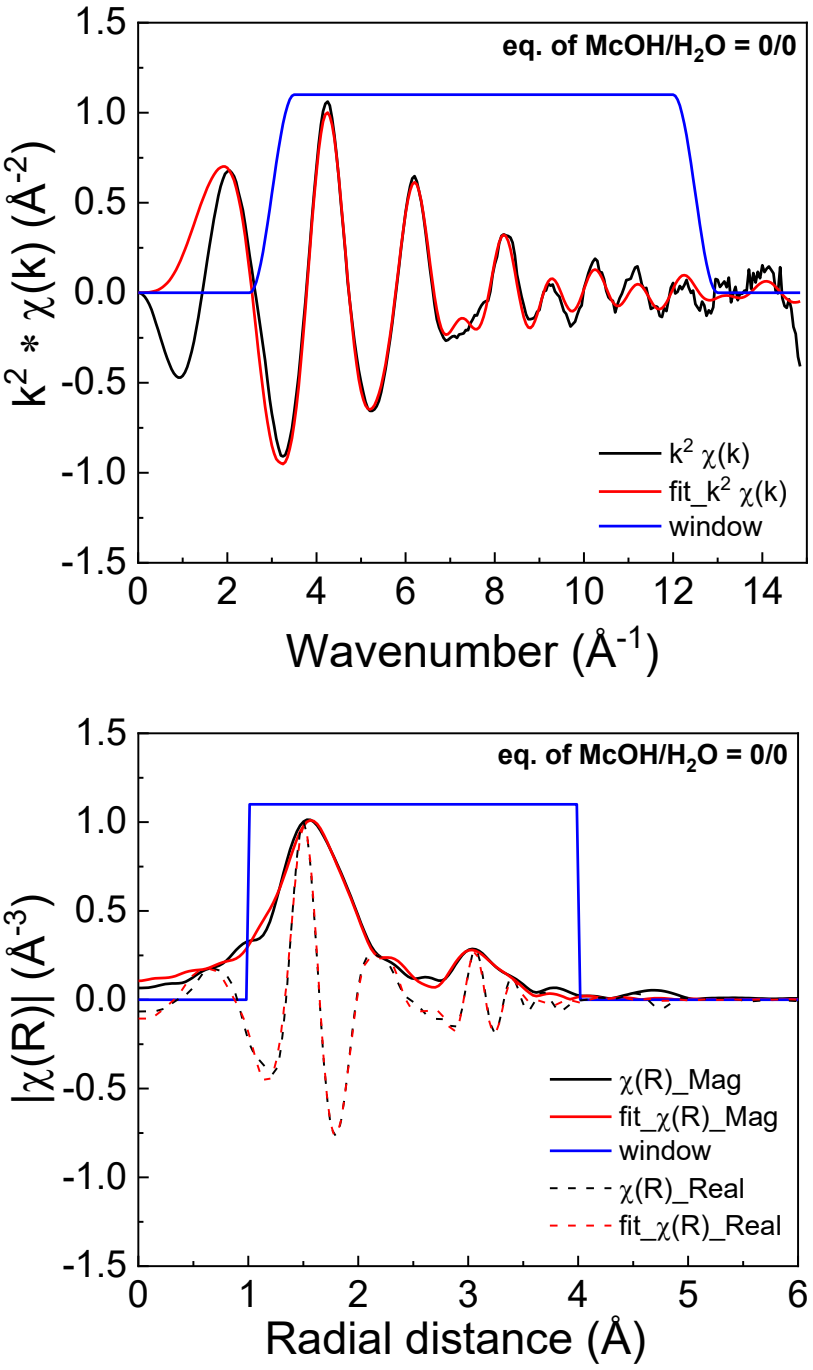

Figure S12: Comparison between the experimental EXAFS data (black) and the best fit showing the R-factor of 0.0148 and the reduced $\chi^2$of 464.38 (red) of the powder synthesized without using modulators; (a) in k-space showing in k^2-weighted $\chi(k)$ and (b) in R-space showing the magnitude and the real part of the $\chi(R)$. Note that, the desolvated UiO-66 in the *Fm-3m* space group (CCDC 733458) was used as the input model for the EXAFS refinement. This Figure was taken from Semrau, *et al.*[59] permission from ACS Crystal Growth & Design. Copyright (2019) American Chemical Society.

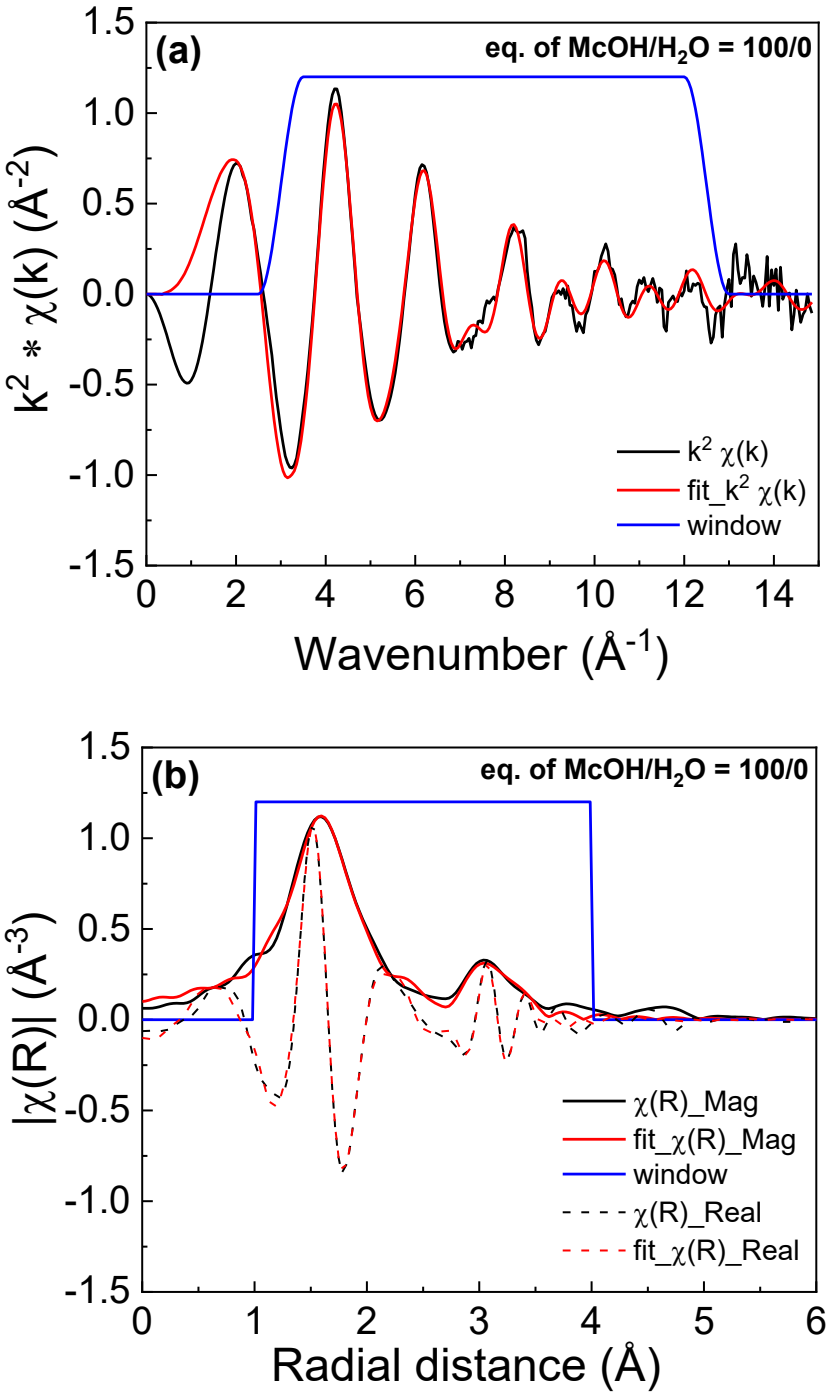

Figure S13: Comparison between the experimental EXAFS data (black) and the best fit showing the R-factor of 0.0146 and the reduced $\chi^2$of 121.96 (red) of the powder synthesized using modulators McOH/H_2O of 100/0 equiv. with respect to the concentration of the Zr_6-SBUs.; (a) in k-space showing in k^2-weighted χ(k) and (b) in R-space showing the magnitude and the real part of the χ(R). Note that, the desolvated UiO-66 in the *Fm-3m* space group (CCDC 733458) was used as the input model for the EXAFS refinement. This Figure was taken from Semrau, *et al.*[59] permission from ACS Crystal Growth & Design. Copyright (2019) American Chemical Society.

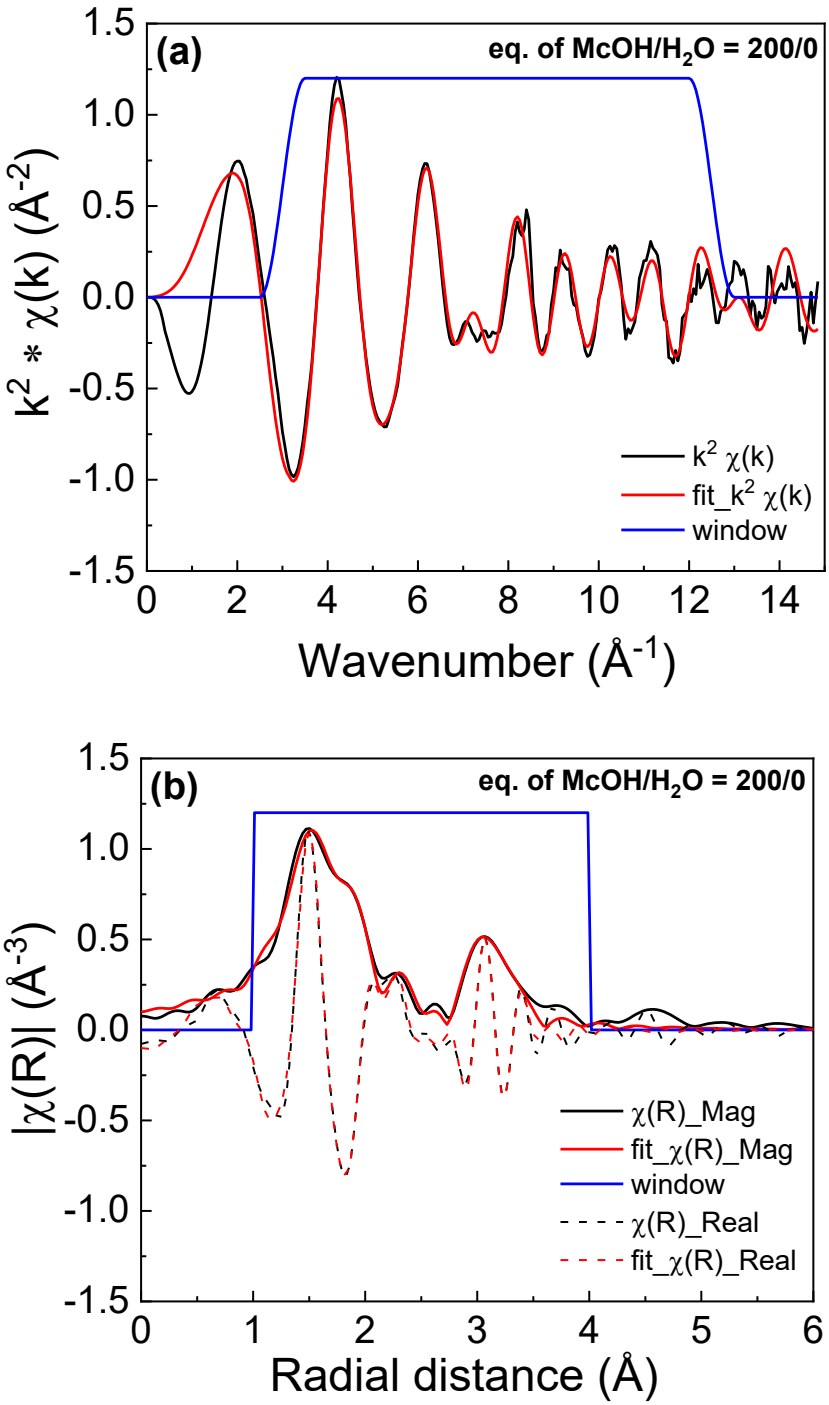

Figure S14: Comparison between the experimental EXAFS data (black) and the best fit showing the R-factor of 0.0204 and the reduced $\chi^2$of 244.35 (red) of the powder synthesized using modulators McOH/H_2O of 200/0 equiv. with respect to the concentration of the Zr_6-SBUs.; (a) in k-space showing in k^2-weighted χ(k) and (b) in R-space showing the magnitude and the real part of the χ(R). Note that, the desolvated UiO-66 in the *Fm-3m* space group (CCDC 733458) was used as the input model for the EXAFS refinement. This Figure was taken from Semrau, *et al.*[59] permission from ACS Crystal Growth & Design. Copyright (2019) American Chemical Society.

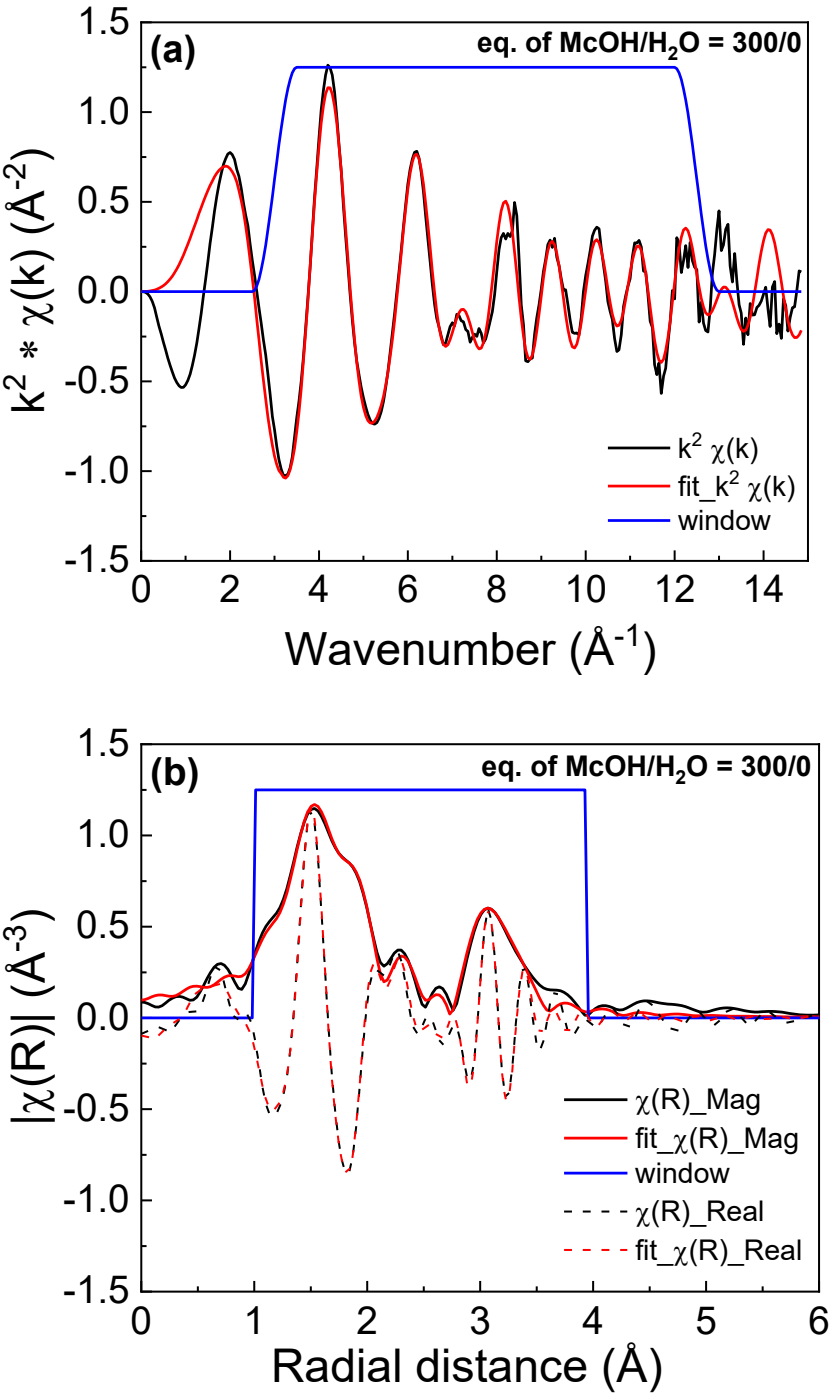

Figure S15: Comparison between the experimental EXAFS data (black) and the best fit showing the R-factor of 0.0135 and the reduced $\chi^2$of 121.52 (red) of the powder synthesized using modulators McOH/H_2O of 300/0 equiv. with respect to the concentration of the Zr_6-SBUs.; (a) in k-space showing in k^2-weighted χ(k) and (b) in R-space showing the magnitude and the real part of the χ(R). Note that, the desolvated UiO-66 in the *Fm-3m* space group (CCDC 733458) was used as the input model for the EXAFS refinement. This Figure was taken from Semrau, *et al.*[59] permission from ACS Crystal Growth & Design. Copyright (2019) American Chemical Society.

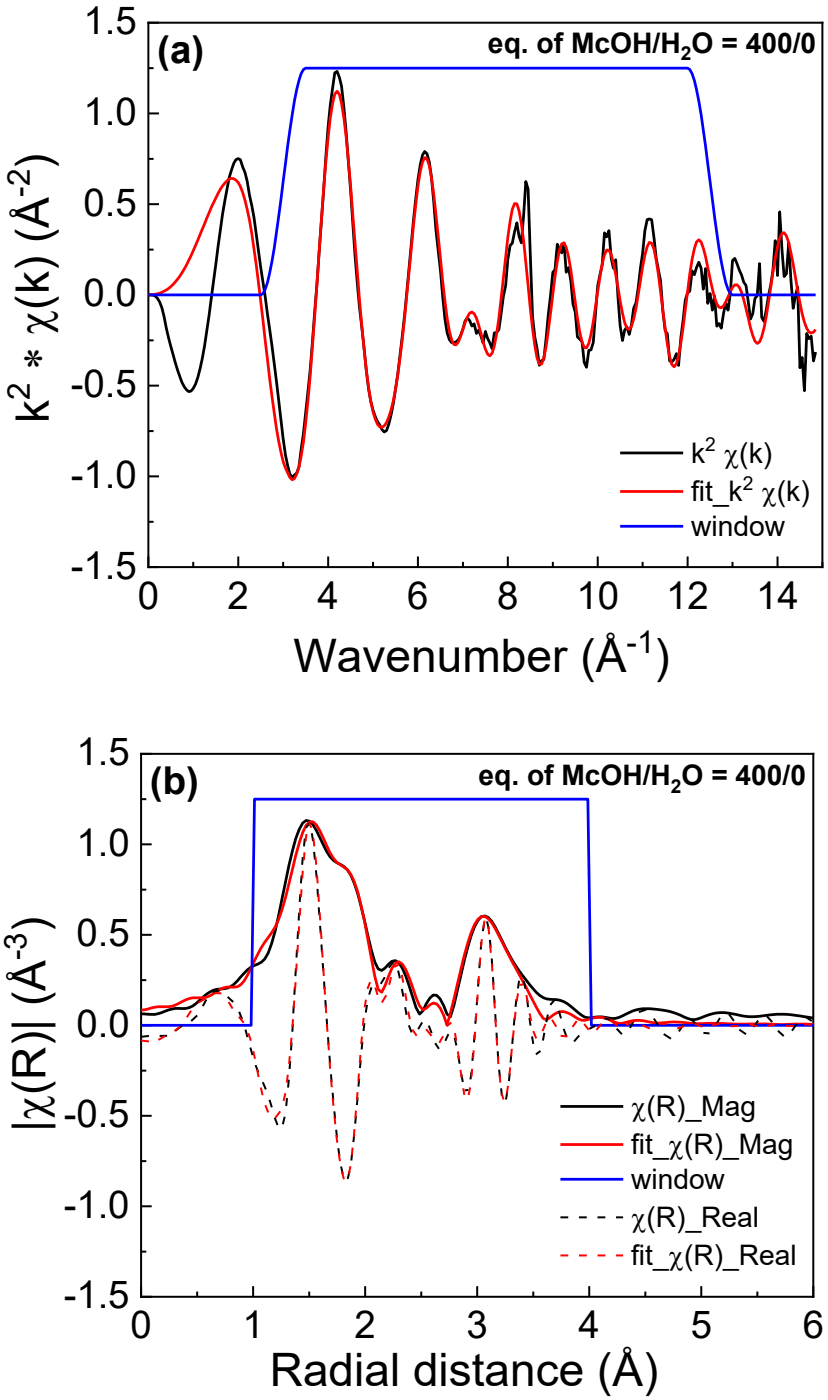

Figure S16: Comparison between the experimental EXAFS data (black) and the best fit showing the R-factor of 0.0259 and the reduced $\chi^2$of 197.57 (red) of the powder synthesized using modulators McOH/H_2O of 400/0 equiv. with respect to the concentration of the Zr_6-SBUs.; (a) in k-space showing in k^2-weighted χ(k) and (b) in R-space showing the magnitude and the real part of the χ(R). Note that, the desolvated UiO-66 in the *Fm-3m* space group (CCDC 733458) was used as the input model for the EXAFS refinement. This Figure was taken from Semrau, *et al.*[59] permission from ACS Crystal Growth & Design. Copyright (2019) American Chemical Society.

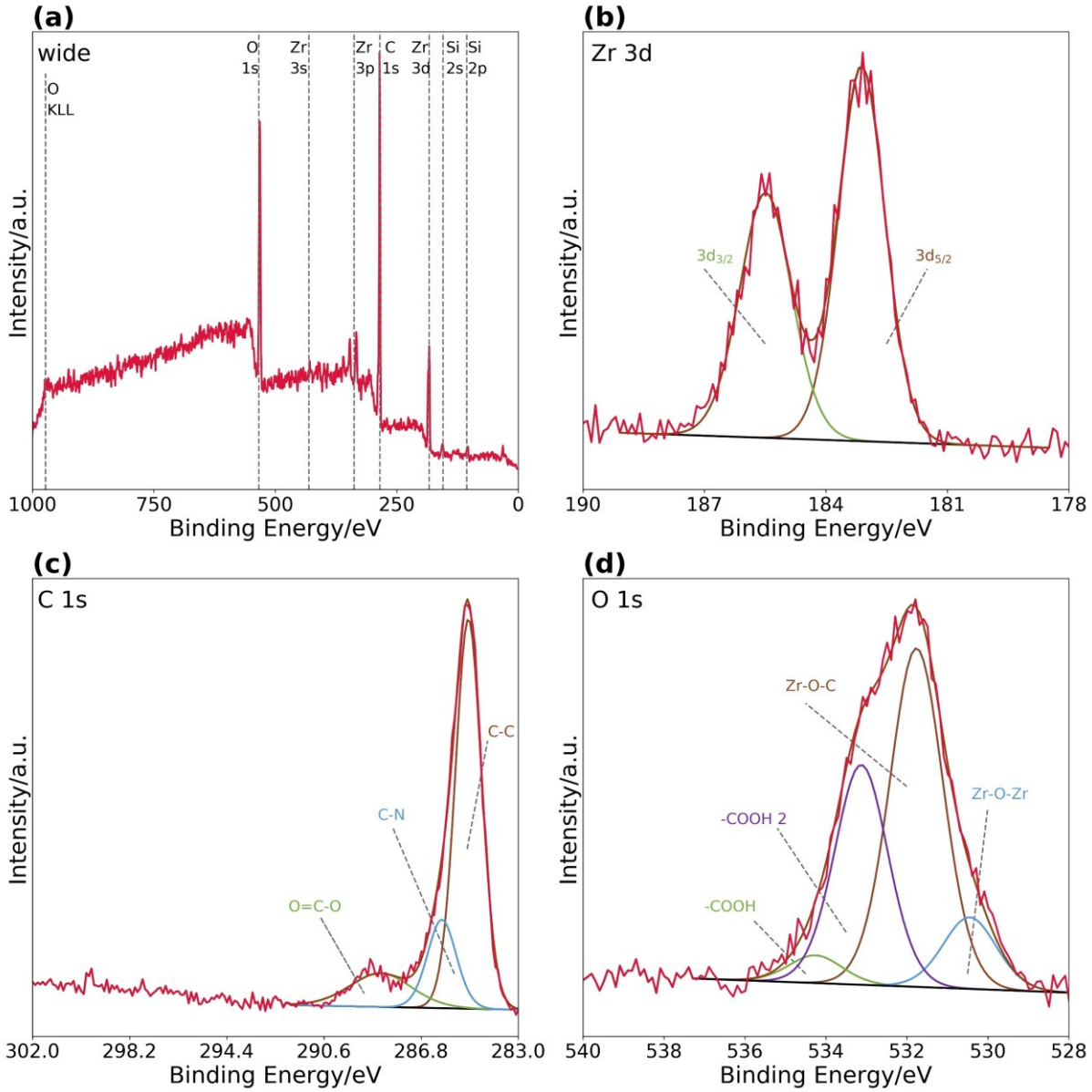

Figure S17: XPS survey scan (a), C 1s (b), O 1s (c), and Zr 3d(d) XPS narrow scans of the activated UiO-66 thin-film deposited by CM-LPE using $[Zr_6O_4(OH)_4(OMc)_{12}]$, H_2bdc and 0 equiv. of methacrylic acid (as modulator).

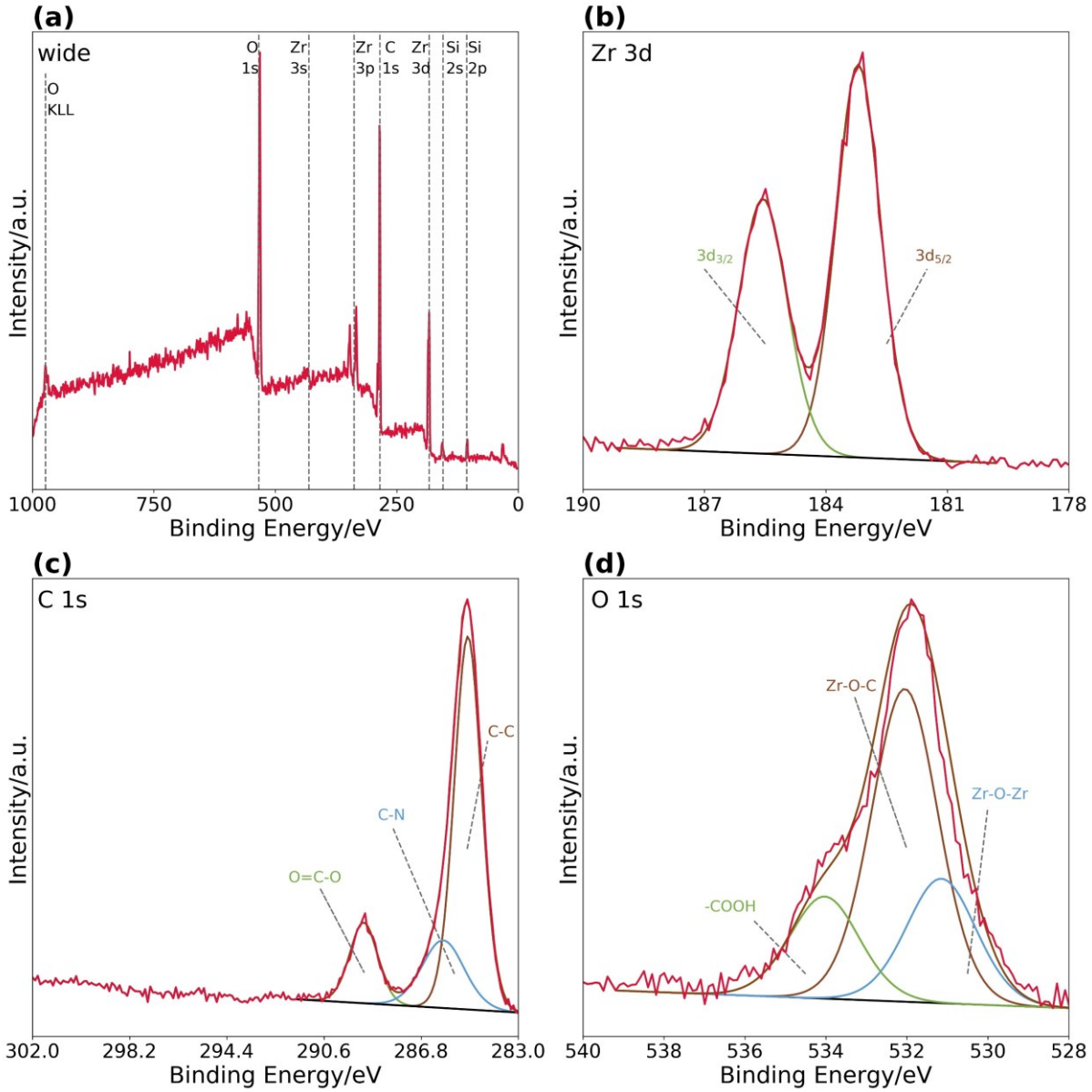

Figure S18: XPS survey scan (a), C 1s (b), O 1s (c), and Zr 3d(d) XPS narrow scans of the activated UiO-66 thin-film deposited by CM-LPE using $[Zr_6O_4(OH)_4(OMc)_{12}]$, H_2bdc and 200 equiv. of methacrylic acid (as modulator).

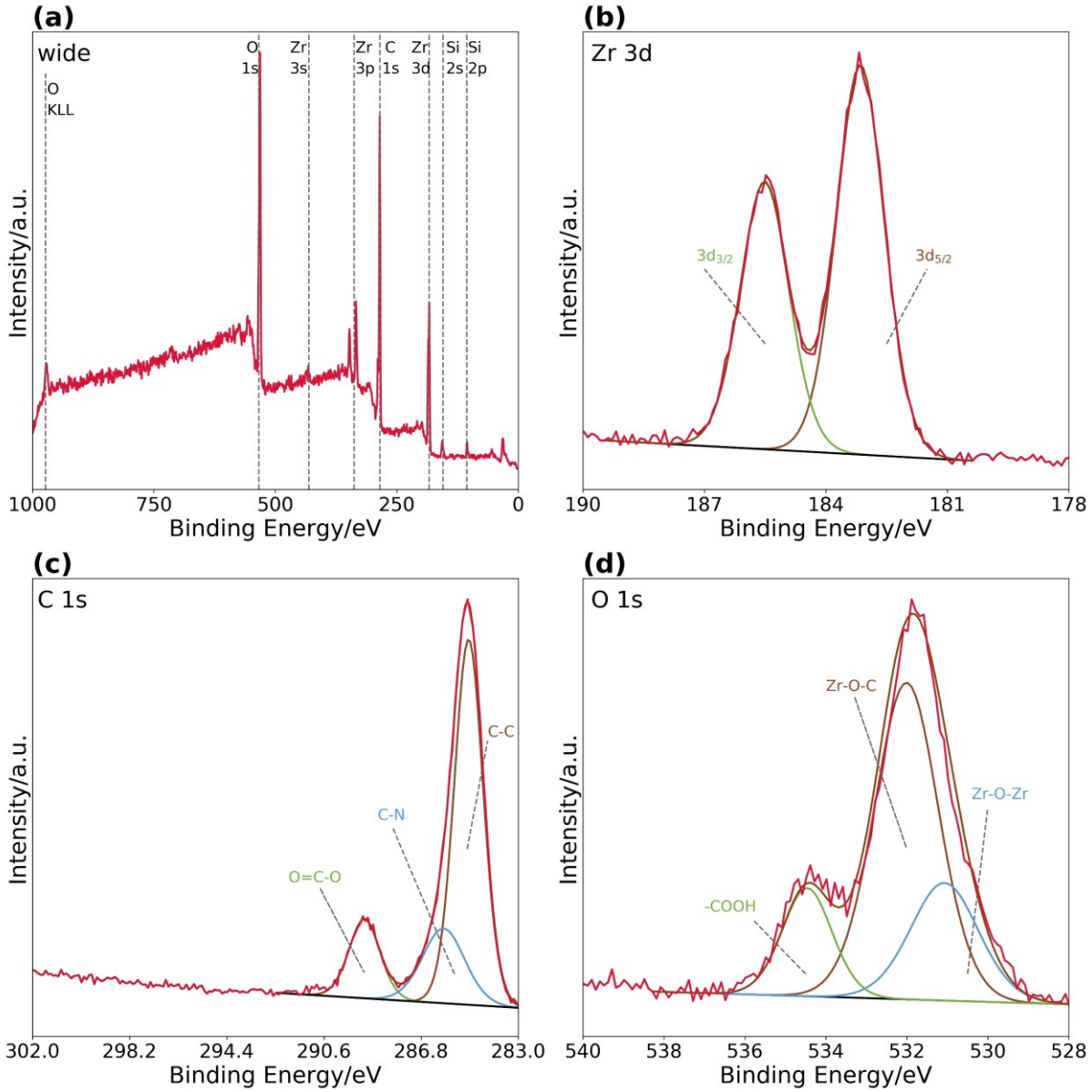

Figure S19: XPS survey scan (a), C 1s (b), O 1s (c), and Zr 3d(d) XPS narrow scans of the activated UiO-66 thin-film deposited by CM-LPE using $[Zr_6O_4(OH)_4(OMc)_{12}]$, H_2bdc and 300 equiv. of methacrylic acid (as modulator).

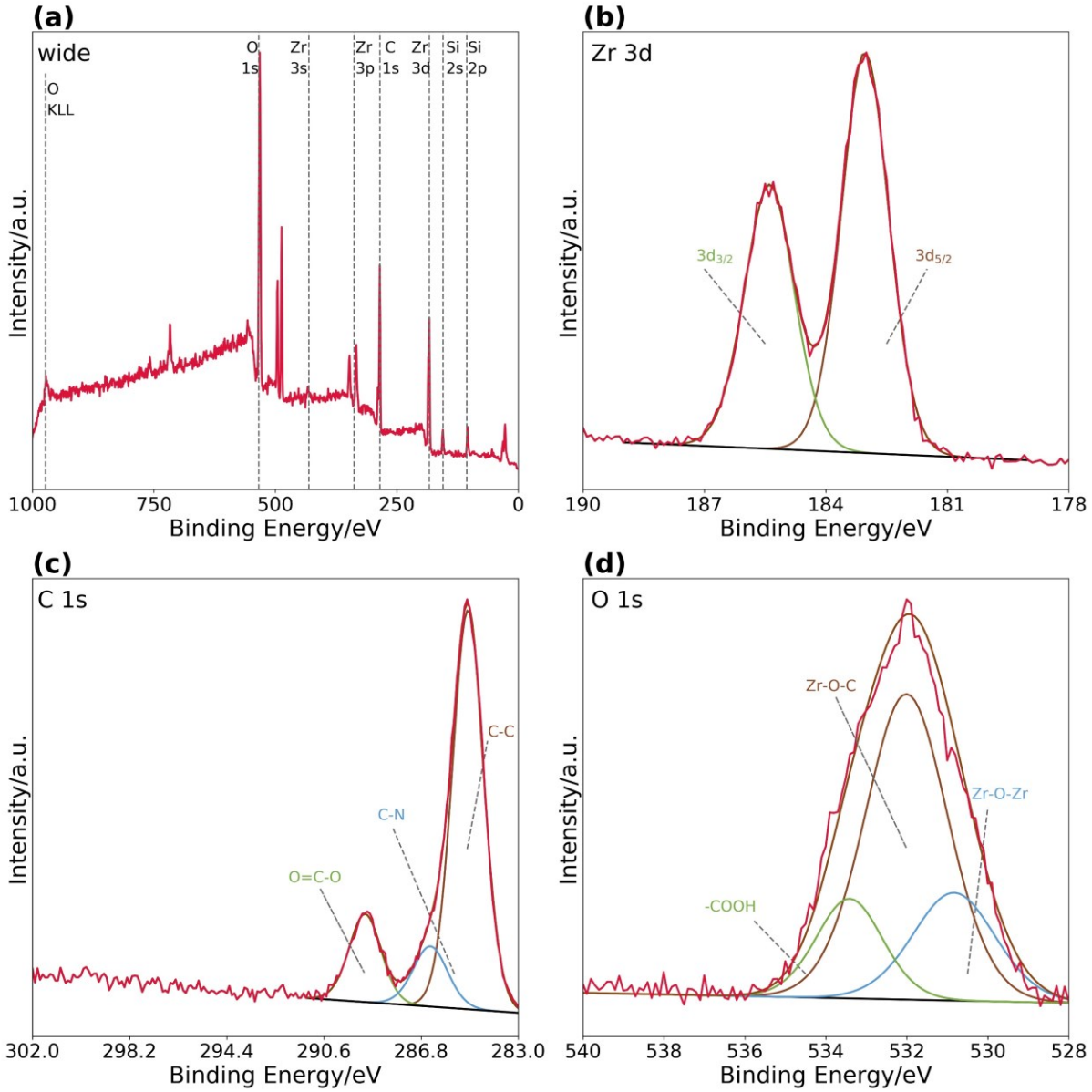

Figure S20: XPS survey scan (a), C 1s (b), O 1s (c), and Zr 3d(d) XPS narrow scans of the activated UiO-66 thin-film deposited by CM-LPE using $[Zr_6O_4(OH)_4(OMc)_{12}]$, H_2bdc and 300 equiv. of methacrylic acid as modulator as well as 1000 equiv. of H_2O as an additive.

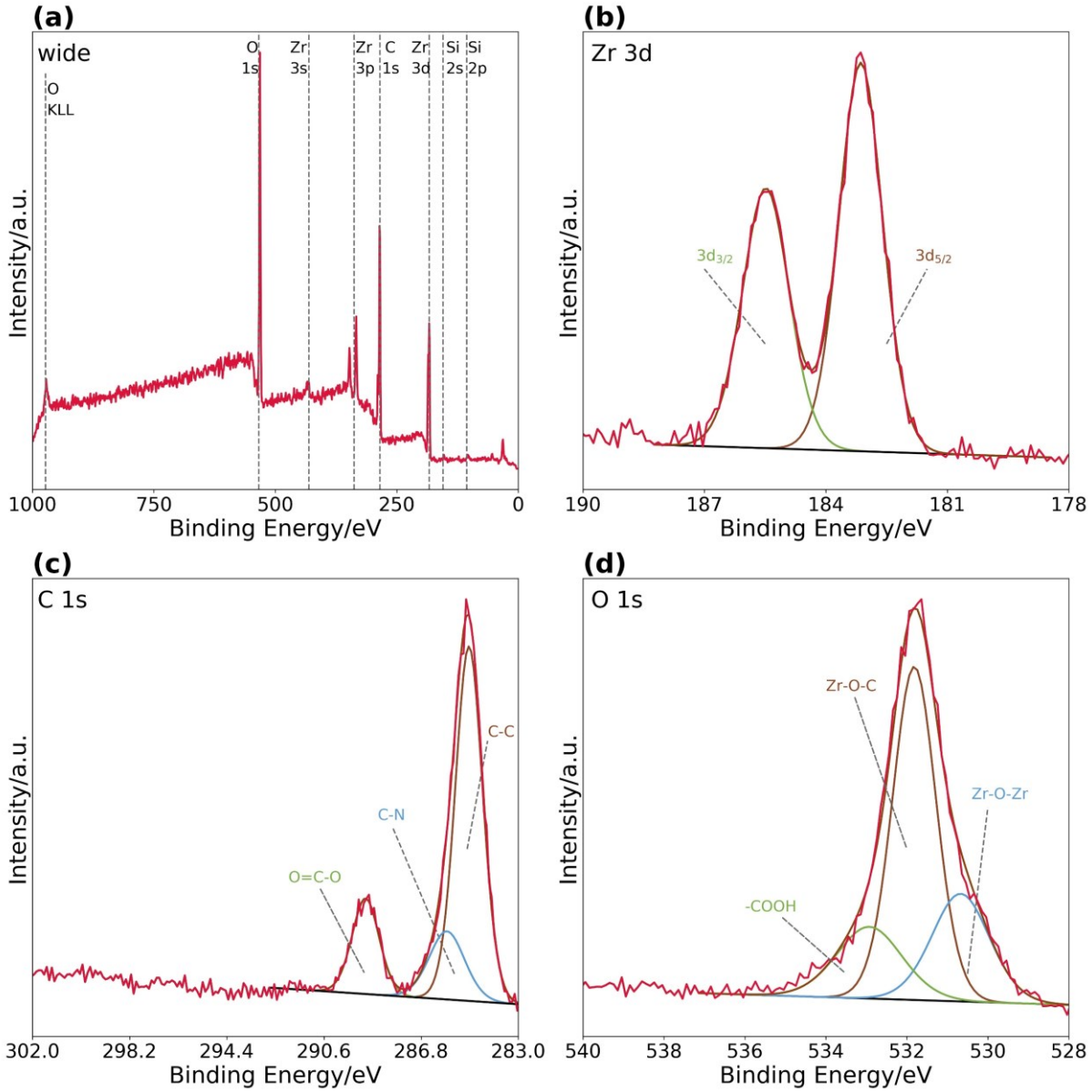

Figure S21: XPS survey scan (a), C 1s (b), O 1s (c), and Zr 3d(d) XPS narrow scans of the activated UiO-66 thin-film deposited by CM-LPE using $[Zr_6O_4(OH)_4(OMc)_{12}]$, H_2bdc and 300 equiv. of methacrylic acid as modulator as well as 2000 equiv. of H_2O as an additive.

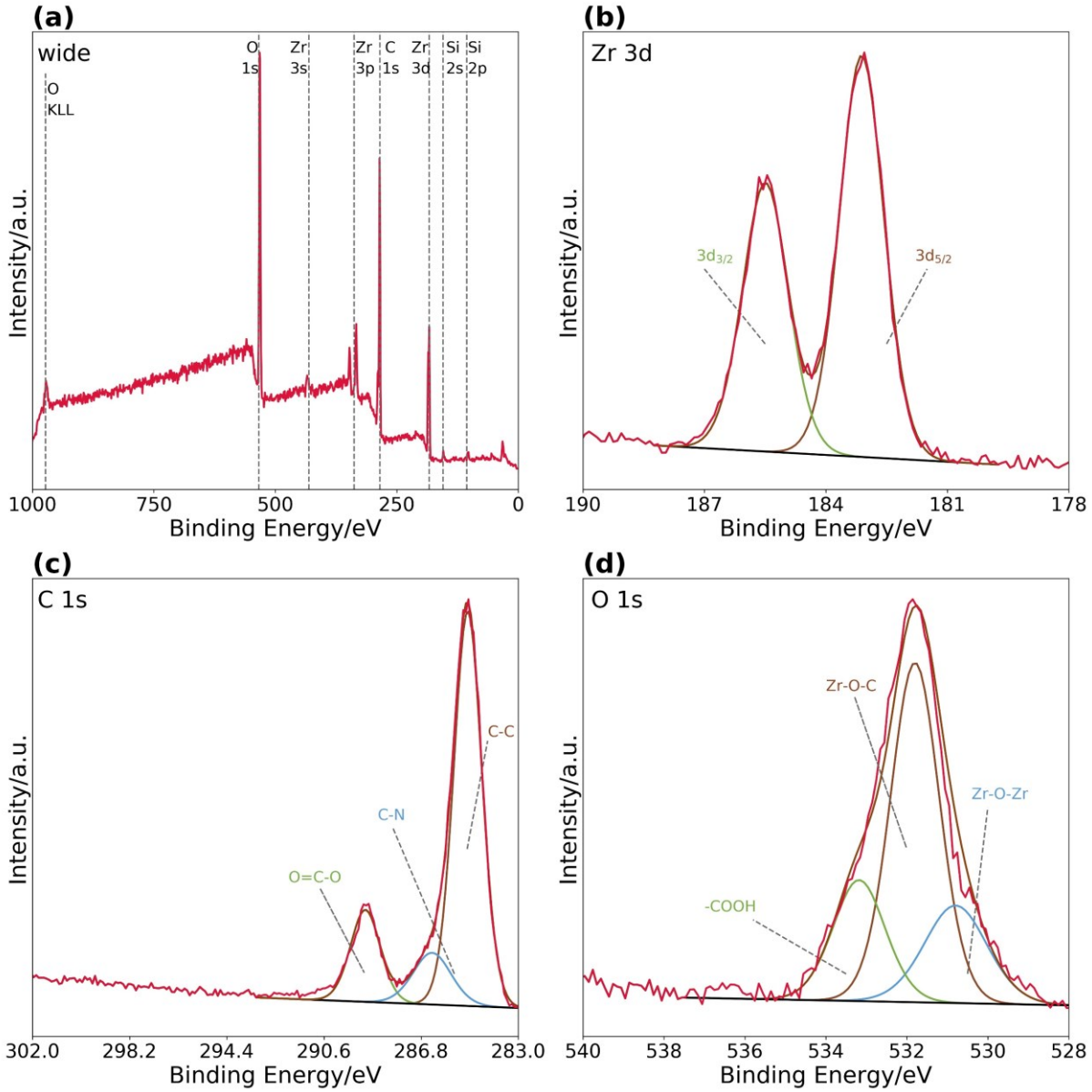

Figure S22: XPS survey scan (a), C 1s (b), O 1s (c), and Zr 3d(d) XPS narrow scans of the activated UiO-66 thin-film deposited by CM-LPE using $[Zr_6O_4(OH)_4(OMc)_{12}]$, H_2bdc and 300 equiv. of methacrylic acid as modulator as well as 3000 equiv. of H_2O as an additive.

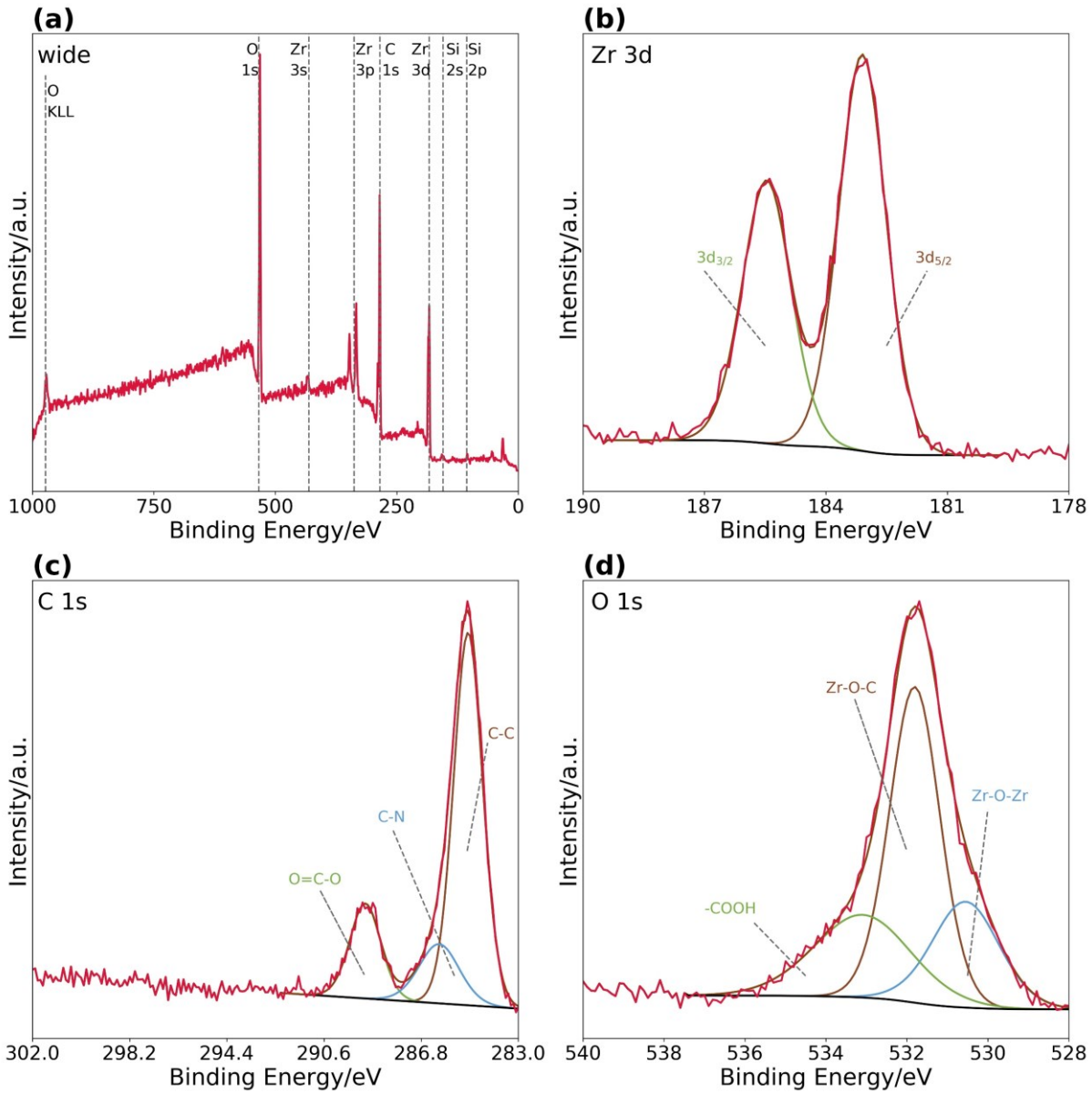

Figure S23: XPS survey scan (a), C 1s (b), O 1s (c), and Zr 3d(d) XPS narrow scans of the activated UiO-66 thin-film deposited by CM-LPE using $[Zr_6O_4(OH)_4(OMc)_{12}]$, H_2bdc and 300 equiv. of methacrylic acid as modulator as well as 4000 equiv. of H_2O as an additive.

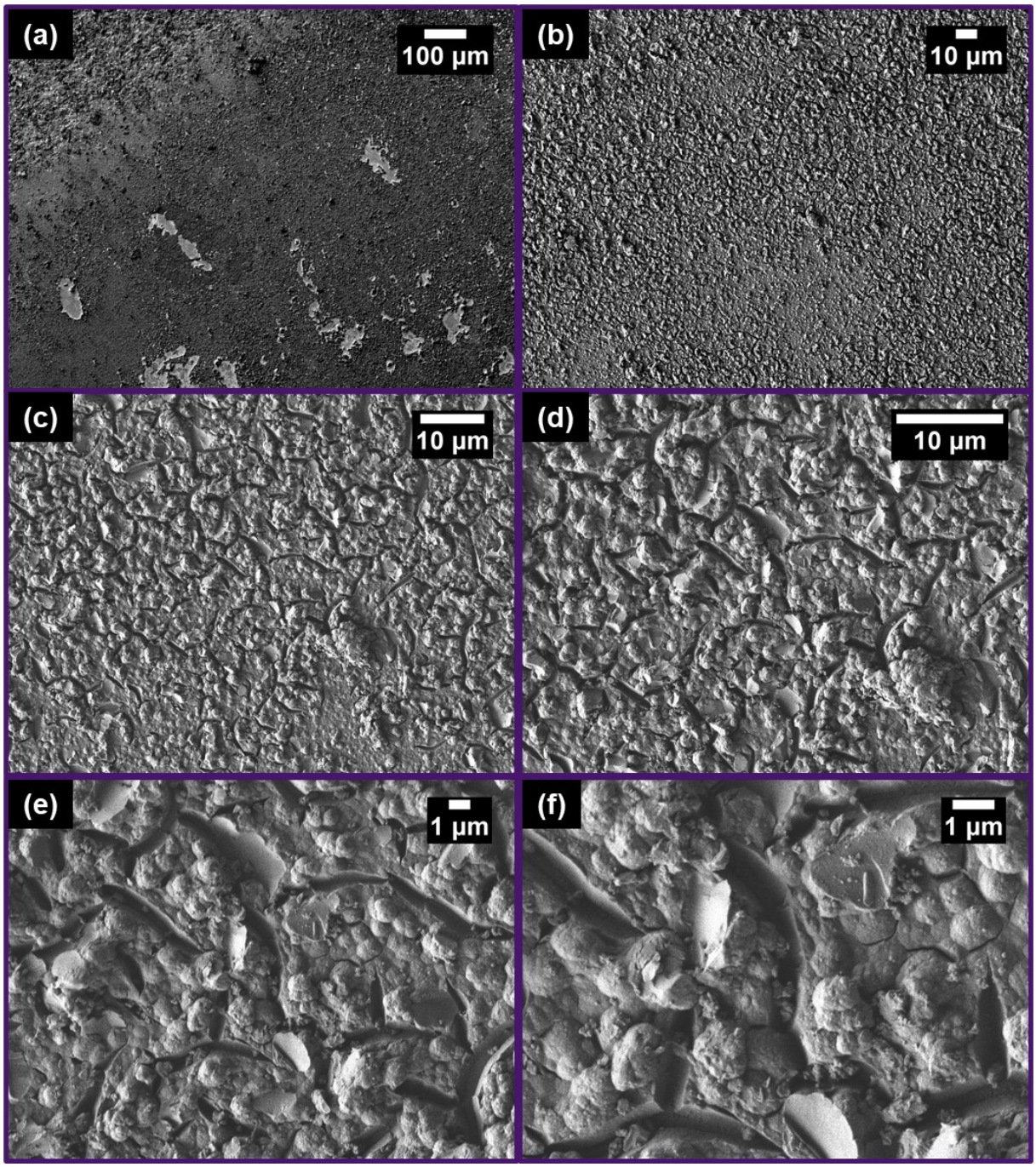

Figure S24: SEM images of UiO-66 thin film grown by CM-LPE. For the deposition, 0 equiv. of methacrylic acid were added to the metal source and linker solution. The instrument settings for the recorded images are 1 kV, LEI, WD 8.0 mm and magnifications of 100 (a), 500 (b), 1500 (c), 2500 (d), 5000 (e), and 10000 (f).

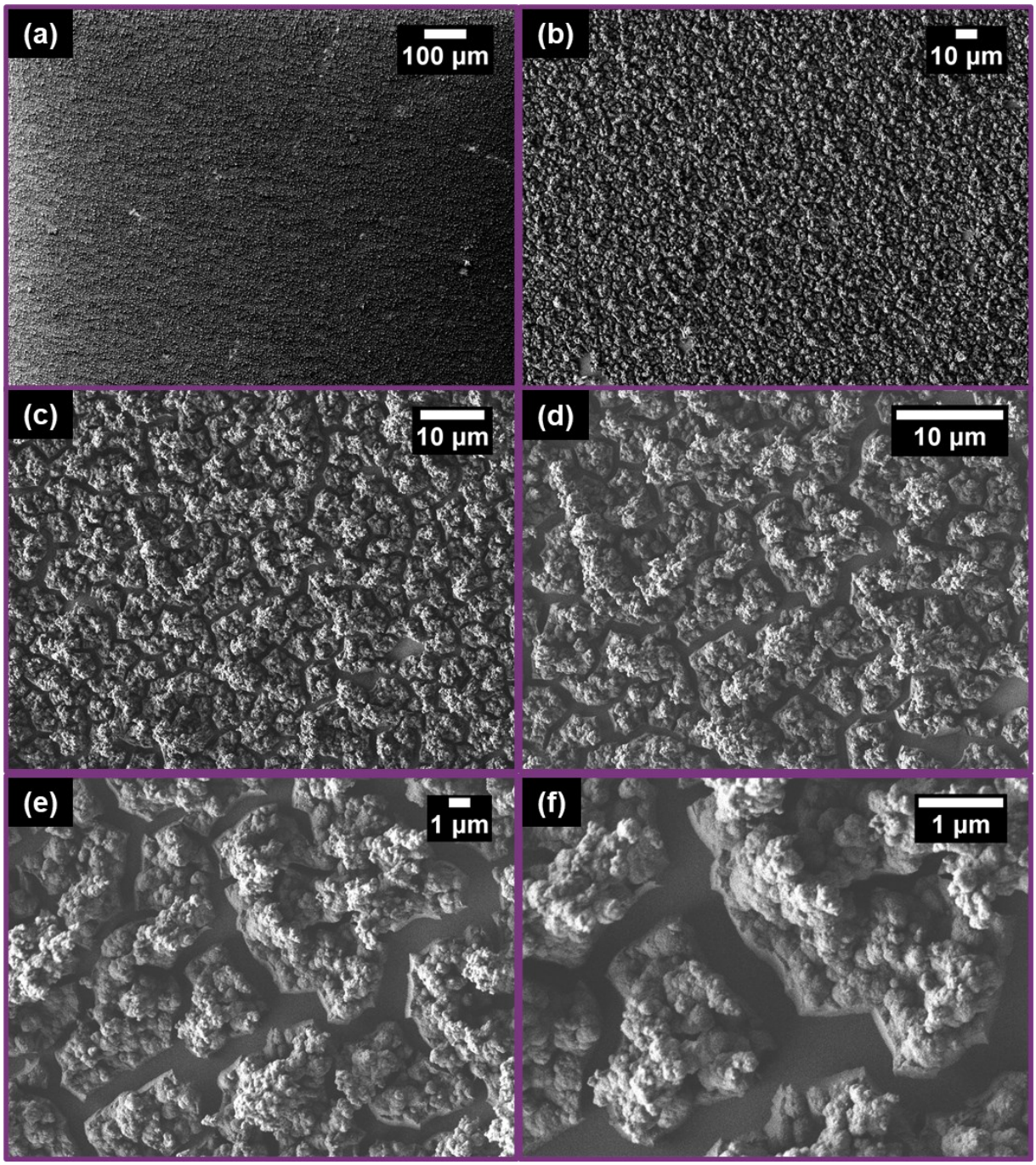

Figure S25: SEM images of UiO-66 thin film grown by CM-LPE. For the deposition, 200 equiv. of methacrylic acid were added to the metal source and linker solution. The instrument settings for the recorded images are 1 kV, LEI, WD 8.0 mm and magnifications of 100 (a), 500 (b), 1500 (c), 2500 (d), 5000 (e), and 10000 (f).

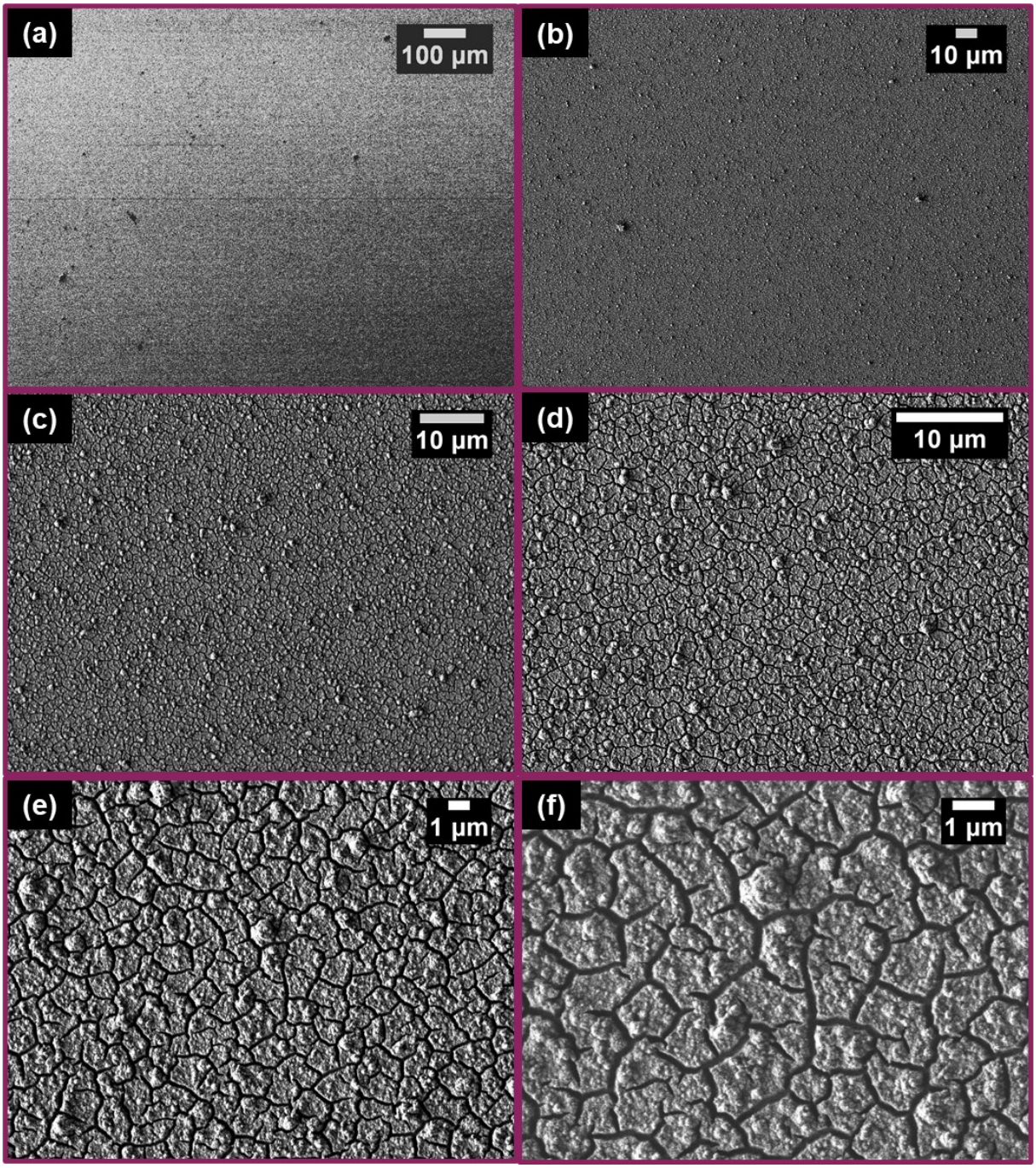

Figure S26: SEM images of UiO-66 thin film grown by CM-LPE. For the deposition, 300 equiv. of methacrylic acid was added to the metal source and linker solution. The instrument settings for the recorded images are 1 kV, LEI, WD 8.0 mm and magnifications of 100 (a), 500 (b), 1500 (c), 2500 (d), 5000 (e), and 10000 (f).

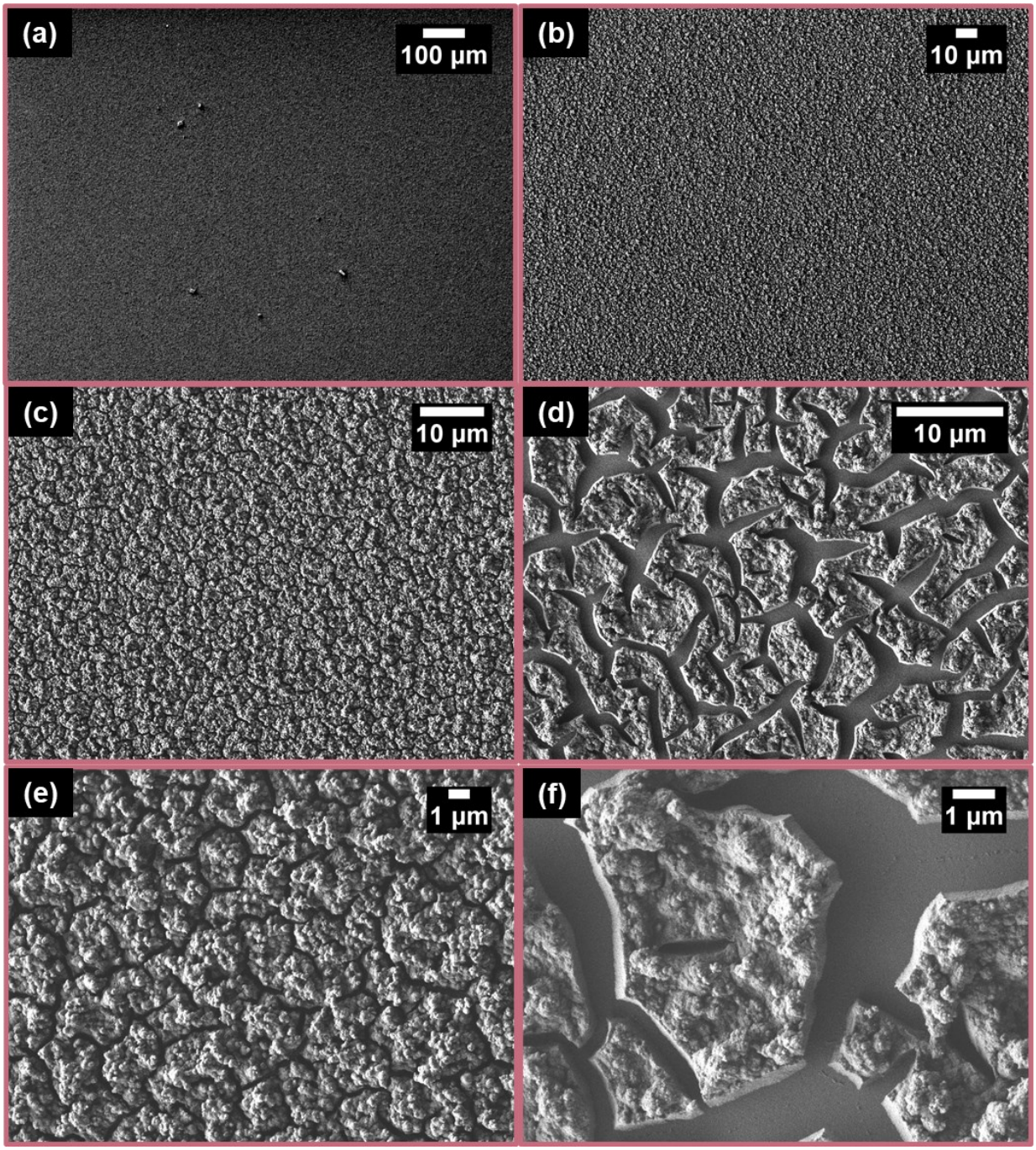

Figure S27: SEM images of UiO-66 thin film grown by CM-LPE. For the deposition, 300 equiv. of methacrylic acid were added to the metal source and linker solution, additionally 1000 equiv. of water were added to the linker solution. The instrument settings for the recorded images are 1 kV, LEI, WD 8.0 mm and magnifications of 100 (a), 500 (b), 1500 (c), 2500 (d), 5000 (e), and 10000 (f).

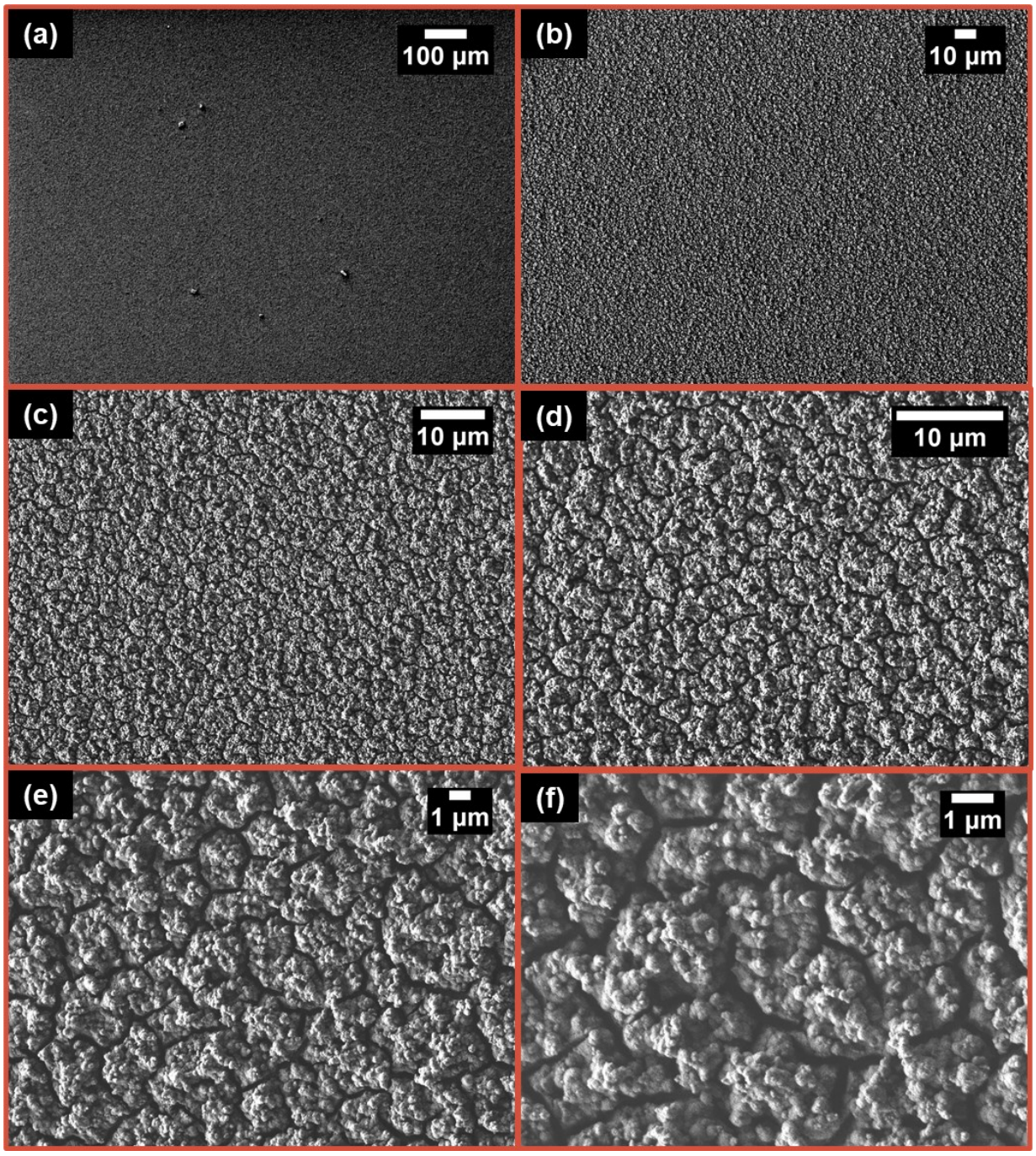

Figure S28: SEM images of UiO-66 thin film grown by CM-LPE. For the deposition, 300 equiv. of methacrylic acid were added to the metal source and linker solution, additionally 2000 equiv. of water were added to the linker solution. The instrument settings for the recorded images are 1 kV, LEI, WD 8.0 mm and magnifications of 100 (a), 500 (b), 1500 (c), 2500 (d), 5000 (e), and 10000 (f).

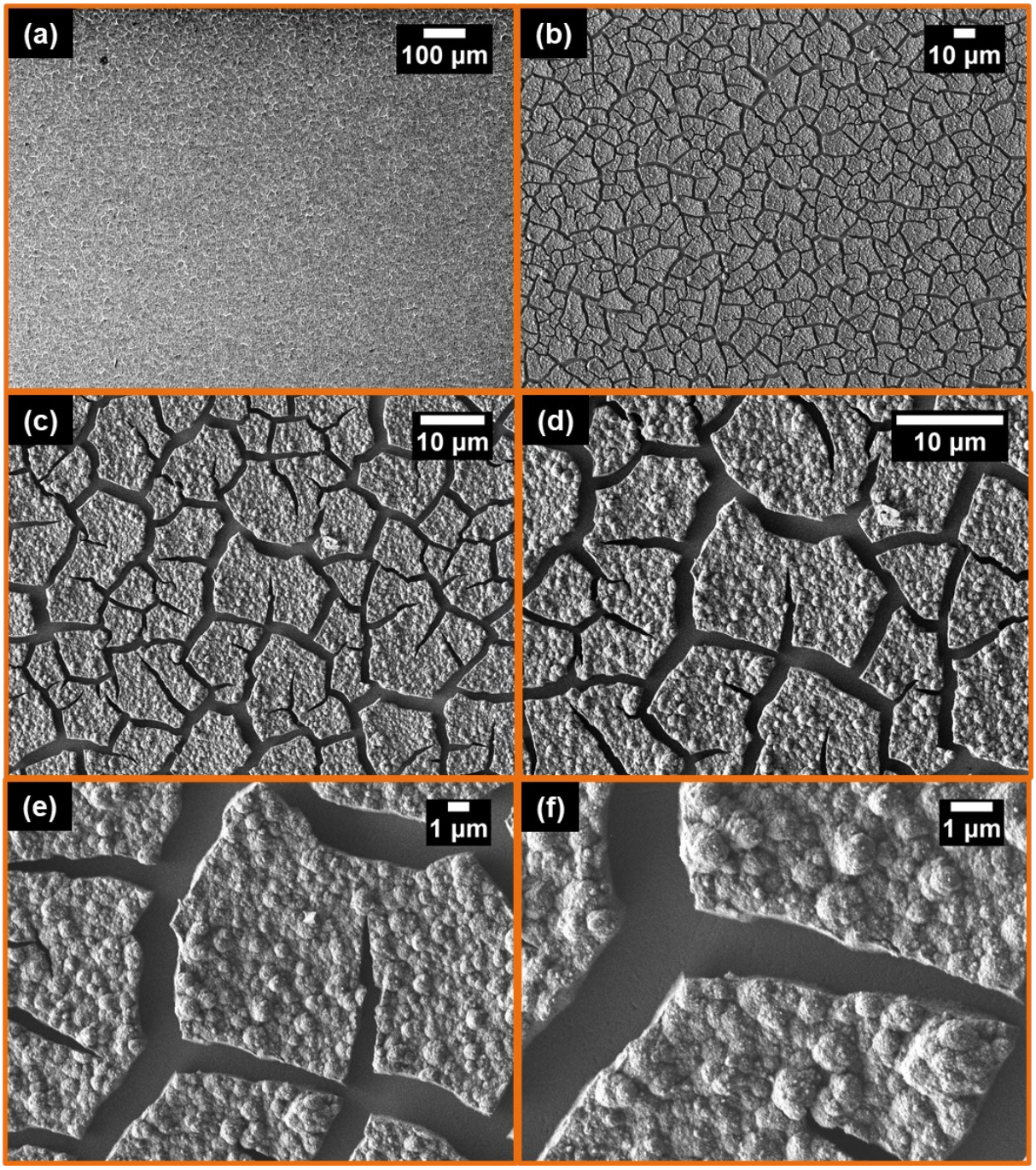

Figure S29: SEM images of UiO-66 thin film grown by CM-LPE. For the deposition, 300 equiv. of methacrylic acid were added to the metal source and linker solution, additionally 3000 equiv. of water were added to the linker solution. The instrument settings for the recorded images are 1 kV, LEI, WD 8.0 mm and magnifications of 100 (a), 500 (b), 1500 (c), 2500 (d), 5000 (e), and 10000 (f).

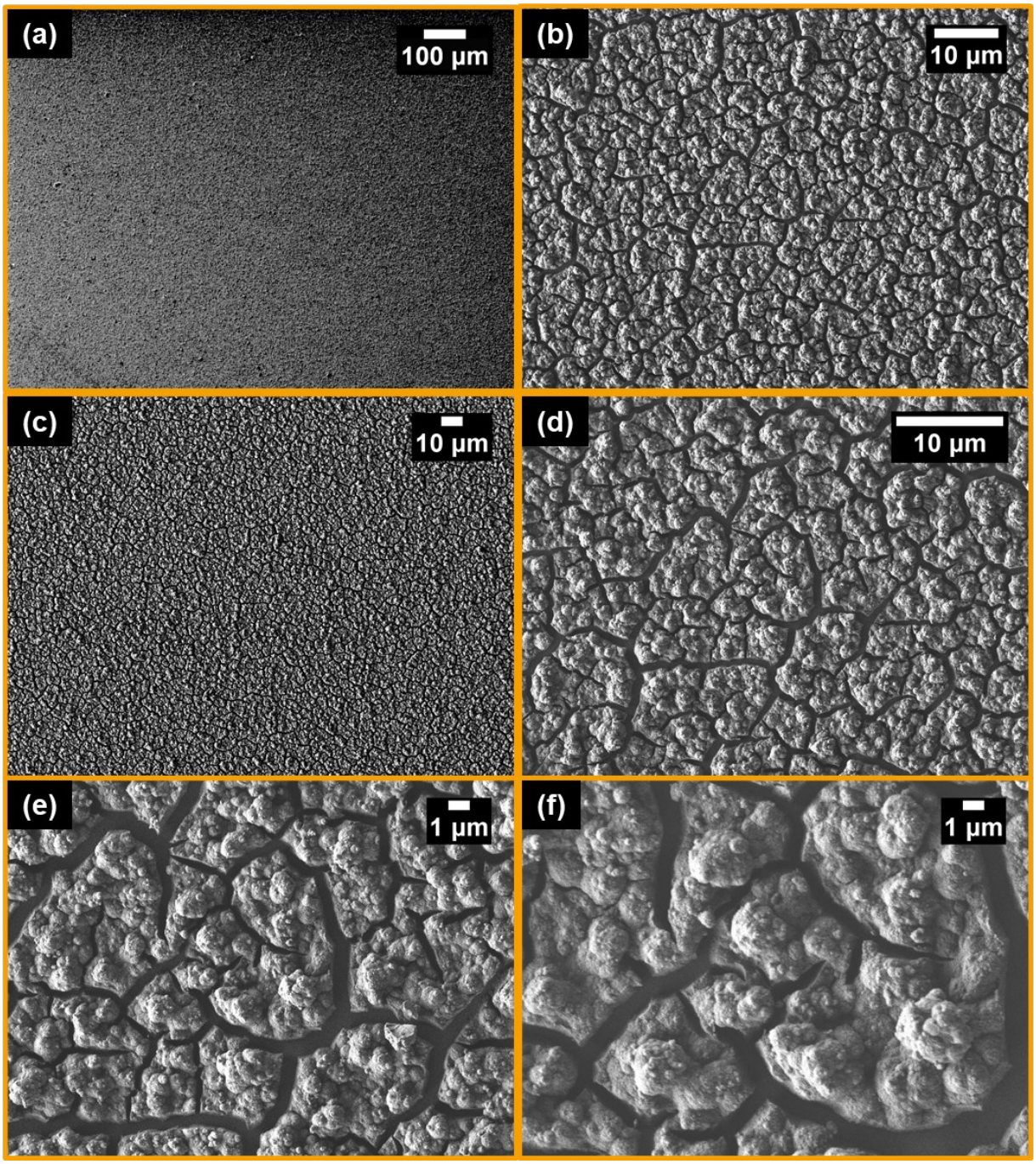

Figure S30: SEM images of UiO-66 thin film grown by CM-LPE. For the deposition, 300 equiv. of methacrylic acid were added to the metal source and linker solution, additionally 4000 equiv. of water were added to the linker solution. The instrument settings for the recorded images are 1 kV, LEI, WD 8.0 mm and magnifications of 100 (a), 500 (b), 1500 (c), 2500 (d), 5000 (e), and 10000 (f).

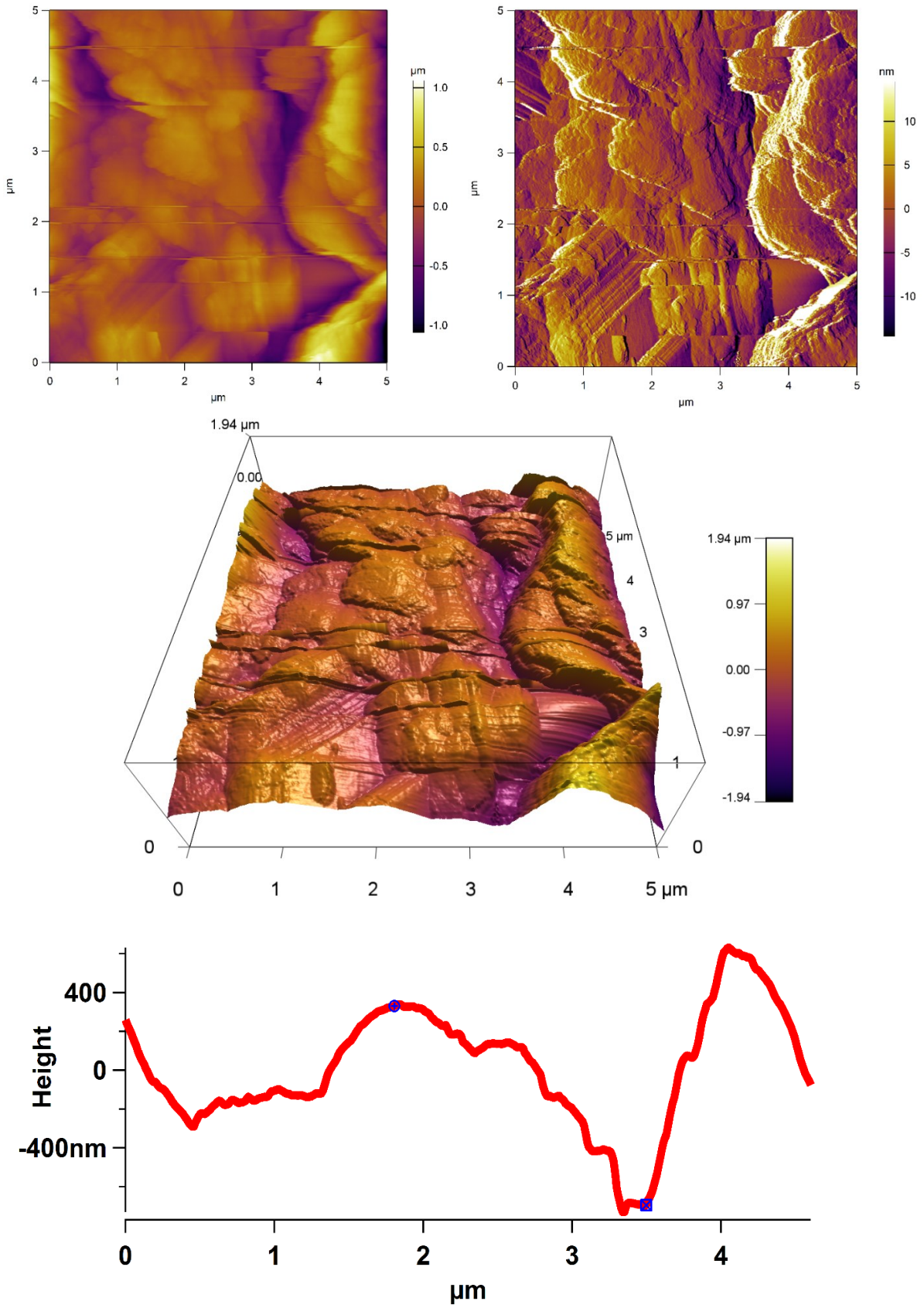

Figure S31: AFM images top height and amplitude, middle height 3D, and bottom height profile of the activated UiO-66 thin-film deposited by CM-LPE using $[Zr_6O_4(OH)_4(OMc)_{12}]$, H_2bdc, 0 equiv. of methacrylic acid. This Figure was taken from Semrau, *et al.*[59] permission from ACS Crystal Growth & Design. Copyright (2019) American Chemical Society.

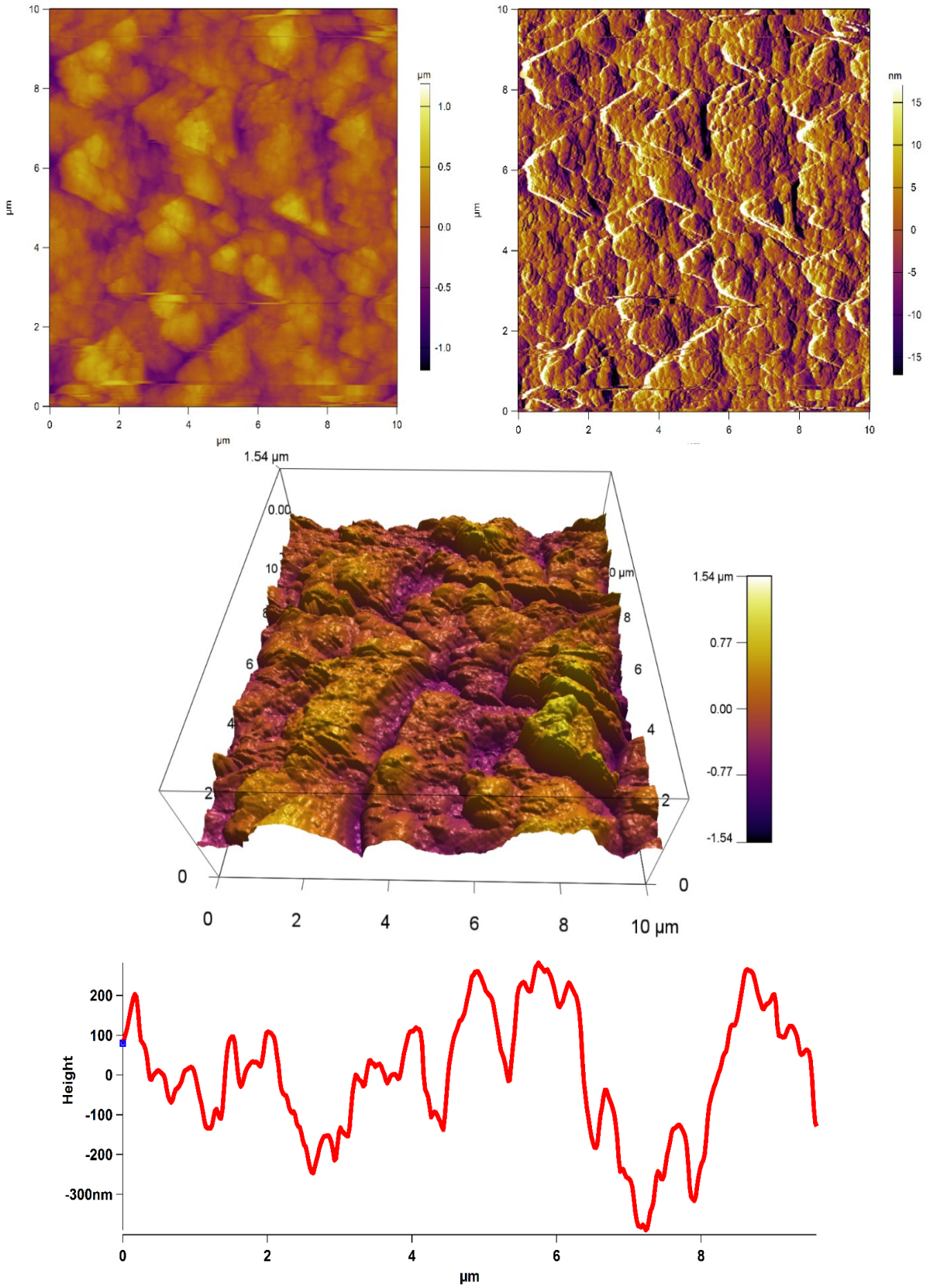

Figure S32: AFM images top height and amplitude, middle height 3D, and bottom height profile of the activated UiO-66 thin-film deposited by CM-LPE using [$Zr_6O_4(OH)_4(OMc)_{12}$], H_2bdc, 200 equiv. of methacrylic acid. This Figure was taken from Semrau, *et al.*[59] permission from ACS Crystal Growth & Design. Copyright (2019) American Chemical Society.

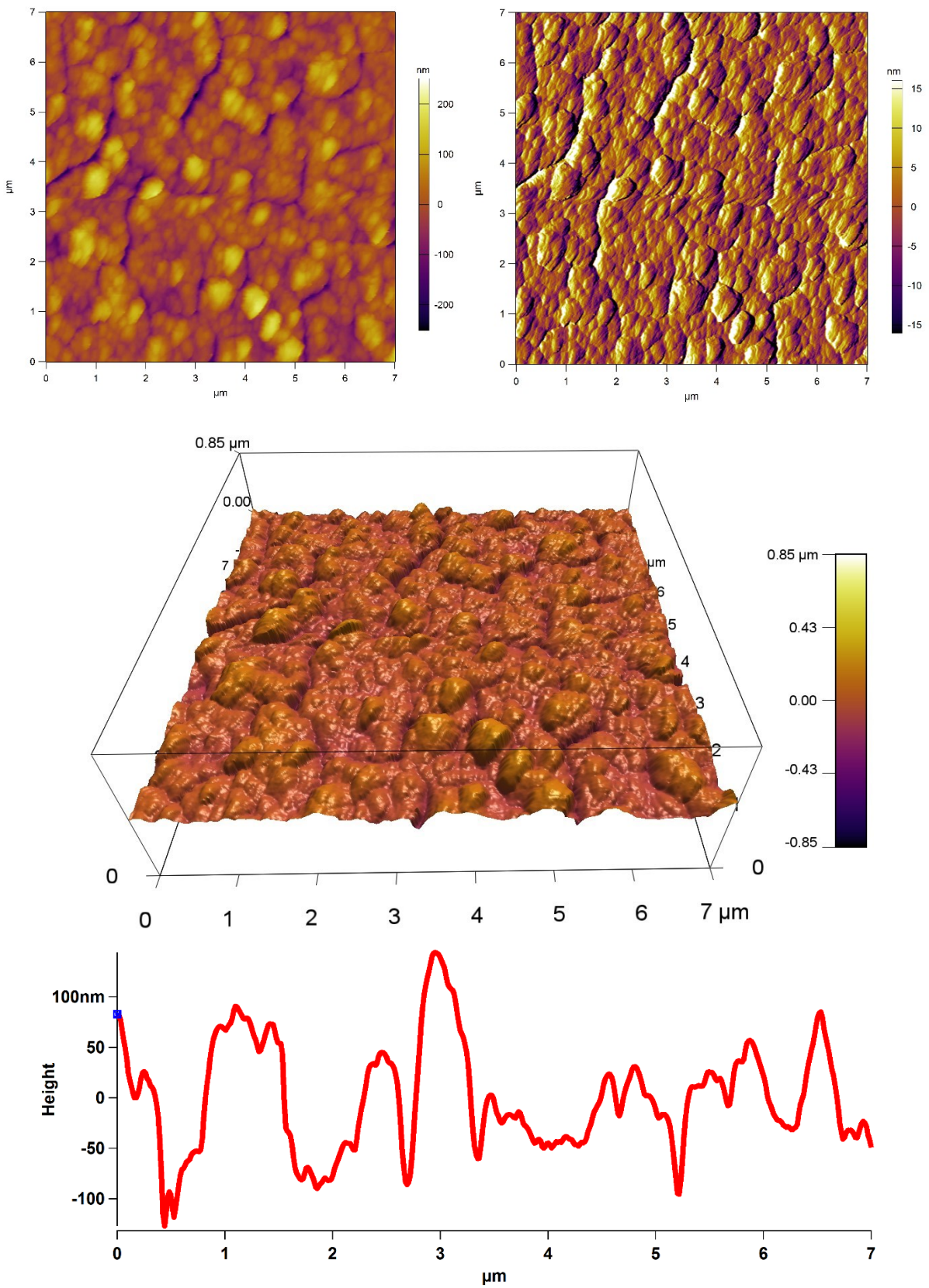

Figure S33: AFM images top height and amplitude, middle height 3D, and bottom height profile of the activated UiO-66 thin-film deposited by CM-LPE using $[Zr_6O_4(OH)_4(OMc)_{12}]$, H_2bdc, 300 equiv. of methacrylic acid. This Figure was taken from Semrau, *et al.*[59] permission from ACS Crystal Growth & Design. Copyright (2019) American Chemical Society.

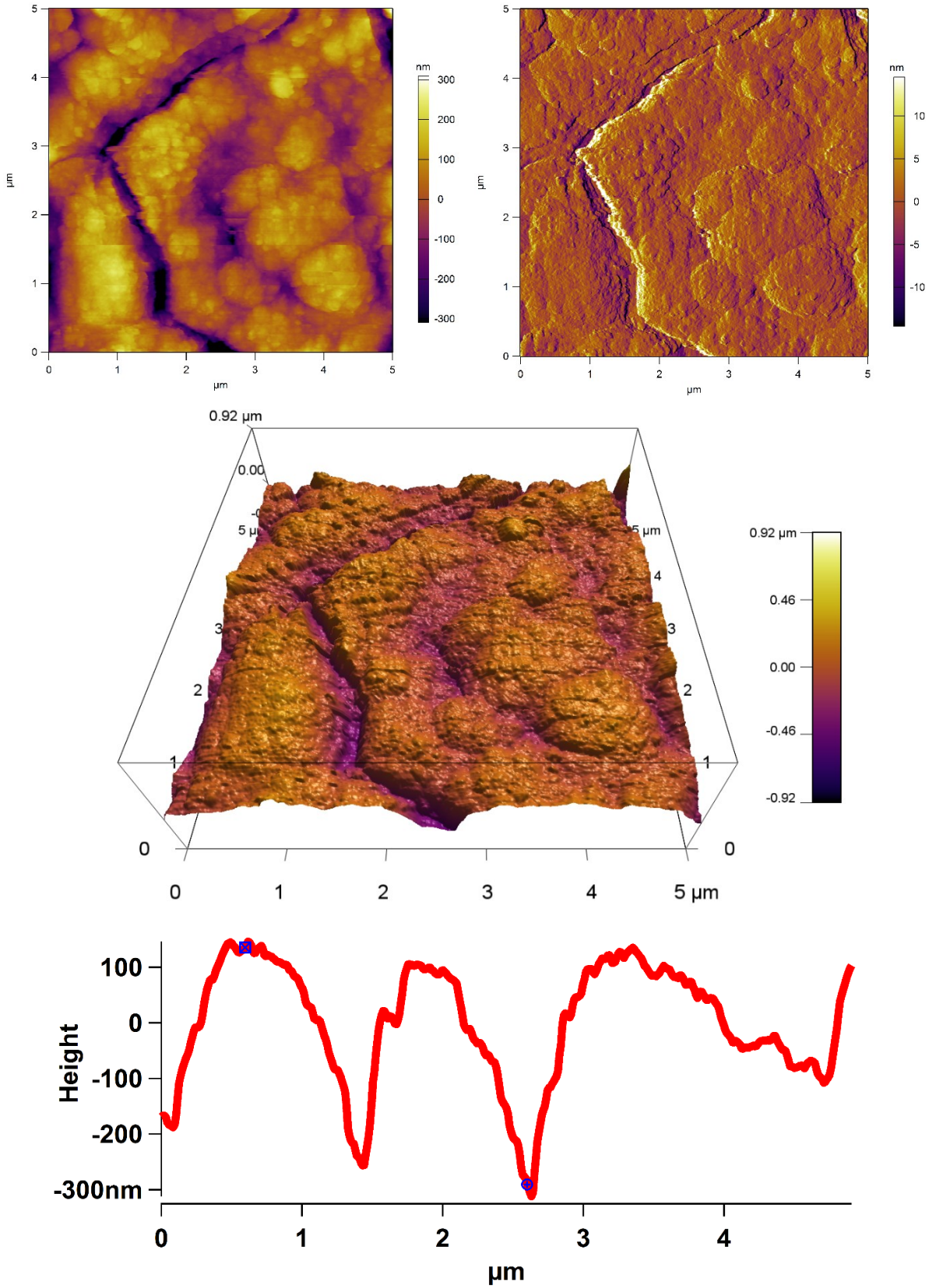

Figure S34: AFM images top height and amplitude, middle height 3D, and bottom height profile of the activated UiO-66 thin-film deposited by CM-LPE using [$Zr_6O_4(OH)_4(OMc)_{12}$], H_2bdc, 300 equiv. of methacrylic acid, and 1000 equiv. of water. This Figure was taken from Semrau, *et al.*[59] permission from ACS Crystal Growth & Design. Copyright (2019) American Chemical Society.

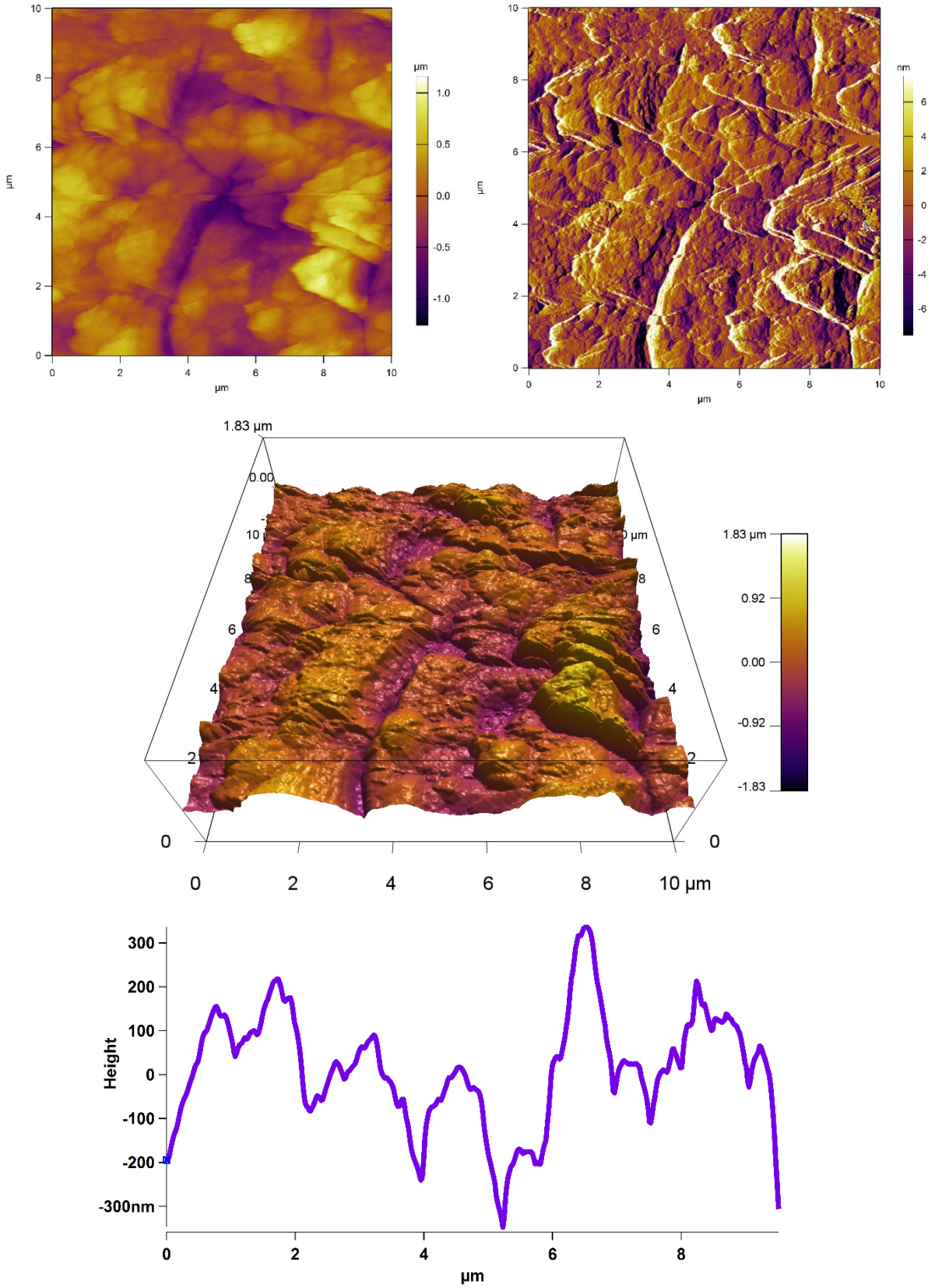

Figure S35: AFM images top height and amplitude, middle height 3D, and bottom height profile of the activated UiO-66 thin-film deposited by CM-LPE using $[Zr_6O_4(OH)_4(OMc)_{12}]$, H_2bdc, 300 equiv. of methacrylic acid, and 2000 equiv. of water. This Figure was taken from Semrau, *et al.*[59] permission from ACS Crystal Growth & Design. Copyright (2019) American Chemical Society.

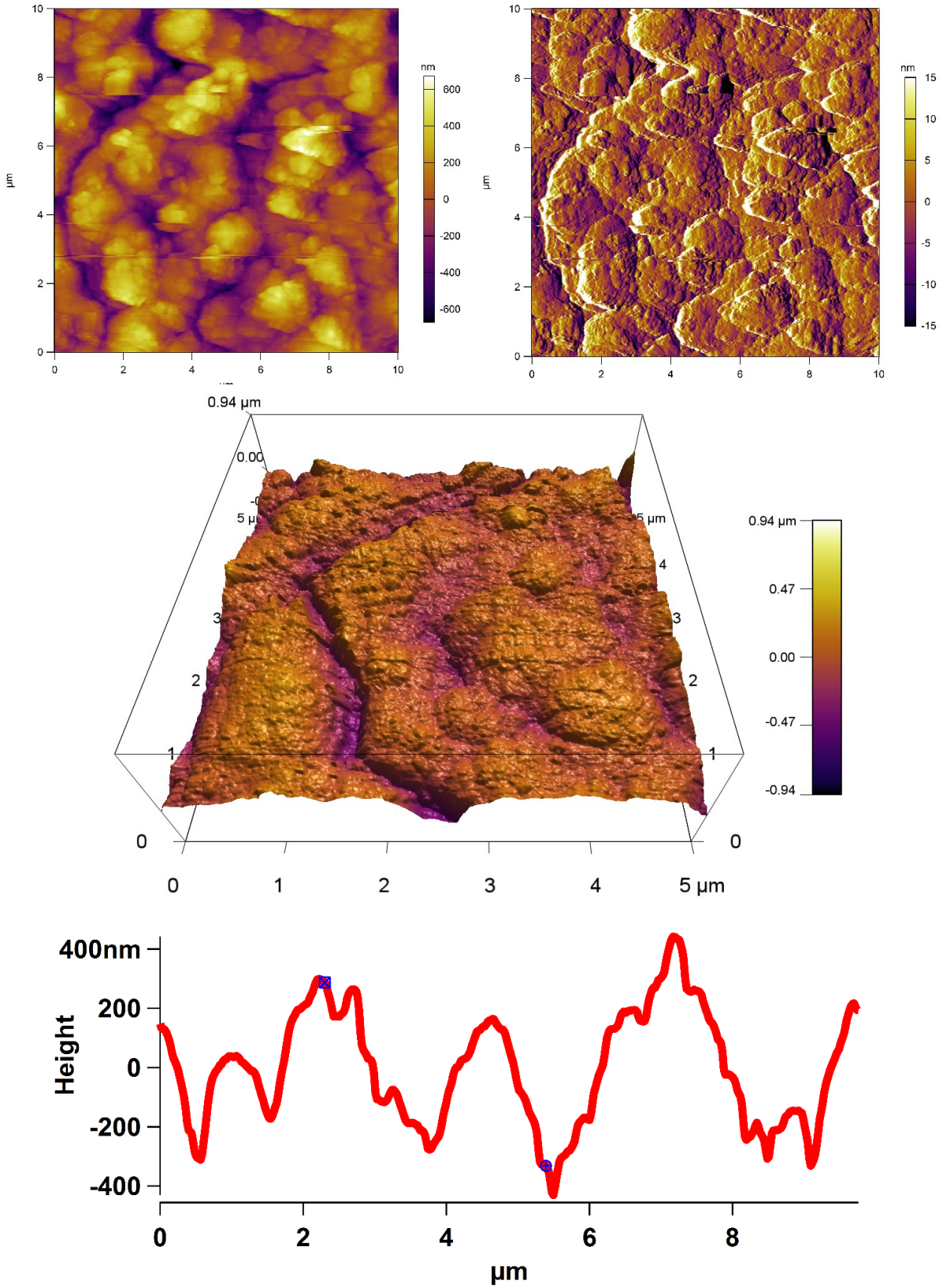

Figure S36: AFM images top height and amplitude, middle height 3D, and bottom height profile of the activated UiO-66 thin-film deposited by CM-LPE using $[Zr_6O_4(OH)_4(OMc)_{12}]$, H_2bdc, 300 equiv. of methacrylic acid, and 3000 equiv. of water. This Figure was taken from Semrau, *et al.*[59] permission from ACS Crystal Growth & Design. Copyright (2019) American Chemical Society.

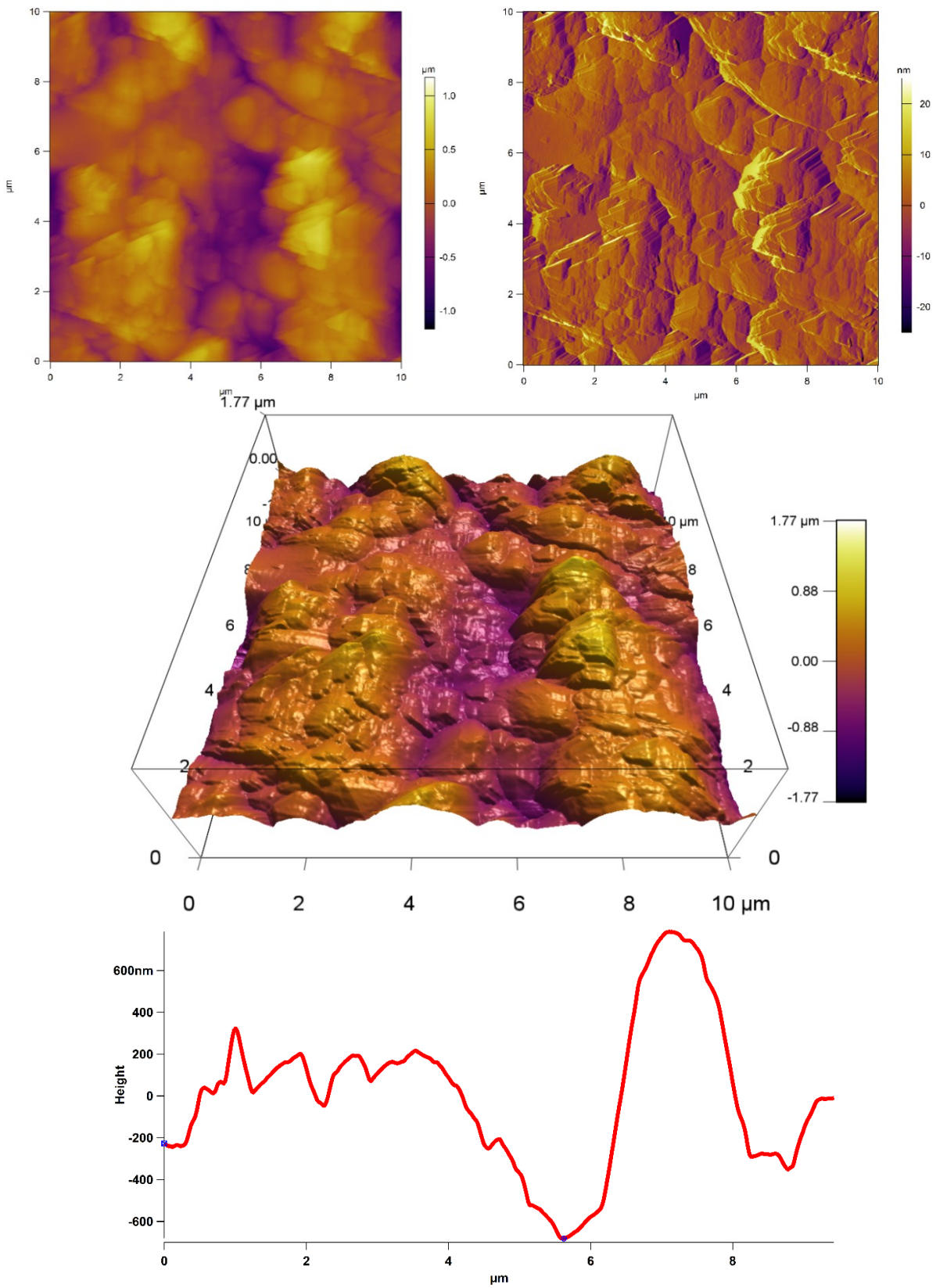

Figure S37: AFM images top height and amplitude, middle height 3D, and bottom height profile of the activated UiO-66 thin-film deposited by CM-LPE using $[Zr_6O_4(OH)_4(OMc)_{12}]$, H_2bdc, 300 equiv. of methacrylic acid, and 4000 equiv. of water. This Figure was taken from Semrau, *et al.*[59] permission from ACS Crystal Growth & Design. Copyright (2019) American Chemical Society.

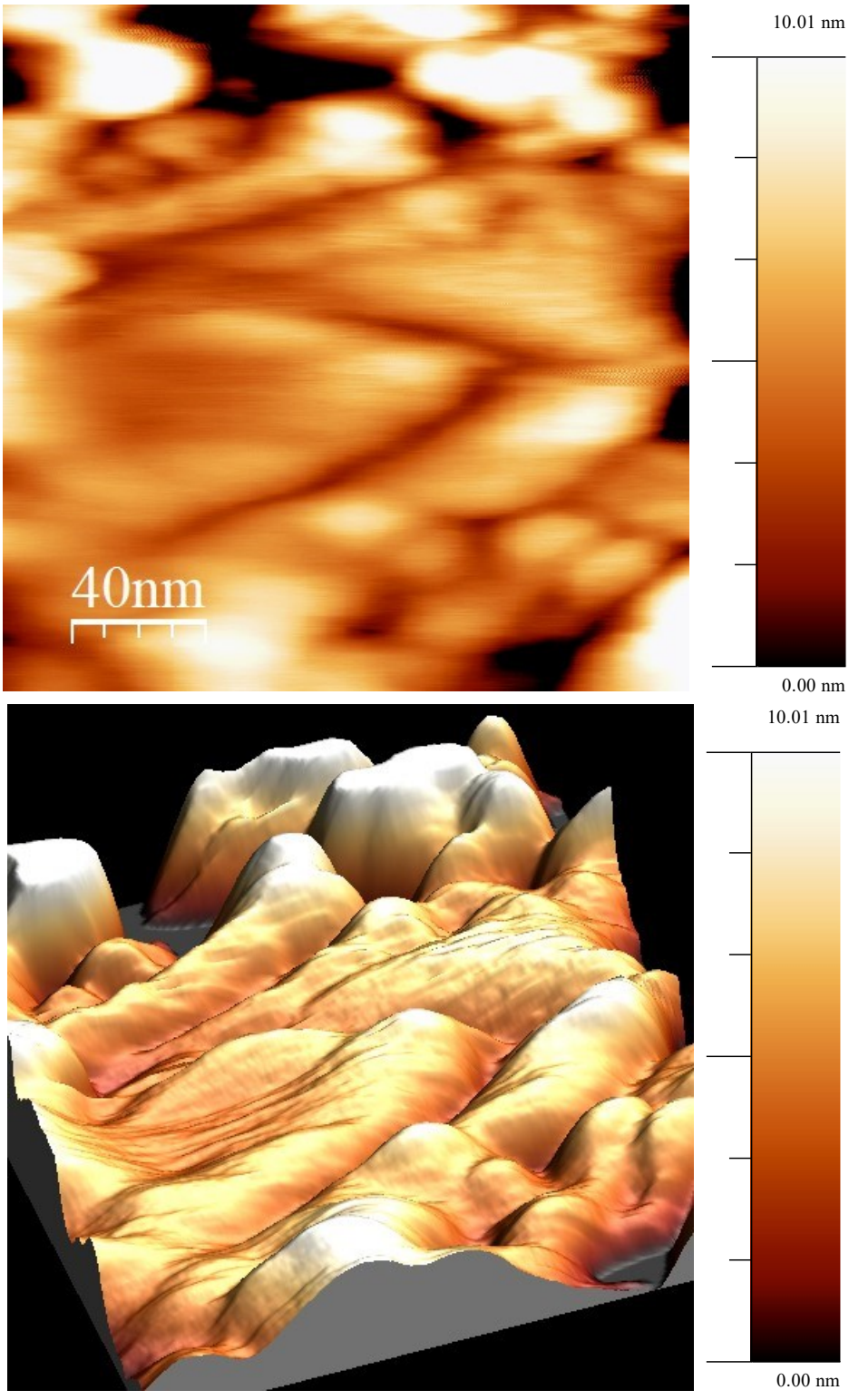

Figure S38: 2D (a) and 3D (b) AFM images of the UiO-66-NH_2 films. The surface roughness was analyzed with WSxM. For the 200 x 200 nm excerpts from the film the root mean square (RSM) of the surface roughness was determined to be 2.0 nm. This Figure was taken from Semrau, *et al.*[59] permission from ACS Crystal Growth & Design. Copyright (2019) American Chemical Society.

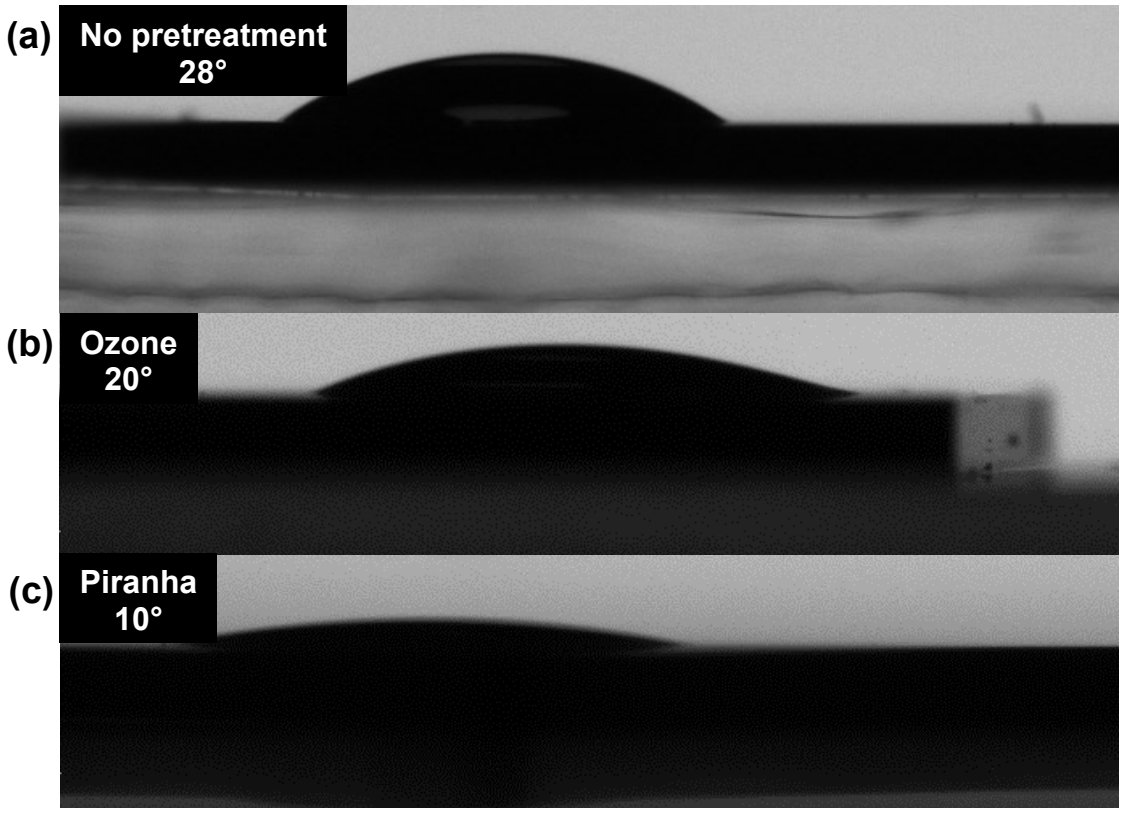

Figure S39: Contact angle measurements of untreated silicon substrates (a), UV/ozone treated silicon substrates (b), and piranha etched silicon substrates (c).

7.5.2. Selective Covalent Immobilization of Preformed Nano-MOFs in Microfluidic Devices Targeting Vectorial Catalysis • (Chapter 3)

7.5.2.1. Study I: Selective Positioning of Nano-Sized Metal-Organic Frameworks Particles at Patterned Substrate Surfaces

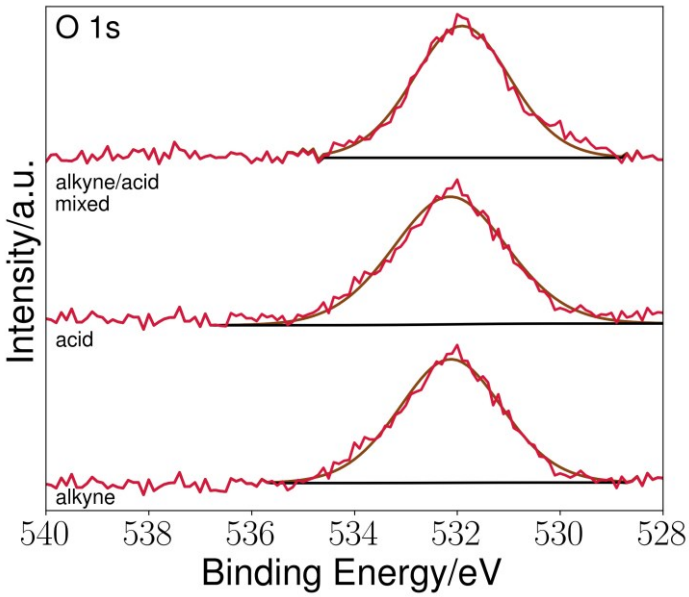

Figure S40: XPS O 1s narrow scan of the alkyne, carboxylic acid, and alkyne/acid mixed surfaces.

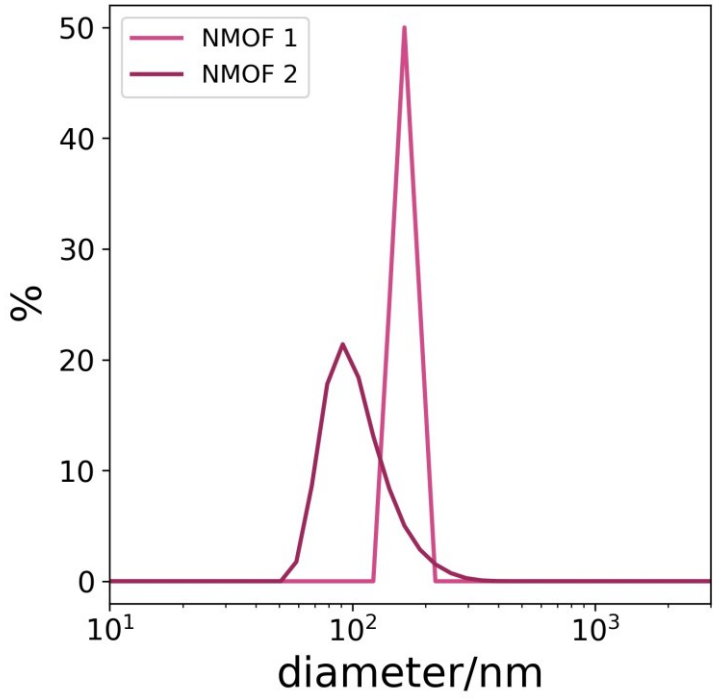

Figure S41: Dynamic Light Scattering of **NMOF 1** (164 ± 24.4 nm) and **NMOF 2** (91.2 ± 37.7 nm) directly after their synthesis.

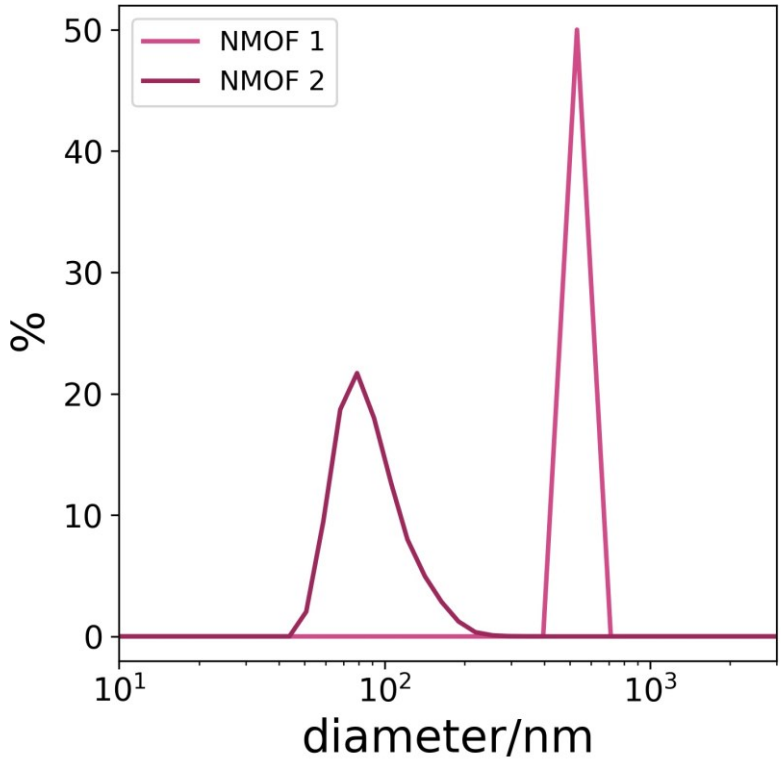

Figure S42: Dynamic Light Scattering of **NMOF 1** (531 ± 76 nm) and **NMOF 2** (78.1 ± 24.4 nm) 4 weeks after the synthesis.

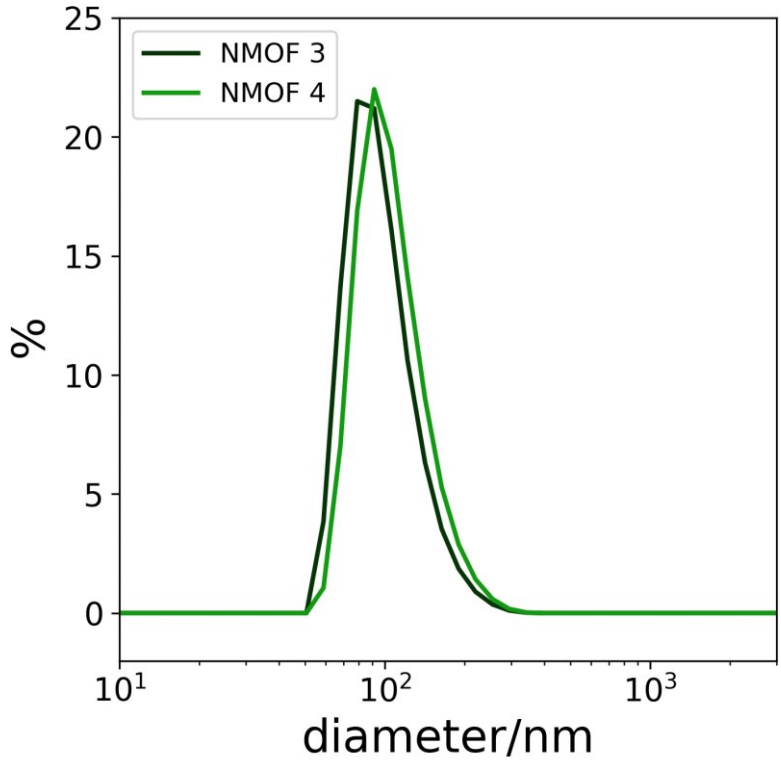

Figure S43: Dynamic Light Scattering of **NMOF 3** (78.8 ± 32.5 nm) and **NMOF 4** (91.3 ± 34.1 nm) directly after their synthesis.

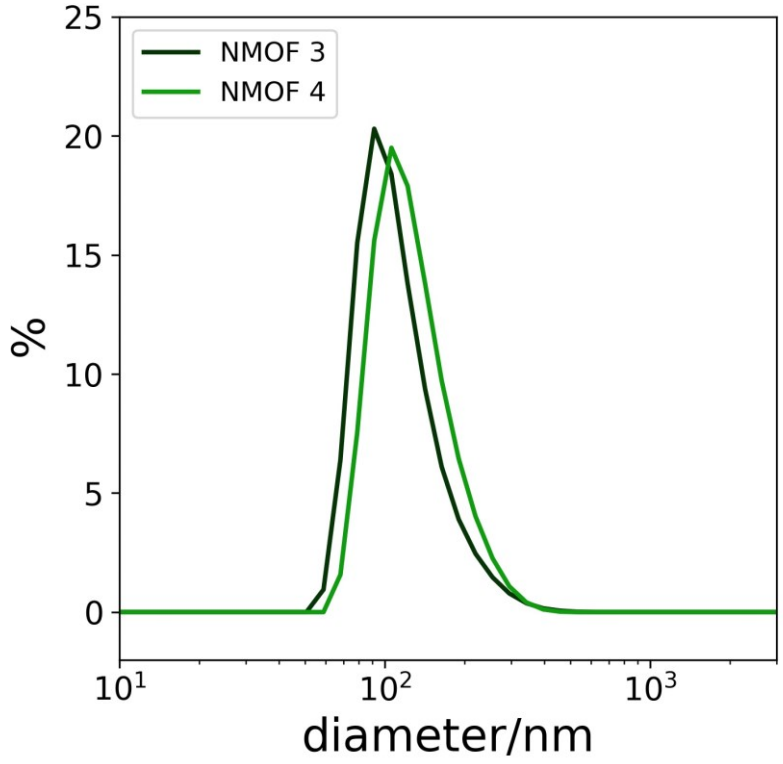

Figure S44: Dynamic Light Scattering of **NMOF 3** (106 ± 47 nm) and **NMOF 4** (91.3 ± 45.6 nm) 4 weeks after the synthesis.

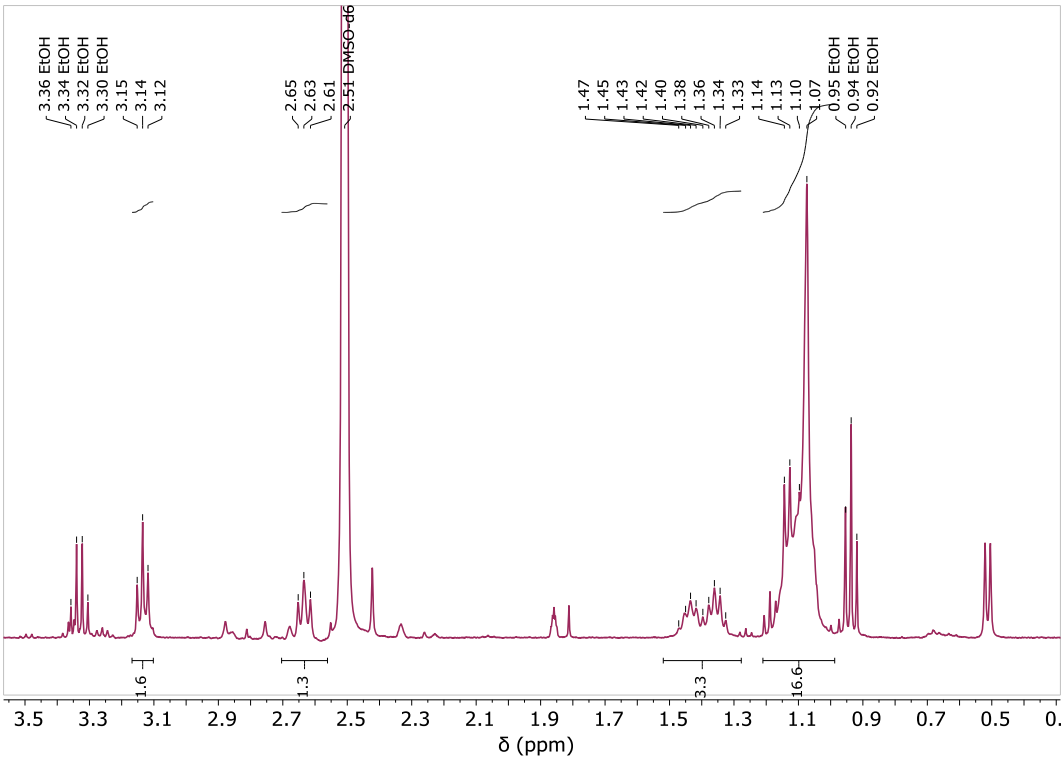

Figure S45: ^{1}H-NMR spectrum of **NMOF 2** after digestion in 0.1 mL DCl and 0.4 mL DMSO-d_6. Range from 0-3.5 ppm.

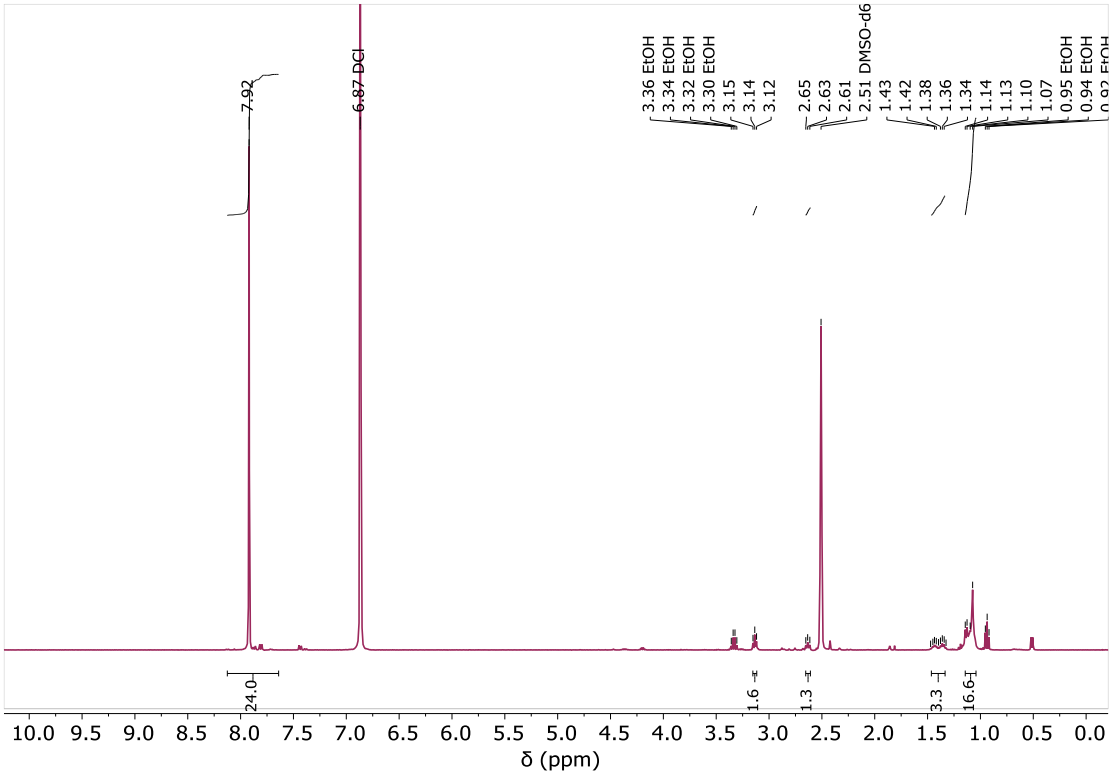

Figure S46: ^{1}H-NMR spectrum of **NMOF 2** after digestion in 0.1 mL DCl and 0.4 mL DMSO-d_6. Full range.

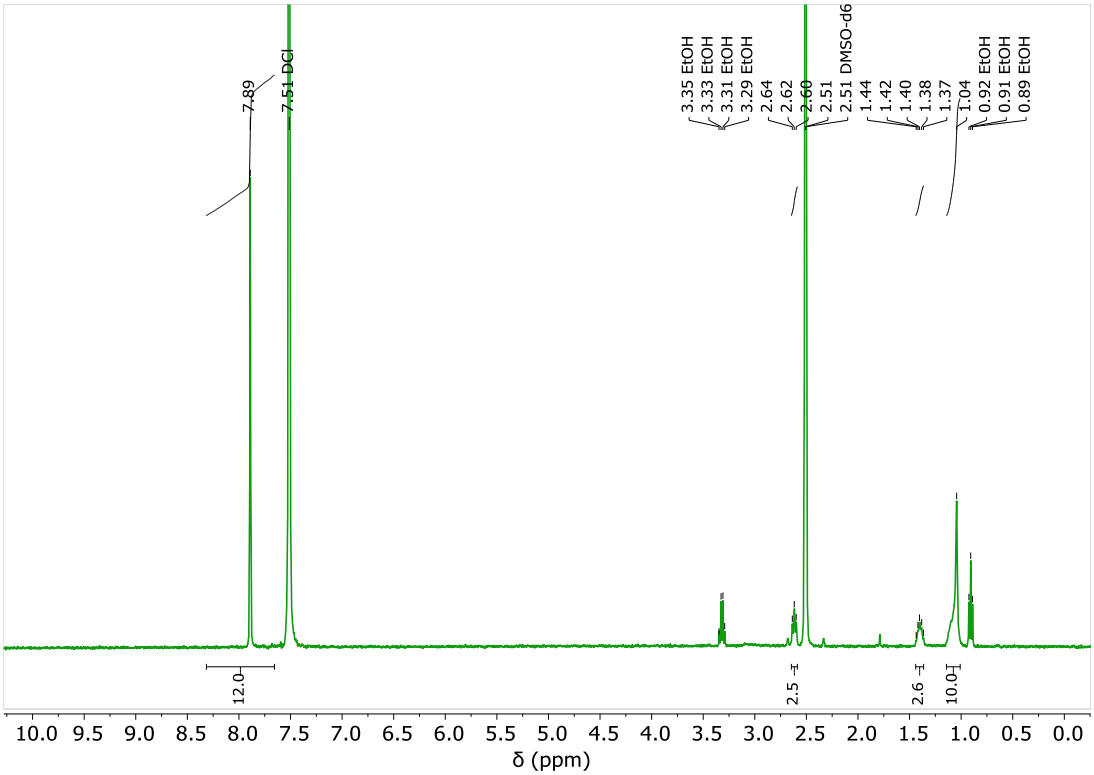

Figure S47: ^{1}H-NMR spectrum of **NMOF 4** after digestion in 0.1 mL DCl and 0.4 mL DMSO-d_6. Range from 0-3.5 ppm.

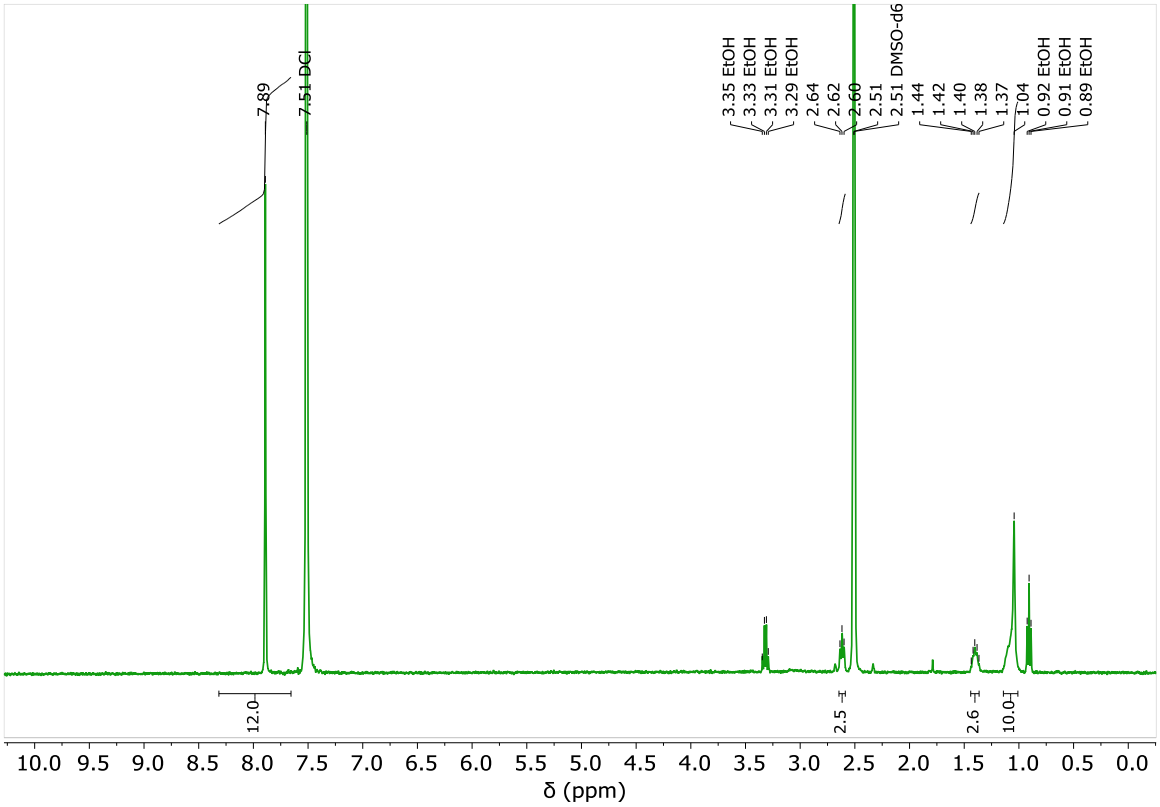

Figure S48: ^{1}H-NMR spectrum of **NMOF 4** after digestion in 0.1 mL DCl and 0.4 mL DMSO-d_6. Full range.

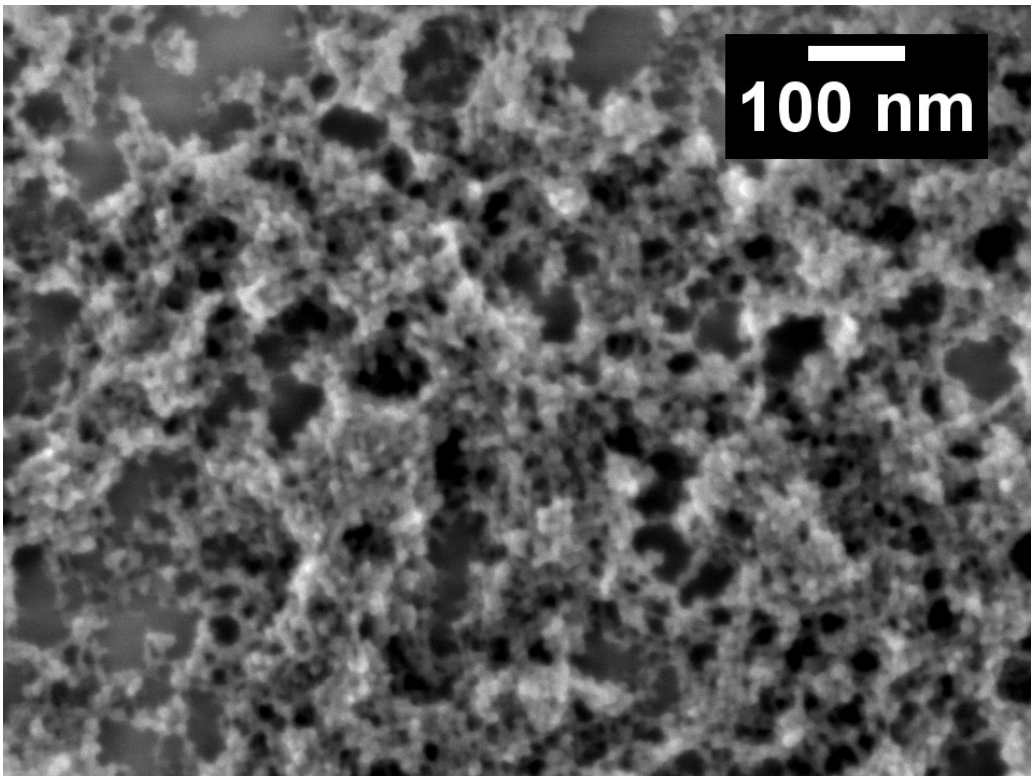

Figure S49: SEM image of **NMOF 1**. Settings: 50,000-fold magnification, 0.50 kV SEI, WD 2.9 mm.

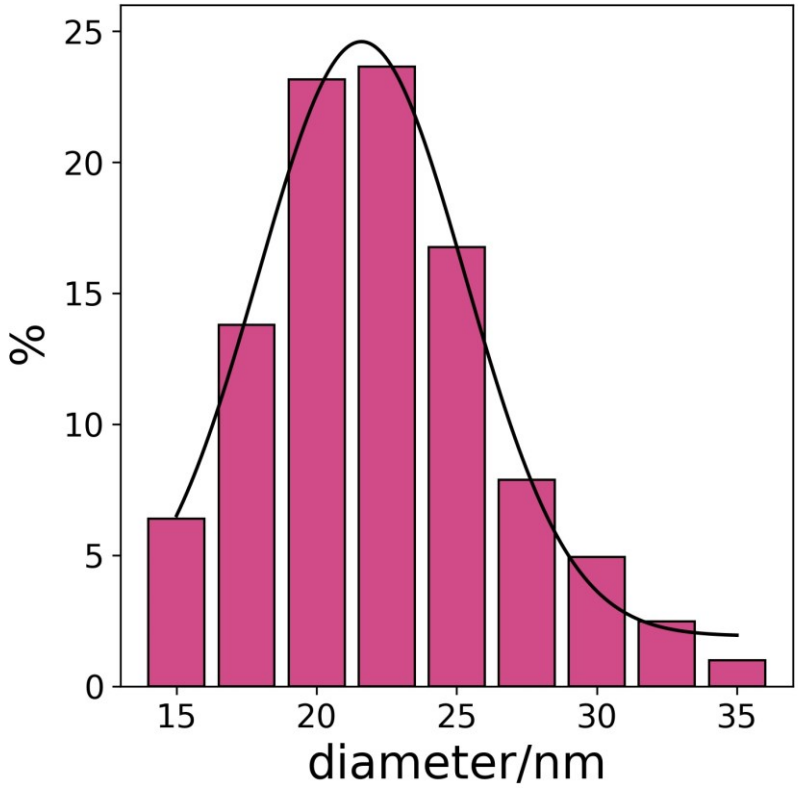

Figure S50: Histogram of **NMOF 1** size distribution. Distribution calculated from the SEM image in Figure S49. The average particle diameter is 21.0 ± 3.3 nm.

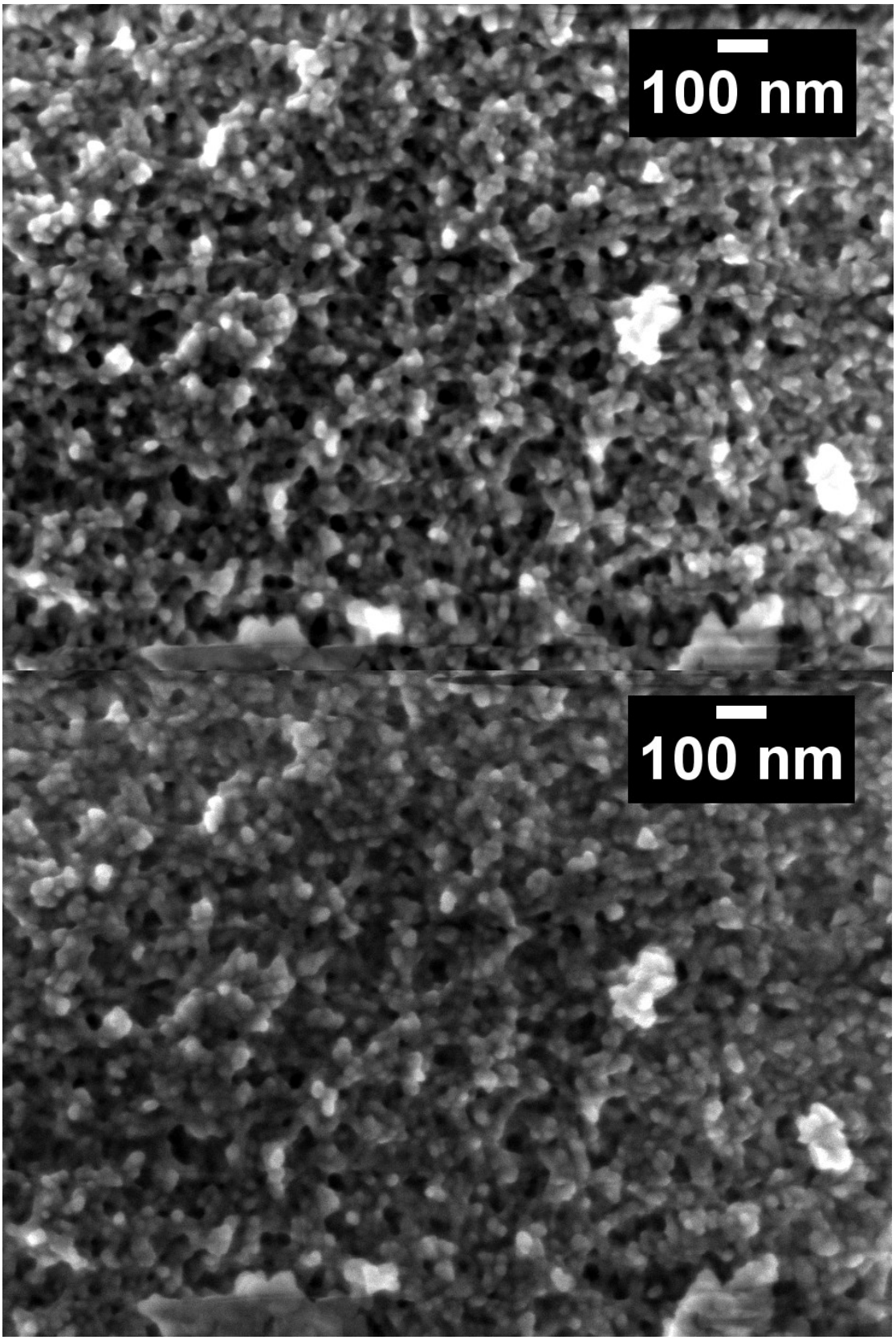

Figure S51: SEM images of **NMOF 2**. Settings: 60,000-fold magnification, 1.50 kV SEI, WD 4.1 mm.

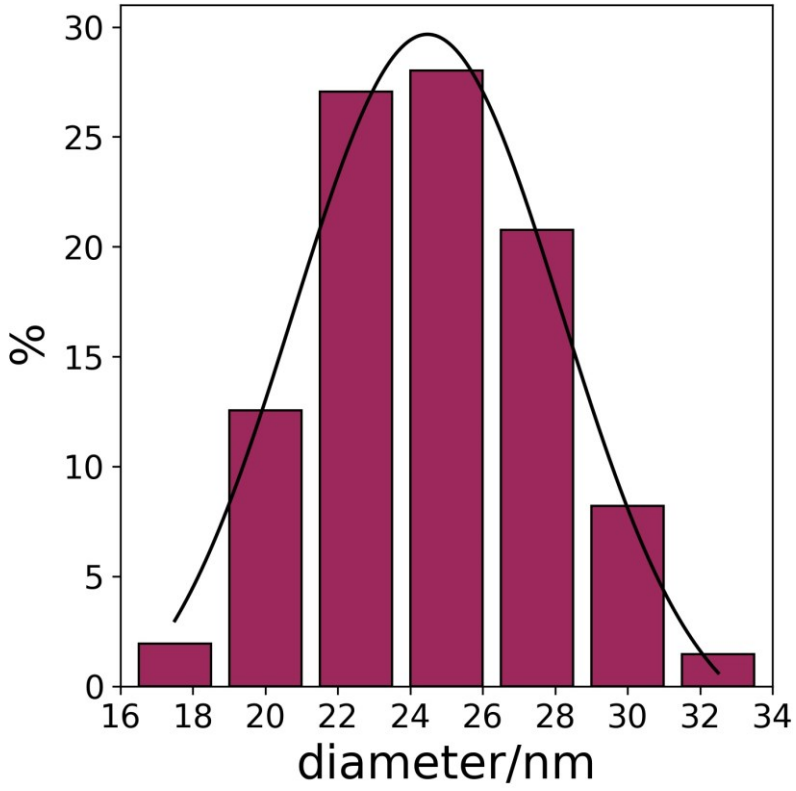

Figure S52: Histogram of **NMOF 2** size distribution. Distribution calculated from the SEM images in Figure S51. The average particle diameter is 23.4 ± 2.5 nm.

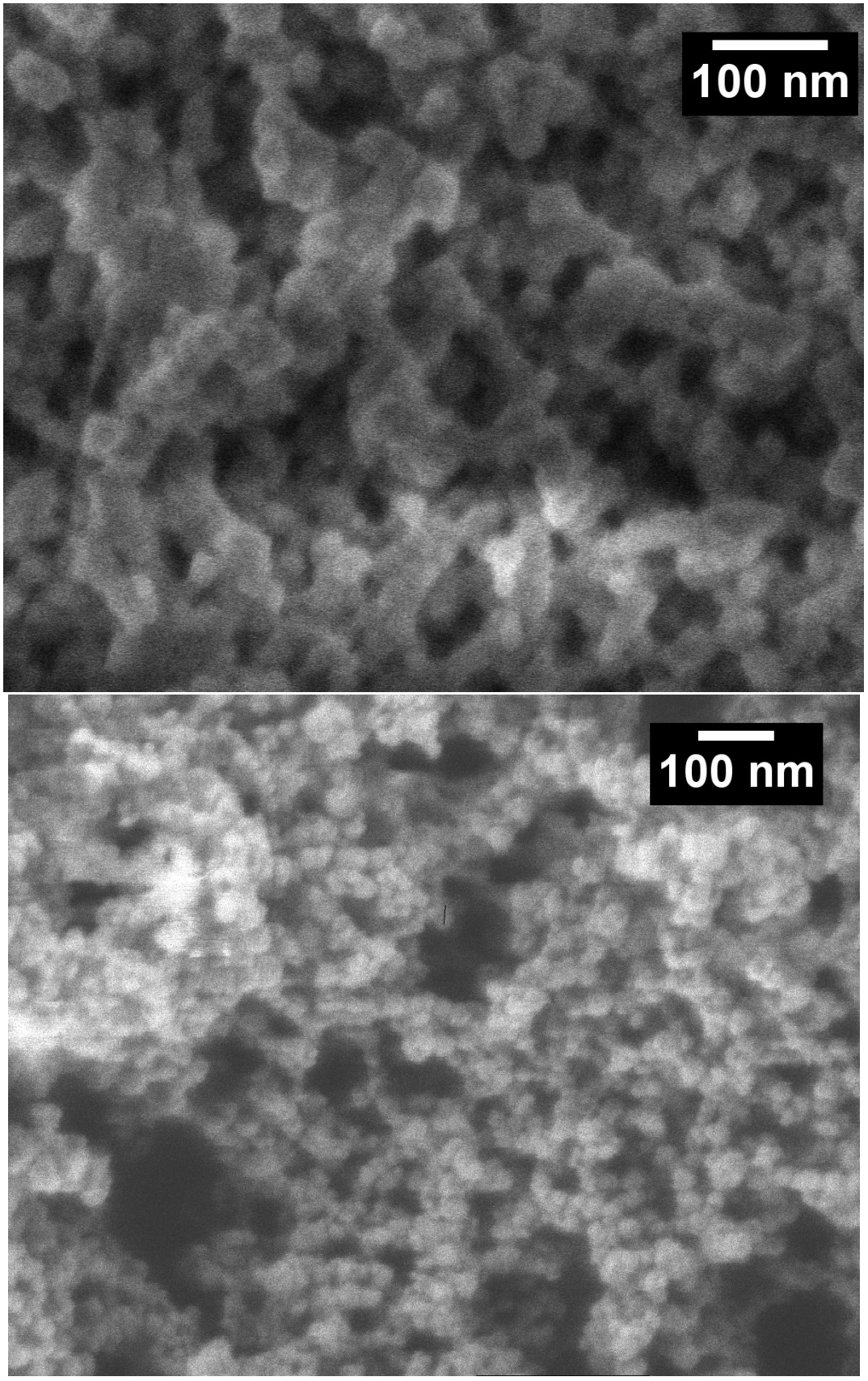

Figure S53: SEM images of **NMOF 3.** Settings: (a) 150,000-fold magnification, 0.80 kV SEI, WD 5.0 mm. (b) 100,000-fold magnification, 0.30 kV SEI, WD 3.5 mm.

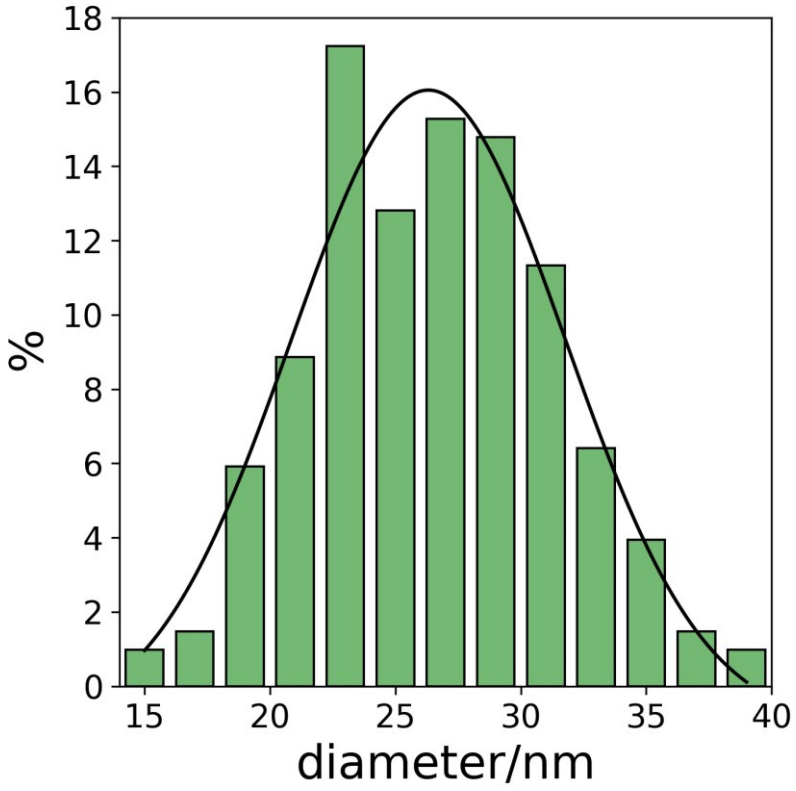

Figure S54: Histogram of **NMOF 3** size distribution. Distribution calculated from the SEM images in Figure S53.The average particle diameter is 26.7 ± 3.9 nm.

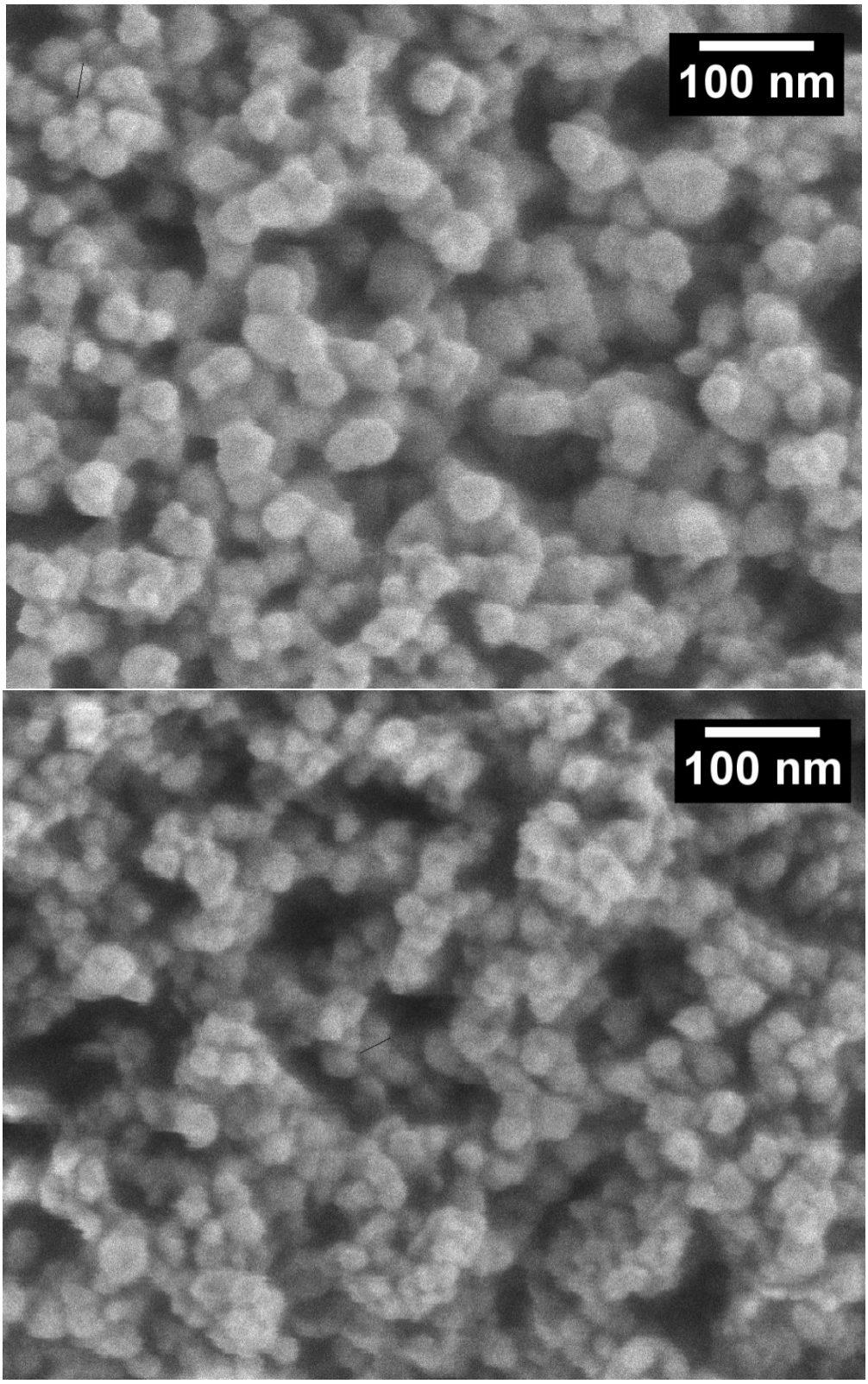

Figure S55: SEM images of **NMOF 4**. Settings: 150,000-fold magnification, 0.30 kV SEI, WD 3.4 mm.

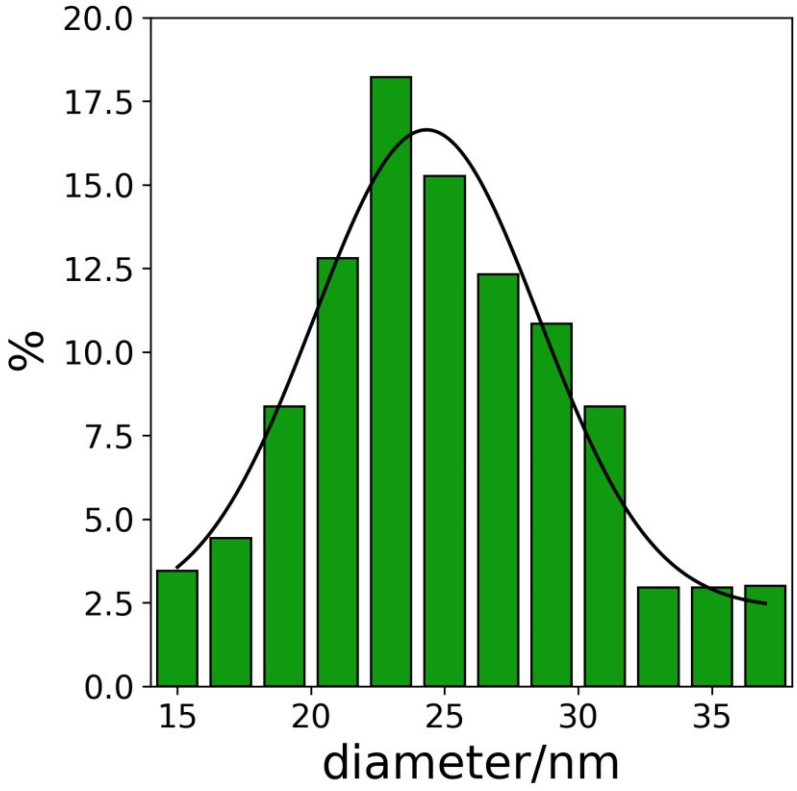

Figure S56: Histogram of **NMOF 4** size distribution. Distribution calculated from the SEM images in Figure S55. The average particle diameter is diameter 24.6 ± 3.8 nm.

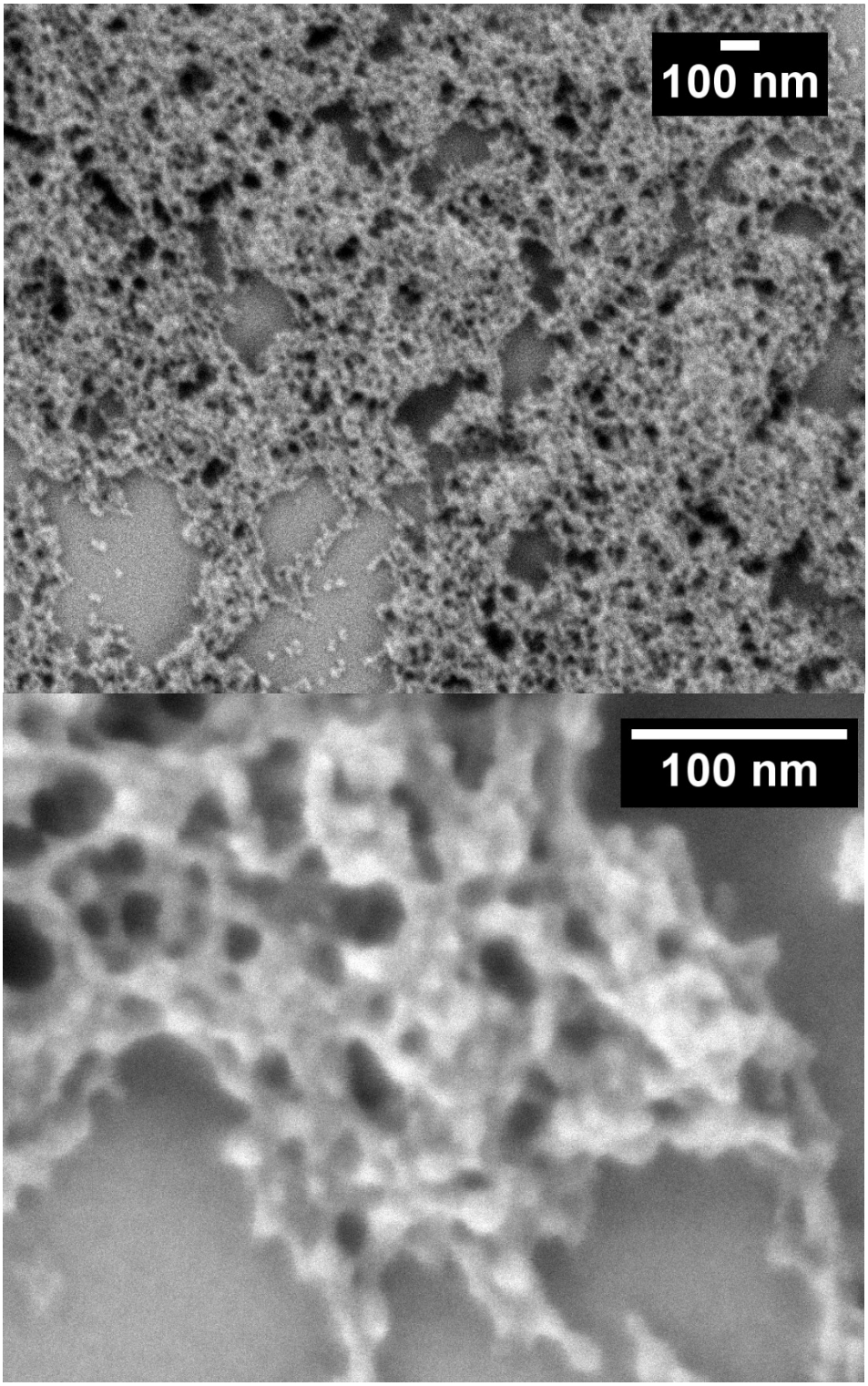

Figure S57: SEM images of **S1**. (a) 50,000-fold magnification, 0.50 kV SEI, WD 2.9 mm. (b) 300,000-fold magnification, 0.50 kV SEI, WD 2.9 mm.

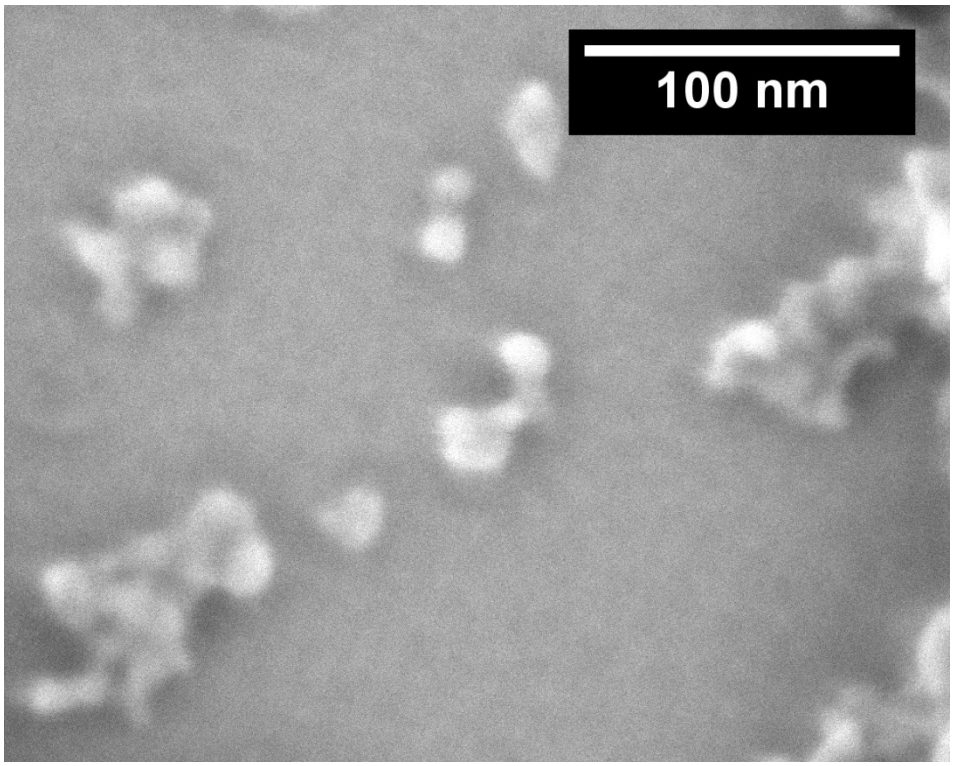

Figure S58: SEM image of **S1**. Settings: 370,000-fold magnification, 0.50 kV SEI, WD 2.9 mm.

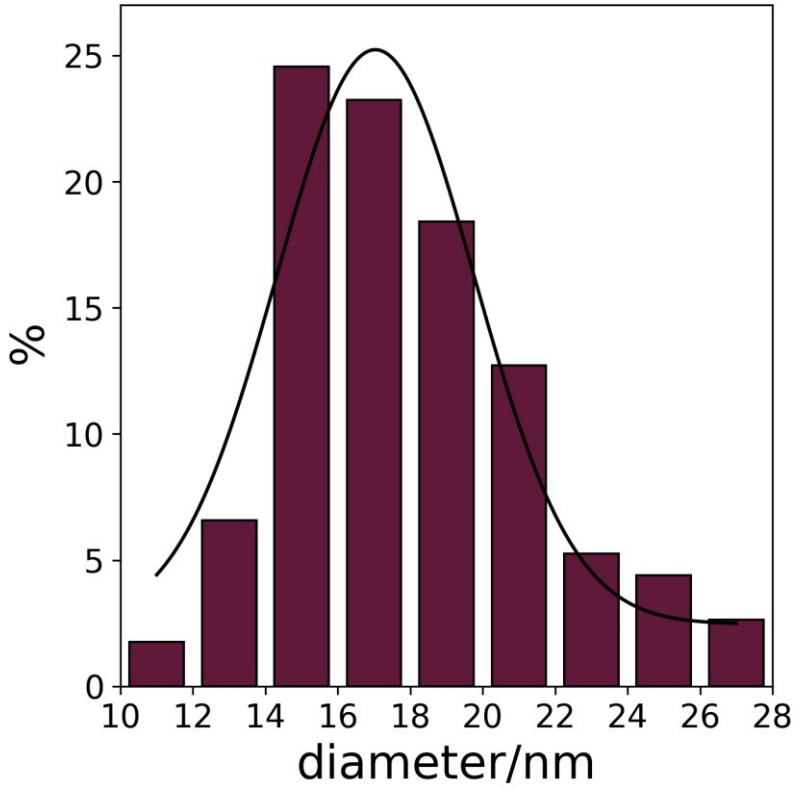

Figure S59: Histogram of **S1** size distribution. Distribution calculated from the SEM images in Figure S57-58. The average particle diameter is diameter 18.0 ± 2.8 nm.

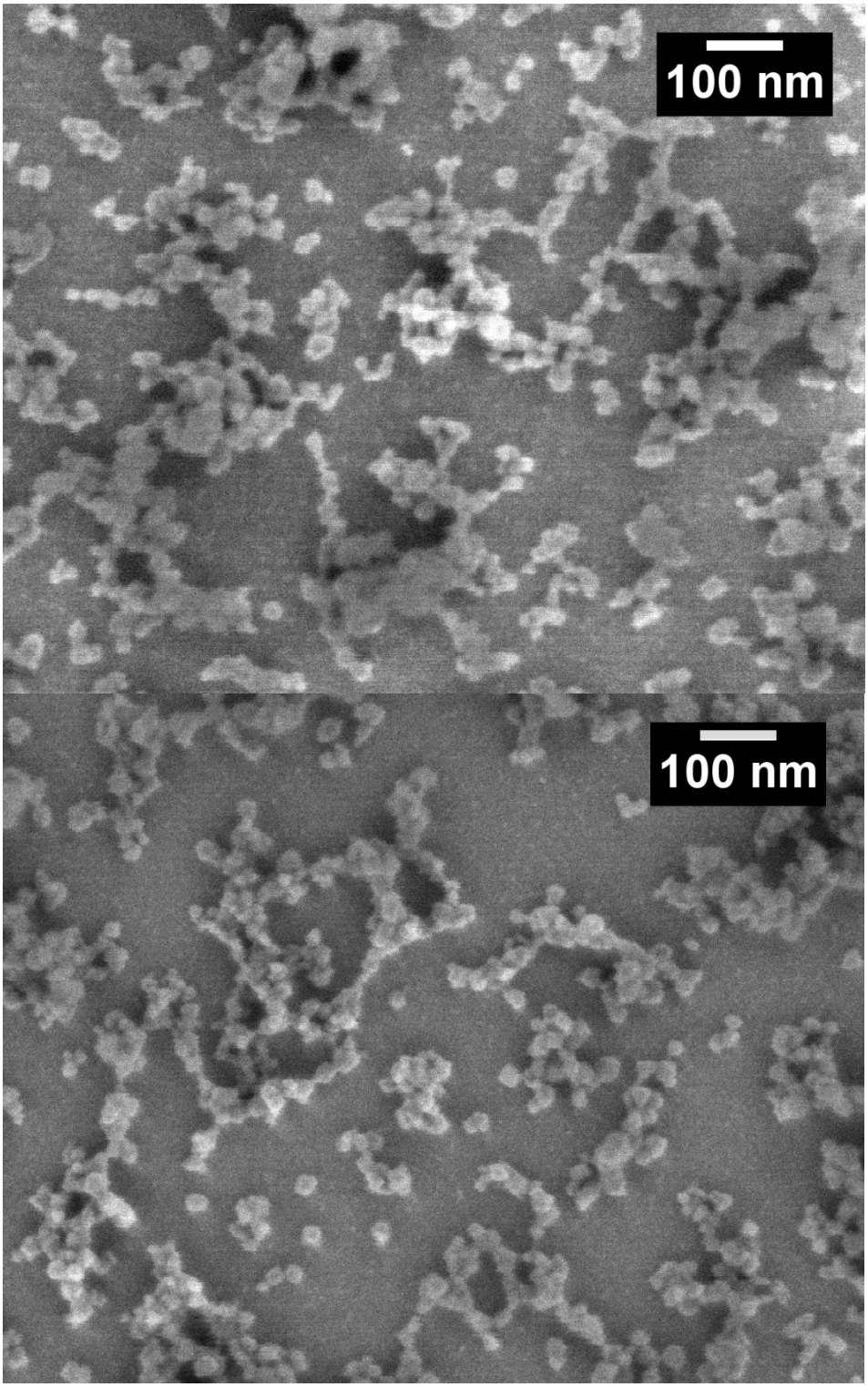

Figure S60: SEM images of **S2**. Settings: 100,000-fold magnification, 0.50 kV SEI, WD 4.8 mm.

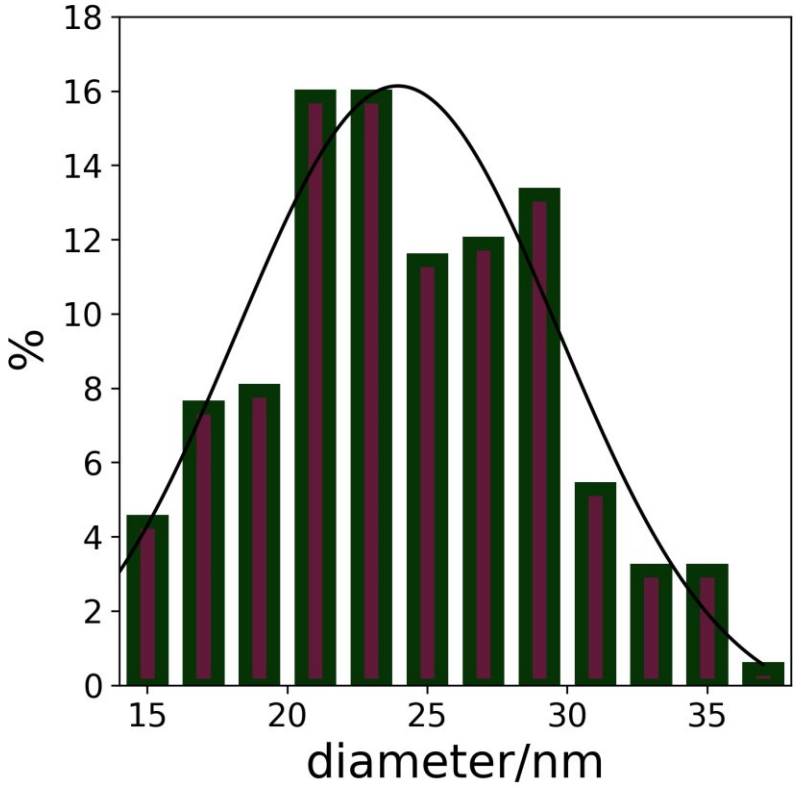

Figure S61: Histogram of **S2** size distribution. Distribution calculated from the SEM images in Figure S60. The average particle diameter is diameter 22.4 ± 3.3 nm.

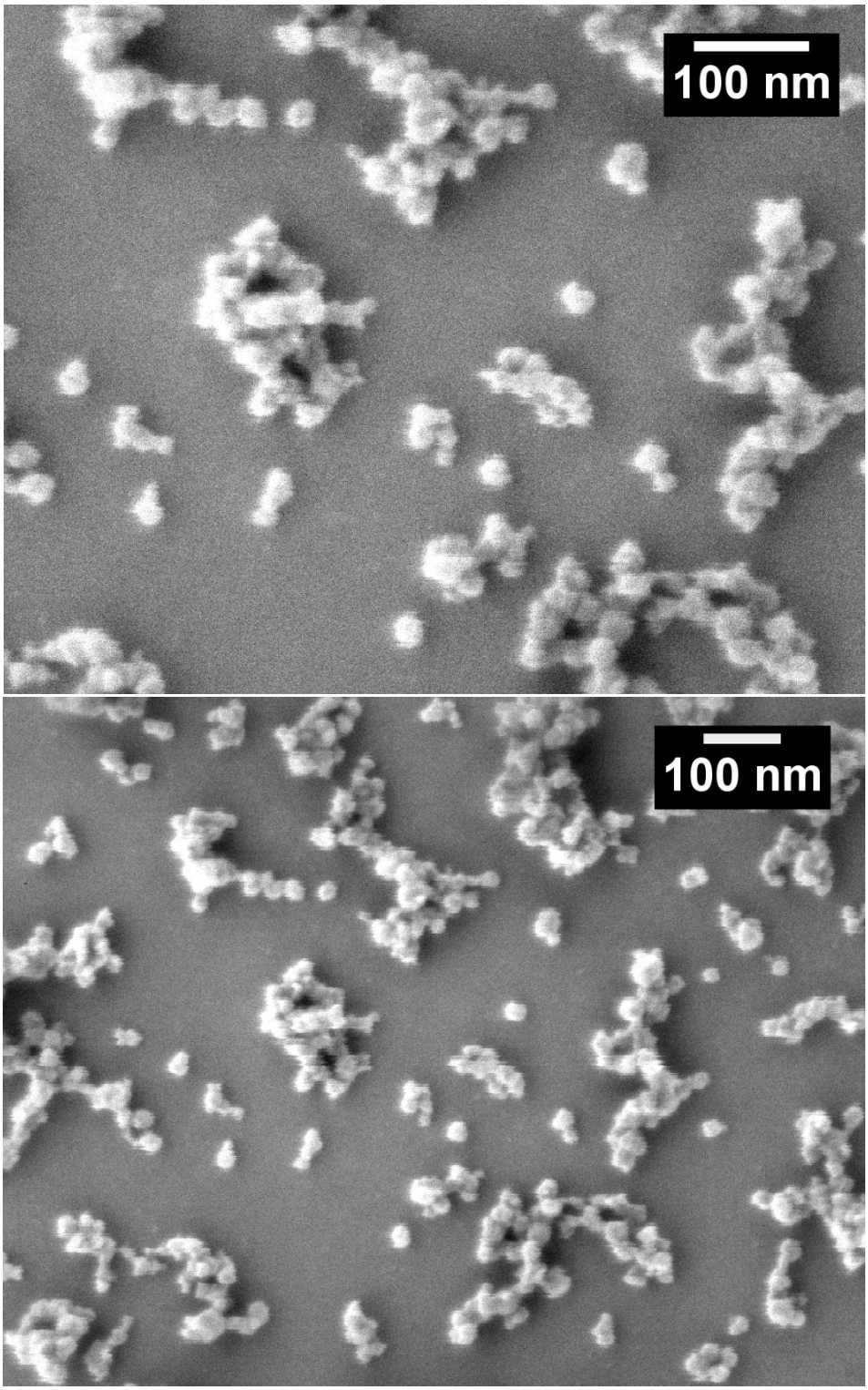

Figure S62: SEM images of **S3.** Settings: 100,000-fold magnification, 0.50 kV SEI, WD 4.9 mm.

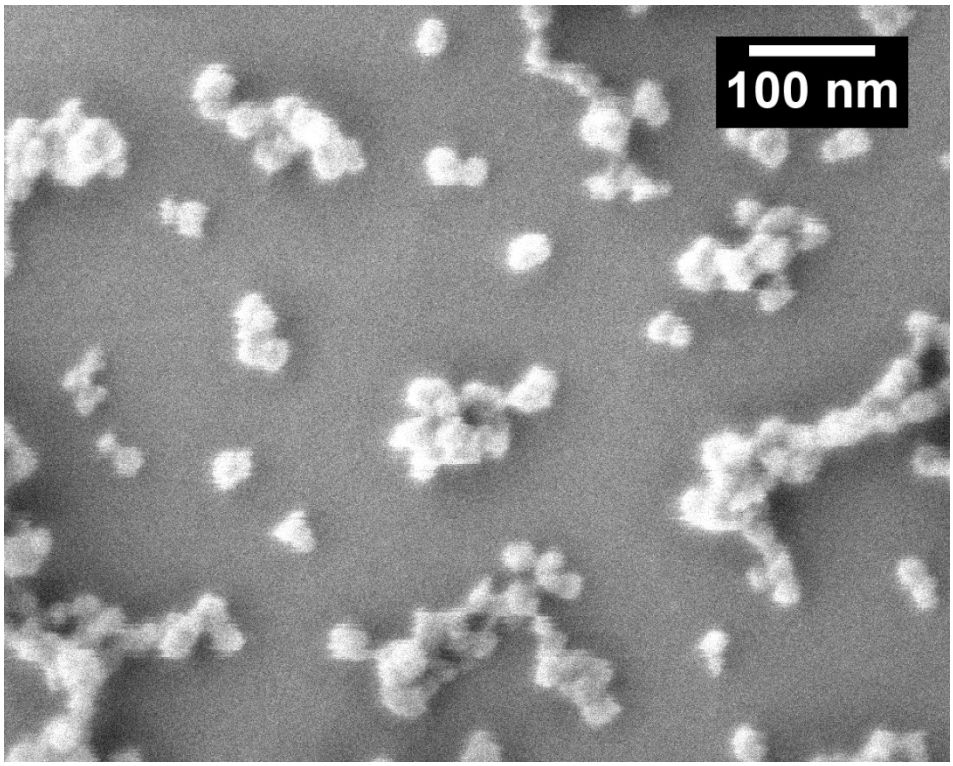

Figure S63: SEM image of **S3.** Settings: 150,000-fold magnification, 0.50 kV SEI, WD 4.9 mm.

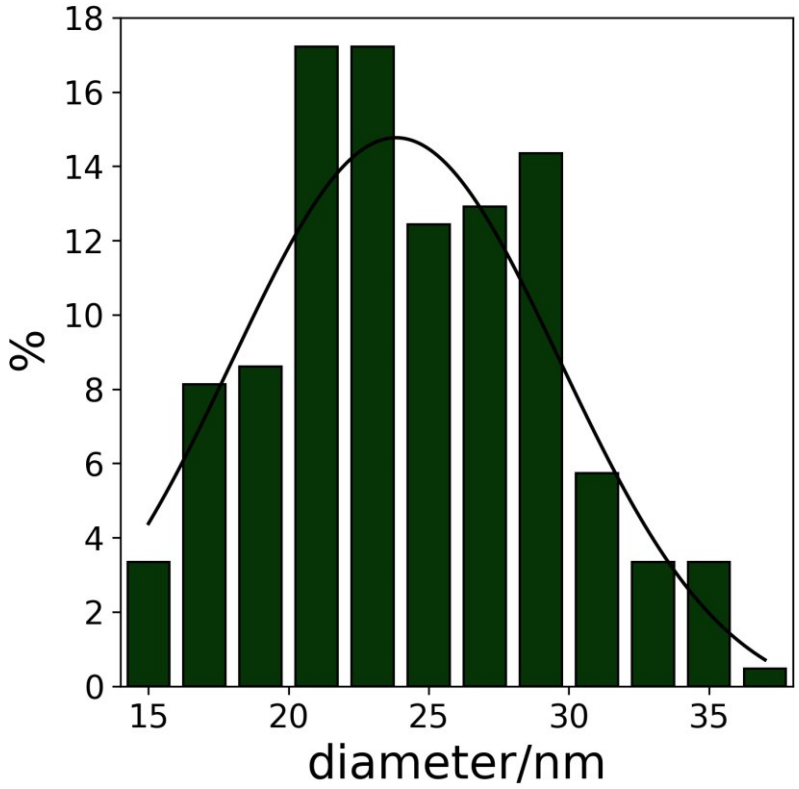

Figure S64: Histogram of **S3** size distribution. Distribution calculated from the SEM images in Figure S62-63. The average particle diameter is diameter 24.2 ± 3.3 nm.

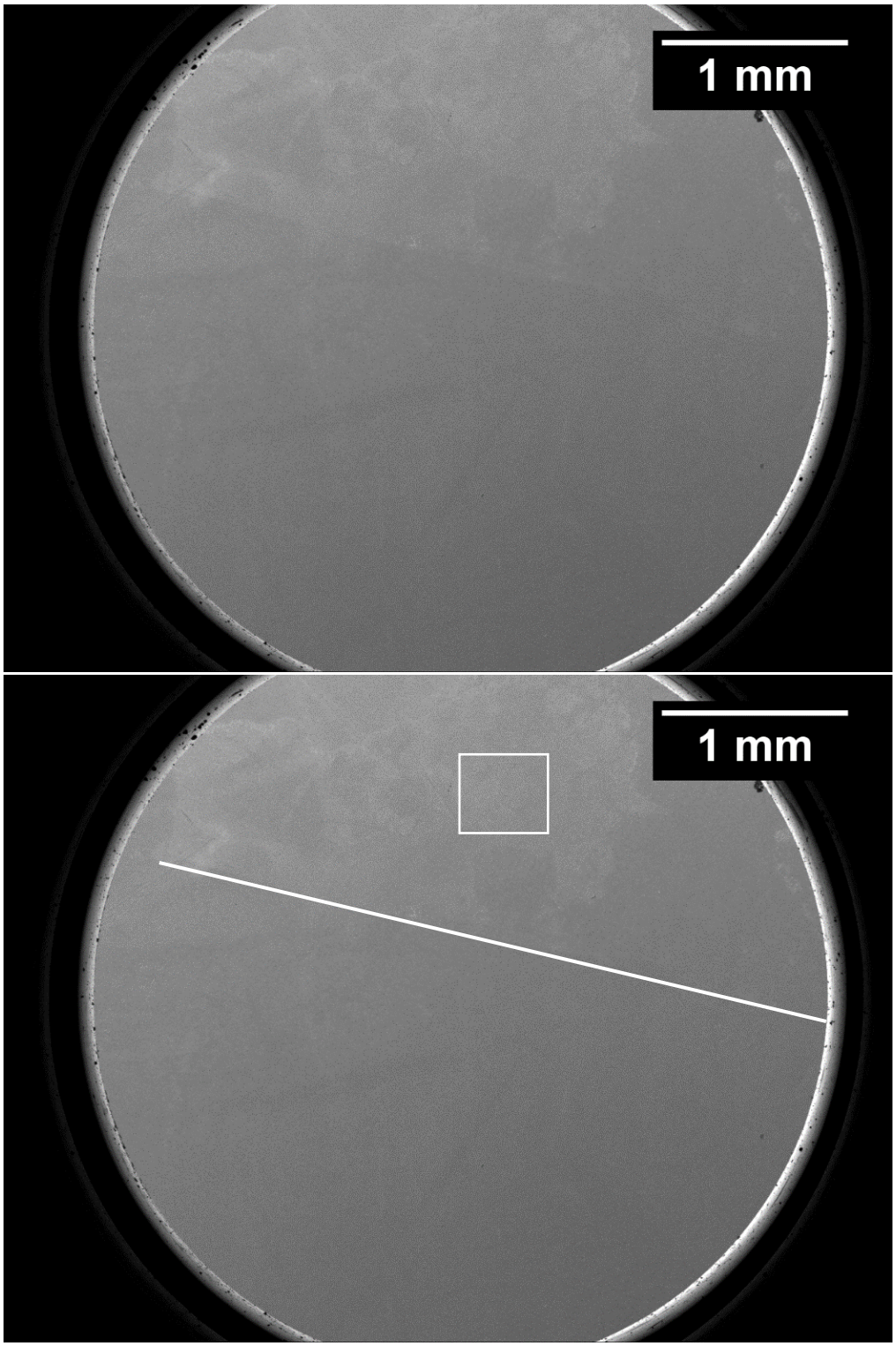

Figure S65: SEM image of an etched silicon surface imprinted with a large PDMS (0.5x0.5cm) stamp, which was immersed in a 1,8-nonadiyne solution and reacted with the silicon surface overnight and coupled with NMOF 2 in a second step. The edge of the stamp can be observed (compare with and without the blue line). shows the magnification of the circled area.

Settings: 25-fold magnification, 1.00 kV LEI, WD 8 mm.

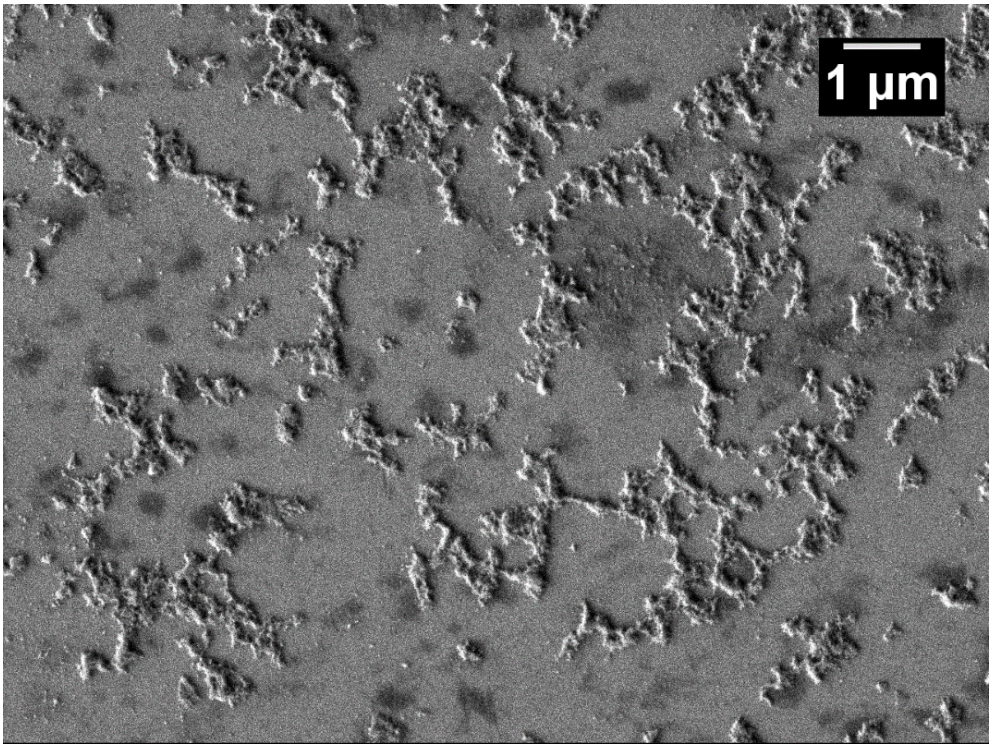

Figure S66: SEM image shows the magnification of the circled area in Figure S65. Settings: 10,000-fold magnification, 1.00 kV LEI, WD 7.8 mm.

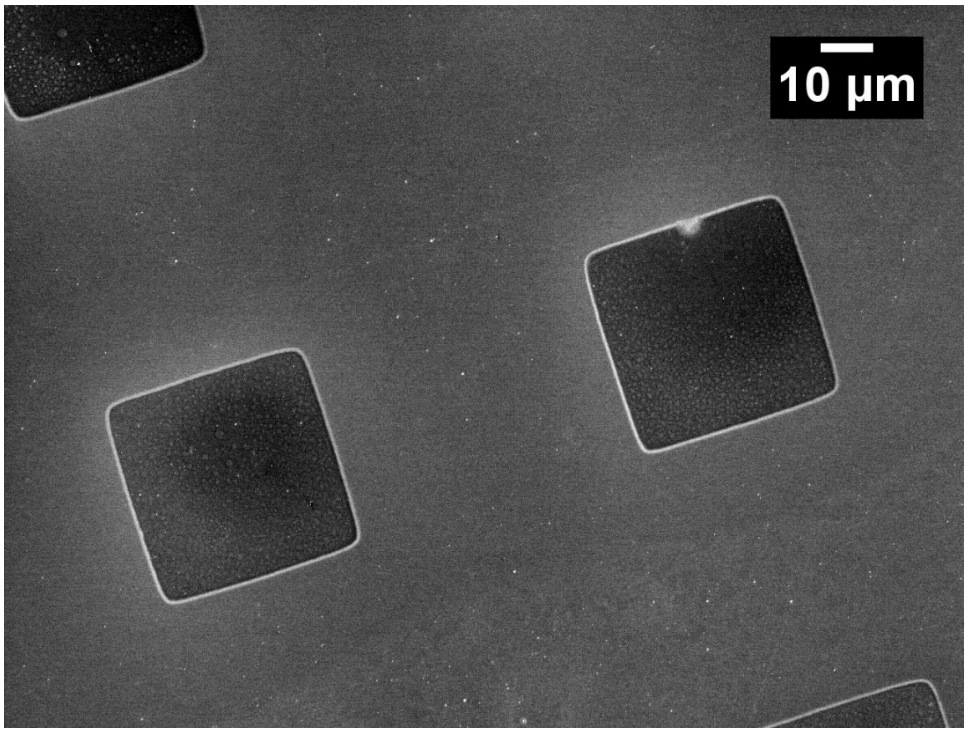

Figure S67: SEM patterning of 1,8-nonadiyne with the backfilling of 10-undecanoic acid in the second step and without further reactions. Settings: 650-fold magnification, 2.00 kV LEI, WD 24.3 mm.

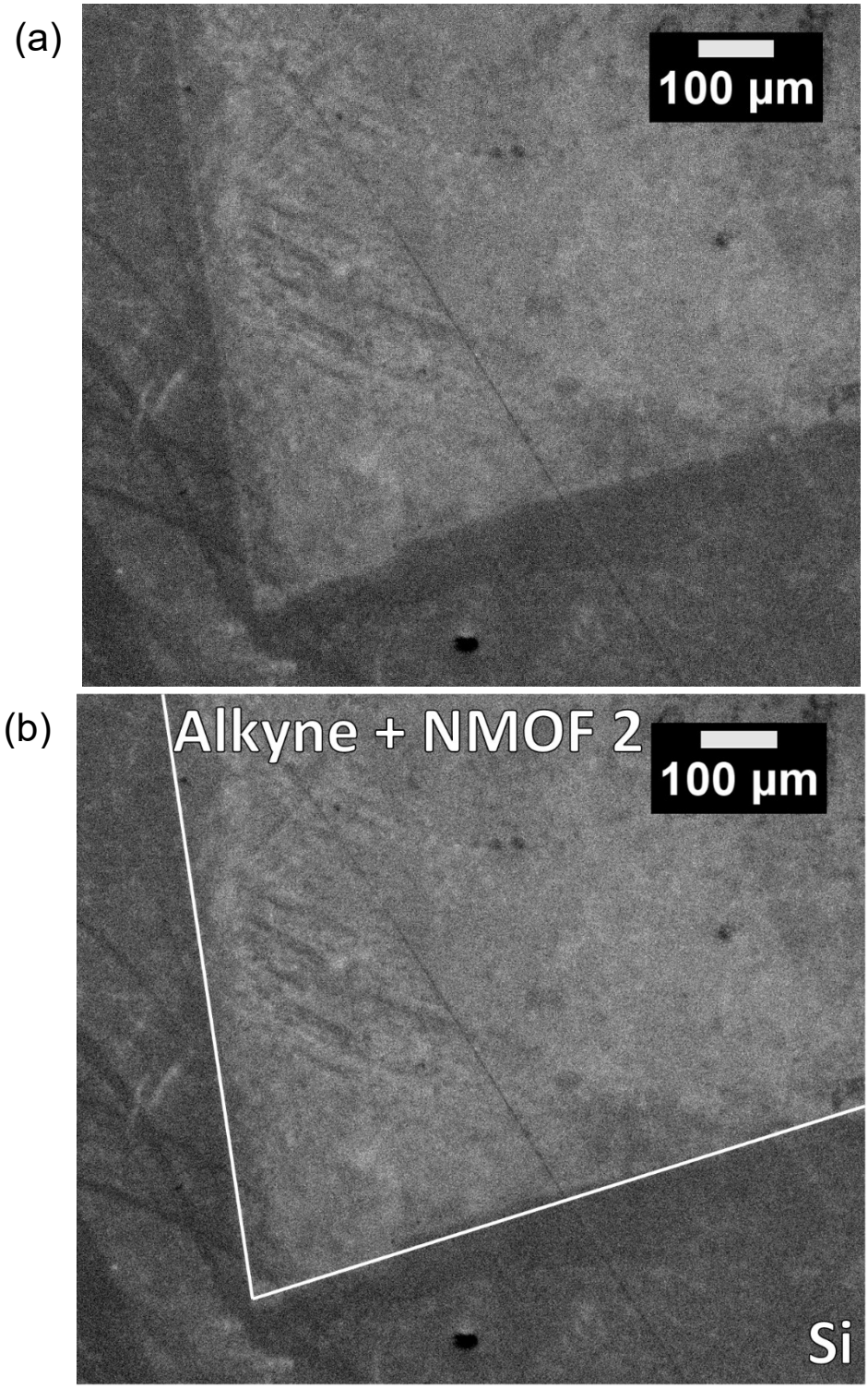

Figure S68: SEM image of an etched silicon surface imprinted with an PDMS (0.35x0.4cm) substrate, which was immersed in neat 1,8-nondiyne and reacted with the silicon surface overnight and coupled with NMOF 2 in a second step. The edge of the functionalized area can be spotted and is marked in (b) for clarification.

Settings: 130-fold magnification, 1.00 kV LEI, WD 15 mm.

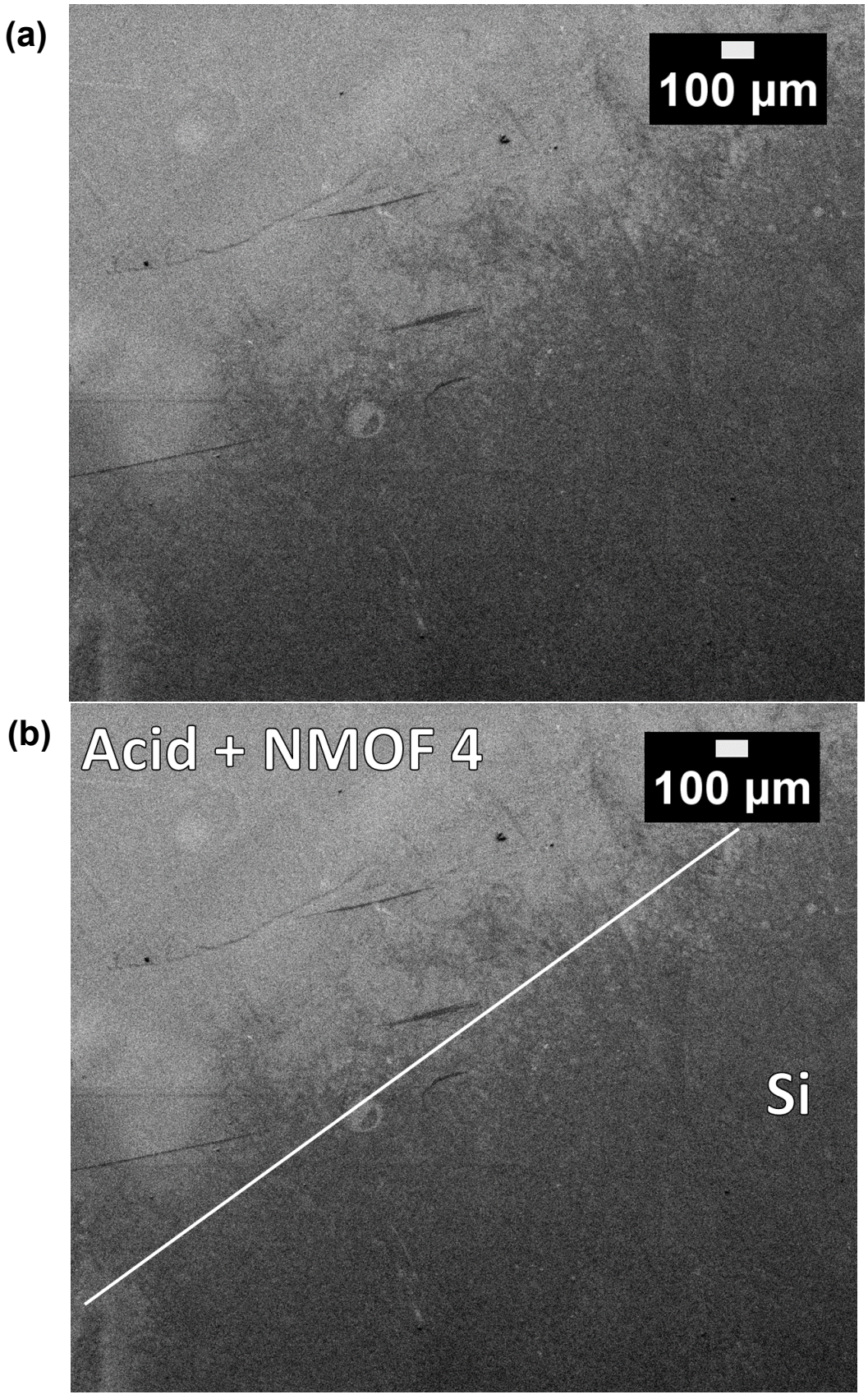

Figure S69: SEM image of an etched silicon surface imprinted with an PDMS (0.35x0.4cm) substrate, which was immersed in neat 10-undecenoic acid and reacted with the silicon surface overnight and coupled with NMOF 4 in the second step. The edge of the functionalized area can be spotted and is marked in (b) for clarification. Settings: Settings: 65-fold magnification, 2.00 kV LEI, WD 15 mm.

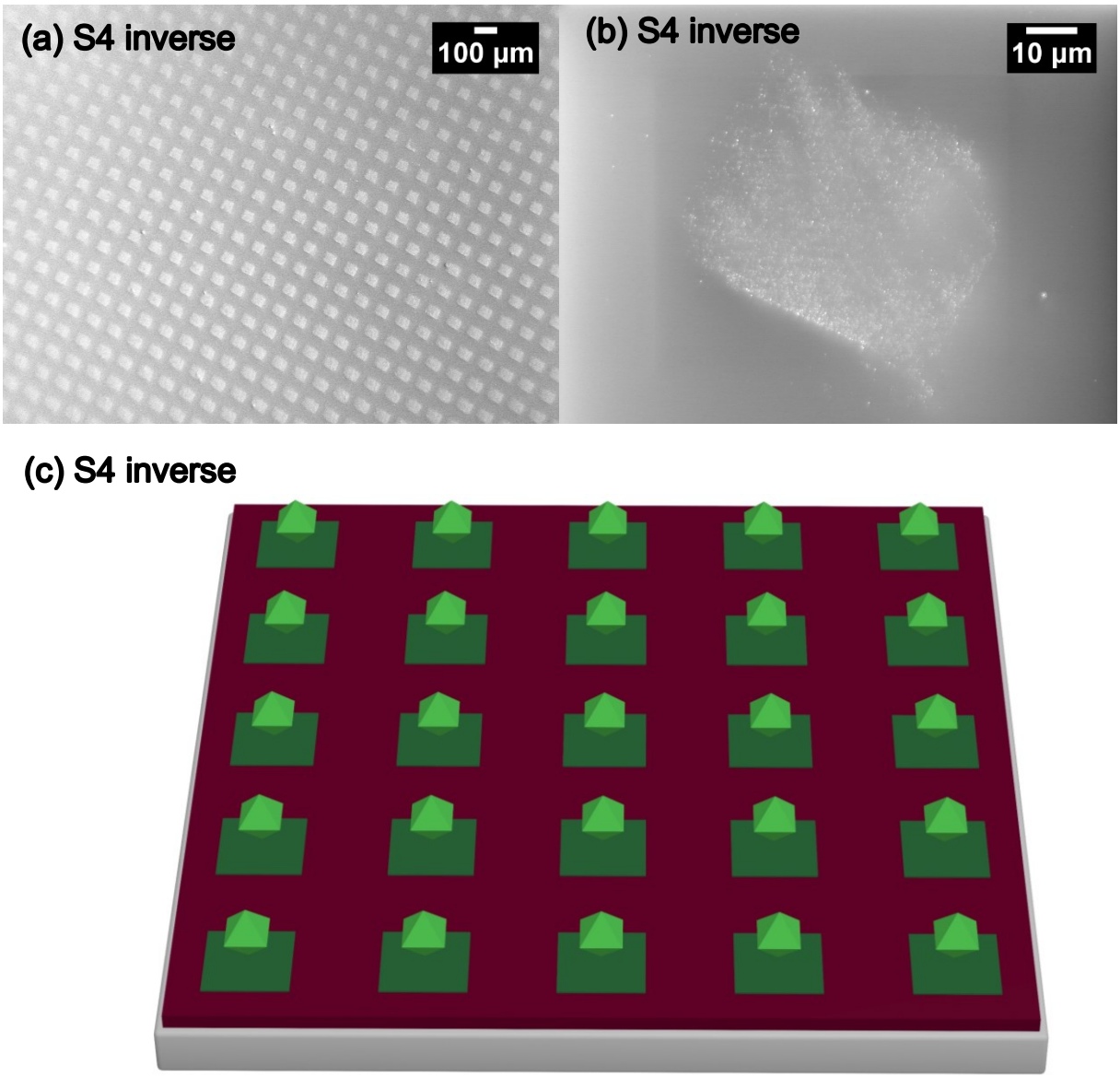

Figure S70: SEM images (a,b) after patterning of 10-undecanoic acid with the backfilling of 1,8-nonadiyne in the second step and further reaction with **NMOF 4** to form **NMOF 4** patterns on the silicon substrate. (c) shows the schematic representation of the S4 inverse surface.

Settings: (a) 50-fold magnification, 2.00 kV SEI, WD 23.3 mm., (b) 1,100-fold magnification, 2.00 kV SEI, WD 23.3 mm.

7.5.2.2. Study II: Substantial Turnover Frequency Enhancement of MOF Catalysts by Crystallite Downsizing Combined with Surface Anchoring

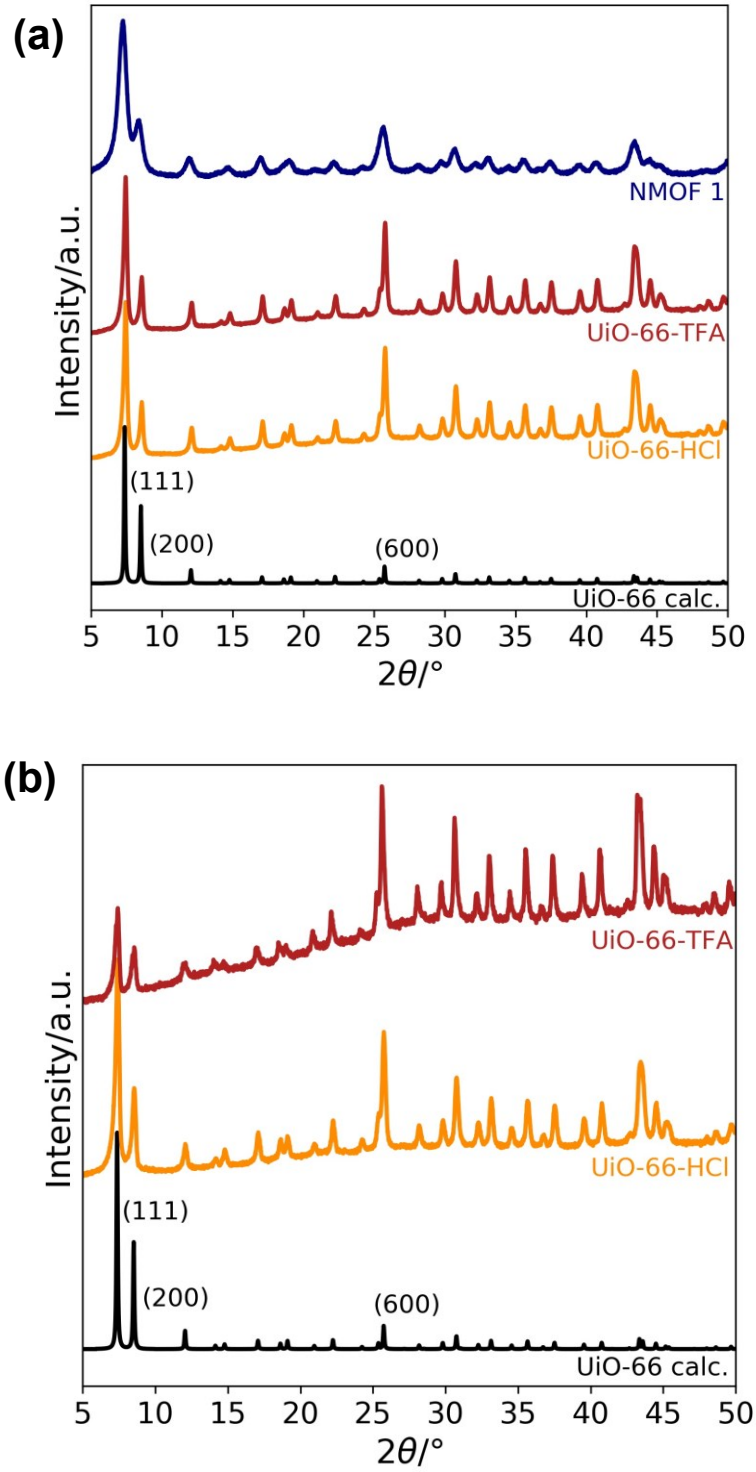

Figure S71: PXRD patterns of UiO-66-HCl (orange), UiO-66-TFA (red) and NMOF 1 (blue) recorded after the cyanosilylation of benzaldehyde (a) and the CO_2 insertion into propylene oxide (b).

7.5.3. Ferroelectric Metal-Free Perovskite [HMDABCO](NH$_4$)I$_3$ Thin Films • (Chapter 3)

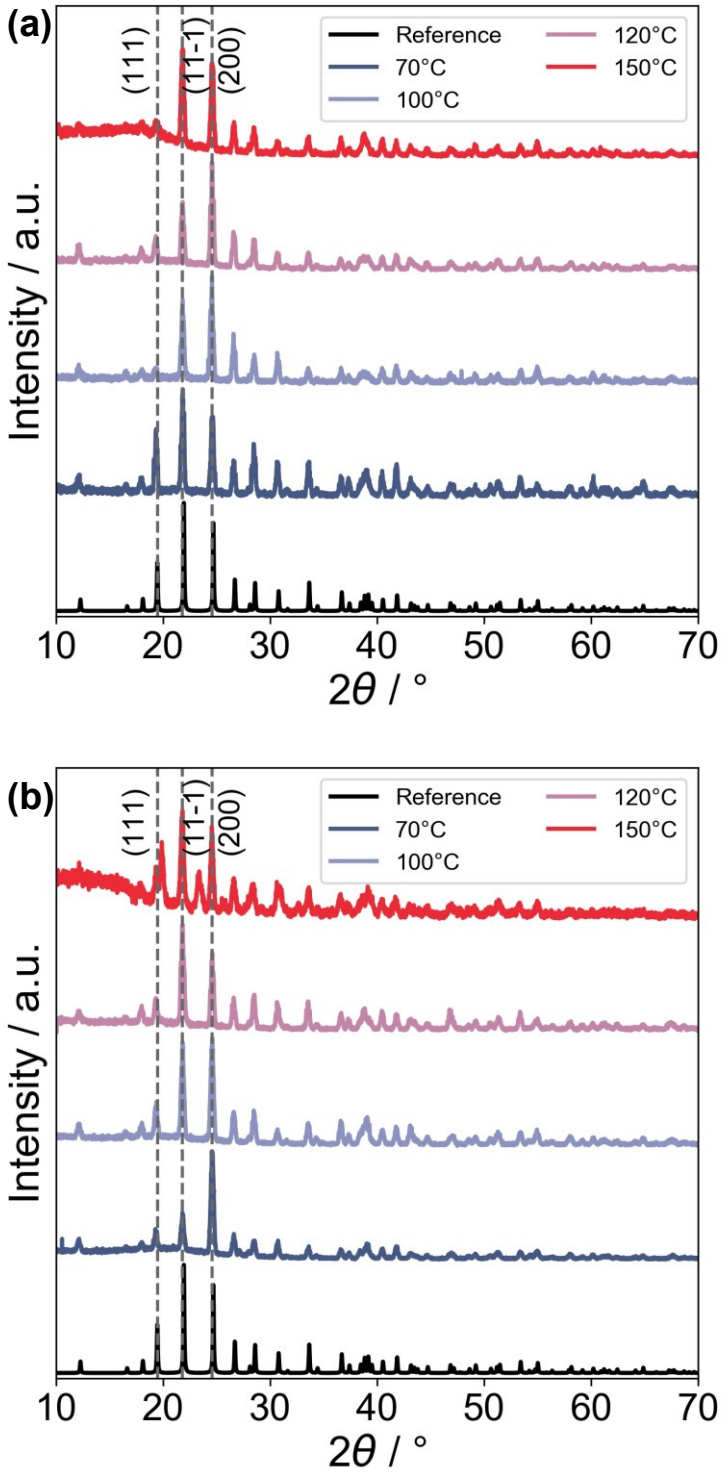

Figure S72: GIXRD of [HMDABCO](NH$_4$)I$_3$ thin films deposited on Au (a) and Si (b) substrates by spray coating and dried in an oven at temperatures between 70-150°C.

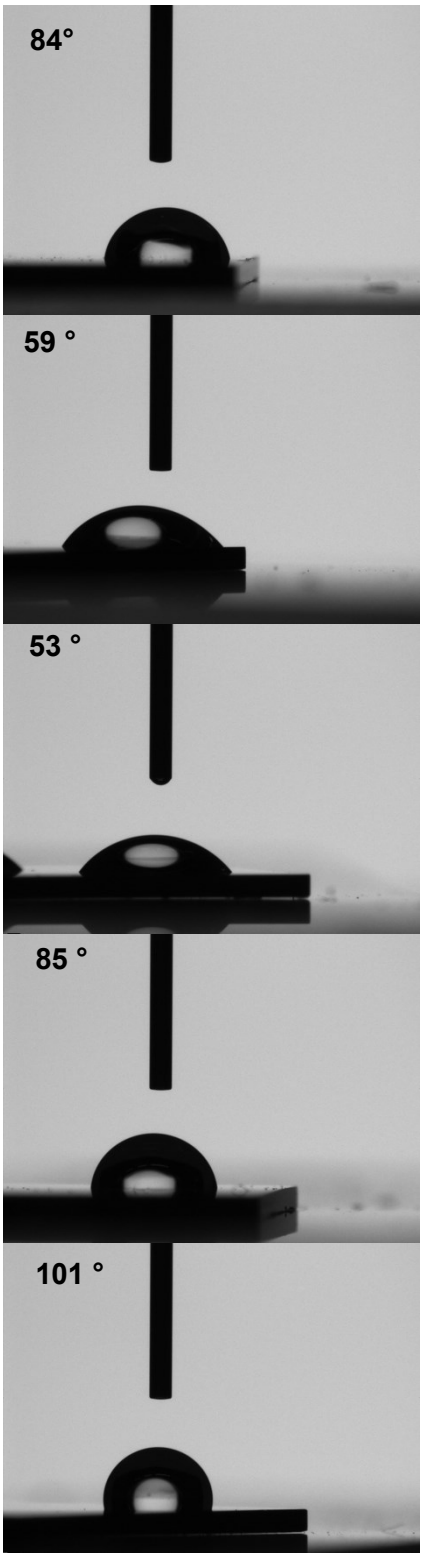

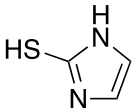

1-imidazole-2-thiol (Imidazole)

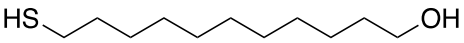

11-mercaptoundecan-1-ol (OH)

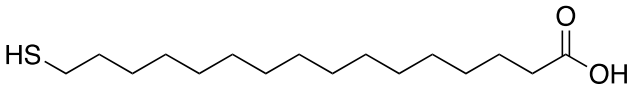

16-mercaptohexadecanoic acid (COOH)

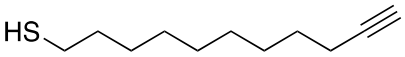

Undec-10-yne-1-thiol (alkyne)

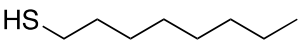

Octan-1-thiol (alkane)

Figure S73: Contact angle measurements (right) of Au substrates functionalized with various thiols (left) measured three times with 2.5 μL of water.

7.6. Tables

7.6.1. Zr-based MOF Thin Films • (Chapter 2)

Table S5: Summary of the EXAFS refinement for the single scattering paths of the obtained powders synthesized using various ratios of modulators McOH/H_2O with respect to the concentration of the Zr_6-SBUs (k from 3 to 12.5 $Å^{-1}$, and R from 1 to 4 Å). This Table was taken from Semrau, *et al.*[59] permission from ACS Crystal Growth & Design. Copyright (2019) American Chemical Society.

EXAFS refinement	**equiv. of McOH/H_2O**				
	0/0	**100/0**	**200/0**	**300/0**	**400/0**
Independent points	17.90	17.90	17.90	17.53	17.90
Number of variables	8	8	8	8	8
R-factor	0.0148	0.0146	0.0204	0.0135	0.0259
Reduced chi-square	463.38	121.96	244.35	121.52	197.57
ΔE_0 (eV)	-0.48436±1.1457	0.48427±1.12868	-1.56022±1.0908	-1.12739±0.99986	-2.60690±1.23421
S_0^2 (from std. ZrO_2)	0.98402	0.98402	0.98402	0.98402	0.98402
delta $R_{(\mu3\text{-}O)}$ (Å) (R_{eff} = 2.1073 Å)	-0.0039±0.0117	0.01252±0.01123	-0.01962±0.0099	-0.01367±0.00906	-0.02137±0.01113
$R_{(\mu3\text{-}O)}$ (Å; N=4)	2.10336	2.11982	2.08768	2.09363	2.08593
$\sigma^2_{(\mu3\text{-}O)}$ ($Å^2$)	0.00503±0.00093	0.00393±0.00091	0.00284±0.00071	0.00231±0.00064	0.00252±0.00082
delta $R_{(O\text{-}carboxylate)}$ (Å) (R_{eff} = 2.2334 Å)	0.01883±0.01287	0.03279±0.01342	0.01310±0.01023	0.01696±0.00928	0.00839±0.01107
$R_{(O\text{-}carboxylate)}$ (Å; N=4)	2.25224	2.26619	2.24651	2.25036	2.24179
$\sigma^2_{(O\text{-}carboxylate)}$ ($Å^2$)	0.00502±0.00112	0.00461±0.00120	0.00202±0.00074	0.00150±0.00067	0.00136±0.00081
delta $R_{(C\text{-}carboxylate)}$ (Å) (R_{eff} = 3.2553 Å)	0.00152	0.01126	0.00003	0.00289	0.00167
$R_{(C\text{-}carboxylate)}$ (Å; N=4)	3.25682	3.26656	3.25533	3.25819	3.25697
$\sigma^2_{(C\text{-}carboxylate)}$ ($Å^2$)	0.01395±0.01137	0.01690±0.02050	0.00884±0.00971	0.01017±0.01148	0.00728±0.00982
delta $R_{(Zr)}$ (Å) (R_{eff} = 3.5098 Å)	0.00164	0.01214	0.00003	0.00312	0.00180
$R_{(Zr)}$ (Å; N=4)	3.51144	3.56218	3.50983	3.51292	3.51160
$\sigma^2_{(Zr)}$ (Å)	0.01010±0.00102	0.00916±0.00095	0.00626±0.00065	0.00530±0.00052	0.00535±0.00065

EXAFS refinement	equiv. of McOH/H_2O				
	0/0	100/0	200/0	300/0	400/0
delta $R_{(\mu3\text{-}O\ \&\ \mu3\text{-}O)}$ (Å) (R_{eff} = 3.2686 Å)	0.00153	0.01131	0.00003	0.00291	0.00168
$R_{(\mu3\text{-}O\ \&\ \mu3\text{-}O)}$ (Å; N=8)	3.27013	3.27991	3.26863	3.27151	3.27028
$\sigma^2_{(\mu3\text{-}O\ \&\ \mu3\text{-}O)}$ ($Å^2$)	0.00754	0.00589	0.00426	0.00347	0.00378
delta $R_{(O\text{-}\ \&\ C\text{-}carboxy)}$ (Å) (R_{eff} = 3.3725 Å)	0.00158	0.01167	0.00003	0.00300	0.00173
$R_{(O\text{-}\ \&\ C\text{-}carboxy)}$ (Å; N=8)	3.37408	3.38417	3.37253	3.37550	3.37423
$\sigma^2_{(O\text{-}\ \&\ C\text{-}carboxy)}$ ($Å^2$)	0.01200	0.01306	0.00644	0.00658	0.00499
delta $R_{(\mu3\text{-}O\ \&\ O\text{-}carboxy)}$ (Å) (R_{eff} = 3.5499 Å)	0.00166	0.01228	0.00003	0.00315	0.00182
$R_{(\mu3\text{-}O\ \&\ O\text{-}carboxy)}$ (Å; N=16)	3.55156	3.56218	3.54993	3.55306	3.55172
$\sigma^2_{(\mu3\text{-}O\ \&\ O\text{-}carboxy)}$ ($Å^2$)	0.00754	0.00624	0.00385	0.00306	0.00320
delta $R_{(O\text{-}\ \&\ O\text{-}carboxy)}$ (Å) (R_{eff} = 3.6283 Å)	0.00169	0.01255	0.00003	0.00323	0.00186
$R_{(O\text{-}\ \&\ O\text{-}carboxy)}$ (Å; N=8)	3.62999	3.64085	3.62833	3.63152	3.63016
$\sigma^2_{(O\text{-}\ \&\ O\text{-}carboxy)}$ ($Å^2$)	0.00753	0.00692	0.00304	0.00225	0.00320
delta $R_{(\mu3\text{-}O\ \&\ Zr)}$ (Å) (R_{eff} = 3.8622 Å)	0.00180	0.01336	0.00003	0.00343	0.00198
$R_{(\mu3\text{-}O\ \&\ Zr)}$ (Å; N=16)	3.86400	3.87556	3.86223	3.86563	3.86418
$\sigma^2_{(\mu3\text{-}O\ \&\ Zr)}$ (Å)	0.01008	0.00851	0.00597	0.00496	0.00519

Table S6: Overview about the publications on UiO-66(-NH_2) thin films (CM: coordination modulated; LPE: liquid phase epitaxy; ALD/MLD: atomic layer deposition/molecular layer deposition; ED: electrophoretic deposition; C-QD: carbon quantum dots; Ln: Lanthanide; AAO: anodic alumina oxide; PP: polypropylene; PES: polyethersolufone; TPU/PSF: thermoplastic polyurethane/polysulfone; PMP: polymethylpentyne; CNF: carbon nanofiber; PEO: polyethylene oxide; PA: polyamide; sPSF: sulfonated polysulfone; GO: graphene oxide; PAN: polyacryl nitrile; MSH: mesoporous synthetic hectorite, PPSU: polyphenylsulfone; SAM: self-assembling monolayer ** not fully covered).

Doi/citation	MOF	Substrate	Method	Thickness	Roughness By RMS	Adsorption capacity	Application (?)
This publication	UiO-66-NH_2 (Zr)	Si/SiO_2	CM-LPE	80 nm(– 744 nm)**	24 nm	3.6-6.6 mmol g^{-1} MeOH	-
10.1021/acs.cgd.8b01719/[59]	UiO-66 (Zr)	Si/SiO_2	CM-LPE	2.6 µm	2.0 nm	3.5 mmol g^{-1} MeOH	-
10.1002/open.201900324/[196]	UiO-66-NH_2 (Zr)	SAM@Au @Si	LPE in DMF +(HCl)	110 nm	-	-	membrane permeance (H_2)
10.1021/acsami.9b16332/[391]	UiO-66-NH_2 (Zr)	Matrimid®	LPE approach in DMF	601 nm	± 41 nm	-	-
10.3390/nano8090676/[392]	UiO-66-NH_2 (Zr)	Si/SiO_2	LPE approach in DMF	153 nm	± 19.3	-	optical properties
10.1021/acsami.9b14099/[393]	UiO-66-NH_2 (Zr)	Fe_3O_4 NP	LPE approach in DMF	-	-	-	degradation of chemical warfare agents
10.1039/C9NR10049K/[394]	UiO-66-NH_2 (Zr)	PP	LPE approach in DMF	40-60 nm	-	-	oil-water separation
10.1021/jacs.7b08174/[20]	UiO-66/ UiO-66-NH_2 (Zr)	SAM@Au @Si	vapour assisted conversion	235 nm (UiO-66-NH_2)	7.4 nm	2.9 mmol g^{-1} EtOH	-
10.1016/j.apsusc.2020.146603/[395]	UiO-66 (Eu)	Si/SiO_2	ALD/MLD	22 µm	0.61 nm	-	luminescence
10.1038/ncomms13578/[396]	UiO-66	Si/SiO_2	ALD/MLD	230 nm/	45 nm	800 ng/cm^{-2}	-

				500 nm after PST		H_2O	
Doi	MOF	Substrate	Method	Thickness	Roughness By RMS	Adsorption capacity	Application (?)
10.1039/c7dt03518g/[397]	UiO-66-NH_2 (Zr)	Si/SiO_2	ALD/MLD	~ 400 nm (100 cycles) After PST	-	474 ng/cm^{-2} H_2O	-
10.1002/adma.201401940/[187]	UiO-66 (Zr)	FTO	ED	4-5 μm	-	-	.
10.1021/acs.inorgchem.7b02595/[398]	C-QD@UiO-66-COOH (Zr)	Zn	ED	100 μm	-	-	ratiometric temperature sensing
10.1021/acsami.7b17947/[399]	Ln@UiO-66 (Zr)	FTO	ED	50 μm	-	-	ratiometric temperature sensing
10.1039/C4CC08218D/[188]	UiO-66	FTO	solvothermal/ directed growth	2-5 μm	-	-	PS linker exchange
10.3390/nano8090676/[392]	UiO-66-NH_2 (Zr)	Si/SiO_2	solvothermal/ directed growth	~1.9 μm	± 56.3**	-	optical properties
10.1016/j.nimb.2015.10.059/[400]	UiO-66-NH_2 (Zr)	Si/SiO_2	solvothermal/ directed growth	-	-	-	ion beams for characterization of thin films
10.1002/asia.201501079/[401]	UiO-66 (Zr)	FTO	solvothermal/ directed growth	1000 nm	-	-	photocatalytic degradation of phenol
10.1364/OL.41.001696/[402]	UiO-66 (Zr)	Optical fiber	solvothermal/ directed growth	1.6-1.9 μm	-	-	contaminant detection
10.1088/1361-6463/aa9cd7/[403]	UiO-66 (Zr)	Optical fiber	solvothermal/ directed growth	1.6-1.9 μm	-	-	contaminant detection

Doi	MOF	Substrate	Method	Thickness	Roughness By RMS	Adsorption capacity	Application (?)
10.1002/anie.201606656/[157]	UiO-66 (Zr)	Nanofiber	solvothermal/ directed growth	-	-	-	degradation of chemical warfare agents
10.1016/j.jhazmat.2020.122431/[404]	Pt-NP@UiO-66-NH_2 (Zr)	Al_2O_3	solvothermal/ directed growth	700-1000 nm	-	-	photocatalytic degradation of phenol
10.1021/acs.iecr.9b07063/[171]	UiO-66-NH_2	MMM	solvothermal/ directed growth	90-500 nm	-	-	desalination/ nanofiltration
10.3390/nano8090676/[392]	UiO-66-NH_2 (Zr)	Si/SiO_2	spin coating	380 nm	± 12.1**	-	optical properties
10.3390/nano8090676/[392]	UiO-66-NH2 (Zr)	Si/SiO_2	drop coating	503 nm	± 42.2**	-	optical properties
10.3390/nano8090676/[392]	UiO-66-NH2 (Zr)	Si/SiO_2	self assembly of pre-synthesized NP	606 nm	± 19.2**	-	optical properties
10.1039/C7CE01801K/[405]	UiO-66 (Zr)	Si/SiO_2	solution shearing	-	-	-	-
10.1002/kin.21328/[406]	UiO-66-NH_2 (Zr)		dip-coating	4.2 μm	-	-	photocatalytic degradation of p-xylene
10.1021/acsami.8b04889/[407]	UiO-66 (Eu&Zr)	glass	drop coating				ratiometric temperature sensing
10.1016/j.cej.2019.123400/[195]	UiO-66 (Zr)	GO@PAN	vacuum filtration				dyes and antibiotics separation

							from wastewater
Doi	MOF	Substrate	Method	Thickness	Roughness By RMS	Adsorption capacity	Application (?)
10.1002/cssc.201900706/[193]	UiO-66-NH_2(Zr)	AAO	In-situ growth, a membrane between to solutions				Ion separation/ desalination
10.1002/aoc.5339/[408]	UiO-66-F	PES/PA	MMM (interfacial polymerization)				desalination
10.1016/j.memsci.2020.118039/[409]	UiO-66-NH_2 (Zr)	PES/PA	MMM (interfacial polymerization)				desalination
10.1016/j.cej.2020.125604/[410]	UiO-66-NH_2 (Zr)	TPU/PSF	MMM (electrospinning/interfacial polymerization)				desalination
10.1016/j.jiec.2020.01.030/[411]	CNF/ UiO-66-NH_2 (Zr)	PEO/PA@ PMP	MMM (dip-coating)				CO_2/CH_4 separation performance
10.1039/C8TA04806A/[412]	UiO-66-NH_2 (Zr)	PMP	MMM (dip-coating)				CO_2/CH_4 separation performance
10.1016/j.memsci.2020.117874/[191]	UiO-66-NH_2 (Zr)	PA	MMM (dip-coating)				desalination
10.1021/acsami.9b17212/[413]	UiO-66-NH_2 (Zr)/	PSU	MMM (interfacial polymerization)				desalination

	UiO-66 (Zr)						
Doi	MOF	Substrate	Method	Thickness	Roughness By RMS	Adsorption capacity	Application (?)
10.1021/acsami.6b14223/[414]	UiO-66 (Zr)	PSU	MMM (interfacial polymerization)				desalination
10.1021/acsami.9b01923/[415]	UiO-66-NH_2 (Zr)	PSF	MMM (interfacial polymerization)				desalination
10.1021/acsnano.8b03994/[169]	UiO-66 (Zr)	sPSF/PSF	MMM (drop coating)				desalination
10.1016/j.memsci.2019.02.072/[416]	UiO-66 (Zr)	PSF	MMM (interfacial polymerization)				boron removal/ desalination
10.1039/c9ew00201d/[417]	UiO-66 (Zr)	PES	MMM (interfacial polymerization)				desalination
10.1016/j.memsci.2020.118212/[418]	UiO-66-NH_2 (Zr)	PSF	MMM (interfacial polymerization)				desalination/ dyes and antibiotics separation from wastewater
10.1016/j.cej.2018.03.154/[194]	UiO-66-NH_2 (Zr)	GO/PPSU	MMM (interfacial polymerization)				kinetic hydrate inhibitor (KHI) separation
10.1002/aic.15508/[419]	UiO-66-NH_2 (Zr)	Matrimid®	MMM (interfacial polymerization)				organic solvent nanofiltration

Doi	MOF	Substrate	Method	Thickness	Roughness By RMS	Adsorption capacity	Application (?)
10.1016/j.memsci.2017.06.061/[192]	UiO-66 (Zr)	PES	MMM (interfacial polymerization)				water decontamination (Se, As) / desalination
10.3390/membranes7020031/[420]	UiO-66 (Zr)	PSF	MMM (interfacial polymerization)				desalination
10.1016/j.jiec.2019.04.057/[421]	UiO-66 (Zr)		MMM (interfacial polymerization)				organic solvent nanofiltration
10.1021/acs.iecr.8b04968/[422]	UiO-66 (Zr)	PSF	MMM (interfacial polymerization)				desalination
10.1039/c9ra04714j/[423]	UiO-66-NH_2 (Zr)	PDA@PSF	MMM (interfacial polymerization)				desalination

Table S7: Overview about chemical stability of UiO-66(-NH_2) thin films towards water or aqueous solutions (AAO: anodic alumina oxide; PES: polyethersolufone; PA: polyamide; GO: graphene oxide; PAN: polyacrylonitrile; PPSU: polyphenylsulfone; SAM: self-assembling monolayer).

doi	MOF	Substrate	Application (?)	Chemical Stability
This work	UiO-66-NH_2 (Zr)	Si/SiO_2	-	Immersion of the thin film into deionized water for 14 days. A slight decrease in intensity in PXRD measurements was observed which can be attributed to a very slow amorphization process
10.1016/j.memsci.2020.117874/[191]	UiO-66-NH_2 (Zr)	PA	desalination	Long term performance experiments with the fabricated membrane for 72 h, at 1-16 bar in an 0.2 mg/mL Na_2SO_4 solution, a slight decrease in Na_2SO_4 rejection performance is observed
10.1016/j.memsci.2017.06.061/[192]	UiO-66 (Zr)	PES	water decontamination (Se, As) / desalination	Long term performance test with the membrane for 160 h, at 10 bar in 1000 ppm SeO_3^{2-} solution -> relative stable rejection performance slight drop in pure water permeability
10.1002/open.201900324/[196]	UiO-66-NH_2 (Zr)	SAM@Au@Si	membrane permeance (H_2)	Immersion of the thin films for 1 h in boiling water -> thin films are still crystalline
10.1002/cssc.201900706/[193]	UiO-66-NH_2(Zr)	AAO	Ion separation/ desalination	Immersion of UiO-66-NH_2 powders into 0.1 M salt solutions of LiCl, $MgCl_2$, NaCl, and mixtures thereof for 120 h, a slight decrease in intensity in PXRD measurements was observed which can be attributed to a slow amorphization
10.1016/j.cej.2018.03.154/[194]	UiO-66-NH_2 (Zr)	GO/PPSU	kinetic hydrate inhibitor (KHI) separation	Long term performance test of the membranes for 70 h at 8 bar with a 0.1 w% aqueous kinetic hydrate inhibitor solution at room temperature -> decrease in flux and rejection at first but then stable for the period of the test

10.1016/j.cej.2019.123400/ [195]	UiO-66 (Zr)	GO@PAN	dyes and antibiotics separation from wastewater	Long term performance test of the membranes for 1000 min (16.7 h) at 3 bar with water or a 0.01 g/L aqueous methyl orange or tetracycline solution at room temperature -> slight decrease in flux (~20%) and rejection (5 %) over time

7.6.2. Selective Covalent Immobilization of Preformed Nano-MOFs in Microfluidic Devices Targeting Vectorial Catalysis • (Chapter 3)

Table S8: Literature overview: Artificial vectorial catalysis catalyzed by different inorganic/metal-organic catalysts.

Nanoreactors			
D. M. Vriezema, P. M. L. Garcia, N. Sancho Oltra, N. S. Hatzakis, S. M. Kuiper, R. J. M. Nolte, A. E. Rowan, J. C. M. van Hest, *Angew. Chem. Int. Ed.* **2007**, *46*, 7378-7382. DOI: 10.1002/anie.200701125	1) CALB 2) GOX 3) HRP	1) Hydrolysis 2) Oxidation 3) Oxidation	Polymer micelle formed by PS-PIAT; CALB in the bulk solution, GOX in the water pool inside the polymersome, HRP membrane immobilized
J. Wang, M. Zhu, X. Shen, S. Li, *Chem. Eur. J.* **2015**, *21*, 7532-7539. DOI:10.1002/chem.201406285	1) 2-acrylamido-2-methylpropanesulfonic acid 2) Pt nanoparticles	1) hydrolysis 2) reduction	Nanoreactor formed by molecular imprinted polymers; diffusion pathway of substrates first leads to acid catalytic sites and then to Pt nanoparticles

Microreactors with Immobilized Catalyst

C. Wiles, P. Watts, S. J. Haswell, *Lab Chip* **2007**, *7*, 322-330. DOI: 10.1039/b615069a	1) Amberlyst 15 2) Silica-supported piperazine	1) acid-catalyzed deprotection of a dimethyl acetal 2) base-catalyzed condensation of the aldehyde with an activated methylene	Electroosmotic flow-based continuous-flow reactor consisting of microporous silica frit and platinum electrodes, both catalysts immobilized in the same reactor
A. Abdul Halim, N. Szita, F. Baganz, *J. Biotechnol.* **2013**, *168*, 567-575. DOI: 10.1016/j.jbiotec.2013.09.001	1) Transketolase 2) Transaminase	1) asymmetric C-C-bond formation 2) amine group addition	His_6-tagged enzymes immobilized on Ni-NTA agarose beads in packed bed microreactors (two-tubes-system)
T. Vong, S. Schoffelen, S. F. van Dongen, T. A. van Beek, H. Zuilhof, J. C. M. van Hest *Chem. Sci.* **2011**, *7*, 1278. DOI: 10.1039/c1sc00146a	1) CALB 2) GOX 3) HRP	1) Hydrolysis 2) Oxidation 3) Oxidation	CALB and HRP are immobilized in fused silica microchannel, GOX dissolved in the glucose acetate solution which is injected to the reactor

Table S9: Literature overview: Tandem reactions catalyzed by different inorganic/metal-organic catalysts.

Nanoparticles			
3	C. Xie, C. Chen, Y. Yu, J. Su, Y. Li, G. A. Somorjai, P. Yang, *Nano Lett.* **2017**, *17*, 3798-3802. DOI: 10.1021/acs.nanolett.7b01139	Nanoparticles with 1) CeO_2−Pt core and mesoporous silica shell decorated with 2) Co nanoparticles	1) reverse water gas shift reaction 2) Fischer-Tropsch reaction
4	H. J. Cho, D. Kim, J. Li, D. Su, B. Xu, *J. Am. Chem. Soc.* **2018**, *140*, 13514-13520. DOI: 10.1021/jacs.8b09568	1) HZSM-5 zeolite matrix encapsulating 2) Pt nanoparticles	1) aldol condensation 2) hydrogenation
Zeolites			
5	L. Xu, C.-g. Li, K. Zhang, P. Wu, *ACS Catalysis* **2014**, *4*, 2959-2968. DOI: 10.1021/cs500653p	Multi-layered MFI zeolites with 1) Brønsted acid sites (zeolite) 2) Lewis and Brønsted base sites (SiO^- and OH^-)	1) deacetalization 2) Knoevenagel condensation
Metal-Organic Frameworks			
6	J. Park, J.-R. Li, Y.-P. Chen, J. Yu, A. A. Yakovenko, Z. U. Wang, L.-B. Sun, P. B.	PCN-124 1) Cu^{2+} sites	1) deacetalization 2) Knoevenagel condensation

	Balbuena, H.-C. Zhou, *Chem. Commun.* **2012**, *48*, 9995-9997. DOI: 10.1039/c2cc34622b	2) pyridine and amide groups	
7	A. Arnanz, M. Pintado-Sierra, A. Corma, M. Iglesias, F. Sánchez, *Adv. Synth. Catal.* **2012**, *354*, 1347-1355. DOI: 10.1002/adsc.201100503	1) Pd, Cu^{2+} 2) Cu^{2+}	1) Sonogashira coupling reaction 2) click reaction
8	B. Li, Y. Zhang, D. Ma, L. Li, G. Li, G. Li, Z. Shi, S. Feng, *Chem. Commun.* **2012**, *48*, 6151-6153. DOI: 10.1039/c2cc32384b	1) MIL-101-SO_3H 2) MIL-101-NH_2	1) deacetalization 2) Henry reaction
9	R. Srirambalaji, S. Hong, R. Natarajan, M. Yoon, R. Hota, Y. Kim, Y. Ho Ko, K. Kim, *Chem. Commun.* **2012**, *48*, 11650-11652. DOI: 10.1039/c2cc36678a	MIL-101(Al)-NH_2 1) Al^{3+} sites 2) -NH_2 groups	1) Meinwald rearrangement 2) Knoevenagel condensation
10	T. Toyao, M. Fujiwaki, Y. Horiuchi, M. Matsuoka, *RSC Advances* **2013**, *3*, 21582-21587. DOI: 10.1039/c3ra44701d	MIL-101(Al)-NH_2 1) -COOH groups 2) -NH_2 groups	1) deacetalization 2) Knoevenagel condensation

11	A. M. Rasero-Almansa, A. Corma, M. Iglesias, F. Sánchez, *ChemCatChem* **2013**, *5*, 3092-3100. DOI: 10.1002/cctc.201300371	1) Zr^{4+} sites or amine/amide groups 2) Rh or Ir (guest)	1) condensation 2) hydrogenation
12	Y.-R. Lee, Y.-M. Chung, W.-S. Ahn, *RSC Advances* **2014**, *4*, 23064-23067. DOI: 10.1039/c4ra02683g	1) MIL-101-SO_3H 2) MIL-101-NH_2	1) deacetalization 2) Henry condensation
13	M. H. Beyzavi, N. A. Vermeulen, A. J. Howarth, S. Tussupbayev, A. B. League, N. M. Schweitzer, J. R. Gallagher, A. E. Platero-Prats, N. Hafezi, A. A. Sarjeant, J. T. Miller, K. W. Chapman, J. F. Stoddart, C. J. Cramer, J. T. Hupp, O. K. Farha, *J. Am. Chem. Soc.* **2015**, *137*, 13624-13631. DOI: 10.1021/jacs.5b08440	1) Fe-Porphyrin 2) Hf	1) oxidation 2) epoxide-opening
14	P. V. Dau, S. M. Cohen, *Inorg. Chem.* **2015**, *54*, 3134-3138. DOI: 10.1021/ic502316v	1) IRMOF-9-dcppy-NH_2 2) Ir(I)	1) Knoevenagel condensation 2) Allylic N-alkylation

15	H. He, F. Sun, B. Aguila, J. A. Perman, S. Ma, G. Zhu, *J. Mater. Chem. A* **2016**, *4*, 15240-15246. DOI: 10.1039/c6ta05098k	Bifunctional MOF (JUC-199) with 1) open metal sites (Zn^{2+}) and 2) Lewis basic sites (amino groups)	1) acetal hydrolysis 2) Knoevenagel condensation
Covalent Organic Frameworks			
16	Q. Sun, B. Aguila, S. Ma, *Mater. Chem. Front.* **2017**, *1*, 1310-1316. DOI: 10.1039/c6qm00363j	COF-TpPa-Py with partially Pd-functionalized pyridine groups 1) Pd 2) free pyridine	1) aerobic oxidation of alcohols to aldehydes 2) Knoevenagel condensation
Porous Aromatic Frameworks			
17	Y. Zhang, B. Li, S. Ma, *Chem. Commun.* **2014**, *50*, 8507-8510. DOI: 10.1039/c4cc04012k	Bifunctionalized PAF-1 with 1) sulfonic groups and 2) amine groups	1) deacetylation 2) Henry reaction
Porphyrin-based Porous Organic Polymers			
18	R. Shen, W. Zhu, X. Yan, T. Li, Y. Liu, Y. Li, S. Dai, Z.-G. Gu, *Chem. Commun.* **2019**, *55*, 822-825. DOI: 10.1039/c8cc08918c	PPOP-1(Pd) with 1) Pd(II)-α-diimine 2) Pd(II)-porphyrin	1) C-H arylation 2) Suzuki coupling

Table S10: Literature overview: cyanosilylation of benzaldehyde with MOFs as catalysts. This Table was taken from Semrau, *et al.*[424] permission from ACS Catalysis. Copyright (2020) American Chemical Society.

doi	T/°C	n(aldehyde)/ mmol	n (TMSCN)/ mmol	Solvent	t/h	cat	m(cat)/ mg	n(Metal)/ mmol	yield/ %	TOF/h^{-1}
this work	40	1	2	toluene	0.5	UiO-66-HCl	8.2	0.03	9.6	6.5
this work	40	1	2	toluene	0.5	UiO-66-10TFA	8.2	0.03	1.02	0.7
this work	40	1	2	toluene	0.5	NMOF 1	8.2	0.03	14.6	9.7
this work	40	1	2	toluene	0.5	NMOF 1	8.2	0.03	10.07	6.7
this work	40	1	2	toluene	0.25	SA-NMOF 3		$4.4 \cdot 10^{-6}$	52.6	$1.96 \cdot 10^{7}$
this work	40	1	2	toluene	0.25	SA-NMOF 4		$6.5 \cdot 10^{-6}$	57.5	$2.82 \cdot 10^{7}$
10.1039/C5RA13149A	40	5	10	DCM	40	UiO-66	135	0.5	85	0.21*
10.1039/C7CE00224F	40	1	2	DCM	2	UiO-66-HCl		0.03	5	0.83*
10.1039/C7CE00224F	40	1	2	DCM	2	UiO-66-10TFA		0.03	60	10*

doi	T/°C	n(aldehyde)/ mmol	n (TMSCN)/ mmol	Solvent	t/h	cat	m(cat)/ mg	n(Metal)/ mmol	yield/ %	TOF/h^{-1}
10.1039/c5dt01456e	25	0.5	1	-	12	Co-MOF 1	3	0.001	98	82.5
10.1039/c7cc03499g	-20	1	1.2	DCM	48	Cd-Ni-MOF		0.01	93	1.9*
10.1039/c4ra13924k	80	0.3	0.45	-	3	InPF-15	10		87	2158
10.1039/c4dt03221g	25	0.5	1.2	CH_3CN	1.5	Sc_2 $(pydc)_2$		0.05	99	6.6*
10.1021/acs.cgd.9b00823	60	2	6	-	6	Co(fma)(ABP)		0.01	96	32
10.1016/j.poly.2015.12.022	50	1	1	toluene	72	Cd-MOF	20	0.0125	49	0.54*
10.1007/s10876-01901714-5	25	0.5	1	DCM	10	Co-MOF		0.01	94	4.7*
10.1021/ja101208s	25	0.5	1.2	CH_3CN	24	Ce-MDIP-2		0.01	94	2.0*
10.1039/C5DT01943E	40	1	2	-	8	NbO-type Cu-MOF 1	24	0.01	99	12*
10.1002/chem.201200046	5	1.5	3	DCM	1	Gd MOF	a	a	92	a
10.1039/C8QI00811F	25	1.5	3	DCM	6	$Zn_{0.29}$-STU-2	15	a	99	a

doi	T/°C	n(aldehyde)/ mmol	n (TMSCN)/ mmol	Solvent	t/h	cat	m(cat)/ mg	n(Metal)/ mmol	yield/ %	TOF/h^{-1}
10.1002/asia.201900853	40	1.5	3	DCM	6	STU-4	15	a	99	a
10.1002/ejic.201501402	25	0.025	0.038	DCM		Gd-psa	10	0.0012		112
10.1002/ejic.201701474	25	0.025	0.038	DCM	0.33	Er-dms	10		97.6	234
10.1039/c1dt11274k	50	1	1	toluene	24	Zn-MOF	10	0.0166	58	1.5*
10.1021/ic5004879	25	0.5	1.2	CH_3CN	24	$[Cu_2(bpy)]_2$ $[H_2W_{11}O_{38}]$		0.01	98	2.0*
10.1021/cg400531j	23	a	a	a	5	$Ln(BDC)_{1.5}$	a	0.02	57	a
10.1039/C5CE00938C	40	0.3	0.6	DCM	12	Cu_3BTC_2	15	0.074	5	0.02*
10.1039/C5CE00938C	40	0.3	0.6	DCM	12	HP- Cu_3BTC_2	15	0.074	55	0.19*
10.1021/acs.cgd.7b01728	25	1	2	hexane	8	Cd-PBA		0.02	99	6.2*
10.1021/jacs.8b09606	25	0.5	0.6	DCM	36	UiO-68-V		0.025	87	0.48*
10.1039/c3cc43384f	25	0.5	1	-	1	La-BBTc		0.05	99	9.9*

doi	T/°C	n(aldehyde)/ mmol	n (TMSCN)/ mmol	Solvent	t/h	cat	m(cat)/ mg	n(Metal)/ mmol	yield/ %	TOF/h^{-1}
10.1002/ejic.201600902	25	0.5	1	DCM	1	Zn (DTD) $(DMF)_2$		0.01	32	16
10.1039/C7DT01056G	25	1	4	-	1	Ce (TPHI) (NO_3)		0.01	64	64
10.1002/ejic.201500431	50	0.48	0.48*	-	24	NaCu (2,4-HPdc) (2,4-Pdc)	1	0.024	85	10.5
10.1080/00958972.2019.1659963	25	1	2	-	3	$Zn_3(BTB)_2$		0.005	98	65*
10.1039/C8DT01145A	25	0.5	1.2	-	2	Cd-MDIP-Fe		0.0025	97	97*
10.1016/j.ica.2014.06.006	40	1	2	pentane	48	$Cu_2(CDB)_2$	100	0.05	27	0.11*
10.1016/j.molstruc.2016.12.005	25	2	4	-	2	Mg(ABTC) (DMI)	1.4	0.001	99	990*
10.1039/C7CC03499G	-20	1	1.2	DCM	48	$[Cd_2(NiPSP)(CdTCPP)]$ $[Cd_2(NiPSP)(H_2TCPP)]$		0.01	93	1.9*
10.1002/ejic.201601242	40	0.5	1	-	4	$Cu_3(TBC)_3$	3.5	0.0025	98	49*
10.1002/asia.201200601	25	0.25	0.5	hexane	12	$Zn_3(TCPB)_2$	7.3	0.00625	100	3.3*

doi	T/°C	n(aldehyde)/ mmol	n (TMSCN)/ mmol	Solvent	t/h	cat	m(cat)/ mg	n(Metal)/ mmol	yield/ %	TOF/h^{-1}
10.1039/C5DT04339E	25	0.5	1	-	14	Pr(LOMe)	10	0.006	99.4	5.9*
10.1039/C5TA03680A	25	2	4	-	2	$Ba(H_2LOMe)_{0.5}$	7.8	0.01	100	384
10.1021/acs.inorgchem.5b00185	40	4	8	DCM	0.75	$Pb_4(C_{12}H_{12}O_4)_4$		0.02	99.8	266
10.1021/acs.cgd.6b00779	5	0.5	1	Hexane	5	Eu-PDC		0.015	93	6.2*
10.1021/acsaem.8b01303	40	0.5	1.2	DCM	6	UiO-67-NS		0.0025	91	30*
10.1039/c5ta00061k	25	0.5	1	-	5	$Yb_2(CTB)_2$		0.007	67	9.6*
10.1002/asia.201500234	25	0.5	1	-	24	UPC-15		0.00078	99	26*
10.1021/ic5012764	25	0.25	0.5	-	24	$Zr_6O_4(OH)_4(OH)_6(H_2O)_6(BTBA)_2$		a	100	a
10.1039/c001659b	25	1.5	3	DCM	24	$[Zn_3(bpy)_4(O_2CCH_2CH_3)_4](bpy)_2(ClO_4)_2(H_2O)_4$	40	0.2	22	26*
10.1016/j.molcata.2008.10.008	25	1.32	2.64	DCM	2	$Zn_2(ptaH)_2$	a	a	32	a

doi	T/°C	n(aldehyde)/ mmol	n (TMSCN)/ mmol	Solvent	t/h	cat	m(cat)/ mg	n(Metal)/ mmol	yield/ %	TOF/h^{-1}
10.1021/ic1019636	25	1.5	3	DCM	3	$Fe_2Ag_2(pca)_4(pcaH)(MeOH)_2(ClO_4)_2$		0.025	51	10
10.1007/s10876-018-1483-2	50	1	2	-	2	$Cu_3(bpt)_2$		0.025	99	9.6*
10.1002/chem.201501486.	0	0.05	0.06	DCM	36	VO(salen)		0.01	93	0.13*
10.1039/C5RA13102B	25	1	1.2	-	4	MIL-101 (Cr)		0.003	96	80*
10.1021/acscatal.6b02359	-78	0.25	0.75	toluene	24	VO(salen)		0.005	98	23
10.1007/s10876-019-01589-6	25	0.5	1	DCM	12	$(Me_2NH_2)\ Ni_3(PPC)_2(OH)(H_2O)$		0.01	94	9.6*
10.1021/ic5009895	25[z]	1	2	-	1	Cu-DDQ		0.025	95	38
10.1080/10426507.2018.1550643	25	0.5	1	-	4	$Cu_7(nbpt)_4$	10	0.081	99	1.5*
10.1021/ic5017092	25	a	a	-	24	Cu-SDU-1		a	97	a
10.1016/j.molcata.2014.06.040	5	5	10	DCM	1	CPO-27-Mn		0.5	100	10

doi	T/°C	n(aldehyde)/ mmol	n (TMSCN)/ mmol	Solvent	t/h	cat	m(cat)/ mg	n(Metal)/ mmol	yield/ %	TOF/h^{-1}
10.1039/c4ra11678j	40	4	4	DCM	1.5	Cd_2 BTCA		0.01	97.4	65
10.1039/C4RA16350H	40	0.5	1	-	2	Cu-MOF 1	13	0.005	96	48*
10.1039/c4cc08003c	25	1	1.2	-	0.5	NiL_2Cl_2		0.033	97	59
10.1016/j.apcata.2019.117190	25	0.87	2.6	-	14	Z_1M_1-110A	12		96	1.17
10.1016/j.catcom.2019.105837	60	0.10	0.12	MeOH	24	Cu-based MOF		0.0015	97	59*
10.1021/ic300816r	50	0.33	0.5	-	2	Nd (DSB) (Phen)	10	0.016	94.8	13
10.1021/ic302662x		1	5	-	16	CoNiBpe 2		0.1	77	0.48*
10.1021/ja4005046	40	0.74	1.1	-	3	(O_2H_3)Sc-MOF		0.037	90	19
10.1039/b900841a	60	1	2	-	12	$Sc_2(C_4O_4)_3$	10	0.02	100	10*
10.1021/acs.inorgchem.9b00963	70	1	1.5	CH_3CN	3	BINAPDA-Zr-MOF (5)		0.02	99	50
10.1039/c5cc09459c	30	0.82	2.46	-	14	Cd-bpdc		0.00205	95	27

doi	T/°C	n(aldehyde)/ mmol	n (TMSCN)/ mmol	Solvent	t/h	cat	m(cat)/ mg	n(Metal)/ mmol	yield/ %	TOF/h^{-1}
10.1039/C5DT01206F	25	0.5	1	-	24	$Cu_4(trz)_2(mal)_2$		0.01	92.5	1.9*
10.1016/j.micromeso.2003.12.027	40	4	8	heptane	48	$Cu_3(BTC)_2$	129	0.21	55	0.22*
10.1002/cssc.200800183	25	0.66	1.32	-	2.5	Er-MCM	10		95	137
10.3390/catal9030284	25	0.1	0.12	MeOH	24	Cu $(en)_2$ (COHBS)		0.005	80	10*
10.1002/chin.199629055	25	2.46	3.2	-	0.5	R_2SnCl_2		0.1	97	`48*
10.1039/c8dt04773a	25	0.5	1	-	1	Cd(2-BPEG) $(ClO_4)_2$		0.01	46	23*
10.1016/j.apsusc.2014.11.064	25	1	1	toluene	12	Cp–Binol–Zr@SBA-15-500	13	0.015	100	5.6*
10.1021/acs.inorgchem.6b03174	25	1	2	-	1	1•Cd		0.006		167
10.1016/j.molcata.2013.07.016	25	1	2	CH_3CN	1	Eu_2 (MELL) $(H_2O)_6$	10	0.027	100	37*
10.1002/chem.201504576	25	1	1	-	0.17	InPF-16		0.01	99	582
10.1039/c8dt01145a	25	0.5	1.2	DCM	2	Cd-MDIP Fe		0.0025	97	97*

1,10-phenanthroline (phen), 3,5-disulfobenzoic acid (DSB), (+)-1,2-Bis((2*S*,5*S*)-2,5-diphenylphospholano)ethane (BPE), mellitic acid (MeLL), biphenyl-4,40-dicarboxylic acid (bpdc), fumaric acid (fma), 3,3‘-azobis pyridine (ABP), methylenediisophthalic acid (H_4MDIP), terephthalic acid (H_2bdc), trimesic acid (H_3BTC), 4,4‘-bpydine (bpy), 5-(4-pyridin-3-ylbenzoylamino)-isophthalic acid ligand (H_2PBA), benzene-1,3,5-tris(2-thiophene-5-carboxylate (BTTc), 3,3"-dipropoxy-[1,1':4',1"-terphenyl]-4,4"-dicarboxylic acid (H_2DTD), 5-[2-{2,4,6-trioxotetrahydropyrimidin-5(2H)-ylidene}hydrazinyl]isophthalate (TPHI), pyridine-2,4-dicarboxylic acid (H_2pdc), 1,3,5-tris(4-carboxyphenyl)benzene (H_3BTB), (S)-4,40-bis(4-carboxyphenyl)-2,20-bis(diphenylphosphinoyl)-1,10-binaphthyl (H_2CDB), 3,3’,5,5’-azobenzene-tetracarboxylic acid (H_4ABTC), 1,3-dimethy-2-imidazolidinone (DMI), 2,2’,6,6’-tetramethoxy-4,4’-biphenyldicarboxylic acid (H_2TBC), (R, R)-N,N’-bis(3-*tert*-butyl-5-(4-pyridyl)salicylidene)-1,2-diphenyldiaminenickel(II) (NiPSP), tetra-(4-carboxyphenyl)porphyrin (H_6TCPP), 1,3,5-Tri(4-carboxyphenoxy)benzene (H_3TCPB), 3,3'-((2,3,6,7-tetramethoxyanthracene-9,10-diyl)bis(4,1-phenylene))diacrylic acid (H_2LOMe), 1,3,5-tris(4-carboxyphenyl-1-ylmethyl)-2,4,6-trimethylbenzene (H_3CTB), 5′-(4-carboxyphenyl)[1,1′:3′,1″-terphenyl]-4,4″-dicarboxylic acid (H_3BTBA), tris-(4-carboxy-2-phenoxyethyl)amine (ptaH_3), 2-pyrazinecarboxylic acid (pcaH), biphenyl-3,40,5-tricarboxylic acid (H_3bpt), 3-phenylpyridine polycarboxylic (H_3PPC), N,N′-dibenzoic acid-2,3-diaminoquinoxaline (H_2DDQ), 3,40,5-tricarboxylic acid (H_3nbpt), 2,3,5,5-biphenyl tetracarboxylic acid (BTCA), 1H-1,2,4-triazole (Htrz), malic acid (H_3mal), 2-(2-(1-cyano-2-oxopropylidene)hydrazinyl)benzenesulfonate ($HCOHBS^-$), 2,2’-(ethane-1,2-diylbis((pyridin-2-ylmethyl)azanediyl)) diacetamide (2-BPEG), 2,3-pyridinedicarboxylic acid (H_2pydc), benzene-1,3,5-tris(2-thiophene-5-carboxylate) (BBTc), (R,R)-N,N′-bis(3-tert-butyl-5-(3,5-dicarboxybenzyl)salicylidene)-1,2-diphenylethylenediame (H_6salen)

a unclear

^{z} ultrasonic reaction

* TOF values were calculated with the data included in the table

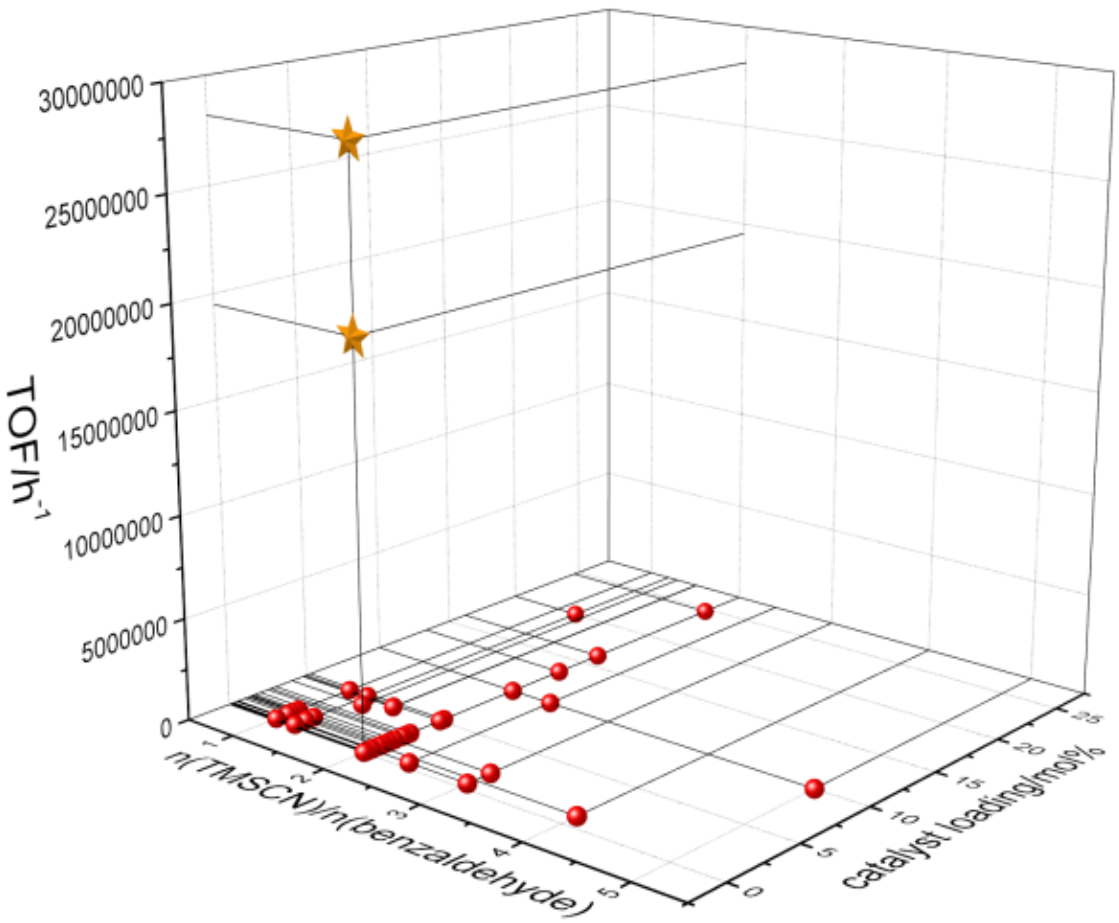

Figure S74:Overview of the TOF values as a function of the catalyst loading and the ratio of TMSCN/benzaldehyde. The TOF values obtained for **SA-NMOF 3** and **4** are marked with stars. This Figure was taken from Semrau, *et al.*[424] permission from ACS Catalysis. Copyright (2020) American Chemical Society.

Table S11: Literature overview: CO_2 insertion in epoxides with MOFs as catalysts. This Table was taken from Semrau, *et al.*[424] permission from ACS Catalysis. Copyright (2020) American Chemical Society.

doi	T/°C	p(CO_2)/ bar	n (Propylene oxide)/ mmol	t/h	cat	m(cat)/ mg	n(cat)/ mmol	n(Metal)/ mmol	n (Bu_4NBr) /mmol	yield/ %	TOF/h^{-1}
this work	100	3	31.05	1	SA-NMOF 3	0.0024	$1.47 \cdot 10^{-6}$	$8.87 \cdot 10^{-6}$	2.49	20.2	$7.74 \cdot 10^{6}$
this work	50	1	31.05	2	SA-NMOF 3	0.0024	$1.47 \cdot 10^{-6}$	$8.87 \cdot 10^{-6}$	2.49	6.48	$1.24 \cdot 10^{6}$
this work	50	1	31.05	2	UiO-66-HCl	43	0.025	0.15	2.49	3.48	5.2
this work	50	1	31.05	2	UiO-66-10TFA	43	0.025	0.15	2.49	6.94	6.4
10.1007/s10853-019-03702-6	50	55	25	0.083	Int-MOF-5		0.0325	0.0325	0.242		5400
10.1002/anie.201803081	25	1	17.2	48	MiL-101-IP	50	0.074	0.022	- (included in cat)	99	16.1*
10.1016/j.apcata.2019.117225	150	17.5	57	4	Pt@Mg-MOF-74	100	0.405	0.810	-	45	7.9*
10.1021/acs.inorgchem.9b00814	80	4	25	4	PNU-21					65	17.5
10.1021/acs.inorgchem.9b00814	80	4			PNU-22						20
10.1016/j.jcat.2012.11.029	RT	8			Cr-MiL-101						3
10.1021/ja508626n	RT	1			Hf-NU-1000						0.5

doi	T/°C	p(CO_2)/ bar	n (Propylene oxide)/ mmol	t/h	cat	m(cat)/ mg	n(cat)/ mmol	n(Metal) / mmol	n (Bu_4NBr) /mmol	yield/ %	TOF/h^{-1}
10.1039/B902550B	50	4			MOF-5						10
10.1016/j.jssc.2019.120906	40	1	20	48	$[Co_6(OH)_2(H_2O)_4(cpt)_9](NO_3)(DMF)_{13}$			0.1	2	96.5	4*
10.1039/c9cc02787d	25	10	10	24	ZnMOF		0.02	0.04	0.25	96	10*
10.1007/s1056 2-019-02874 -9	100	30	344	5	2MeIm@CoBTC	100/50 (CoBTC)	0.186	0.186	0.186	95	351
10.1007/s10853-019-03702-6	50	4	25	4	MOF-5		0.0325	0.0325	0.242		87
10.1007/s10853-019-03702-6	50	55	25	4	Int-MOF-5		0.0325	0.0325	0.242		180
10.1021/acs.inorgchem.9b01762	80	5	34.5	6	Zn (Bmic) (AT)	-	0.187	0.187	0.5	96	29.5*
10.1016/j.cej.2019.05.061	50	12	25	6	MOF-5-MIX		0.125	0.125	0.125	93	31*
10.1016/j.apcata.2018.11.035	60	12	25	8	UiO-66/Cu-BTC		0.04	0.04	0.125	91	71*
10.1039/c9dt01249d	80	1	2	8	$[Mn_4(L)_2(H_2O)_4]_n \cdot 4DMF \cdot H2O$		0.1	0.4	2	99	0.62*
10.1007/s11814-019-0255-5	40	10	42.8	24	MIL-47(V)		0.342	0.342	0.342	93	4.9*
10.1021/acsami.9b05091	90	1	5	20	PCN-224(Co)-		0.02	0.02	-	93	11.6*

					BPDC-CH_2NBu_3Br						
doi	T/°C	p(CO_2)/ bar	n(Epoxide)/ mmol	t/h	cat	m(cat)/ mg	n(cat)/ mmol	n(Metal)/ mmol	n (Bu_4NBr) /mmol	yield/ %	TOF/h^{-1}
10.1002/cssc.201802990	120	10	13	2	MIL-101-tzmOH-Br		0.022	0.066	0.033	97	96
10.1002/cctc.201800137	40	10	10	3.5	Zn(BDC)(PCDH)	82		0.18	0.18	98	15.6*
10.1002/cssc.201802990	80	10	13	10	MIL-101-tzm-Br		0.022	0.066	0.033	93	18
10.1016/j.cattod.2014.05.022	120	11.7	18.1	6	F-ZIF-90	20	0.177	0.177		94	89
10.1039/C5GC02153G	120	10	18.1	3	IL-ZIF-90		0.088	0.088	0,08869	83	56
10.1039/c5ta07026k	80	20	30	8	MIL-101-$N(nBu)_3Br$		0.27	0.81	-	99	4.6
10.1039/C6DT01282E	50	10	100.2	24	MIL-47	100			2.5	95	33
10.1021/acs.inorgchem.7b02983	140	1	5	14	ZnTCPP⊂(Br−)Etim-UiO-66		0.015	0.015	-	87	87
10.1021/acscatal.7b03404	70	1	1	24	polyILs@MIL-101	100		0.103	-	94	0.13
10.1039/C6SC04357G	120	1	10	24	(I-)Meim-UiO-66	50		0.052	-	93	3.9
10.1021/acs.inorgchem.6b03169	90	1		8	UiO-67-IL			0.7mol%	1 mol%	95	7.9

doi	T/°C	p(CO_2)/ bar	n(Epoxide)/ mmol	t/h	cat	m(cat)/ mg	n(cat)/ mmol	n(Metal)/ mmol	n (Bu_4NBr) /mmol	Yield /%	TOF/h^{-1}
10.1039/C7CC08630J	80	1	5	12	FJI-C10		0.017	0.0175	-	87	5.2
10.1039/c1ee02234b	100	20		1	Mg-MOF-74					50	27
10.1021/cs200638h	100	7	18	4	ZIF-8-f	100		0.44		49.1	28
10.1016/j.apcata.2012.12.018	100	20	5	1	UIO-66-NH_2			0.105	-	58	28
10.1002/cctc.201200288	150	8	1.75	8	MIL-(In)NH2	50		0.159	-	74	1
10.1016/j.cattod.2011.08.019	100	20.2	5	4	Co-MOF-74	20		0.08	-	96	15
10.1166/jnn.2013.6878	120	12	25.3	6	IRMOF-1	300		0.149	-	20.1	5.6
10.1166/jnn.2013.6878	120	12	25.3	6	IRMOF-3	300		0.139	-	44.1	13.6
10.1166/jnn.2013.6878	120	12	25.3	6	F-IRMOF-3(BuI)	300		0.109	-	92.3	35.8
10.1166/jnn.2013.6879	120	12	18.6	6	ZnHipBipy-B			0.3	-	40.7	4.1
10.1002/asia.201900147	30	10	20	12	MgBipyD $(H_2O)_2$	58.4		0.4	0.5	99	4.2
10.1002/anie.201901786	70	1	2	12	$Ni_3Th_6O_4$ $(OH)_4(IN)_{12})$ $(H_2O)_{12}]$ · $(OH)_6$ ·5DMF ·2 H_2O	40		0.05	0.05	89	2.9*

doi	T/°C	p(CO_2)/ bar	n(Epoxide)/ mmol	t/h	cat	m(cat)/ mg	n(cat)/ mmol	n(Metal)/ mmol	n (Bu_4NBr) /mmol	Yield /%	TOF/h^{-1}
10.1021/acsami.9b16834	80	12	25	6	DUT-52(Zr)/ TBAB			0.125	0.125	96	32
10.1016/j.jcou.2019.09.019	100	15	34,5	3	$Zn_2Py(Atz)_2$ · DMF · 2 H_2O	100			0.311	84	37
10.1007/s10311-018-0793-9	100	10	20	2	MIL-53(Cr)	15	0.064	0.064	1.2^X	98	153*
10.1039/c8dt01297k	80	8	20	8	Zn(ATA) (PMIH)] $\cdot H_2O$	100		0.21	0.5	91	11*
10.1016/S1872-2067(17)62916-4	120	12	25.5	12	CuTrp			0.212	0.212	99.3	10*
10.1021/acssuschemeng.8b01055	80	10	34.5	3	$Zn_2L_2MA_2$ DMF	100	0.148	0.297	0.311	99	38*
10.1039/C8DT01405A	80	20.6	73.9	24	$(NH_4)_3[In_3Cl_2(BPDC)_5]$			0.0367	0.739	77	64
10.1002/cctc.201800336	50	4	34.5	24	PCN-224			0.0288	2.5	99	210
10.1021/acs.inorgchem.8b01713	80	1	2	4	$[Zn_2(TCA)(BIB)_{2.5}] \cdot (NO_3)$		0.01	0.02	0.02	99	167
10.1016/j.apcata.2018.08.011	100	10	55	7	Co(tp)(bpy)	31.9		0.084	0.084	93	87*
10.1002/cssc.201801585	RT	12	40	48	MOF-74-III(Co)			0.02	1.5	98	41
10.1002/chem.201802387	80	10	42.6	18	[Zn(CHDC)(PCAH)]H_2O			0.767	0.767	97	3.0*

doi	T/°C	p(CO_2)/ bar	n(Epoxide)/ mmol	t/h	cat	m(cat)/ mg	n(cat)/ mmol	n(Metal)/ mmol	n (Bu_4NBr) /mmol	Yield /%	TOF/h^{-1}
10.1016/j.cherd.2018.10.034	100	30	344	6	$Zn_2(C_9H_3O_6)(C_4H_5N_2)(C_4H_6N_2)_3$	150	0.226	0.452	-	69	88*
10.1039/c8cc07865c	RT	1	20	48	Cu-Nb-Ni	80		0.1	2.0	99	4.1*
10.3390/catal8110565	100	10	10	2	DMOF(Zn)			0.2	0.1	78	20*
10.1039/c8nj04947e	120	1	10	8	$\{Co(TCPB)_{0.5}(H_2O)\}DMF$			0.01	0.25	99	110
10.1016/j.apsusc.2017.09.040	80	8	18:6	4	MIL-101-IMBr-6	90				94	28
10.1021/acs.chemmater.8b04792	80	20	20	4	InDCPN-Cl			0.01	1	95	475*
10.1039/C8QI01396A	80	8	20	5	SNNU-5-In			0.058	0.3	97	67*
10.1021/acs.inorgchem.8b03612	80	8	20	15	$\{[Co_6(TATAB)_4(DABCO)_3(H2O)_3]$ 12 DMF · 9 $H_2O\}_n$			0.04	-	94.6	31.5
10.1016/j.molstruc.2019.02.076	80	25	10	5	$[(Cu_2BPDSDC$ .4 DMF) 2 DMF$]_n$	50	0.051	0.103	0.315	99	19*
10.1016/j.micromeso.2019.02.026	RT	1	10	24	$Mn(TCPP)_{0.5}$			0.05	0.25	100	8.33
10.1021/acs.inorgchem.8b03525	RT	1	12.5	48	Cu_4L_8			0.0313	0.9	96	200

doi	T/°C	p(CO_2)/ bar	n(Epoxide)/ mmol	t/h	cat	m(cat)/ mg	n(cat)/ mmol	n(Metal)/ mmol	n (Bu_4NBr) /mmol	Yield /%	TOF/h^{-1}
10.1002/cjoc.201800587	70	1	2	12	$Na[Zn_{1.5}(O)(H_2DOHD)]$	20		0.1	0.05	99	1.6*
10.1002/cssc.201702193	90	12		1	IL-$[In_2(dpa)_3(1,10phen)_2]$			0.0856	-	99	495
10.1002/cssc.201702193	100 W[z]	12	42.8	1/6	IL-$[In_2(dpa)_3(1,10phen)_2]$			0.0856	-	99	3100
10.1021/acs.inorgchem.7b00323	60	1	2	12	$[Tb_4Mn(BPDC)_3(OH)_4(HCOO)_{1.5}(H2O)_4]_{2.5}OH \cdot 8\ H_2O\}$	25	0.04	0.16	0.05	95	1*
10.1021/acsami.7b16163	80	1	6.87	23	MOF-893			0.0229	0.0687	88	12*
10.1002/ejic.201700871	80	10	10	12	Cd_2(Ni(salen)			0.05	0.05	99	16
10.1021/acsami.7b06497	RT	1	17.5	24	WM-MOF			0.0595	0.875	90	11*
10.1002/ange.201801122	RT	1	20	48	HKUST-1			0.05	2.019	62	5.2*
10.1002/ange.201801122	RT	1	20	48	MOF-505			0.05	2.019	61	5.1*
10.1002/ange.201801122	RT	1	20	48	JUC-1000			0.05	2.019	96	8.0*
10.1039/c7ra13245j [flow]	100	5	165mM 0.25mL/min		MIL-101 (Cr)	42				40	19
10.1021/acs.cgd.8b00068	80	1	5	12	$[TbCPC(H_2O)_2]\cdot H_2O$	76		0.175	0.175	90.1	2.2*

doi	T/°C	p(CO_2)/ bar	n(Epoxide)/ mmol	t/h	cat	m(cat)/ mg	n(cat)/ mmol	n(Metal)/ mmol	n (Bu_4NBr) /mmol	Yield /%	TOF/h^{-1}
10.1039/C7DT04882C	50	5	1	2	[Co(TDA)(H_2O)] ·0.5 H_2O (PVP)	50		0.19	0.05	43.6	1.2*
10.1039/C7DT00583K	RT	1	100	48	MOPGr-2			0.03	3	56	39*
10.1039/C7CY02063E	90	12	25	8	Ni-Co-MOF(M)			0.15	0.15	95	20*
10.1016/j.inoche.2019.05.031	25	1	2	6	Ni-MOF-1a			0.01	0.02	99	6.6
10.1016/j.inoche.2017.12.014	80	20	20	4	CdPDIA	100		0.166	1.801	95	29*
10.1002/chem.201704027	80	20	20	4	Ni(btzip)(H_2btzip)] ·2 DMF ·2 H_2O		0.2	0.2	2	99	25*
10.1039/c7cc08315g	25	1	20	8	[Cu_6(ATPT)$_3$(H_2O)$_6$]		0.04	0.08	1.00	85	27*
10.1021/acsami.8b01291	25	1	20	48	Ba_2(BDPO)(H_2O) ·DMA			0.1	0.4	98	4.0
10.1021/acs.chemmater.7b03183	25	1	20	48	Cu_2($C_{20}H_{12}N_2O_2$)(COO)$_4$		0.8	0.4	1.55	96	5.0
10.1016/j.jiec.2018.04.010	50	10	10	12	UiO-66			0.2	TBAI: 0.1	77	3.2*
10.1016/j.jiec.2018.04.010	140	10	10	2	UiO-66			0.2	TBAI: 0.1	67	16*
10.1039/C3CC47542E		1			MMPF-9						14

doi	T/°C	p(CO_2)/ bar	n(Epoxide)/ mmol	t/h	cat	m(cat)/ mg	n(cat)/ mmol	n(Metal)/ mmol	n (Bu_4NBr) /mmol	Yield /%	TOF/h^{-1}
10.1016/j.jiec.2018.04.010	140	10	10	2	UiO-66-NO_2			0.2	TBAI: 0.1	73	18*
10.1016/j.jiec.2018.04.010	140	10	10	2	UiO-66-NH_2			0.2	TBAI: 0.1	77	19*
10.1016/j.jiec.2018.04.010	140	10	10	2	UiO-66-Cl			0.2	TBAI: 0.1	75	19*
10.1016/j.jiec.2018.04.010	140	10	10	2	UiO-66-Br			0.2	TBAI: 0.1	70	18*
10.1016/j.jiec.2018.04.010	140	10	10	2	UiO-66-OH			0.2	TBAI: 0.1	91	23*
10.1039/C7DT02819A	80	1	2	12	$Zn_3(tza)_2(OH)_2(H_2O)_2 \cdot H_2O$	20		0.1	0.05	97	1.6*
10.1016/j.jiec.2018.04.010	140	10	10	2	UiO-66-OH			0.2	TBAI: 0.1	80	20*
10.1016/j.jiec.2018.04.010	140	10	10	2	UiO-66-naphtyl			0.2	TBAI: 0.1	62	16*
10.1039/c7cc08315g	25	1	20	8	$[Cu_6(ATPT)_3(H_2O)_6]$		0.04	0.08	1.00	85	27*
10.1002/asia.201701706	100	16	2.2	2	NH_2-MIL-125 (Ti)	2.5	0.015	0.121	0.013	19.8	1.8*
10.1039/C7DT03754F	120	18	105	6	NH_2–MIL–101(Al)			0.17	0.14	96	141
10.1039/c7nj01055a	100	10	38	1	Zr-BDC-MOF	100					326
10.1039/c7nj01055a	100	10	38	1	Zn-BTC-MOF	100					110

doi	T/°C	p(CO_2)/ bar	n(Epoxide)/ mmol	t/h	cat	m(cat)/ mg	n(cat)/ mmol	n(Metal)/ mmol	n (Bu_4NBr) /mmol	Yield /%	TOF/h^{-1}
10.1039/c7nj01055a	100	10	38	1	Zn-BDC-MOF	100					112
10.1039/c7nj01055a	100	10	38	1	Zn-MeIMI-MOF	100					42
10.1039/c7nj01055a	100	10	38	1	Cu-BTC-MOF	100					18
10.1039/c7nj01055a	100	10	38	1	DMAP-Zr-BDC-MOF	100					1095
10.1021/acs.cgd.7b00063	70	1	2	12	$TbZnBPDC_2$ (H_2O) Cl (H_2O)$_3$	20	0.024	0.048	0.1	99	3.4*
10.1021/acs.cgd.7b00198	25	1	25	48	Cu_2(pbpta)	20		0.059	1.8	89	7.9*
10.1021/acs.inorgchem.7b01286	50	10	25	6	$[(CH_3)_2NH_2^+]_2[Zn_3O(ATTA)_2(H_2O)] \cdot 4\,DMF \cdot 2\,H_2O$	145	0.103	0.309	0.125	98	13*
10.1021/acs.cgd.8b00065	80	1	20	15	{Sm (BTB) (H_2O)} ·H_2O			0.1	0.2	100	13
10.1021/acs.cgd.7b00274	80	8bar/ 1atm CO_2	20	12	Co (muco) (bpa)			0.1	1	100	16.7
10.1039/C7TA09082J	70	31	10	6	RD Au/Zn-MOF nanocage			0.07	-	96	11.4

doi	T/°C	p(CO_2)/ bar	n(Epoxide)/ mmol	t/h	cat	m(cat)/ mg	n(cat)/ mmol	n(Metal)/ mmol	n (Bu_4NBr) /mmol	Yield /%	TOF/h^{-1}
10.1002/anie.201802661	50	1	5	20	PCN-900-Eu-CoTCPP-CoBPYDC			0.006	0.216	97	40*
10.1002/cctc.201800411	120	12	830mg/mL	14	UiO-66/SnS_2			80.36 mg/mL		100	-
10.1016/j.jiec.2017.09.040	105	30	213	9	$[(CH_3)_2NH_2][Mn_3(BTC)(HCOO)_4(H_2O)]$	300	0.453	1.360	-	94	16*
10.1016/j.apcatb.2017.07.085	60	10	20	12	Yb-DDIA			0.05	0.1	93	31
10.1016/j.micromeso.2018.03.011	120	13	29	1	IL^z/MIL-101-NH_2			0.126	-	91	209*
10.1021/acsami.7b03835	25	1	20	48	Co_2(tzpa)			0.2	2	93.8	1.9*
10.1039/C5GC01763G	50	12	42.8	24	UMCM-1-NH_2			0.274	-	91	25
10.1039/C6CC05289D	25	1	25	48	CuBTC		0.031	0.063	1.801	79	6.5*
10.1021/acs.inorgchem.6b00937	25	1	10	48	MMPF-18	17.6		0.025	0.698	97	8.1*
10.1021/acs.cgd.6b01132	90	10	34.5	6	$Co_3(Hbtc)_2(atz)_2$	100	0.132	0.395	0.310	72	11*
10.1038/NCHEM.1982	120	20	100	0.75	gea-MOF-1	60		0.15	0.15	94	105
10.1002/ejic.201600218	25	1	25	48	Zn-MOF	20		y	1.801	92	

doi	T/°C	p(CO_2)/ bar	n(Epoxide)/ mmol	t/h	cat	m(cat)/ mg	n(cat)/ mmol	n(Metal)/ mmol	n (Bu_4NBr) /mmol	Yield /%	TOF/h^{-1}
10.1002/ejic.200900509	140	615 mmol	615	3	MIXMOF (MOF-5)			0.125	0.1	90	400
10.1039/C5CC07781H	25	10	42.6	24	ZnGlu			0.682	0.682	91	2.3*
10.1039/c5ta05688h	80	12	42.6	6	ZnGlu			0.2	0.4	98	35
10.1039/c3gc41833b	120	12	18.6	6	CHB(M)			0.3	0.3	88	9.1*
10.1039/c3cc49187k	160	30	20	8	BIT-103			3.76	-	90.8	27
10.1039/C5CE01843A	25	1	15	6	N-MOF-NP		0.75	1.5	1.5	89	1.5*
10.1039/C6GC00413J	100	1	20	16	$Zn_6(TATAB)_4(DABCO)_3(H_2O)_3$			0.184	1.5	99	15
10.1016/j.jcis.2013.10.041	80	60	20	2	Zn_3BTC_2	51	0.083	0.251	0.378	97	39*
10.1039/C5NJ03169A	100	30	70.15	6	Zn(DPDD)(aip) ·(H2O)			0.07		91	110
10.1016/j.jcat.2012.11.029	25	8	40	48	MIL-101(Cr)			0.5	1.5	95	10
10.1016/j.micromeso.2016.12.009	25	1	80	48	UTSA-16			0.12	3.602	78	11*
10.1039/C2RA22550F	80	20	10	4	Ni(salphen)-MOF	50	0.036	0.145	0.3	80	14*
10.1021/jacs.5b13335	25	1	20	48	$Cu_4[(C_{57}H_{32}N_{12})(COO)_8$		0.040	0.08	2.019	96	5*

doi	T/°C	p(CO_2)/ bar	n(Epoxide)/ mmol	t/h	cat	m(cat)/ mg	n(cat)/ mmol	n(Metal)/ mmol	n (Bu_4NBr) /mmol	Yield /%	TOF/h^{-1}
10.1021/acs.inorgchem.6b00050	80	20	20	12	$In_2(OH)(btc)(Hbtc)_{0.4}(PCBDC)_{0.6}\cdot 3\ H_2O$			0.026	0.5	57	110
10.1002/smll.201503741	25	12	40	60	$(Zn_4O)_2(Zn_2)_{1.5}CPPD_6(H_2O)_3$		0.0064	0.0032	1.5	99	103
10.1021/acs.chemmater.6b02511	25	1	20	48	TMOF-1			0.2	2	99	2.1*
10.1002/anie.201604313	50	1	5	10	PCN-700-Me_2-o			0.019	0.3	93	24
10.1021/acs.inorgchem.6b01407	70	1	2	12	[Eu (BTB) (phen)]	40		0.07	0.1	98	2.3*
10.1021/acssuschemeng.6b02972	80	20	20	5	Gd-MOF	100	0.093	0.186	0.5	98	21*
10.1021/acs.inorgchem.6b01569	80	8	20	12	Ni (muco) (bpa)			0.1	0.1	100	17
10.1002/cplu.201402395	120	12	18.6	8	ZIF-90	30		0.11	-	83	18*
10.1021/acs.inorgchem.9b01762	80	5	34.5	6	Zn (Bmic) (AT)	-	0.187	0.187	0.5	96	29.5*
10.1021/acsami.6b12458	RT	12			MOF-205						6
10.1002/anie.201309778	RT	1			MMCF-2						15
10.1021/acs.inorgchem.9b01977	45	5	20	10	$[PMo_8VMo_4$	83.5		0.04	0.5	99	49.5*

	$VIO_{37}(OH)_{3v}$ $Zn_4][BPE]_2$ · [BPE]

trans-1,2-bis(4-pyridyl)ethylene ligand (BPE), 5-aminotetrazole (AT), 1*H*-benzimidazole-5-carboxylic acid (Bmic), 4-(4′-carboxyphenyl)-1,2,4-triazole (Hcpt), Melamine (MA), 2,5-thiophenedicarboxylic acid (H_2L), tricarboxytriphenylamine (H_3TCA), 1,3-bis(imidazol-1-ylmethyl)benzene (BIB), 2,2'-bipyridyl-4,4'-dicarboxylic acid (BipyD), 4-pyridylcarboxaldehydeisonicotinoylhydrazone (PCAH) in combination with flexible 1,4-cyclohexane-dicarboxylic acid (H_2CHDC), H_4TCPB =1,2,4,5-tetrakis(4-carboxyphenyl)benzene, biphenyl-3,3'-disulfonyl-4,4'-dicarboxylic acid (H4BPDSDC), diphenic acid (H_2dpa), 6,6-Dimethyl-3-oxabicyclo[3.1.0]hexane-2,4-dione (H_2DOHD); (R,R)-N,N′-bis(3-tert-butyl-5-(3,5-dicarboxybenzyl)salicylidene)-1,2-diphenylethylenediame (H_6salen), thiazolidine 2,4-dicaboxlic acid (H_2TDA), 1-(4-carboxybenzyl)-1H-pyrazole-3,5-dicarboxylic acid (H_3CPC), 5-(phenyldiazenyl)isophthalic acid (H_2PDIA), 4,6-bis(triazol-1-yl)isophthalic acid (H_2btip), N,N′-bis(isophthalic acid)-oxalamide (H_4BDPO), G lattice guests (G), 4-pyridyl carboxaldehydeisonicotinoylhydrazone (PCDH), (E)-N-(pyridin-4-ylmethylene)isonicotinohydrazide (PMIH),
2-aminoterephthalic acid (H_2ATA), 5'-amino-[1,1':3',1"-terphenyl]-3,3",5,5"-tetracarboxylic acid (H_4ATPT), 4,4'-Biphenyldicarboxylic acid (H_2BPDC), 4,4',4",4"'-(1,4-phenylenbis(pyridine-4,2-6-triyl))-tetrabenzoic acid (H4pbpta), 2'-amino-[1,1':3',1"-terphenyl]-4,4",5'-tricarboxylic acid (H_3ATTA), 1,3,5-tris(4-carboxyphenyl)benzoic acid (H_3BTB), trans, trans-muconate dianion (muco), 1,2-bis(4-pyridyl)ethane (bpa), 4,4',4"-*s*-triazine-1,3,5-triyl-tri-*p*-aminobenzoic acid (H_3TATAB) , 1,4-diazabicyclo[2.2.2]octane (DABCO), 5-aminoisophthalic acid (H_2aip), N4,N4' -di(pyridin-4-yl)biphenyl-4,4'-dicarboxamide (DPDD), 2-(piperazine-1-carbonyl)terephthalic acid (H_2PCBDC), 10-(4-carboxy-phenyl)-10H-phenoxazine-3,6-dicarboxylicacid (H_3CPPD), 1,10-phenanthroline (phen)
X: $P_{12,4,4,4}$ (tributyldodecylphosphoniumbromide) is used instead of nBu_4NBr
Y:Sum formula unknown
Z: IL instead of TBAB
*TOF values were calculated with the data included in the table

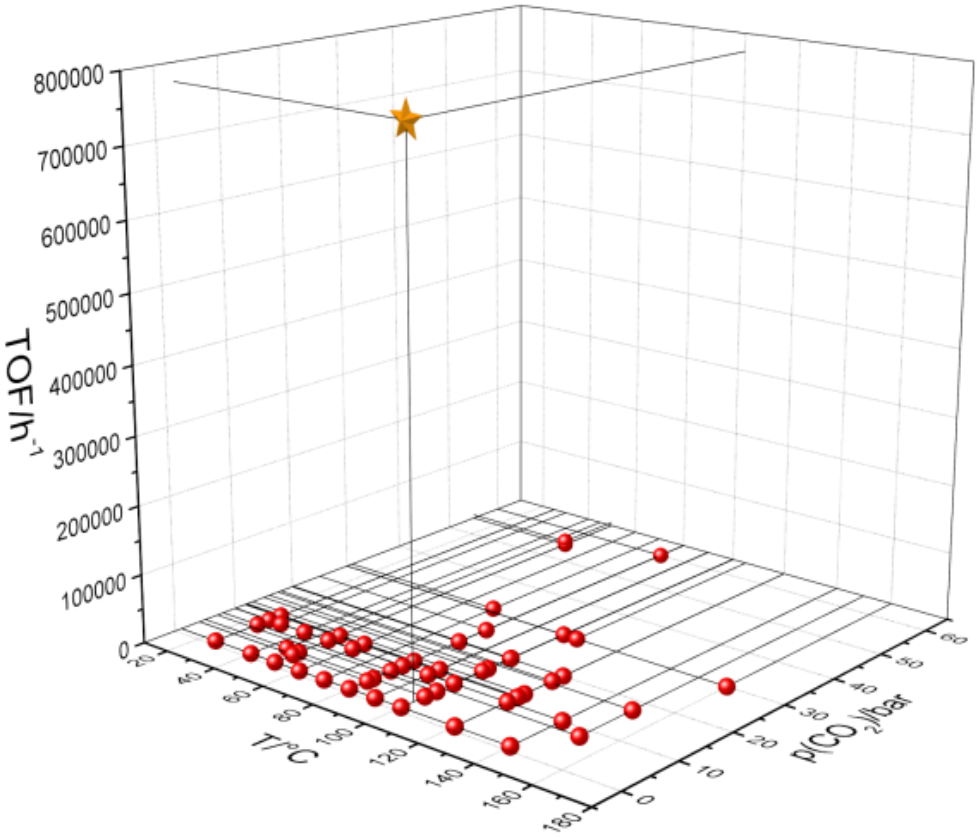

Figure S75: Overview of the TOF values as a function of the temperature and the partial pressure of CO_2. The TOF values obtained for **SA-NMOF 3** is marked with a star. This Figure was taken from Semrau, *et al.*[424] permission from ACS Catalysis. Copyright (2020) American Chemical Society.

Table S12: Literature overview: Benzaldehyde dimethyl acetal (BADMA) hydrolysis to benzaldehyde (BA) followed up by Knoevenagel condensation

Paper	cat	solvent	T/°C	t/h	n (BADMA)/ mmol	n (MAN)/ mmol	n (metal)/ mmol	Yield (BA)/ %	Yield (BACN)/ %	TOF (R1)/h^{-1}	TOF (R2)/ h^{-1}
[329]	PCN-124	DMSO	50	12	2.00	1.05	0.02	0.00	100.00	8.33	8.33
[328]	MIL-101-NH_2(Al)	dioxane	90	3	1.00	5.00	0.43	6.00	94.00	0.78	0.74
[332]	UiO-67-$(NH_2)_2$	ethanol	60	10	1.00	1.00	0.04	1.00	98.00	2.75	2.72
[333]	MIL-101 (Cr)@citosan	acetonitrile	80	12	2.00	1.05	0.07	0.00	99.00	2.27	2.27
[336]	Zn-MOF I	DMF	80	0.50	1.00	2.00	0.01	16.00	10.00	52.00	20.00
[336]	Zn-MOF I	DMF	80	0.50	1.00	2.00	0.01	27.00	5.00	64.00	10.00
[337]	Cd-MOF I	DMF	90	5	1.00	1.00	0.01	0.00	84.00	30.00	30.00
[337]	Cd-MOF II	DMF	90	5	1.00	1.00	0.01	0.00	95.00	33.93	33.93

with malononitrile (MAN) to 2-benzylidene malononitrile (BACN).

Paper	cat	solvent	T/°C	t/h	n (BADMA)/ mmol	n (MAN)/ mmol	n (metal)/ mmol	Yield (BA)/ %	Yield (BACN)/ %	TOF (R1)/h^{-1}	TOF (R2)/ h^{-1}
[334]	Cr-MIL-101-AB-x	DMF	90	0.08	1.00	2.00	0.04	44.00	17.00	183	51
[335]	Yb-BDC-NH_2	DMSO	50	24	2.00	1.05	0.04	0.00	97.00	1.98	1.98
[335]	Sm-BDC-NH_2	DMSO	50	24	2.00	1.05	0.04	0.00	82.00	1.58	1.58
[335]	Dy-BDC-NH_2	DMSO	50	24	2.00	1.05	0.04	0.00	76.00	1.51	1.51
[425]	Fe_3O_4@Cu-HKUST-1	DMSO	90	5.00	1.00	3.00	0.08	0.00	99.00	2.39	2.39
[426]	Cu-HNUST-8	DMSO	50	48	4.00	1.05	0.02	0.00	99.00	4.13	4.13
[427]	Cu-HNUST-6	DMSO	50	48	4.00	1.05	0.02	0.00	99.50	4.15	4.15
[428]	PBSA/Cr-MIL-101 + PMAP/Cr-MIL-101	DMSO. H_20	70	12	0.30	1.20	0.01	0.00	89.00	1.78	1.78
[429]	PCN-700-AB	DMSO	50	12	1.00	1.00	0.05	6.48	83.52	1.50	1.39

Paper	cat	solvent	T/°C	t/h	n (BADMA)/ mmol	n (MAN)/ mmol	n (metal)/ mmol	Yield (BA)/ %	Yield (BACN)/ %	TOF (R1)/h^{-1}	TOF (R2)/ h^{-1}
[338]	PCN-905(Eu)-SO_2-SO_3H	toluene. H_2O	90	1	0.36	1.43	0.04	4.50	95.50	10.00	9.55
[430]	PCN-222-Co@TpPa-1	DMSO-d6	50	10	0.10	1.10	5.00	0.00	99.30	-	-
[431]	Zn-MOF 3	toluene	90	3	1.00	1.20	0.25	0.00	99.00	1.31	1.31
[432]	MIL-101(Al/Fe)-NH_2 (15:1)	toluene	90	0.17	1.00	1.50	0.03	unknown	35.00		74.11
[433]	Zr_{12}-BDC-NH_2	CDCl3	55	24	1.00	1.10	0.08	9.00	22.00	0.15	0.11
[434]	JUC-199	dioxane	90	4	1.00	1.20	0.06	0.00	99.00	4.05	4.05
[435]	ZSM-5@UiO-66	MeCN	80	2	1.36	0.96	0.18	8.00	27.00	1.35	1.04

"Mischief Managed!"

— Harry Potter

in Harry Potter and the Prisoner of Azkaban

by Joanne K. Rowling